CONTENS

Editorial

POLISH MARITIME RESEARCH is the scientific journal with a worldwide circulation. This journal is published quarterly (four times a year) by Gdansk University of Technology (GUT). On September, 1994, the first issue of POLISH MARITIME RESEARCH was published. The main objective of this journal is to present original research, innovative scientific ideas, and significant findings and application in the field of :

Naval Architecture, Ocean Engineering and Underwater Technology,

The scope of the journal covers selected issues related to all phases of product lifecycle and corresponding technologies for offshore floating and fixed structures and their components.

All researchers are invited to submit their original papers for peer review and publications related to methods of the design; production and manufacturing; maintenance and operational processes of such technical items as:

- all types of vessels and their equipment,
- fixed and floating offshore units and their components,
- autonomous underwater vehicle (AUV) and remotely operated vehicle (ROV).

We welcome submissions from these fields in the following technical topics:

- ship hydrodynamics: buoyancy and stability; ship resistance and propulsion, etc.,
- structural integrity of ship and offshore unit structures: materials; welding; fatigue and fracture, etc.,
- marine equipment: ship and offshore unit power plants: overboarding equipment; etc.

INVESTIGATION OF ASYMMETRIC TWIN-RUDDER LOAD BEHAVIOUR THROUGH FREE-RUNNING MODEL TESTS

Dobrin Efremov [ID]
Evgeni Milanov [ID]

Bulgarian Ship Hydrodynamics Centre - Bulgarian Academy of Sciences, Varna, Bulgaria,

---

* Corresponding author: *d.efremov@bshc.bg (Dobrin Efremov)*

ABSTRACT

During tight manoeuvres, twin-screw ships equipped with two rudders located in the propeller slip stream experience a fairly large imbalance in the hydrodynamic loads on the propeller and rudders. To investigate the phenomenon of rudder asymmetric load in some depth, manoeuvring experiments based on a free-running model were set up in which the kinematics of the model, the forces on the rudder and the stock moment were recorded. In parallel, with the aim of obtaining an exact estimation of free-stream characteristics of the rudder blade, corresponding wind tunnel experiments were also performed. Based on the results of this investigation, an analysis of the interaction effects within the hull-propeller-rudder system was performed and some conclusions were drawn.

Keywords: Manoeuvrability, Twin screw–twin rudder ship, Rudder, Resistance, Rudder normal force, Interactions

LIST OF SYMBOLS

A_R	Rudder area
B	Breadth of the ship
b_R	Mean chord of the rudder blade
C_B	Block coefficient
F_N	Normal force on the rudder
F_D	Drag force on the rudder
f	Lift gradient coefficient for the rudder
h_R	Rudder height
U	Approach speed
U_R	Resultant rudder inflow velocity

u_R, v_R	Components of the rudder inflow velocity
X_R, Y_R	Surge and sway forces due to the rudder
α_R	Effective angle of inflow to the rudder
β_{R0}	Geometrical angle of inflow to the rudder
δ	Rudder angle order
δ_{N0}	Angle of the rudder at which the normal force on the rudder becomes zero

Note: Superscript symbols P, S denote port and starboard, respectively.

INTRODUCTION

Twin-screw twin-rudder propulsion and steering systems have been installed on many types of ship. In view of their very good manoeuvring performance, they are used for coastal, inland and naval vessels. Under service conditions, however, there are indications that a relatively large load imbalance can be observed between the external and internal rudders.

The asymmetry in the rudder forces on the port and starboard sides of a single-rudder manoeuvring ship is well known, and is related to the propeller slipstream twist [1]. In addition, during tight manoeuvres, the propulsion system of a twin-screw twin-rudder ship may experience significant fluctuation in the shaft loads [2,3]. Similar effects can be observed for a rudder system also, but limited investigations have been carried out [4,5].

The interactions between the hull, propeller and rudder are associated with the flow field viscosity. CFD calculations can be used to simulate the flow around rudder, including the three-dimensional separation [6]. In the case of a twin-screw twin-rudder ship, the solution becomes more difficult, due the presence of complicated interactions [7,8], and this gives rise to a need to perform experimental investigations to study this problem. There are two main goals in this case: firstly, to obtain reliable empirical results for a twin-rudder steering unit load and to analyse the asymmetry between the rudder forces during a manoeuvring motion, and secondly, to obtain data for benchmarking of the CFD results. It should be noted that the experiments reported in this paper were done with a model, meaning that the problem of scale effects of the phenomena considered here remains and will need attention in the future.

The present study focuses on EFD investigations of the forces on a twin-rudder steering system. Measurements of the rudder blade characteristics were carried out in a free stream, and were followed by free-running manoeuvring tests in which the rudder forces were recorded during both turning motion and specific tight manoeuvres. A preliminary analysis of the results and some assessments of the interaction effects are presented.

SHIP MODEL

A scale model of a fast twin-screw twin-rudder ship was used. The model was designed and produced in Bulgarian Ship Hydrodynamics Centre (BSHC). The main particulars of the hull are given in Table 1, and the body sections and a 3D view of the hull are shown in Figs. 1 and 2.

Tab. 1. Main particulars of the hull

Non-dimensional hull data	Symbol	Value
Length-to-beam ratio	L_{pp}/B	6.269
Beam-to-draft ratio	B/T	3.395
Rudder lateral area	A_R/LT	0.011
Block coefficient	C_B	0.460
Number of propellers	[–]	2
Number of rudders	[–]	2
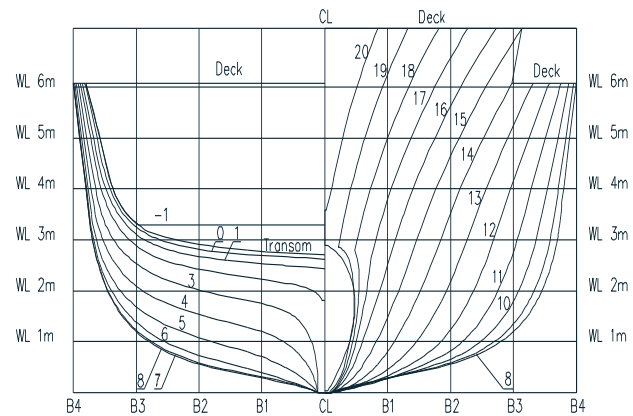
Fig. 1. View of the body sections

Fig. 2. 3D view of the hull of the model

The ship model was equipped with fixed pitch stock propellers (FPP) (Fig. 3), for which the main characteristics are shown in Table 2.

Tab. 2. Data for the propeller model

Propeller	№1	№2
Propeller diameter, mm	110.3	
Design pitch ratio at 0.7R	1.04	
Expanded blade area ratio	0.446	
Number of blades	4	
Direction of rotation	Right	Left
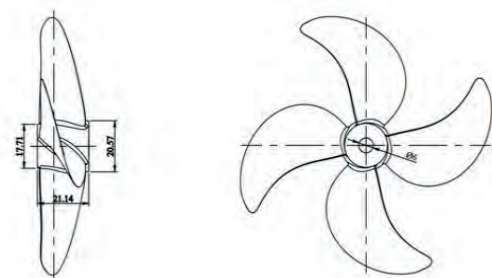
Fig. 3. View of the propeller

The model was equipped with two rudders, as summarised in Table 3. The geometry of each rudder is shown in Fig. 4. The arrangement of propellers and rudders on the model is illustrated in Fig. 5.

Tab. 3. Data for the rudder model

Characteristic	Symbol	Dimensions	Model
Rudder area	A_R	m²	0.00545
Rudder height	h_R	m	0.1016
Rudder mean chord	b_R	m	0.0537
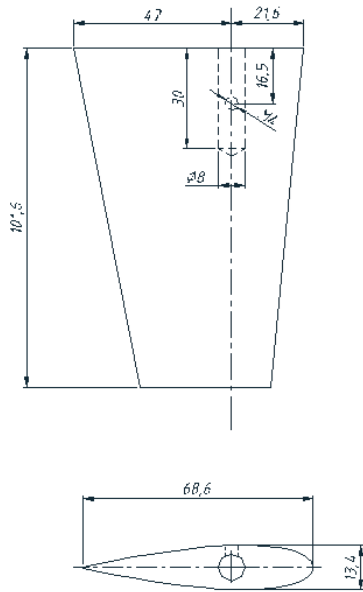
Fig. 4. Rudder geometry

Fig. 5. View showing the arrangement of rudders and propellers

FREE STREAM RUDDER CHARACTERISTICS OBTAINED VIA WIND TUNNEL EXPERIMENTS

Experimental wind tunnel setup

To obtain the free-stream rudder characteristics of the model, an experiment was carried out in the BSHC wind tunnel. The experimental model was located in the test section of the wind tunnel, labelled **1** in Fig. 6. The closed-circuit wind tunnel had an open test section of 800 × 466 mm, and was assembled from straight parts of a closed-return passage with a rectangular cross section, elbows with corner vanes, a nozzle, and an open test section (**1**). The honeycomb and two screens were placed in a closed-return passage. The rudder blade of the model (**2**) was fastened firmly via the stock (**3**) to the α mechanism (**4**), which changed the angle of attack of the rudder profile. The α mechanism was rigidly joined to the aerodynamic balance (**5**). The measurement system included the low-speed wind tunnel system and the aerodynamic balance and data processing software (based on LabVIEW and Matlab).
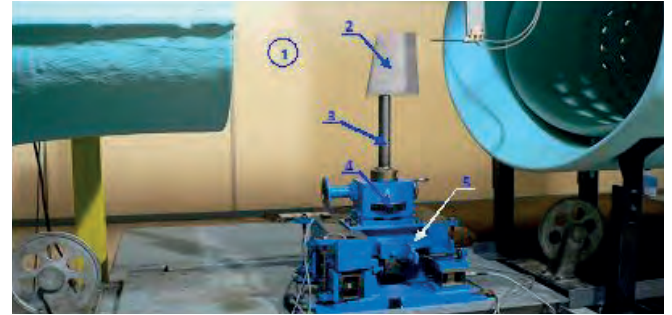
Fig. 6 Experimental setup in the wind tunnel (1 - Working section; 2 - Rudder blade; 3 - Rudder stock; 4 - Rotating mechanism; 5 - Six-component balance)

Results of measurements

The characteristics of the rudder blade profile are given in Fig. 7. The critical angle at which separation started was observed at an angle of attack greater than 20°. Under these conditions, the lift coefficient dropped to low values and the drag on the blade increased sharply. This region was examined using smoke visualisation, as shown in Fig. 8.
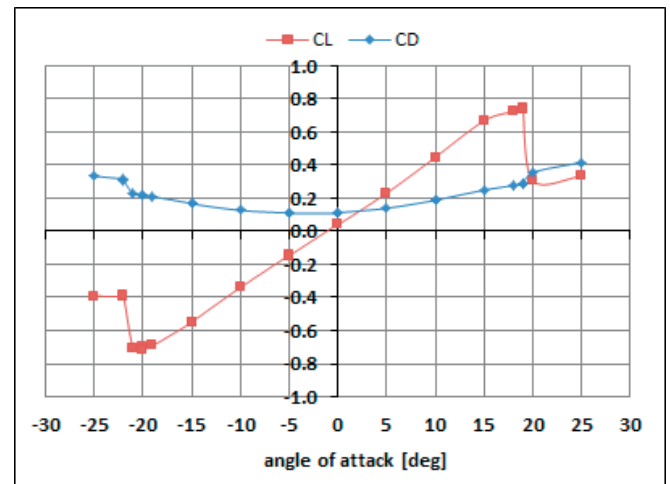
Fig. 7. Rudder lift and drag coefficients versus angle of attack, Rn=1.93*10⁵
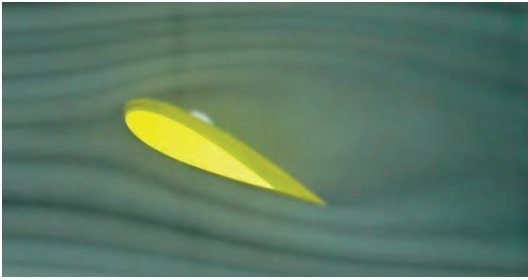
Fig. 8. Flow separation region observed with smoke visualisation

RUDDER CHARACTERISTICS FROM FREE-RUNNING MODEL TESTS

EXPERIMENTAL SETUP IN THE MANOEUVRING BASIN

Manoeuvring tests with the model were carried out in the BSHC Manoeuvring & Seakeeping Basin (Figs. 9 and 10), with main dimensions $L \times B \times T = 60 \times 40 \times 2.5$ m (maximum depth). The wave making by the model motion was damped by a wave-absorbing beach, located at the opposite side from the wave generator.
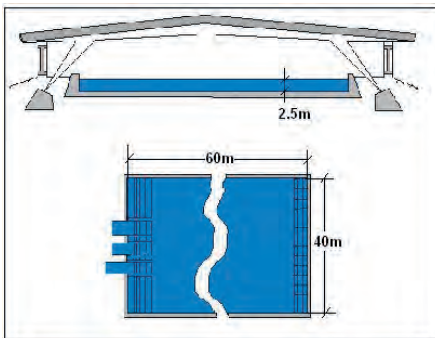
Fig. 9. Main dimensions of the manoeuvring basin
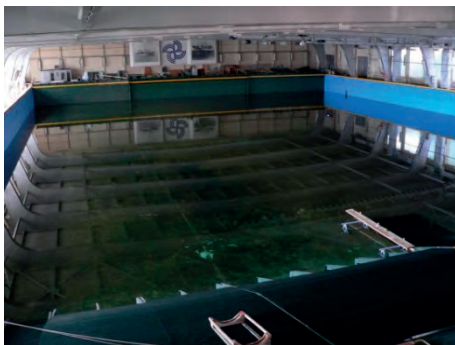
Fig. 10. The BSHC manoeuvring basin

Model equipment

The equipment needed for the free-running tests was physically divided into two types, onboard and onshore equipment, which worked together synchronised by a radio link. The onboard equipment contained all the units needed for remote control of the model and for the measurements, data acquisition and data recording, both onboard and onshore (Fig. 11).
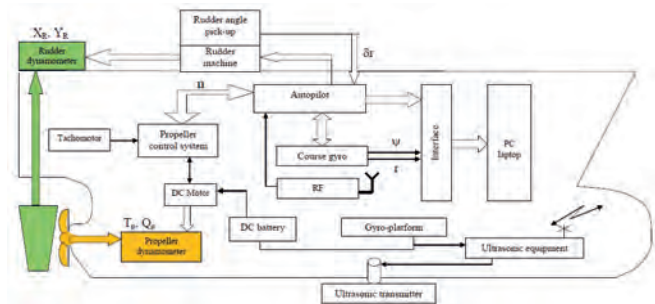
Fig. 11. Block diagram of the equipment used for the experiments

The complete model equipped for the free-running manoeuvring tests is shown in Fig. 12, and the rudder forces dynamometer is illustrated in Fig. 13.

Fig. 12. Fully equipped ship model
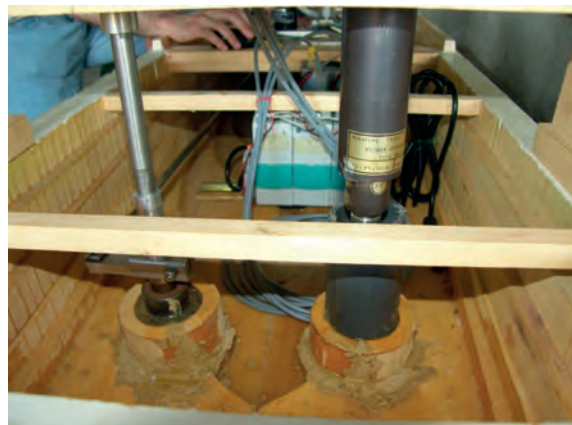
Fig. 13. Rudder force dynamometer

Experimental results and analysis

Table 4 shows a matrix of the parameters used for the experimental program. Two approach speeds were used during the free-running manoeuvring tests by varying the rudder angle. The rudder forces were originally measured in a coordinate system fixed to the rudder, and were then recalculated in a coordinate system fixed to the model. In addition to the rudder force measurements, all of the other kinematic parameters of the manoeuvring motion were recorded. During the tests, a constant RPM strategy was applied [2,9].

Tab 4. Matrix of parameters for the experiments

Manoeuvre	Initial speed [m/s]	Fn [-]	Rudder angle [deg]
Turning	1.9; 2.48	0.34; 0.44	20, 25,30,35
Williamson turn	1.9; 2.48	0.34; 0.44	$\delta = 35° \rightarrow \psi=60/$ $\delta = -35° \rightarrow \psi=180$
Steering gear test	1.9; 2.48	0.34; 0.44	35°/−35°

Time series data for the rudder resistance force F_D and the normal force F_N are given in Figs. 14–17, where the external and internal rudder (according to the direction of turning) are denoted as "ext" and "int", respectively.
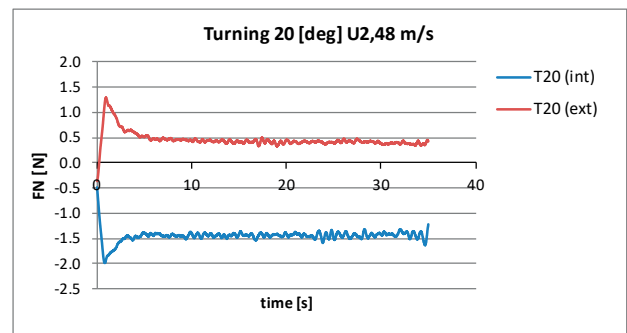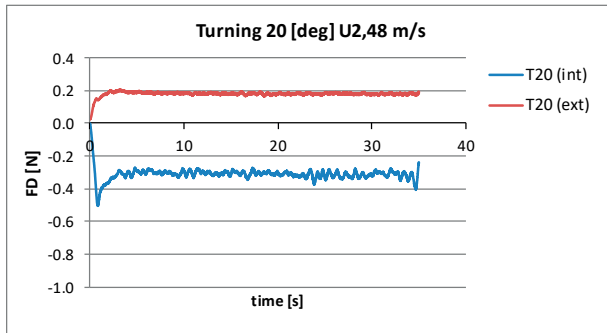
Fig. 14. Resistance F_D (left) and normal force F_N (right) for rudder turning through 20°
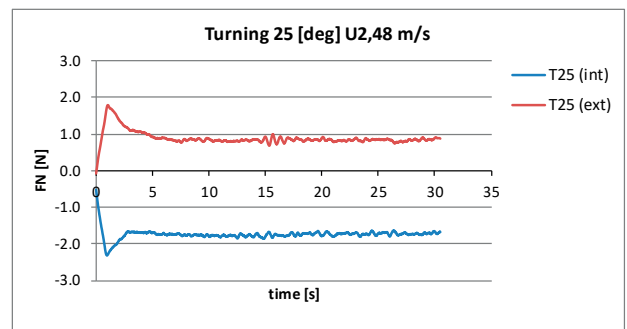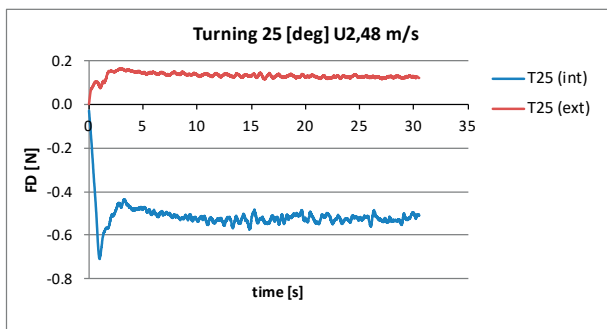
Fig. 15. Resistance F_D (left) and normal force F_N (right) for rudder turning through 25°
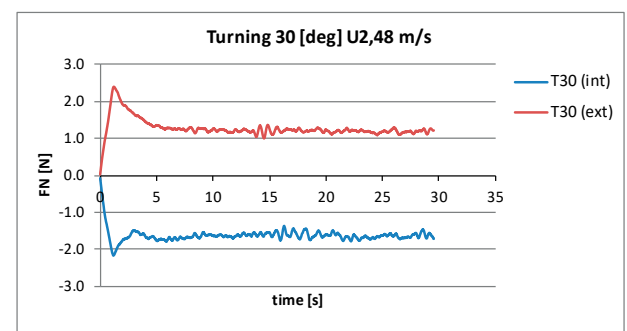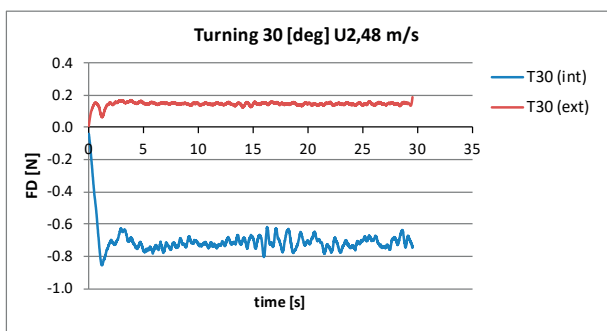
Fig. 16. Resistance F_D (left) and normal force F_N (right) for rudder turning through in 30°
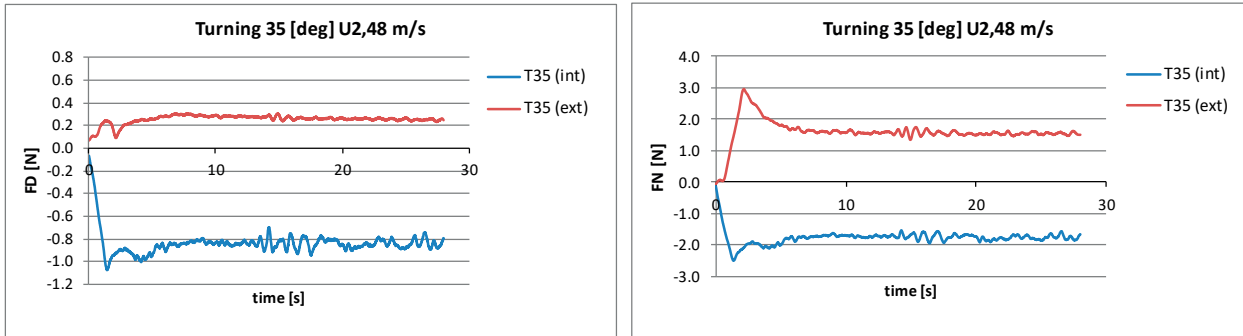
Fig. 17. Resistance F_D (left) and normal force F_N (right) for rudder turning through 35°

From the above figures, the following preliminary conclusions can be drawn. Regarding the resistance force F_D, the internal rudder load systematically increases with a characteristic peak value according the bigger rudder angle value. At the same time, the external rudder resistance increases almost monotonically. The normal rudder force F_N increases in similar way, but the difference between the two rudder loads is large. For accuracy, we note that under steady turning conditions, the periodic fluctuations in the F_D and F_N values observed after 13–15 s are likely to be due to entering of the model in the initially wave system generated by the model motion. The peak values of the rudder resistance and normal forces are illustrated in Figs. 18 and 19.

Under ship service conditions, there are two extreme manoeuvres that can take place in which the rudder system is subjected to high loads, which are known as the Williamson turn and a steering gear test. For this reason, the rudder forces were recorded as the free-running model tests were performed. Due to the specific method of rudder control in these manoeuvres, in which rudder orders are applied to both ship boards (i.e. a given rudder becomes partly external and partly internal), the measurement results are compared with time series data for a tight manoeuvre with a 35° rudder order. Fig. 20 shows a comparison of time series data for the normal rudder force recorded in a Williamson turn and in
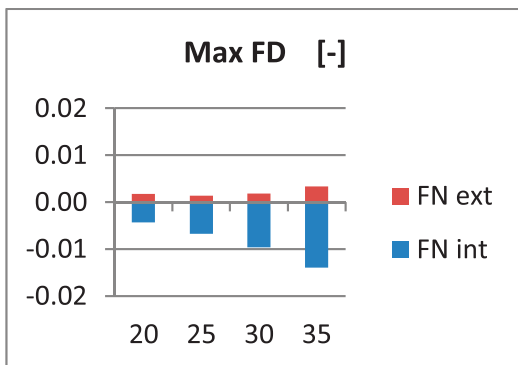
Fig. 18. Maximum values of F_D
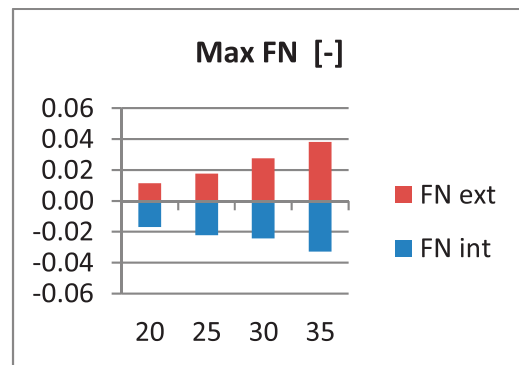
Fig. 19. Maximum values of F_N
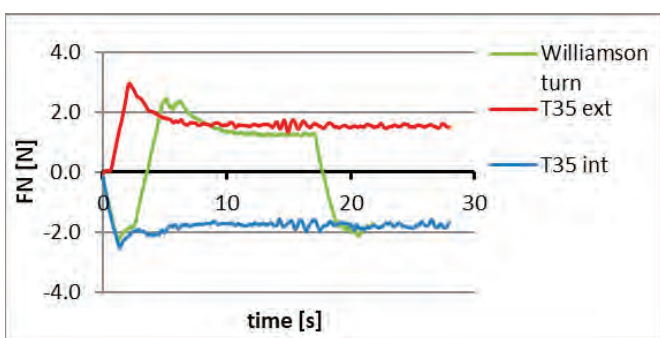
Fig. 20. F_N force over time for a Williamson turn and a 35° turning manoeuvre
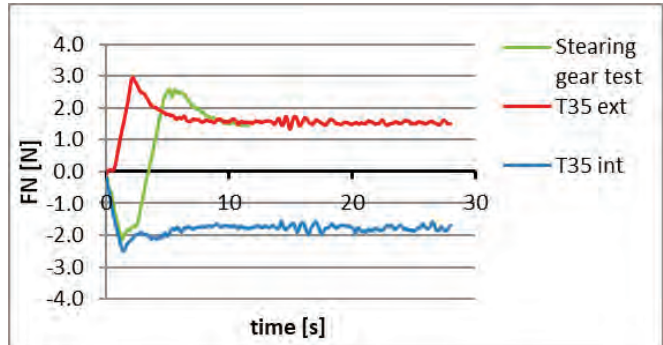
Fig. 21. F_N force over time for a steering gear test and a 35° turning manoeuvre

a 35° tight turning manoeuvre. Maximum and steady values were recorded in the latter case.

Another manoeuvre during which the maximum rudder angle needs to be applied dynamically from port to starboard and vice versa is the steering gear test, which is normally performed in a sea trial of a ship. In this manoeuvre the maximum and also the steady rudder normal force values do not exceed those in tight circulation (Fig. 21).

Estimation of interaction effects

To perform a complete analysis of the hull-propeller-rudder interactions, the results of captive model tests are needed [7]. In our case, we had data from the free-running model test, and it was therefore possible to determine reliable values for the components of the inflow velocity in the rudder region when the rudder force was equal to zero [4,5]. Following the work in [10,11], we assumed that the rudder force on the port (p) and starboard (s) rudders took the form:

$$F_N^{P,S} = 0.5\rho A_R U_R^{P,S} f_a \sin \alpha_R^{P,S} \qquad (1)$$

The resultant rudder inflow velocities $U_R^{P,S}$ then have the following components:

$$U_R^{P,S} = \sqrt{u_R^{P,S\,2} + v_R^{P,S\,2}} \qquad (2)$$

The effective rudder angles are:

$$\alpha_R^{P,S} = \delta + \delta_f^{P,S} - \tan^{-1}(\frac{v_R^{P,S}}{u_R^{P,S}}) \approx \delta + \delta_f^{P,S} - \frac{v_R^{P,S}}{u_R^{P,S}} \qquad (3)$$

where $\delta_f^{P,S}$ is a correction to the port or starboard position in relation to the centre plane of the ship.

When the model is moving straight ahead, i.e., without drift or yaw, the lateral velocity component can be expressed as:

$$v_R^{P,S} = U\gamma_R^{P,S}\beta_{R0}^{P,S} \qquad (4)$$

where $\gamma_R^{P,S}$ are the flow straightening coefficients, and $\beta_{R0}^{P,S}$ are the geometrical inflow angles for a particular rudder. If we substitute $U_R^{P,S}$ and $\alpha_R^{P,S}$ in Eq. (1) for the corresponding expressions in Eqs. (2) and (3), then in non-dimensional form we have:

$$F_N^{P,S\,'} = \frac{A_R}{L_{pp}T}(u_R^{P,S\,'2} + v_R^{P,S\,'2})f_a \sin\left(\delta + \delta_f^{P,S} - \frac{v_R^{P,S\,'}}{u_R^{P,S\,'}}\right) \qquad (5)$$

After differentiation by δ we obtain:

$$\frac{dF_N^{P,S\,'}}{d\delta} = \frac{A_R}{L_{pp}T}(u_R^{P,S\,'2} + v_R^{P,S\,'2})f_a \cos\left(\delta + \delta_f^{P,S} - \frac{v_R^{P,S\,'}}{u_R^{P,S\,'}}\right) \qquad (6)$$

By making use of the relation $\delta_{N\,0}^{P,S} = \dfrac{v_R^{P,S\,'}}{u_R^{P,S\,'}}$, we can write Eq. (6) as follows:

$$\frac{dF_N^{P,S\,'}}{d\delta}\bigg|_{\delta=\delta_{FN0}^{P,S}} = \frac{A_R}{L_{pp}T}u_R^{P,S\,'2}(1+\delta_{FN0}^{P,S\,2})f_a \qquad (7)$$

The axial component of the rudder's inflow velocity can then be calculated:

$$u_R^{P,S\,'} = \sqrt{\frac{dF_N^{P,S\,'}}{d\delta}\bigg|_{\delta=\delta_{FN0}^{P,S}} \frac{L_{pp}T}{A_R f_a (1+\delta_{FN0}^{P,S\,2})}} \qquad (8)$$

Based on the above expression, the lateral single rudder inflow velocities are estimated in the following way. The non-dimensional normal force for each rudder and the dimensional approach speed measured in a steady turn are given by Figs. 22 and 23, respectively.
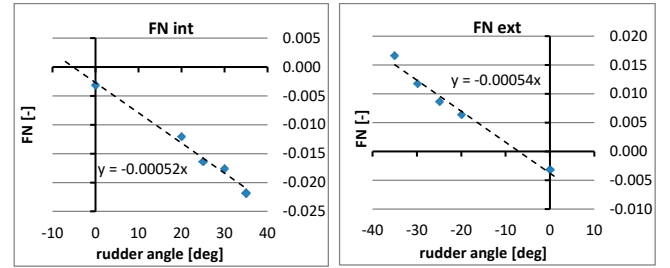
Fig. 22. Non-dimensional normal force F_N on the internal and external rudders
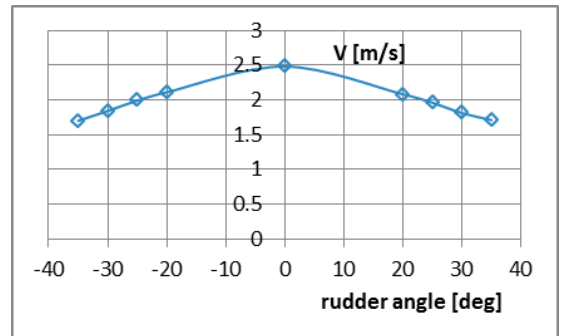
Fig. 23. Dimensional approach speed measured in a steady turn

The rudder neutral angle $\delta_{FN0}^{p'}$ is reached to -7.8° when rudder normal force $F_N^{p'}$ is equal to zero. Based on this value, the estimated rudder inflow velocity components are then as follows.

The external rudder:

$u_R^{p'} = 0.94$; $v_R^{P'} = 0.13$, i.e. $u_R^P = 1.99$ m/s; $v_R^P = 0.27$ m/s.

The rudder neutral angle $\delta_{FN0}^{s\prime}$ is reached 5.4° when the rudder normal force $F_N^{s\prime}$ is equal to zero . Based on this value, the estimated rudder inflow velocity components are as follows.

The internal rudder:

$u_R^{s\prime} = 0.93;$ $v_R^{P\prime} = 0.09,$ i.e. $u_R^P = 1.96$ m/s; $v_R^P = 0.19$ m/s.

CONCLUSIONS AND FUTURE WORK

This paper represents an attempt to look more deeply at the characteristics of twin-rudder steering systems, with a particular focus on the asymmetry in the rudder load. The present work formed part of a BSHC project involving research in the field of hull-propeller-rudder interaction effects in the case of multi-rudder systems.

These results will form the basis for further investigations, including captive static drift model tests with the propulsion ratio and measurements of the rudder and hull forces.

ACKNOWLEDGMENTS

REFERENCES

1. A. Kamis, A. Fuad, A. Ashaari, C. Noor, and S. Ali, "Development of WOP mathematical model for optimum track-keeping. A ship simulation study using VLCC, focusing on hard over rudder turning circle with three stages of validation analysis," *Polish Maritime Research*, vol. 28, no. 3, pp. 156–174, 2021, eISSN 2083-7429, https://doi.org/10.2478/pomr-2021-0043.

2. A. Coraddu, G. Dubbioso, S. Mauro, and M. Viviani, "Analysis of twin screw ships' asymmetric propeller behaviour by means of free running model tests," *Ocean Engineering*, vol. 68, pp. 47–64, 2013, ISSN 0029-8018, https://doi.org/10.1016/j.oceaneng.2013.04.013.

3. G. Dubbioso and M. Viviani, "Aspects of twin screw ships semi-empirical maneuvering models," *Ocean Engineering*, vol. 48, pp. 69–80, 2012, ISSN 0029-8018, https://doi.org/10.1016/j.oceaneng.2012.03.007.

4. S. Khanfir, V. Nagarajan, K. Hasegawa, and S. K. Lee, "Estimation of mathematical model and its coefficients of ship manoeuvrability for a twin-propeller twin-rudder ship," in *Proceedings of MARSIM*, Panama City, vol. 9, pp. M159–M166, 2009.

5. S. Khanfir, K. Hasegawa, E. Kobayashi, and V. Nagarajan, "Mathematical model for manoeuvring of twin-propeller twin-rudder ship considering peculiar rudder normal force phenomenon," in *Proceedings of the International Conference on Marine Simulation and Ship Maneuverability*, Singapore, vol. 1, 2012.

6. G. Dubbioso, D. Durante, A. Di Mascio, and R. Broglia, "Turning ability analysis of a fully appended twin screw vessel by CFD. Part II: Single vs. twin rudder configuration," *Ocean Engineering*, vol. 117, pp. 259–271, ISSN 0029-8018, 2016, https://doi.org/10.1016/j.oceaneng.2016.03.001.

7. S. Khanfir et al., "Manoeuvring characteristics of twin-rudder systems: Rudder-hull interaction effect on the manoeuvrability of twin-rudder ships," Journal of Marine Science and Technology, vol. 16, no. 4, pp. 472–490, 2011, https://doi.org/10.1007/s00773-011-0140-3.

8. D. Kang, V. Nagarajan, K. Hasegawa, and M. Sano, "Mathematical model of single-propeller twin-rudder ship," *Journal of Marine Science and Technology*, vol. 13, no. 3, pp. 207–222, 2008, https://doi.org/10.1007/s00773-008-0027-0.

9. G. Dubbioso and M. Viviani, "Experimental investigation of asymmetrical propeller behavior of twin screw ships during manoeuvers," in *Proceedings of the International Conference on Marine Simulation and Ship Maneuverability*, Singapore, vol. 1, 2012.

10. H. Yasukawa and Y. Yoshimura, "Introduction of MMG standard method for ship maneuvering predictions," *Journal of Marine Science and Technology*, vol. 20, no. 1, pp. 37–52, 2015, https://doi.org/10.1007/s00773-014-0293-y.

11. Y. Yoshimura, "Mathematical model for manoeuvring ship motion (MMG model)," in *Workshop on Mathematical Models for Operations Involving Ship-Ship Interaction*, Tokyo, pp. 1-6, August, 2005.

MODELLING OF LAKE WAVES TO SIMULATE ENVIRONMENTAL DISTURBANCE TO A SCALE SHIP MODEL

Andrzej Rak* ID
Anna Miller ID

Gdynia Maritime University, Faculty of Electrical Engineering, Department of Ship Automation, Gdynia, Poland,

* Corresponding author: *a.rak@we.umg.edu.pl (Andrzej Rak)*

ABSTRACT

In the development of ship motion control systems, software simulations or scale model experiments in pools or open water are very often carried out in the verification and testing stages. This paper describes the process of building a software wave simulator based on data gathered on the Silm Lake near Iława, Poland, where scale ship models are used for research and training. The basis of the simulator structure is a set of shaping filters fed with Gaussian white noise. These filters are built in the form of transfer functions generating irregular wave signals for different input wind forces. To enable simulation of a wide range of wind speeds, nonlinear interpolation is used. The lake wave simulation method presented in this paper fills a gap in current research, and enables accurate modelling of characteristic environmental disturbances on a small lake for motion control experiments of scale model ships.

Keywords: wave modelling, environmental disturbances, scale ship model, ship motion simulation

INTRODUCTION

One of the main developments that seems likely to change the *modus operandi* of the global transportation system the most over the coming decades involves autonomous vehicles, including maritime shipping [21]. When designing an autonomous seagoing vessel, one vital factor is the motion control system for all phases of the cruise, from berth to berth. For a fully autonomous ship, this type of voyage will include port manoeuvres, as well as moving in restricted water areas at low speeds. Under such conditions, it is crucial to take into account the impact of environmental disturbances when

designing the control system to ensure that these manoeuvres are fully safe [7].

Except for software simulations, research projects in this area typically include the testing and verification of control systems using scale model ships sailing in open waters, such as lakes or ponds [1, 3, 15, 20]. A model of the environmental load on a scale ship caused by waves and wind blowing over a small inland lake is therefore needed. Unfortunately, the currently available models of environmental disturbance, which are widely used for simulations of marine control systems, are equivalent to fully developed ocean or open sea conditions [6, 18]. Existing research on the description of lake waves

has used several different types of models, and has focused mostly on geophysical and environmental issues [2, 9]. This work describes the process of designing a unidirectional, nonlinear wave model that is suitable for simulating the influence of a lake surge on a scale ship. Source data for the project were collected from the Silm Lake, Poland, which is used as a research area for the manoeuvring of scale ships [17]. Introductory analyses of the wind and wave phenomena in this location have been reported in previous papers by the current authors [12, 13]. A corresponding elaboration of a wind model is being prepared for a separate publication.

MODELLING OF THE WAVE SIGNAL

Sea waves can be described as a stationary random process [5], and the reconstruction of these waves can be achieved by appropriate shaping of the frequency components of a continuous standard input signal. Of the shaping methods in the literature [10], the most commonly used for this purpose are filters implemented in the form of approximate state-space structures, convolution filters with directly specified power spectral densities (PSDs), or compositions of orthogonal basis functions, typically cosine ones, which directly correspond to the PSD, with variable phase shifts or amplitudes at the boundary of the periodic signal. Shaping filters are usually designed as linear time-invariant (LTI) systems driven by white noise. These give good simulation performance, and a suitable PSD approximation assuming correctly identified the LTI system. Based on the ITTC guidelines [18], it was decided in this project to model wave PSDs as an LTI system.

It is known that the PSD of a Gaussian white noise signal (GWN) is equal to:

$$S_x(f) = \frac{N_0}{2} \qquad (1)$$

for all frequencies f. An LTI system is characterised in the time domain by the impulse response:

$$h(t) = T[\delta(t)], \qquad (2)$$

where $\delta(t)$ is a Dirac delta function. The output signal $y(t)$ of the filter may be determined as the convolution of an LTI system impulse response with a GWN input signal $x(t)$:

$$y(t) = h(t) * x(t). \qquad (3)$$

Since $x(t)$ is a GWN random signal, the system output $y(t)$ is also a Gaussian process. Hence, for a discrete system, the output signal can be defined as:

$$y_n = \sum_k h_k x_{n-k}, \qquad (4)$$

where n is the sample number, and k is the time shift. An LTI system transfer function is defined as:

$$H(f) = \sum_n h_n e^{-j2\pi n f}. \qquad (5)$$

Taking into account Eq. (3) in the frequency domain, the desired frequency component $\hat{Z}(f)$ corresponding to the measured wave spectrum $Z(f)$ can be expressed as:

$$\hat{Z}(f) = H(f)W(f), \qquad (6)$$

where $W(f)$ is a white noise spectrum. Hence, the power density function to be realised is given by:

$$S_z(f) = |H(f)|^2 S_x(f) = |H(f)|^2 \frac{N_0}{2}. \qquad (7)$$

In the relationship above, the PSD can be approximated by a suitable transfer function, which can be computed from the PSD for a measured wave, $S_w(f)$, using the least squares method (LSM) as follows:

$$\min_{a_k, b_m} \sum_{j=1}^m \left(|H(j2\pi f)| - \sqrt{\left(S_w(j2\pi f)\right)^2} \right), \qquad (8)$$

where a_k, b_m are LTI filter coefficients, $H(2\pi f)$ is the desired frequency response, and $m \geq k$. The corresponding discrete filter transfer function with sample time corresponding discrete filter transfer function with sample time $T_s = 0.1$ [s] can be calculated as follows:

$$H(z) = \sum_{n=-\infty}^{+\infty} h(n)z^{-n}, \qquad (9)$$

and has the form:

$$H(z) = \frac{a_0 + a_1 z^{-1} + \ldots + a_p z^{-p}}{1 + (b_1 z^{-1} + \ldots + b_q z^{-q})}. \qquad (10)$$

A corresponding analogue filter, which reproduces the wave parameters, can be designed based on the assumptions of the bilinear transformation method. The following function [8] can be used to convert a digital filter with transmittance $H(z)$ to an analogue filter with transmittance $H(s)$:

$$z = \phi(s) = \frac{1 + s\frac{T_s}{2}}{1 - s\frac{T_s}{2}}, \qquad (11)$$

where T_s is the discrete signal sampling time. Finally, the resulting LTI object can be obtained in the form of a transfer function:

$$T(s) = k \frac{b_n s^n + \cdots + b_1 s + b_0}{a_m s^m + \cdots + a_1 s + a_0}. \tag{12}$$

DESIGN OF A LAKE WAVE DIGITAL SIMULATOR

A lake wave simulator was designed based on the assumption that all waves are generated by winds. The structure of our simulator is shown in Fig. 1, where the mean wind speed v_w [m/s] is the input value, and the wave height h_w [mm] is the output signal.
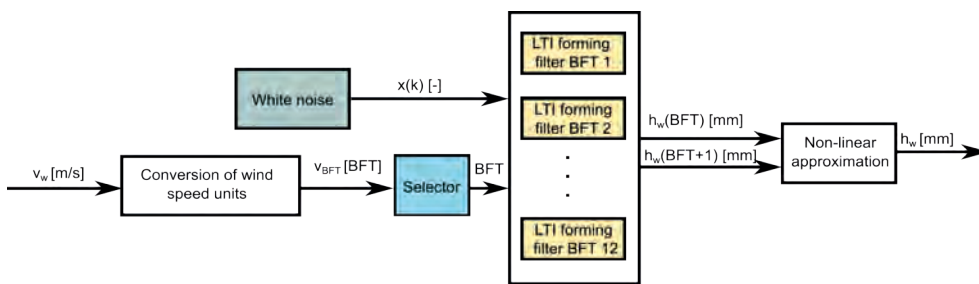
Fig. 1. Block diagram of the wave generation algorithm

A white noise generator is used as a signal source. A noise seed can be defined rather than a random selection of parameters, which leads to reproducible results from the wave signal specification. The "Selector" module rounds the force of the wind to the integers on the Beaufort wind scale (BFT), and acts as a switch for the appropriate pair of LTI forming filters. The wind speed is recalculated based on the BFT at the scale of the ship model to avoid confusion from an assessment of the wind impact based on two different reference measures in metres per second caused by the scaling of the ship. The transformation of wind speed v_w to BFT is done using the empirical formula [11]:

$$v_{BFT} = 1.42 \left(v_w \sqrt{1/sc} \right)^{0.61}, \tag{13}$$

where sc is the model scale ($sc = 1{:}24$); v_{BFT} is the wind force in BFT, proportional to the ship's scale; and v_w is the wind speed in [m/s]. The relationship between wind speed and BFT force at the scale of the ship, and a comparison with the reference points given in [6], is shown in Fig. 2.
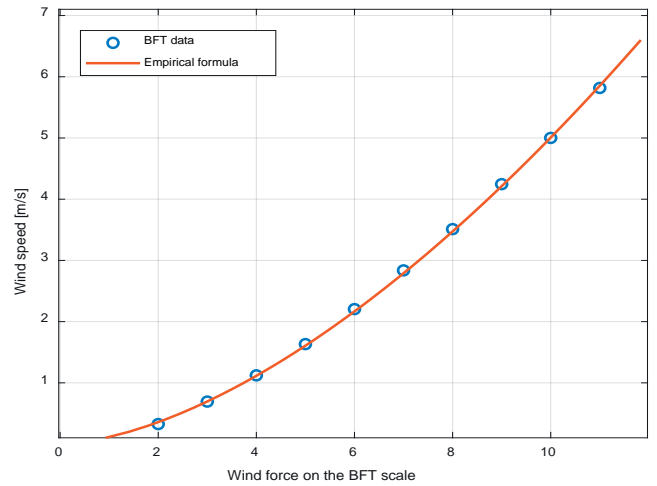
Fig. 2. Wind force [BFT] at the scale of the model ship

The wind speed at the scale of the model corresponding to the 0–1 BFT range caused no measurable wave effects on the surface of the lake, and the curve shown above therefore begins at 1 BFT. Interpolation between the outputs of the two consecutive forming filter blocks (see Fig. 1) used nonlinear weighting functions, and is described in the next section.

Measurements were taken with a device consisting of two ultrasonic anemometers, a wavemeter and a data recording computer working in real time. Details of the measurement equipment can be found in [12-14]. Data from all three instruments were acquired at a sampling rate of 10 Hz. The software was developed using the Real-Time Target Toolbox of the MATLAB package, as well as low-level functions coded in C.

EXTRAPOLATION OF RESULTS AND DEPENDENCY ANALYSIS OF WAVE HEIGHT AND WIND SPEED

Wave height and wind speed measurements were collected in several sessions between the spring of 2019 and the autumn of 2021. The measuring equipment was located on the Silm Lake, and each measurement session lasted 12 h. Detailed analyses of the acquired data and the results of spectrum modelling have been presented in [13]. The results of these studies confirmed that the wave height on a lake is strongly correlated with the wind speed. The distributions of the height deviations from the mean value and the wave amplitude were Gaussian and Rayleigh, respectively, and the wave PSD function was analogous to the ITTC formulation for the sea waves spectrum. These factors formed the basis for the construction of a digital wave simulator. The measured wave spectrum was modelled as a scaled ITTC spectrum [18] as follows:

$$s(\omega) = A\omega^{-5} exp(-B\omega^{-4}), \tag{14}$$

where:

$$A = 1.51 \frac{\bar{H}_{1/3}^2}{\bar{T}_z^4}, \tag{15}$$

$$B = 105.44 \bar{T}_z^4, \tag{16}$$

and $\bar{H}_{1/3}$ [mm] is the mean of the significant wave height, and $\bar{T}_z$ [s] is the mean of the significant wave period. Based on the measured values of $\bar{H}_{1/3}$ and $\bar{T}_z$ for wind forces of 4, 5, 6, 7 and 9 BFT, dependencies for $\bar{H}_{1/3}(BFT)$ and $\bar{T}_z(BFT)$ were extrapolated to obtain continuous relationships. These are shown in Figs. 3 and 4, respectively.
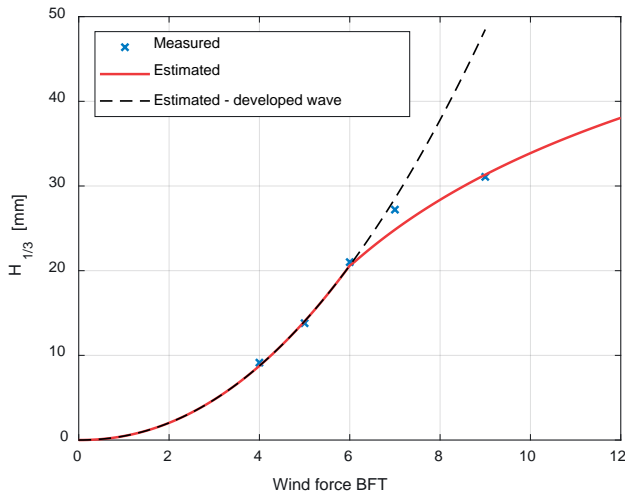
Fig. 3. Dependency of the significant wave height on the wind force
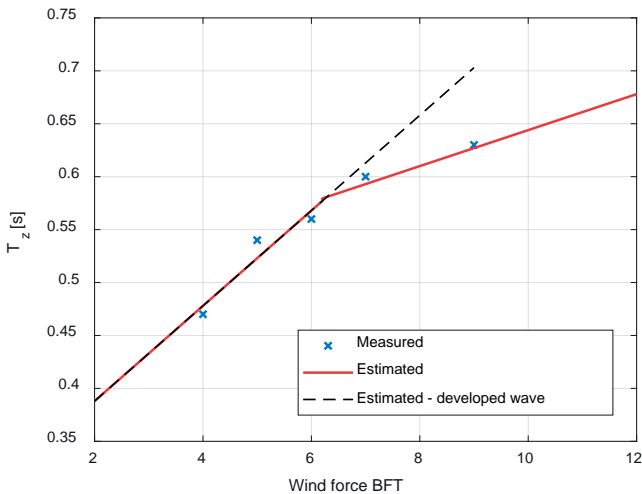
Fig. 4. Dependency of the significant wave period on the wind force

The dependence of the significant wave height on the wind speed, for fully developed sea waves, is described by a second-order polynomial [19]. The same dependence for Lake Erie is described by the square function for wind speeds between zero and 15 m/s and for higher wind speeds it is linear [4], due to the limited depth of the lake. On the Silm Lake, fully developed waves were observed for winds less than or equal than 6 BFT at the scale of the ship, and above this value, a characteristic flattening was observed (see Fig. 3). The dependence of the significant wave height on the BFT scale can be expressed as:

$$\hat{H}_{1/3} = \begin{cases} 0.47 v_{BFT}^{2.11} & \text{for} \quad v_{BFT} \leqslant 6BFT \\ -149.4 v_{BFT}^{-0.38} + 96.16 & \text{for} \quad v_{BFT} > 6BFT. \end{cases} \tag{17}$$

For fully developed sea waves, the dependence of the significant wave priod on the wind speed is linear [16]. For the waves measured on Silm Lake, consistency with this general rule was observed for wind forces not exceeding 6 BFT at the scale of the ship, in the same way as for the wave heights. Above this value, due to the restricted area and depth of the lake, characteristic flattening was observed, as shown in Fig. 4. The dependence of the significant wave period on scaled BFT is described by:

$$\hat{T}_z = \begin{cases} 0.045 v_{BFT} + 0.298 & \text{for} \quad v_{BFT} \leqslant 6BFT \\ 0.017 v_{BFT} + 0.474 & \text{for} \quad v_{BFT} > 6BFT. \end{cases} \tag{18}$$

These dependencies were estimated using an LSM curve fitting, with the fit factors shown in Table 1.

Tab. 1. Accuracy of significant wave height and period estimates

	$\hat{T}_z$ [Hz]		$\hat{T}_{1/3}$ [mm]	
	$v_{BFT} \leq 6$ [BFT]	$v_{BFT} > 6$ [BFT]	$v_{BFT} \leq 6$ [BFT]	$v_{BFT} > 6$ [BFT]
R^2	0.813	0.923	0.996	0.992
$RMSE$	0.024	0.011	0.510	1.110

NONLINEAR WAVE HEIGHT APPROXIMATION

The wave generator structure shown in Fig. 1 requires a selector for the consecutive reconstruction filters designed for each BFT. To obtain a continuous wave height signal, interpolation is required between the outputs of the selected filters. This interpolation is done based on a sigmoid function:

$$\Delta h_{coeff}(\Delta BFT) = 1 - \frac{1}{1 + e^{5(1 - \Delta BFT)}}, \tag{19}$$

where Δh_{coeff} is the forming filter output multiplier, and ΔBFT is the difference between the mean wind speed value (recalculated to the BFT scale for the ship) and the next integer on the BFT scale.

The shape of this nonlinear function is shown in Fig. 5.
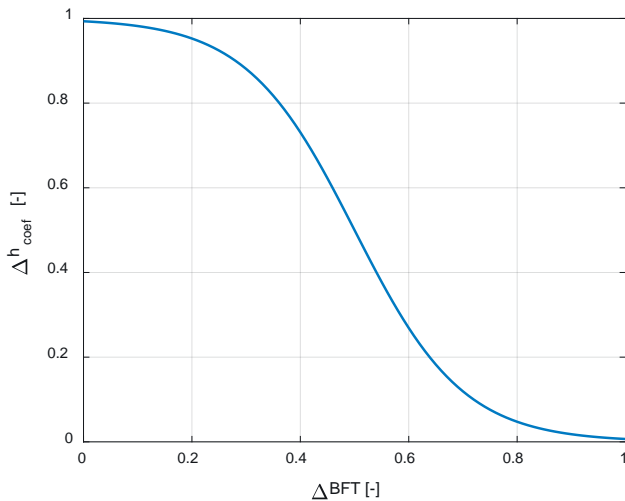
Fig. 5. Nonlinear wave height interpolation function

RESULTS

The workflow described in the section entitled "Modelling of the Wave Signal" was applied to the design of a digital wave generator. The MATLAB-Simulink package was used as a software development environment, and the parameters of the scaled ITTC spectrum (see Eqs. (15) and (16)) were calculated using the estimated significant wave height and period for each point on the BFT scale.

DESIGN OF THE FORMING FILTERS

Twelve IIR forming filters were designed, for which the parameters were estimated using the LSM optimisation in Eq. (8). These IIR filter factors were stored in second-order section (SOS) matrices and used to determine the parameters for the discrete transfer functions. In the real world, wave height is modelled as a continuous analogue signal, and to remain consistent with this assumption, continuous transfer functions were computed as shown in Eq. (12). A decision

was made to keep the order of the filter transfer functions as low as possible, at the cost of an acceptable level of simulator inaccuracy. A second-order transfer function of general form was therefore proposed as follows:

$$T(s) = k \frac{b_2 s^2 + b_1 s + b_0}{a_2 s^2 + a_1 s + a_0}. \qquad (20)$$

The values of the filter coefficients a, b and k (gain) for each point on the BFT scale are shown in Table 2.

Tab. 2. Coefficients for filter transfer functions

BFT	k	b_2	b_1	b_0	a_2	a_1	a_0
2	14	0.0065	0.034	$2.4 \cdot 10^{-5}$	1	2.35	161.5
3	6.4	0.36	0.22	0.011	1	2.45	138.1
4	3.2	0.074	0.51	0.0031	1	2.10	116.1
5	3	0.22	1.74	0.028	1	1.86	87.12
6	1.7	0.59	4.83	0.026	1	1.92	80.65
7	1.1	1.02	8.59	0.20	1	1.67	69.44
8	0.6	2	17.00	1.08	1	1.51	65.89
9	0.82	1.47	12.54	0.30	1	1.50	63.52
10	0.75	1.93	16.77	0.13	1	1.54	58.44
11	0.78	1.20	17.57	0.15	1	1.54	56.44
12	0.83	2	17.81	0.024	1	1.58	55.00

Using the nonlinear interpolation mechanism described in the previous section, a system of forming filters was created to digitally model wind-generated waves on the Silm Lake. An example of the output from our digital wave simulator is shown in Fig. 6. This diagram includes three separate waveforms generated by winds of force 2, 2.5 and 3 BFT at the scale of the ship, corresponding to winds with average speeds of 0.35 m/s, 0.5 m/s and 0.7 m/s, respectively. From Fig. 6, it can be seen that the height and period of the waves increase with the wind speed; this pattern is consistent with the nature of the phenomena observed on the lake.
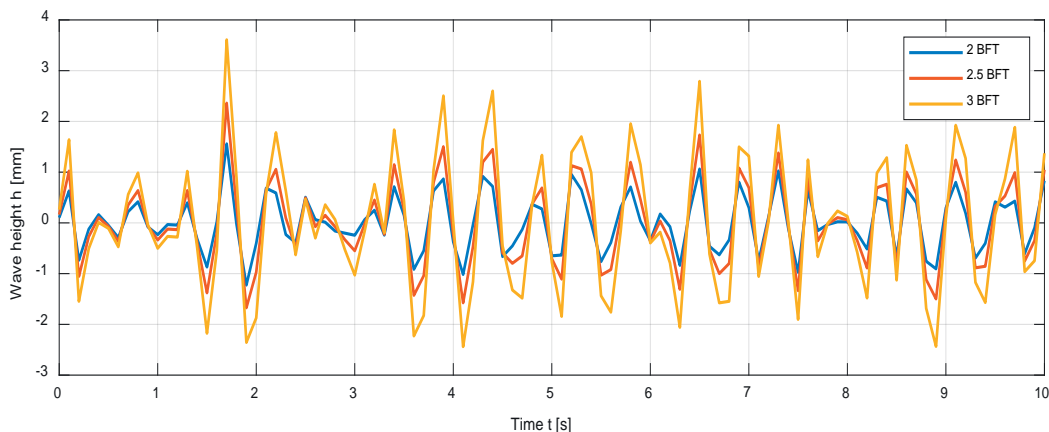
Fig. 6. Example of the output from the wave generator

A discussion of the results is presented below, and is divided into two subsections dealing with a spectral analysis of the simulated waves and their statistics.

SPECTRAL ANALYSIS OF SIMULATED WAVES

The proposed digital wave generator takes the mean value of the wind speed and a white noise signal as input, and based on these, the wave height is simulated as a function of time.
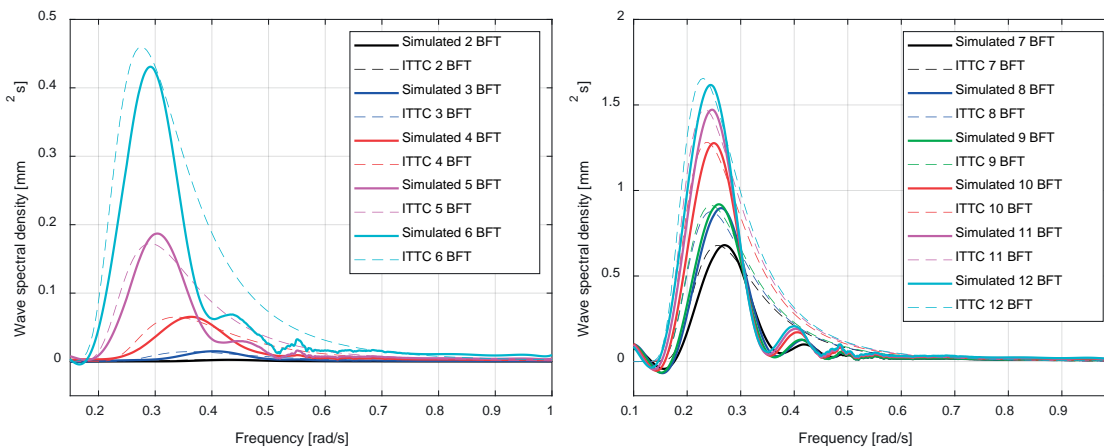
Fig. 7. Comparison of simulated and ITTC spectra

The outputs of the generator for each point on the BFT scale were compared to the standard ITTC scaled wave spectra. The results of this comparison are shown in Fig. 7, for winds of strength 2–6 BFT and 7–12 BFT. The diagram is separated into two parts to ensure readability. The simulation results are shown by the solid lines, and the corresponding ITTC spectra by the dashed lines. A high level of convergence of the results was seen over the full range of wind forces. A modal frequency shift toward lower frequencies was observed as the wind strength increased, which is consistent with the principles of ITTC spectrum modelling. The value of the wave spectral density also increased at higher points on the wind BFT scale. Moreover, narrowing of the spectrum compared with the ITTC wave spectral model was observed in the higher frequency range.

To enable a quantitative evaluation of the spectrum modelling, RMSE values were determined using the formula:

$$RMSE = \sqrt{\frac{1}{n} \sum \left(S_{ITTC}(\omega) - \hat{S}(\omega) \right)^2}, \qquad (21)$$

where S_{ITTC} is the ITTC scaled standard spectrum, $\hat{S}$ is the spectrum computed on the basis of the digital generator output, and n is the number of bands in the spectrum. The values of the RMSE are listed in Table 3.

Table 3. RMSE values for the simulated spectrum

BFT [-]	2	3	4	5	6	7	8	9	10	11	12
RMSE [mm²s]	$8.18\cdot10^{-4}$	0.0048	0.021	0.055	0.13	0.19	0.25	0.26	0.35	0.41	0.45

The resulting values did not exceed 2% of the sum of the ITTC spectrum elements for each BFT. We therefore conclude that a high degree of convergence in the results was obtained, and that our model is sufficiently accurate to be used as a digital wave generator.

STATISTICS FOR THE SIMULATED WAVES

The mode of operation and reproduction accuracy of each filter wave were analysed separately. Based on the results of the simulation, the heights and periods of the significant waves were determined, and a statistical analysis of the obtained data was carried out. The distributions of deviations from the mean values and the distributions of the wave amplitudes were computed and compared with the distributions estimated on the basis of real measurements.

Table 4 shows the relative errors in the simulated heights and periods of significant waves for each point on the BFT scale.

Tab. 4. Relative error in the simulated wave parameters

BFT	Measured		Simulated		Error	
	$H_{1/3}$ [mm]	T_z [s]	$\hat{H}_{1/3}$ [mm]	$\hat{T}_z$ [s]	$e_{H1/3}$ [%]	e_{Tz} [%]
2	2.00	0.38	1.80	0.40	10	5.3
3	4.50	0.40	4.33	0.43	3.8	7.5
4	9.24	0.45	9.14	0.47	1.1	4.4
5	14.00	0.52	13.80	0.54	1.4	3.8
6	22.23	0.55	21.01	0.56	5.5	1.8
7	26.07	0.59	24.94	0.60	4.3	1.7
8	28.90	0.62	28.00	0.62	3.1	0
9	29.50	0.62	28.32	0.63	4	1.6
10	34.40	0.65	33.51	0.65	2.6	0
11	36.60	0.65	36.04	0.66	1.5	1.5
12	38.50	0.66	39.04	0.66	1.4	0

The mean error of the significant wave height was equal to 3.5%. The maximal value was obtained for the weakest wind force of 2 BFT, where the wave height reached 2 mm, and this value had a negligible effect on the movement of the model ship. In the other cases, the error did not exceed 5.5%. The maximal error of significant wave period reached 7.5% for winds at 3 BFT, and the mean inaccuracy of significant waves period was 2.5%. These error values indicate that the wave parameters are sufficiently well chosen to simulate the environmental disturbance generated in the motion of the ship. The distributions of the wave amplitudes and deviations from the mean values for the waves generated by weak (4 BFT), mean (6 BFT) and strong (9 BFT) winds are shown in Fig. 8. The blue bars represent data obtained from the digital generator, which are compared to the estimated distributions based on real lake measurements [13].
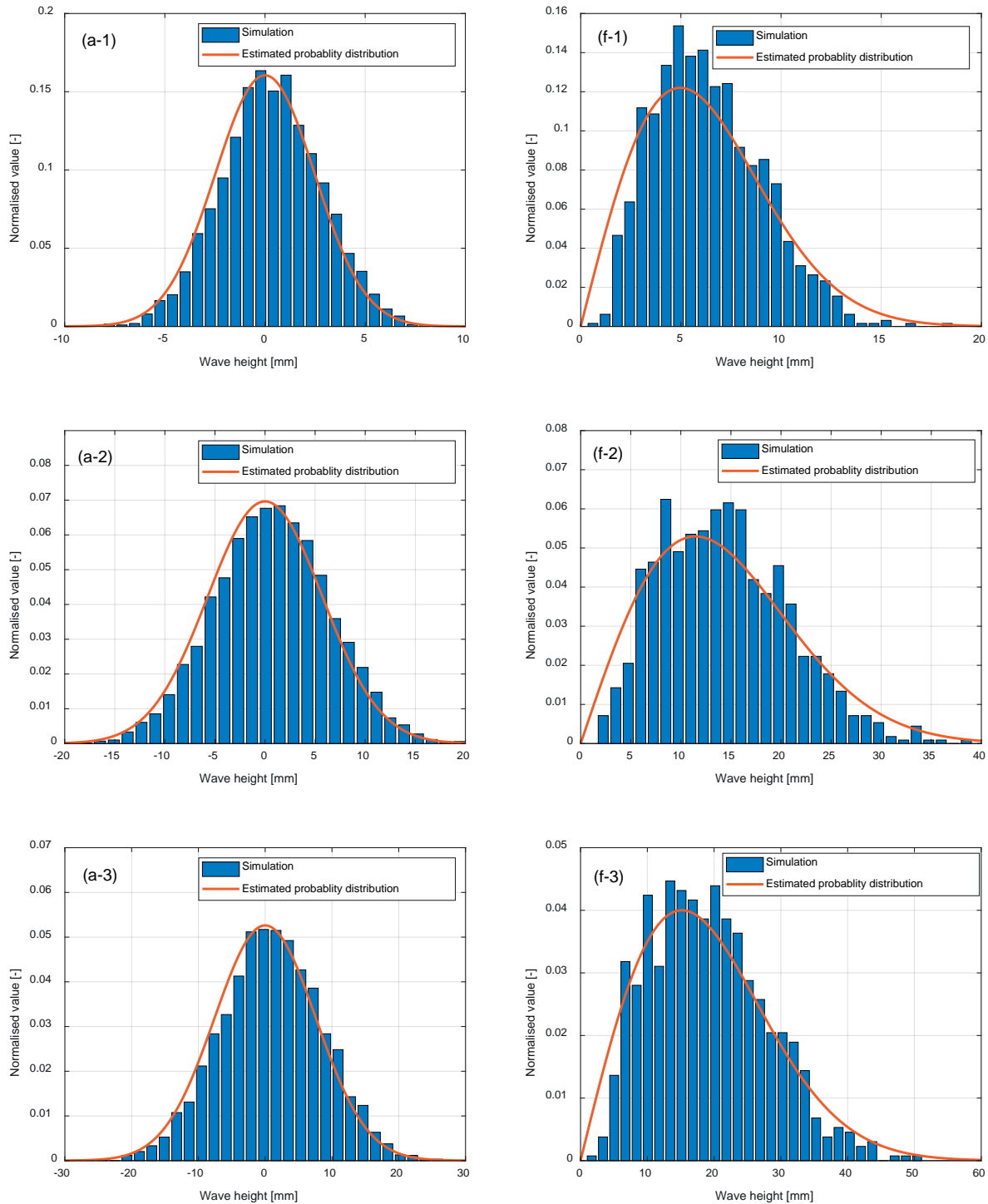
Fig. 8. Distributions of (a) wave amplitudes and (f) frequency of deviations from the mean value for (1) weak, (2) medium and (3) strong winds

The frequency of the wave height deviations from the mean value for the simulated waves had a Gaussian distribution, which coincides with the estimated probability of the wind-generated waves for each point on the BFT scale. A high level of compliance was observed for the model in this regard. All wave amplitudes were characterised by a Rayleigh distribution. The highest level of alignment with the estimation was observed for the strongest wind force (Fig. 8f-3). For a weak wind (4 BFT), the amplitudes of the generated waves were higher than expected, close to the maximum of the distribution function. In the case of a medium wind (6 BFT), a high degree of compliance was seen for the maximum of the distribution, although more waves were generated in its vicinity than expected from theory.

Fig. 9 shows examples of (a) measured and (b) digitally generated wave heights for a mean wind force of 4 BFT. Statistical parameters such as the minimal, maximal, and mean values and the standard deviation are marked by dashed lines. Their numerical values are summarised in Table 5.
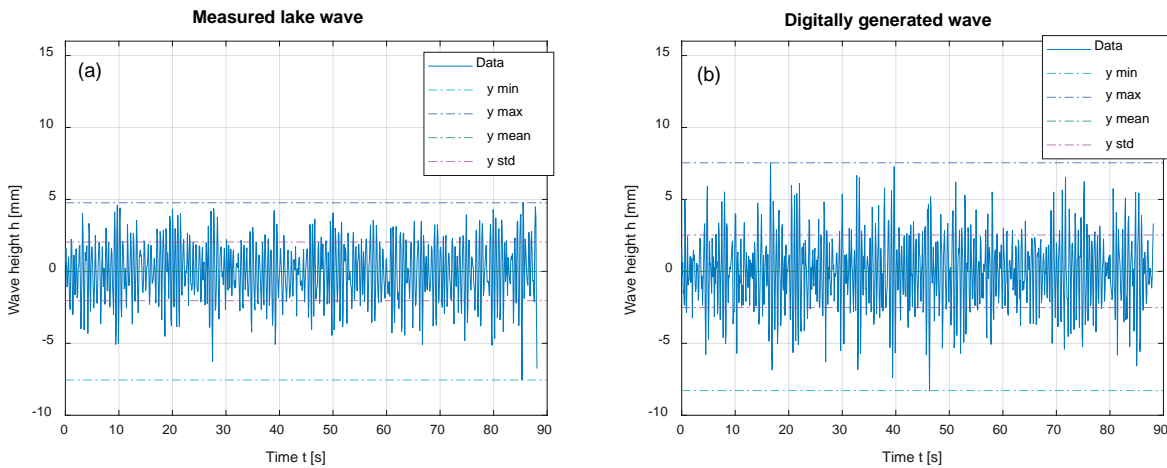
Fig. 9. Statistical parameters for waves under a wind of 4 BFT: (a) measured, (b) digitally generated
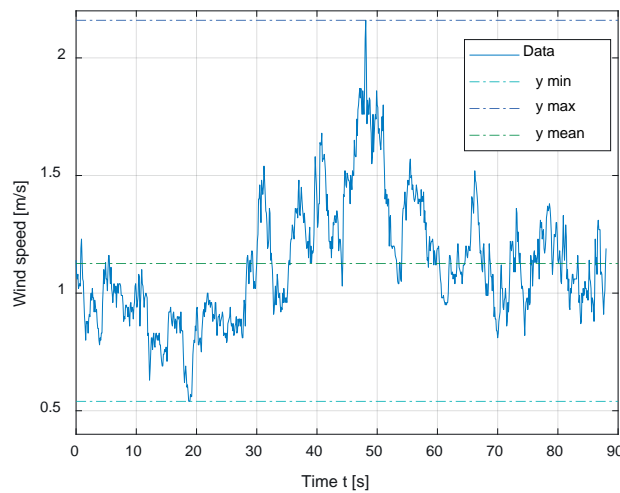
Fig. 10. Time series data for measured wind speeds

Tab. 5. Statistics for wave time histories for a wind of 4 BFT

Parameter	Measured	Simulated
Min. value [mm]	−7.55	−8.28
Max. value [mm]	4.76	7.54
Mean value [mm]	0	0
Standard deviation [mm]	2.04	2.54

In the simulation, a wave was generated under a constant mean wind speed $\bar{v}_w$ [m/s] (4 BFT), as indicated by the green dashed line in Fig. 10, while the wave measured on the lake was induced by a real, variable wind, marked on this figure by the solid line. The wind speed stabilised over the last 30 s, and the wave amplitudes in this time period varied by about 15% (0.75 mm). A difference of 25% can be observed in the standard deviation between the measured and digitally generated waves. The main reason for the difference in the amplitudes of the waves is the inconsistency in the wind causing the waves. Both wave signals are shown in Fig. 11.
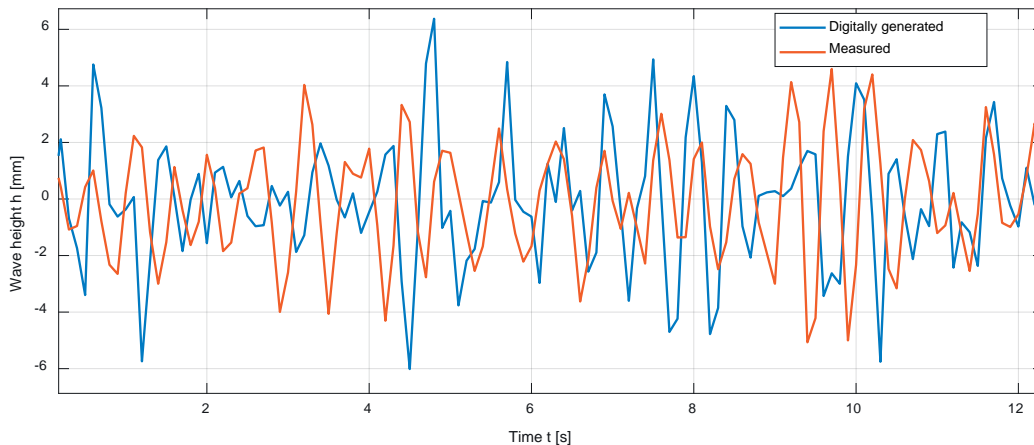
Fig. 11. Direct comparison of measured and generated waves as a function of time

In contrast, however, a distinctive similarity in the results can be seen for both the period and the amplitude. In the digitally generated signal, single waves of higher amplitude than the measured waves were observed. The data presented in Fig. 11 correspond to a wind force of 4 BFT. The occurrence of higher amplitudes is correlated with the distribution of wave amplitudes (Fig. 8f-1), where higher values for the wave heights are seen than expected from theory. The above-mentioned discrepancies do not exceed 2 mm, meaning that when modelling the external disturbances to the motion of the ship, this can be considered to have a negligible impact on the operation of the model ship.

CONCLUSIONS

The following conclusions may be drawn from the research reported in this paper:
- Based on an empirical description of the PSD of waves generated by the wind on a small lake, a digital simulator of this process could be constructed.
- The simulator consisted of a group of parallel connected shaping filters for the reconstruction of the wave signal for particular wind BFT, and was easy to implement, analyse and verify.
- The relative errors in the wave reproduction did not exceed 10%. This is an acceptable level for a wave generator for a motion control simulation of a ship.
- Unlike in open sea conditions, the dependencies of the heights and periods of significant waves on the wind force did not follow quadratic and linear relationships, respectively, for all values of force. Flattening was shown above a certain range of values.
- The time series of irregular waves generated by the simulator exhibited properties characteristic of real waves, such as a proportionally increasing height and a lengthening period as the wind strength increased.

ABBREVIATIONS USED

BFT – Beaufort wind scale
GWN – Gaussian white noise
IIR – Infinite impulse response filter
ITTC – International Towing Tank Conference
LSM – Least squares method
LTI – Linear time-invariant
PSD – Power spectral density
RMSE – Root mean square error
SOS – Second-order section

REFERENCES

1. H. L. Alfheim, K. Muggerud, M. Breivik, E. F. Brekke, E. Eide, and Ø. Engelhardtsen, "Development of a dynamic positioning system for the ReVolt model ship," IFAC-PapersOnLine, vol. 51, no. 29, pp. 116–121, Sept. 2018, doi: 10.1016/j.ifacol.2018.09.479.

2. J. C. Allan and R. M. Kirk, "Wind wave characteristics at Lake Dunstan, South Island, New Zealand," New Zeal. J. Mar. Fresh., vol. 34, no. 4, pp. 573–591, Mar. 2000, doi: 10.1080/00288330.2000.9516959.

3. A. M. Bassam, A. B. Phillips, S. R. Turnock, and P. A. Wilson, "Experimental testing and simulations of an autonomous, self-propulsion and self-measuring tanker ship model," Ocean Eng., vol. 186, pp. 106065, Aug. 2019, doi: 10.1016/j.oceaneng.2019.05.047.

4. C. Drews, "Using wind setdown and storm surge on Lake Erie to calibrate the air-sea drag coefficient," PLOS ONE, vol. 8, no. 8, pp. 1–16, Aug. 2013, doi: 10.1371/journal.pone.0072510.

5. O. M. Faltinsen, Sea Loads on Ships and Offshore Structures, Cambridge University Press, Cambridge – New York, 1990.

6. T. I. Fossen, Handbook of Marine Craft Hydrodynamics and Motion Control, John Wiley & Sons, Ltd, 2011, doi:10.1002/9781119994138.

7. W. Gierusz and M. Rybczak, "Effectiveness of multidimensional controllers designated to steering of the motions of ship at low speed," Sensors, vol. 20, no. 12, p. 3533, Jun. 2020, doi: 10.3390/s20123533.

8. T. Holton, Digital Signal Processing: Principles and Applications, Cambridge University Press, 2021, doi:10.1017/9781108290050.

9. K-R. Jin and Z-G Ji, "Calibration and verification of a spectral wind–wave model for Lake Okeechobee," Ocean Eng., vol. 28, no. 5, pp. 571–584, May 2001, doi: 10.1016/S0029-8018(00)00009-3.

10. A. Klockner, A. Knoblach and A. Hackmann, "How to shape noise spectra for continuous system simulation," Math. Comp. Model. Dyn., vol. 23, no. 3, pp. 284–300, Feb. 2017, doi:10.1080/13873954.2017.1298622.

11. J. Ley and O. el Moctar, "A comparative study of computational methods for wave-induced motions and loads," J. Mar. Sci. Eng., vol. 9, no. 1, p. 83, Jan. 2021, doi: 10.3390/jmse9010083.

12. A. Miller and A. Rak, "Measurement system for the environmental load assessment of the scale ship model," Sensors, vol. 23, no. 1, p. 306, Dec. 2022, doi: 10.3390/s23010306.

13. A. Miller and A. Rak, "A measurement system for the environmental load assessment of a scale ship model–Part II," Sensors, vol. 23, no. 7, p. 3415, Mar. 2023, doi: 10.3390/s23073415.

14. L. Morawski, J. Pomirski, P. Sikora, and R. Sokół, "Measurement system for wind and waves characteristics registration on the Silm Lake," TransNav: International Journal on Marine Navigation and Safety of Sea Transportation, vol. 4, no. 2, pp. 205–207, Jun. 2010, doi:10.1201/9780203869345.ch83

15. L. P. Perera, L. Moreira, F. P. Santos, V. Ferrari, S. Sutulo, and C. Guedes Soares, "A navigation and control platform for real-time manoeuvring of autonomous ship models," IFAC Proc. Vol., vol. 45, no. 27, pp. 465–470, 2012, doi: 10.3182/20120919-3-IT-2046.00079.

16. W. J. Pierson Jr. and L. Moskowitz, "A proposed spectral form for fully developed wind seas based on the similarity theory of S. A. Kitaigorodskii," J. Geophys. Res., vol. 69, no. 24, pp. 5181–5190, Dec. 1964, doi:10.1029/JZ069i024p05181.

17. Shiphandling Research and Training Centre. [Online]. Available: http://www.ilawashiphandling.com.pl [Accessed 15 April 2023].

18. C. T. Stansberg, G. Contento, S. Hong, M. Irani, S. Ishida, and R. Mercier, "The Specialist Committee on Waves final report and recommendations to the 23rd ITTC," In: Proceedings of the 23rd ITTC, Venice, Italy, 8–14 Sep. 2002, pp. 505–736.

19. D. N. Sugianto, M. Zainuri, A. Darari, S. S. Darsono and N. Yuwono, "Wave height forecasting using measurement wind speed distribution equation in Java Sea, Indonesia," International Journal of Civil Engineering and Technology, vol. 8, no. 5, pp. 604–619, May 2017.

20. M. Tomera, "Hybrid switching controller design for the maneuvering and transit of a training ship," Int. J. Appl. Math. Comput. Sci., vol. 27, no. 1, Mar. 2017, pp. 63–77. doi:10.1515/amcs-2017-0005.

21. A. Tsvetkova and M. Hellström, "Creating value through autonomous shipping: An ecosystem perspective," Marit. Econ. Logist., vol. 24, no. 2, pp. 255–277 Jun. 2022, doi: 10.1057/s41278-022-00216-y.

APPLICATION OF FUEL COLD ENERGY IN CO₂ BOG RELIQUEFACTION SYSTEM ON AMMONIA-POWERED CO₂ CARRIER

Yiqun Lin [ID]
Jie Lu [ID]
Boyang Li [ID] *
Yajing Li
Qingyong Yang
College of Electromechanical Engineering, Qingdao University of Science and Technology, China

* Corresponding author: *qdlby@126.com (Boyang Li)*

ABSTRACT

A CO₂ boiled off gas (CO₂ BOG) reliquefaction system using liquid ammonia cold energy is designed to solve the problems of fuel cold energy waste and the large power consumption of the compressor in the process of CO₂ BOG reliquefaction on an ammonia-powered CO₂ carrier. Aspen HYSYS is used to simulate the calculation, and it is found that the system has lower power consumption than the existing reliquefaction method. The temperature of the heat exchanger heater-1 heat flow outlet node (node C-4) is optimised, and it is found that, with the increase of the node C-4 temperature, the power consumption of the compressor gradually increases, and the liquefaction fraction of CO₂ BOG gradually decreases. Under 85% conditions, when the ambient temperature is 0°C and the temperature of node C-4 is -9°C, the liquid fraction of CO₂ BOG reaches the maximum, which is 74.46%, and the power of Compressor-1 is the minimum, which is 40.90 kW. According to this, the optimum temperature of node C-4 under various working conditions is determined. The exergy efficiency model is established, in an 85% ship working condition with the ambient temperature of 40°C, and the exergy efficiency of the system is the maximum, reaching 59.58%. Therefore, the CO₂ BOG reliquefaction system proposed in this study could realise effective utilisation of liquid ammonia cold energy.

Keywords: mmonia-powered CO₂ carrier; liquid ammonia cold energy; CO₂ BOG; reliquefaction system; Aspen HYSYS

INTRODUCTION

In recent years, a large amount of CO₂ emission has intensified the greenhouse effect, so reducing man-made CO₂ emission has become an urgent problem to solve. Bui et al. [1], Aradottir et al. [2], and Onarheim et al. [3]considered that carbon capture and storage (CCS) is an effective method to reduce carbon dioxide emissions, so CCS technology has attracted wide attention from various industries. At present, the common storage methods are CO₂ hydrate seafloor sequestration [4], liquefied seafloor sequestration [5], mine sealing [6], ore carbonisation [7] and so on. In this study, the

liquefaction method in the liquefaction seafloor storage will be studied. Usually when CO₂ is sequestered, it needs to be transported across regions and countries to specific locations for sequestering, for example, in Iceland, where storage capacity is high [8], but for the long-distance transport of liquefied carbon dioxide (LCO₂), ship transportation is a better choice than pipeline transportation [9].

LCO₂ is usually transported on ships by placing storage tanks in the ship's cargo hold, so the temperature and pressure for LCO₂ transport should be considered. Hegerland [5] points out that, in order to reduce the investment cost of the LCO₂ storage tanks, it is necessary to get as close to the triple point of CO₂ as

possible (5.17 bar, -56.6℃). However, in practical engineering applications, the temperature of the LCO₂ should not be lower than -50℃, because when the temperature and pressure are close to the triple point of CO_2 [10], LCO_2 easily forms dry ice, which will lead to the risk of pipeline blockage. Due to the low storage and transportation temperature of LCO_2, there is a large temperature difference with the outside environment, so the LCO_2 storage tank will generate infiltration heat, which leads to CO_2 boiled off gas (CO_2 BOG). In order to reduce the infiltration heat, it is necessary to add an insulation layer on the LCO_2 storage tank, but there is still a large temperature difference between the tank and the outside environment and it still generates infiltration heat, with the result that the LCO_2 produces a small amount of BOG. Due to the long route and sailing time of CO_2 carriers, more and more CO_2 BOG will be generated. If the CO_2 BOG is not processed and is directly discharged into the atmosphere, it will also contribute further to the greenhouse effect. Therefore, a CO_2 reliquefaction system must be set up on CO_2 carriers to reliquefy a small amount of CO_2 BOG [11].

More and more scholars are looking for new technologies to apply for BOG reliquefaction on ships [12]]. Alabdulkarem et al. [13] carried out research on the CO_2 liquefaction process and proposed to use NH3 as the refrigerant, which can reduce the energy consumption of the CO_2 reliquefaction system. Other scholars have also studied more novel methods, such as absorption refrigeration [14] and turbine expander applications [15]. Seo et al. [16] proposed four different CO_2 liquefaction systems and determined their design parameters through multiple process simulations and optimisation. Decarre et al. [17] proposed a CO_2 liquefaction process using two cooling cycles and a reliquefaction system. Duan et al. [18] proposed a liquefaction method that uses waste heat to drive ammonia refrigeration, and then uses a booster pump to achieve CO_2 supercharging. Zahid et al. [19] proposed a new method of CO_2 liquefaction with low energy consumption. Awoyomi et al. [20] proposed the use of a two-stage reliquefaction cycle to recover evaporated gas and capture emitted carbon dioxide. Sang and Min [21] and Deng et al. [22]] studied the influence of impurities on the CO_2 BOG reliquefaction system, and concluded that impurities may increase the risk of the system reliquefaction and affect the cost of CO_2 liquefaction; the cost of liquefaction is lower for pure CO_2, and 34% higher for CO_2 containing impurities Y. Lee et al. [23] studied the reliquefaction characteristics of CO_2 and proposed a feasible scheme for a CO_2 BOG reliquefaction process suitable for large carriers, which is conducive to the further development of liquefied CO_2 carriers. Muhammad et al. [24] proposed a CO_2 liquefaction system and found that a lower pressure and cooling temperature could improve the system performance. A CO_2 BOG reliquefaction system will consume a large amount of energy, and a research focus in the industry is now to seek a method to reduce the energy consumption of ships [25]. Therefore, it is particularly important to find a method to reduce the energy consumption of CO_2 BOG reliquefaction.

In recent years, in order to reduce the emission of ship exhaust pollutants, the International Maritime Organization (IMO) has put forward increasingly strict ship exhaust emission policies [26], in which clean fuels such as ammonia [27], LNG [28], and hydrogen [29] keep emerging. Frankl et al. [30] and Mounaim-Rousselle et al. [31] proposed that the combustion of ammonia fuel can achieve "zero carbon" emission, making it undoubtedly a more ideal carbon-free fuel for CO_2 carriers. Ammonia fuel is usually stored on the ship in the form of low-temperature liquid (liquid ammonia), and the storage temperature is -33.5℃ [32]. Liquid ammonia fuel needs to be heated to the supply temperature of the ship's main engine before being used. In this process, the ammonia fuel will release cold energy, but most of this cannot be fully utilised and is therefore wasted. Liquid ammonia has just started to be used as a clean marine fuel and has not been widely used, and research on the utilisation technology of liquid ammonia cold energy is relatively scarce. In addition, the cold energy released by liquid ammonia fuel is relatively small. Therefore, how to make full use of this part of the cold energy is another research hotspot in the industry.

As cold energy is required to reliquefy the small amount of CO_2 BOG produced by an ammonia-powered CO_2 carrier, the cold energy released on the carrier can therefore be used in the CO_2 BOG reliquefaction process. However, the temperature of liquid ammonia is -33.5℃, which may be higher than that of LCO_2 under different transport temperatures. Therefore, it is urgent to find a solution that can use liquid ammonia cold energy in the CO_2 reliquefaction process on CO_2 carriers.

In this study, it is proposed to utilise the liquid ammonia cold energy of the CO_2 BOG reliquefaction process in an ammonia-powered CO_2 carrier, which can not only greatly reduce the power consumption in the process of reliquefaction, but also make full use of the ammonia fuel cold energy released by the carrier, thus solving the problem of wasting this cold energy. This makes the super environment-friendly ammonia-powered CO_2 carrier more in line with the requirements of energy conservation and emission reduction. In this study, a CO_2 BOG reliquefaction system using liquid ammonia cold energy is first proposed. The process and numerical calculation are carried out for the system using Aspen HYSYS, the parameter optimisation of the system is completed, and the node parameters affecting the heat exchanger heat transfer rate, the compressor power consumption and the liquefaction fraction rate of CO_2 BOG are optimised. An exergy efficiency model is established to verify the feasibility of the system, and can provide a theoretical basis and technical support for large-scale application in ammonia-powered CO_2 carriers in the future.

RESEARCH BASIS

ESTABLISHMENT OF MODEL

The CO_2 carrier of a shipyard in China is selected as the research object. Its conceptual ship model is shown in Fig. 1. The main engine power of the ship is 15,000 kW, the ship can carry 50,000 m³ of LCO_2, and liquid ammonia is used as fuel. Other parameters of the ship are shown in Table 1.
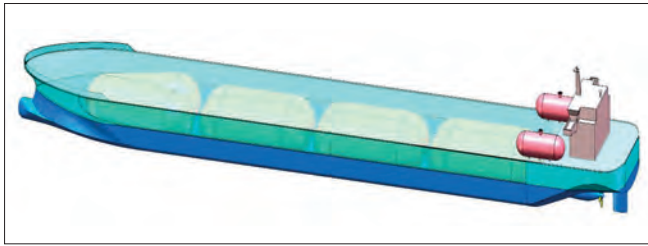
Fig. 1. Research object model diagram

Tab. 1 Main parameters of the CO_2 carrier

Parameter	Value	Parameter	Value
Length overall (m)	230.15	Draft (m)	13.5
Breadth moulded (m)	31.6	Loading (m³)	50780.7
Depth (m)	21.9	Main engine power (kW)	15000
Pressure of LCO2 (kPa)	659	Cargo hold temperature (°C)	-50

At a certain temperature, CO_2 is in liquid state when it reaches the saturation pressure of CO_2 at this temperature. At different temperatures, the liquefaction pressure of CO_2 is different, and the corresponding relationship between the saturation pressure and temperature is shown in Fig. 2.
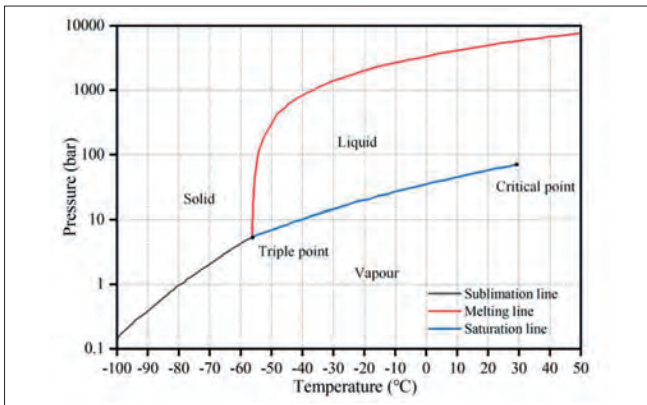
Fig. 2. Phase diagram of CO_2 pressure and temperature

As can be seen from Fig. 2, when the temperature of the CO_2 is less than -40℃, its saturation pressure is less than 10 bar; when the temperature is more than -40℃, the saturation pressure is more than 10 bar. A higher saturation temperature can reduce the cold energy required for CO_2 liquefaction, but a higher temperature requires a higher transport pressure. Thus, this means a higher requirement on the pressure of the LCO₂ storage tank. Usually, the temperature range of LCO₂ transported by ships is -50 ~ -20℃ [11], and the corresponding saturation pressure is 6.59 ~19.7 bar. In addition, the density of LCO₂ is different at different transport temperatures, which will also affect the transport volume of the LCO₂. Its density can be calculated by Aspen HYSYS when the temperature is between -50℃ and -20℃ (5℃ is a temperature gradient). Li and Yan [33] proposed that the Peng–Robinson (PR) and Soave–Redlich–Kwong (SRK) equations of state can both be used to calculate the saturation pressure, and the average absolute deviation compared with the actual measured data is less than

3%. However, SRK should be excluded during liquefaction and reliquefaction as they are not recommended if the temperature is below 290 K. Therefore, in this study, the PR equation of state is adopted and the results are summarised in Table 2.

Tab. 2. LCO₂ density at different temperatures

Temperature (°C)	-50	-45	-40	-35	-30	-25	-20
Density (kg/m³)	1151	1132	1114	1094	1074	1053	1031

As can be seen from Table 2, as the liquefaction temperature of the CO_2 increases, its density gradually decreases. Compared with low transport temperature, to transport the same mass of LCO₂, a larger tank volume is required at a high transport temperature, which increases the investment cost of tank construction. Irrespective of low- or high-temperature transportation, there is still a large temperature difference between the temperature of the LCO₂ and the ambient temperature, and the existence of infiltration heat will cause the evaporation of LCO₂. In order to reduce the evaporation, it is still necessary to add an insulating layer on the LCO₂ tank. Therefore, compared with low-temperature transportation, the insulating layer does not decrease but, on the contrary, increases the cost, with the requirement for the tank to have a greater bearing capacity. Since the LCO₂ storage temperature on land is -20.0°C [34], and on ships is roughly between -50°C and -20.0°C, considering the density of LCO₂, the higher the temperature, the lower the density, so the tank at -50.0°C may be more advantageous than at -20.0°C. That is, the amount of LCO₂ stored per unit of storage volume can be increased by 12%. The transport temperature of -50°C and the transport pressure of 6.59 bar are used in this study. Y. Lee et al. [23] and Engel et al. [35] also proposed that a -50°C transport temperature is desirable.

PREREQUISITES

Although the insulating layer is added to the LCO₂ storage tank, due to the large temperature difference between the inside and outside of the tank, the LCO₂ in the tank will still have heat exchange with the outside air, generating infiltration heat and resulting in the generation of CO_2 BOG. However, the volume of the storage tank is fixed. If there is more CO_2 BOG, the pressure in the storage tank will be too high and can easily cause damage to the tank, so the CO_2 BOG should be treated or released. If it is discharged directly into the atmosphere, it will aggravate the greenhouse effect, so it should instead be reliquefied.

Based on the route characteristics of the ammonia-powered LCO₂ carrier, the external ambient temperature of the storage tank varies greatly during the voyage. Under different external ambient temperatures, the amount of CO_2 BOG in the storage tank is different. In order to calculate the amount of CO_2 BOG in the tank under different external environments, a variety of ambient temperatures are selected in this study, which are 0°C, 10°C, 20°C, 30°C and 40°C, respectively, and the amount of CO_2 BOG under the different ambient temperatures is calculated. The calculation method is as follows:

(1) Calculation of heat transfer coefficient k

Heat transfer coefficient k:

$$k = \frac{1}{\frac{1}{h_w} + \frac{\delta_i}{\lambda_i} + \frac{1}{h_n}} \qquad (1)$$

In the formula,

h_n is the heat transfer coefficient of the inner wall, W/(m²·k).

It is calculated as follows: the LCO₂ storage tank is made of 5Ni steel with a thickness of 7 mm and the temperature inside the tank is -50°C. The data in Table 3 are the heat conduction coefficient of the 5Ni steel at different temperatures [36]. The heat conduction coefficient of the tank inner wall can be calculated by interpolation.

Tab. 3. Heat conduction coefficient of 5Ni steel at different temperatures

Temperature (k)	75.15	97.15	103.2	120.2	151.2	201.2	251.2	300.2
Heat conduction coefficient (W/(m))	13.1	16.1	17.3	19.3	21	24.8	27.4	29.2

The heat conduction coefficient of the storage tank inner wall is as follows:

$$\frac{(27.4-24.8)\times(223-201.2)}{251.2-201.2} + 24.8 = 25.93 \text{ W/(m·}k)$$

The thickness of the storage tank is designed as 7 mm, and the heat transfer coefficient of the inner wall can be calculated:

$$h_n = \frac{25.93}{0.007} = 3704.29 \text{ W/(m²·}k)$$

h_w is the convective heat transfer coefficient of the outer wall, W/(m²·k).

Using the same method, taking the external temperature of 20°C as an example, the thermal conductivity of the tank outer wall can be calculated:

$$\frac{(29.2-27.4)\times(293-251.2)}{300.20-251.20} + 27.4 = 28.94 \text{ W/(m·}k)$$

Thus, the heat transfer coefficient of the tank outer wall can be calculated:

$$h_w = \frac{28.94}{0.007} = = 4134.29 \text{ W/(m²·}k)$$

δ_i is the thickness of the thermal insulation material.

The thickness of the insulation layer of the LCO₂ tank is usually 80 ~ 120 mm. In this study, the thickness of the insulation layer is 100 mm.

λ_i is the heat conductivity coefficient of the thermal insulation material, W/(), 0.02 W/(m·k).

The insulation material is the commonly used rigid polyurethane foam, which has a good insulation effect and low heat conductivity of only 0.018~0.024 W/(m·k). In this article, the value is 0.02 W/(m·k), which is obtained through actual investigation.

Through calculation, the heat transfer coefficient k can be calculated:

$$k = \frac{1}{\frac{1}{h_w} + \frac{\delta_i}{\lambda_i} + \frac{1}{h_n}} = \frac{1}{\frac{1}{4134.29} + \frac{0.1}{0.02} + \frac{1}{3704.29}} =$$

$$= 0.199 \text{W/(m²·}k)$$

Since the value of h_w has little influence on the total heat transfer coefficient k, when the external temperatures are 0°C, 10°C, 30°C and 40°C, respectively, the value of the total heat transfer coefficient k remains unchanged at 0.199 W/(m²·k), so this value will be used in subsequent calculations.

(2) Calculation of heat transfer rate Q

$$Q = A \cdot k \cdot \frac{\Delta T}{1000} \qquad (2)$$

In the formula,

A – is the surface area of the tank, m³;
k – is the heat transfer coefficient, W/(m²·k);
Q – is the total heat transfer rate of the tank, kW.

(3) Calculation of evaporation rate R

$$R = \frac{Q \times 24 \times 3600}{r \times V \times \rho} \qquad (3)$$

In the formula,

r – is the vaporisation heat of LCO₂, kJ/kg, here 339.737 kJ/kg [20];
V – is the volume of the tank, m³, and taken in this study as 50780.707 m³;
ρ – is the density of LCO₂ at -50°C, kg/m³, here 1151 kg/m³;
R – is the evaporation rate of LCO₂, %.

(4) Calculation of evaporation capacity Q_{BOG}

$$Q_{BOG} = \frac{v\rho R}{24} \qquad (4)$$

Eqs. (1)~(4) can be used to calculate the amount of CO₂ BOG at different ambient temperatures, and the results are summarised in Table 4.

Tab. 4. Amount of CO₂ BOG at different ambient temperatures

Ambient temperature (°C)	0	10	20	30	40
Evaporation capacity (kg/h)	1299.86	1559.90	1819.83	2079.76	2339.80

DESIGN OF CO₂ BOG RELIQUEFACTION SCHEME

COMPARISON SCHEME

Recently, some scholars have studied using seawater as a cold source for CO₂ BOG reliquefaction [37]. However, the temperature of seawater is higher and so also is the corresponding liquefaction pressure of CO₂. Whether single-stage or multistage compression is adopted, the power consumption of the refrigeration compressor is greater. In addition, the temperature difference between the liquefaction temperature of CO₂ BOG

using seawater as a cold source and the transport temperature of LCO_2 is large, so the LCO_2 needs to be expanded and cooled after liquefaction. However, when the temperature difference is large, the expanded LCO_2 will partially vaporise, resulting in a low liquefaction fraction of CO_2 BOG. The CO_2 BOG reliquefaction system with seawater as the cold source is shown in Fig. 3. It is necessary to compress the CO_2 BOG to the saturation pressure (57.26 bar) corresponding to CO_2 at a temperature higher than that of seawater (20°C). Due to the large compression ratio of the compressor, in order to save compressor power consumption, the method of multistage compression is adopted to realise the liquefaction of the CO_2.
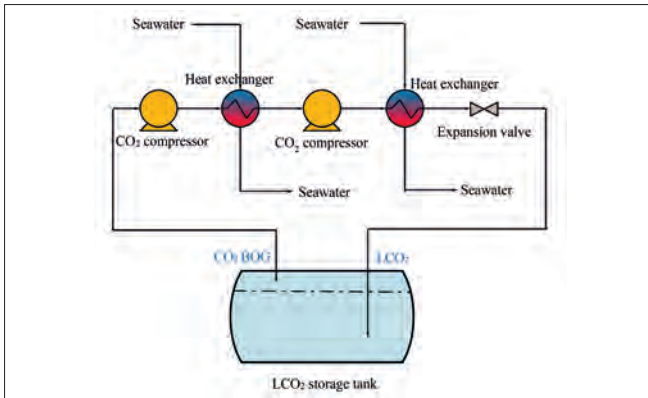
Fig. 3. System diagram of CO_2 BOG liquefaction process

Aspen HYSYS simulation software was used to simulate the liquefaction system in Fig. 3. The setting of the node parameters refers to part of the data in the literature [37], and the flow of CO_2 BOG adopts the calculated value of CO_2 BOG when the external temperature is 20°C in Table 4, which is 1819.83 kg/h. The simulation system diagram and the parameter settings of the key nodes are shown in Fig. 4. Through simulation, it can be obtained that the power consumption of compressor K-1 is 73.36 kW, and compressor K-2 is 28.67 kW, so the total power consumption of the compressor is 102.03 kW. In addition, the vaporisation fraction of node 6 is 51.58%, and the liquefaction fraction rate is only 48.42%.
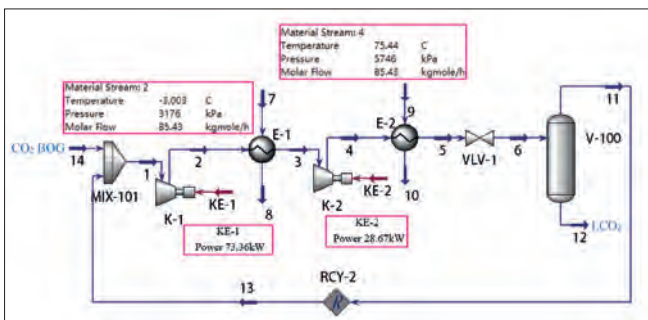
Fig. 4. System simulation diagram of comparison scheme

DESIGN OF CO_2 BOG RELIQUEFACTION SCHEME WITH LIQUID AMMONIA AS COLD SOURCE

According to the above calculation, the main power consumption in the CO_2 BOG reliquefaction system is by

the compressor. To reduce this, it is necessary to reduce the compression ratio of the compressor. The temperature of liquid ammonia is -33.5°C. If it can be used as the cold source of CO_2 BOG reliquefaction, the liquefaction temperature can be reduced, and thus the liquefaction pressure and the power consumption can also be reduced. Based on this, a system that utilises liquid ammonia cold energy in the process of CO_2 reliquefaction is proposed, as shown in Fig. 5.
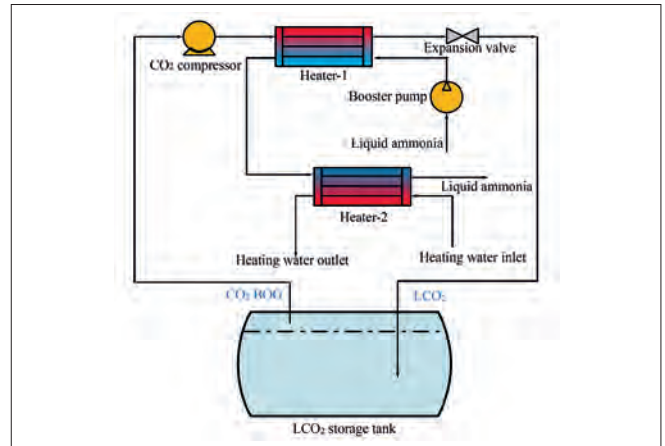
Fig. 5. CO_2 BOG reliquefaction system with liquid ammonia as cold source

The system working principle is as follows: CO_2 BOG produced by the LCO_2 storage tank is first pressurised by the compressor and then enters the heat exchanger Heater-1 to realise liquefaction by using the liquid ammonia cold energy. LCO_2 is a high pressure liquid after liquefaction. In order to meet the storage conditions of the LCO_2, an expansion valve is needed to expand the LCO_2 pressure to the storage pressure and temperature. Then the LCO_2 is returned to the LCO_2 storage tank; liquid ammonia is first supercharged to 80 bar by the booster pump, and then heated by the heat exchanger Heater-1 to release cold energy. However, the temperature of the liquid ammonia still cannot meet the supply temperature of the ship's main engine, so it needs to be heated by the heat exchanger Heater-2 using cylinder liner water heated to about 40°C.

SIMULATION CALCULATION AND RESULTS

The ship uses liquid ammonia as fuel, the calorific value of which is only 18.568 MJ/kg, but the power of the ship's main engine is higher, so it needs a greater ammonia fuel supply. In different ship operating conditions, the supply of liquid ammonia fuel is different, so the cold energy released is also different. In order to study the cold energy release of liquid ammonia under various ship conditions, 55%, 65%, 75%, 80%, and 85% ship working conditions are taken as examples. The amount of liquid ammonia fuel supplied can be calculated, and the results are summarised in Table 5.

Tab. 5. Amount of liquid ammonia fuel supplied under different working conditions

Working condition (%)	55%	65%	75%	80%	85%
Amount of liquid ammonia (kg/h)	3359	3969.7	4580.5	4885.8	5191.2

Based on the system diagram in Fig. 5, a simulation flow diagram is created using Aspen HYSYS, as shown in Fig. 6. In this simulation, the NBS steam equation is selected as the physical property method for the cylinder liner heating water in the system, and the P–R equation is selected as the physical property method for other fluid components. The efficiency of the pump is set at 85%. In this simulation, the entire process is assumed to be static and stable.
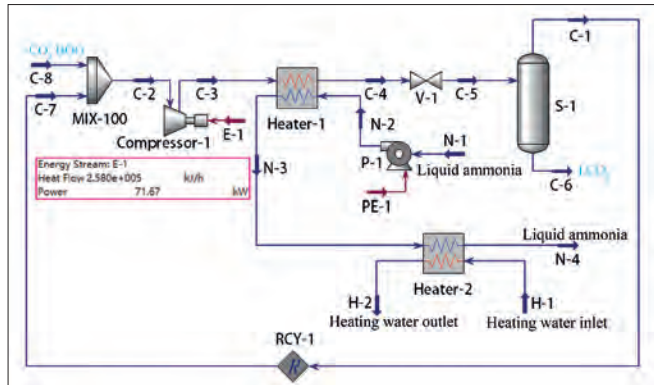
Fig. 6. Simulation system diagram of liquid ammonia as cold source in CO_2 BOG reliquefaction process

Taking the 85% ship working condition and the ambient temperature of 20°C as an example, the parameters of the simulation system in Fig. 6 are set. It can be seen from Table 4 that when the ambient temperature is 20°C, the amount of CO_2 BOG is 1819.83 kg/h, so the flow of node C-2 is set to 1819.83 kg/h. As can be seen from Table 5, when the ship working condition is 85%, the liquid ammonia supply is 5191.2 kg/h, so the flow of node N-1 is set at 5191.2 kg/h. The liquefaction pressure of node C-4 can be calculated according to the liquefaction temperature of node C-4, so as to figure out the pressure of node C-3. The liquefaction temperature of node C-4 is mainly related to the flow of LCO_2 and liquid ammonia, but the temperature of node C-4 should be selected within a range that ensures that no temperature crossing occurs in heat exchanger Heater-1. In order to ensure the normal operation of the simulation system, the temperature of node C-4 is initially selected as -2°C. The settings of the other main simulation parameters are shown in Table 6, and the simulation results of the main nodes are shown in Table 7.

Tab. 6. Setting of main simulation parameters

Nodes	C-2	C-4	C-5	N-1	N-2	N-4	H-1	H-2
Fluid	CO_2	CO_2	CO_2	LNH_3	LNH_3	LNH_3	H_2O	H_2O
Temperature (°C)	-50	-2	-	-33.5	-	40	80	68
Pressure (kPa)	659	-	659	200	8040	-	200	-
Mass flow (kg/h)	1820	-	-	5191	-	-	-	-

By comparing the simulation results of the two systems in Fig. 4 and Fig. 6, it can be found that, when the CO_2 BOG flow is the same, using the liquefaction system shown in Figure 5, the vaporisation fraction of CO_2 is lower, the vaporisation fraction is 30.78% and the liquefaction fraction is 69.22%. In the system,

Tab. 7. Main node simulation results

Nodes	Fluid	Temperature (°C)	Pressure (kPa)	Mass flow (kg/h)	Vapour fraction (%)
C-1	CO_2	-50	659	809.3	100
C-3	CO_2	80.64	3285	2629	100
C-4	LCO_2	-2	3265	2629	0
C-5	CO_2/LCO_2	-50	659	1820	30.78
C-6	LCO_2	-50	659	1820	0
N-1	LNH_3	-33.5	200	5191	0
N-2	LNH_3	-31.82	8040	5191	0
N-3	LNH_3	5.859	8020	5191	0
N-4	LNH_3	40	8000	5191	0
H-1	H_2O	80	200	22540	0
H-2	H_2O	68	500	22540	0

the main power consumption is by Compressor-1, which can be calculated as 71.67 kW by simulation. The compressor power consumption comparison scheme is 102.03 kW. Therefore, the compressor consumes less power in the CO_2 BOG reliquefaction system using liquid ammonia cold energy. This is because, compared with seawater, when using liquid ammonia cold energy the cold source temperature is lower, the liquefaction temperature and saturation pressure corresponding to CO_2 BOG are lower, and the power consumption of the compressor is also lower. In this simulation, the temperature of node C-4 is randomly selected under the condition that temperature crossing does not occur in heat exchanger Heater-1. The corresponding temperature may not be the temperature where the system cold energy is fully utilised and the compressor power consumption is minimal. Therefore, the temperature of node C-4 should be optimised.

RESULT OPTIMISATION

ANALYSIS OF HEAT TRANSFER RATE

When the working condition of the ship is constant, the supply of liquid ammonia fuel is constant. Therefore, the heat transfer rate of Heater-1 indicates the amount of liquid ammonia cold energy that can be used. The heat transfer rate of the heat exchanger is related to the heat exchange temperature difference. For cold flow and heat flow of Heater-1, the temperature of node N-2 (Heater-1 cold flow inlet) is determined according to the temperature of node N-1 (liquid ammonia fuel imports) and the pressure of node N-2. The temperature of node N-1 is equal to the liquid ammonia temperature, so the pressure and temperature of node N-2 are determined. The temperature of node C-3 (Heater-1 heat flow inlet) and N-3 (Heater-1 cold flow outlet) is determined according to the temperature of node C-4 (Heater-1 heat flow outlet). Therefore, the temperature difference of the hot and cold flow of Heater-1 mainly depends on the

temperature of node C-4, which may affect the heat transfer rate of Heater-1. Under a certain ship working condition, with different ambient temperatures, the influence of the node C-4 temperature on Heater-1 is studied by changing the temperature of node C-4. Taking the 85% ship working condition as an example, simulation calculation is carried out for the CO_2 BOG reliquefaction system with liquid ammonia cold energy under different external ambient temperatures, so as to study the heat transfer of Heater-1 under the different temperatures. According to these different temperatures, different node C-4 temperatures are then selected. Under the condition that no temperature crossing occurs in Heater-1, five different temperatures of node C-4 are taken, respectively, including the lowest temperature of node C-4 on the premise of ensuring the normal operation of the heat exchanger. The results are summarised in Fig. 7.

Suppose the heat transfer rate of the heat exchanger is expressed in Q (kJ/h), $Q = LMTD \cdot UA$, where $LMTD$ (°C) is the logarithmic mean temperature difference of the cold flow and heat flow of the heat exchanger and UA (kJ/°C*h) represents the total heat transfer coefficient. As can be seen from Fig. 7 (a)~(e), with the increase of the node C-4 temperature, the LMTD value of Heater-1 is increasing. This is because, as the node C-4 temperature increases,

the temperature difference between the heat flow and cold flow also increases, so the value of LMTD increases. In addition, as the temperature of node C-4 increases, the heat transfer rate of Heater-1 gradually decreases, and according to the formula $Q = LMTD \cdot UA$, as the temperature of node C-4 increases, the value of UA becomes smaller and smaller. It can be seen that the decrease of temperature of node C-4 will increase the heat transfer rate of Heater-1. Under 85% ship working conditions, when the ambient temperature is 0°C and the temperature of node C-4 is -5°C, the heat transfer rate of Heater-1 is the smallest, at 4.46×10^5 kJ/h. When the external ambient temperature is 40°C and the temperature of node C-4 is 3°C, the heat transfer rate of Heater-1 is the highest, at 7.96×10^5 kJ/h.

RELATIONSHIP BETWEEN COMPRESSOR POWER, CO_2 BOG LIQUID FRACTION AND C-4 TEMPERATURE

The temperature of node C-4 is the liquefaction temperature of CO_2 BOG, and the liquefaction pressure of node C-4 can be calculated according to the temperature of node C-4. The pressure drop of Heater-1 is 20 kPa, so the pressure of node C-3
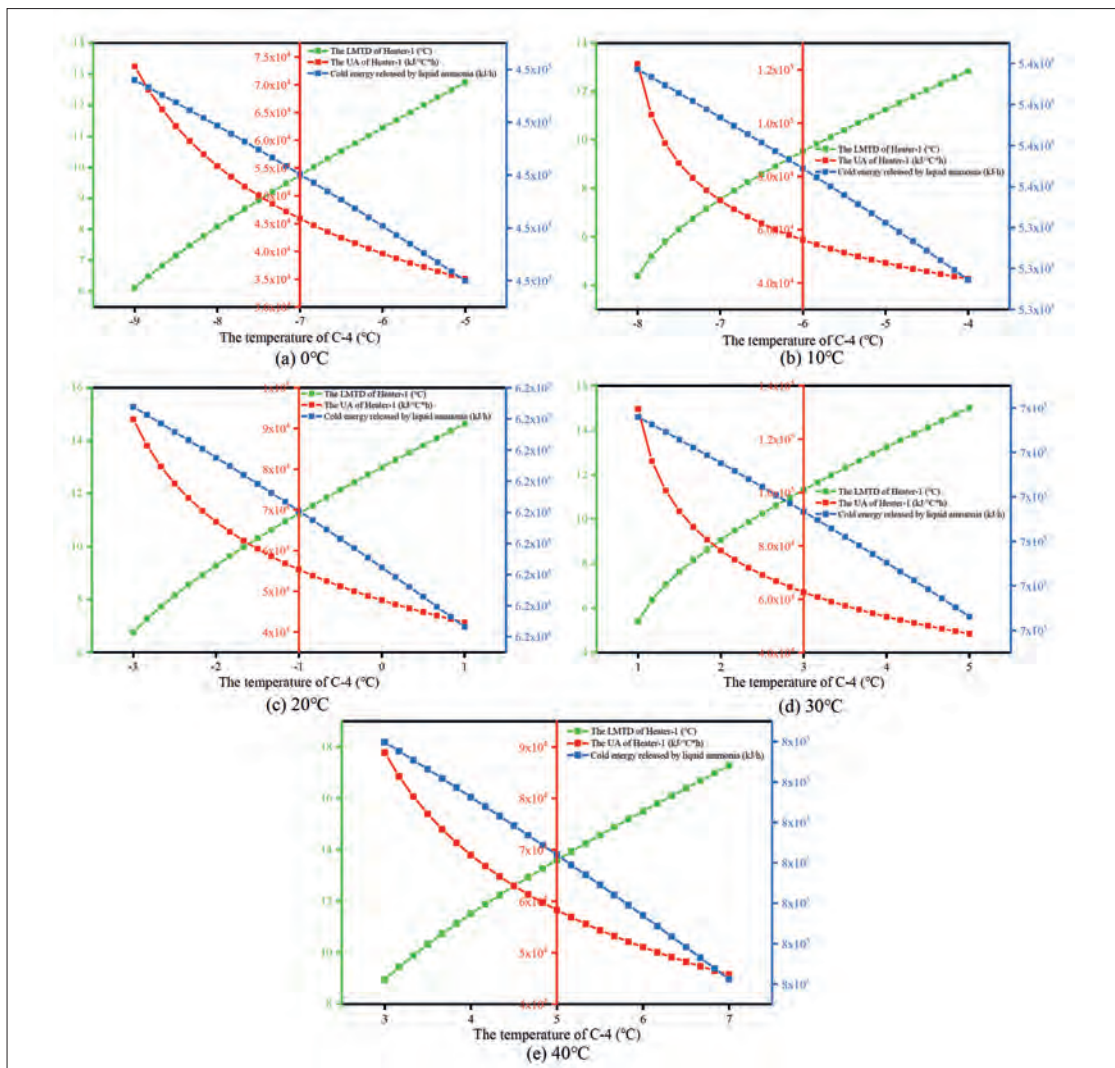
Fig. 7. Variation curves of heat transfer rate of Heater-1 and node C-4 temperature

and compressor power consumption can be calculated, and the compressor power consumption is related to the temperature of node C-4. Meanwhile, at node C-4, the LCO2 is at high pressure and low temperature, but the temperature is still higher than the storage temperature of LCO2. In order to meet the storage conditions, it is necessary to expand and cool the LCO2. After passing through the expansion valve V-1, both the temperature and pressure of the LCO2 are reduced, with the pressure dropping to 659 kPa and the temperature dropping to -50°C. However, partial vaporisation of the LCO2 will occur at this time, and the vaporisation fraction is related to the temperature difference between node C-4 and node C-5. The temperature between node C-5 is set at -50°C, so the value of the vaporisation fraction is determined by the temperature of node C-4. At this time, the proportion of LCO2 is called the liquefaction fraction rate of CO2 BOG. Taking the 85% ship working condition as an example, the relationship between the compressor power and the liquefaction fraction of CO2 BOG and the node C-4 temperature under different external ambient temperatures is studied. A summary of the results is shown in Fig. 8.

From Fig. 8 (a)~(e), it can be seen that, with the increase of the node C-4 temperature, the node C-3 pressure and the power of Compressor-1 gradually increase, while the liquefaction fraction of CO2 BOG gradually decreases. This is because, as the temperature of node C-4 increases, the liquefaction temperature of the CO2 and the corresponding liquefaction pressure also increase gradually. Therefore, the pressure of node C-3 and the power of Compressor-1 increase gradually. At the same time, the temperature and pressure of node C-4 increase, but the temperature and pressure of node C-5 are set and unchanged, so the difference between the temperature and pressure of node C-4 and node C-5 increases, resulting in an increase in the vaporisation fraction of CO2 BOG and a decrease in the liquefaction fraction. By comparing Fig. 8 (a)~(e), it can be found that, under the same ship working condition, the liquefaction fraction gradually decreases and the compressor power consumption gradually increases with the increase of the ambient temperature. This is because, with the increase of the ambient temperature, the temperature difference between the LCO2 storage tank and the ambient environment becomes larger, so the infiltration heat increases and the amount of CO2 BOG also increases; the cold energy required for reliquefaction of the CO2 BOG also increases, but the working conditions of the ship remain unchanged, and the
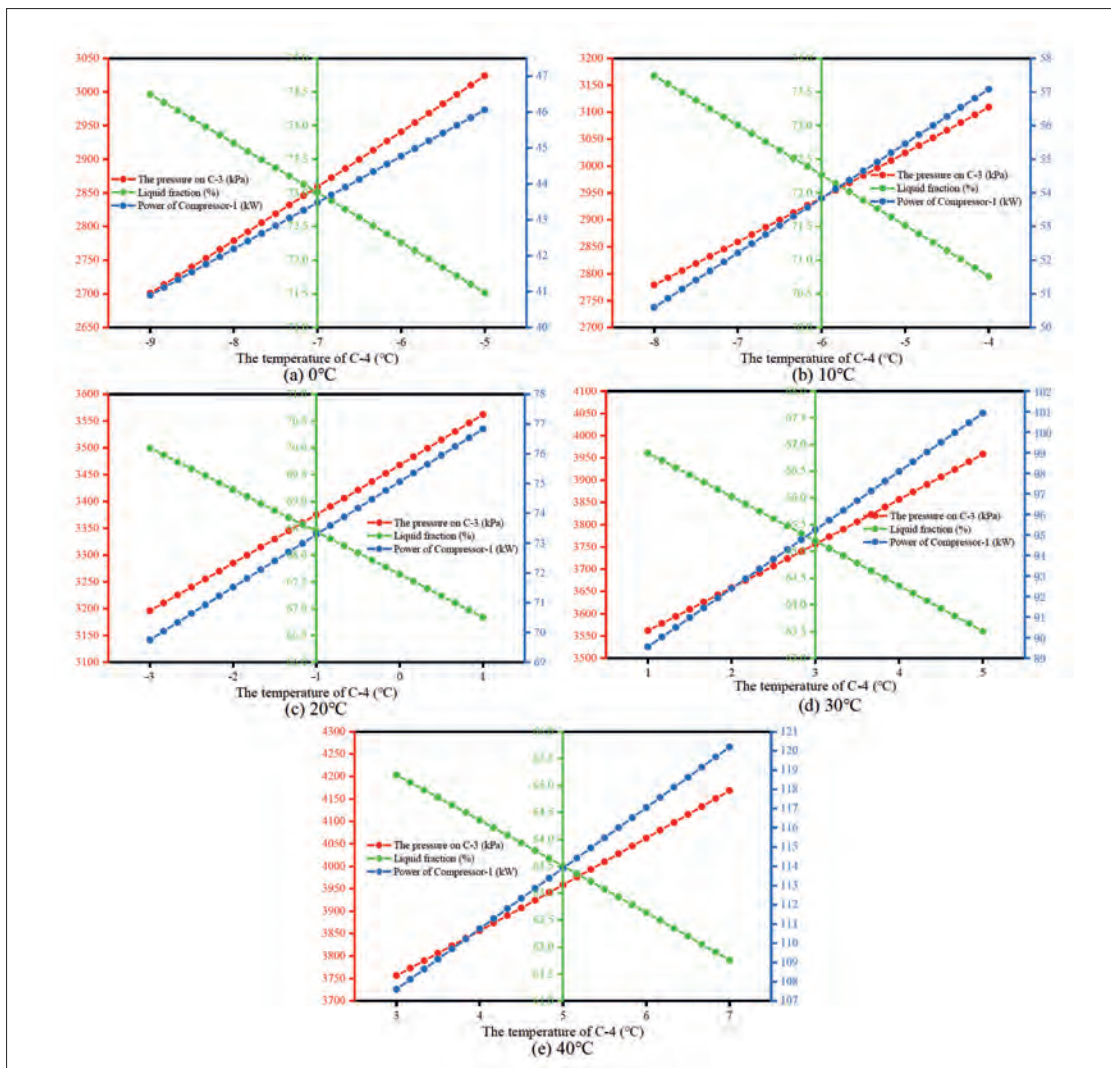
Fig. 8. The relationship between compressor power consumption, CO2 BOG liquid fraction and node C-4 at different ambient temperatures

amount of liquid ammonia consumed per hour is also basically unchanged, so the maximum cold energy released by the system is constant. In order to ensure that temperature crossing does not occur in the normal operation of Heater-1, the higher the ambient temperature is, the higher the temperature setting of node C-4 is. As a result, the liquefaction temperature of CO_2 and the liquefaction pressure increase, as do the pressure of node C-3 and the power of Compressor-1, and the corresponding liquefaction fraction decreases. Under 85% conditions, when the ambient temperature is 0°C and the node C-4 temperature is -9°C, the liquid fraction of CO_2 BOG is the maximum, at 74.46%, and the power of Compressor-1 is the minimum, at 40.90 kW. When the ambient temperature is 40°C and the node C-4 temperature is 7°C, the liquid fraction of CO_2 BOG is the minimum, at 61.76%, and the power of Compressor-1 is the maximum, at 120.2 kW. Under these conditions, when the node C-4 temperature is 3°C, the CO_2 BOG liquefaction fraction is 65.20%, and the power of Compressor-1 is 107.6 kW. In conclusion, reducing the temperature of node C-4 has a positive effect on improving the liquefaction fraction of CO_2 BOG, and also reduces the power consumption of the compressor.

TEMPERATURE DETERMINATION OF NODE C-4

According to the above studies, it can be found that reducing the temperature of node C-4 can increase the heat transfer rate of Heater-1, increase the liquefaction fraction of CO_2 BOG, and reduce the power consumption of the compressor. Therefore, the temperature of node C-4 should be reduced as much as possible in order to ensure the normal operation of the system. Based on this, the lowest temperature of node C-4 under different working conditions and different ambient temperatures of the

ship, as well as the liquefaction fraction of CO_2 BOG and the power consumption of the compressor under the temperature of the C-4 node, are summarised in Fig. 9.

From Fig. 9 (a)~(c), it can be seen that with the increase of ambient temperature, the node C-4 temperature and the power consumption of Compressor-1 gradually increase, while the node C-5 liquefaction fraction decreases under the same ship operating condition. This is because, when the ship is under a certain working condition, the amount of ammonia fuel supplied and the cold energy it can release are also certain. As the ambient temperature increases, the amount of CO_2 BOG that needs to be liquefied keeps increasing. Therefore, the temperature of node C-4 keeps rising; that is, the liquefaction temperature of the CO_2 BOG keeps rising, so the liquefaction pressure corresponding to node C-3 and the power consumption of the compressor gradually increase. The liquefied CO_2 BOG is expanded by the V-1 expansion valve, the LCO_2 will partially vaporise, and an increase in the node C-4 temperature increases the pressure and temperature difference between node C-4 and node C-5. Therefore, the vaporisation fraction of node C-5 will increase, resulting in the reduction of the liquefaction fraction of CO_2 BOG.

From Fig. 9 (a)~(c), it can also be seen that, at the same ambient temperature, the node C-4 temperature and the power consumption of Compressor-1 gradually decrease or remain unchanged, while the node C-5 liquefaction fraction increases or remains unchanged with the increase of ship operating conditions. This is because, when the ambient temperature remains unchanged, the amount of CO_2 BOG that needs to be liquefied remains unchanged. With the increase of the ship working conditions, the liquid ammonia supply and the cold energy that can be released by the system keep increasing.
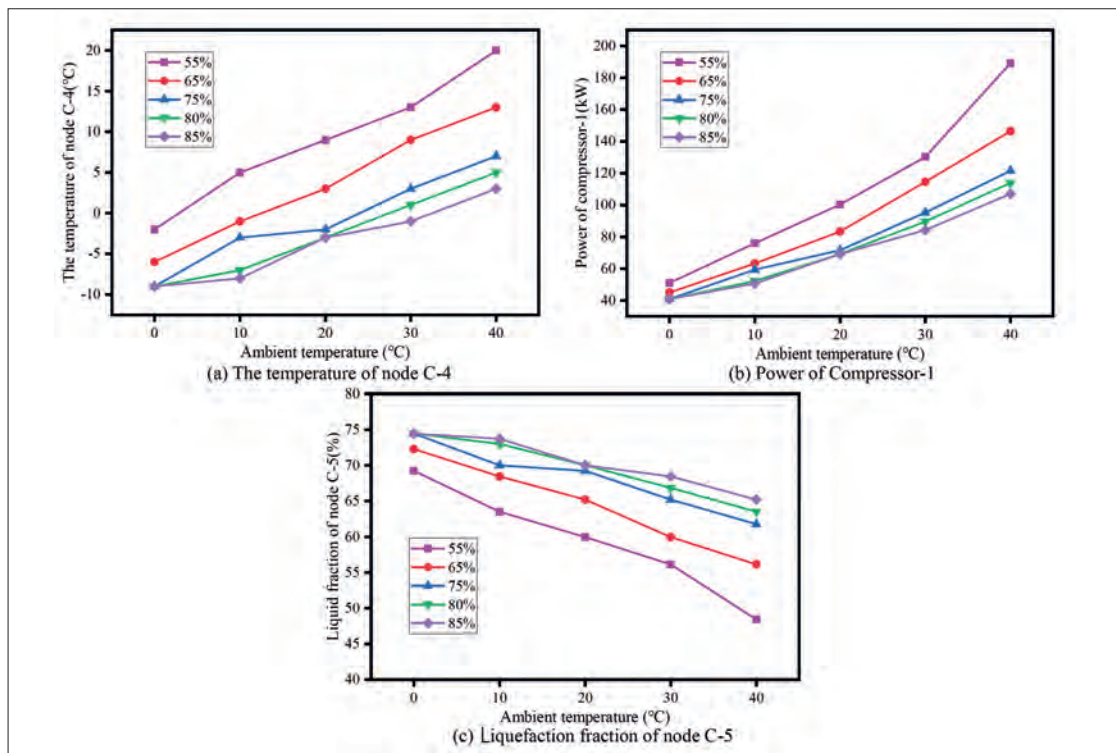
Fig. 9 Variation relationship between main parameters and ambient temperature under different working conditions

Therefore, the temperature of node C-4 keeps decreasing; that is, the liquefaction temperature of the CO_2 BOG decreases and the corresponding liquefaction pressure also decreases. As a result, the power consumption of Compressor-1 decreases gradually, and the temperature difference and pressure difference between node C-4 and node C-5 decrease gradually. After expansion in the expansion valve V-1, the LCO_2 vapour fraction decreases gradually, so the liquefaction fraction increases gradually.

At the same ambient temperature, the node C-4 temperature and the power consumption of Compressor-1 are the minimum when the ship working condition is 85%, and node C-5 has the maximum liquefaction fraction. Taking 85% as an example, when the ambient temperature is 0°C, the node C-4 temperature is -9°C, and the power consumption of Compressor-1 and the liquefaction fraction of node C-5 are 40.81 kW and 74.46%, respectively. When the ambient temperature is 10°C and the node C-4 temperature is -8°C, the power consumption of Compressor-1 and the liquefaction fraction of node C-5 are 50.56 kW and 73.74%, respectively. When the ambient temperature is 20°C and the node C-4 temperature is -3°C, the power consumption of Compressor-1 and the liquefaction fraction of node C-5 are 69.24 kW and 70%, respectively. When the ambient temperature is 30°C, the node C-4 temperature is -1°C, and the power consumption and liquefaction fraction of node C-5 are 84.18 kW and 68.44%, respectively. When the ambient temperature is 40°C and the node C-4 temperature is 3°C, the power consumption of Compressor-1 and the liquefaction fraction of node C-5 are 107.1 kW and 65.2%, respectively.

EXERGY EFFICIENCY ANALYSIS

Exergy of logistics

Assume that the medium of the system is stable flow. For the stable flow system:

$$E_{x,mass} = m[(h - h_0) - T_0(s - s_0)] \tag{5}$$

In the formula, m is the mass flow of the medium; h and s are the specific enthalpy and specific entropy of each medium, respectively.

Exergy efficiency calculation

Exergy efficiency can be used as an important index to evaluate the ability of a system to do external work [38]. In this study, the exergy efficiency can be reflected in the utilisation of liquid ammonia cold energy in the CO_2 BOG reliquefaction system. The exergy efficiency η is equal to the ratio of revenue exergy to payout exergy. The exergy efficiency of each device can be calculated to get the exergy efficiency of the whole system.

(1) Exergy efficiency of heat exchanger

$$\eta_H = \frac{E_{x,in}}{E_{x,p}} \times 100\% \tag{6}$$

In the formula,
$E_{x,in}$ is the revenue exergy, $E_{x,p}$ is the payout exergy.

The revenue exergy of heat-exchanger Heater-1 is the difference between the import exergy and exit exergy of the

heat logistics, while the payout exergy is the difference between the exit exergy and import exergy of the cold logistics. The revenue exergy of heat exchanger Heater-2 is the difference between the exit exergy and import exergy of the cold logistics, while the payout exergy is the difference between the import exergy and exit exergy of the heat logistics.

(2) Exergy efficiency of compressor

The exergy efficiency of the compressor is the ratio of the effective revenue exergy $E_{x,c}$ of a compressor to the power P_C of the compressor. The exergy efficiency of the compressor is as follows:

$$\eta_C = \frac{E_{x,c}}{P_C} \times 100\% \tag{7}$$

The effective revenue exergy $E_{x,c}$ of compressor is the difference between the exit exergy and import exergy of the compressor.

(3) Exergy efficiency of pump

The exergy efficiency of the pump is the ratio of effective power consumption E_{xefc} to the pump power P, and is as follows:

$$\eta = \frac{E_{xeft}}{P} \times 100\% \tag{8}$$

The effective power consumption of the pump E_{xefc} is the difference between the exit exergy and import exergy.

(4) Exergy efficiency of the system

The exergy efficiency of the system is the ratio of the sum of the effective revenue exergy to the sum of the payout exergy in the system, and the calculation formula is as follows:

$$\eta = \frac{\sum E_{x,in}}{\sum E_{x,p}} \times 100\% \tag{9}$$

In the formula,

$$\sum E_{x,in} = E_{x,in} + E_{x,c} + E_{xeft} \tag{10}$$

$$\sum E_{x,p} = E_{x,p} + P_C + P \tag{11}$$

The exergy efficiency of the different equipment and the whole system can be calculated in 55%, 65%, 75%, 80%, and 85% working conditions and in different ambient temperatures according to Eqs. (5)~(11), and is shown in Fig. 10.

The exergy efficiency of Heater-1 mainly represents the effect of the utilisation of cold energy in the system. As can be seen from Fig. 10 (a), the exergy efficiency of Heater-1 decreased gradually with the increase of the ambient temperature, which is because the exergy efficiency of the heat exchanger is mainly related to the heat exchange temperature difference. As can be seen from Fig. 9, with the increase of the ambient temperature, the temperature of node C-4 keeps rising. It can also be seen from Fig. 7 that, as the temperature of node C-4 rises, the LMTD of Heater-1 gradually rises, so the exergy loss of the heat exchanger increases and the exergy efficiency decreases. It can also be seen from Fig. 10 (a) that, under the same ambient temperature, the exergy efficiency of Heater-1 increases with the increase of the ship working conditions. This is because the higher the ship working
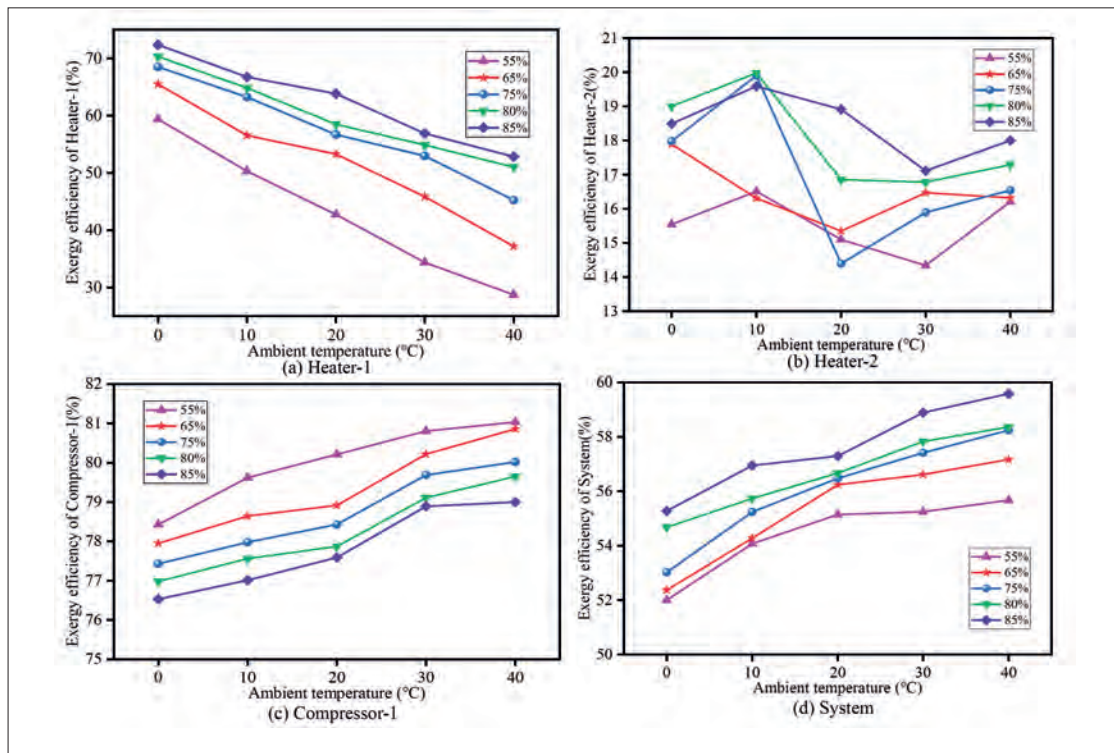
Fig. 10. Exergy efficiency of different devices and system

conditions, the greater the ammonia fuel supply, the richer the cold energy released, and the lower the minimum temperature that node C-4 can achieve. As the LMTD of Heater-1 becomes smaller, its exergy loss will decrease and the exergy efficiency will increase. When the ship working condition is 55% and the ambient temperature is 40°C, the exergy efficiency of Heater-1 is the lowest, at 28.71%; when the ship working condition is 85% and the ambient temperature is 0°C, the exergy efficiency of Heater-1 is the highest, at 72.36%. As can be seen from Fig. 10 (d), when the ship working condition is 85% and the ambient temperature is 0°C, the exergy efficiency of the system is the least, reaching 51.99%. When the ship working condition is 85% and the ambient temperature is 40°C, the exergy efficiency of the system reaches the maximum, which is 59.58%. Therefore, the system proposed in this study could effectively utilise the cold energy of liquid ammonia.

CONCLUSIONS

To address the problems of the waste of liquid ammonia cold energy and the high power consumption in the CO_2 BOG reliquefaction process of ammonia-powered CO_2 carriers, a CO_2 BOG reliquefaction system using liquid ammonia cold energy is proposed. The main conclusions are as follows:

1. A CO_2 BOG reliquefaction system with liquid ammonia as the cold source is designed. Under the same conditions, compared with the existing reliquefaction technology, Aspen HYSYS simulation software is used to establish the process and simulate two systems. The compressor power consumption of the two systems is 102.03 kW and 71.67 kW,

respectively. It can be seen that the use of liquid ammonia cold energy can greatly reduce the compressor power consumption in the process of CO_2 BOG reliquefaction.

2. In order to reduce the compressor power consumption and improve the liquefaction fraction of CO_2 BOG, the node C-4 temperature is optimised and analysed. The results show that, with the increase of the external temperature, the node C-4 temperature and the power consumption of Compressor-1 gradually increase, while the liquefaction fraction of CO_2 BOG decreases. At the same external temperature, the node C-4 temperature and the power consumption of Compressor-1 decrease with the increase of ship operating conditions, while the liquefaction fraction of CO_2 BOG increases; thus, the optimal temperature values of node C-4 in the system under different working conditions are determined. The maximum CO_2 BOG liquefaction fraction after optimisation is 74.46%, and the minimum value of compressor power is 40.81 kW.

3. The exergy efficiency models of the main equipment and the system are established. It is found that, with the increase of the external temperature, the exergy efficiency of Heater-1 decreases gradually. At the same external temperature, the exergy efficiency of Heater-1 increases gradually with the increase of ship working conditions, while the exergy efficiency of the whole system decreases gradually with the increase of the external temperature. The maximum exergy efficiency value of Heater-1 is 72.36%, and the maximum exergy efficiency value of the whole system is 59.58%.

4. In view of this, the CO_2 BOG reliquefaction system using liquid ammonia fuel cold energy proposed in this study

solves the problems of the waste of liquid ammonia cold energy and the high power consumption in the CO_2 BOG reliquefaction process of ammonia-powered CO_2 carriers. This provides a new form of fuel cold energy utilisation for ammonia-powered ships in the future and promotes the development of energy-saving and emission reduction technologies for ships.

REFERENCES

1. M. Bui, C. S. Adjiman, A. Bardow, E. J. Anthony, A. Boston, S. Brown, and N. MacDowell, "Carbon capture and storage (CCS): the way forward," *Energy & Environmental Science*, vol. 11, no. 5, pp. 1062-1176, 2018, doi: 10.1039/C7EE02342A.

2. E. S. P. Aradóttir, H. Sigurdardóttir, B. Sigfússon, and E. Gunnlaugsson, "CarbFix: a CCS pilot project imitating and accelerating natural CO_2 sequestration," *Greenhouse Gases: Science and Technology*, vol. 1, no. 2, pp. 105-118, 2011, doi: 10.1002/ghg.18.

3. K. Onarheim, A. Mathisen, and A. Arasto, "Barriers and opportunities for application of CCS in Nordic industry–A sectorial approach," *International Journal of Greenhouse Gas Control*, vol. 36, pp. 93-105, 2015, doi: 10.1016/j.ijggc.2015.02.009.

4. P. Mekala, M. Busch, D. Mech, R. S. Patel, and J. S. Sangwai, "Effect of silica sand size on the formation kinetics of CO_2 hydrate in porous media in the presence of pure water and seawater relevant for CO_2 sequestration," *Journal of Petroleum Science and Engineering*, vol. 122, pp. 1-9, 2014, doi: 10.1016/j.petrol.2014.08.017.

5. G. Hegerland, T. Jørgensen, and J. O. Pande, "Liquefaction and handling of large amounts of CO_2 for EOR," *Proc. Seventh International Conference on Greenhouse Gas Control Technologies*, vol. 2, pp. 2541–2544, 2005, doi: 10.1016/B978-008044704-9/50369-4.

6. D. E. Clark, E. H. Oelkers, I. Gunnarsson, B. Sigfússon, S. Ó. Snæbjörnsdóttir, E. S. Aradóttir, and S. R. Gíslason, "CarbFix2: CO_2 and H_2S mineralization during 3.5 years of continuous injection into basaltic rocks at more than 250°C," *Geochimica et Cosmochimica Acta*, vol. 279, pp. 45-66, 2020, doi: 10.1016/j.gca.2020.03.039.

7. H. Wu, R. S. Jayne, R. J. Bodnar, and R. M. Pollyea, "Simulation of CO_2 mineral trapping and permeability alteration in fractured basalt: Implications for geologic carbon sequestration in mafic reservoirs," *International Journal of Greenhouse Gas Control*, vol. 109, p. 103383, 2021, doi: 10.1016/j.ijggc.2021.103383.

8. T. M. P. Ratouis, S. Ó. Snæbjörnsdóttir, M. J. Voigt, B. Sigfússon, G. Gunnarsson, E. S. Aradóttir, and V. Hjörleifsdóttir, "Carbfix 2: A transport model of long-term CO_2 and H_2S injection into basaltic rocks at Hellisheidi, SW-Iceland," *International Journal of Greenhouse Gas Control*, vol. 114, p. 103586, 2022, doi: 10.1016/j.ijggc.2022.103586.

9. H. A. Baroudi, A. Awoyomi, K. Patchigolla, K. Jonnalagadda, and E. J. Anthony, "A review of large-scale CO_2 shipping and marine emissions management for carbon capture, utilisation and storage," *Applied Energy*, vol. 287, p. 116510, 2021, doi: 10.1016/j.apenergy.2021.116510.

10. S. Trædal, J. H. J. Stang, I. Snustad, M. V. Johansson, and D. Berstad, "CO_2 liquefaction close to the triple point pressure," *Energies*, vol. 14, p. 8220, 2021, doi: 10.3390/en14248220.

11. S. H. Jeon and M. S. Kim, "Compressor selection methods for multi-stage re-liquefaction system of liquefied CO_2 transport ship for CCS," *Applied Thermal Engineering*, vol. 82, pp. 360-367, 2015, doi: 10.1016/j.applthermaleng.2015.02.080.

12. J. R. Gómez, M. R. Gómez, R. F. Garcia, and A. D. Catoira, "On board LNG reliquefaction technology: a comparative study," *Polish Maritime Research*, vol. 21, pp. 77-88, 2013, doi: 10.2478/pomr-2014-0011.

13. A. Alabdulkarem, Y. H. Wang, and R. Radermacher, "Development of CO_2 liquefaction cycles for CO_2 sequestration," *Applied Thermal Engineering*, vol. 33, pp. 144-156, 2012, doi: 10.1016/j.applthermaleng.2011.09.027.

14. K. Aliyon, M. Mehrpooya, and A. Hajinezhad, "Comparison of different CO_2 liquefaction processes and exergoeconomic evaluation of integrated CO_2 liquefaction and absorption refrigeration system," *Energy Conversion and Management*, vol. 211, p. 112752, 2020, doi: 10.1016/j.enconman.2020.112752.

15. L. E. Øi, N. Eldrup, U. Adhikari, M. H. Bentsen, J. L. Badalge, and S. Yang, "Simulation and cost comparison of CO_2 liquefaction," *Energy Procedia*, vol. 86, pp. 500-510, 2016, doi: 10.1016/j.egypro.2016.01.051.

16. Y. Sen, H. You, S. Lee, C. Huh, and D. Chang, "Evaluation of CO_2 liquefaction processes for ship-based carbon capture and storage (CCS) in terms of life cycle cost (LCC) considering availability," *International Journal of Greenhouse Gas Control*, vol. 35, pp. 1-12, 2015, doi: 10.1016/j.ijggc.2015.01.006.

17. S. Decarre, J. Berthiaud, N. Butin, and J. L. Guillaume-Combecave, "CO_2 maritime transportation," *International Journal of Greenhouse Gas Control*, vol. 4, no. 5, pp. 857-864, 2010, doi: 10.1016/j.ijggc.2010.05.005.

18. L. Duan, X. Chen, and Y. Yang, "Study on a novel process for CO_2 compression and liquefaction integrated with the refrigeration process," *International Journal of Energy Research*, vol. 37, pp. 1453-1464, 2013, doi: 10.1002/er.2951.

19. U. Zahid, J. An, U. Lee, S. P. Choi, and C. Han, "Techno-economic assessment of CO_2 liquefaction for ship transportation," *Greenhouse Gases: Science and Technology*, vol. 4, no. 6, pp. 734-749, 2015, doi: 10.1002/ghg.1439.

20. A. Awoyomi, K. Patchigolla, and E. J. Anthony, "CO_2/SO_2 emission reduction in CO_2 shipping infrastructure," *International Journal of Greenhouse Gas Control*, vol. 88, pp. 57-70, 2019, doi: 10.1016/j.ijggc.2019.05.011.

21. H. J. Sang and S. K. Min, "Effects of impurities on re-liquefaction system of liquefied CO_2 transport ship for CCS," *International Journal of Greenhouse Gas Control*, vol. 43, no. 2, pp. 225-232, 2015, doi: 10.1016/j.ijggc.2015.10.011.

22. H. Deng, S. Roussanaly, and G. Skaugen, "Techno-economic analyses of CO_2 liquefaction: Impact of product pressure and impurities," *International Journal of Refrigeration*, vol. 103, pp. 301-315, 2019, doi: 10.1016/j.ijrefrig.2019.04.011.

23. Y. Lee, K. H. Baek, S. Lee, K. Cha, and C. Han, "Design of boil-off CO_2 re-liquefaction processes for a large-scale liquid CO_2 transport ship," *International Journal of Greenhouse Gas Control*, vol. 67, pp. 93-102, 2017, doi: 10.1016/j.ijggc.2017.10.008.

24. H. A. Muhammad, C. Roh, J. Cho, Z. Rehman, H. Sultan, Y. J. Baik, and B. Lee, "A comprehensive thermodynamic performance assessment of CO_2 liquefaction and pressurization system using a heat pump for carbon capture and storage (CCS) process," *Energy Conversion and Management*, vol. 206, p. 112489, 2020, doi: 10.1016/j.enconman.2020.112489.

25. J. Kropiwnicki, "Application of Stirling engine type alpha powered by the recovery energy on vessels," *Polish Maritime Research*, vol. 27, no. 1, pp. 96-106, 2020, doi: 10.2478/pomr-2020-0010.

26. H. P. Nguyen, A. T. Hoang, S. Nizetic, X. P. Nguyen, A. T. Le, C. N. Luong, V. D. Chu, and V. V. Pham, "The electric propulsion system as a green solution for management strategy of CO_2 emission in ocean shipping: A comprehensive review," *International Transactions on Electrical Energy Systems*, vol. 31, E12580, 2020, doi: 10.1002/2050-7038.12580.

27. L. C. Law, B. Foscoli, E. Mastorakos, and S. Evans, "A comparison of alternative fuels for shipping in terms of lifecycle energy and cost," *Energies*, vol. 14, no. 24, p. 8502, 2021, doi: 10.3390/en14248502.

28. N. R. Sharma, D. Dimitrios, A. I. Olcer, and N. Nikitakos, "LNG a clean fuel – the underlying potential to improve thermal efficiency," *Journal of Marine Engineering and Technology*, vol. 21, pp. 111-124, 2020, doi: 10.1080/20464177.2020.1827491.

29. M. Comotti and S. Frigo, "Hydrogen generation system for ammonia-hydrogen fuelled internal combustion engines," *International Journal of Hydrogen Energy*, vol. 40, no. 33, pp. 10673-10686, 2015, doi: 10.1016/j.ijhydene.2015.06.080.

30. S. Frankl, S. Gleis, S. Karmann, M. Prager and G. Wachtmeister, "Investigation of ammonia and hydrogen as CO_2-free fuels for heavy duty engines using a high pressure dual fuel combustion process," *International Journal of Engine Research*, vol. 22, no. 10, pp. 3196-3208, 2021, doi: 10.1177/1468087420967873.

31. C. Mounaïm-Rousselle, P. Bréquigny, C. Dumand, and S. Houillé, "Operating limits for ammonia fuel spark-ignition engine," *Energies*, vol. 14, no. 14, p. 4141, 2021, doi: 10.3390/en14144141.

32. A. Valera-Medina, F. Amer-Hatem, A. K. Azad, I. C. Dedoussi, M. D. Joannon, R. X. Fernandes, P. Glarborg, H. Hashemi, X. He, S. Mashruk, J. McGowan, C. Mounaim-Rouselle, A. Ortiz-Prado, A. Ortiz-Valera, I. Rossetti, B. Shu, M. Yehia, H. Xiao, and M. Costa, "Review on ammonia as a potential fuel: From synthesis to economics," *Energy and Fuels*, vol. 35, pp. 6964-7029, 2021, doi: 10.1021/acs.energyfuels.0c03685.

33. H. Li and J. Yan, "Evaluating cubic equations of state for calculation of vapor–liquid equilibrium of CO_2 and CO_2-mixtures for CO_2 capture and storage processes," *Applied Energy*, vol. 86, no. 6, pp. 826-836, 2009, doi: 10.1016/j.apenergy.2008.05.018.

34. U. Lee, S. Yang, Y. S. Jeong, Y. Lim, C. S. Lee, and C. Han, "Carbon dioxide liquefaction process for ship transportation," *Industrial and Engineering Chemistry Research*, vol. 51, no. 46, pp. 15122-15131, 2012, doi: 10.1021/ie300431z.

35. F. Engel and A. Kather, "Improvements on the liquefaction of a pipeline CO_2 stream for ship transport," *International Journal of Greenhouse Gas Control*, vol. 72, pp. 214-221, 2018, doi: 10.1016/j.ijggc.2018.03.010.

36. Y. Shi, J. Shen, D. Qiu, and T. Qin, "Thermal analysis of type C independent tank," *Ships and Ocean Engineering*, vol. 36, no. 3, p. 5, 2020, doi: 10.14056/j.cnki.naoe.2020.03.001.

37. B. Y. Yoo, "The development and comparison of CO_2 BOG re-liquefaction processes for LNG fueled CO_2 carriers," *Energy*, vol. 127, pp. 186-197, 2017, doi: 10.1016/j.energy.2017.03.073.

38. Y. Li, B. Li, F. Deng, Q. Yang, and B. Zhang, "Research on the application of cold energy of largescale LNG-powered container ships to refrigerated containers," *Polish Maritime Research*, vol. 28, no. 4, pp. 107-121, 2022, doi: 10.2478/pomr-2021-0053.

REVERSE ENGINEERING-INSPIRED PARAMETRIC 3D GEOMETRY MODEL OF MARINE PROPELLER

Long Zheng (iD)
Shunhuai Chen* (iD)
Xinyu Chen (iD)
Shengchen Ji

School of Naval Architecture, Ocean and Energy Power Engineering, Wuhan University of Technology, Wuhan, China

Corresponding author: *shchen@whut.edu.cn (Shunhuai Chen)*

ABSTRACT

In this study, an effective parametric 3D geometry model of a propeller was established with the aid of reverse engineering. The goal is to reduce the free parameters while automating the modelling of the propeller. The process of building the parametric model begins by generating an initial point cloud by defining the feature matrix associated with the propeller blade profile shape. Subsequently, the initial point cloud is deformed and refined by the deformation feature matrix and resampling. Finally, a 3D geometry model of the propeller is generated by surface reconstruction. The model can be built automatically by interactively modifying the feature matrices. Two numerical analyses illustrate the performance of the parametric 3D geometry model. Specifically, two propellers are constructed using the proposed model to estimate the shape error between the reconstructed propellers and the original offset of the propellers. These propellers are selected as research objects to determine the hydrodynamic performance error between the propeller constructed by the proposed model and a benchmark propeller. According to the results of the numerical study, the parametric 3D geometry model can precisely reconstruct the aforementioned geometry within a valid error range. The hydrodynamic error analysis demonstrates that the geometric inaccuracy from the reconstructed model has less impact on the propeller performance. This indicates that the model described in this study is generalised and robust. Moreover, some uncommon propeller CAD models were generated in batches using the parametric 3D geometry model.

Keywords: marine propeller; geometric modeling; parametric 3D geometry model; surface reconstruction

INTRODUCTION

For nearly a decade, there has been a lot of focus on propeller design. Król presented a simplified lifting surface method, replacing the 3D task for the full blade with a series of 2D tasks for accomplishing blade section profiles [1]. Moreover, Król also analysed the uncertainty of full-scale propeller open water performance testing [2]. Nadery et al. used a numerical method to study the hydrodynamic performance of aft propellers with and without wake equalisation ducts

[3]. Greeley used numerical approaches for the design and study of propellers [4]. Recently, simulation-based design (SBD) has been widely applied in the naval architecture design field [5]-[11]. The geometry parameterisation is critical in SBD. The parametric 3D geometry model will facilitate the automated modelling and optimisation design of the propeller [12]. However, the number of 3D geometric parametric models currently available for propeller design and design optimisation is relatively limited. These parametric models are usually associated with the specific parameters

that the researcher is trying to optimise so they are not directly applicable as common models to automatically construct CAD models of propellers. For example, Bertetta et al. described the camber and thickness distributions of a propeller with B-spline parametric curves [13]. Furthermore, most parameters employed in the parametric model are coordinates of control points, which have less physical significance. To achieve automatic parametric modelling of the propeller, Ye fitted the given data points with the least square method and constructed the propeller blade surface based on the B-spline curve and surface [14]. Vickers carried out coordinate conversion of propeller data points through computer programming, and further built the three-dimensional model of a propeller [15]. Kim focused on the geometric modelling steps of marine propeller blades, blade roots and propeller hubs. Further, a comprehensive analysis of the leaf surface and the leaf back was carried out [16]. Lee established a propeller surface modelling system that can connect the propeller blade surface and blade back by building the side. The final surface constructed by this system can maintain G1 continuity of the surface at the joint part [17]. Pérez-Arribas generated the B-spline surface representation of the propeller blade while reducing the number of control points used. The effectiveness of the proposed method was verified by using it to reconstruct the model and compare it with a benchmark model [18]. Arapakopoulos et al. provided two propeller mathematical expression methods based on non-uniform rational B-splines (NURBS) and T-splines, respectively. These methods can quickly and automatically generate effective geometric representations of marine propellers [19]. However, the number of parameters in these parametric models is high and there are some barriers to using them directly for design optimisation.

In this study, the parametric modelling of a marine propeller is achieved by constructing 3D point cloud data through the inspiration of reverse engineering combined with parametric ideas. The goal of this work is to reduce the number of free parameters needed for parametric modelling while maintaining generality. Initially, a thorough explanation of the parametric calculation method for the propeller point cloud and the reverse engineering technique for the propeller surface reconstruction is provided. Several examples of error validation studies are additionally employed to explain the parametric model. Finally, some uncommon propeller CAD models were generated in batches via the developed model.

MATERIALS AND METHODS

Reverse engineering is a viable method to create a 3D virtual CAD model of an existing physical part. The reverse engineering process involves measuring an object and then reconstructing it as a 3D model. The measured data is usually represented as a point cloud [20]. The reverse engineering procedure can be characterised by the flowchart in Fig. 1.

In classical reverse engineering, the physical object can be measured using 3D scanning technologies like structured light digitisers, or industrial computerised tomography (CT) scanning. However, the surface point cloud of a propeller can usually be calculated using mathematical methods. The flowchart of the parametric 3D geometry model of a marine propeller based on reverse engineering is updated to Fig. 2.

PROPELLER BLADE 3D POINT CLOUD

In Fig. 2, the initial step is the parametric point cloud calculation of the propeller. There are three processes in constructing the 3D point cloud of the propeller: the initial point cloud, the deformation point cloud and the fine point cloud. The general steps in constructing the 3D point cloud of the propeller blade are shown in Algorithm 1.

Algorithm 1: General steps in constructing the 3D point cloud of the propeller blade

1	**begin**
2	H: defining the feature matrix associated with the propeller blade profile.
3	D: propeller diameter $\rightarrow R_N$.
4	Create initial point cloud based on Eq. (4).
5	R: defining the deformation feature matrix.
6	Create deformation point cloud based on Eq. (12) and Eq. (13).
7	Resample based on Eq. (14) $\rightarrow$ fine point cloud.
8	**end**
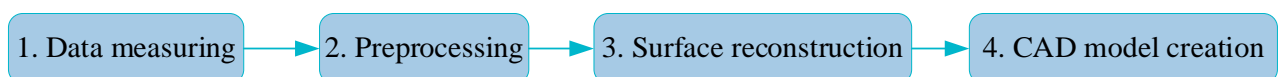
Fig. 1. Basic phases of reverse engineering
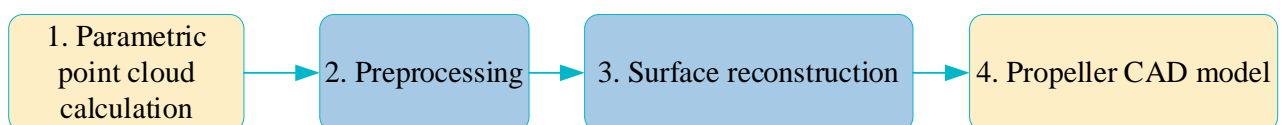
Fig. 2. Basic phases of parametric 3D geometry model of marine propeller based on reverse engineering

The computation process of the initial point cloud starts with defining the feature matrix associated with the propeller blade profile. The feature matrix is formulated as Eq. (1).

$$H = \begin{bmatrix} H_{1,1} & H_{1,2} & \dots & H_{1,i} \\ H_{2,1} & H_{2,2} & \dots & H_{2,i} \\ \dots & \dots & \dots & \dots \\ H_{N,1} & H_{N,2} & \dots & H_{N,i} \end{bmatrix} \quad i = 1,2 \dots 8, N = 1,2 \dots \quad \textbf{(1)}$$

where N is the number of blade profiles composing the blade.

The initial point cloud is generated from H according to Eq. (2) to (4).

$$\textbf{(2)}$$
$$X_N = [0, \ H_{N,1} * \cos(H_{N,2}), \ 1 - H_{N,3} * \cos(H_{N,4}), \ 1, \ 1 - H_{N,5} * \cos(H_{N,6}), \ H_{N,7} * \cos(H_{N,8}), \ 0]$$

$$\textbf{(3)}$$
$$Y_N = [0, \ H_{N,1} * \sin(H_{N,2}), \ H_{N,3} * \sin(H_{N,4}), \ 0, \ H_{N,5} * \sin(H_{N,6}), \ H_{N,7} * \sin(H_{N,8}), \ 0]$$

$$IP = \begin{bmatrix} IPX \\ IPY \\ IPZ \end{bmatrix} = \begin{bmatrix} \sum_{i=0}^{3} N_{i,3}(u) X_N(i) & \sum_{i=0}^{3} N_{i,3}(u) X_N(i+3) \\ \sum_{i=0}^{3} N_{i,3}(u) Y_N(i) & \sum_{i=0}^{3} N_{i,3}(u) Y_N(i+3) \\ R_N & R_N \end{bmatrix} \quad \textbf{(4)}$$

where u [0,0,0,0,1,1,1,1]. $N_{i3}(u)$ is the De Boor Cox function [21][22]. R_n is the radius of the propeller, such as 0.2r/R,0.3r/R…0.9r/R,1r/R.
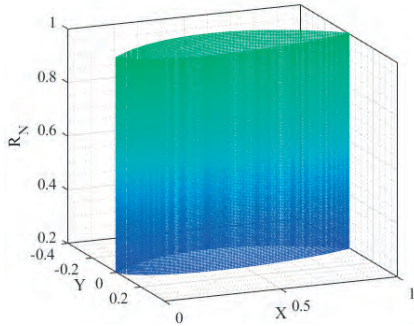
Fig. 3. Schematic diagram of initialised point cloud

The shape of the initialised point cloud is a "columnar" structure, similar to an airplane wing, as shown in Fig. 3. Therefore, a deformation feature matrix needs to be defined to deform the initialised point cloud. The deformation feature matrix is written as Eq. (5).

$$R = \begin{bmatrix} R_{1,1} & R_{1,2} & \dots & R_{1,i} \\ R_{2,1} & R_{2,2} & \dots & R_{2,i} \\ \dots & \dots & \dots & \dots \\ R_{N,1} & R_{N,2} & \dots & R_{N,i} \end{bmatrix} \quad i = 1,2 \dots 6, N = 1,2 \dots 4 \quad \textbf{(5)}$$

where $R_{N,i}$ is the feature parameters of the propeller's chord distribution, rake distribution, skew distribution, and pitch distribution. The detailed explanation is given in the appendix.

The deformation process of the initialised point cloud is based on Eq. (6) to (13).

$$\textbf{(6)}$$
$$X_i = [R_{root}, \ R_{root} + R_{i,2} * \cos(R_{i,3}), \ R_{tip} - R_{i,4} * \cos(R_{i,5}), \ R_{tip}]$$

$$\textbf{(7)}$$
$$Y_i = [R_{i,1}, \ R_{i,1} + R_{i,2} * \sin(R_{i,3}), \ R_{i,6} + R_{i,4} * \sin(R_{i,5}), \ R_{i,6}]$$

$$RCX(t)_i = X_i(1)(1-t)^3 + 3X_i(2)t(1-t)^2 + \\ + 3X_i(3)t^2(1-t) + X_i(4)t^3, t \in [0,1] \quad \textbf{(8)}$$

$$RCY(t)_i = Y_i(1)(1-t)^3 + 3Y_i(2)t(1-t)^2 + \\ + 3Y_i(3)t^2(1-t) + Y_i(4)t^3, t \in [0,1] \quad \textbf{(9)}$$

where R_{root} is the radius ratio at the propeller blade root, the recommended value of which is 0.2r/R. The same R_{tip} is the radius ratio at the blade tip. $i=1,…,4$, meaning the chord distribution, skew distribution, rake distribution, and pitch distribution, respectively.

$$UCX(u)'_N = IPX * RCX(t_N)_1 \quad \textbf{(10)}$$

$$LCX(u)'_N = IPY * RCX(t_N)_1 \quad \textbf{(11)}$$

where N is the n-th section in the radial direction of the propeller, and is the chord distribution function.

$$Xu_N = -[RCX(t_N)_2 + RCX(t_N)_3 * \tan(RCX(t_N)_4)] + (0.5 * RCX(t_N)_1 - UCX(u)'_N) \\ * \sin(RCX(t_N)_4) + UCY(u)'_N * \cos(RCX(t_N)_4)$$
$$Yu_N = \sin[RCX(t_N)_3 - (0.5 * RCX(t_N)_1 - UCX(u)'_N) * \cos(RCX(t_N)_4) - UCY(u)'_N \\ * \sin(RCX(t_N)_4)]$$
$$Zu_N = \cos[RCX(t_N)_3 - (0.5 * RCX(t_N)_1 - UCX(u)'_N) * \cos(RCX(t_N)_4) - UCY(u)'_N \\ * \sin(RCX(t_N)_4)] \quad \textbf{(12)}$$
$$Xl_N = -[RCX(t_N)_2 + RCX(t_N)_3 * \tan(RCX(t_N)_4)] + (0.5 * RCX(t_N)_1 - LCX(u)'_N) \\ * \sin(RCX(t_N)_4) + LCY(u)'_N * \cos(RCX(t_N)_4)$$

$$Yl_N = \sin[RCX(t_N)_3 - (0.5 * RCX(t_N)_1 - LCX(u)'_N) * \cos(RCX(t_N)_4) - LCY(u)'_N \\ * \sin(RCX(t_N)_4)]$$
$$Zl_N = \cos[RCX(t_N)_3 - (0.5 * RCX(t_N)_1 - LCX(u)'_N) * \cos(RCX(t_N)_4) - LCY(u)'_N \\ * \sin(RCX(t_N)_4)] \quad \textbf{(13)}$$

The $Xu_N, Yu_N, Zu_N, Xl_N, Yl_N, Zl_N$ form the form the deformation point cloud. It should be noted that when

defining H, N in Eq. (1) usually takes the value of 10, that is, ten blade sections are used to express the propeller blade. This results in sparse initialisation point clouds and distorted point clouds. Therefore, the sparse deformed point cloud is refined by resampling. The resampling method is written as Eq. (14).

$$\begin{bmatrix} X_N^{re} \\ Y_N^{re} \\ Y_N^{re} \end{bmatrix} = [\frac{M-j}{M}, \frac{j}{M}] \begin{bmatrix} X_N^{i+1} - X_N^i \\ Y_N^{i+1} - Y_N^i \\ Z_N^{i+1} - Z_N^i \end{bmatrix} \qquad \textbf{(14)}$$

where $j = 1, 2, …, M$. M is the number of the resample.

Fig. 4 summarises the aforementioned procedure using an example of a propeller with a diameter of 2.5 m. Interactively defining H, R, and D leads to the parametric production of 3D point clouds for propellers.
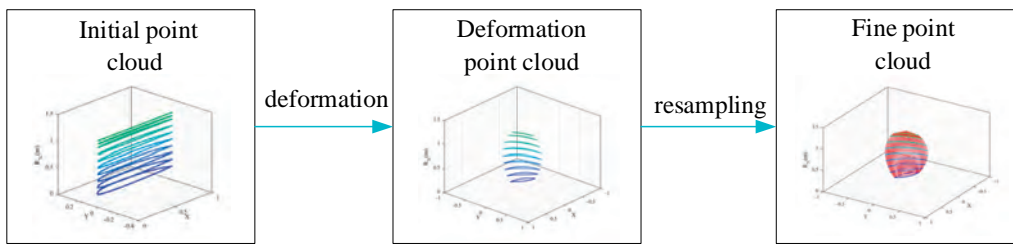
Fig. 4. Phases of creating parametric point cloud of propeller

SURFACE RECONSTRUCTION TO FORM POINT CLOUD

There is essentially no noise data since the point cloud data in this study was produced using mathematical techniques. As a result, the traditional surface reconstruction methodology based on the moving least squares (MLS) method [23][24] can be utilised to conclude the propeller's surface reconstruction. The basic idea of using the MLS for surface reconstruction is to grid the reconstruction area first, then calculate the node values on the grid points, and finally connect the grid nodes to form a surface. Algorithm 2 shows the process of surface reconstruction. The specific properties of this method are described in the literature [23][24].

Algorithm 2: Surface reconstruction based on MLS

1	begin
2	Grid the reconstruction area.
3	**for** =1: *n* (*Number of grid points*) **do**
4	Determine the area of influence of grid points.
5	Determine the nodes of the area of influence.
6	Compute shape functions.
7	Compute the node value at the grid point.
8	**end**
9	Connect mesh points to form surface.
10	end

ANALYSIS AND VERIFICATION

SHAPE ERROR ANALYSIS

This work aims to reconstruct the propeller geometry by using a parametric 3D geometry model of a marine propeller based on reverse engineering. Therefore, the shape error analysis of the propeller reconstruction will be performed. The shape error is represented by the distance between the offset and the surface of the propeller. In this analysis, two typical propellers, AU series and B series, are chosen as the research objects. Table 1 lists the main parameters of the propellers.

Tab. 1. General parameters for the construction of a generic marine propeller

Item	AU series	B series
Diameter (m)	2.5	2.5
Number of sections	4	4
Area ratio	0.55	0.55
Pitch ratio	1.00	1.00

Fig. 5 shows the propeller constructed using the method proposed in this article and the corresponding offset. Similarly, the shape errors of the two propellers are also depicted in Fig. 5.

As shown in Fig. 5, at the part of the face side, the maximum error positions for the AU series and B series at each radius are close to the leading edge of the blade section. At the part of the back side, the distance error of the AU series and B series is relatively evenly distributed on each radius. Comparatively, Fig. 5 further demonstrates that the error near the blade root is larger than the error at the tip. The error of the blade back side is greater than the error of the blade face side when the method proposed in this paper is used to construct the aforementioned propeller. The highest deviation for all the propellers that were previously reconstructed is commonly less than 0.2 m (8% D). As a consequence, the method described in this research can be applied to the geometric representation and reconstruction of propellers with high precision and flexibility. All of the aforementioned shape errors, taken collectively, fall within a fair range of engineering standards.

	Propeller CAD model and offset	Face side shape error	Back side shape error
AU series			
B series			
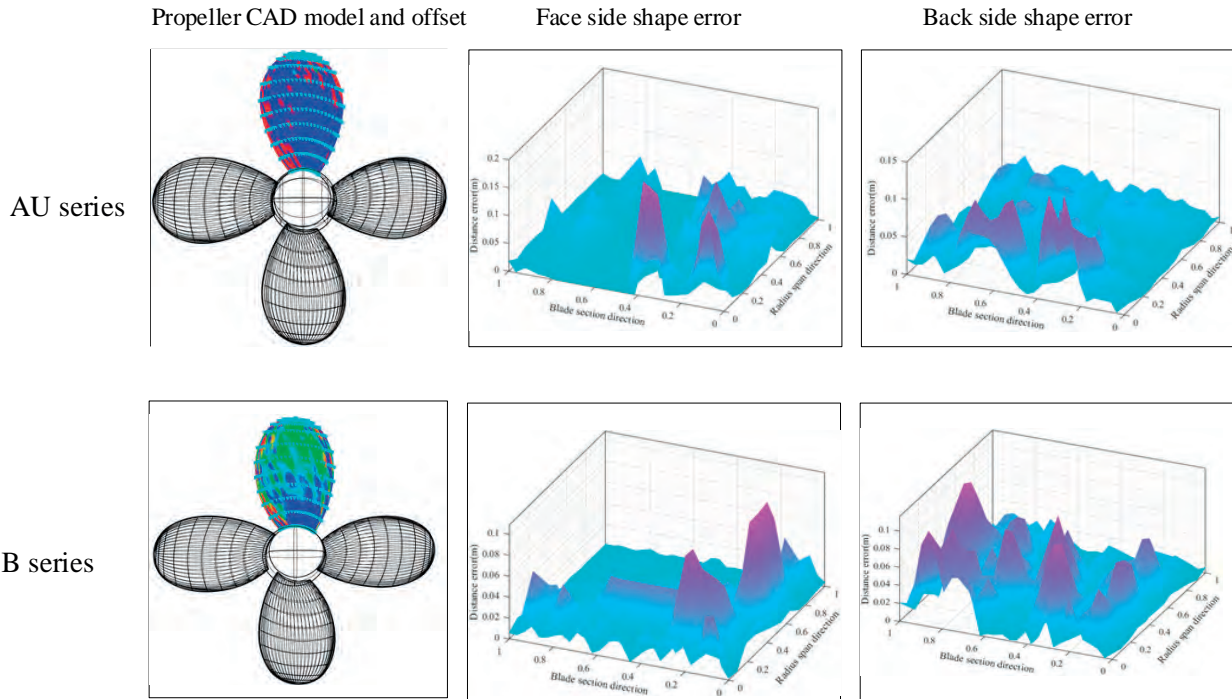
Fig. 5. The shape error of AU series and B series

HYDRODYNAMIC PERFORMANCE ERROR ANALYSIS

The purpose of the marine propeller CAD model is to design or optimise the propeller. Therefore, the primary focus of this analysis is to investigate whether the shape error produced during the reconstruction of the propeller model will have a seriously negative effect on the propeller's hydrodynamic performance. The specific operation for hydrodynamic performance error analysis is to operate computational fluid dynamics (CFD) simulations on both the reconstructed propeller model at a scale of 10 and the benchmark propeller model, also at a scale of 10, and then to investigate whether the distance error generated by the reconstruction will lead to a large performance error by comparing the error between the open water performance

obtained by CFD calculation. The grid reliability analysis, boundary condition setting, and solver settings involved in the numerical calculation refer to previous publications [25][26][27]. The open water performance of the propeller obtained by the CFD solver of the reconstructed propeller and the benchmark propeller is shown in Fig. 6. Fig. 6 (a) is the open water performance for the AU series, and Fig. 6 (b) is the open water performance for the B series. As observed in Fig. 6, the reconstructed AU series and benchmark propeller exhibit considerable hydrodynamic performance differences, whereas the reconstructed B series and prototype propeller exhibit similar hydrodynamic performance. This matches with Fig. 5. In terms of the distance error between the benchmark propeller and the reconstructed propeller, the error of the AU series is greater than that of the B series.

(a) AU series

(b) B series
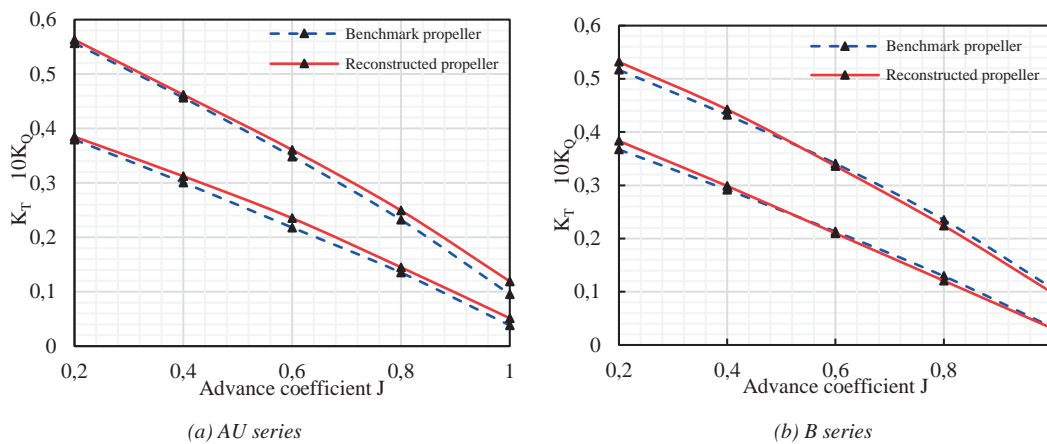
Fig. 6. Open water performance curve obtained by CFD

In addition, when the propeller works, the pressure at the blade back decreases to form a suction surface. Cavitation will take place if the pressure at a particular location falls below the critical level. The pressure distribution on the propeller surface will have a great impact on the cavitation performance of the propeller. Therefore, in order to investigate whether the errors generated during the reconstruction will lead to drastic changes in the pressure distribution of the propeller, the pressure distribution of the benchmark propeller and the reconstructed propeller at the corresponding advance coefficient (J) is shown in Fig. 7 to Fig. 9.
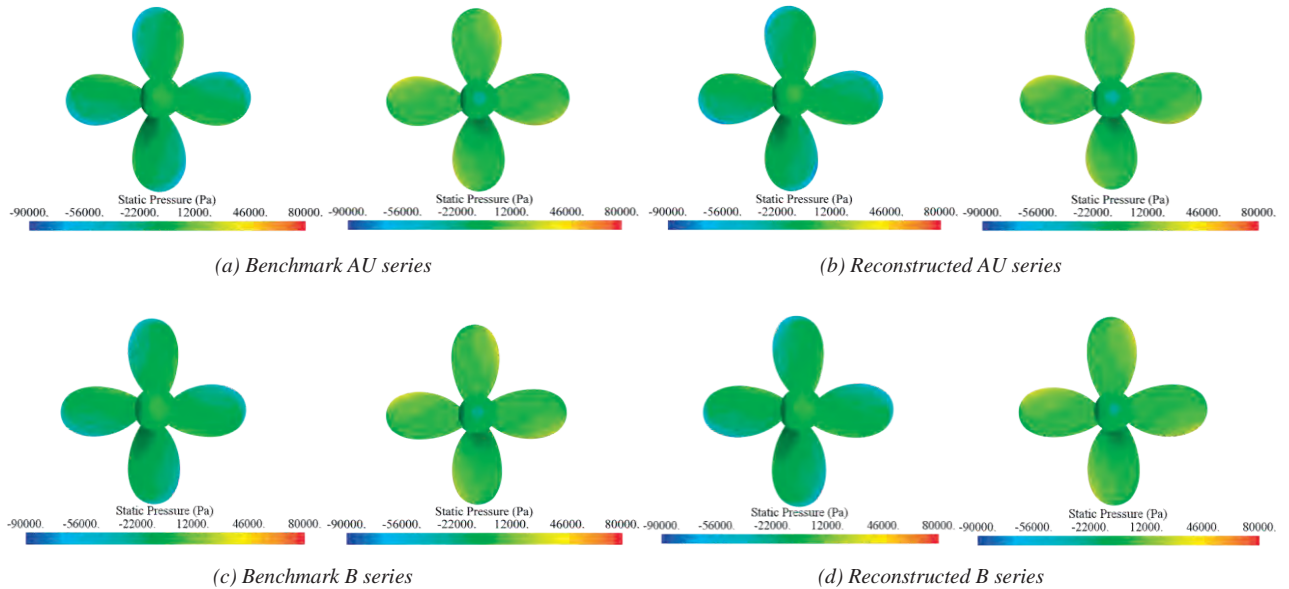
(a) Benchmark AU series

(b) Reconstructed AU series

(c) Benchmark B series

(d) Reconstructed B series

Fig. 7. Pressure distribution of benchmark blade and reconstructed blade (J=0.4)

(a) Benchmark AU series

(b) Reconstructed AU series

(c) Benchmark B series

(d) Reconstructed B series

Fig. 8. Pressure distribution of benchmark blade and reconstructed blade (J=0.6)

(a) Benchmark AU series

(b) Reconstructed AU series

(c) Benchmark B series
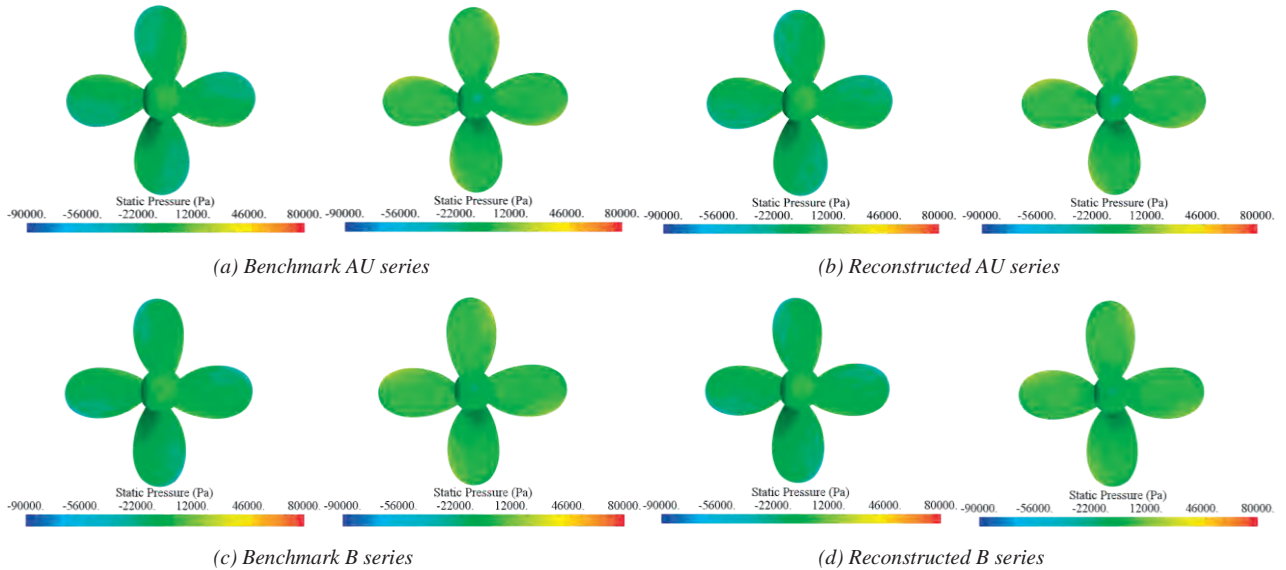
(d) Reconstructed B series
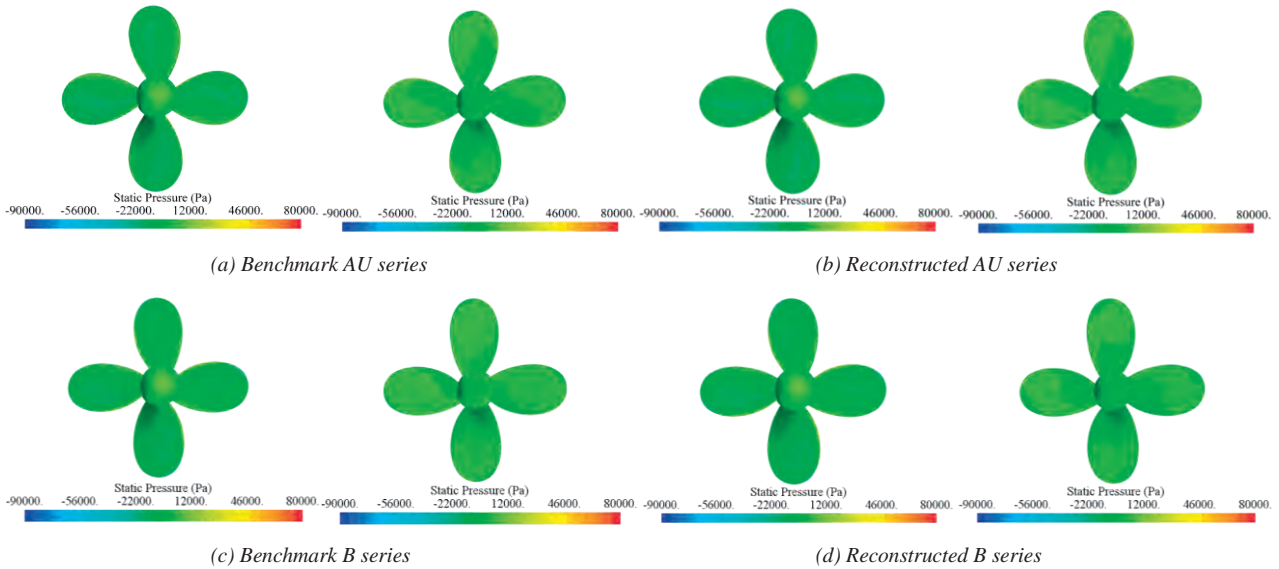
Fig. 9. Pressure distribution of benchmark blade and reconstructed blade (J=0.8)

Fig. 7 to Fig. 9 show that the surface pressure distribution of the reconstructed propeller is not significantly different from that of the benchmark propeller. In order to further investigate the variation of the pressure distribution, the pressure coefficients at different radii as the advance coefficient increases are given in Fig. 10 to Fig. 12, which show that, for various advance speed coefficients, the pressure distribution change of 0.6 r/R is rather minimal. Moreover, when J=0.4, the change in the AU series' pressure distribution is more visible than the change in the B series, when J=0.6,

the change in the AU series is also merely moderately obvious and when J=0.8, the B series is relatively larger. The results indicate that the geometric error produced when utilising the method proposed in this paper to reconstruct the propeller geometric model does not significantly affect the reconstructed propeller's performance (including open water performance and pressure distribution). As a consequence, it can be demonstrated that the method presented in this research can be utilised to deform and reconstruct propeller geometry in an efficient manner.

(a) AU series r/R=0.3

(b) AU series r/R=0.6

(c) AU series r/R=0.9

(d) B series r/R=0.3

(e) B series r/R=0.6

(f) B series r/R=0.9
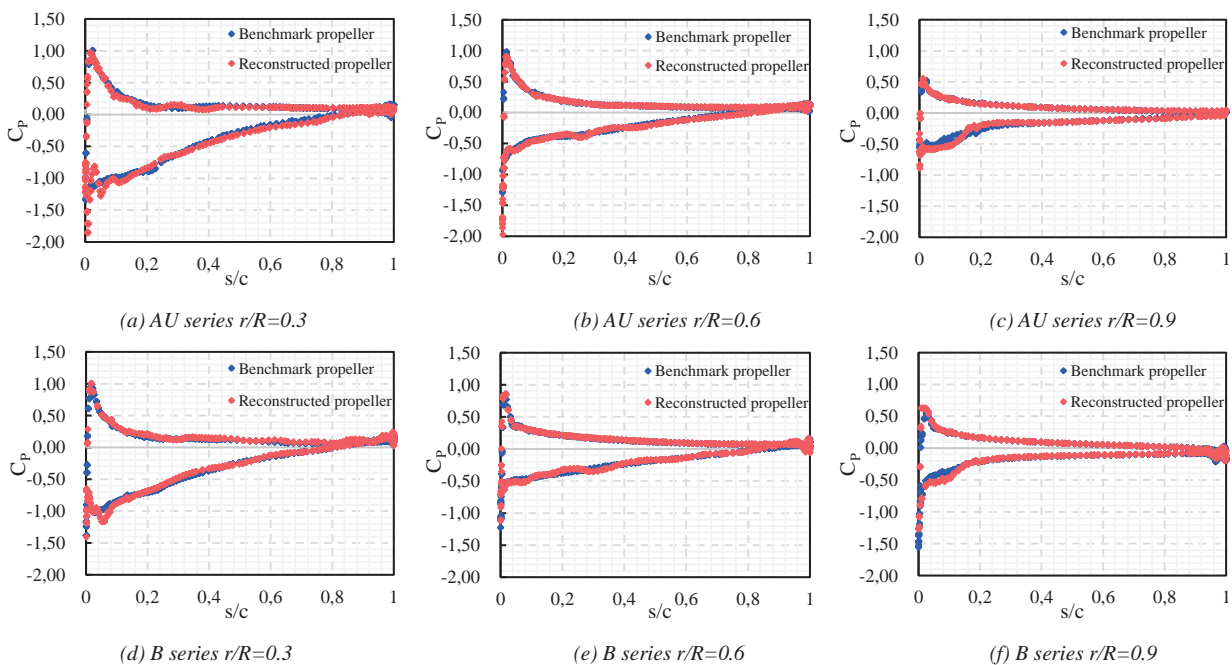
Fig. 10. Pressure coefficient at J=0.4

(a) AU series r/R=0.3 *(b) AU series r/R=0.6* *(c) AU series r/R=0.9*

(d) B series r/R=0.3 *(e) B series r/R=0.6* *(f) B series r/R=0.9*
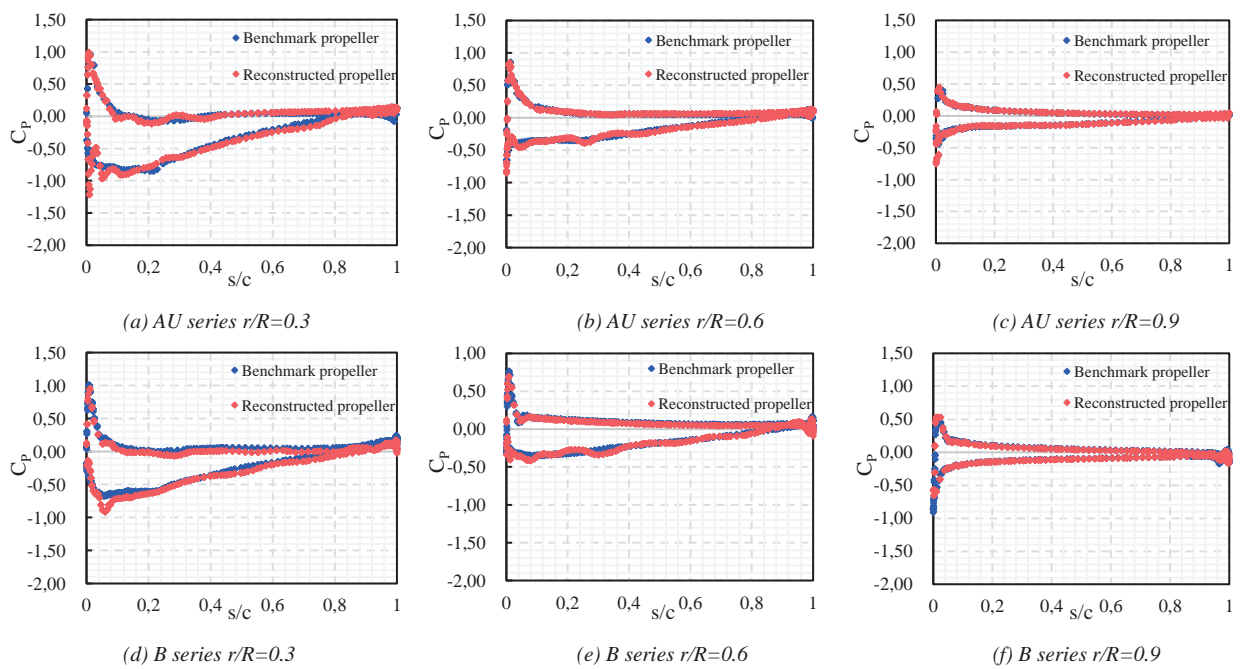
Fig. 11. Pressure coefficient at J=0.6

APPLICATION OF PARAMETRIC

(a) AU series r/R=0.3 *(b) AU series r/R=0.6* *(c) AU series r/R=0.9*

(d) B series r/R=0.3 *(e) B series r/R=0.6* *(f) B series r/R=0.9*
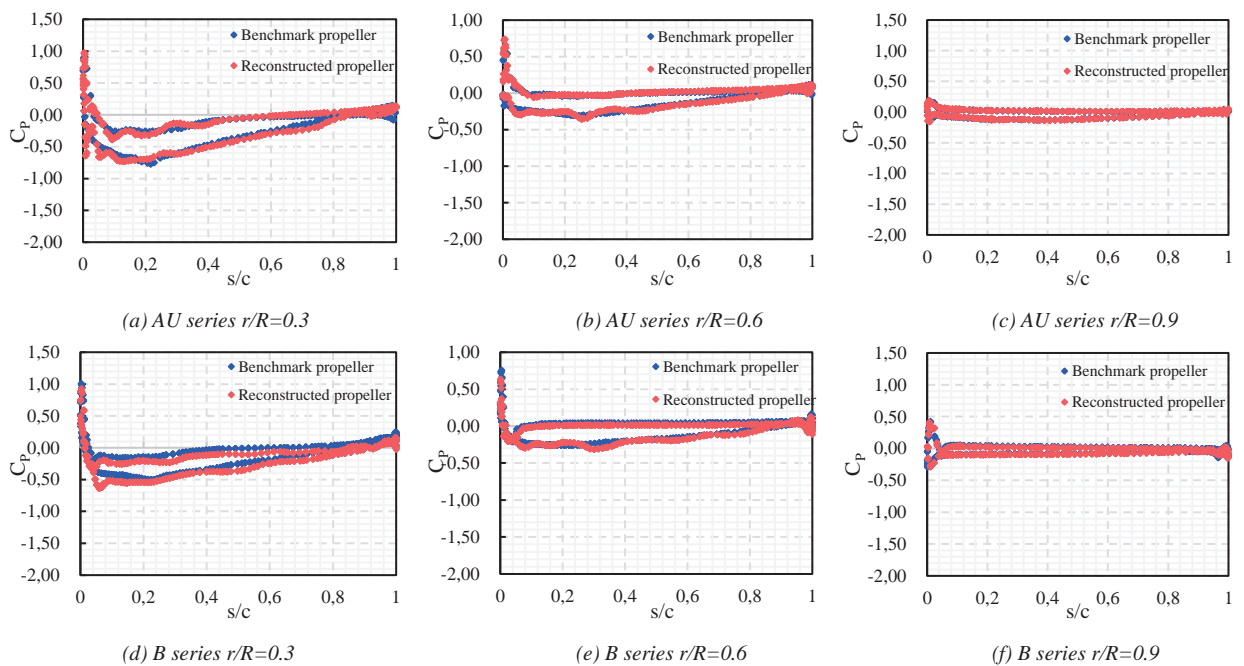
Fig. 12. Pressure coefficient at J=0.8

CONSTRUCTION OF PROPELLER

In theory, an infinite number of propeller CAD models can be generated by different combinations of feature parameters. In practical engineering applications, the propeller CAD model often needs to be generated under specific constraints. In this part using NACA 66 as the blade profile (constraint), the initial point cloud is generated; thus, H remains unaltered and constant, and several propeller CAD models are produced by specifying various R. R contains 24 parameters, among which and represent the information at the propeller blade root and blade tip, which are also unchanged as constraints. The remaining 16 parameters are used as design variables, and the upper and lower bounds are listed in Table 2. The diameter (D) of the generated propellers is 0.25 m. The values of the constraint parameters (and) are listed in Table 3.

Tab. 2. Boundaries of design variables used for sample generation

NO.	Name	Lower Bound	Upper Bound
1	$R_{1,2}$	0.001	0.15
2	$R_{1,3}$	30°	90°
3	$R_{1,4}$	0.05	0.2
4	$R_{1,5}$	80°	90°
5	$R_{2,2}$	0.001	0.09
6	$R_{2,3}$	0°	5°
7	$R_{2,4}$	0.001	0.02
8	$R_{2,5}$	0°	5°
9	$R_{3,2}$	0.001	0.09
10	$R_{3,3}$	-10°	10°
11	$R_{3,4}$	0.001	0.02
12	$R_{3,5}$	0°	10°
13	$R_{4,2}$	0.001	0.09
14	$R_{4,3}$	0°	10°
15	$R_{4,4}$	0.001	0.02
16	$R_{4,5}$	0°	10°

Tab. 3. Values of constraint parameters

NO.	Name	Value
1	$R_{1,1}$	0.058
2	$R_{1,6}$	0
3	$R_{2,1}$	0°
4	$R_{2,6}$	0°
5	$R_{3,1}$	-4.72°
6	$R_{3,6}$	24.18°
7	$R_{4,1}$	0.209
8	$R_{4,6}$	0.209

The design variables were sampled using the Sobol algorithm [28]. With the aim of uniformly sampling the design space, this technique propagates the design solution throughout the variable domain space in a standard manner by using a Sobol sequence that imitates the behaviour of a series of random numbers. The technique can cover the full design area and is primarily utilised for experimental ideas.

The Sobol algorithm was used to randomly select 12 samples within that range as cases. Fig. 13 shows the distribution of the parameters in their respective value ranges.
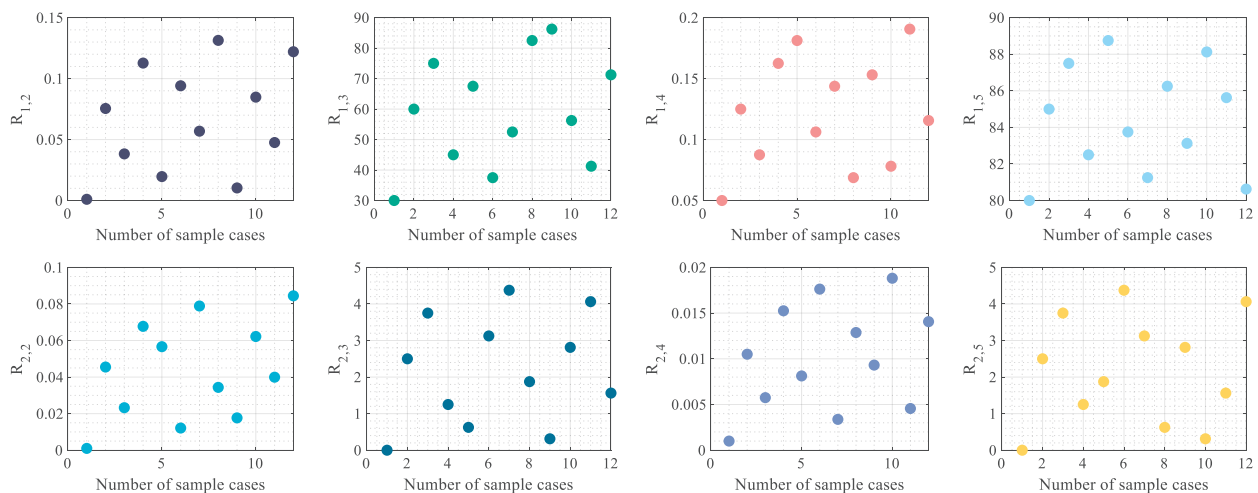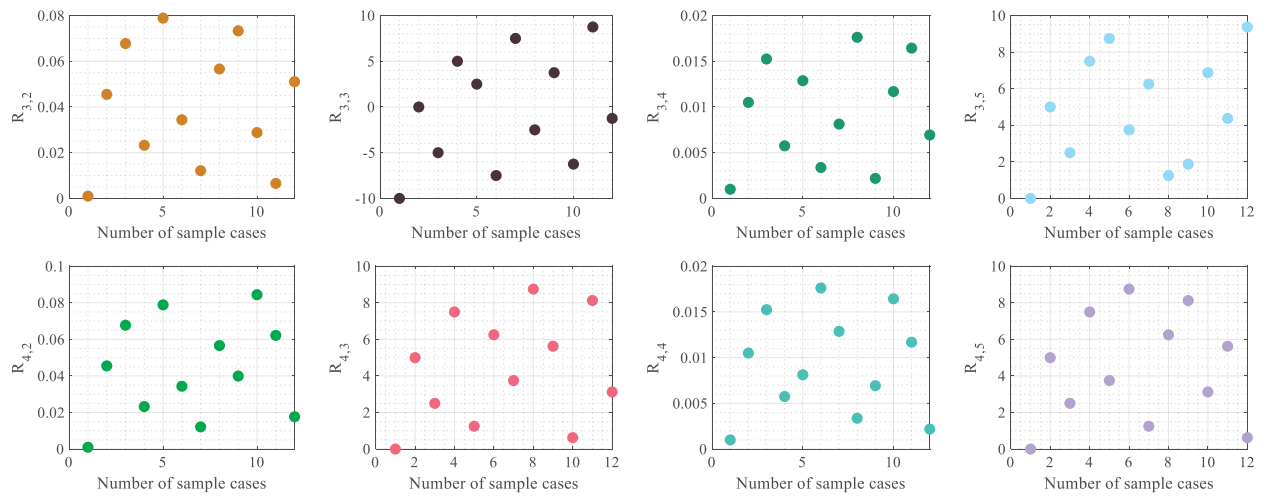
Fig. 13. Distribution of design variables in space
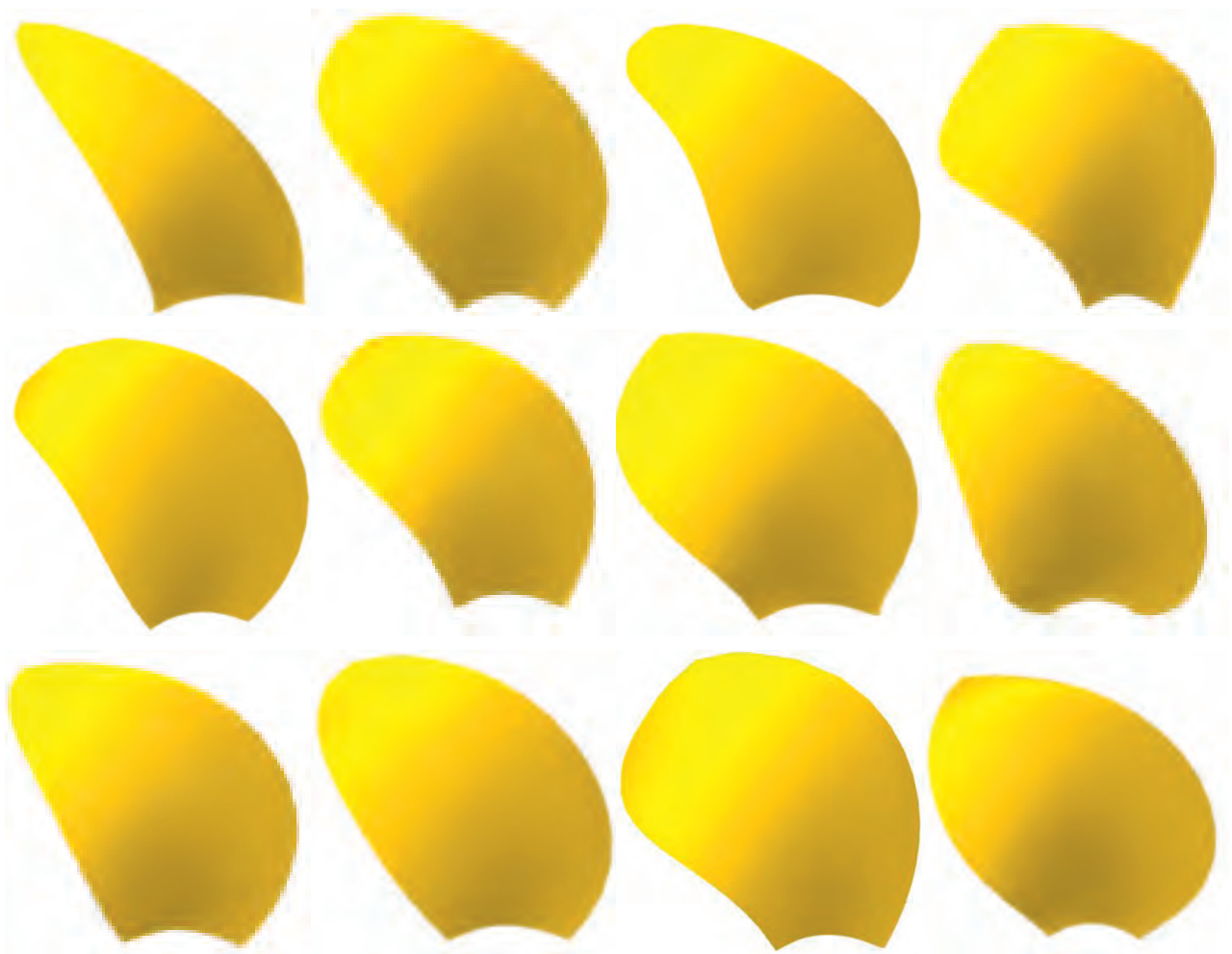
Fig. 14. Propeller blade model for each case

According to the combination of parameters corresponding to each case, the CAD model is driven to automatically generate the corresponding propeller. Fig. 14 depicts the propeller geometry model corresponding to each case. It can be seen that the model in this article can construct a series of uncommon propeller geometries to help designers explore novel design space.

CONCLUSION AND FUTURE WORKS

In this article, a parametric 3D geometry model of a marine propeller is constructed. The basic idea of the model is inspired by reverse engineering. The point cloud of the propeller generated is parameterised by a mathematical calculation method. The surface reconstruction algorithm based on MLS is used to generate the propeller surface. Different propeller CAD models can be built smoothly by modifying the corresponding parameters interactively. By using this technique, the parameter-driven creation of propeller surfaces is realised. This may quickly supply designers with a large number of sample propellers, saving the time required for manual modelling and modification, considerably increasing design efficiency, and offering certain engineering benefits. Simultaneously, the propellers created by this technique have good smoothness and satisfy the fundamental design criteria, so they can be utilised as the foundational model for subsequent performance investigation. In future research, we will work on the feature extraction of the parameters in this model by means of sensitivity analysis and feature selection methods. In addition, we hope to combine feature selection work to realise a propeller automation optimisation framework that comprehensively considers propeller efficiency, propeller cavitation and propeller vibration noise.

FUNDING SOURCES

DECLARATION OF COMPETING INTEREST

The authors declare that they have no known competing financial interests or personal relationships that could have appeared to influence the work reported in this paper.

REFERENCES

1. P. Król, "Blade section profile array lifting surface design method for marine screw propeller blade," *Polish Maritime Research*, vol. 26, no. 4, 3919, pp.134-141, 2019. doi: /10.2478/pomr-2019-0075.

2. P. Król, "Analysis of model-scale open-water test uncertainty," *Polish Maritime Research*, vol. 29, no. 4, 3922, pp. 4-11, 2022. doi: /10.2478/pomr-2022-0039.

3. A. Nadery and H. Ghassemi, "Numerical investigation of the hydrodynamic performance of the propeller behind the ship with and without Wed," *Polish Maritime Research*, vol. 27, no. 4, 3920, pp. 50-59, 2020. doi: /10.2478/pomr-2020-0065.

4. D. S. Greeley, "Numerical method for propeller design and analysis in steady flow," *SNAME Transactions*, vol. 90, pp. 415-453, 1982.

5. M. Diez, A. Serani, E. F. Campana, et al., "Design space dimensionality reduction for single-and multi-disciplinary shape optimization," *Proceedings of AIAA/ISSMO Multidisciplinary Analysis and Optimization Conference (MA&O). AVIATION 2016*, Washington DC, USA. 13-17 June, 2016. doi: 10.2514/6.2016-4295.

6. I. Marinić-Kragić, D. Vučina, and M. Ćurković, "Efficient shape parameterization method for multidisciplinary global optimization and application to integrated ship hull shape optimization workflow," *Computer-Aided Design*, vol. 80, 2016, ISSN 0010-4485. doi: 10.1016/j.cad.2016.08.001.

7. A. Miao, M. Zhao, and D. Wan, "CFD-based multi-objective optimisation of S60 Catamaran considering demihull shape and separation," *Applied Ocean Research*, vol. 97, 2020. doi:10.1016/j.apor.2020.102071.

8. A. Serani, F. Stern, E. F. Campana, et al., "Hull-form stochastic optimization via computational-cost reduction methods," *Engineering with Computers*, vol. 38 (Suppl. 3), pp. 2245-2269, 2022. doi:10.1007/s00366-021-01375-x.

9. S. Gaggero, "Numerical design of a RIM-driven thruster using a RANS-based optimization approach," *Applied Ocean Research*, vol. 94, 101941, 2020. doi:10.1016/j.apor.2019.101941.

10. S. Gaggero, J. Gonzalez-Adalid, and M. P. Sobrino, "Design and analysis of a new generation of CLT propellers," *Applied Ocean Research*, vol. 59, pp. 424-450, 2016. doi:10.1016/j.apor.2016.06.014.

11. S. Gaggero, G. Tani, D. Villa, M. Viviani, P. Ausonio, P. Travi, G. Bizzarri, and F. Serra, "Efficient and multi-objective cavitating propeller optimization: An application to a high-speed craft," *Applied Ocean Research*, vol. 64, pp. 31-57, 2017. doi:10.1016/j.apor.2017.01.018.

12. S. Gaggero, G. Vernengo, and D. Villa, "A marine propeller design method based on two-fidelity data levels," *Applied Ocean Research*, vol. 123, 103156, 2022. doi:10.1016/j.apor.2022.103156.

13. D. Bertetta, S. Brizzolara, S. Gaggero, M. Viviani, and L. Savio, "CPP propeller cavitation and noise optimization at different pitches with panel code and validation by cavitation tunnel measurements," *Ocean Engineering*, vol. 53, pp. 177-195, 2012. doi:10.1016/j.oceaneng.2012.06.026.

14. X. Ye, T. R. Jackson, and N. M. Patrikalakis, "Geometric design of functional surfaces," *Computer-Aided Design*, vol. 28, no. 9, pp. 741-52, 1996. doi:10.1016/0010-4485(95)00080-1.

15. G. W. Vickers, "Computer-aided manufacture of marine propellers," *Computer-Aided Design*, vol. 9, no. 4, pp. 267-74, 1977. doi:10.1016/0010-4485(77)90008-2.

16. Y. C. Kim, Y. M. Lee, M. J. Son, T. W. Kim, and J. C. Suh, "Generating cutter paths for marine propellers without interference and gouging," *Journal of Marine Science and Technology*, vol. 14, no. 3, pp. 275-84, 2009. doi:10.1007/s00773-008-0033-2.

17. C. S. Lee and J. H. Lee, "Geometric modeling and tool path generation of model propellers with a single setup change," *The International Journal of Advanced Manufacturing Technology*, vol. 50, no. 1, pp. 253-63, 2010. doi:10.1007/s00170-009-2495-8.

18. F. Pérez-Arribas and R. Pérez-Fernández, "B-spline design model for propeller blades," *Advances in Engineering Software*, vol. 118, pp. 35-44, 2018. doi:10.1016/j.advengsoft.2018.01.005.

19. A. Arapakopoulos, R. Polichshuk, Z. Segizbayev, S. Ospanov, A. I. Ginnis, and K. V.Kostas, "Parametric models for marine propellers," *Ocean Engineering*, vol. 192, 106595, 2019. doi:10.1016/j.oceaneng.2019.106595.

20. T. Várady, R. R. Martin, and J. Cox, "Reverse engineering of geometric models—an introduction," *Computer-Aided Design*, vol. 29, no. 4, pp. 255–268, 1997. doi:10.1016/s0010-4485(96)00054-1.

21. M. G. Cox, The numerical evaluation of B-splines. Technical report, National Physics Laboratory DNAC 4, 1971. doi:10.1093/imamat/10.2.134.

22. C. De Boor, "On calculation with B-splines," *Journal of Approximation Theory*, vol. 6, pp. 50–62, 1972. doi:https://doi.org/10.1016/0021-9045(72)90080-9.

23. P. Lancaster and K. Salkauskas, "Surfaces generated by moving least squares methods," *Mathematics of Computation*, vol. 37, no. 155, pp. 141-158, 1981. doi:10.2307/2007507.

24. Q. H. Zeng and D. T. Lu, "Curve and surface fitting based on moving least-squares methods," *Journal of Engineering Graphics*, vol. 25, no. 1, pp. 84-89, 2004. doi:1003-0158(2004)01-0084-06.

25. A. Yazaki, E. Kuramochi, and T. Kumasaki, "Open water test series with modified AU-type four-bladed propeller models," *Journal of Zosen Kiokai*, vol. 108, pp. 99-104, 1960.

26. S. Leone, C. Testa, L. Greco, and F. Salvatore, "Computational analysis of self-pitching propellers performance in open water," *Ocean Engineering*, vol. 64, pp. 122-134, 2013. doi:https://doi.org/10.1016/j.oceaneng.2013.02.012.

27. W. Zhu and H. Gao, "Hydrodynamic characteristics of bioinspired marine propeller with various blade sections," *Ships and Offshore Structures*, 2020. doi:10.1080/17445302.2020.1713039.

28. S. Joe and F. Y. Kuo, "Remark on Algorithm 659: Implementing Sobol's Quasirandom Sequence Generator," *ACM Transactions on Mathematical Software*, vol. 29, no. 1, pp. 49–57, 2003. doi:10.1145/42288.214372.

APPENDIX

PHYSICAL MEANING OF PARAMETERS IN *H* AND *R*

H is related to the blade profile shape of the propeller. These parameters are provided in Table 4.

Tab. 4. Parameters used in blade profile shape

Nr.	Name	Symbol
0	Chord	L
1	Upper-side leading edge shift length	$H_{N,1}$
2	Upper-side leading edge angle of advance	$H_{N,2}$
3	Upper-side trailing edge shift length	$H_{N,3}$
4	Upper-side trailing edge angle of departure	$H_{N,4}$
5	Lower-side leading edge shift length	$H_{N,5}$
6	Lower-side leading edge angle of advance	$H_{N,6}$
7	Lower-side trailing edge shift length	$H_{N,7}$
8	Lower-side trailing edge angle of departure	$H_{N,8}$
Note:	The angle at the leading edge point, specified as the positive direction of the x-axis, is 0 degrees, the clockwise direction is negative, and the counterclockwise direction is positive. The angle at the trailing edge point, specified as the negative direction of the x-axis, is 0 degrees, the clockwise direction is positive, and the counterclockwise direction is negative.	

The coordinate system needs to be specified. Assuming that the origin of the coordinate system is at the leading edge point of the hydrofoil, the longitudinal axis coincides with the line connecting the leading edge point and the trailing edge point, and the positive direction is toward the trailing edge. Fig. 15 shows the corresponding meanings of each parameter. The ordinates of the hydrofoil's upper side will always be non-negative numbers, while the lower side values can be either negative or mixed, depending on the hydrofoil's camber.

(15)
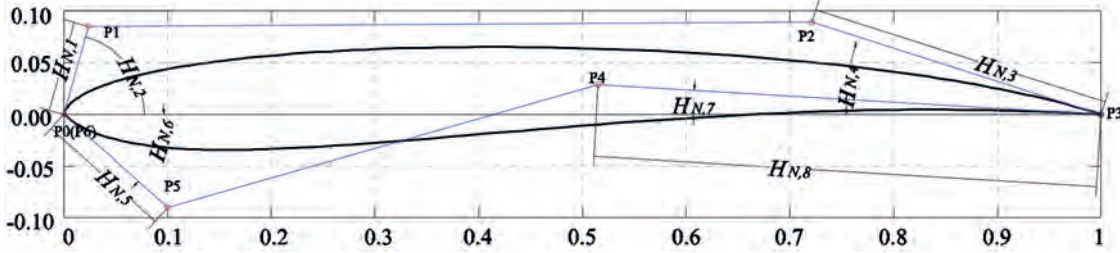
Fig. 15. Schematic diagram of feature parameters

R is related to the radial distribution of the propellers. These radial distributions include the chord distribution, rake distribution, skew distribution and pitch distribution. The definitions of the parameters in R are listed in Table 5. Fig. 16 shows a graphical explanation of the corresponding parameters.

Tab. 4. Parameters used in radial distribution

Nr.	Name	Symbol
1	The value of the root	$R_{N,1}$
2	Corresponding radial parameters, leading edge shift length	$R_{N,1}$
3	Corresponding radial parameters, angle of advance	R
4	Corresponding radial parameters, trailing edge shift length	$R_{N,1}$
5	Corresponding radial parameters, angle of departure	$R_{N,1}$
6	The value of the tip	$R_{N,1}$
Note:	The angle at the leading edge point, specified as the positive direction of the x-axis, is 0 degrees, the clockwise direction is negative, and the counterclockwise direction is positive. The angle at the trailing-edge point, specified as the negative direction of the x-axis, is 0 degrees, the clockwise direction is positive, and the counterclockwise direction is negative.	

$$P_N : x = [R_{root}, \ R_{root} + R_{N,2} * cos(R_{N,3}), \ R_{tip} - R_{N,4} * cos(R_{N,5}), \ R_{tip}] \quad (16)$$

$$P_N : y = [R_{N,1}, \ R_{N,1} + R_{N,2} * sin(R_{N,3}), \ R_{N,6} + R_{N,4} * sin(R_{N,5}), \ R_{N,6}] \quad (17)$$

$$\frac{A_e}{A_0} = \frac{4Z \int_{r_n}^{R} \sum_{i=0}^{3} C_3^i P_1^i (1 - t(x))^{3-i} (t(x))^i dr}{\pi D^2} \quad (18)$$

$$Rake = P_2^3 : y$$
$$Skew = P_3^3 : y \quad (19)$$
$$\bar{P} = \frac{\int_{r_n}^{R} \sum_{i=0}^{3} C_3^i P_4^i (1 - t(x))^{3-i} (t(x))^i dr}{\int_{r_n}^{R} r \, dr}$$

An example of $R =$
$$\begin{bmatrix} 0.66 & 0.65 & 20° & 0.25 & 75° & 0 \\ 0 & 0.5 & 0° & 0.5 & 0° & 0 \\ 0 & 0.5 & 0° & 0.5 & 0° & 0 \\ 0.6 & 0.5 & 0° & 0.5 & 0° & 0.6 \end{bmatrix} \quad (20)$$

is depicted in Fig. 17.

Fig. 16. Schematic diagram of feature parameters
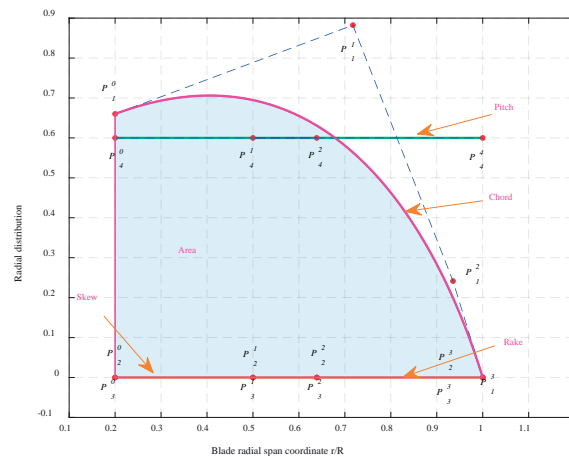
Fig. 17.. The radial parameter generated from the R

The relationship between R and the propeller parameters (propeller area ratio, pitch, skew, rake) is shown in Eq. (15) to Eq. (20).

The rake and skew of this propeller are both 0, and the pitch of the fixed pitch propeller is constant along the span direction of the propeller.

EXPERIMENTAL STUDY OF FUEL COMBUSTION AND EMISSION CHARACTERISTICS OF MARINE DIESEL ENGINES USING ADVANCED FUELS

Li Changxiong * (ID)
Yihuai Hu
Zy Yang
Hao Guo
Shanghai Maritime University, China

* Corresponding author: *cxli@shmtu.edu.cn (Li Changxiong)*

ABSTRACT

In order to explore the potential application of oxygenated fuels, polyoxymethylene dimethyl ethers (PODE), as an alternative fuel for marine diesel engines, the fuel combustion performance and gas emission characteristics of pure diesel oil, diesel-blended PODE, and pure PODE were tested on a marine diesel engine under different running conditions. The experimental results indicate that oxygen consumption can be reduced by diesel-blended PODE and pure PODE. The in-cylinder pressure and exothermic curve were consistent with the trend of diesel oil. Also, the ignition delay of diesel-blended PODE and pure PODE decreased, and the diffusion rate was accelerated, which helped to improve the combustion performance of diesel engines. Diesel blended PODE and pure PODE reduced the particulate matter (PM) emissions by up to 56.9% and 86.8%, respectively, and CO emissions by up to 51.1% and 56.3%, respectively. NOx emissions were gradually decreased with engine load. CO2 emissions were slightly increased, and the effective fuel consumption was increased up to 48% and 132%, respectively. It was shown that PODE could provide comparable power in a marine diesel engine and improve the fuel combustion and gas emission of the engine as a clean alternative fuel for marine diesel engines.

Keywords: Marine diesel engine; PODE; Combustion characteristics; Emission performance

INTRODUCTION

Diesel engines are widely used in ships due to their high thermal efficiency, power, and reliability, but one of the main technical challenges is the increase in environmental hazards from the generated exhaust emissions. To address this, the International Maritime Organization has issued a series of strict emission regulations to limit harmful emissions from ships [1-2]. The existing in-engine treatment and outside-engine pre-treatment technologies for diesel engines are unable to meet the Tier III emission standards, while clean alternative fuel-efficient combustion technologies and exhaust after-treatment have become the main technological ways to reduce harmful emissions from marine engines. Although the exhaust after-treatment can meet the requirements of Tier III emission regulations, it will also increase engine operation costs. Cleaner alternative fuels can reduce harmful gas emissions and effectively cope with the fossil energy crisis. This has become one of the hot research topics in the field of energy conservation and emission reduction for ships.

Oxygenated fuels are effective in reducing carbon soot emissions from engines [3-4]. This is due to their high cetane number, which not only enhances compression ignition performance but also reduces the emission of soluble organic

compounds in the particulate matter [5-7]. Lipids, alcohols, and other fuels can be used as alternative fuels in internal combustion engines. Biodiesel, as a lipid fuel with a high cetane number, is suitable for compression ignition engines. So it can help improve combustion performance and reduce harmful emissions while blending with Ultra Low Sulphur Diesel-Fuel for marine ancillary diesel engines [8]. However, the oxygen content of biodiesel is only about 20%. This helps to reduce particulate matter but not in-cylinder combustion very significantly [9]. Alcohol fuels with a low cetane number, mostly below 20, are commonly used in spark plug ignition engines [10]. Michal Puˇskár et al. [11] conducted experimental research using ethanol and gasoline fuel mixtures in the intake pipe of a 4-cylinder turbocharged direct injection engine. This showed that nitrogen oxide, carbon monoxide, and unburned hydrocarbon emissions were all reduced. Ether fuels with both a high cetane number and a high oxygen content are suitable for compression ignition diesel engines and have good particulate reduction performance. Ether fuels have potential as an alternative fuel for marine diesel engines [12-13].

Polymethoxydimethyl ether ($CH_3O(CH_2O)_nCH_3$, PODE) is a new type of coal-based ether-oxygenated fuel. It is produced by the polymerisation of methanol in formaldehyde solution. PODE production will be low cost due to China's "rich coal, lack of oil, less gas" energy structure. So, PODE is beneficial for optimising the energy structure as an alternative fuel for marine diesel engines in China. With strong solubility, high oxygen content, high cetane number, and no carbon-carbon bonds, PODE has properties close to that of diesel fuel and shows excellent combustion and emission characteristics in diesel engine applications [14-16]. PODE has gradually received attention from the clean fuel industry.

In recent years, much research has been carried out domestically and internationally on the properties, preparation, emission characteristics, and compatibility of PODE with diesel fuel [17-21], especially on diesel engines with blended PODE [22-24]. Wang et al. [25] conducted experimental studies on diesel blended with different ratios of PODE. It was found that soot, HC and CO emissions decreased with the increase of blended PODE ratio, and the effective thermal efficiency increased at low and medium engine load conditions, while the effective thermal efficiency changed less at high load conditions. The results on the combustion and emission characteristics of PODE/diesel blended fuels from Liu H et al. [26] showed that diesel blended PODE can significantly reduce HC, CO, and carbon soot emissions, and the thermal efficiency of blended fuel combustion is higher than that of pure diesel at low and medium loads. Liu et al. [27] tested the combustion characteristics of diesel blended with PODE in a diesel engine. The results showed that HC, CO, and carbon soot emissions were significantly reduced, and NOx emissions were slightly increased after using diesel blended with PODE. Wang H.F et al. [28] tested the emission characteristics of diesel blended PODE in an electronically controlled high-pressure common rail diesel engine under low load conditions. It was confirmed that the effective thermal efficiency of diesel-blended PODE increased, HC and CO emissions decreased, soot decreased significantly, and NOx emissions increased. Wang Z et al. [29] verified that diesel blended PODE could significantly reduce HC, CO and carbon soot emissions, and the thermal efficiency of the blended fuel combustion was higher than that of pure diesel. Feng et al. [30] studied the effect of PODE-diesel fuel blends on diesel combustion and emissions. The tests showed that when diesel engines were blended with PODE, the ignition delay period was shortened, and the maximum in-cylinder pressure increased. The specific fuel consumption increased slightly, and the effective thermal efficiency increased. CO, HC, and exhaust smoke were significantly reduced. NOx emissions were nearly unchanged. Zhu et al. [31] evaluated the effect of blending PODE on the combustion and emission performance of inter-cooled supercharged diesel engines, and the results proved that the combustion duration was shortened, and the maximum in-cylinder combustion temperature was increased when PODE was blended in diesel oil. With the increase of the blended PODE ratio, the peak pressure and pressure rise rate in the cylinder increased, the combustion duration was shorter, and the combustion temperature was higher. The NOx emission of diesel engines increased, and HC emission decreased with PODE blends, but the effect on CO emission was not significant. In addition, PODE blends reduced the equivalent fuel consumption rate of the engine and improved its economy.

As mentioned above, many researchers have carried out the application of PODE in automotive diesel engines, but there are few research papers about marine diesel engines using PODE. Since marine diesel engines are different from automotive diesel engines in their operating environment, thermal system, power requirements, and working characteristics, it is necessary to analyse and study the combustion performance and emission characteristics of marine diesel engines with PODE. In this paper, pure PODE, PODE/diesel blends, and diesel oil were tested on a marine diesel engine to compare and analyse their effects on the combustion performance and emission characteristics of diesel engines and to provide evidence for PODE as a clean alternative fuel in marine diesel engines.

EXPERIMENTAL SETUP

The marine diesel engine of the experimental setup is a Dongfeng 4135ACa, an inline 4-cylinder, naturally aspirated, water-cooled, four-stroke marine diesel engine. For the injection system, the tested fuel was pressurised by an injection pump and supplied to the injectors of each cylinder for injection into cylinders. There were 4 holes 0.37mm in diameter in each injector. The fuel was injected at 22-24°CA before TDC with 24 MPa injection pressure and 15°CA injection duration. The main structure and technical parameters are listed in Table 1. The engine was coupled with a hydraulic dynamometer and a control system that could adjust the torque and speed of the diesel engine, and a

constant speed and constant torque mode was used to obtain the test conditions.

Table 1. Structure and technical parameters of the 4135ACa marine diesel engine

Description	Parameter
Compression ratio	17:1
Bore/Stroke (mm/mm)	135/150
Displacement (L)	8.6
Rated power/kW	66.2
Rated speed/(r·min^{-1})	1500
Intake valve closing timing /°CA	48 after BDC
Exhaust valve opening timing /°CA	48 before BDC
Maximum valve lift /mm	16
Fuel advance injection angle /°CA	22~24 before TDC
Fuel injection quantity /(mm 3 /CY)	130
Combustion chamber shape	ω
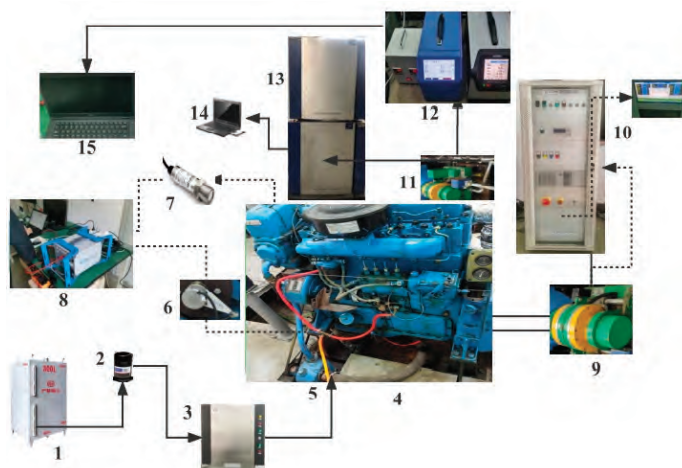
1-Diesel fuel tank, 2-Fuel filter, 3-Fuel consumption monitor, 4-Marine diesel engine, 5-Oil pipe, 6-Crank angle sensor, 7-Pressure sensor, 8-Data acquisition 9-Hydraulic dynamometer, 10-Dynamometer controller, 11-Exhaust pipe, 12-Gas analyser, 13-Particulate analyser, 14- Control Computer, 15- Monitoring Computer

Fig. 1. Schematic diagram of the experimental system.

The experimental setup schematic is shown in Fig 1. The combustion condition in the cylinder was monitored by a 6613CG1 pressure sensor, Kistler 2614CK1 angular scaler and Kistler KiBox 2893BK8 combustion analyser. The fuel consumption rate was measured with a ToCeil-CMFD015 dynamical fuel consumption meter with 0.12% accuracy. A Hariba PG-350 analyser was used to measure carbon monoxide, carbon dioxide, and nitrogen oxide emissions. An AVL SPC478 particulate sampling system was used to collect particulate emissions under steady-state and transient engine conditions to determine whether the diesel engine met the relevant marine pollutant emission measurement regulations under a constant temperature and humidity environment. The

PM was sampled on filter paper and weighed with a Sartorius MSA2.7S-0CE-DF super microgram balance with a 0-2.1 mg range and 0.01μg resolution in an RXCH500-II environmental weighing chamber. The main technical parameters of the data acquisition and analysis instruments are listed in Table 2.

Table 2. Technical parameters of data acquisition and analysis instruments

Instrument	Type	Parameter	Range	Resolution/ Uncertainty
Cylinder pressure sensor	6613CG1	Cylinder pressure	0-250 bar	0.05 mA/ bar
Crank angle detector	Kistler 2614CK1	Crank angle	0-1200 r/min	0.1 °CA
Combustion Analyzer	KiBox 2893Bk8	--	--	--
Hydraulic Dynamometer Changtong		Speed Torque	0-5000 rpm 0-1200 Nm	1 rpm 0.4%
Fuel consumption meter	ToCeil-CMFD015	Fuel consumption	0-400 g/ kWh	0.12%
Particulate collector	AVL SPC478	PM	--	--
Weighing chamber	RXCH500-II	PM	--	--
Ultramicrogram balance	MSA2.7S-0CEDF	PM	0-2.1 mg	0.01μg
NOx Analyzer	Hariba PG-350	NOx	0-2500 ppm	0.2%
CO Analyzer	Hariba PG-350	CO	0-5000 ppm	0.2%
CO$_2$ Analyzer	Hariba PG-350	CO$_2$	0-30 vol%	0.2%
O$_2$ Analyzer	Hariba PG-350	O$_2$	0-25 vol%	0.2%

For new types of marine fuels, it is valuable to conduct engine tests in laboratory conditions to comprehensively assess their suitability [32]. To verify the effect of the blended PODE fuel on the performance of marine diesel engines, three fuels, including pure diesel, diesel blended PODE and pure PODE, were used. D100 was 100% diesel, D/P50 was a diesel/PODE blend with a 1:1 mass ratio, and P100 was 100% PODE. The main physicochemical parameters are listed in Table 3.

Table 3. Physicochemical properties of tested fuels

Fuels	D100	D/P50	P100
Oxygen content/%	0	28.72	47.85
Cetane number	50	69	85
Density (20°C/g·cm⁻³)	0.83	0.97	1.06
Viscosity(20 °C (mm²·s⁻¹)	4.74	3.76	1.05
Flash point/°C	69	65	63
Low calorific value /(MJ·kg⁻¹)	42.8	30.9	18.3
Latent heat of vaporization /(kJ·kg⁻¹)	260	320	393
Boiling point /°C	200	191.23	161.3

The experimental procedure was arranged based on the "Emission Limits and Measurement Methods for Marine Engine Exhaust Pollutants (China Stage I and II)" (GB15097-2016) to set the working conditions as listed in Table 4.

Table 4. Working condition of the tests

Working condition NO.	1#	2#	3#	4#
Speed n (r/min)	525	705	945	1200
Power Pe (kW)	1.9	6.6	16.6	33.1

EXPERIMENTAL SETUP RESULTS AND COMBUSTION CHARACTERISTICS ANALYSIS

COMBUSTION CHARACTERISTICS
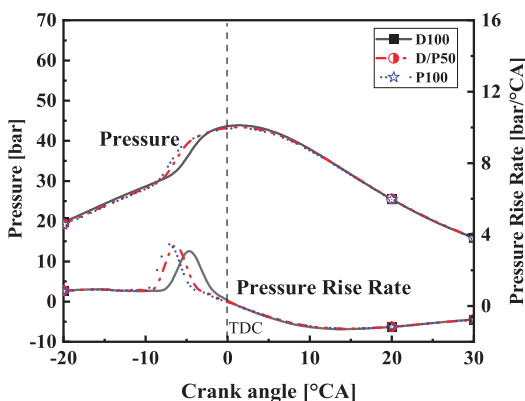
(a) n = 525 r/min, Pe = 1.9kW
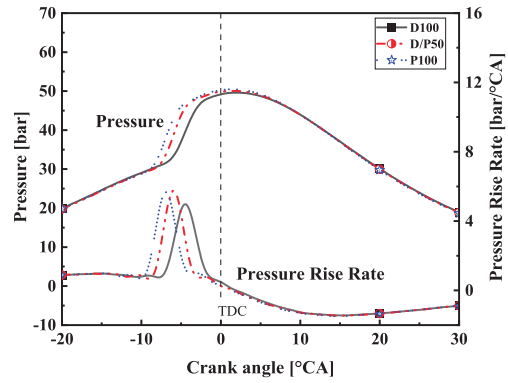
(b) n = 705 r/min, Pe = 6.6kW
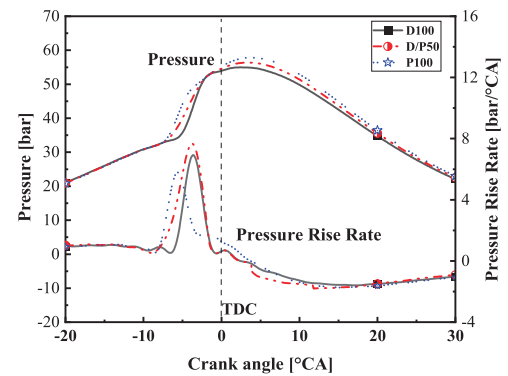
(c) n = 945 r/min, Pe = 16.6kW
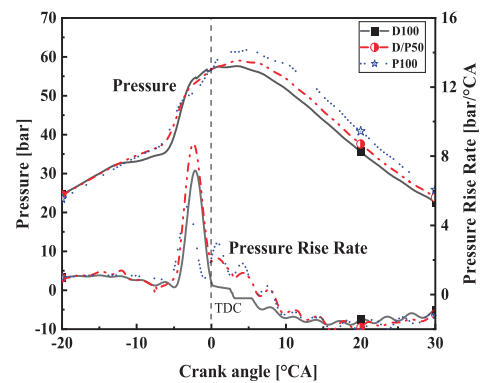
(d) n = 1200 r/min, Pe = 33.1kW

Figure 2. Cylinder pressure and pressure rise rate.

The curves of the engine in-cylinder pressure, p, and its rise rate, dp/dϕ, with crankshaft angle are shown in Fig. 2 with D100, D/P50, and P100 fuels under marine diesel engine propulsion characteristics. It can be seen that the in-cylinder maximum pressure, P_{MAX}, increases with all three fuels when the load increases. There is little difference between the peak pressures under the 1# condition and the 2# condition. There is a significant difference between the 3# condition and the 4# condition. Comparatively, the peak pressure increase of D/P50 is the highest, reaching 14.6 bar, with an increase of 49.8%, followed by P100 at 12 bar, with an increase of

39.2%, and D100 at 10.1 bar, with an increase of 31.2%. This is because PODE contains oxygen and has better combustion performance in low and medium load conditions compared to diesel oil, so its peak pressure increases more than diesel oil. Since the test diesel engine is designed for burning diesel oil, P100 cannot fully show its own advantages. Blended fuel can provide good combustion performance in the diesel engine, as the addition of PODE further improved the performance of blended fuel, and its pressure peak increased the most among the three fuels. It can be seen that PODE can effectively improve the combustion performance of the diesel engine under low load conditions.

Overall, due to the characteristics of the engine itself, the ignition time of the three fuels showed a pattern of firstly advancing and then delaying with the increase of speed and load. However, the variation of the ignition delay period of the three fuels was different. Under 1# and 2# operating conditions, the ignition point of D/P50 was earlier, and the ignition delay period was shorter than that of D100. P100 had a shorter ignition delay period than that of D/P50, which is due to the lower cetane number and high oxygen content of PODE. The earlier combustion starting point and longer time resulted in a more uniform mixture at low load and low speed. Under the 3# working condition, due to the increase in speed, the combustion start point of the three fuels was delayed, but D/P50 was delayed the most, very close to the TDC, while pure diesel changed the least. Under the 4# working condition, the P100 combustion start point was delayed the most, followed by D100 and D/P50 (the smallest). The main reason for this change is that PODE helped improve the performance of diesel, and a second reason is that the increase in engine load improves the combustion performance. PODE provided a good advantage in the low load but showed little advantage in the combustion performance with the speed and load increase.
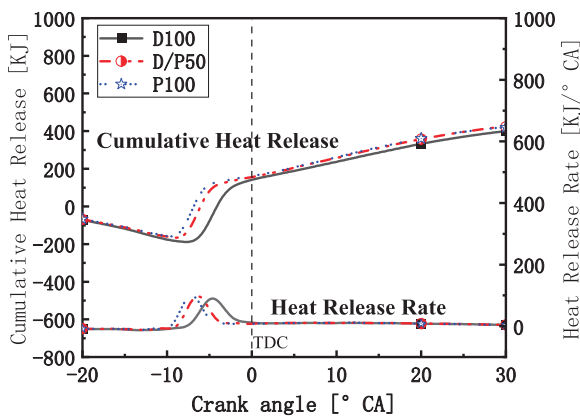
（a）n = 525 r/min, Pe = 1.9kW
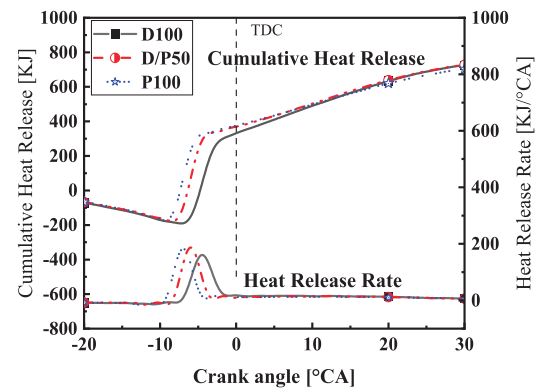
（b）n = 705 r/min, Pe = 6.6kW
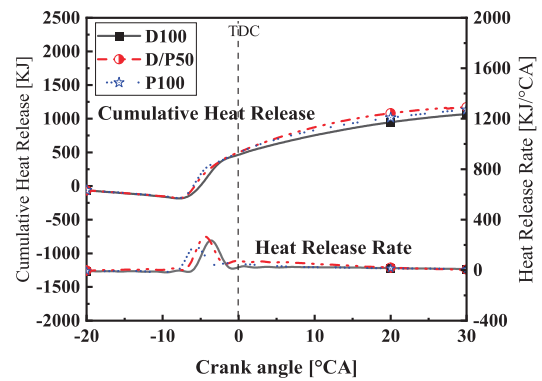
（c）n = 945 r/min Pe = 16.6kW
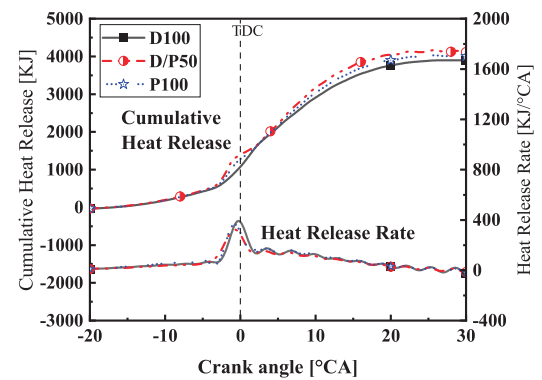
（d）n = 1200 r/min, Pe = 33.1kW

Fig. 3. Cumulative heat release and heat release rate with different fuels.

The cumulative heat release (CHR) and heat release rate curves with crankshaft angle are shown in Fig. 3 with P100, D100, and D/P50 blended fuels under marine diesel engine propulsion characteristics. The CHR shows that the change of ignition timing and delay period of the three fuels is consistent with the above. The CHR of P100 and D/P50 under the 1# working condition is larger than that of D100, which indicates that P100 and D/P50 burn more fully than D100, which is also an advantage of highly oxygenated fuel. Although the latent heat of vaporisation of PODE is greater, the CHR curves of P100 and D/P50 presented higher values than D100 because the fuel injection was less, and the combustion heat release was greater than the heat absorbed by fuel vaporisation. At

low load, the increase of D100 CHR was greater than P100 and D/P50, which indicates that the effect of vaporisation heat absorption increased when the load and the fuel injection increased. Due to the lower latent heat of vaporisation of diesel fuel, the CHR curves of the three fuels are not much different under the 2# working conditions. The CHR of the single fuels under the 3# and 4# working conditions is not as good as that of blended fuel. Although the low calorific value of PODE is only half that of diesel, the density of PODE is greater, resulting in a larger mass of fuel injected into the cylinder. In summary, PODE can meet the power requirements under diesel engine low load conditions, and in-cylinder combustion was more efficient due to the high oxygen content. PODE makes the blended fuel provide the combined advantages of diesel oil and high oxygen fuel, having more outstanding performance.

EFFECTIVE FUEL CONSUMPTION RATE

Fig.4 shows the effective fuel consumption (EFC) rates of the three fuels under different operating conditions. Under the same engine conditions, D100 has the lowest EFC rate, followed by D/P50, and P100 was the highest as the load increased. The EFC rate of all three fuels decreased to different extents. Compared with D100, the EFC rates of D/P50 and P100 increased by 33% and 80% under the 2# working load, respectively. Under the 3# working condition, the EFC rates of D/P50 and P100 increased by 36% and 110%, respectively. Under 4#, the EFC rates of D/P50 and P100 increased by 48% and 132%, respectively.

The EFC rate is influenced by the fuel calorific value and effective combustion. A higher fuel calorific value and better combustion will result in a lower EFC rate. The calorific value of D/P50 is 30.9 MJ·kg^{-1} and P100 is 18.3 MJ·kg^{-1}, which are 27.8% and 57.2% lower than that of D100 (42.8 MJ·kg^{-1}). Therefore, under the same load condition, the effective fuel consumption rate of D100 is the lowest, and the effective fuel consumption rate of P100 is the highest. As the load increases, the EFC rates of all three fuels decrease. This is because when the load increases, the temperature and pressure inside the cylinder increases, and the combustion quality improves. Since PODE has a higher cetane number than diesel, it can take advantage of highly oxygenated fuel under low engine load.
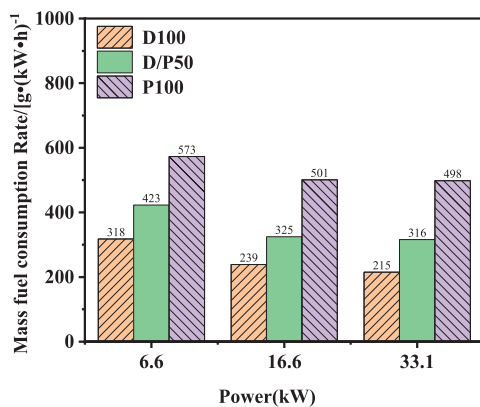
Fig. 4. Effective specific fuel consumption

EXPERIMENTAL SETUP RESULTS AND EMISSION CHARACTERISTICS ANALYSIS

ANALYSIS OF PARTICULATE MATTER EMISSIONS

Fig. 5 shows the engine particulate matter (PM) emissions with the three fuels under different working conditions. It can be seen that the PM emissions of the three fuels firstly decreased significantly, then decreased slowly, and finally increased slightly with the increase of load. The PM emissions of the three fuels decreased significantly from the 1# to the 2# working conditions. D100 dropped the most at 85.7%, D/P50 dropped the least at 73.8%, and P100 dropped between the two at 80.5%. From 2# to 3#, the PM emissions decreased slightly for the other two fuels except P100. The reduction rates of D100, D/P50, and P100 were 8%, 1.8%, and 55.4%, respectively. From 3# to 4#, the PM emissions increased slightly for the other two fuels except P100. D100, D/P50, and P100 increased by 17.1%, 0.7%, and 256.1%, respectively. Overall, the change in PM emissions for the three fuels was small at low and medium engine loads. In terms of magnitude, D100 and D/P50 did not fluctuate much, while P100 fluctuated more, mainly because PODE, as an oxygenated fuel, had sufficient burnout and almost no PM emissions under the 3# condition. With the increase in engine load and speed, the fuel injected into the cylinder increased, and the in-cylinder combustion time shortened, so the particulate ratio emissions increased slightly.

Under the same engine working conditions, D100 had the highest PM emissions, followed by D/P50 and P100, the lowest. Compared with D100, the PM emissions of D/P50 and P100 were reduced by 56.9% and 80.1% under the 1# working conditions, respectively. Under 2#, the PM emissions of D/P50 and P100 were reduced by 20.8% and 72.7%, respectively. Under 3#, the PM emissions of D/P50 and P100 were reduced by 15.5% and 86.8%, respectively. Under 4#, the PM emissions of D/P50 and P100 were reduced by 25.3% and 59.8%, respectively.

Compared with diesel fuel, the PM emissions of both blended PODE and pure PODE were significantly reduced after in-cylinder combustion mainly because of the following: (1) PODE is a chain of C-O bonded highly oxygenated fuel with nearly 50% oxygen content, and the oxygen in the fuel aids the combustion, especially in the high fuel concentration region, such as the spray core, and significantly reduces the incomplete combustion in this region [31, 33]. (2) PODE has no C-C bond, does not contain aromatic hydrocarbons, and has few C_2H_2 and C_2H_4 fragments in the combustion products, which reduces the formation of the carbon soot precursor PAH. The -OH group generated during combustion has a strong oxidising effect [33], which not only inhibits the formation of carbon soot but also adsorbs the SOF on carbon soot. (3) The low viscosity of PODE facilitates good atomisation, and both high oxygen content and high cetane number make the combustion faster and more complete with higher combustion temperature and accelerate the oxidation

of PM. (4) The lowest PM emission was under the 3# working condition, mainly because carbon soot was mainly generated in the diffusion combustion process. Under 3#, the ignition delay period of the three fuels was extended, and the diffusion combustion was shortened, which significantly reduced the generation of carbon soot [33].
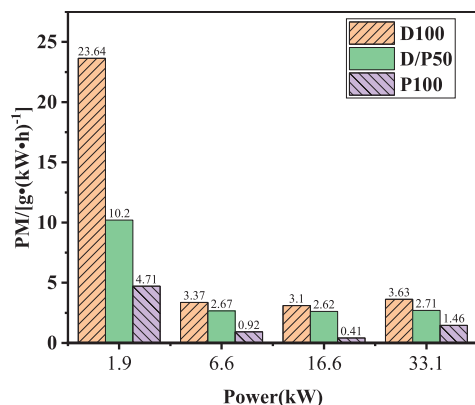
Fig. 5. Specific particulate matter emissions

ANALYSIS OF CO EMISSIONS

Fig. 6 shows the CO emissions of the three fuels under different working conditions. With the increase in engine load, the CO emissions of the three fuels showed a decreasing trend, and the decreasing range of CO emissions from the 1# to 4# working conditions showed an increasing and then a gradually decreasing trend. From the 1# to 2# working conditions, the CO emissions of all three fuels decreased significantly. The largest decrease was 44.2% for D100, while the smallest was 20.2% for D/P50, and it was 27.7% for P100. From 2# to 3# working conditions, the CO emission rate of all three fuels decreased more substantially. D100, D/P50, and P100 decreased by 49.4%, 48.5%, and 52.8%, respectively. From 3# to 4# working conditions, the CO emission rate of all three fuels decreased slightly. D100, D/P50, and P100 were 26.8%, 35.3%, and 33.8%, respectively. Overall, the CO emissions of the three fuels showed a decreasing trend with an increase in engine load. The main reason is that as the load increases, the in-cylinder pressure and temperature increase, the chemical reaction becomes more and more complete, and more CO is oxidised to CO_2. The decreasing range of CO emissions of the three fuels firstly increased and then decreased with the increase of load, mainly because the pressure and temperature of fuel combustion in the cylinder increased from 2# to 3# working conditions, while the engine speed was low, the combustion lasted longer, so there was sufficient time for chemical reaction, resulting in better combustion in the cylinder. The test engine is a naturally aspirated engine, so the air drawn in at low load conditions can provide sufficient oxygen for fuel combustion. However, as the engine load increased from 3# to 4# conditions, more fuel was injected into the cylinder. Meanwhile, more fresh air was needed accordingly, but not enough fresh air was actually sucked in. Furthermore, the engine speed increased, and the chemical reaction time of in-cylinder combustion decreased, so the CO emission decreased extent reduced.

Under the same engine operating conditions, D100 had the highest CO emissions, followed by D/P50, and P100 was the lowest. Compared with D100, the CO emissions of D/P50 and P100 were reduced by 51.1% and 56.3%, respectively, under 1# working conditions. Under 2# working conditions, the CO emissions of D/P50 and P100 were reduced by 30.1% and 43.3%, respectively. Under 3# working conditions, the CO emissions of D/P50 and P100 were reduced by 28.9% and 47.1%, respectively. The CO emissions of D/P50 and P100 were reduced by 37.1% and 52.1% under 4# working conditions, respectively.

Under the same engine running conditions, both blended PODE and pure PODE resulted in significantly lower CO emissions from in-cylinder combustion. The main reason is that the high oxygen content of PODE is equivalent to increasing the air-fuel ratio and strengthening the intensity of CO conversion to CO_2, especially in the high-fuel concentration area. PODE can significantly improve the incomplete combustion in this area due to its own oxygen content. In addition, the high temperature in the cylinder and high cetane number also promote the oxidation of CO, and the lower viscosity of PODE makes it easier to form a homogeneous mixture, which is conducive to full combustion, thus significantly reducing CO emissions.
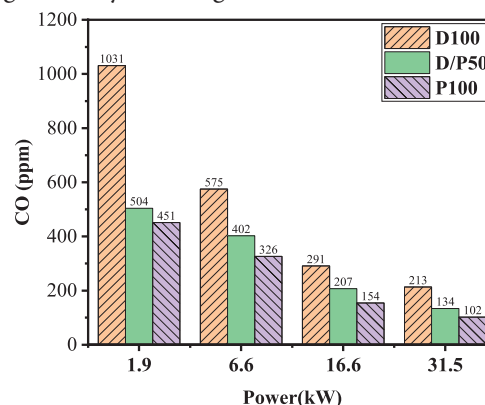
Fig.6. CO emissions under different running conditions

ANALYSIS OF CO_2 EMISSIONS

Fig. 7 shows the CO_2 emissions of the three fuels under different running conditions. With the increase in load, the CO_2 emissions of the three fuels showed an increasing trend. From 1# to 2# operating conditions, the CO_2 emissions of all three fuels increased. D100, D/P50, and P100 increased by 0.77%, 0.84%, and 0.87%, respectively. From 2# to 3#, the CO_2 emissions of D100, D/P50 and P100 increased by 1.13%, 1.19%, and 1.36%, respectively. The increase of CO_2 emissions of all three fuels decreased slightly from #3 to #4 operating conditions. D100, D/P50, and P100 increased by 0.82%, 0.89%, and 1.06%, respectively. Overall, the CO_2 emissions of the three fuels showed an increasing trend with the increase of

engine load, mainly because the fuel injected into the cylinder for combustion increases with the increase of engine load, and the corresponding CO_2 emissions increased.

Under the same operating conditions, D100 had the lowest CO_2 emission, followed by D/P50, and P100 was the highest. Compared with D100, the CO_2 emissions of D/P50 and P100 increased by 0.02% and 0.07% under 1# working conditions, respectively. Under 2# working conditions, the CO_2 emissions of D/P50 and P100 increased by 0.09% and 0.17%, respectively. Under 3# working conditions, CO_2 emissions increased by 0.15% and 0.4% for D/P50 and P100, respectively. Under 4# working conditions, CO_2 emissions increased by 0.22% and 0.64% for D/P50 and P100, respectively.

Under the same engine running conditions, CO_2 emissions of D/P50 and P100 presented an increasing trend compared to D100, and the magnitude of the increase increased as the engine load increased. Although the carbon content of PODE is lower compared to diesel, theoretically, the CO_2 emission is lower with complete combustion of PODE. However, because of the low viscosity of PODE, the in-cylinder injection fuel atomisation quality is higher, which helped the formation of a homogeneous mixture. Also, the high oxygen content and high cetane number of PODE are more conducive to complete combustion at low and medium loads, especially in the high fuel concentration area in the cylinder. The fuel's own oxygen content helped convert CO into CO_2, resulting in more CO_2 emissions.
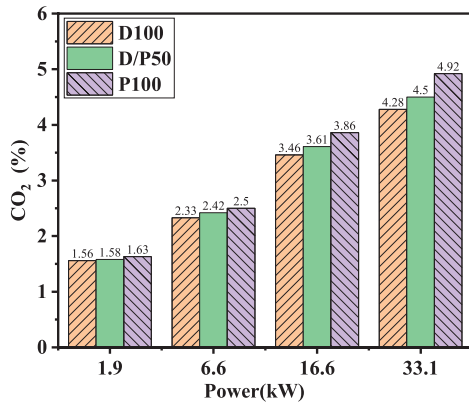
Fig. 7. CO_2 emissions under different running conditions

ANALYSIS OF NOX EMISSIONS

Fig. 8 shows the NOx emissions of the three fuels under different working conditions. With the increase in load, the NOx emissions of the three fuels showed an increasing trend. The NOx emissions of D100 were the lowest and P100 the highest under 1# working conditions. Under 2# working conditions, D100 was the lowest, and D/P50 was the highest. Under 2# working conditions, the NOx emissions of D100 and D/P50 were comparable and both higher than P100 under 3# working conditions. D100 emissions were the highest, and P100 emissions were the lowest under 4# working conditions. From 1# to 2#, NOx emissions of all three fuels increased, with the largest increase of 147.5% for D100, the smallest

increase of 70.1% for P100, and an increase of 91.8% for D/P50 between the two. The NOx emissions of D100, D/P50, and P100 increased by 59.4%, 40.7%, and 29% from 2# to 3#, respectively. From 3# to 4# working conditions, the increases in NOx emissions of D100, D/P50, and P100 were 23.8%, 6.36%, and 5.8%, respectively. Overall, the NOx emissions of the three fuels steadily increased at low and medium engine loads. In terms of magnitude, the increase gradually decreased with increasing load. Among these, D100 increased the most, while P100 increased the least.

Although the latent heat of vaporisation of PODE is larger than that of diesel, the effect of latent heat of vaporisation is not obvious because the fuel consumption is smaller at low engine load. Due to the lower calorific value, more fuel must be injected to meet the load requirements when the load increases. Meanwhile, PODE vaporisation latent heat increased, resulting in lowering the temperature in the cylinder. Therefore, the NOx emissions increase was consequently lower than diesel.
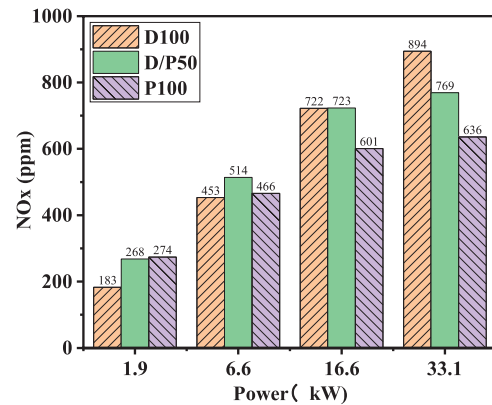
Fig. 8. NOx emissions under different running conditions

ANALYSIS OF O_2 EMISSIONS

Fig. 9 shows the O_2 emissions of the three fuels under different working conditions. With the increase in engine load, the O_2 emissions of the three fuels show a decreasing trend. The O_2 emissions of the three fuels showed slight differences under the 1# and 2# operating conditions, and the differences in the O_2 emissions of the three fuels widened under the 3# and 4# operating conditions. The main reason is that the test engine is a naturally aspirated engine, which requires less fuel and low oxygen consumption at low load, but as the load increases, the fuel required increases, and the corresponding oxygen consumption increases.

Under the same engine operating conditions, the D100 had the lowest O_2 emissions, followed by the D/P50 and the P100 the highest. Compared with D100, the O_2 emissions of D/P50 and P100 increased by 0.19% and 0.23% under 1# working conditions, respectively. Under the 2# working conditions, the O_2 emissions of D/P50 and P100 increased by 0.05% and 0.12%, respectively. Under 3# working conditions, the O_2 emissions of D/P50 and P100 increased by 0.71% and 0.91%,

respectively. Under 4# working conditions, the O_2 emissions of D/P50 and P100 increased by 0.46% and 1.38%, respectively. Obviously, blended PODE and pure PODE had higher O_2 emissions than diesel, mainly because PODE contains oxygen, which can replace part of the oxygen consumption of air in-cylinder combustion.
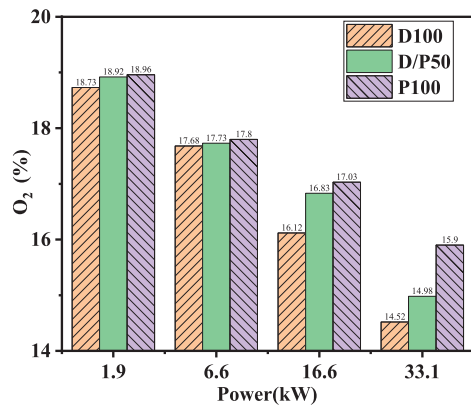
Fig.9. O_2 emissions under different running conditions

CONCLUSIONS

This paper studied the improvement of combustion performance of a diesel engine with blended PODE and pure PODE under low and medium engine load conditions. It was shown that with the increase in engine load, the effective fuel consumption rate of all three fuels was reduced to a different extent. Under low and medium engine load conditions, both blended PODE and pure PODE can provide power comparable to diesel oil, but the effective fuel consumption rate of PODE-blend and pure PODE increased. Furthermore, the NOx emission of the three fuels tends to increase with increasing engine load, and the NOx emission of D/P50 and P100 is higher than that of D100 under 1# and 2#working conditions, while the NOx emission of D100 is higher than that of D/P50 and P100 under medium engine load conditions. The blended PODE and pure PODE can significantly reduce the particulate matter and CO emissions, but the CO_2 emissions increase. The O_2 emissions of the three fuels showed a decreasing trend with increasing load, as the addition of oxygenated fuels helped to reduce the in-cylinder O_2 consumption. In general, PODE can improve the combustion performance of marine diesel engines and can obtain power comparable to diesel oil; besides, the emissions can be reduced significantly. PODE will be an ideal alternative clean fuel oil for marine diesel engines in the future.

DECLARATION OF COMPETING INTEREST

The authors declare that they have no known competing financial interests or personal relationships that could influence the work reported in this paper.

REFERENCES

1. J.E. Jonson, M. Gauss, J.P. Jalkanen, L. Johansson, Effects of strengthening the Baltic Sea ECA regulations. Atmospheric Chemistry and Physics, 2019,19, pp.13469-13487.

2. M. Karl, J.E. Jonson, A. Uppstu, A. Aulinger, M. Prank, M. Sofiev, J.P. Jalkanen, L. Johansson, M. Quante, V. Matthias, Effects of ship emissions on air quality in the Baltic Sea region simulated with three different chemistry transport models. Atmospheric Chemistry and Physics, 2019, 519, pp. 7019-7053.

3. Y.J. Wei, W. Kun, W.R. Wang, S.H. Liu, X. Chen, YJ. Yang, S.W. Bai, Comparison study on the emission characteristics of diesel- and dimethyl ether originated particulate matters. Applied Energy, 2014;130, pp. 357–369. doi:10.1016/j.apenergy.2014.05.058.

4. H. Chen, J. He, H. Hua, Investigation on combustion and emission performance of a common rail diesel engine fueled with diesel/biodiesel/polyoxymethylene dimethyl ethers blends, Energy Fuel, 2017, 31, pp. 11710–11722.

5. J.X. Wang, FJ. Wu, J.H. Xiao, S.J. Shuai, Oxygenated blend design and its effects on reducing diesel particulate emissions. Fuel, 2009, 88,pp.2037–2045. doi:10.1016/j.fuel.2009.02.045.

6. N. Miyamoto, H. Ogawa, T. Arima, G.H. Cao, Improvement of diesel combustion and emissions with addition of various oxygenated agents to diesel fuels. 1998, 19, pp.154-156. https://doi.org/10.1016/S0389-4304(97)00065-9.

7. N. Miyamoto, H. Ogawa, M. Nurun, K. Obata, T. Arima, Smokeless, low NOx, high thermal efficiency, and low noise diesel combustion with oxygenated agents as main fuel. 1998 SAE International Congress and Exposition, 1998. doi:10.4271/980506.

8. M. Puškár, P. Tarbajovský, M. Lavčák, M. Soltesova, Marine Ancillary Diesel Engine Emissions Reduction Using Advanced Fuels. Journal of Marine Science and Engineering. 2022, 10. doi:10.3390/jmse10121895.

9. K. Cheikh, A. Sary, L. Khaled, L. Abdelkrim, T. Mohand, Experimental assessment of performance and emissions maps for biodiesel fueled compression ignition engine. Applied Energy, 2016, 161, pp. 320–329.doi:10.1016/j.apenergy.2015.10.042.

10. [10] B. Choi, X.L. Jiang, Y.K. Kim, G. Jung, C. Lee, I. Choi, C.S Song, Effect of diesel fuel blend with n-butanol on the emission of a turbocharged common rail direct injection diesel engine. Applied Energy, 2015, 146, pp. 20–28. doi:10.1016/j.apenergy.2015.02.061.

11. M. Puškár, J. Živcák , M. Lavcák, M. Soltesova, M. Kopas, Analysis of Combustion Conditions for Sustainable Dual-Fuel Mixtures. Sustainability, 2022, 14. doi:10.3390/su142113962.

12. Y.Y. Zheng, Q. Tang, T.F. Wang, Y.H. Liao, J.F. Wang, Synthesis of a green diesel fuel additive over cation resins. Chemical Engineering & Technology, 2013, 36, pp. 1951–1956. doi:10.1002/ceat.201300360.

13. R.Y. Sun, I. Delidovich, R. Palkovits, Dimethoxymethane as a Cleaner Synthetic Fuel: Synthetic Methods, Catalysts, and Reaction Mechanism. ACS Catalysis, 2019, 9, pp.1298–1318. doi:10.1021/acscatal.8b04441.

14. J. Burger, M. Siegert, E. Strofer, H. Hasse, Poly(oxymethylene) dimethyl ethers as components of tailored diesel fuel: Properties, synthesis and purification concepts. Fuel, 2010, 89, pp. 3315-3319. doi:10.1016/j.fuel.2010.05.014.

15. J. Burger, E. Strofer, H. Hasse, Production process for diesel fuel components poly(oxymethylene) dimethyl ethers from methane-based products by hierarchical optimization with varying model depth. Chemical Engineering Research & Design, 2013, 91, pp.2648-2662. doi:10.1016/j.cherd.2013.05.023.

16. D. Wang, G.L. Zhu, Z. Li, C.G. Xia, Polyoxymethylene dimethyl ethers as clean diesel additives: Fuel freezing and prediction. Fuel, 2018, 237, pp. 933-839. doi: 10.1016/j.fuel.2018.10.014.

17. X. Xiao, T. Zheng, Y.F, Wang, Research on compatibility of PODE and diesel fuel. Diesel Engine, 2015, 37 ,pp.24–28.

18. Z.B. Yang, C.X. Ren, S.Q Jiang, Y.Y Xin, Y.F Hu, Z.C Liu, Theoretical predictions of compatibility of polyoxymethylene dimethyl ethers with diesel fuels and diesel additives. Fuel, 2022, 307. doi: 10.1016/j.fuel.2021.121797.

19. J.X. Ning, Q.Y. Qiu, H.X. Ma, L.Y Chen, Development and catalytic mechanism of ionic liquid catalysts for polyoxymethylene dimethyl ethers. Chemical Physics Letters,2023, 822. doi:10.1016/j.cplett.2023.140471.

20. F.K. Yang, J.W. Wang, Research progress on the synthesis of diesel additive polymethoxydimethyl ether. Applied Chemical Industry, 2012, 41, pp.1803-1806.

21. Y. Meng, H. Li, C.N. Dai, B.H. Chen, Z.G. Lei, X.G. Li, X. Gao, Innovative reactive distillation process for the eco-friendly Poly (oxymethylene) dimethyl ethers synthesis from methylal and trioxane. Separation and Purification Technology, 2021, 278. doi: 10.1016/j.seppur.2021.119538.

22. R.J Zhu, X.B. Wang, H.Y. Miao, Z.H. Huang, J. Gao, D.M. Jiang, Performance and emission characteristics of diesel engines fueled with diesel-dimethoxymethane (DMM) blends. Energy&Fuels, 2009, 23, pp .286–293. doi: 10.1021/ef8005228.

23. Z. Wang, H.Y. Liu, J. Zhang, J.X. Wang, S.J. Shuai, Performance, combustion and emission characteristics of a diesel engine fueled with polyoxymethylene dimethyl ethers (PODE3-4)/diesel blends. Applied Energy, 2015, 75, pp.2337-2344. https://doi.org/10.1016/j.egypro.2015.07.479.

24. W.X. Yang, Y. Wang, Y.Q. Bai, L. Hao, X. Liu, Experimental study of the bioethanol substitution rate and the diesel injection strategies on combustion and emission characteristics of dual-fuel-direct-injection (DFDI) engine. Journal of the Energy Institute,2023,106. https://doi.org/10.1016/j.joei.2022.101153.

25. J.H. Liu, P. Sun, H. Huang, J. Meng, X.H. Yao, Experimental investigation on performance, combustion and emission characteristics of a common-rail diesel engine fueled with polyoxymethylene dimethyl ethers-diesel blends. Applied Energy, 2017,202, pp. 527-536. https://doi.org/10.1016/j.apenergy.2017.05.166.

26. H.Y. Liu, Z. Wang, J. Zhang, JX. Wang, SJ. Shuai, Study on combustion and emission characteristics of polyoxymethylene dimethyl ethers/diesel blends in light-duty and heavy-duty diesel engines. Applied Energy, 2017, 185, pp.1393-1402. https://doi.org/10.1016/j.apenergy.2015.10.183.

27. H.Y. Liu, Z. Wang, J.X. Wang, X. He, Improvement of emission characteristics and thermal efficiency in diesel engines by fueling gasoline/diesel/PODEn blends. Energy, 2016, 97, pp. 105-112. https://doi.org/10.1016/j.energy.2015.12.110.

28. H.F. Wang, W.X. Ma, Research on the emission characteristics of diesel blended with PODE mixed fuel under small load conditions. Small Internal Combustion Engine and Vehicle Technology, 2020, 49, pp. 82-90.

29. H.Z. Huang, Q.S. Liu, W.W. Teng, Q.X. Wang, The Potentials for Improving Combustion Performance and Emissions in Diesel Engines by Fueling n-butanol/diesel/PODE3-4 Blends. Energy Procedia, 2017.105, pp. 914-920. https://doi.org/10.1016/j.egypro.2017.03.415.

30. H.Chen, J.J. He, Z.M. Chen, L.M. Geng, A comparative study of combustion and emission characteristics of dual-fuel engine fueled with diesel/methanol and diesel–polyoxymethylene dimethyl ether blend/methanol. Process Safety and Environmental Protection, 2021, 147, pp.714-722. https://doi.org/10.1016/j.psep.2021.01.007.

31. J.H. Liu, Y. Liu, Q. Ji, P. Sun, X.C. Zhang, X.D. Wang, H.J. Ma, Effects of split injection strategy on combustion stability and GHG emissions characteristics of natural gas/diesel RCCI engine under high load. Energy,2023,266. https://doi.org/10.1016/j.energy.2022.126542.

32. Z. Korczewski. Energy and emission quality ranking of newly produced low-sulphur marine fuels. Polish Marine Research, 2022, 29, pp. 77-87.doi:10.2478/pomr-2022-0045.

33. G. Wu, G.H. Jiang, Z.Y. Yang, H.J. Wei, Z.J. Huang, Mechanism of emission and smoke elimination of marine diesel engine fueled with biodiesel. Journal of Harbin Engineering University, 2019, 40,pp.136-142.

ECONOMIC ANALYSIS AND THE EEXI REDUCTION POTENTIAL OF PARALLEL HYBRID DUAL-FUEL ENGINE–FUEL CELL PROPULSION SYSTEMS FOR LNG CARRIERS

Nader R. Ammar (ORCID)

a) Department of Marine Engineering, Faculty of Maritime Studies, King Abdulaziz University, Jeddah, Saudi Arabia

b) Department of Naval Architecture and Marine Engineering, Faculty of Engineering, Alexandria University, Egypt

Majid Almas,

Qusai Nahas

Department of Marine Engineering, Faculty of Maritime Studies, King Abdulaziz University, Jeddah, Saudi Arabia

* Corresponding author: *nammar@kau.edu.sa (Nader R. Ammar)*

ABSTRACT

One potential solution for reducing carbon dioxide emissions from ships and meeting the Energy Efficiency Existing Ship Index (EEXI) requirements is to use a hybrid propulsion system that combines liquid hydrogen and liquefied natural gas fuels. To improve energy efficiency for diesel-electric dual-fuel ship propulsion systems, an engine power limitation system can also be used. This paper examines the potential use of these systems with regard to several factors, including compliance with EEXI standards set by the International Maritime Organization, fuel ratio optimisation, installation requirements, and economic feasibility. As a case study, an LNG carrier is analysed, with dual-fuel diesel-electric and two hybrid systems adjusted to meet IMO-EEXI requirements with engine power limitation percentages of 25%, 0% (hybrid option 1), and 15% (hybrid option 2), respectively. From an economic standpoint, the liquid hydrogen-based system has competitive costs compared to the dual-fuel diesel-electric system, with costs of 2.1 and 2.5 dollars per kilogram for hybrid system options 1 and 2, respectively.

Keywords: EEXI, EPL, alternative fuels, LNG carrier, economic analysis

INTRODUCTION

The transport of goods worldwide generates multiple exhaust gas emissions that have negative effects on the environment. These emissions include carbon monoxide (CO), carbon dioxide (CO_2), sulfur oxides (SO_x), particulate matter, and nitrogen oxides (NO_x) [1–3]. Stricter rules on greenhouse gas emissions (GHG) in the maritime industry have become a recent topic of debate due to the fact that over 90% of global trade is transported by ships [4, 5]. Shipping is responsible for more than 5% of overall SO_x emissions and 3% of overall CO_2 emissions [1]. To address this issue, the

International Maritime Organization (IMO) has introduced several regulations aimed at promoting energy efficiency and reducing emissions from ships [6]. One such regulation is the Energy Efficiency Existing Ship Index (EEXI), which aims to improve the energy efficiency of existing ships and ensure that they meet minimum requirements for carbon emissions. The EEXI is part of the IMO's strategy to reduce greenhouse gas emissions from international shipping by at least 50% by 2050 [7, 8]. It is based on a calculation of a ship's Energy Efficiency Design Index (EEDI), which assesses a ship's carbon emissions based on its size, speed, and other design features [9, 10]. The EEXI uses a similar methodology

and calculation to determine the energy efficiency rating of existing ships. Ships that fail to meet the minimum energy efficiency requirements set by the EEXI must take measures to reduce their emissions or face penalties. The EEXI regulation is a significant step towards reducing emissions from the shipping industry and improving energy efficiency. However, it presents challenges for ship owners and operators who must comply with the new standards while ensuring the economic viability of their vessels [11].

Various applications can be implemented on marine vessels to comply with EEXI requirements, including hull cleaning, design modifications, energy-saving devices, route optimisation, engine modifications, engine power limitation (EPL), and shaft power limitation (ShaPoLi) [12, 13]. Alternative energy or waste heat recovery systems can also be implemented to reduce the accommodation service resourced load [13, 14]. Cleaning the hull and propeller surfaces can reduce water resistance and save up to 5% in fuel, while improvements to the propeller design, such as variable structure propellers, can increase energy efficiency by up to 5% when compared to conventional propellers [15‒17].

Engine power limitation is a highly applicable and easy method for older vessels to comply with EEXI requirements because minimal modifications are necessary. EPL ensures a changeable limit on the maximum continuous rating (MCR) power output, which also limits the vessel's speed. It can be implemented using a mechanical stopping screw for mechanical engines or fuel-limiting software for electronic engines. Moreover, several studies have investigated the potential of alternative propulsion systems and fuels to improve energy efficiency and reduce emissions in the shipping industry, including the use of LNG and LH_2 fuels in hybrid propulsion systems [18, 19] and the potential for engine power limitation (EPL) systems to improve the energy efficiency of diesel-electric dual-fuel propulsion systems [12]. These studies highlight the importance of considering a range of factors, including technical feasibility, safety considerations, and economic viability, when evaluating alternative propulsion systems and fuels for compliance with EEXI standards.

Moreover, there are many projects aimed at using fuel cell engines onboard ships to reduce emissions. The ZEMSHIP program aimed to operate a hybrid vessel employing proton exchange membrane fuel cells (PEMFCs), batteries, and compressed hydrogen from 2008 to 2010 [20]. The supply vessel, Viking Lady, adopted a hybrid propulsion system of dual-fuel diesel-electric engines (DFDE) and a molten carbonate fuel cell (MCFC) to provide secondary power as a part of the low-pollution vessel project (Fellow Vessel). The Viking Lady was the first hybrid ship to use an MCFC [21]. Hybrid engines with high-temperature fuel cells can be used in large ships by reforming hydrocarbon fuels [22]. However, due to their CO_2 emissions, reforming fossil fuels is unable to achieve the higher energy efficiency criterion. Korkmaz et al. conducted a comparative environmental study that examined the CO_2 reduction potentials of a ship using phosphoric acid fuel cells (PAFC), MCFC, and a diesel engine, and found that a 50% CO_2 emission reduction is hard to achieve [23]. In order to use hydrogen fuel onboard ships, it should be stored in compressed or liquefied forms. Compressed hydrogen storage techniques can be used at high pressures up to 800 bar, which results in a storage density of less than 39 kg/m³ [24]. Alternatively, liquefied hydrogen (LH_2) can be stored at atmospheric pressure and a temperature of -250 °C, which results in a higher density of 71 kg/m³ [25]. Due to the substantial volume of fuel storage tanks on ships, it is impractical to bunker while at sea. Therefore, the high density of LH_2 makes it a good option for maritime vessels, especially for large ships. On the other hand, PEMFCs have many desirable properties that make them a good option for ships' propulsion systems. PEMFCs work at low temperature and pressure, which allows for quick startup [26]. They also have high power density and efficiency compared to other fuel cell types [27]. Additionally, PEMFCs exhibit superior heat and reaction stability compared to SOFCs and perform better at low engine loads compared to DFDE engines [28].

The research gap in the previous literature on studying EEXI, EPL systems, alternative fuels, and hybrid propulsion systems for ships lies in the need to evaluate their combined effectiveness. While EPL and hybrid propulsion systems are individual solutions for improving energy efficiency and reducing emissions, their combined effectiveness has not been thoroughly studied. This study aims to contribute to this growing body of research by evaluating the potential of hybrid propulsion systems that combine LH_2 and LNG fuels, as well as the use of the EPL system for improving energy efficiency in DFDE ship propulsion systems. Additionally, this research focuses on several factors, including compliance with EEXI standards, fine-tuning fuel ratios, installation requirements, and economic feasibility. The investigated case study focuses on an LNG carrier and provides valuable insights for ship owners and operators who are seeking to comply with regulations and improve the environmental and economic performance of their vessels.

SYSTEM DESCRIPTION

LNG CARRIER VESSEL SPECIFICATIONS

The present case study is one of the Q-Max LNG carriers operated by Qatargas II, with an IMO number of 9337755. The vessel is currently berthed at the Ras Laffan terminal in Qatar. Its gross tonnage is 163,922, and its deadweight is 130,102. Gross tonnage refers to the total enclosed volume of a ship, while deadweight refers to the maximum weight of cargo, fuel, and supplies that a ship can carry. The vessel's main dimensions are 345 m for overall length, 53 m for breadth, and 12 m for summer draft. Table 1 summarises the main specifications for the ship [29, 30], including information such as its propulsion system, cargo capacity, and crew size. The vessel is powered by 2 MAN B&W 7S70ME-C two-stroke low-speed diesel engines, which have a total output power of 43.54 MW at 91 rpm.

Item	Value
Vessel classification	LNG tanker
Port of registry	Marshall Islands
Dimensions	345 (length) × 53 (beam) × 12 (draft) in m
Deadweight	130,102 ton
Cargo volume	266,000 m³
Speed	19 knots
Engine	Dual-fuel diesel-electric engine
Installed power	43,540 kW (58,390 hp) at 91 rpm
Propulsion	2 x MAN B&W 7S70ME-C diesel engines
Main engine SFC	175 g/kWh
Liquefied natural gas fuel consumption	4.75 tons per hr

LNG CARRIER PROPULSION SYSTEM OPERATED BY DUAL-FUEL DIESEL-ELECTRIC ENGINE

Fig. 1 depicts a typical propulsion system operated by a DFDE for LNG ships. The LNG is stored at a pressure less than 1.2 bar and a temperature of -163 °C. During ship operations, the LNG's boil-off gas (BOG) is utilised as fuel to operate the main engines [31]. The compressor pressurises the BOG before supplying it to the DFDE system. The produced BOG is not enough to run the DFDE during operations. Therefore, the LNG fuel pump, submerged in the fuel tank, is used to transfer liquefied natural gas to the fuel vaporiser. The pump raises the LNG's pressure to 6 bar, at which point it is vaporised into natural gas. In a BOG vaporiser, the liquefied natural gas is heated using glycol water. After being heated to the required inlet temperature, which usually ranges from 25 °C to 35 °C, the LNG and boil-off gas are fed to the DFDE.
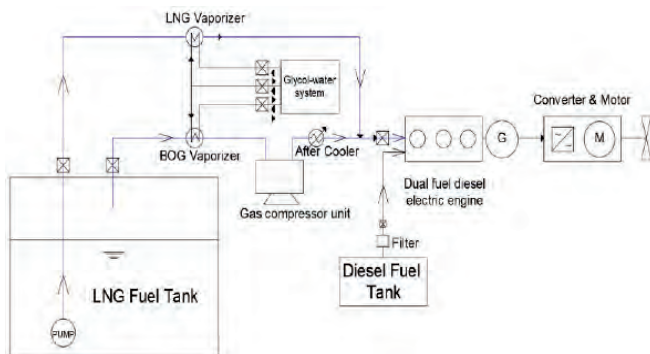
Fig. 1. LNG carrier propulsion system operated by dual-fuel diesel-electric engine

LNG CARRIER PROPULSION SYSTEM OPERATED BY HYBRID ENGINES

Fig. 2 shows the hybrid propulsion system of an LNG carrier, which operates using LNG and LH_2 fuels. The method for using the produced BOG in the liquefied gas storage tanks in the hybrid system is similar to that of the DFDE system explained earlier. PEMFC requires hydrogen at a pressure greater than 3 bar, which is achieved by pressurising the LH_2 using a submerged pump in the fuel tank. The BOG–LH_2 mixture is then pressurised using a compressor to the required inlet pressure for the fuel cell. Meanwhile, glycol water heats the pressurised liquid hydrogen and supplies it to the PEMFC electrode. The air is compressed and cooled before being delivered to the cathode of the PEMFC stack. Any unreacted hydrogen gas that passes through the fuel cell anode is recirculated back to the inlet line. At the cathode, the produced water vapour is discharged to the atmosphere.
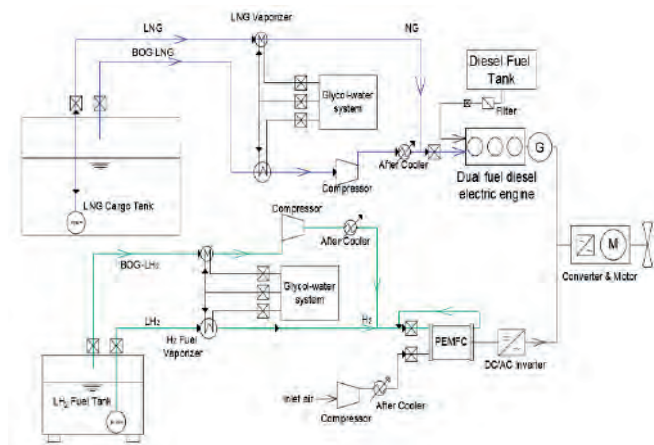
Fig. 2. LNG carrier hybrid propulsion system operated by LNG and LH_2 fuels

ASSUMPTIONS FOR THE CURRENT CASE STUDY

The assumed ship route for the case study involves transporting LNG between Ras Laffan port in Qatar and Vizag port in India, as shown in Fig. 3. Ras Laffan port is one of the largest LNG export facilities in the world, with the largest artificial harbour and a strategic location on the international maritime trade route [32]. India is currently the world's fourth-largest importer of LNG, with Qatar contributing 42% of India's imports and making it the top supplier of liquefied natural gas to India [33]. Table 2 provides a description of the voyage scenario and the schedule for the assumed 18 round trips per year of the vessel, including information such as the cargo capacity, loading and unloading times, and estimated fuel consumption for each leg of the journey.

Fig. 3. LNG carrier case study vessel and ship route

Tab. 2 Voyage circumstances for the case study vessel

Voyage	Operating conditions	Voyage time	Engine working time	BOG producing time
Loaded	LNG loading, h.	32	-	-
	Sea routing, h.	197	197	197
Ballast	LNG discharging, h.	32	-	-
	Sea routing, h.	197	197	197
Overall	Two-way trip in hours	455	395	395
	Two-way trip in days	19	17	17
Number of annual round trips	18	-	-	-

Tab. 3 PEM fuel cell main specifications [34, 36]

Rated power	200 kW
Minimum power	55 kW
Voltage	350–720 VDC
Volume	0.5 m³ without H_2 storage
Dimensions (mm)	1209 × 741 × 2195
Efficiency	53.5% @ nominal power
Peak efficiency	60% @ 50% power
Ambient temperature	-30 °C to +40 °C
Emission	Water vapour
Operating temperature	60–65 °C
Lifetime	40,000 – 80,000 hours
Certifications	DNV-type approval

The specifications of the selected PEMFC module, which is used in the hybrid propulsion system, are listed in Table 3. The Ballard 200 kW PEMFC system is designed to provide zero-emission power to ships. The selected PEMFC module is specifically developed and tested for marine environments, and it has been approved by Det Norske Veritas (DNV) ship class for marine applications. The module is scalable from 200 kW to MWs to accommodate the power requirements of different ships based on the demands of their routes [34]. To comply with safety requirements, onboard the case study vessel, liquid hydrogen tanks are stored in IMO class C tanks, with vacuum-perlite insulation and stainless steel 304 tanks being used [35]. For this study, the capacity of the LH_2 tank was estimated by adding a 15% margin to the calculated amount of liquid hydrogen. This margin was added to ensure that the calculated storage volume would cover the required power onboard the ship. Additionally, it is difficult to maintain the vacuum insulation of liquid gas storage tanks, particularly for large volumes, which further justifies the use of the margin.

From an economic viewpoint, the following capital costs have been assumed for the current study. The cost of the dual-fuel engine is assumed to be 520 $/kW [37]. The cost of the PEMFC stack is assumed to be 150 $/kW, while the cost of the PEMFC system is assumed to be 210 $/kW [38, 39]. The cost of the liquefied natural gas vaporiser is assumed to be 40 $/kW, while the cost of the liquid hydrogen vaporiser is assumed to be 60 $/kW. The cost of the natural gas compressor is assumed to be 1200 $/kW [40], while the cost of the air compressor is assumed to be 450 $/kW [41]. Finally, the cost of the after-cooler is assumed to be 90 $/kW [42-44]. In addition, maintenance and repair costs are assumed to be 6% of the capital costs, while operating supplies costs are assumed to be 15% of the maintenance and repair costs [45]. According to the latest fuel prices, the prices of natural gas and hydrogen fuels are 190 $/ton and 5200 $/ton, respectively [46, 47].

METHODOLOGY AND MODELLING

In this section, the energy efficiency existing index and economic modelling of conventional DFDE and hybrid propulsion systems operated by alternative fuels are assessed. The fuel ratios of LNG and LH_2 that satisfy EEXI-IMO requirements for both the hybrid and DFDE propulsion

systems are estimated. Finally, the breakeven price of LH_2 for the hybrid systems is estimated in the economic analysis.

ATTAINED AND REFERENCE ENERGY EFFICIENCY EXISTING INDEX VALUES

The Energy Efficiency Existing Ship Index is a regulatory requirement under the International Maritime Organization's (IMO) MARPOL Annex VI regulations. The EEXI requirements were adopted by the IMO's Marine Environment Protection Committee (MEPC) in November 2020 and became mandatory on January 1, 2023. Starting on that date, all ships over 400 gross tonnage (GT) will be required to have an EEXI that meets the required level of energy efficiency, based on the ship's technical specifications, design characteristics, and operational profile. Each existing ship must meet two EEXI parameters specified by the IMO in 2022: the required and the attained. In order to meet the minimum energy efficiency standards recommended by the IMO, the attained EEXI (expressed in gCO_2/ton.nm) must be equal to or less than the required EEXI. The required EEXI for each ship is based on its baseline value of the Energy Efficiency Design Index (EEDI) after accounting for a reduction factor as shown in Eqs. (1) and (2) [48, 49].

$$\text{EEXI baseline value} = 2253.7 \times DWT^{-0.474} \quad (1)$$

$$\text{Required EEXI} = \left(1 - \frac{X}{100}\right) \times \text{EEXI baseline value} \quad (2)$$

where (DWT) is the ship's deadweight in tons and (X) is the reduction factor, based on the ship type, and is 30% for LNG carriers.

The attained EEXI value for LNG carriers, on the other hand, depends on several factors such as the type of fuel used in the main and auxiliary engines, the ship's deadweight (DWT) in tons, and other ship specifications, as well as the sea state. The formula for calculating the attained EEXI for diesel-electric LNG carriers (expressed in gCO_2/ton.nm) is presented in Eq. (3) [48-50]. In this case, dual-fuel diesel-electric engines do not have separate main engines (MEs) and auxiliary engines (AEs) but have a number of 4-stroke dual-fuel gensets, all acting as MEs.

$$\text{EEXI}_{attained} = \frac{(P_{ME} + P_{AE}) \times \begin{bmatrix} (C_{fME(pilot)} \times SFC_{ME(pilot)}) + \\ (C_{fME(gas)} \times SFC_{ME(gas)}) \end{bmatrix}}{f_i \cdot f_c \cdot f_w \cdot \text{Capacity} \cdot V_{ref}} \quad (3)$$

where (P_{ME}) and (P_{AE}) are the main and auxiliary engines powers, respectively, (SFC_{ME}) is the specific fuel consumption at 75% for the main engines, respectively, (C_f) is the fuel conversion factor to CO_2 emissions, and (V_{ref}) is the vessel speed in knots at the summer load line. (f_i) is the capacity

factor for any technical/regulatory limitation on ship capacity, (f_c) is the cubic capacity correction factor for chemical tankers, gas carriers and RO-RO passenger ships, and (f_w) is the coefficient for the decrease in ship speed due to weather and environmental conditions. Capacity is the deadweight tonnage (DWT) for LNG carriers.

(P_{ME}) is the engine power, assumed to be 75% of the rated power in normal conditions. In the case of using electric propulsion and Engine Power Limitation (EPL), (P_{ME}) can be calculated using Eq. (4) [50].

$$P_{ME} = \frac{\sum_{i=1}^{n}(0.83 \cdot MPP_{limit})}{\eta_{(elec)}} \quad (4)$$

where (MPP_{limit}) is the rated limited output power in kW of electric engine (i), and ($\eta_{(elec)}$) is the electric systems' efficiencies including the transformer, converter, and propulsion motor.

In addition, (P_{AE}) used in Eq. (3) can be predetermined based on the main engine power as expressed in Eq. (5).

$$P_{AE(MCR(ME)>10,000 \text{ kW})} = \left[0.025 \cdot \left(\sum_{i=1}^{nME} MCR_{ME}\right)\right] + 250 \quad (5)$$

where (MCR) represents the maximum continuous rating power in kilowatts for the main engine (i), and (n) represents the number of main engines on the ship.

Calculating the reference ship speed (V_{ref}) depends on whether or not it complies with Energy Efficiency Design Index (EEDI) requirements. If the ship complies with EEDI requirements, (V_{ref}) can be obtained from the certified speed–power curve. If the ship does not comply with EEDI requirements, an approximated speed–power curve can be used to determine (V_{ref}). If the ship's sea trial results are validated by tank tests but it does not comply with EEDI requirements, (V_{ref}) can be calculated using Eq. (6) [48].

$$V_{ref} = V_s \times \left(\frac{P_{ME}}{P_s}\right)^{\frac{1}{3}} \quad (6)$$

where (V_s) is the sea trial speed, and (P_s) is the main engine power according to (V_s). For tankers, container ships, or bulk carriers not subject to the EEDI but whose sea trials have been calibrated by the tank test under the design load draught and sea conditions, (V_{ref}) can be calculated using Eq. (7).

$$V_{ref} = k^{\frac{1}{3}} \times \left(\frac{DWT_s}{\text{Capacity}}\right)^{\frac{2}{9}} \times V_s \times \left(\frac{P_{ME}}{P_s}\right)^{\frac{1}{3}} \quad (7)$$

where (DWT_s) is the deadweight regarding the design load draught. The scale coefficient is represented by k depending on the ship type and capacity [48].

In the case of using liquefied fuels for operating ship engines, the boil-off gas rate (BOR) can be calculated using Eq. (8). It shows the amount of evaporated LNG fuel per day as a share of the overall cargo (%/day) [51–53].

$$BOR = \left(\frac{Q}{H_{latent}} \times 3600 \times 24\right) \times \frac{100}{\rho_{LH_2} V_{cargo}} \quad \text{(8)}$$

where (Q) is the power of the heat exchange rate in the storage tanks (kW), (ρ) is the LNG density in kg/m³, and (H_{latent}) is the vaporisation heat in kJ/kg. The average BOR values for new LNG tankers range from 0.1 to 0.15% /day for the laden voyage and from 0.06 to 0.1 %/day for the ballast voyage [54].

ECONOMICS MODELLING

A system's initial investment cost, or CAPEX, is made up of both direct and indirect costs [55]. Direct costs include the installation and purchase costs of the equipment, while indirect costs include incidental costs such as system design, manpower, and surcharges. The formula for calculating CAPEX is shown in Eq. (9), which takes into account both direct and indirect costs associated with the installation of the equipment.

$$CAPEX = \sum_{1}^{x} TP_{C,x} \left(1 + IPER_{c,x}\right) \quad \text{(9)}$$

where (TP_c) represents the total purchase and initial costs of the equipment (x), and ($IPER_c$) represents the percentage of indirect costs related to (TP_c) costs. ($IPER_c$) can be calculated using the following Eq. (10) [56, 57]:

$$IPER_c = \frac{C_{lab} + C_{mat} + C_{overhead} + C_{reg} + C_{test}}{TP_c} \quad \text{(10)}$$

where (C_{lab}) represents the indirect labour costs for equipment installation, like wages, benefits, and training costs for the workers who install the equipment. (C_{mat}) is the indirect material costs, such as costs of materials that are necessary for the installation of the equipment but are not part of the equipment itself. Examples include wiring, cables, nuts, bolts, and other small parts. ($C_{overhead}$) represents the overhead indirect costs, like costs associated with running the business that cannot be directly attributed to the installation of the equipment. (C_{reg}) represents the indirect permitting and regulatory costs, like costs associated with obtaining the necessary permits and complying with regulatory requirements for the installation of the equipment. (C_{test}) is the testing and commissioning indirect costs, for example, costs associated with testing and commissioning the equipment to ensure that it operates correctly.

On the other hand, the overall operating expenses (OPEX) of a propulsion system over the course of its lifetime include the costs of fuel, electricity, and operations and maintenance (O&M). The value of operating expenditures is divided into four main components as shown in Eq. (11).

$$OPEX = C_{O\&M} + C_{fuel} + C_{elec.} + C_{fixed} \quad \text{(11)}$$

where ($C_{O\$M}$) is the operating and maintenance costs, (C_{fuel}) is the total fuel costs, ($C_{elec.}$) is the electricity consumption for operating the system, and (C_{fixed}) is the fixed charges like insurance. (C_{fixed}) can be assumed as 0.7% of the fixed capital investment [45].

Net present value (NPV) is the difference between the present value of cash inflows and the present value of cash outflows over a period of time. The investment will be more valuable if NPV is higher than 0. The NPV formula is given in Eq. (12) [58, 59].

$$NPV = \sum_{t=1}^{N} \frac{C_{tot}}{(1 + i)^t} - C_o \quad \text{(12)}$$

where (t) is the finances interval, (N) denotes the lifetime, (C_{tot}) denotes the net finances at interval (t), (C_o) denotes the current amount of capital expenditure, and (i) refers to the annual interest rate. (i) ranges from (2% to 8%) and from (8% to 30%) for industrialised and developing countries, respectively [60]. (i) is assumed to be 5% for the current study.

RESULTS AND DISCUSSION

ENERGY EFFICIENCY RESULTS

Fig. 4 shows the energy efficiency index values for existing LNG carriers based on ship deadweight. The calculated energy efficiency index value for the case study, which is operated by LNG fuel without installing an EPL system, is 7.19 gCO_2 per ton-nautical mile. This value does not meet the IMO-EEXI standard. To comply with the reference EEXI value, an EPL system should be installed for the DFDE propulsion system.

Reducing the consumption of LNG and increasing the power produced by hydrogen fuel cells are two important factors that can reduce the attained EEXI for a hybrid propulsion system. In order to comply with the IMO-EEXI standard for the year 2023, a hybrid system is incorporated with variable fuel cell and hydrogen output powers. The fuel cells should generate 11.6 MW of the required propulsion power, or 26.64% of the total maximum continuous rating (MCR), to comply with the reference EEXI value. For this scenario, hybrid system option 1 will attain an energy efficiency index value of 5.93 gCO_2 per ton-nautical mile, which complies with the IMO-EEXI value. Hybrid system option 1will not require the installation of an EPL system. On the other hand, a proposed hybrid propulsion system, operated by 5.8 MW PEMFC with an installed EPL system, will be investigated in the current study. This system, hybrid

system option 2, is being investigated to show the effect of using EPL in the hybrid system while reducing the fuel cell output power.
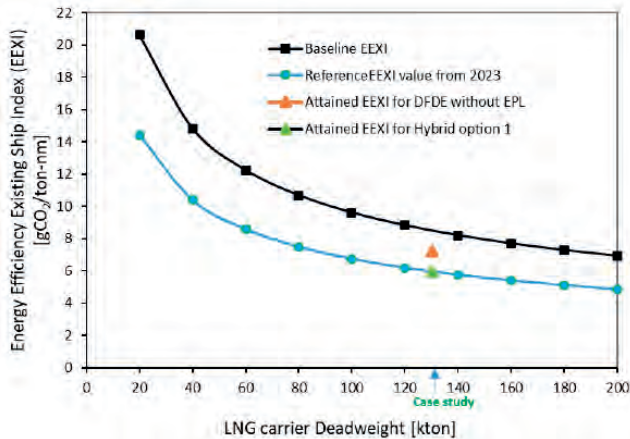
Fig. 4. Reference EEXI for the LNG carriers at different capacities

Limiting engine power is a method that can be used to reduce a ship's EEXI. This involves reducing the maximum power output of the ship's engines, which in turn limits the ship's speed. By reducing the ship's speed, the fuel consumption is lowered, resulting in lower emissions. To implement engine power limitation, the ship's engine performance needs to be analysed to determine its maximum power output. The ship's operational profile also needs to be analysed to determine the most effective engine power limitation strategy. Once the optimal strategy is determined, it needs to be implemented through the use of engine control systems that can limit the engine's maximum power output based on the ship's operational requirements. From the case study sea trial report, the relationship between ship speed, engine output power, and RPM can be drawn, as shown in Fig. 5 (a). Based on the case study specifications and main engine performance, the effect of engine power limitation on the ship speed is shown in Fig. 5 (b). The reference ship speed of 19 knots is reduced by 4%, 7%, and 11% when the engine power is limited by 10%, 20%, and 30%, respectively.

(a)   (b)
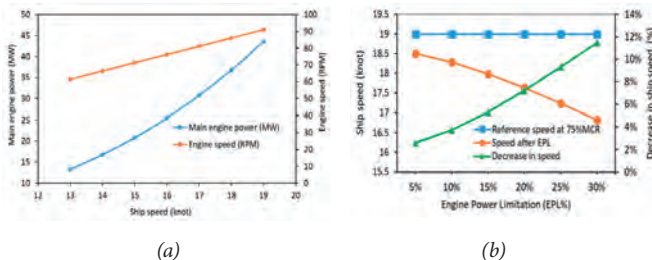
Fig. 5. Relation between ship speed and main engine power (I)
as well as EPL (II)

Fig. 6 shows the values of the attained EEXI at different EPL values for the DFDE and hybrid system option 2. It can be noted that the DFDE system has relatively high EEXI values compared to the hybrid system. As a result, it will require high

power limitation values to comply with the reference EEXI compared to the hybrid system. The reference value for the EEXI for the current case study is 5.941 gCO_2/ton-nautical mile. In order to comply with the reference EEXI, the main engine power should be limited by 25% and 15% for the DFDE and hybrid option 2 systems, respectively. In these scenarios, the attained EEXI will improve by 17% and 10%, respectively. Moreover, the operational ship speed will be reduced from 19 knots to 17.2 knots and 17.98 knots with speed reduction percentages of 9% and 5%, respectively.

(a)   (b)
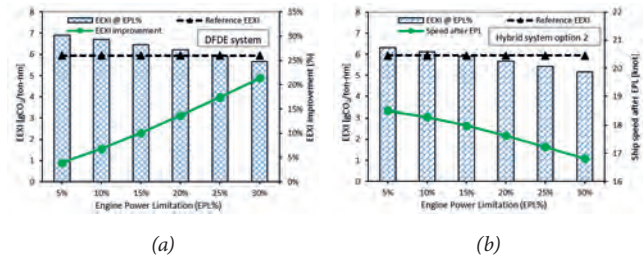
Fig. 6. EEXI at different EPL for DFDE system (i) and hybrid system option 2 (ii)

Fig. 7 illustrates the calculated weight percentages of liquid hydrogen and natural gas fuels in the DFDE and hybrid systems to comply with the required IMO-EEXI value. To achieve the requirements, only hybrid system option 1 can be used to power the case study vessel without installing an EPL system. The required weight percentages of liquid hydrogen fuel are 4% and 7% of the overall LNG and LH_2 fuels weight to comply with the IMO-EEXI requirements for hybrid system options 1 and 2, respectively. In comparison to a traditional liquefied natural gas system, the energy percentage is between 26.64% and 13.32% of the maximum continuous rating, respectively. In addition, proton exchange membrane fuel cells (PEMFCs) that use hydrogen have higher power-generating efficiency than conventional natural gas-operated systems.
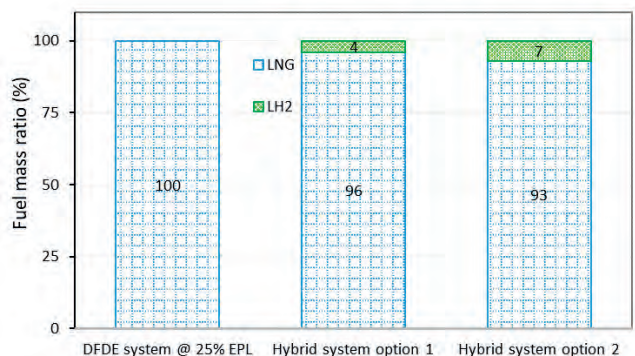
Fig. 7. Fuel mass percentage for conventional system and the hybrid systems

COMPARING THE VOLUME RATIO OF THE PROPULSION ENGINES

The required fitting space of the propulsion engines, which includes the DFDE engine, fuel cell, and liquid hydrogen tank volumes, can be seen in Fig. 8. Hybrid system options 1 and 2 require higher volumes than the conventional DFDE system by 93.76% and 48.84%, respectively. A significant contributor to the increased capacity of the overall system is the volumetric increase of the liquid hydrogen storage tanks, which accounts for 52.84% and 34.16% of the overall volume rise in hybrid system options 1 and 2, respectively. The volume of the PEMFCs is less than that of the DFDE engines, accounting for 14.91% and 9.73%, respectively, of the entire system capacities. However, the fitting of extra tubes or valves cannot have a considerable influence on the propulsion area because they are mounted on the ship deck. Table 4 displays the required capacities for fuel cell and liquid hydrogen tanks for the two hybrid systems.
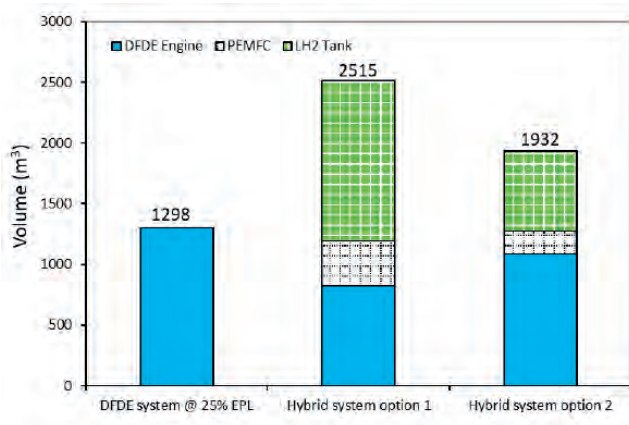
Fig. 8. Comparing the required engine volumes for the investigated propulsion systems

Tab. 4 Fuel cell and storage tank volumes onboard the ship

Hybrid system	Option 1	Option 2
Tank type	IMO type C	IMO type C
Tank volume	1320 m³	660 m³
PEMFC's power	11,600 kW	5,800 kW
Number of stacks	58	4
PEMFC volume	340 m³	160 m³

ECONOMIC RESULTS

Fig. 9 (a) shows the capital expenditures for the conventional DFDE and hybrid propulsion systems. The CAPEX of hybrid system option 1 and option 2 are 18.6% and 10.8% less than that of the conventional liquefied natural gas system, respectively. This is due to the low hydrogen consumption rate for the hybrid systems, which does not have a high impact on the CAPEX costs. Additionally, compared to using a DFDE system, the CAPEX cost of producing a lower power output

by utilising a fuel cell is quite low. Therefore, future fuel cell technology advances and an increase in the volume of stack manufacturing might accelerate the adoption of hybrid propulsion systems. On the other hand, using hybrid systems will increase the operating expenditures for propulsion systems, as shown in Fig. 9 (b). This is due to the fuel cost of liquid hydrogen being more than liquefied natural gas and due to the additional equipment required for producing electricity in the hybrid system. Additionally, the PEM fuel cell stack will need to be replaced every 43,800 working hours (5 years) during the ship's expected lifetime of 25 years. The cost of fuel cell stacks, included in the operating and maintenance costs (O&M), will be 8.7 and 4.35 million USD for hybrid system options 1 and 2, respectively, over the ship's lifetime. The liquid hydrogen cost to operating expenditure ratio is highest for hybrid system options 1 and 2, at 29.4% and 15.8%, respectively. Compared to the liquefied natural gas system, the cost of liquefied natural gas fuel is reduced by 27.5% and 13.7% for hybrid system options 1 and 2, respectively. Finally, the total operating costs for hybrid system options 1 and 2 are estimated to be 374 and 315 million USD, respectively. These costs represent an increase of 27.6% and 7.5%, respectively, compared to the DFDE system.
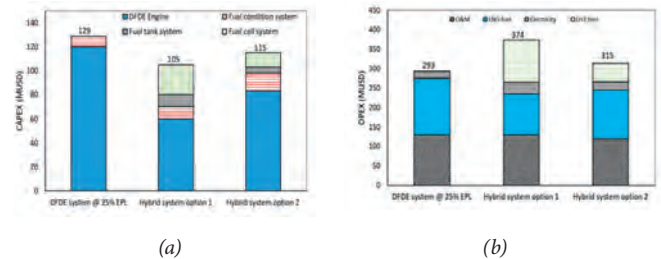
Fig. 9. CAPEX and OPEX expenses for the investigated propulsion systems

The life cycle costs of each propulsion system are the sum of the CAPEX and OPEX expenses, as shown in Fig. 10. The life cycle cost of the hybrid system increases as the EEXI requirements become more challenging. In comparison to the liquefied natural gas system, the life cycle cost for hybrid system option 1 and option 2 increased by 13.5% and 1.9%, respectively. Based on the expected lower future prices for hydrogen fuels, the predicted life cycle costs for the hybrid systems can be reduced. Therefore, the cost of LH_2 fuel needs to be reduced to operate a hybrid propulsion system profitably and to comply with the new IMO emissions requirements. Consequently, this will increase the opportunities for using hydrogen fuel onboard ships.
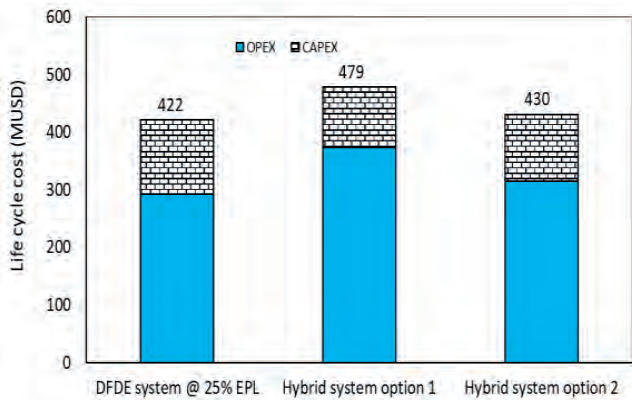
Fig. 10. Life cycle costs of the investigated propulsion systems

Fig. 11 (a and b) illustrates the breakeven liquid hydrogen fuel prices required to achieve the IMO-EEXI value for the hybrid systems compared to the conventional natural gas system. The results show that the cost of viable liquid hydrogen fuel is expected to be $2.10 per kg for hybrid system option 1 and $2.50 per kg for option 2. The left region between the life cycle cost of the conventional LNG and the hybrid systems, as shown in Fig. 11, illustrates the economic range for using the hybrid system. However, the right region in the figure is more costly compared to the conventional DFDE propulsion system.
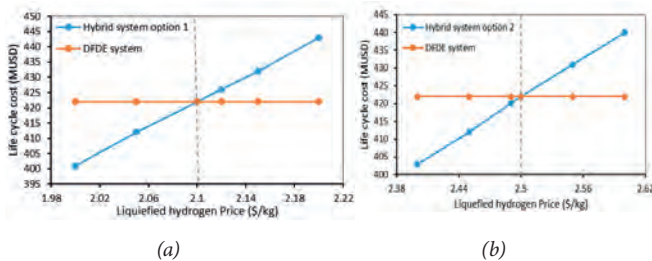
Fig. 11. Breakeven of liquid hydrogen fuel price for achieving IMO-EEXI requirements

Finally, the price of hydrogen fuel, as well as the CAPEX and OPEX expenses for the fuel cell engines, are key factors for a cost-effective hybrid propulsion system onboard a ship. Based on the current case study, the LNG–LH$_2$ hybrid system may be a cost-effective choice that satisfies EEXI requirements at a hydrogen fuel cost of less than $2.10 per kg.

CONCLUSIONS

In conclusion, the current paper has explored the potential of using hybrid propulsion systems that combine LH$_2$ and LNG fuels, as well as the use of the engine power limitation (EPL) system for improving energy efficiency for dual-fuel diesel-electric engine (DFDE) ship propulsion systems. The study has focused on several factors, including compliance with the EEXI standards set by the IMO, fine-tuning fuel ratios, installation requirements, and economic feasibility. As a case study, an LNG carrier was investigated. The main findings from the current study are as follows:

- From the energy efficiency viewpoint, the DFDE and two hybrid systems could be adjusted to comply with IMO-EEXI requirements with EPL percentages of 25%, 0% (hybrid option 1), and 15% (hybrid option 2), respectively. The attained energy efficiency existing index value for the hybrid system option 1, is 5.93 gCO$_2$ per ton-nm. In order to comply with the reference EEXI, the main engine power should be limited by 25% and 15% for the DFDE and hybrid option 2 systems, respectively. In these scenarios, the attained EEXI will be improved by 17% and 10%, respectively. Moreover, the operational ship speed will be reduced from 19 knots to 17.2 knots and 17.98 knots with speed reduction percentages of 9% and 5%, respectively. Finally, options 1 and 2 of the hybrid system require higher volumes than the natural gas system by 93.76% and 48.84%, respectively.

- From an economic viewpoint, the CAPEX expenses of the hybrid options 1 and 2 are 18.6% and 10.8% less than that of the conventional liquefied natural gas system, respectively. On the other hand, the OPEX expenses rise by 27.6% and 7.5%, respectively. Therefore, the total life cycle cost for the hybrid system options 1 and 2 increased by 13.5% and 1.9%, respectively. The LH$_2$-based system had competitive costs compared to the DFDE system, with costs of 2.1 and 2.5 dollars per kg corresponding to hybrid system options 1 and 2, respectively. Finally, the cost of hydrogen fuel needs to be reduced to operate a hybrid propulsion system profitably and to comply with the new IMO emissions requirements. Consequently, this will increase the opportunities for using hydrogen fuel onboard ships.

Finally, the findings of the present study provide valuable insights for ship owners and operators looking to comply with regulations and improve the environmental and economic performance of their vessels. As the shipping industry continues to face increasing pressure to reduce emissions and improve energy efficiency, the use of innovative technologies such as hybrid propulsion systems and EPL technology will play an increasingly important role in achieving these goals.

REFERENCES

1. H. Huang *et al.*, "Inland ship emission inventory and its impact on air quality over the middle Yangtze River, China," *Sci. Total Environ.*, vol. 843, p. 156770, 2022, https://doi.org/10.1016/j.scitotenv.2022.156770.

2. B. Ryu, P. A. Duong, and H. Kang, "Comparative analysis of the thermodynamic performances of solid oxide fuel cell–gas turbine integrated systems for marine vessels using ammonia and hydrogen as fuels," *Int. J. Nav. Arch.*

Ocean Eng., p. 100524, 2023, https://doi.org/10.1016/j.ijnaoe.2023.100524.

3. N. R. Ammar and I. S. Seddiek, "Hybrid/dual fuel propulsion systems towards decarbonization: Case study container ship," *Ocean Eng.,* vol. 281, p. 114962, 2023, https://doi.org/10.1016/j.oceaneng.2023.114962.

4. M. M. Elgohary, I. S. Seddiek, and A. M. Salem, "Overview of alternative fuels with emphasis on the potential of liquefied natural gas as future marine fuel," *Proc. IMechE, Part M: Journal of Engineering for the Maritime Environment,* vol. 229, no. 4, pp. 365-375, 2014, doi: 10.1177/1475090214522778.

5. V. Yalama, O. Yakovleva, V. Trandafilov, and M. Khmelniuk, "Future sustainable maritime sector: Fishing carriers and their adoption to the environmental regulations. Part I," *Pol. Marit. Res.,* vol. 29, no. 3, pp. 69-77, 2022, doi:10.2478/pomr-2022-0027.

6. O. Konur, M. Bayraktar, M. Pamik, B. Kuleyin, and M. Nuran, "The energy efficiency gap in Turkish maritime transportation," *Pol. Marit. Res.,* vol. 26, no. 3, pp. 98-106, 2019, doi:10.2478/pomr-2019-0050.

7. IMO, "Resolution MEPC.254(67). Guidelines on survey and certification of the energy efficiency design index (EEDI). International Maritime Organization," 2014.

8. IMO, "Energy efficiency of ships, comments received by the correspondence group on possible introduction of EEDI Phase 4, Submitted by Japan. Marine environment protection committee, 75th session agenda item 6," 2019.

9. IMO, "Fourth IMO Greenhouse Gas Study 2020: Safe, secure and efficient shipping on clean oceans," London: International Maritime Organization (IMO), 2020.

10. M. Kalajdžić, M. Vasilev, and N. Momčilović, "Evaluating an inland waterway cargo vessel's energy efficiency indices," *Pol. Marit. Res.,* vol. 29, no. 2, pp. 27-34, 2022, doi:10.2478/pomr-2022-0014.

11. V. Yalama, O. Yakovleva, V. Trandafilov, and M. Khmelniuk, "Future sustainable maritime sector: Energy efficiency improvement and environmental impact reduction for fishing carriers older than 20 years in the fleet Part II," *Pol. Marit. Res.,* vol. 29, no. 3, pp. 78-88, 2022, doi:10.2478/pomr-2022-0028.

12. M. Bayraktar and O. Yuksel, "A scenario-based assessment of the energy efficiency existing ship index (EEXI) and carbon intensity indicator (CII) regulations," *Ocean Eng.,* vol. 278, p. 114295, 2023, https://doi.org/10.1016/j.oceaneng.2023.114295.

13. E. Czermański *et al.*, "Implementation of the Energy Efficiency Existing Ship Index: An important but costly step towards ocean protection," *Marine Policy,* vol. 145, p. 105259, 2022, https://doi.org/10.1016/j.marpol.2022.105259.

14. F. Baldi and A. Coraddu, "Appendix B - Towards halving shipping GHG emissions by 2050: the IMO introduces the CII and the EEXI," in *Sustainable Energy Systems on Ships*, F. Baldi, A. Coraddu, and M. E. Mondejar, Eds. Elsevier, 2022, pp. 513-517.

15. A. Farkas, N. Degiuli, I. Martić, and C. G. Grlj, "Is slow steaming a viable option to meet the novel energy efficiency requirements for containerships?" *J. Clean. Prod.,* vol. 374, p. 133915, 2022, https://doi.org/10.1016/j.jclepro.2022.133915.

16. M. Schroer, G. Panagakos, and M. B. Barfod, "An evidence-based assessment of IMO's short-term measures for decarbonizing container shipping," *J. Clean. Prod.,* vol. 363, p. 132441, 2022, https://doi.org/10.1016/j.jclepro.2022.132441.

17. H. Wang, Y. Hou, Y. Xiong, and X. Liang, "Research on multi-interval coupling optimization of ship main dimensions for minimum EEDI," *Ocean Eng.,* vol. 237, p. 109588, 2021, https://doi.org/10.1016/j.oceaneng.2021.109588.

18. S. E. Damian *et al.*, "Review on the challenges of hybrid propulsion system in marine transport system," *Journal of Energy Storage,* vol. 56, p. 105983, 2022, https://doi.org/10.1016/j.est.2022.105983.

19. S. Hyeon, J. Lee, and J. Choi, "Evaluation of fuel gas supply system for marine dual-fuel propulsion engines using LNG and ammonia fuel," *Energies*, vol. 15, no. 17, doi: 10.3390/en15176303.

20. Á. Benet, A. Villalba-Herreros, R. d'Amore-Domenech, and T. J. Leo, "Knowledge gaps in fuel cell-based maritime hybrid power plants and alternative fuels," *J. Power Sources,* vol. 548, p. 232066, 2022, https://doi.org/10.1016/j.jpowsour.2022.232066.

21. J. Ahn, S. H. Park, S. Lee, Y. Noh, and D. Chang, "Molten carbonate fuel cell (MCFC)-based hybrid propulsion systems for a liquefied hydrogen tanker," *Int. J. Hydrogen Energ.,* vol. 43, no. 15, pp. 7525-7537, 2018, https://doi.org/10.1016/j.ijhydene.2018.03.015.

22. L. van Biert and K. Visser, "Chapter 3 - Fuel cells systems for sustainable ships," in *Sustainable Energy Systems on Ships*, F. Baldi, A. Coraddu, and M. E. Mondejar, Eds. Elsevier, 2022, pp. 81-121.

23. S. A. Korkmaz, K. E. Erginer, O. Yuksel, O. Konur, and C. O. Colpan, "Environmental and economic analyses of fuel cell and battery-based hybrid systems utilized as auxiliary

power units on a chemical tanker vessel," *Int. J. Hydrogen Energ.,* 2023, https://doi.org/10.1016/j.ijhydene.2023.01.320.

24. Z. Chen, Y. Chen, W. Wang, K. Lu, H. Yang, and W. Zhu, "Failure pressure analysis of hydrogen storage pipeline under low temperature and high pressure," *Int. J. Hydrogen Energ.,* vol. 45, no. 43, pp. 23142-23150, 2020, https://doi.org/10.1016/j.ijhydene.2020.06.129.

25. Y. Rong *et al.*, "Techno-economic analysis of hydrogen storage and transportation from hydrogen plant to terminal refueling station," *Int. J. Hydrogen Energ.,* 2023, https://doi.org/10.1016/j.ijhydene.2023.01.187.

26. A. Farsi and M. A. Rosen, "PEM fuel cell-assisted lithium ion battery electric vehicle integrated with an air-based thermal management system," *Int. J. Hydrogen Energ.,* vol. 47, no. 84, pp. 35810-35824, 2022, https://doi.org/10.1016/j.ijhydene.2022.08.153.

27. A. Pramuanjaroenkij and S. Kakaç, "The fuel cell electric vehicles: The highlight review," *Int. J. Hydrogen Energ.,* vol. 48, no. 25, pp. 9401-9425, 2023, https://doi.org/10.1016/j.ijhydene.2022.11.103.

28. A. S. Mohammed, S. M. Atnaw, A. O. Salau, and J. N. Eneh, "Review of optimal sizing and power management strategies for fuel cell/battery/super capacitor hybrid electric vehicles," *Energy Reports,* vol. 9, pp. 2213-2228, 2023, https://doi.org/10.1016/j.egyr.2023.01.042.

29. Marine Traffic, "MOZAH, LNG TankerLNG Tanker IMO: 9337755," https://www.marinetraffic.com/en/ais/details/ships/shipid:712524/mmsi:538003212/imo:9337755/vessel:MOZAH (accessed 25 March 2023.

30. Vessel tracking, "MOZAH (IMO 9337755) - LNG Tanker," https://www.vesseltracking.net/ship/mozah-9337755 (accessed 25 March 2023.

31. M. S. Khan *et al.*, "Graphical approach for estimating and minimizing boil-off gas and compression energy consumption in LNG regasification terminals," *J. Nat. Gas Sci. Eng.,* vol. 101, p. 104539, 2022, https://doi.org/10.1016/j.jngse.2022.104539.

32. Qatar Energy, "Ports Information," https://www.qatarenergy.qa/en/MarketingAndTrading/Pages/PortsInformation.aspx (accessed 3 March 2023.

33. Statista, "Distribution of liquefied natural gas imported into India in 2021, by country of origin," https://www.statista.com/statistics/1237488/lng-import-share-india-by-country/#:~:text=India's%20primary%20supplier%20of%20liquefied,world's%20fourth%2Dlargest%20LNG%20importer (accessed 2 March 2023.

34. Ballard, "Fuel cell power module for marine applications," https://www.ballard.com/docs/default-source/spec-sheets/fcwavetm-specification-sheet.pdf?sfvrsn=6e44dd80_12 (accessed 2 February 2023.

35. M. Cavo, E. Gadducci, D. Rattazzi, M. Rivarolo, and L. Magistri, "Dynamic analysis of PEM fuel cells and metal hydrides on a zero-emission ship: A model-based approach," *Int. J. Hydrogen Energ.,* vol. 46, no. 64, pp. 32630-32644, 2021, https://doi.org/10.1016/j.ijhydene.2021.07.104.

36. S. Dirkes, J. Leidig, P. Fisch, and S. Pischinger, "Prescriptive lifetime management for PEM fuel cell systems in transportation applications, Part I: State of the art and conceptual design," *Energ. Convers. Manage.,* vol. 277, p. 116598, 2023, https://doi.org/10.1016/j.enconman.2022.116598.

37. Y. Wang and L. A. Wright, "A comparative review of alternative fuels for the maritime sector: Economic, technology, and policy challenges for clean energy implementation," *World,* vol. 2, no. 4, pp. 456-481, 2021, doi: 10.3390/world2040029.

38. R. Jing *et al.*, "Economic and environmental multi-optimal design and dispatch of solid oxide fuel cell based CCHP system," *Energ. Convers. Manage.,* vol. 154, pp. 365-379, 2017, https://doi.org/10.1016/j.enconman.2017.11.035.

39. H. Xing, C. Stuart, S. Spence, and H. Chen, "Fuel cell power systems for maritime applications: Progress and perspectives," *Sustainability,* vol. 13, no. 3, 2021, doi: 10.3390/su13031213.

40. X. Tian, W. Jiao, L. Ren, S. Liu, and T. Liu, "Research on climate zoning indicators for operating environment of liquefied natural gas ambient air vaporizer," *Sustainable Cities and Society,* vol. 60, p. 102186, 2020, https://doi.org/10.1016/j.scs.2020.102186.

41. M. Sermsuk, Y. Sukjai, M. Wiboonrat, and K. Kiatkittipong, "Feasibility study of a combined system of electricity generation and cooling from liquefied natural gas to reduce the electricity cost of data centres," *Energy,* vol. 254, p. 124397, 2022, https://doi.org/10.1016/j.energy.2022.124397.

42. Y. Li and H. Luo, "Integration of light hydrocarbons cryogenic separation process in refinery based on LNG cold energy utilization," *Chemical Engineering Research and Design,* vol. 93, pp. 632-639, 2015, https://doi.org/10.1016/j.cherd.2014.04.009.

43. N. T. Stetson and R. C. Bowman, " Fuel cell system cost. Department of Energy Hydrogen and Fuel Cells Program Record," 2016.

44. R. E. Ciez and J. F. Whitacre, "Comparison between cylindrical and prismatic lithium-ion cell costs using a process based cost model," *J. Power Sources,* vol. 340, pp. 273-281, 2017, https://doi.org/10.1016/j.jpowsour.2016.11.054.

45. M. S. Peters, K. D. Timmerhaus, and R. E. West, *Plant design and economics for chemical engineers.* McGraw-Hill, 2003.

46. MAN, "Hydrogen in shipping, MAN Energy Solutions," https://www.man-es.com/campaigns/download-Q2-2023/Download/hydrogen-in-shipping/faffa612-4edc-4a2a-a5f9-df89c632a431/Future-Fuels-Hydrogen (accessed 30 March 2023).

47. EIA, *US Energy Information Administration, Natural Gas Statistics,* https://www.eia.gov/dnav/ng/hist/rngwhhdD.htm (accessed 30 January 2023.

48. IMO, Guidelines on the method of calculation of the attained Energy Efficiency Existing Ship Index (EEXI). Resolution MEPC.333(76), https://wwwcdn.imo.org/localresources/en/KnowledgeCentre/IndexofIMOResolutions/MEPCDocuments/MEPC.333(76).pdf (accessed 10 May 2023.

49. ABS, "Energy Efficiency Existing Ship Index (EEXI)," https://ww2.eagle.org/content/dam/eagle/regulatory-news/2022/ABS%20Regulatory%20News%20-%20EEXI.pdf (accessed 10 May 2023.

50. IACS, "EEXI Implementation Guidelines," https://iacs.org.uk/download/14308 (accessed 10 May 2023.

51. IMO, "Report of the marine environment protection committee on its sixty-second session," http://www.crs.hr/Portals/0/MEPC%2062-24.pdf (accessed 27 October 2018).

52. J. Ahn, H. You, J. Ryu, and D. Chang, "Strategy for selecting an optimal propulsion system of a liquefied hydrogen tanker," *Int. J. Hydrogen Energ.,* vol. 42, no. 8, pp. 5366-5380, 2017, https://doi.org/10.1016/j.ijhydene.2017.01.037.

53. N. R. Ammar, "Environmental and cost-effectiveness comparison of dual fuel propulsion options for emissions reduction onboard LNG carriers," *Brodogradnja/Shipbuilding,* vol. 70(3), no. 3, pp. 61-77, 2019. [Online]. Available: https://hrcak.srce.hr/221116.

54. D. Dobrota, B. Lalić, and I. Komar, "Problem of boil-off in LNG supply chain," *Transactions on Maritime Science,* vol. 2, pp. 91-100, 2013.

55. J. Blazquez, R. Fuentes, and B. Manzano, "On some economic principles of the energy transition," *Energy Policy,* vol. 147, p. 111807, 2020, https://doi.org/10.1016/j.enpol.2020.111807.

56. D. Lukić *et al.*, "Manufacturing cost estimation in the conceptual process planning," *Machine Design,* vol. 8, pp. 83-90, 2016.

57. Ihsan, "The analysis of the effect of indirect costs on the performance of construction project implementation," *Jurnal PenSil,* vol. 12, pp. 100-119, 2023, doi: 10.21009/jpensil.v12i1.30978.

58. N. R. Ammar and I. S. Seddiek, "An environmental and economic analysis of emission reduction strategies for container ships with emphasis on the improved energy efficiency indexes," *Environ. Sci. Pollut. R.,* vol. 27, no. 18, pp. 23342-23355, 2020, doi: 10.1007/s11356-020-08861-7.

59. N. R. Ammar and I. S. Seddiek, "Evaluation of the environmental and economic impacts of electric propulsion systems onboard ships: case study passenger vessel," *Environ. Sci. Pollut. R.,* vol. 28, no. 28, pp. 37851-37866, 2021, doi: 10.1007/s11356-021-13271-4.

60. P. Thoft-Christensen, "Infrastructures and life-cycle cost-benefit analysis," *Structure and Infrastructure Engineering,* vol. 8, no. 5, pp. 507-516, 2012, doi: 10.1080/15732479.2010.539070.

REDUCTION OF CO₂ EMISSIONS FROM OFFSHORE COMBINED CYCLE DIESEL ENGINE-STEAM TURBINE POWER PLANT POWERED BY ALTERNATIVE FUELS

Wojciech Olszewski [1] *
Marek Dzida [2]
Van Giao Nguyen [3]
Dao Nam Cao [4]

[1] Gdansk University of Technology, Poland

[2] Gdansk University of Technology, Institute of Naval Architecture and Ocean Engineering, Gdansk, Poland

[3] Institute of Engineering, HUTECH University, Ho Chi Minh City, Viet Nam

[4] PATET Research Group, Ho Chi Minh City University of Transport, Ho Chi Minh City, Viet Nam

* Corresponding author: *wojolsze@pg.gda.pl (Wojciech Olszewski)*

ABSTRACT

Diverse forms of environmental pollution arise with the introduction of materials or energy that exert adverse effects on human health, climate patterns, ecosystems, and beyond. Rigorous emission regulations for gases resulting from fuel combustion are being enforced by the European Union and the International Maritime Organization (IMO), directed at maritime sectors to mitigate emissions of SO_x, NO_x, and CO_2. The IMO envisions the realisation of its 2050 targets through a suite of strategies encompassing deliberate reductions in vessel speed, enhanced ship operations, improved propulsion systems, and a transition towards low and zero-emission fuels such as LNG, methanol, hydrogen, and ammonia. While the majority of vessels currently depend on heavy fuel or low-sulphur fuel oil, novel designs integrating alternative fuels are gaining prominence. Technologies like exhaust gas purification systems, LNG, and methanol are being embraced to achieve minimised emissions. This study introduces the concept of a high-power combined ship system, composed of a primary main engine, a diesel engine, and a steam turbine system, harnessing the energy contained within the flue gases of the main combustion engine. Assumptions, constraints for calculations, and a thermodynamic evaluation of the combined cycle are outlined. Additionally, the study scrutinises the utilisation of alternative fuels for ship propulsion and their potential to curtail exhaust emissions, with a specific focus on reducing CO_2 output.

Keywords: ship power plants, alternative marine fuels, greenhouse gases, CO_2 emissions, combined power systems, diesel engines, steam turbine, gas turbine

Nomenclature

CO_2	Carbon dioxide	EUA	EU Allowance
CCU	Carbon capture and utilisation,	GHG	Greenhouse gas
CCS	Carbon capture and storage	GTL	Gas to liquid
CTL	Coal to liquid	HFO	Heavy fuel oil
DF	Diesel-ignited engines with pilot fuel injection	IMO	International Maritime Organization
		LBSI	Lean-Burn Spark-Ignited gas engine
		LMG	Liquefied methane gas
EEX	European Energy Exchange	LNG	Liquefied natural gas
EEXI	Energy Efficiency Existing Ship Index	LP	Low-pressure
EGR	Exhaust gas recirculation	LPG	Liquefied petroleum gas

LSFO	Low sulphur fuel oil
MARPOL	The International Convention for the Prevention of Pollution from Ships
MFO	Marine fuel oil
MGO	Marine gas oil
MDO	Marine diesel oil
NOX	Nitrogen oxides
SCR	Selective catalytic reduction
SOX	Sulphur oxides
VLSFO	Very low sulphur fuel oil

INTRODUCTION

Decarbonisation has already become a reality but the pace of its implementation is much slower than originally assumed. The direction to take, in terms of selecting the best technology and energy sources to replace conventional fuels, is also not entirely clear. There is also no clear path for choosing the best methods of their storage and, in the case of some sources, such as liquid hydrogen, a proven method of transporting them. This will particularly apply to wind energy, hydrogen energy and the storage of carbon dioxide. These activities are strongly influenced by the 2015 Paris Agreement, which aims to limit global warming to 1.5°C by 2100, thus reducing the amount of CO_2 released into the atmosphere [1].

Environmental pollution can be defined and classified in various ways. According to the Act of 17 January 1980 on the protection and shaping of the environment, as amended (1994), environmental pollution means the introduction of solid, liquid or gaseous substances or energy into the environment in such quantities or such compositions that may adversely affect human health, climate, living nature, soil, or water, or cause other changes in the environment [2].

Increasingly stringent standards for the emission of gases from fuel combustion on floating plants, mainly SO_x, NO_x and CO_2, are being introduced by the EU (Directive 2012/33/EU) and IMO – MARPOL Annex VI [3]. The International Convention for the Prevention of Pollution from Ships, known as MARPOL 73/78 (Marine Pollution), has a global character and covers all seas [2]. Poland is a party to the Convention. The Convention applies only to pollution from ships and it divides sea areas into two categories:

- special areas, and
- other areas.

Current environmental conditions increase the need to reduce CO_2 emissions, the main factor responsible for global climate change. The most commonly considered technologies to reduce CO_2 emissions are CCS technologies, which consist of the separation of CO_2 and its transport, as well as its underground storage. CCU technologies aimed at the use of captured carbon dioxide and its conversion into other substances or products (e.g. plastic, concrete, biofuel) are also being considered [4].

The maritime industry has set ambitious targets to reduce CO_2 emissions in the future. The IMO aims to reduce the ratio of CO_2 emissions from propulsion by at least 40% by 2030 and up to 70% by 2050, compared to 2008 levels (Fig. 1).
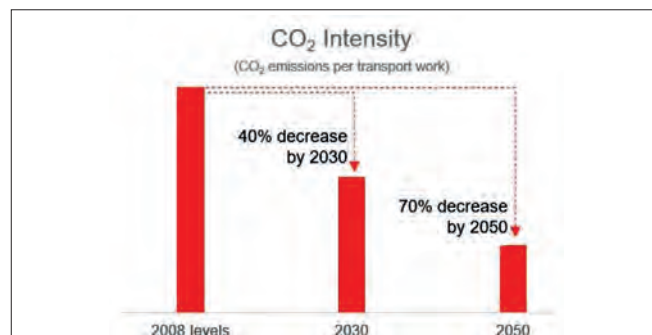
Fig. 1. Significant decreases in the carbon intensity of international shipping
Source: International Maritime Organization (November 2020).
Reducing greenhouse gas emissions from ships (Article). Retrieved from https//www.imo.org/

At the meeting in November 2020, the IMO's Marine Environment Protection Committee (MEPC 75) agreed on the following measures to achieve the above-mentioned targets [5]:

- the introduction of the Energy Efficiency Existing Ship Index (EEXI), with the aim of making older ships perform to a similar standard as newer tonnage,
- energy-efficient technologies/designs,
- alternative low-emission fuels,
- reduction in ship speed.

In July 2021, the European Commission [3] presented its legislative proposal to enable the European Union (EU) to meet its 2030 goal of reducing EU-wide greenhouse gas emissions by at least 55% compared to 1990. The 'Fit for 55' package includes 10 proposals, four of which are directly related to the maritime economy:

1. the inclusion of shipping in the EU Emissions Trading System (EU ETS) Directive from 2023;
2. the FuelEU Maritime regulation, new policy measures to switch to low-emission fuels, introducing requirements to gradually reduce the carbon intensity of marine fuels from 2025;
3. revision of the Alternative Fuels Infrastructure Directive: LNG and shore-side electricity in major ports by 2025 (LNG) and 2030; and
4. revision of the Energy Taxation Directive on the abolition of the tax exemption for marine fuels.

The IMO's target for 2050 is expected to be achieved through the simultaneous introduction of [6, 7]:

- slow-steaming ships – a reduction of the sailing speed of merchant ships (cargo ships) leading to a simultaneous reduction in fuel consumption and carbon emissions;
- better management of ship operations;
- improved propulsion efficiency;
- a massive shift to low and zero-emission fuels, such as LNG, LPG, methanol, hydrogen, ammonia (and other e-fuels), and biofuel; and
- the use of electricity for short sea shipping and port stops.

Today, the vast majority of the fleet runs on marine heavy fuel (HF) or low-sulphur fuel oil (LSFO) but significant orders have recently been placed for new designs that use alternative fuels.

Ship owners can achieve low emission levels in various ways through the use of exhaust gas cleaning systems, LNG

or low-sulphur fuels. The Polish shipbuilding industry engages in the manufacture or collaboration in the construction of LNG-powered floating structures. The availability of an LNG-powered ship bunkering service does not require additional investment in the construction of complex onshore infrastructure in Polish ports [8].

Not only LNG, but also methanol, has stepped into the spotlight. Currently, less than 1% of the existing fleet uses alternative fuels. Currently, the main alternative fuels available in the marine industry are [9]:

- LNG (and LPG), which can reduce CO_2 intensity by 15-25%. LNG technology is well-developed and the rapid growth of LNG bunkering infrastructure can also be observed. Methanol, usually produced from natural gas, reduces CO_2 intensity by about 10%.
- In addition to carbon-based fuels, the use of ammonia as a fuel is being extensively developed, and suitable engine technology is expected to be commercially available from 2024 onwards. The use of biofuels and synthetic fuels (also known as electrofuels or e-fuels) could provide opportunities to replace the above hydrocarbons with their low-emission equivalents.
- The supply of electricity from quays to merchant ships, while in port, is intended to eliminate the operation of ship's generator sets (reducing noise and pollution in the port area, caused by exhaust gases).

Changing macro-environmental conditions, greater customer requirements, as well as intensifying competition, forces economic entities to take systematic actions to increase the efficiency of their functioning. Making accurate decisions without access to reliable technical and economic information is not feasible. Nevertheless, the mere possession of this information is insufficient to assess the effectiveness of a company's operations. A reliable assessment can be obtained by analysing the financial and environmental impacts using technical and economic information.

THE CONCEPT OF A MOBILE FLOATING POWER PLANT

The proposed concept [10, 11] of electricity production in floating power plants for coastal regions has the following advantages (Fig. 2):

- it provides environmental protection;
- it reduces CO_2 and NO_x emissions, increasing system efficiency, and lower emissions result from the engine design. In addition, there is a reduction of SO_x emissions through the use of desulphurisation systems;
- diversification of primary energy sources reduces coal consumption in favour of liquid fuels;
- there is no slag and ash;
- there are no complications with condenser cooling water and a low impact on the environment related to water management;
- there is an increase in electricity production in northern Poland;

- there is shorter construction time, compared to conventional power plants and the possibility of starting it in stages;
- general mobile capabilities of the power plant complex – floating platform.
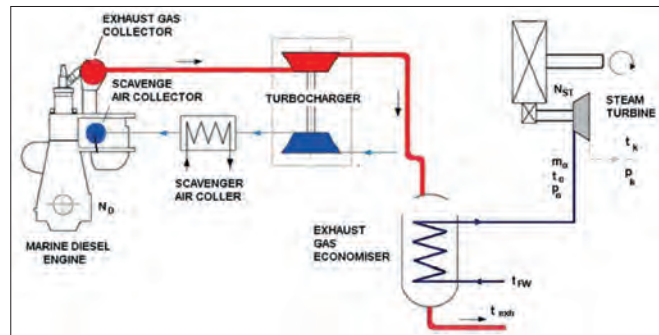
Fig. 2. Combined mobile floating power plant with a diesel engine and a steam turbine system. [10]

LOW-SPEED MARINE DIESEL ENGINES IN THE COMBINED CYCLE

MAN B&W MC-S two-stroke engines, designed by MAN Diesel, are low-speed engines with unit outputs of up to 80 MW. The low-speed two-stroke engines meet all the requirements of medium and large power units, up to 250-300 MW. They are suited to combust all liquid and gaseous fuels with high efficiency and good reliability.

Such engines can operate at a low load without restriction, up to approximately 10% of the maximum continuous rated output. In addition, they can operate at 10% overload for approximately one hour every 12 consecutive operating hours. The installation of such engines can be justified in mobile floating power plants, as it shortens the construction time of the power unit, reduces space requirements, and reduces investment, operating and maintenance costs while ensuring high efficiency, reliability and rapid relocation.

The engine manufacturer WinGD is designing marine engines with CCS technology, which will be available commercially in 2024 and 2025. The engines will be multi-fuel and use zero-emission or carbon-neutral fuels, such as ammonia and methanol, providing ship owners with reduced greenhouse gas (GHG) emissions and CO_2 emissions by up to 50%.

New engine designs launched in 2021 [2] are expected to reduce the loss of methane, which is considered a greenhouse gas when it enters the atmosphere:

- Two-stroke engines: For high pressures – 23% reduction in GHG emissions; for low pressures – 14% reduction in GHG emissions.
- Four-stroke engines (both low pressure): – DF engines with diesel ignition and pilot fuel injection: 6% reduction in GHG emissions. LBSI engines: 14% reduction in GHG emissions.

Methanol-fuelled diesel engines operate on the same principles as dual-fuel gas engines. A small pilot fuel injection, usually less than 5% of the total energy consumed, is required to ignite the methanol-air mixture [12]. The design of the MAN ME-LGI 2-stroke engine [13], which is already in operation, is

not significantly different from conventional diesel engines; its methanol-fuelled engine is at least as efficient, the lower energy density of methanol means that fuel consumption will be higher by volume or mass. ME-LGI can switch to MGO fuel mode without any speed or load limits. They can combust liquid and gaseous fuel in almost any ratio without affecting their power or efficiency. The use of methanol as a fuel reduces NO_x emissions by 30-50% and slightly improves engine efficiency in comparison to MGO fuel. EGR systems or SCR catalysts can be installed to reduce NO_x emissions further, to comply with NO_x Tier III standards.

Due to global climate change and various international agreements on CO_2 emissions, there has been a growing interest in the use of various liquid biofuels of animal or plant origin in the last few years. MAN B&W low-speed two-stroke diesel engines are a viable option for use wherever reliable and economical diesel installations are required, especially if the fuel is scarce and of poor quality.

THERMODYNAMIC ANALYSIS OF THE COMBINED CYCLE OF A MOBILE POWER PLANT

One solution for a mobile floating power plant could be to combine a diesel engine with a gas turbine and steam turbine cycle into a combined cycle using the waste heat contained in the flue gases of the main combustion engine [14]. Such a solution was presented by the authors of this article, in papers [10] and [11]. The leading engine in this system is a low-speed diesel engine.

A low-speed diesel engine combusting heavy fuel (HFO) was used for the main propulsion. Nowadays, the efficiency of such engines reaches 45-50%. With the high power of propulsion engines, the fuel gases leaving the engine contain large amounts of heat that can be further utilised. Table 1 shows the basic parameters of a low-speed marine engine.

Tab. 1. Basic ship parameters of a low-speed diesel engine

Company		MAN DIESEL & TURBO
Engine type		9K98 MC, Two- Stroke
Power	kW	48,762
Ambient air temperature	°C	25
Exhaust gas mass flow	kg/s	134.25
Exhaust gas temperature	°C	232.8
Fuel	kJ/kg	42,700
Fuel mass flow	kg/s	2.369

Combined systems of a steam turbine, in combination with a single-pressure or dual-pressure exhaust gas collector, were analysed (Figs. 3 and 4).

In the single-pressure system (Fig. 3), one exchanger was used in the steam system, namely a de-aerator heated by steam from the steam turbine exhaust.
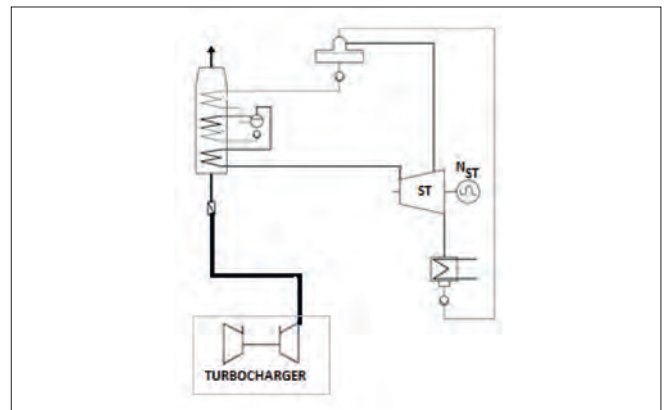
Fig. 3. Flow diagram of a single pressure system [10]
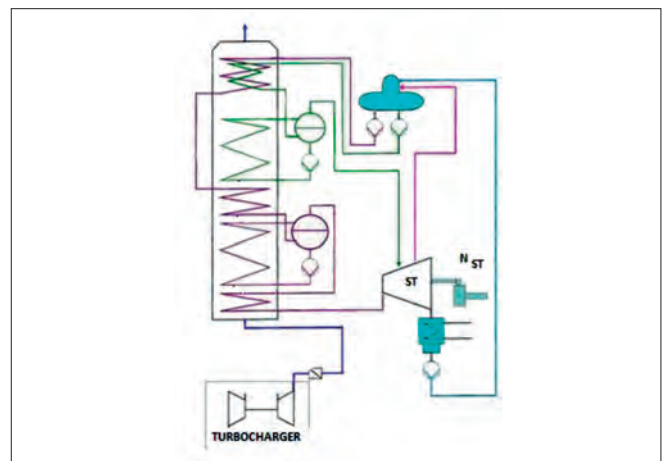
Fig. 4. Flow diagram of a two-pressure system [10]

In the two-pressure system (Fig. 4), two steam pressures were applied in the evaporators, with saturated steam (x = 1) in the low-pressure evaporator feeding the steam turbine. One regenerative exchanger was also applied, with a de-aerator heated by the steam from the turbine exhaust.

Both steam turbine circuits used a condensing type steam turbine, with the condenser cooled by seawater.

In the calculations, the temperature of the fresh steam in the steam turbine system was assumed to be 10°C lower than the flue gas temperature of the diesel engine. The condenser pressure was the same for the single and two-pressure system.

The calculation results for other variants of the combined system are presented in the papers [10], [11] and [4].

Fig. 5 shows the course of the steam turbine power, depending on the fresh steam pressure for a constant feed water temperature and the circuit with a single or double-pressure boiler for boiler feed water temperatures of 85°C and 120°C. The charts show that the two-pressure boiler for both engines provides the maximum steam turbine power with an appropriately adjusted low-boiling evaporator pressure. Increasing the pressure of the low-boiling evaporator reduces the steam turbine power. In both cases, the maximum steam turbine power of the single-pressure boiler is less than the maximum power of the two-pressure boiler. At the same time, the optimum fresh steam pressure of a single-pressure boiler

is lower than the fresh steam pressure of a two-pressure boiler. For a lower feed water temperature, the steam turbine power parameters for both variants are higher than the assumed higher feed water temperature. For a lower feed water temperature, the de-aerator will be more expensive and its operation will be more difficult because it works at lower than atmospheric pressures.
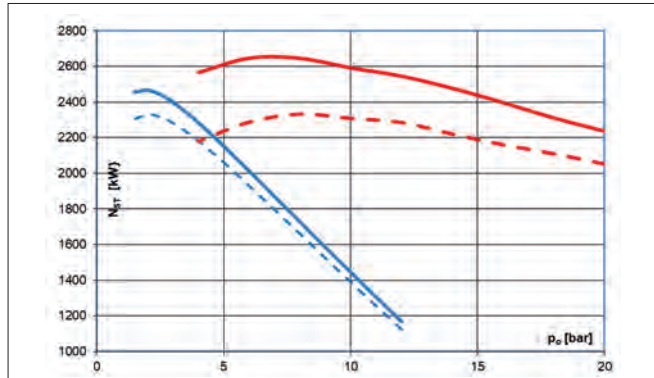
Fig. 5. The power of the steam turbine for constant feed water temperature (MAN Diesel & Turbo engine 9K98MC) t_{FW} = 85°C
——— *Single-Pressure System* ——— *Two-Pressure System t_{FW} = 120°C*
- - - - *Single-Pressure System* - - - - *Two-Pressure System*

Calculations of combination systems consisting of a diesel engine with a steam turbine circuit show that [10, 11]:

- it is possible to use a combined system, consisting of a diesel combustion engine as the main engine and a steam turbine circuit using the heat contained in the flue gas of the diesel engine;
- Such systems achieve thermodynamic efficiencies comparable to combined circuits of gas turbines with steam turbines;
- Depending on the variant and load of the main engine, the use of a combined system makes it possible to increase the power of the power plant by 7-15%, compared with a conventional power plant for the same fuel stream;
- The additional power of the system is possible because of the recovery of energy contained in the flue gases of the diesel engine; and
- The combined system reduces specific fuel consumption by 6.4-12.8%, compared to a conventional power plant.

Using a combined system for the propulsion of a mobile floating power plant increases the propulsion system's efficiency, thereby reducing specific fuel consumption and increasing the propulsion power; this results in additional environmental benefits.

ALTERNATIVE FUELS

The EU Directive '2012/33/EU' defines alternative fuels as fuels or power sources which serve, at least partly, as a substitute for fossil oil sources in the energy supply which have the potential to reduce the dependence of EU Member States on oil imports and contribute to the decarbonisation and improvement of environmental performance in this sector [3].

These fuels include:
- electricity;
- hydrogen;
- biofuels;
- synthetic and paraffin fuels;
- natural gas (including biomethane) in the form of compressed natural gas (CNG) and liquefied natural gas (LNG); and
- liquefied petroleum gas (LPG).

Synthetic fuels can be divided according to the raw material used:
1. natural gas-derived fuels (GTL);
2. coal-derived fuels (CTL);
3. biomass-derived fuels; and
4. plastic-derived fuels (municipal waste).

The use of synthetic fuels does not involve the construction of new refuelling infrastructure in ports.

Table 2 presents data from a Polish government report [15], forecasting the structure of fuels in electricity production. In 2050, only 38% of electricity is expected to be produced from fossil fuels (coal and lignite) whereas, in 2020, solid fuels constituted 78% of electricity production.

In terms of environmental protection, marine fuels (existing, emerging and future marine fuels) [16] are divided into:

Grey: Fossil fuels – typically used today, such as HFO, LNG, LPG, methanol, hydrogen (H_2), and ammonia – produced from natural gas/coal;

Blue Hydrogen, ammonia – produced from natural gas/coal with CCS, e-fuels – produced with CO_2 from carbon capture during another combustion process;

Green: Hydrogen (H_2), ammonia – produced from carbon-free electricity, e-fuels – produced with CO_2 directly extracted from the atmosphere, and biofuels – (sustainability requirements apply).

Tab. 2. 2017 electricity production forecast by fuel (%) [15]

	2010	2015	2020	2025	2030	2035	2040	2045	2050
coal	0.558	0.457	0.432	0.405	0.382	0.381	0.387	0.359	0.334
lignite	0.309	0.368	0.302	0.265	0.184	0.050	0.049	0.047	0.046
natural gas	0.043	0.037	0.066	0.063	0.063	0.083	0.076	0.102	0.091
renewable energy sources	0.074	0.130	0.191	0.197	0.251	0.276	0.284	0.294	0.328
nuclear energy	0.000	0.000	0.000	0.063	0.113	0.204	0.198	0.193	0.194
other	0.017	0.009	0.008	0.007	0.007	0.006	0.006	0.006	0.006
total	1.000	1.000	1.000	1.000	1.000	1.000	1.000	1.000	1.000

Fig. 6. Current and future methanol production by source
Source: www. methanol.org/join-us

We consider the production of methanol as an example. Depending on the technology used, grey, blue or green fuel can be obtained. Fig. 6 shows the methanol production capacity by fuel type for each year. In 2020, only methanol derived from fossil fuels was available and the widespread use of methanol as bio or e-fuel was dependent on production capacity. Methanol produced from natural gas increases greenhouse gas emissions by a few per cent (2-3%) when produced from LNG, although emissions are reduced by 10 to 25%, depending on the technology applied. When methanol is produced from LPG, it typically leads to a 17% reduction in greenhouse gases. The production of green methanol as bio and synthetic e-methanol is currently very limited. In 2050, methanol, as a low-carbon fuel, will account for 80% of production. In the decarbonisation of exhaust gases, it is important to use low and zero-emission fuels. Their production depends on the available technologies and legal regulations, as well as safety standards for the transport and use of these fuels on floating facilities. Fig. 7 presents the possibilities for the use of a given fuel on floating facilities, enabling the safe use of such fuels. The technology of using hydrogen in transport is the least developed of all alternative fuels; however, commercial development is expected by around 2040-2050 [12], [15].
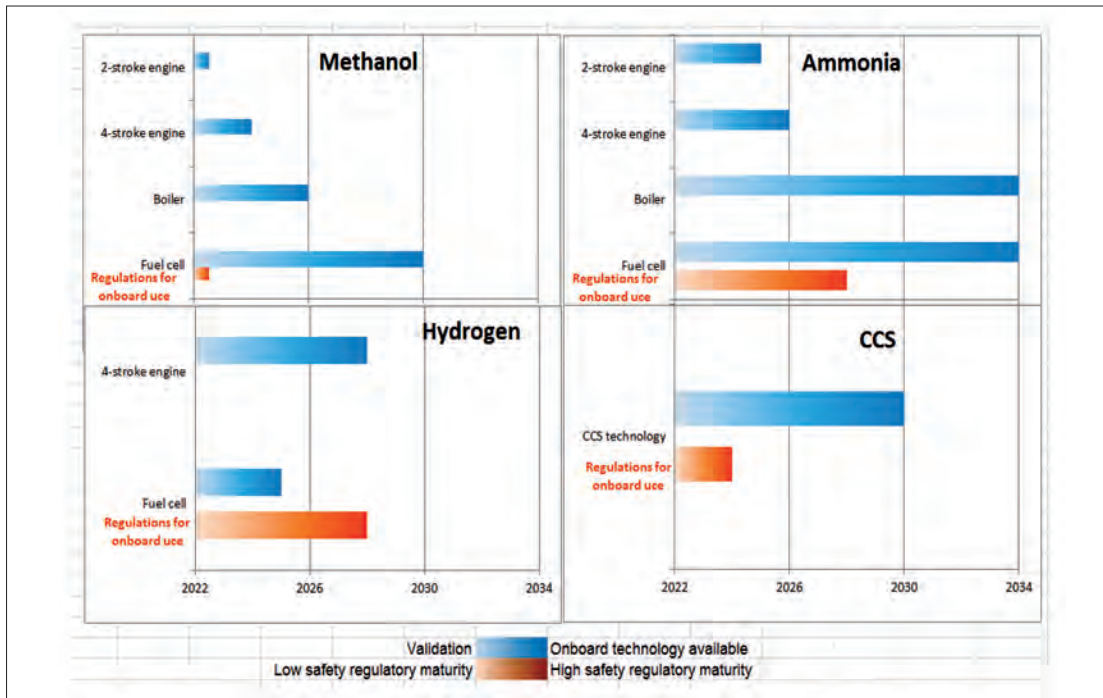
Fig.7. Estimated maturation timelines for energy converters onboard CCS technologies and corresponding safety regulations for onboard use.
Source: https://www.dnv.com/maritime/publications/maritime-forecast-2022/index.html
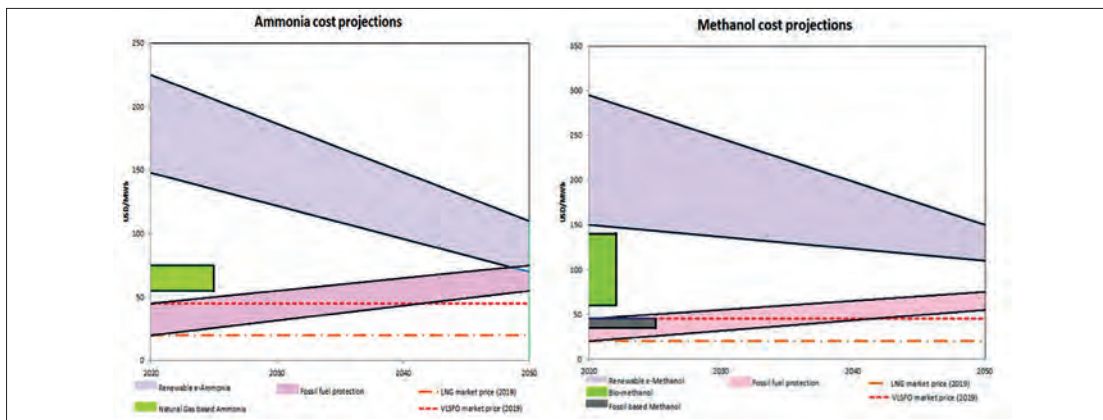
Fig. 8. Fuel cost projections. Source: A Pathway to Decarbonise the Shipping Sector by 2050 (International Renewable Energy Agency, 2021) www.methanol.org/renewable/

The cost of producing zero and low-carbon fuels will play a significant role in the use of alternative fuels. Ammonia is of great interest as a source of zero-emission fuel for shipping [17]. Fig. 8 shows the expenditure on the production of ammonia and methanol for various technologies. At the moment, the price of low and zero-emission fuels is high, compared to grey or fossil fuels. In the future, the prices of such fuels will be comparable to current fossil fuels. Almost all ammonia currently in use is produced from hydrocarbons and, as such, provides almost no benefit, in terms of reducing CO_2 emissions, but increases costs. In 2020, the costs of ammonia production in zero-emission e-fuel technology were three times higher than VLFSO fuel and it will be five times higher than LNG gas fuel in 2050. Their price is expected to fall, so that the cost will be two times higher than the cost of VLFSO fuel and 2.5 times more expensive than LNG gas fuel, respectively. This constitutes a barrier to the use of this fuel. Ammonia prices vary significantly over time and are not the same in all geographical regions. The cost of natural gas accounts for 70-85% of the cost of ammonia production. The cost of renewable ammonia production will largely depend on two parameters: the price of electricity and capital expenditure [10].

On the other hand, green ammonia (produced by electrolysis powered by renewable or nuclear energy) is an excellent source of zero-emission fuel, provided that the associated NO_x emissions are appropriately technology-dependent [18]. Greenhouse gas emissions will be close to zero.

There are many other alternative fuels that can be used in shipping, such as dimethyl ether, ethanol, biodiesel, electricity, liquefied biogas (LBG), hydrogen and nuclear power.

Synthetic fuels, produced from a combination of pure hydrogen and CO_2 obtained from the atmosphere or other biogenic processes, can also be carbon neutral at the cost of very high fuel prices. For this reason, the conversion of CO_2 into fuels appears to be a good way forward, both to dispose of CO_2 and to store renewable and excess electricity [19].

Options that will lead to a near 100% reduction in greenhouse gas emissions include nuclear fission reactors and onboard carbon capture and storage. The former is controversial and capital-intensive, while the latter is currently complex, expensive and dependent on the reception facilities in ports. Greenhouse gas emissions from electricity production, and even more from hydrogen, have the potential for virtually emission-free production from renewable energy. However, those energy carriers are difficult to store, which significantly limits the range of ships, in the case of battery propulsion and pressurised hydrogen storage.

THE USE OF ALTERNATIVE FUELS ON FLOATING FACILITIES

Ethanol fuel, like conventional fuel, causes the emission of toxic chemicals and greenhouse gases [11]. It is generally accepted that CO_2 emissions, during the use of ethanol fuel, are offset by CO_2 captured during its cultivation, compared to those powered by standard motor gasoline. A reduction of 54% NO_x emissions, 27% non-methane hydrocarbon emissions, and 18% CO_2 emissions has been shown, on average.

LNG gives the opportunity to reduce emissions of greenhouse gases (GHG) [5], NO_x and particulate matter (PM). NO_x emissions

can be reduced by 20-80%, depending on the technologies used, Exhaust Gas Recirculation (EGR) or Selective Catalytic Reduction (SCR) systems ensure that Tier III IMO NO_x levels are achieved. In greenhouse gases, both CO_2 and methane emissions should be considered, the latter being emitted as a result of incomplete combustion. Methane leaks throughout the entire chain of fuel installations (including fuel production, transportation and distribution), affecting the overall GHG footprint. The emission reduction depends on the type of engine used and it is: 95-98% for SO_x, 20-80% for NO_x and 14-25% for CO_2. In the case of internal combustion engines powered by LNG gas, additional pilot fuel is required (about 8% of MDO fuel) [20].

Methanol is the simplest alcohol, with the lowest carbon content and the largest amount of hydrogen. Methanol can be produced from several different feedstocks, mainly natural gas or coal, but also from renewable resources such as black liquor from pulp and paper mills, as a result of forest clearing or from agricultural waste, or even directly from CO_2 captured from power plants. It can also be converted into dimethyl ether (DME), which can be used as a fuel for diesel engines. Methanol requires modified engines. The key differences between methanol and HFO marine fuel are as follows:

- Methanol has a low flash point of 11-12°C compared to over 50°C for HFO.
- Emission reductions: SO_x (95-98%) and CO_2 (5-10%); but for green methanol: NO_x (25-80%); and with exhaust gas recirculation (EGR) or selective catalytic reduction (SCR) systems: CO_2 up to 80%.
- The volume of the methanol tank is 2.5 times that of HFO.
- Methanol engine technology is already available and in use.

Ammonia is an alkaline compound with a distinctly strong, suffocating odour. It is corrosive to certain materials, such as copper, copper alloys and zinc, and, therefore, care must be taken in the selection of motor construction materials. Ammonia has a lower air-fuel stoichiometric ratio compared to diesel and, with the same amount of air, more ammonia can be introduced to compensate for the lower energy content and maintain the motor power density. Additional fuel is required for internal combustion engines. Usually, MGO is used as a pilot fuel but it could also be renewable diesel (HVO) with about 60% lower GHG emissions. The use of ammonia as fuel, like LNG, almost completely eliminates particulate and soot emissions. However, there are NO_x emissions, which depend on the engine technology applied. In the case of ammonia, toxicity is a major concern but flammability and reduced temperatures also need to be considered. Ammonia is a zero-emission fuel that can potentially play an important role in the decarbonisation of marine propulsion systems. Although ammonia is toxic and has a lower energy density than currently used petroleum fuels, ammonia is preferable to hydrogen and may be a suitable option for future use in marine applications.

REDUCTION OF CO_2 EMISSIONS BY USING ALTERNATIVE FUELS

The calculations presented in [10, 11] apply to a combined cycle with a steam turbine system at a feed water temperature for a waste heat boiler t_{FW} = 85°C and t_{FW} = 120°C. The fuel burned in the engine was Heavy Fuel Oil, HFO. The system with

a dual-pressure utilisation boiler has a higher steam turbine power compared to the system with a single-pressure boiler; however, the increase in the power of the steam turbine compared to the dual-pressure system is small, approximately 6%. A system with a single-pressure boiler in the steam turbine system is adopted in further considerations. This solution is cheaper and easier to use from the point of view of investment costs.

The temperature of a boiler feed water affects the power of the steam turbine and the design of the de-aerator: the lower the temperature, the more powerful the steam turbine but, also, the lower the pressure in the de-aerator. For a supply water temperature of 85°C, the de-aerator must be of a vacuum design, which causes more operational difficulties; it is a more expensive solution than

a positive pressure de-aerator. The increase in steam turbine power is small. Further calculations of the combined system will be carried out for a single-pressure utilisation boiler and a feed water temperature of 120°C (positive pressure de-aerator).

A combined system was analysed for different alternative marine fuels with the mass compositions and calorific values given in Table 2. The results were compared with a power plant powered by a low-speed marine engine without a steam turbine system and powered by MDO fuel.

The combined system was analysed under the following additional assumptions:
– engine efficiency and power were identical, regardless of the type of fuel;

Tab. 3. Fuel specifications

Fuel		MDO	LNG 1	LNG 2	methanol	ethanol	ammonia	dual fuel 8% MDO & 92% LNG 1
		in 1 kg						
C		0.829						0.06632
CH_4			0.885	0.911				0.81420
H		0.122						0.00976
S		0.028						0.00224
O_2		0.010						0.00080
N_2		0.011		0.006				0.00088
CO_2				0.005				
H_2O								
C_2H_2			0.046	0.047				0.04232
C_3H_8			0.054	0.017				0.04968
C_4H_{10}			0.015	0.014				0.01380
CH_3OH					1			
C_2H_5OH						1		
NH_3							1	
Lower calorific value [13] [21]	kJ/kg	42700	49170	48390	22693	26800	18600	48652

Tab. 4. Exhaust gas composition of a combined system for alternative marine fuels

Fuel		Power of Steam turbine	Emission						
			CO_2	SO_2	H_2O	O_2	N_2	Exhaust gases	Specific Fuel Consumption
		kW	kg/kWh						
MDO	without steam turbine	0	0.5316	0.0098	0.1920	1.6984	7.4796	9.9114	0.1749
MDO	Combined cycle	2450	0.5062	0.0093	0.1829	1.6171	7.1217	9.4372	0.1665
dual fuel 8% MDO & 92% LNG 1		2820	0.4087	0.0007	0.2977	1.5733	7.0690	9.3493	0.1451
LNG 1		2740	0.4022	0.0000	0.3070	1.5733	7.0798	9.3623	0.1438
LNG 2		2740	0.4037	0.0000	0.3115	1.5687	7.0807	9.3646	0.1461
methanol		2730	0.4285	0.0000	0.3506	1.6716	7.0812	9.5319	0.3116
ethanol		2100	0.5111	0.0000	0.3136	1.6081	7.1689	9.6017	0.2672
ammonia		2260	0.0000	0.0000	0.5756	1.6472	7.4449	9.6676	0.3837

Tab. 5. Reduction of CO_2 emissions of a combined system with alternative marine fuels.

Fuel		MDO	MDO	dual fuel 8% MDO & 92% LNG 1	LNG 1	LNG 2	methanol	ethanol	ammonia
		without steam turbine	Combined cycle						
CO_2	kg/kWh	0.5316	0.5062	0.4087	0.4022	0.4037	0.4285	0.5111	0.0000
$\Delta CO_2/CO_2$ MDO	%	0	-4.78	-23.13	-24.34	-24.06	-19.40	-3.87	-100.00

– the charge air was identical, irrespective of fuel type;
– fuel flow was variable and dependent on calorific value;
– engine exhaust gases were dependent on fuel stream; and
– temperature of the exhaust gases from the engine were identical, regardless of the type of fuel used.

With the above assumptions, a combined cycle was recalculated for different types of alternative marine fuel (Table 2). Two types of LNG-based fuel were adopted for different contents of methane, methanol, ethanol and ammonia. For a slow-speed engine [13], according to the manufacturer's requirements, a fuel consisting of 8% of MDO pilot fuel and 92% of LNG 1 gas was adopted.

The maximum power of the steam turbine was determined for each variant (Table 3). The power of the steam turbine, depending on the type of fuel, changed by +/– 14% in relation to the power of the steam turbine from the combined system variant fuelled with standard MDO fuel. Changes in the power of the entire combined drive system differed by +/– 0.7% in relation to the variant of the system powered by MDO fuel.

Greenhouse gas emissions for alternative fuels in the system are presented in Table 4; Table 5 presents the CO_2 reductions compared to a simple drive system without a steam turbine for the standard MDO fuel.

CO_2 gas emissions depend on the fuel composition. The use of a steam turbine for a simple drive with no fuel change (MDO) results in a 4.8% reduction in emissions. This is due to an increase in system efficiency and, thus, a reduction in specific fuel consumption. The use of low-emission alternative fuels further reduces CO_2 emissions. For low-emission fuels, the greatest reduction in emissions is the result of the use of LNG fuels at 23-24%. The use of the zero-emission fuel, ammonia, leads to the complete elimination of CO_2 from the exhaust gases.

SO_x gas emissions depend on the sulphur content in the fuel. The use of a combined system without changing the type of fuel (MDO) reduces emissions of sulphur compounds by approximately 5%. In dual-fuel engines fuelled with a mixture of LNG and MDO control fuel, this reduction reaches 93%, compared to the standard fuel. By using alternative sulphur-free fuels, sulphur compounds are completely eliminated.

The emission of water vapour $H2O$, which is also a greenhouse gas for renewable low and zero-emission fuels increases, in relation to the system powered by standard fuel. Technologies can be used in this area to eliminate this problem.

This article does not consider NO_x emissions in a combined system. Emissions of these compounds can be reduced by using appropriate SCR engine technologies.

CONCLUSIONS

Based on the analysis conducted, the following conclusions can be drawn regarding the utilisation of mobile floating power plants in relation to greenhouse gas emissions.

• The adoption of a combined system powered by conventional fuel leads to a reduction in CO_2 emissions.
• Alternative fuels that replace the standard marine fuel, MDO, contribute to a decrease in CO_2 emissions. The specific type of fuel and the technologies employed for its production significantly influence the extent of CO_2 reduction.
• Low and zero-emission marine fuels, derived from environmentally friendly technologies and known as e-fuels, offer the potential to achieve CO_2 emission reduction in line with EU Directives and IMO Conventions within specified timeframes. Complete decarbonisation can be realised through the utilisation of zero-emission green ammonia.
• The surplus electricity production from offshore wind farms on the Polish Baltic Sea shelf (Offshore Wind Energy) will play a significant role in alternative fuel production (green technology).
• The incorporation of low-emission fuels within the maritime sector and mobile floating power plants has the capacity to eliminate or substantially reduce SO_x emissions.
• Alternative fuels containing methane necessitate appropriate technologies to prevent methane release into the atmosphere, as methane is classified as a greenhouse gas due to its potential escape through leaks in storage and power supply systems, as well as incomplete fuel combustion.
• The integration of slow-speed reciprocating engines within a combined system, encompassing steam and gas turbines in mobile floating power plants, results in reduced CO_2 and SO_x emissions when utilising conventional MDO fuels. The advantages of such emission reduction are further enhanced by the incorporation of low and zero-emission fuels within the combined system.

REFERENCES

1. A.T. Hoang et al., "Energy-related approach for reduction of CO_2 emissions: A critical strategy on the port-to-ship pathway," J. Clean. Prod., vol. 355, p. 131772, Jun. 2022, doi: 10.1016/j.jclepro.2022.131772.

2. M. Julian, "MARPOL 73/78: the International Convention for the Prevention of Pollution from Ships," Marit. Stud., vol. 2000, no. 113, 2000, doi: 10.1080/07266472.2000.10878605.

3. EC, "Directive 2012/33/EU of the European Parliament and of the Council of 21 November 2012 amending Council Directive 1999/32/EC as regards the sulphur content of marine fuels," OJ L, 2012.

4. J. Liu, Q. Zhang, H. Li, S. Chen, and F. Teng, "Investment decision on carbon capture and utilisation (CCU) technologies—A real option model based on technology learning effect," Appl. Energy, vol. 322, 2022, doi: 10.1016/j.apenergy.2022.119514.

5. IMO - Marine Environment Protection Committee, "Reduction of GHG emissions from ships. Fourth IMO GHG Study 2020. MEPC 75/7/15.," International Maritime Organization. 2020.

6. P. Balcombe et al., "How to decarbonise international shipping: Options for fuels, technologies and policies," Energy Conversion and Management. 2019, doi: 10.1016/j.enconman.2018.12.080.

7. F. Baldi and A. Coraddu, "Towards halving shipping GHG emissions by 2050: the IMO introduces the CII and the EEXI," in Sustainable Energy Systems on Ships, 2022.

8. J. Herdzik, "Decarbonization of Marine Fuels—The Future of Shipping," Energies, vol. 14, no. 14, p. 4311, Jul. 2021, doi: 10.3390/en14144311.

9. A.T. Hoang and V.V. Pham, "A review on fuels used for marine diesel engines," J. Mech. Eng. Res. Dev., vol. 41, no. 4, pp. 22–32, 2018.

10. M. Dzida and W. Olszewski, "Comparing combined gas tubrine/steam turbine and marine low speed piston engine/steam turbine systems in naval applications," Polish Marit. Res., vol. 18, no. 4, 2011, doi: 10.2478/v10012-011-0025-8.

11. W. Olszewski and M. Dzida, "Selected Combined Power Systems Consisted of Self-Ignition Engine and Steam Turbine," Polish Marit. Res., vol. 25, no. s1, 2018, doi: 10.2478/pomr-2018-0042.

12. DNV, "Alternative fuels for containerships," 2022.

13. MAN Diesel & Turbo, "Using Methanol Fuel in the MAN B&W ME-LGI Series," MAN. 2014.

14. A.T. Hoang, "Waste heat recovery from diesel engines based on Organic Rankine Cycle," Applied Energy, vol. 231. 2018, doi: 10.1016/j.apenergy.2018.09.022.

15. "National policy framework for the development of alternative fuels infrastructure (in Polish). Ministry of Energy 2017"
https://www.gov.pl/web/aktywa-panstwowe/rzad-przyjal-krajowe-ramy-polityki-rozwoju-infrastruktury-paliw-alternatywnych-3.

16. D. GL, "Comparison of Alternative Marine Fuels; DNV GL AS Maritime: Høvik, Norway," 2019.

17. K. Machaj et al., "Ammonia as a potential marine fuel: A review," Energy Strategy Reviews, vol. 44. 2022, doi: 10.1016/j.esr.2022.100926.

18. S. Giddey, S.P.S. Badwal, C. Munnings, and M. Dolan, "Ammonia as a Renewable Energy Transportation Media," ACS Sustain. Chem. Eng., 2017, doi: 10.1021/acssuschemeng.7b02219.

19. C.G. Okoye-Chine et al., "Conversion of carbon dioxide into fuels - A review," Journal of CO_2 Utilisation, vol. 62. 2022, doi: 10.1016/j.jcou.2022.102099.

20. I. Domić, T. Stanivuk, L. Stazić, and I. Pavlović, "Analysis of LNG Carrier Propulsion Developments," J. Appl. Eng. Sci., vol. 20, no. 4, 2022, doi: 10.5937/jaes0-36809.

21. A. Szklo and R. Schaeffer, "Fuel specification, energy consumption and CO_2 emission in oil refineries," Energy, vol. 32, no. 7, 2007, doi: 10.1016/j.energy.2006.08.008.

DETERMINATION OF RATIONAL DESIGN VALUES FOR GAS-AIR COOLERS COMPONENTS OF EXHAUST GASES OF MARINE POWER PLANTS

Svitlana Kuznetsova [ID] [1]
Valerii Kuznetsov [ID] [1] *
Andrii Voloshyn [ID] [2]

[1] Admiral Makarov National University of Shipbuilding, Mykolaiv, Ukraine

[2] State Research Design & Shipbuilding Centre, Mykolaiv, Ukraine

* Corresponding author: *valeriy.kuznetsov@nuos.edu.ua (Valerii Kuznetsov)*

ABSTRACT

Modernisation of marine power plants in the transport vessel fleet to satisfy the requirements of the International Maritime Organization is an urgent scientific and technical problem. Currently, the use of catalytic selective filters, dry and wet scrubber systems and exhaust gas recirculation for marine diesel engines is widely used for this purpose. An analysis of the use of ejection gas-air coolers is presented as an additional method of emission reduction. However, the use of such device does not neutralise the harmful emissions of power plant engines, but only increases the volume concentration of their exhaust gases. But this will help to increase the efficiency of dispersion of harmful emissions, by reducing the concentration of harmful emissions to values not exceeding the maximum permissible concentrations. Its efficiency depends on the load mode of the diesel engine. It is found that the initial concentration of harmful substances in combustion products due to their dilution with fresh air at 100% engine load is reduced by about 50%. The values of the reduction of the concentration and temperature of exhaust gases with the reduction of the engine load to 75% and 50% depending on the louvre angle are obtained. It is proved that ejection gas-air coolers can be an effective additional means for compliance with modern environmental parameters, especially when vessels are in special areas of the world's oceans.

Keywords: vessel, marine power plant, environmental parameters, emissions, gas-air cooler, nozzle.

INTRODUCTION

Today, maritime transportation is one of the most cost-effective ways of transporting goods for different purposes around the world. United Nations data [1] shows that in 2019 there was a 4.1% growth of the world merchant fleet, and that by the beginning of 2020 the total number of merchant vessels was 98,140.

In spite of the fact that the percentage of harmful emissions of marine power plants does not exceed 7–9% of the world total, the International Maritime Organization (IMO) rules are consistently strengthening the requirements to limit the level of harmful emissions into the atmosphere during the operation of the power plants of sea transport vessels. The greatest attention is given to the levels of sulphur oxides and nitrogen oxides, which ship owners are obliged to reduce (Fig. 1). This applies particularly to the 'special' areas of the world's oceans – the Black Sea, Mediterranean Sea, Baltic Sea, North Sea, Red Sea, the Antarctic area, and the Caribbean Sea area, including the Gulf of Mexico [2, 3].
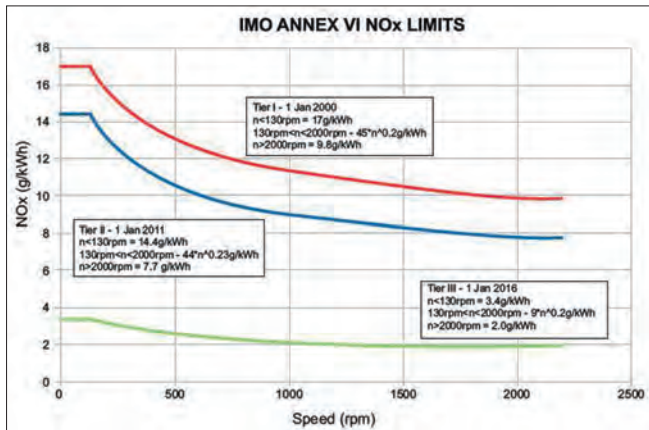
Fig. 1. IMO emission reduction requirements

In 2010, Annex VI to the International Convention on the Prevention of Air Pollution (MARPOL - 73/78) [4] introduced a requirement to improve the energy efficiency of vessels, which is directly related to the amount of fuel that is used, and the emissions of carbon dioxide – CO_2. Strictly, this gas is not a pollutant but a greenhouse gas, the control of emissions of which is covered by the UN Framework Convention on Climate Change and the Kyoto Protocol. Besides, an indirect cause of the development of the greenhouse effect is thermal pollution of the environment due to the relatively high temperature level and quantity of exhaust gases during the operation of sea transport vessel power plants. Moreover, the operation of vessels in different climatic zones of the world's oceans can cause a decrease in the efficiency of the cooling systems of the main and auxiliary engines, which can additionally increase the level of thermal emissions by up to 3% [5].

So, in today's practice it is considered necessary to ensure environmental efficiency in the operation of power plants of marine transport vessels by reducing their thermal and harmful emissions.

LITERATURE ANALYSIS OF EXISTING BASIC TECHNICAL SOLUTIONS HIGHLIGHTING THE UNRESOLVED PART OF THE PROBLEM

The specific challenge of measures to reduce environmental pollution by marine power plants is the need to implement them in the limited space of the vessel's engine room. This task is relatively easy to solve when designing and building new vessels, but problems can arise when retrofitting the propulsion systems of vessels currently in service.

The manufacturers of equipment for marine power engineering offer several directions for the "greening" of marine power plants – the use of catalytic selective filters, dry and wet scrubber systems, as well as recirculation of exhaust gases of ship diesel engines.

Fig. 2 shows the *Wärtsilä NO$_x$ Reducer* (*NOR*) wet system for additional treatment of the exhaust gas flow to comply with IMO Tier III [6].
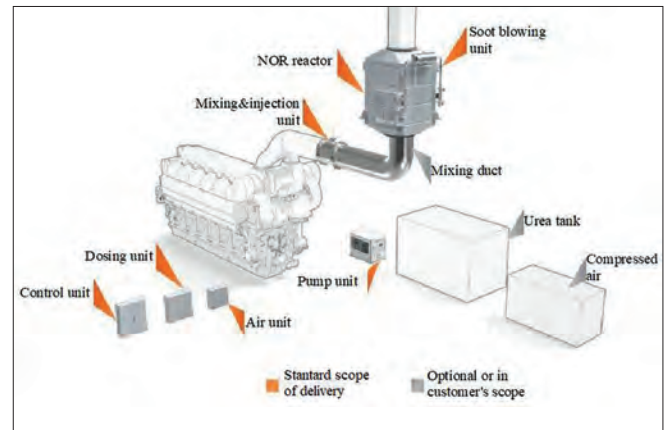
Fig. 2. Wärtsilä NOx Reducer system

The final elements of the catalytic reaction in the selective catalytic filter are pure nitrogen and water, i.e., the main constituents of the environment. No liquid or solid by-products are formed. The result is lower NO_x levels, but no significant change in the temperature of the flue gas.

Alfa Laval offers the *Pure SO$_x$ Express* system (Fig. 3) [7] to reduce SO_x levels.

Fig. 3. Pure SOx Express system by Alfa Laval

This system allows vessels to continue to use heavy fuel and still meet Tier II and Tier III emission requirements for SO_x levels. In addition, the temperature of the exhaust gases is significantly reduced.

In these systems, simultaneously with the reduction of harmful emissions, the temperature of the exhaust gases is also reduced.

However, the use of these scrubber systems causes problems with the selection of scrubber elements depending on the operating mode [8] and also with the disposal of the scrubber wash water, especially when the vessel is at sea [9].

Dry cleaning can also be used to reduce the amount of SO_x in the exhaust gases.

The company SodaFlexx has developed and implemented a technology for neutralising sulphur components SO_x by injecting sodium bicarbonate $NaHCO_3$ into the exhaust gas stream [10, 11]. Due to the chemical reaction, a highly stable and non-toxic salt – sodium sulphate Na_2SO_4 – is formed. It can be removed into the atmosphere or captured by special cyclone separators.

Solvay and Andritz have proposed the Bicar dry scrubber [12]. This was installed on the ferry "Piana". According to the independent third party CERTAM, about 96% of the SO_x was removed from use. According to [12], the scrubber is certified by DNV GL.

To neutralise harmful components in the exhaust gases, it is possible to use the Dry Exhaust Gas Scrubber manufactured by Crystec Technology Trading GmbH [13]. However, its use is possible with an exhaust gas flow rate of up to 72 m³/h, which limits its use by diesel generators

Another direction of the reduction of the NO_x level in exhaust gases of diesel engines is gas recirculation, the principle of which is illustrated in the diagram in Fig. 4 [14, 15], and it is shown that recirculation is economically justified in partial engine operation modes and at a recirculation rate of 12‑20%.
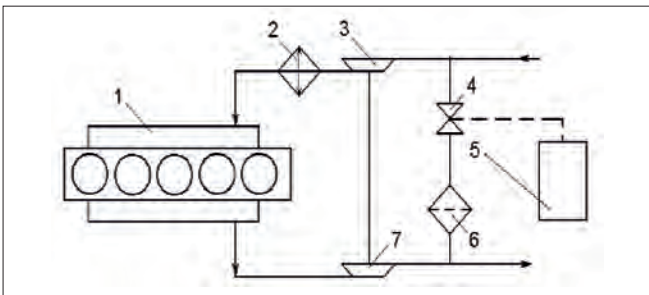
Fig. 4. Schematic diagram of gas recirculation: 1 - diesel engine; 2 - cooler; 3 - compressor; 4 - valve; 5 - control unit; 6 - filter; 7 - turbine

But at the same time, it has been shown in [15, 16] that such degrees of recirculation can increase the exhaust gas temperature by 4.5‑9.1%. So, it can increase the thermal load on the environment (Fig. 5).

The ecological parameters of marine power plants depend on many factors and can deteriorate during their operation. One effective way to control them is vibroacoustic diagnostics and monitoring of the working process of diesel engines [17, 18, 19, 20]. However, this method requires the installation of additional equipment on the main and auxiliary engines of the power plant.
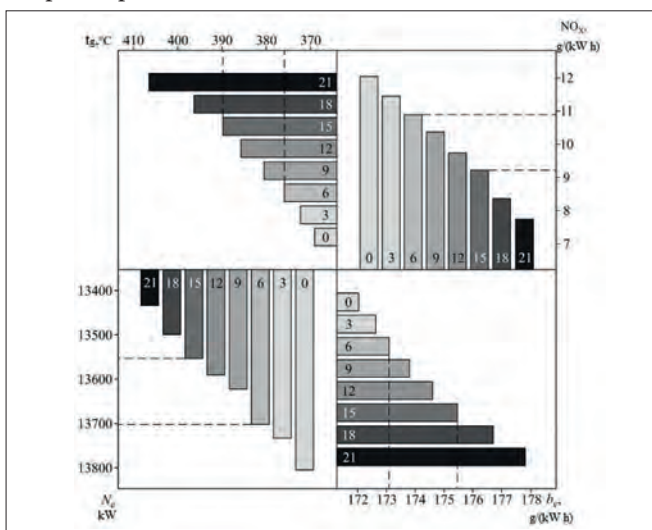
Fig. 5. Variation of exhaust gases NOx emissions, specific effective fuel consumption be, effective power Ne, exhaust gas temperature tg at 100% load of 7S60MC Kawasaki MAN-B&W diesel engine at various EGR

Wang and Yao [21] presented the results of their research on the effect of dimethyl ether on methyl decanoate HCCI on the emission characteristics of a low-speed diesel engine. However, in our opinion, it is still necessary to conduct more detailed research on the direct effect of these additives on the structural elements of a diesel engine ‑ injectors, cylinder walls, exhaust valve, etc. In addition, the fuel preparation system before feeding into the engine is significantly complicated, which will accordingly increase the cost of operating such systems.

In [22], Korczewski proposes to determine the parameters of chemical emissions in the exhaust gases of marine diesel engines on the basis of the emission calculation model that he developed. He presented the results of a comparison of the computational model with the results of the operation of a four-stroke marine diesel engine, which showed good convergence. However, he noted that it is advisable to use the proposed method at a steady state of engine operation. He does not specify measures to reduce emissions if they exceed the values of the maximum permissible norms.

Research on the features of the cold start of the main engine of the vessel is the subject of work by Adamkiewicz et al. [23]. Typical damage to the structural elements of a diesel engine is presented. Recommendations are made to reduce the harmful effects of transient processes on these elements. However, there are no data on the changes in the level of emissions of harmful substances during the cold start of the engine.

The analysis of current methods for neutralising harmful emissions showed that, in order to achieve the required efficiency, it is necessary to install a large amount of additional equipment and measuring instruments in the limited volume of the engine room and directly on the engines. These methods do not provide complete emission control of the exhaust gases and are costly to install and operate on a ship in service. Selection of these methods depends on the ship type and operation mode [24], which can considerably limit their application. In addition, the literature data on the efficiency of such systems in the transient modes of operation of the marine power plant ‑ entry and exit from the port, loading and unloading operations ‑ are very limited. This necessitates the development of additional ways to comply with the environmental standards of ship power plants.

In [25], in order to reduce the exhaust gas temperature and concentration of harmful emissions, the use of gas-air coolers of power plant exhaust gases is proposed (Fig. 6). It is explained that the use of such coolers will not require a significant modernisation of the gas exhaust system of power plant engines and the vessel's funnel.
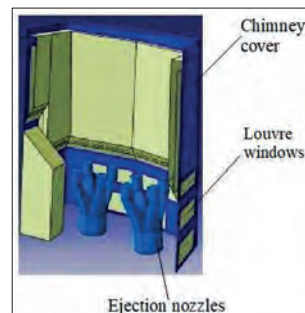
Fig. 6. Injection gas-air cooler

A positive effect of their operation will be a reduction in the volumetric concentration of the emission level by diluting the exhaust gases with ejected cold air, which will also reduce the exhaust gas temperature. This can be an effective additional means of improving the environmental parameters of vessels, especially when operating in "special" areas of the world's oceans.

At the same time, the proposed gas-air coolers are designed with the same 45° angle as the air supply louvre windows. When operating in "special" areas, it is typical to change the engine load of both the main and auxiliary marine power plant. This will change the flow rate and consequently the velocity of the flue gases as an ejection flow of gases, which in turn will change the efficiency of the unit, which can be corrected by changing the angle of opening of the louvre windows. So, it is advisable to consider the dependences of the pollutant concentration at the outlet and the exhaust gas temperature on the angle of the louvre windows and the temperature of outside ejected air under different operating modes of the diesel engine.

INVESTIGATION METHOD

The modern method for studying the processes of heat transfer and mixing in the elements of power plants is CFD – the computer fluid dynamics method. The mathematical model that describes these processes includes the continuity, momentum and energy conservation equations. These are presented in the following form [26]:

Continuity equation

$$\frac{\partial \rho}{\partial t} + \nabla (\rho \vec{V}) = 0, \tag{1}$$

where ρ is the mass flow density, and $\vec{V}$ is the vector of the local fluid velocity;

Momentum equation

$$\frac{\partial (\rho \vec{V})}{\partial t} + \nabla(\rho \vec{V} \vec{V}) = \nabla p + \nabla \tau + \rho \vec{g} + \vec{F}, \tag{2}$$

where p is the static pressure, $\rho \vec{g}$ is the gravitational force per unit mass, $\vec{F}$ are the external forces acting on the flow, and τ is the pressure tensor;

Equation of energy conservation

$$\frac{\partial (\rho E)}{\partial t} + \nabla (\vec{V}(\rho E + p)) = \nabla (-\vec{J_q} + (\tau_{eff} \vec{V})), \tag{3}$$

where $\vec{J_q}$ is the heat flow density, $E = h - \frac{p}{\rho} + \frac{V^2}{2}$ is the total energy of the working fluid, h is the working fluid enthalpy, and the expression $\tau_{eff} \vec{V}$ represents viscous heating.

The closure of the system of equations is performed by adding semi-empirical equations for the pressure tensor, the heat flux, the equation of state for ideal gases, and the differential equations of the turbulence model.

Newton's law equation: by neglecting the bulk viscosity, the stress tensor can be represented as

$$\tau = \mu \left[\nabla \vec{V} + (\nabla \vec{V})^T - \frac{2}{3} \nabla (\vec{V} I) \right], \tag{4}$$

where μ is the coefficient of molecular viscosity, and I is the unit vector.

Fourier's law equation: The heat flow is determined by the expression

$$\vec{J_q} = -\lambda_{eff} \nabla T, \tag{5}$$

where $\lambda_{eff} = \lambda + \lambda_t$ is the coefficient of effective conductivity.

Mendeleev−Clapeyron's law equation is presented in the form

$$p = R \cdot \rho \cdot T, \tag{6}$$

where R is the individual gas constant for the working fluid.

To calculate the processes of mixing flows the species transport equation was used. It is presented in the form

$$\frac{\partial}{\partial t}(\rho Y_i) + \nabla \cdot (\rho \vec{v} Y_i) = - \nabla \cdot \vec{J_i} + R_i + S_i, \tag{7}$$

where R_i is the net rate of production of species I and S_i is the rate of creation by addition from the dispersed phase plus any user-defined sources. An equation of this form will be solved for N-1 species, where N is the total number of fluid phase chemical species present in the system. The mass fraction of the species must sum to unity. To minimise numerical error, the Nth species should be selected as that species with the overall largest mass fraction, such as N_2 when the oxidiser is air.

On the basis of the recommendations given in [27, 28], the *RSM* turbulence model was used to close the system of equations (1)–(7). To solve the resulting system, the *RANS* approach was implemented using the *Code-Saturne* software package with a free license [29] and the *SimScale* cloud service [30].

The mathematical model with the adopted turbulence model was verified by comparing the results of numerical modelling with experimental data from a full-scale bench test of a model of a ship's gas-air cooler. The discrepancy between the results did not exceed 5% [31].

DETERMINATION OF THE EFFICIENCY OF THE GAS-AIR COOLER

Modelling of gas-air cooler operation was carried out for the following conditions: exhaust gas temperature at the cooler inlet $t_{gas} = 375°C$, $G_{gas} = 1.25$ kg/s, which corresponds to the characteristics of the engine 7L16/24 of MAN B&W company, used as a drive engine of marine diesel generators [32], ambient air temperature 17°C, with diesel oil as fuel. The fuel currently used in marine power plants, both liquid and gaseous, has a rather diverse chemical composition. Therefore, in order to summarise the results obtained, the change in the total
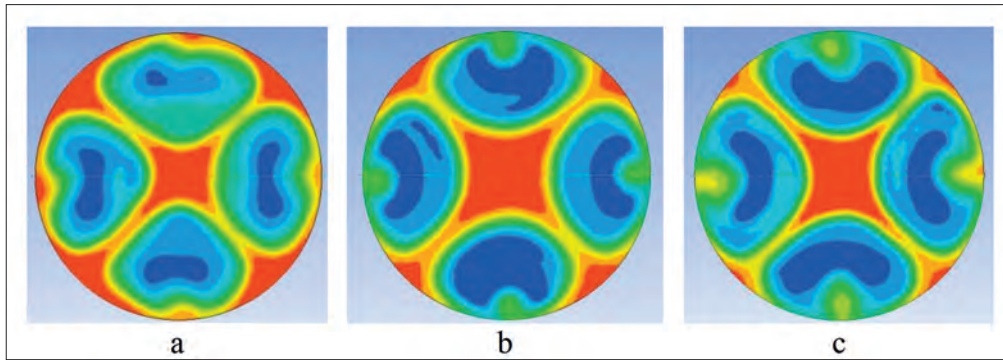
Fig. 7. Variation of output concentration at 45° louvre opening angle as a function of engine load: a - 100%; b - 75%; c - 50%

concentration of the $CO_2 + NO_x$ components of diesel fuel combustion products at the outlet of the gas-air cooler was researched.

Changes in the combustion product yield for the 45° louvre opening angle at 100%, 75% and 50% engine load are shown in Fig. 7.

The processing of similar results in the form of dependences $n\_out = f(v\_rel)$, where n_out is the diesel fuel vapour output concentration, v_rel is the relative engine load, %, for different louvre opening angles is shown in Fig. 8a-11. Fig. 8b shows the results of calculations of the output concentrations and the exhaust gas temperature as a function of the external air temperature. Their values are defined as the average integral in the outlet section.

Analysis of the results shows the following.

Changes in the outdoor temperature have an insignificant effect on the investigated performance of the device. The

changes in output concentration and temperature do not exceed 3% (Fig. 8b). Much stronger influence is exerted by the change of engine load and the louvre windows opening angle (Fig. 8a-11).

Thus, for the louvre opening angle of 45° (Fig. 8a), the temperature drop with a change in motor load from 100% to 75% and 50% is 12.5% and 19.5%, respectively. At the same time, the corresponding reductions in concentration are 13.8% and 22.7%.

At an opening angle of 60° (Fig. 9), there is a slightly smaller temperature drop of 11.2% and 14.3%, but a larger concentration drop of 14.4% and 19.7%, respectively.

At an opening angle of 30° (Fig. 10), the reduction in temperature and concentration when the load is reduced from 100% to 75% is 10.1% and 12.6%, respectively. At the same time, the largest reductions in temperature and concentration of up to 50% are observed at 22.8% and 27.7%, respectively.
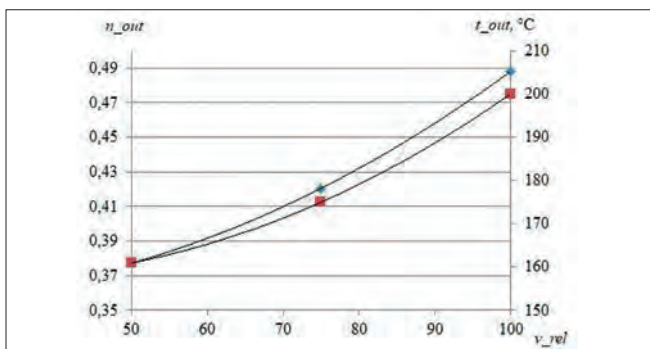
Fig. 8a. Effectiveness of the gas-air cooler operation at 45° louvre opening angle as a function of engine load: ▪ – temperature change; ♦ - concentration change
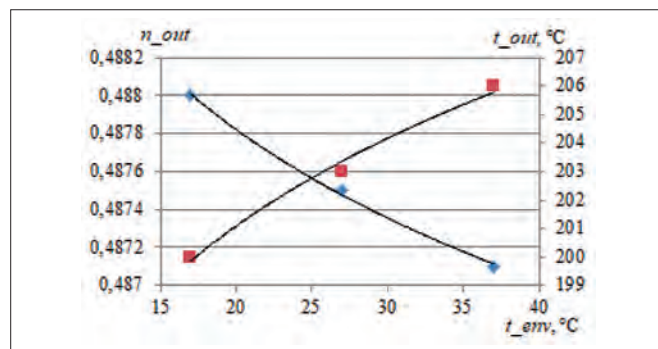
Fig. 8b. Effectiveness of the gas-air cooler operation at 45° louvre opening angle as a function of environmental temperature: ▪ – temperature change; ♦ - concentration change
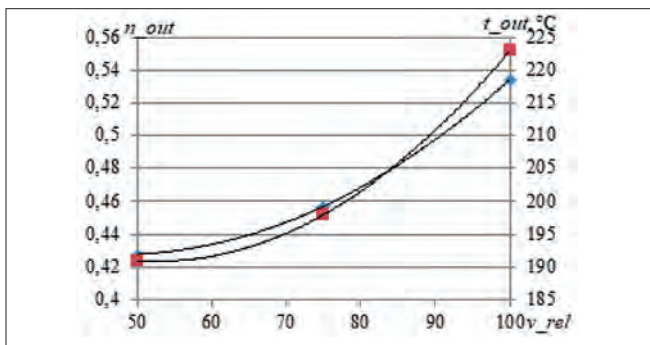
Fig. 9 Effectiveness of the gas-air cooler operation at 60° louvre opening angle as a function of engine load: ▪ – temperature change; ♦ - concentration change
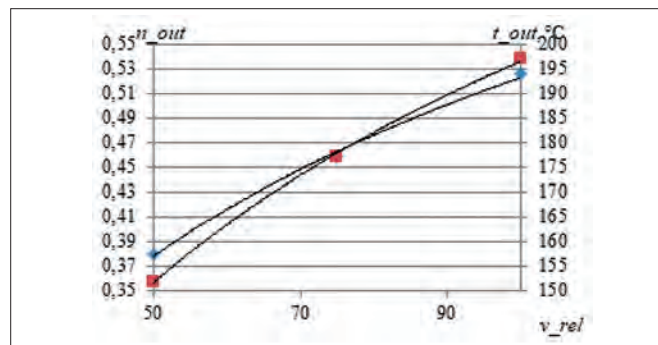
Fig. 10. Effectiveness of the gas-air cooler operation at 30° louvre opening angle as a function of engine load: ▪ – temperature change; ♦ - concentration change
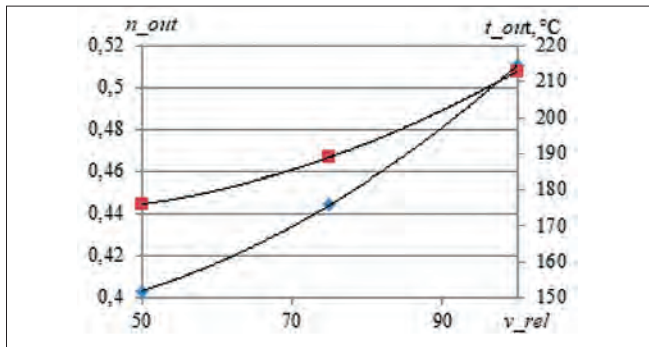
Fig. 11. Effectiveness of the gas-air cooler operation at 45° and 60° louver opening angles as the function of engine load: ■ – temperature change; ♦ - concentration change

The expected effect of the combined louvre opening of 45° and 60° was not significant (Fig. 11). The reductions in temperature and concentration from 100% to 75% and 50% are 11.3% and 17.3%, 13.1% and 21.06%, respectively.

DISCUSSION OF THE RESULTS

The modernisation of shipboard propulsion systems in operation to comply with IMO Tier III is a current scientific and technical issue. The results show that gas-air coolers for diesel engine exhaust gases can be an effective additional means of reducing concentration and temperature.

Running at 100% engine load, the concentration reduction efficiency is around 50%. With a standard louvred window opening of 45° and a reduction in engine load from 100% to 75%, it is reasonable to increase the opening angle to 60°, and with a further reduction to 50% to reduce the angle to 30°.

The proposed technical solution of the gas-air exhaust gas cooler does not neutralise the harmful emissions of power plant engines, but only increases the volume concentration of exhaust gases. However, at the same time, this will help *to increase the efficiency of dispersion* of harmful emissions, by reducing the concentration of harmful emissions to values not exceeding the maximum permissible concentrations. This will enable the use of gas-air coolers as an effective additional means of ensuring the environmental friendliness of power plants, especially in transient modes of operation. More detailed results can be obtained by analysing the operation of a particular ship power plant, taking into account the load schedule and the location of the vessel.

Further research can be aimed at studying the efficiency of the device depending on specific ship operating conditions in various areas of the world's oceans, as well as determining the total efficiency of the gas-air cooler when low-speed and medium-speed diesel engines work together.

FINAL CONCLUSIONS

The effectiveness of the ejection gas-air cooler for the diesel engine exhaust gases of the marine power plant as an additional means of improving its environmental performance is shown.

It is demonstrated that, in order to ensure effective operation of the device at varying engine loads, the louvre windows opening angle should be 30–60°.

The explanation of the mathematical model and the open-source software implementing it make it possible to correctly estimate the decrease in the level of harmful emissions depending on the loading of the engines, selecting separate components of fuel for specification.

It is expedient to further investigate the effectiveness of the device in the case of joint operation of low-speed and medium-speed engines and considering the availability of their load schedule.

REFERENCES

1. United Nations Conference on Trade and Development. "Executive Summary. Review of Maritime Transport." 2020. [Online]. Available: https://unctad.org/system/files/official-document/rmt2020summary_en.pdf. [Accessed: Mar. 30, 2023].

2. "ABS Advisory on NOx TIER III. Compliance." [Online]. Available: https://ww2.eagle.org/content/dam/eagle/advisories-and-debriefs/ABS-Advisory-on-NOx-Tier-III-Compliance-20068.pdf. [Accessed: Mar. 30, 2023].

3. "Resolution MEPC.198(62)." Adopted on 15 July 2011. 2011 Guidelines Addressing Additional Aspects to the NOx Technical Code 2008 with Regard to Particular Requirements Related to Marine. Diesel Engines Fitted with Selective Catalytic Reduction (SCR) Systems. [Online]. Available: https://wwwcdn.imo.org/localresources/en/KnowledgeCentre/IndexofIMOResolutions/MEPCDocuments/MEPC.198(62).pdf. [Accessed: Mar. 30, 2023].

4. "MARPOL Annex VI and the Act to Prevent Pollution from Ships (APPS)." [Online]. Available: https://www.epa.gov/enforcement/marpol-annex-vi-and-act-prevent-pollution-ships-apps. [Accessed: Mar. 30, 2023].

5. Y. Moshentsev, O. Gogorenko, and O. Dvirna, "Possibilities for improving the cooling systems of IC engines of marine power plants," *Advances in Science and Technology Research Journal*, vol. 16(3), pp. 183–192, 2022. https://doi.org/10.12913/22998624/149658.

6. "Wärtsilä Environmental Product Guide." [Online]. Available: https://cdn.wartsila.com/docs/default-source/product-files/egc/product-guide-o-env-environmental-solutions.pdf. [Accessed: Mar. 31, 2023].

7. "New system PureSOx Express (in Ukrainian)." [Online]. Available: https://www.alfalaval.ua/media/news/2020/new-alfa-laval-puresox-express-offers-easy-access-to-sox-scrubber-advantages/ [Accessed: Mar. 31, 2023].

8. Y. S. Choi and T. W. Lim, "Numerical simulation and validation in scrubber wash water discharge from ships," *Journal of Marine Science and Engineering*, vol. 8(4), p. 272, 2020. https://doi.org/10.3390/jmse8040272.

9. S. Endres, F. Maes, F. Hopkins, K. Houghton, E. M. Mårtensson, J. Oeffner, and D. Turner, "A new perspective at the ship-air-sea-interface: The environmental impacts of exhaust gas scrubber discharge," *Frontiers in Marine Science*, vol. 5, 2018. https://doi.org/10.3389/fmars.2018.00139.

10. "SodaFlexx - Clean exhaust from ships." [Online]. Available: https://sodaflexx-int.com [Accessed: Mar. 31, 2023].

11. "Dry exhaust cleaning system installed on bulker." [Online]. Available: https://maritime-executive.com/article/dry-exhaust-cleaning-system-installed-on-bulker [Accessed: Mar. 31, 2023].

12. "Dry exhaust gas cleaning system certified by DNV GL." [Online]. Available: https://www.seatrade-maritime.com/europe/dry-exhaust-gas-cleaning-system-certified-dnv-gl [Accessed: Mar. 31, 2023].

13. "Dry exhaust gas scrubber." [Online]. Available: https://www.crystec.com/ksicate.htm [Accessed: Mar. 31, 2023].

14. V. V. Le, T. H. Truong, "A simulation study to assess the economic, energy and emissions characteristics of a marine engine equipped with exhaust gas recirculation," *1st International Conference on Sustainable Manufacturing, Materials and Technologies*, 2020. https://doi.org/10.1063/5.0000135.

15. O. A. Kuropyatnyk and S. V. Sagin, "Exhaust gas recirculation as a major technique designed to reduce NOx emissions from marine diesel engines," *OUR SEA: International Journal of Maritime Science & Technology*, vol. 66, iss. 1, pp. 1–9, 2019. https://doi.org/10.17818/ NM/2019/1.1.

16. S. V. Sagin and O. A. Kuropyatnyk, "The use of exhaust gas recirculation for ensuring the environmental performance of marine diesel engines," *OUR SEA: International Journal of Maritime Science & Technology*, vol. 65, no. 2, pp. 78–86, June 2018. https://doi.org/10.17818/NM/ 2018/2.3.

17. R. Varbanets, O. Shumylo, A. Marchenko, D. Minchev, V. Kyrnats, V. Zalozh, N. Aleksandrovska, R. Brusnyk, and K. Volovyk, "Concept of vibroacoustic diagnostics of the fuel injection and electronic cylinder lubrication systems of marine diesel engines," *Polish Maritime Research*, vol. 29, no. 4, pp. 88‒96, 2022. https://doi.org/10.2478/pomr-2022-0046.

18. D. Minchev, R. Varbanets, N. Aleksandrovskaya, and L. Pisintsaly, "Marine diesel engines operating cycle simulation for diagnostics issues," *Acta Polytechnica*, vol. 3, no. 61, pp. 428‒440, 2021. [Online]. Available: https://ojs.cvut.cz/ojs/index.php/ap/article/view/6833 [Accessed: Mar. 31, 2023].

19. S. Neumann, R. Varbanets, D. Minchev, V. Malchevsky, and V. Zalozh, "Vibrodiagnostics of marine diesel engines in IMES GmbH systems," *Ships Offshore Struct.*, 2022. https://doi.org/10.1080/17445302.2022.2128558.

20. M. H. Ghaemi, "Performance and emission modelling and simulation of marine diesel engines using publicly available engine data," *Polish Maritime Research*, vol. 28, pp. 63‒87, 2021. https://doi.org/10.2478/pomr-2021-0050.

21. S. Wang and L. Yao, "Effect of engine speeds and dimethyl ether on methyl decanoate HCCI combustion and emission characteristics based on low-speed two-stroke diesel engine," *Polish Maritime Research*, vol. 27, pp. 85‒95, 2020. https://doi.org/10.2478/pomr-2020-0030.

22. Z. Korczewski, "Test method for determining the chemical emissions of a marine diesel engine exhaust in operation," *Polish Maritime Research*, vol. 28, pp. 76‒87, 2021. https://doi.org/10.2478/pomr-2021-0035.

23. A. Adamkiewicz, J. Fydrych, and J. Drzewieniecki, "Studies on the effects of cold starts of the ship main engine," *Polish Maritime Research*, vol. 29, pp. 109‒118, 2022. https://doi.org/10.2478/pomr-2022-0031.

24. Y. Zhao, Y. Fan, K. Fagerholt, and J. Zhou, "Reducing sulfur and nitrogen emissions in shipping economically," *Transportation Research Part D: Transport and Environment*, vol. 90, January 2021. [Online]. Available: https://www.sciencedirect.com/science/article/abs/pii/S1361920920308269?via%3Dihub [Accessed: Mar. 31, 2023].

25. V. Kuznetsov, B. Dymo, S. Kuznetsova, M. Bondarenko, and A. Voloshyn, "Improvement of the cargo fleet vessels power plants ecological indexes by development of the exhaust gas systems," *Polish Maritime Research*, vol. 28, pp. 97‒104, 2021. https://doi.org/10.2478/pomr-2021-0009.

26. Y. A. Bystrov, S. A. Isayev, N. A. Kudryavtsev, and A. I. Leont'yev, *Numerical simulation of heat transfer vortex intensification in the pipe packs*. St. Petersburg: Shipbuilding, 2005.

27. T. B. Gatski, M. Y. Hussaini, and J. L. Lumley, *Simulation and Modelling of Turbulent Flows*. Oxford University Press. Oxford, New York, 1996 [Online]. Available: https://vdoc.pub/documents/simulation-and-modelling-of-turbulent-flows-60gogpq1fom0. [Accessed: Apr. 5, 2023].

28. S. Sarkar and L. Balakrishnan, *Application of a Reynolds-Stress Turbulence Model to the Compressible Shear Layer*. ICASE Report 90-18NASA CR 182002, 1990. [Online]. Available: https://apps.dtic.mil/dtic/tr/fulltext/u2/a227097.pdf. [Accessed: Apr. 10, 2023].

29. About Code_Saturne. [Online]. Available: https://www.code-saturne.org/cms/web/ [Accessed: Apr. 10, 2023].

30. SimScale CFD. [Online]. Available: https://www.simscale.com/product/cfd/ [Accessed: Apr. 10, 2023].

31. B. V. Dymo, A. Y. Voloshyn, A. A. Yepifanov, and V. V. Kuznetsov, "Increase of ship power plants gas-air cooler efficiency," *Problemele Energeticii Regionale*, vol. 2 (34), pp. 113‒124, 2017. https://doi.org/10.5281/zenodo.1189332

32. Marine Engine Programme. *MAN Energy Solutions 2023*. [Online]. Available: https://www.man-es.com/marine/products/planning-tools-and-downloads/marine-engine-programme. [Accessed: Apr. 10, 2023].

DIAGNOSTIC ANALYSIS OF EXHAUST GAS WITH A QUICK-CHANGING TEMPERATURE FROM A MARINE DIESEL ENGINE PART II / TWO FACTOR ANALYSIS

Patrycja Puzdrowska [ORCID]
Gdansk University of Technology, Institute of Naval Architecture, Poland

* Corresponding author: *patrycja.puzdrowska@pg.edu.pl (Patrycja Puzdrowska)*

ABSTRACT

The article presents a continuation of research carried out to determine the effect of input parameters (changes in engine structure parameters) on selected output parameters (diagnostic measures), based on quickly changing exhaust gas temperature. A method of determining the simultaneous influence of two input factors (the structure parameter and the engine load) on one output factor was presented, as well as an evaluation of which of the analysed input factors has a stronger influence on the output parameter. The article presents the stages of the experimental research conducted and statistical inference based on the results. Three changing parameters for the structure were reviewed: the active cross-sectional area of the inlet air channel, the injector opening pressure and the compression ratio. Based on the quickly changing temperatures of the exhaust gases, three diagnostic measures were defined and subjected to statistical tests. The following data were averaged over one cycle for a 4-stroke engine operation: the intensity of changes, the specific enthalpy and the peak-to-peak value of the exhaust gas temperature. The results of the two-factor analysis are presented. Conclusions on the analysis are given and a criterion for the selection of a diagnostic measure, depending on the analysed parameter of the structural design of the diesel engine, is proposed.

The previous part of the article presented the results of the first stage of the elimination study: the one-factor statistical analysis (randomised complete plan). This paper presents the results of the second stage of the studies: two-factor analysis (block randomised plan), where the significance of the effect of changing the values of the structural parameters on the diagnostic measures were analysed in the background of a variable engine load. The next (third) part will present the results of the calculations and analysis of the interaction coefficient of significance.

Keywords: marine diesel engine, exhaust gas temperature, diagnostic information, F-statistic of Fisher-Snedecor distribution

INTRODUCTION

The first part of this series of articles presented the results of a single-factor statistical analysis [15], which made it possible to evaluate the influence of a single input factor (load or structural parameter) on diagnostic measures determined from the course of quickly varying exhaust gas temperature. These were: the intensity of changes $(\Delta T/\Delta \tau \uparrow)_{śr}$, the specific enthalpy $h_{spśr}$ and the peak-to-peak value $\Delta T_{spśr}$ of the quick-changing exhaust gas temperature. All diagnostic measures were for a single cycle of compression-ignition engine operation. One-factor analysis was performed to eliminate output factors deemed not to be statistically significant. It was then concluded that the reduced injector opening pressure p_{wtr} did not significantly affect the specific enthalpy of the exhaust gas $h_{spśr}$ of the test engine. In the next step (in this article), the results of a two-factor analysis are presented to determine the effect of the structural parameters in the background of the variable engine load on the mentioned diagnostic measures. The second goal was to determine

which of the two input factors analysed has a greater influence on the output parameter. The research, the statistical analysis results of which are presented in this article, was carried out on a test bench of a small-scale model of a marine engine [15].

The utilitarian goal of the research was to formulate a methodology for diagnostic testing of a ship's engine under operating conditions, based on measurements of the rapidly changing exhaust gas temperature. The novelty of the proposed method is that the quickly changing exhaust gas temperature is not monitored in the standard measurement system of control parameters of a marine engine. However, there is an average temperature measurement point required by classification societies, so that it can be used for fast variable measurements. Analysis of the rapidly changing signal gives more diagnostic information about the condition of the structural components of the compression ignition engine and injection system under consideration.

QUICK-CHANGING EXHAUST GAS TEMPERATURE AS A DIAGNOSTIC PARAMETER

Diagnostics of marine diesel engines is a current and important issue. Piston engines, which are the main propulsion systems of ships, as well as their power plants, generate operating costs that account for more than 70% of the cost of maintaining the entire ship's power plant, mainly due to the high price of fuel and lubricating oils [19]. There is a strong relationship between engine reliability and ship safety. A very important issue is also the emission of harmful, including toxic, components of exhaust gases by marine engines and the associated effects on the environment. Taking into account these three aspects (safety of shipping, costs of ship operation and reduction of emissions of harmful and toxic components of exhaust gases), diagnostic methods and equipment are mainly being developed with a focus on the reliability of marine engines, but also on environmental protection [3, 7, 11, 17].

The exhaust gas temperature is the main diagnostic symptom of a marine engine (main and auxiliary). It is an intensive parameter of the state of the thermodynamic (working) medium, which characterises the quality of the process of transforming the chemical energy of fuel into mechanical energy, via work and heat, as a result of the realisation of complex physicochemical processes in its cylinder systems. The temperature of the exhaust gas also determines the quality of the thermal-flow processes taking place in the separated gaseous spaces of the channels for transporting the working medium from the cylinders directly to the environment or indirectly, through the turbine(s) of the turbocharging system. The thermo-chemical reactions that occur during the combustion of fuel in cylinders are essential for the realisation of the working process but, at the same time, they can be the cause of many destructive processes that negatively affect the technical condition of the structural components confining the engine's working spaces. These mainly comprise the corrosive and erosive effects of flowing (hot) exhaust gases. The consequences of successive transformations of the thermodynamic cycle of a compression-ignition engine are cyclically varying thermal and mechanical stresses, resulting in material exhaustion, in turn. Wear processes (tribological, erosive and corrosive) result in the progressive degradation of the engine's design structure, consequently contributing to the state of its operational unfitness [8, 9, 12].

F − STATISTIC AS A TOOL FOR TWO-FACTOR IMPACT SIGNIFICANCE ANALYSIS

An experimental study was carried out, the main purpose of which was diagnostic inference, on the basis of rapidly changing exhaust gas temperature, as a result of the proposed diagnostic measures determined on the basis of the course of rapidly changing exhaust gas temperature. After the single-factor analysis, the next step was to test the significance of the influence of two input factors, varying to a specific degree and determined by the engine's design and operating capabilities. This made it possible to assess which of the analysed input factors has a stronger influence on the output parameter. The matrix of this stage of experimental research is shown in Table 1.

Tab. 1. Matrix of the experimental research program - static randomised block plan with two input factors: engine load P and active cross-sectional area of the intake air flow to the engine A_{dol}

Level of variation of factor I: engine load	Level of variation of factor II: structural parameter			$\bar{h}_i$
	A_{dol1}	A_{dol2}	A_{dol3}	
P_1	h_{11}	…	h_{11}	$\bar{h}_{1w}$
P_2	⋮ ⋅	⋮ ⋅	⋮ ⋅	⋮ ⋅
P_3	h_{31}	…	h_{33}	$\bar{h}_{3w}$
$\bar{h}_j$	$\bar{h}_{1k}$	…	$\bar{h}_{3k}$	$\bar{h}$

When the number of factors is greater than one, it is said to be a multiple classification, in which the essence of the method remains the same as with a single-factor, but is more complex. The idea of variation analysis for this case is based on decomposing the sum of squares of deviations from the overall average, into components corresponding to the individual factors whose influence was studied [1, 18]. The calculation scheme of the two-factor analysis of variation can be presented in tabular form, see Table 2. Statistical reasoning is carried out analytically, as in the case of one-factor analysis.

Tab. 2. Calculation scheme for two-fold analysis of variation

Variation	Sum of squares	Number of degrees of freedom	Empirical variation
relative to the rows	$S_I = q\,\bar{h}_i^2 - p \cdot q \cdot \bar{h}^2$	$p-1$	S_I^2
relative to the columns	$S_I = p \sum\limits_{j=1}^{q} \bar{h}_j^2 - p \cdot q \cdot \bar{h}^2$	$q-1$	S_{II}^2
residual (error)	$S_R = \sum\limits_{i=1}^{p} \sum\limits_{j=1}^{q} h_{ij}^2 - q \sum\limits_{i=1}^{p} \bar{h}_i^2$ $- p \sum\limits_{j=1}^{q} \bar{h}_j^2 + p \cdot q \cdot \bar{h}^2$	$(p-1) \cdot (q-1)$	S_R^2

where $\bar{h}_i$ is the average specific enthalpy from the results of the measurements in the i-th row, $\bar{h}_j$ is the average specific enthalpy from the results of the measurements in the j-th column, $\bar{h}$ is the average specific enthalpy of the results from all measurements, h_{ij} is the value of the j-th specific enthalpy at the level of i, p and q are the number of levels of variation of input factor I (engine load) and input factor II (active cross-sectional area of inlet air flow to the engine), accordingly.

At the level of variation of the first factor, the same number of experiments must be performed as for the level of variation of the second factor, and the individual experiments should be performed in random order. Mathematical processing of the results carried out for the discussed program consisted of calculating the value of the F_{obl} coefficient for the two input factors under study, according to the equations [5]:

$$F_{obl\_I} = \frac{S_I}{S_R} \cdot \frac{(p-1) \cdot (q-1)}{(p-1)}$$
$$F_{obl\_II} = \frac{S_{II}}{S_R} \cdot \frac{(p-1) \cdot (q-1)}{(p-1)} \tag{1}$$

After calculations according to (1), the obtained values of the coefficients were compared with the critical value of the statistic determined on the basis of Fisher-Snedecor's F-distribution tables, with the assumed significance level α and the number of degrees of freedom for the denominator:

$$f_2 = f_m = (p-1) \cdot (q-1) \tag{2}$$

and for the numerator (for factor I and factor II, respectively, e.g. P and A_{dol}):

$$f_{1I} = p - 1$$
$$f_{1II} = q - 1 \tag{3}$$

where p and q are the numbers of levels of variation in factor I and factor II, respectively.

The influence of the considered input factor on the result factor is deemed significant when the empirical value for a given factor calculated from (1), F_{obl}, was greater than or equal to the critical value Fkr [5].

To complement the statistical analysis, the values of the impact significance confidence factor ΔF were determined as a measure of the power of the statistical test, i.e. the difference between the value of the F_{obl} statistic, calculated for the input factor under study, and the critical value for the assumed values of the numerator and denominator degrees of freedom and the significance level:

$$\Delta F_I = F_{obl\_I} - F_{krI}$$
$$\Delta F_{II} = F_{obl\_II} - F_{krII} \tag{4}$$

Comparing the values of the confidence coefficients ΔF_I and ΔF_{II} made it possible to assess which of the two input factors has a greater influence on the output parameters, with the previously proven significance of the influence of both input factors.

RESEARCH PROCEDURE

Analysis was carried out on the effects of changes in structural parameters using the DIESEL-RK program on selected engine operating parameters, such as flame temperature, temperature and pressure of the working medium in the cylinder, and the temperature and chemical composition and speed of the exhaust gas in the exhaust channel [10, 13]. Literature searches were also carried out on the most common states of inoperability of functional engine systems [19]. It was concluded that the most critical functional systems of a marine compression-ignition engine are the fuel supply system [4, 6], the intake air duct [19] and the structural elements that limit the combustion chamber [2, 20]. On the basis of the above analyses, in the next step, tests were conducted during which the most common malfunctions in the functional systems of a diesel engine were simulated (Table 3). The empirical research was carried out on a laboratory test stand comprising a single-cylinder, type D10 four-stroke Farymann Diesel marine engine, as described in the first part of the article [15]. The input variables were the structural parameters listed in the same article and shown in Table 3 and Figure 1.

Tab. 3. Values of engine load and its structural parameters, which are input factors in the diagnostic tests carried out

Structural parameter (input factor)	Desig-nation	Unit	Reference value	Assigned changes
Engine load	P	W	1200 (0.2·P_{NOM})	768 (0.64·P_{REF}) 432 (0.36·P_{REF})
Active cross-sectional area of the inlet air channel flow	A_{dol}	mm² (%)	(100%)	603 (0.75·A_{REF}) 401 (0.5·A_{REF})
Opening pressure of the injector	p_{wtr}	MPa	12	10
Compression ratio	ε	-	22:1	22:1

In order to obtain the value of the F_{obl} statistic and the confidence coefficient ΔF, and thus to answer the key question about the significance of the influence of selected input factors (structural engine parameters) on the defined diagnostic measures, the procedure was followed according to the developed scheme for the implementation of statistical tests (Figure 1). The recorded signal of exhaust gas temperature in the first step was subjected to mathematical processing, the purpose of which was to remove disturbances from the measurement network using the method of least sum of squares. An important element when evaluating the dynamic properties of the thermocouple is to determine its response to the sinusoidal forcing of the exhaust gas temperature of the compression-ignition test engine (the phase shift and amplitude of the temperature changes recorded by the thermocouple in relation to the forced, real exhaust gas temperature changes) [16]. Diagnostic measures were determined from the obtained waveform of the real and disturbance-free fast-changing exhaust gas temperature. By using the complete randomised plan, non-significant input values were extracted and eliminated from further diagnostic analyses [15]. The final stage of the study was the implementation of the block randomised plan and the statistical and merit analysis of the significance of
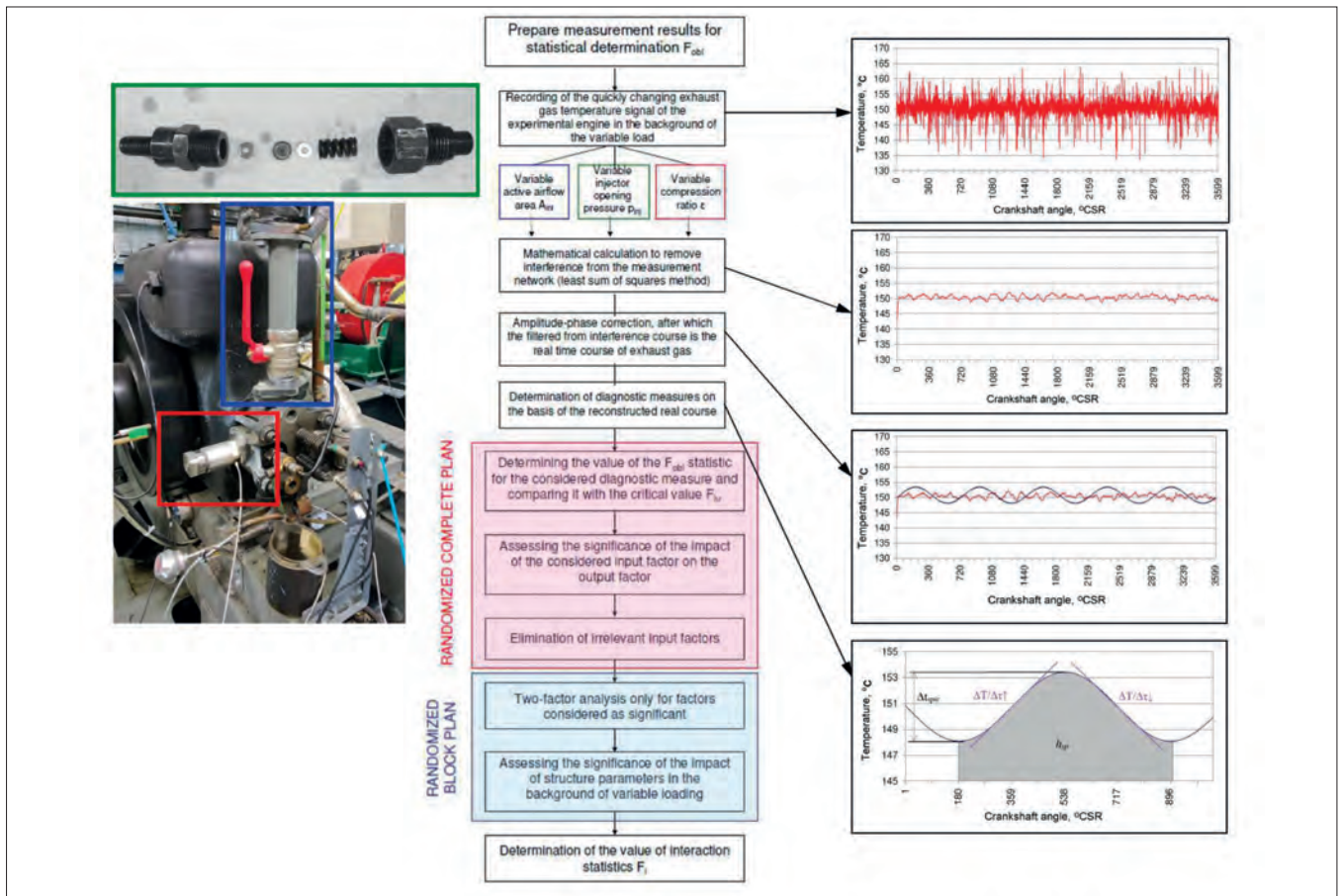
Fig. 1. Steps for determining the F-statistic of the Fisher-Snedecor distribution for diagnosing a diesel test engine

the effect of the structural parameters on the defined diagnostic measures in the background of the changed load condition (presented in this article), The determination of the interaction coefficient of significance will be described in the next part of the article and will allow assessment as to whether and how two input factors statistically affect the output factor.

RESULTS

In the case of two-factor statistical analysis, the simultaneous effect of the structural parameter (A_{dol}, p_{wtr}, ε) in the background of the variable engine load P on the defined diagnostic measures ($h_{spśr}$, $\Delta T_{spśr}$, $(\Delta T/\Delta \tau \uparrow)_{śr}$) was evaluated. Accordingly, the following null hypotheses were formulated:

H01: the value of the analysed structural parameter with a background of variable load has no influence on the value of the specific enthalpy of the exhaust gas stream, averaged over one engine operating cycle ($S_{II}^2 = S_I^2$).

H02: the value of the analysed structural parameter with a background of variable load has no influence on the peak-to-peak value of the exhaust gas stream temperature within one engine operating cycle ($S_{II}^2 = S_I^2$).

H03: the value of the analysed structural parameter with a background of variable load has no influence on the value of the intensity of changes in the exhaust gas temperature within one engine operating cycle ($S_{II}^2 = S_I^2$).

Table 4 shows the results of the statistical analysis, evaluating which of the two input parameters (the engine load P or the structural parameter (A_{dol}, p_{wtr}, ε) has a greater effect on the determined diagnostic measures ($h_{spśr}$, $\Delta T_{spśr}$, $(\Delta T/\Delta \tau \uparrow)_{śr}$). Calculations were performed according to the algorithm presented in this article (1-4).

In the first step, a statistical analysis was performed to evaluate which of the two input parameters (engine load P or active cross-sectional area of the intake air channel A_{dol}) has a greater impact on all diagnostic measures ($h_{spśr}$, $\Delta T_{spśr}$, $(\Delta T/\Delta \tau \uparrow)_{śr}$). The number of degrees of freedom for the denominator f_2 was 4 and the number of degrees of freedom for the numerator of the first factor (P) was $f_{1I} - 2$. The number of degrees of freedom was the same for the numerator of the second factor (A_{dol}) f_{1II}. The number of levels of variation of both factors p and q was the same, i.e. 3. The critical value of the statistic read from the tables was for rows and columns $F_{kr(0.05;2;45)} = 3.20432$ (table data [5]).

In the case of statistical analysis of the diagnostic parameters, which are the average peak-to-peak value $\Delta T_{spśr}$ and the average intensity of changes of exhaust gas temperature $(\Delta T/\Delta \tau)_{śr}$, which of the two input parameters (engine load P or injector opening pressure p_{wtr}) has a greater influence on the diagnostic measures was evaluated. The number of degrees of freedom for the numerator of the first factor (P) was $f_{1I} - 2$, the number of degrees of freedom for the numerator of the second factor (p_{wtr}) was $f_{1II} - 1$, and the number of degrees of freedom for the denominator f_2 was 2. The number of levels of variation of the

factors was p = 3 and q = 2, respectively. The critical value of the statistics read from the tables was for rows $F_{kr(0.05; 2; 18)}$ = 3.55456 and columns $F_{kr(0.05; 1; 18)}$ = 4.41387 (table data [5]).

Table 4 also shows the results of the statistical analysis for evaluating which of the two input parameters, the engine load P or its compression ratio ε, has a greater effect on all diagnostic measures ($h_{spśr}$, $\Delta T_{spśr}$, $(\Delta T/\Delta \tau)_{śr}$) within one engine cycle. The number of degrees of freedom for the denominator of f_2 was 2, the number of degrees of freedom for the numerator of the first factor (P) f_{II} was also 2, the number of degrees of freedom for the numerator of the second factor (p_{wtr}) f_{III} was 1, and the number of levels of variation of the input factors was: p = 3 and q = 2. The critical value of the statistic was for rows $F_{kr(0.05; 2; 18)}$ = 3.55456, while for columns $F_{kr(0.05; 1; 18)}$ = 4.41387 (table data [5]).

In all three cases, a significance level of α = 0.05 was applied and a right-hand critical area was assumed. Confidence coefficient values ΔF_I and ΔF_{II} were calculated, based on the significance of the effect of the two input factors on the determined diagnostic measures.

Tab. 4. Values of the confidence coefficient ΔF for the simultaneous influence of the engine load P (first input factor - index 'I') and the structural parameter (second input factor - index 'II') on the diagnostic measures considered

Input factors influencing simultaneously	The value of the confidence coefficient ΔF for the diagnostic measures		
	$h_{spśr}$	$\Delta T_{spśr}$	$(\Delta T/\Delta \tau)_{śr}$
P (I)	ΔF_I = 1011.55	ΔF_I = −3.19	ΔF_I = −3.19
A_{dol} (II)	ΔF_{II} = 559.80	ΔF_{II} = 53.57	ΔF_{II} = 53.57
P (I)		ΔF_I = 12.81	ΔF_I = 1.65
p_{wtr} (II)		ΔF_{II} = 486.66	ΔF_{II} = 309.73
P (I)	ΔF_I = 432.53	ΔF_I = 8.75	ΔF_I = 8.75
ε (II)	ΔF_{II} = 65.83	ΔF_{II} = 273.84	ΔF_{II} = 274.30

Based on the numerical data summarised in Table 4, it was possible to observe (within the analysed range of variation of input parameters) a very significant effect of engine load P on the specific enthalpy of the exhaust gas stream $h_{spśr}$ (confidence coefficient ΔF_I = 1011.55). The value of the active cross-sectional area of the intake air flow A_{dol} on the specific enthalpy of the exhaust gas stream hspśr was also statistically significant (ΔF_{II} = 559.8). When the effects of the engine load P and the active cross-sectional area of the intake air flow A_{dol} on the diagnostic measures of the average peak-to-peak value of the exhaust gas temperature $\Delta T_{spśr}$ and the value of the average intensity of changes in the exhaust gas temperature $(\Delta T/\Delta \tau)_{śr}$ are evaluated, the conclusions for both measures are analogous. A significant effect of the A_{dol} cross-sectional area on both diagnostic measures $\Delta T_{spśr}$ and $(\Delta T/\Delta \tau)_{śr}$ was observed, with a confidence coefficient ΔF_{II} of 53.57. However, there was no effect of engine load P on these diagnostic measures (ΔF_I = -3.19).

The highly significant effect of injector opening pressure pwtr on the average peak-to-peak value of exhaust gas temperature $\Delta T_{spśr}$ was also confirmed (confidence coefficient ΔF_{II} = 486.66). The value of engine load P also had a statistically significant effect on the same diagnostic measure (ΔF_I = 12.81). Based on

the data presented in Table 4, it is also possible to confirm the highly significant effect of injector opening pressure pwtr on the average intensity of changes in exhaust gas temperature $(\Delta T/\Delta \tau)_{śr}$; the confidence coefficient ΔF_{II} = 309.73. Statistically significance was also affected by the change in engine load P on $(\Delta T/\Delta \tau)_{śr}$ but the value of the confidence coefficient was much smaller (ΔF_I = 1.65).

The results summarised in Table 4 allow us to conclude that there is a very significant effect of engine load P on the specific enthalpy of the exhaust gas stream $h_{spśr}$ (confidence coefficient ΔF_I = 432.53) but the value of compression ratio ε on the specific enthalpy $h_{spśr}$ was also statistically significant (ΔF_{II} = 65.83). The results of the calculations summarised in Table 4 also allow confirmation of a highly significant effect of the compression ratio ε on the average peak-to-peak value of the exhaust gas temperature $\Delta T_{spśr}$ (confidence coefficient ΔF_{II} = 273.84). A statistically significant effect of engine load change P on the same diagnostic measure (ΔF_I = 8.75) was also confirmed. The data allows confirmation of a highly significant effect of the compression ratio ε on the average intensity of change in exhaust gas temperature $(\Delta T/\Delta \tau)_{śr}$ (confidence coefficient ΔF_{II} = 274.3). The effect of engine load P on $(\Delta T/\Delta \tau)_{śr}$ was also statistically significant at ΔF_I = 8.75.

To evaluate the significance of the influence by means of two-factor statistical analysis (Figure 2a), for the question as to which of the input parameters (the load P or the active cross-sectional area of the intake airflow A_{dol}) has a greater effect on the diagnostic measures studied, the result is not so clear. It can be seen that some values of the F_{obl} statistic are below the critical value of F_{kr}, which means that there is no significant influence of these input factors on the determined measures of the diagnostic signal of the quickly changing exhaust gas temperature. These include the effect of engine load P on the average intensity of changes in exhaust gas temperature $(\Delta T/\Delta \tau)_{śr}$ and on the average peak-to-peak value of exhaust gas temperature $\Delta T_{spśr}$. In other cases, however ($F_{obl} > F_{kr}$), different values of the confidence factor ΔF are evident for the evaluation of the effect of A_{dol} on $\Delta T_{spśr}$ and $(\Delta T/\Delta \tau)_{śr}$, where the confidence factor was less than 54. Meanwhile, the effect of A_{dol} on $h_{spśr}$ is greater than that for $(\Delta T/\Delta \tau)_{śr}$ and $\Delta T_{spśr}$. It is also interesting to note that the specific enthalpy of the exhaust gas stream is more influenced by the engine load than by the amount of air supplied to the combustion chamber, but both input factors interacting simultaneously have a significant effect, as the values of the confidence factor ΔF are very high (559.8 and 1011.55).

When using two-factor statistical analysis (Figure 2b) to assess the significance of the influence which the input parameters engine load P and injector opening pressure p_{wtr} have on the considered diagnostic measures, the result is more clear. It can be seen that all the values of the confidence coefficient ΔF are positive and so $F_{obl} > F_{kr}$, which means there is a significant simultaneous influence of these input parameters on the determined diagnostic measures. Figure 2b also indicates the result of two-factor analysis for a diagnostic measure such as $h_{spśr}$, despite its elimination after the first stage of statistical testing (one-factor analysis). The result of the two-factor analysis indicates that both input factors (interacting simultaneously) have a significant effect on this diagnostic measure. By analysing

the values of the confidence coefficient ΔF, it is apparent that p_{wtr} has a much more significant effect on $(\Delta T/\Delta \tau)_{śr}$ and $\Delta T_{spśr}$ than on $h_{spśr}$, and the opposite is true for the effect of load.

In the case of evaluating the significance of the influence as a result of two-factor statistical analysis (Figure 2c), to answer the question as to which of the input parameters (engine load P or compression ratio ε) has a greater influence on the diagnostic measures considered, the result is also quite clear. A significant influence of both input factors on all diagnostic measures is evident; however, the values of the confidence coefficient ΔF differ significantly. In the case of engine load P, the greatest influence occurs for $h_{spśr}$ ($\Delta F = 432.53$), while the degree of compression ε had the most significant effect on $(\Delta T/\Delta \tau)_{śr}$ and $\Delta T_{spśr}$ ($\Delta F = 274.3$ and $\Delta F = 273.84$).
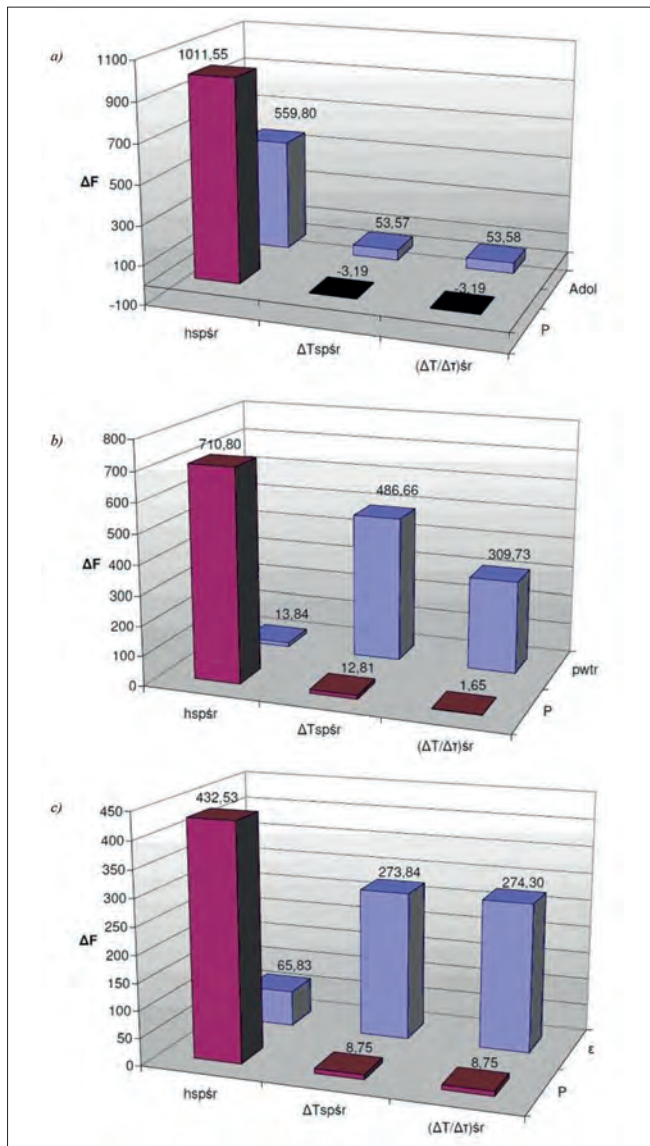

Fig. 2. Values of significance coefficient ΔF for two-factor analysis of the simultaneous effect of engine load P and structural parameters: active cross-sectional area of intake airflow A_{dol} (a), injector opening pressure p_{wtr} (b), and compression ratio ε (c) on values of defined diagnostic measures

In summary, it is possible to formulate the following general conclusions for the two-factor analysis, where the input factors are engine load P and engine structure parameters (A_{dol}, p_{wtr}, ε):

1. Injector opening pressure and compression ratio affects $(\Delta T/\Delta \tau)_{śr}$ and $\Delta T_{spśr}$ more significantly than engine load, which should be interpreted as the high sensitivity of these two diagnostic measures to their (p_{wtr} and ε) changes in the range being studied. Thus, a change in p_{wtr} and ε causes an evident increase in the fluctuation of the course of the rapidly changing exhaust gas temperature.
2. Both A_{dol} and load P have the strongest effect on $h_{spśr}$, which is due to the direct and simultaneous influence of these two input factors on the value of the quickly changing exhaust gas temperature.

From the statistical hypotheses tested, it is also possible to conclude the following methodological findings, which are also presented graphically in Table 5:

1) During diagnostic investigations, the engine should be loaded to the maximum degree, then the specific enthalpy of the exhaust gas stream within one engine cycle $h_{spśr}$ responds most strongly.
2) The loss of permeability of the inlet channel, e.g. as a result of its pollution, demonstrated by a reduced value of the active cross-sectional area of the inlet air channel flow A_{dol}, is best indicated by the specific enthalpy of the exhaust gas stream within one engine cycle $h_{spśr}$.
3) The greatest diagnostic sensitivity to reduced injector opening pressure p_{wtr} is characterised by the average peak-to-peak value $\Delta T_{spśr}$ and the average intensity of change in exhaust gas temperature $(\Delta T/\Delta \tau)_{śr}$. At higher engine loads, the sensitivity of these diagnostic measures is greater.
4) Damage or impurities (carbon deposits), which can result in a reduced value of the compression ratio ε, can best be inferred on the basis of the average inter-peak value $\Delta T_{spśr}$ and the average intensity of changes in exhaust gas temperature $(\Delta T/\Delta \tau)_{śr}$. These measures show high diagnostic sensitivity over the entire range of specified engine load changes.
5) Inference on the basis of the proposed diagnostic measures can be made for measurements made with a thermocouple with sufficiently low values of the time constant, of the order of a few to a few tens of milliseconds, designed for measurements of rapidly changing exhaust gas temperatures [14]. It is crucial to apply the proposed mathematical and statistical processing of the recorded signal.

Tab. 5. Criterion for the selection of a diagnostic measure depending on the analysed parameter of the structural design of a diesel engine: blue boxes indicate a diagnostic measure especially recommended for inference with a significant influence on the selected parameter of the structure, pink boxes indicate a diagnostic measure with low significant influence

Diagnostic measure Load / Structure parameter	$h_{spśr}$	$\Delta T_{spśr}$	$(\Delta T/\Delta \tau)_{śr}$
P			
A_{dol}			
p_{wtr}			
ε			

FINAL REMARKS AND CONCLUSIONS

In the proposed one-factor and two-factor analysis, it was shown that the quickly changing temperature of the exhaust gas from a compression-ignition engine is a suitable diagnostic parameter. The proposed diagnostic measures allow the diagnostic inference of selected malfunctions of engine systems with a reduced active cross-sectional area of intake airflow A_{dol}, a reduced injector opening pressure p_{wtr} or with a reduced engine compression ratio ε. The two-factor analysis method presented in this article introduces a lot of diagnostic information about the condition of selected engine functional systems, but it is worth developing further. Therefore, in the next part of this article, the interaction value of the statistic F_i and the interaction confidence coefficient ΔF_i will be characterised, allowing us to assess whether, and how much, the two input factors 'interact' with each other, affecting the output factor, and the results of the presented statistical analyses will also be discussed. Conducting the analysis in three stages allows us to present a method for diagnosing selected functional systems of engines similar to the one researched, based on the course of the quickly changing exhaust gas temperature.

REFERENCES

1. A. Borokov, Mathematical statistics. 2019.

2. B.K. Debnath, N. Sahoo and U.K. Saha, 'Thermodynamic analysis of variable compression ratio diesel engine running with palm oil methyl ester', Energy Conversion and Management. 2013, https://doi.org/10.1016/j.enconman.2012.07.016.

3. M. Ghaemi, 'Performance and Emission Modelling and Simulation of Marine Diesel Engines using Publicly Available Engine Data', Polish Maritime Research. 2021, https://doi.org/10.2478/pomr-2021-0050.

4. J. Grochowalska, 'Analysis of the macrostructure of the fuel spray atomized with marine engine injector', Combustion Engines. 2019, doi:10.19206/CE-2019-413.

5. M. Jesussek, 'F distribution table.' https://datatab.net/tutorial/f-distribution (accessed 1.07.2023)

6. O. Klyus, P. Rajewski, S. Lebedevas and S. Olszowski, 'Determination of fuel atomization quality in compression ignition engines using acoustic emission signal', Combustion Engines. 2022, doi:10.19206/CE-149370.

7. Z. Korczewski, 'Test Method for Determining the Chemical Emissions of a Marine Diesel Engine Exhaust in Operation', Polish Maritime Research. 2021, https://doi.org/10.2478/pomr-2021-0035.

8. Z. Korczewski, 'Endoscopic diagnostics of marine engines', Diagnostyka. 2008, bwmeta1.element.baztech-article-BAR0-0038-0044.

9. R. Krakowski, 'Diagnosis modern systems of marine diesel engine', Journal of KONES. 2014.

10. A. Kuleshov, 'Diesel-RK is an engine simulation tool.' https://diesel-rk.com/Eng/ (accessed 1.07.2023)

11. M. Liang and M. Chen, 'Monitoring the Performance of a Ship's Main Engine Based on Big Data Technology', Polish Maritime Research. 2022, https://doi.org/10.2478/pomr-2022-0033.

12. J. Monieta, 'Selection of Diagnostic Symptoms and Injection Subsystems of Marine Reciprocating Internal Combustion Engines', Applied Sciences. 2019, doi.org/10.3390/app9081540.

13. V. Pham, 'Research on the application of diesel-RK in the calculation and evaluation of technical and economic criteria of marine diesel engines using the unified ULSD and biodiesel blended fuel', Journal of Mechanical Engineering Research and Developments. 2019, https://doi.org/10.26480/jmerd.02.2019.87.97.

14. P. Puzdrowska, 'Determining the time constant using two methods and defining the thermocouple response to sine excitation of gas temperature', Journal of Polish CIMEEAC. 2016.

15. P. Puzdrowska, 'Diagnostic information analysis of quickly changing temperature of exhaust gas from marine diesel engine part I single factor analysis', Polish Maritime Research. 2021, https://doi.org/10.2478/pomr-2021-0052.

16. P. Puzdrowska, 'Signal filtering method of the fast-varying diesel exhaust gas temperature', Combustion Engines. 2018, doi: 10.19206/CE-2018-407.

17. R. Varbanets, O. Shumylo, A. Marchenko, D. Minchev, V. Kyrnats, V. Zalozh, N. Aleksandrovska, R. Brusnyk and K. Volovyk, 'Concept of Vibroacoustic Diagnostics of the Fuel Injection and Electronic Cylinder Lubrication Systems of Marine Diesel Engines', Polish Maritime Research. 2022, https://doi.org/10.2478/pomr-2022-0046.

18. M. Verbeek, A guide to modern econometrics. 2017.

19. K. Witkowski, 'The Increase of Operational Safety of Ships by Improving Diagnostic Methods for Marine Diesel Engine', TransNav the International Journal on Marine Navigation and Safety of Sea Transportation. 2017, doi:10.12716/1001.11.02.15.

20. P. Woś, A. Jaworski, H. Kuszewski, K. Lejda and A. Ustrzycki, 'Technical and operating problems yielded from setting up the optimum value of geometric compression ratio in piston engines', Combustion Engines. 2016, doi:10.19206/CE-116483.

FAULT DIAGNOSIS OF ME MARINE DIESEL ENGINE FUEL INJECTOR WITH NOVEL IRCMDE METHOD

Qingguo Shi * ORCID
Yihuai Hu
Guohua Yan ORCID
Shanghai Maritime University, Shanghai, China

* Corresponding author: *892158956@qq.com (Qingguo Shi)*

ABSTRACT

As an important component of the fuel injection system, the fuel injector is crucial for ensuring the power, economy, and emissions for a whole ME (machine electronically-controlled) marine diesel engine. However, injectors are most prone to failures such as reduced pressure at the opening valve, clogged spray holes and worn needle valves, because of the harsh working conditions. The failure characteristics are non-stationary and non-linear. Therefore, to efficiently extract fault features, an improved refined composite multi-scale dispersion entropy (IRCMDE) is proposed, which uses the energy distribution of sampling points as weights for coarse-grained calculation, then fast correlation-based filter(FCBF) and support vector machine (SVM) are used for feature selection and fault classification, respectively. The experimental results from a MAN B&W 6S35ME-B9 marine diesel engine show that the proposed algorithm can achieve 92.12% fault accuracy for injector faults, which is higher than multiscale dispersion entropy (MDE), refined composite multiscale dispersion entropy (RCMDE) and multiscale permutation entropy (MPE). Moreover, the experiment has also proved that, due to the double-walled structure of the high-pressure fuel pipe, the fuel injection pressure signal is more accurate than the vibration signal in reflecting the injector operating conditions.

Keywords: marine diesel engine; fuel injector; improved refined composite multi-scale dispersion entropy; fault diagnosis

INTRODUCTION

A diesel engine has the advantages of high reliability, high fuel economy and easy operations; it has been the main propulsion source for marine ships [1]. For a diesel engine, the fuel injection system is one of most important parts, its safe and reliable operation is crucial to ensuring the power, economy, and reliability of the whole engine [2]. With the development of technology and more stringent emission regulations, high pressure common rail fuel injection systems have become a hot research topic because of their good performance, in terms of power, economy and emissions [3]. The MAN B&W ME-type diesel engine has the largest

scale of application of all marine two-stroke diesel engines. However, injector failure occurs at a higher rate, affecting the energy efficiency and emission performance of diesel engines [4]. Therefore, fault diagnosis in diesel fuel injectors is crucial to ensure the safe and efficient operation of marine diesel engines.

For the process of fault diagnosis, there are mainly three steps: signal acquisition, feature extraction, and pattern classification. Many researches have conducted fault diagnosis of diesel engines. Thurson et al. [5] measured the exhaust temperature to diagnose faults in diesel engine fuel injectors. Li et al. [6] analysed the cylinder pressure to reflect the whole

combustion process and identify the malfunctions of diesel engines. Zhang et al. [7] used the instantaneous crankshaft speed to realise the fault diagnosis of uneven firing intervals of V-type marine diesel engines. Yang et al. [8] collected vibration signals by installing a transducer on a fuel injection pump, and then used discriminative non-negative matrix factorisation and KNN classifier to realise the fault diagnosis of diesel engines. Ftoutou et al.[9] measured vibration signals on the cylinder block and used modified S-transform, two-dimensional non-negative matrix factorisation, and three fuzzy clustering algorithms to realise the fault diagnosis of a diesel engine's injection faults. Ramteke et al. [10] used signal processing techniques to extract fault-related features from vibration signals, and then monitored the effect of liner scuffing faults. Alireza et al. [11] presented a condition monitoring and combustion fault detection method based on the vibration signal obtained from both intake manifold and cylinder heads. Although vibration signals are easy to measure, they are more susceptible to contamination, especially under weak faults. For a marine two-stoke diesel engine, the vibration on a ship is inherently serious, so the vibration signals measured from the surface of diesel engines may not be accurate for fault diagnosis. Similarly for the fuel injection system, the fuel injection pipeline is relatively thick and may be a double-walled pipe, which makes it difficult to measure the vibration signal on the surface of the pipeline to reflect the pressure fluctuation inside the pipeline. Therefore, in order to obtain better fault diagnosis accuracy, our research measures the fuel pressure and vibration signals of the high-pressure fuel line at the same time, and compares the two signals for analysis.

When acquiring the original fluctuation signal, the next step is feature extraction. Many methods had been used to extract the fault features, mainly including time-domain analysis [12], frequency-domain analysis [13], and time-frequency analysis [14]. Because the pressure and vibration signals of high pressure pipes have nonlinear and non-stationary characteristics, nonlinear dynamic-based entropy methods are a powerful tool for extracting these features and they have been widely used in the field of fault diagnosis, e.g. approximate entropy (AE), sample entropy (SE), fuzzy entropy (FE), and permutation entropy (PE). Chen et al. [15] used SE for rolling bearing fault diagnosis. Shang et al. [16] used modified SE for the fault diagnosis of lithium-ion battery strings. Zhu et al. [17] used the FE to extract fault features. Ma et al. [18] used fuzzy distribution entropy for fault diagnosis in rotating machinery. However, these methods made comparisons between data, which may have reduced the calculation efficiency. Ma et al. [19] used PE for the early fault diagnosis of rotating machinery. Wu et al. [20] used multi-scale permutation entropy (MPE) for the fault diagnosis of bearings. However, PE values are relatively sensitive to noise [21]. In order to extract fault features more efficiently, Azami et al. [22] proposed dispersion entropy (DE). Gu et al. [23] used DE to realise the misfiring diagnosis of diesel engines. Yan et al. [24] used multi-scale dispersion entropy (MDE) to extract multidimensional fault characteristics and

validated their effectiveness by experiments. Ke et al. [25] used hierarchical fluctuation dispersion entropy for fault diagnosis in common-rail injectors. Dhandapani et al. [26] used a generalised Gaussian distribution to refine composite multiscale dispersion entropy for the diagnosis of rolling bearings. Inspired by these references, we decided to use MDE to extract fault features from the pressure signal. However, the coarse-graining process in MDE has two main defects. Firstly, when the scale factor increases, the data length is reduced, and this reduces the reliability of the entropy value. Secondly, there are no overlap segments, and calculating the average of each segment will cause the loss of potentially useful information [27]. The coarse-graining process of refined composite MDE can solve these problems, to some extent, but it only considers the first-order moment in the coarse-graining process. Therefore, in this research, we propose an improved refined composite MDE (IRCMDE) to extract more hidden features for fault diagnosis, in which the second-order moment is used. After using IRCMDE, the fault features of the pressure signal can be extracted. However, these fault features are large and so feature reduction is needed for the improvement of calculation efficiency. Generally speaking, distance measures, dependency measures, consistency measures and information measures are used to evaluate the quality of a feature [28]; mutual information is most frequently used to measure the correlation and redundancy of features. The fast correlation-based filter (FCBF) has faster calculation efficiency and robustness, compared to the relevance filter, minimum redundancy maximum relevance (mRMR) and conditional mutual information maximisation (CMIM). Therefore, this study uses FCBF for feature selection and then constructs the feature set. After feature extraction and selection, state classification is the final step in fault diagnosis. Support vector machine (SVM) is one of the most commonly used fault classification methods, showing great advantages when fault sample data is insufficient. Zhang et al. [29] proposed the support vector machine (SVM)-based intelligent fault diagnosis method and obtained good results under different fault degrees at various engine speeds and load conditions. Zhao et al. [30] proposed PSO-SVM, to realise the fault classification. SVM is selected in this research, to classify the fault mode. Simulations and experiments were conducted to illustrate the diagnosis performance and generalisation ability of the proposed method.

The rest of this paper is organised as follows: in Section 2, theoretical analysis of IRCMDE is introduced. In Section 3, the influence of parameter changes on the IRCMDE value is discussed in detail and the effectiveness of the algorithm is demonstrated through simulation signals. In Section 4, the whole fault diagnosis procedure is proposed. In Section 5, experiments are employed to verify the proposed method. The conclusion is summarised in Section 6.

IMPROVED REFINED COMPOSITE MULTISCALE DISPERSION ENTROPY

For the original time series with N points, the length of the coarse-grained time series at scale factor τ is equal to N/τ after using the MDE method, as shown in Eq. (1). So, when a larger scale factor is used, the generated time series will become shorter. Besides, MDE divides the time series into non-overlapping segments of equal length and then calculates the average of all data points in each segment, which will inevitably cause the loss of potentially useful information. So, RCMDE is proposed to overcome the above defects; there two main steps to calculate the RCMDE value.

$$y_j^\tau = \frac{1}{\tau} \sum_{i=(j-1)\tau+1}^{j} x_i, 1 \le j \le N/\tau \quad \text{(1)}$$

Step 1. For a given time series u with length N, its k-th coarse-grained time sequence $y_k^{(\tau)} = \{y_{k,1}^{(\tau)}, y_{k,2}^{(\tau)}, \cdots, y_{k,\frac{N}{\tau}}^{(\tau)}\}$ can be calculated by Eq. (2).

$$y_{k,j}^{(\tau)} = \frac{1}{\tau} \sum_{i=k+\tau(j-1)}^{k+j\tau-1} u_i$$
$$k = 1, 2, \cdots, \tau$$
$$j = 1, 2, \cdots, \frac{N}{\tau} \quad \text{(2)}$$

Step 2. For each scale τ, the DE of each coarse-grained time series $y_k^{(\tau)}(k=1,2,\cdots,\tau)$ is calculated (the detailed calculation can be found in [23]). Then these DE values are averaged according to Eq. (3).

$$RCMDE(x,m,c,d,\tau) = \frac{1}{\tau} \sum_{k=1}^{\tau} DE(y_k^{(\tau)},m,c,d) \quad \text{(3)}$$

However, the RCMDE algorithm still uses the original coarse-grained mean processing, which affects the accuracy of entropy values. Inspired by this, the energy distributions between sampling points $(x_1, x_2,..., x_n)$ are used as coefficients to fuse the corresponding time scale factors $y_k^{(\tau)}$ and preserve the impact characteristics of the original signal to the greatest extent possible. The calculation flowchart of IRCMDE is shown in Fig.1. For the IRCMDE method, there are two main steps to calculate the IRCMDE value.

Step 1. For a given time series u with length N, its k-th coarse-grained time sequence $y_k^{(\tau)} = \{y_{k,1}^{(\tau)}, y_{k,2}^{(\tau)}, \cdots, y_{k,\frac{N}{\tau}}^{(\tau)}\}$ can be calculated by Eq. (4).

$$y_{k,j}^\tau = \left. \sum_{i=(j-1)\tau+k}^{j\tau+k-1} (x_i - \bar{x})^2 \middle/ \sum_{i=(j-1)\tau+k}^{js+k-1} |x_i| \right.$$
$$k = 1, 2, \cdots, \tau$$
$$j = 1, 2, \cdots, \frac{N}{\tau} \quad \text{(4)}$$

Step 2. Calculate the DE for each $y_{k,j}^\tau$ $(k=1,2,\cdots,\tau)$ sequence separately and then the final IRCMDE value for scale factor τ can be calculated by Eq. (5).

$$IRCMDE(u,m,c,d,\tau) = \frac{1}{\tau} \sum_{k=1}^{\tau} DE(y_k^\tau, m, c, d) \quad \text{(5)}$$
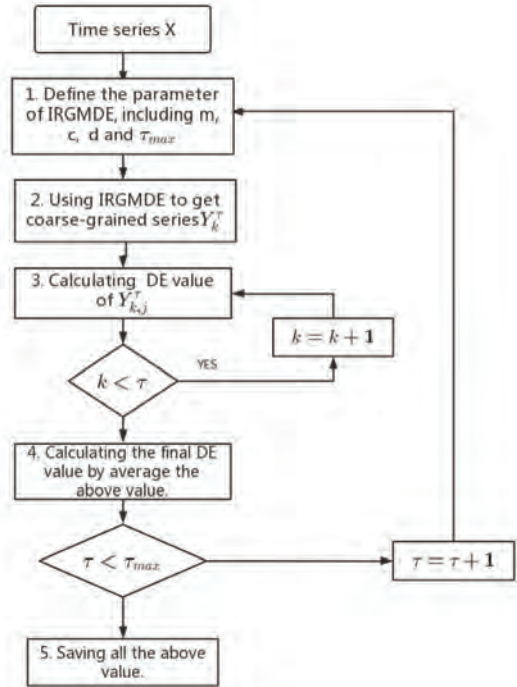
Fig. 1. the flowchart of the IRCMDE method

PARAMETER SELECTION AND ANALYSIS

When using the IRCMDE method to analyse data, there are five main parameters which need to be set in advance: signal length N, embedding dimension m, the number of classes c, time delay d and scale factor τ. According to the relevant reference, the time delay is usually selected as 1, which has no influence on the computational efficiency and reliability of the DE value. The scale factor τ is selected as 18, which will fully extract fault information at different scales. Because white Gaussian noise (WGN) and 1/f noise are two commonly occurring noises in nature, we decide to analyse the impact of the other four parameters on the DE results by using these two signals. The coefficient of variation (CV) value and Euclidean distance (ED) value are calculated for evaluating the effectiveness of the DE results. The CV equation is defined as standard deviation divided by the mean and ED value, as shown in Eq. (6).

$$ED = \sqrt{\sum_{i=1}^{\tau} (DE_1(i) - DE_2(i))^2} \quad \text{(6)}$$

where DE_1 and DE_2 denote WGN and 1/f noise IRCMDE values, respectively.

PARAMETER OF SIGNAL LENGTH

In order to analyse the influence of signal length N on the DE value, we select 20 times WGN and 1/f noise with lengths of 512, 1024, 2048 and 4096, respectively, for calculating the IRCMDE value. The results are shown in Fig. 2, Table 1, Table 2 and Table 3. Fig. 2 shows that the entropy values of both WGN and 1/f noise are very similar, which indicates that the signal length has little influence on the multiscale entropy value. Moreover, it can be seen from Tables 1-3 that, with increasing signal length, the CV value becomes smaller, the ED value becomes larger and time become longer. Overall, it is more reasonable when the signal length is 2048, so N is chosen to be equal to 2048 in this study.
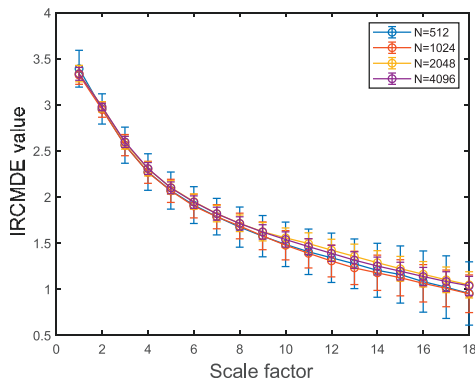
(a)   Entropy value of WGN

(b)   Entropy value of 1/f noise

Fig. 2. IRCMDE value of different signal lengths

Table 1. CV value of different data lengths

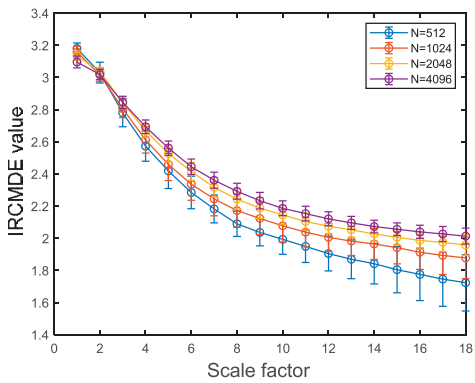| Data length	512	1024	2048	4096
WGN	0.1732	0.1098	0.0703	0.0536
1/f noise	0.0537	0.0429	0.0224	0.0190

Table 2.Consuming time with different data lengths

Data length	512	1024	2048	4096
WGN	0.0950s	0.0879s	0.1288s	0.2130s
1/f noise	0.0851s	0.1138s	0.1203s	0.2134s

Table 3. ED value with different data lengths

Data length	512	1024	2048	4096
ED	2.0693	2.6295	2.6430	2.8253

PARAMETER OF EMBEDDING DIMENSION

The embedding dimension *m* has a great influence on the entropy value. If *m* is too small, the dynamic information from the signal may not be detected. If *m* is too large, the small variations in the signal may not be displayed and it is also more time-consuming. Therefore, we decided to select *m* values equal to 2, 3, 4 and 5, respectively, for calculating the IRCMDE value. The calculation results are shown in Fig. 3, Table 4, Table 5 and Table 6. Fig. 3 shows that the entropy value will become larger with an increase of embedding dimension *m*. This is because there will be more dispersion patterns when *m* is larger, and so a larger DE value will be produced. Moreover, it can be seen from Tables 4-6 that, when *m* is equal to 3, the CV value is relatively lower, the consuming time is relatively shorter and the ED value is relatively longer. So, an embedding dimension *m* of 3 was chosen in this study.

(a)b Entropy value of WGN

(b) Entropy value of 1/f noise

Fig. 3. IRCMDE values of different embedding dimensions

Table 4. CV values of different embedding dimensions

Embedding dimension	2	3	4	5
WGN	0.0738	0.0805	0.0552	0.0883
1/f noise	0.0311	0.0258	0.0215	0.0260

Table 5. Time consumed with different embedding dimensions

Embedding dimension	2	3	4	5
WGN	0.0721s	0.1223s	0.4427s	2.2708s
1/f noise	0.0695s	0.1151s	0.4292s	2.2589s

Table 6. ED values with different embedding dimensions

Embedding dimension	2	3	4	5
ED	1.7316	2.5567	3.2294	3.6448

THE NUMBER OF CLASS C

The parameter c is one of the important parameters determining the number of dispersion patterns. When c is too small, there are not enough patterns to reflect signal information, resulting in two signals with different amplitudes being divided into the same class. However, when c is too large, the calculation time will become very long and the signal may be divided into different classes when encountering noise pollution. Therefore, we decided to select c equal to 4, 5, 6 and 7, respectively, for calculating IRCMDE values. The calculation results are shown in Fig. 4, Table 7, Table 8 and Table 9. Fig. 4 shows that the entropy value will increase with the increase in class number because there will be more possible dispersion patterns under a larger class number c. In other words, when c is larger, there will be more information which can be extracted, yielding a larger DE value. However, when c is larger, the calculation time will become longer and the ED value will become shorter. Therefore, after comprehensive analysis, a c value of 6 was chosen, which is more reasonable.
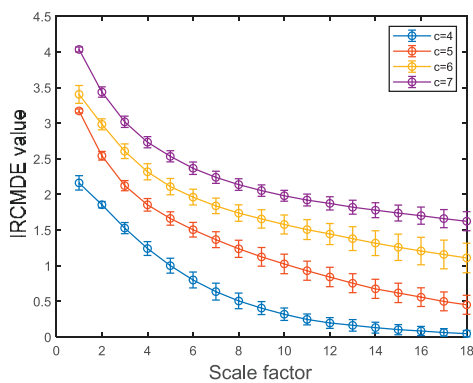
(a) Entropy values of WGN
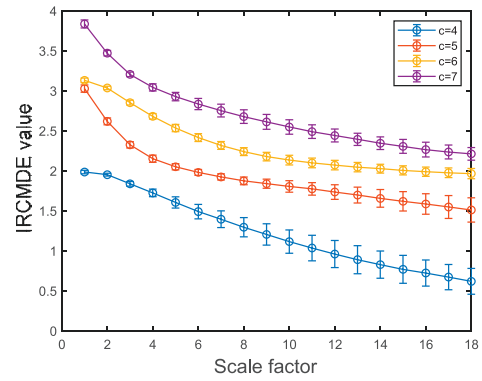
(b) Entropy values of 1/f noise

Fig.4. IRCMDE values of different class numbers

Table 7. CV values of different class numbers

Class number	4	5	6	7
WGN	0.2603	0.1507	0.0566	0.0495
1/f noise	0.1018	0.0508	0.0284	0.0224

Table 8. Consuming time with different class numbers

Class number	4	5	6	7
WGN	0.0819s	0.1257s	0.1627s	0.2556s
1/f noise	0.1033s	0.1051s	0.1472s	0.1538s

Table 9. ED values with different class numbers

Class number	4	5	6	7
ED	2.6069	3.5288	2.4144	1.8705

COMPARISON OF IRCMDE, RCMDE, MDE AND MPE

When a fault occurs, the fault signal usually contains modulation components. Our research selected five AM-FM signals containing different frequencies and amplitudes as simulation signals, as shown in Eq. (7) [31].

$$x = (1 + a * \cos(6\pi t)) * \cos(b * 20\pi t + 2 * \cos(10\pi t)) + $$
$$+ c * (0.8 \sin(\pi t) * \sin(30\pi t)) \tag{7}$$

The sample frequency is 2048 Hz, and a, b, and c are coefficients forming five different modulation signals, which are expressed as a=[0.5,1,1.5,2,2.5], b=[1,2,3,4,5], and c=[1,2,3,4,5].

The calculation results are shown in Fig 5. It can be seen that the DE values of the five signals have obvious intersections when using the MDE method. The entropy value of IRCMDE and RCMDE are separated on most scales. This indicates that multi-scale analysis is very important when evaluating the information from practical fault signals, which is beneficial for achieving fault diagnosis in mechanical equipment.
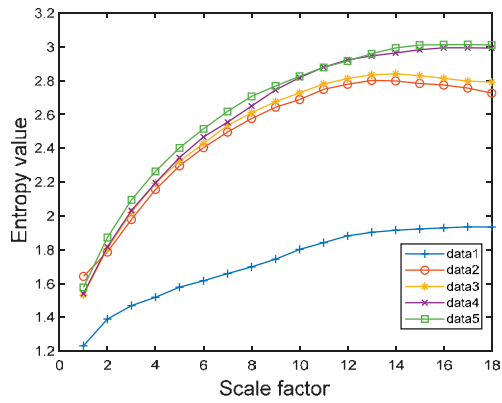
(a)   Entropy values of IRCMDE
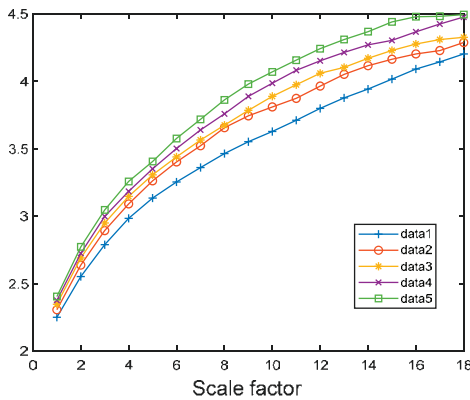
(b) Entropy values of RCMDE
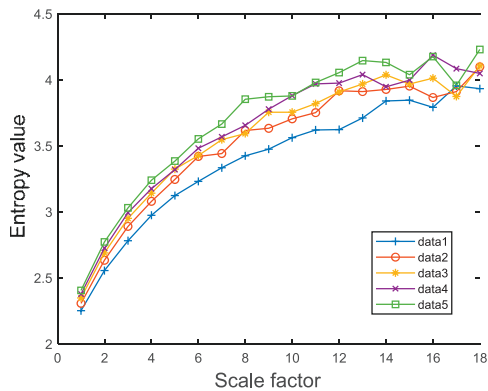
(c)   Entropy values of MDE
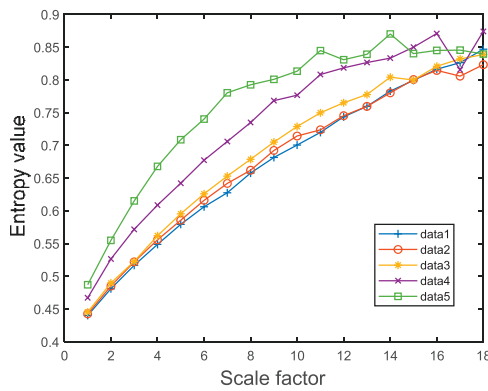
(d) Entropy values of MPE

Fig. 5. Entropy values of five modulation signals

When an engine's fuel injection system appears to have faults, the measured signal is often affected by background noise. Therefore, five different levels of signal to noise ratio (SNR) were used to form a synthetic signal, with the aim of further demonstrating the noise reduction ability of the proposed algorithm. The SNRs used were: 10, 15, 20 and 25. Fig. 6 shows the calculation results of entropy value from the four methods, using synthetic signals. It can been seen that, when the SNR is different, there are fluctuations and severe crossovers between different scales in the IRCMDE, MDE and MPE entropy curves, but the IRCMDE entropy is much smoother. Therefore, the IRCMDE method has a better noise reduction effect and is more suitable for the feature extraction of actual signals.
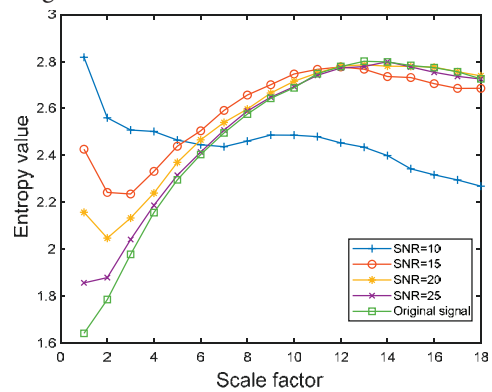
(a)   Entropy values of IRCMDE
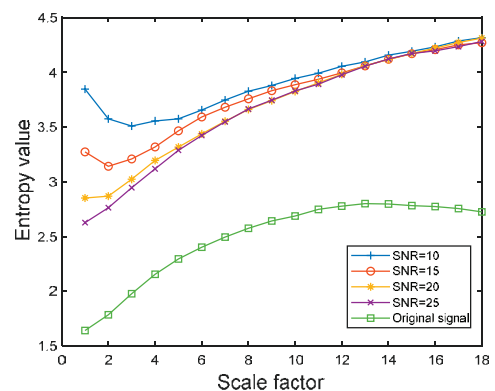
(b) Entropy values of RCMDE
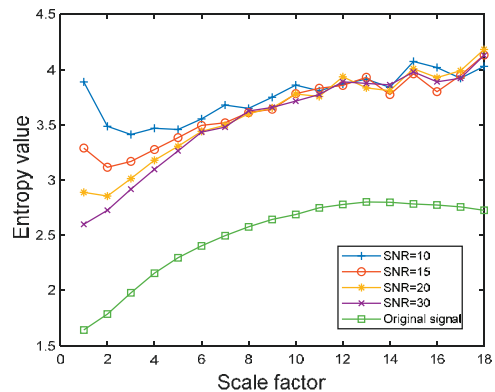
(b)   Entropy values of MDE
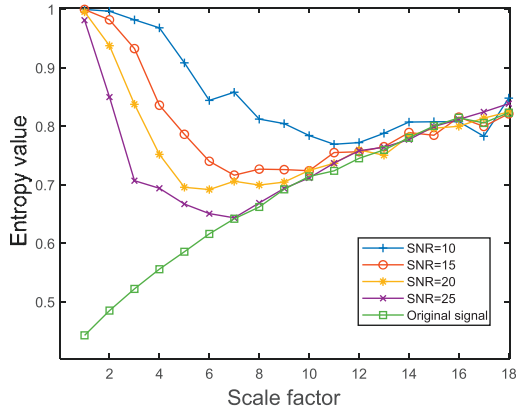
(d) Entropy values of MPE

Fig. 6. Entropy values of five modulation signals

THE PROPOSED FAULT DIAGNOSIS METHOD

FAST CORRELATION-BASED FILTER FOR FEATURE SELECTION

Fault diagnosis is required after feature extraction. However, if all of these features are used, the classification accuracy rate may not be high and the calculation time is also very long. Therefore, the feature selection method is needed for further improving the effectiveness of fault diagnosis. Fast correlation-based filter (FCBF) is one of the most widely used non-liner correlation measures, which is used for feature selection [32].

Definition 1. Information entropy solves the measurement of complexity of random information variables. If X is a discrete signal, then the entropy of X is expressed as:

$$H(X) = -\sum_{i=1}^{n} p(x_i) \log p(x_i) \tag{8}$$

Definition 2. The conditional entropy is expressed as the conditional probability distribution of the occurrence of random variable X when random variable Y occurs alone.

$$H(X|Y) = -\sum p(y) \sum p(x|y) \log p(x|y) \tag{9}$$

Definition 3. Mutual information of discrete signal X and Y can be defined as:

$$I(X,Y) = H(X) - H(X|Y) \tag{10}$$

From Eq. (10), it can be seen that the upper limit of *I(X,Y)* is the minimum value between *H(X)* and *H(Y)*, and its lower limit is 0. Due to the significant variation in entropy, uncertain entropy values can lead to unreasonable values of *I(X,Y)*. Therefore, it is necessary to process the maximum information coefficient of *I(X,Y)* because the maximum information coefficient can compensate for the deviation of

mutual information in the multi value feature, and limit its value range to [0, 1]. Therefore, the maximum information coefficient of random variables X and Y can be determined by the minimum value of *H (X)* and *H (Y)*, as shown below.

$$I_{\max}(X,Y) = \frac{I(X,Y)}{\min(H(X), H(Y))} \tag{11}$$

Definition 4. Symmetrical uncertainty (SU) is defined as:

$$SU_{\max}(X,Y) = \frac{2I_{\max}(X,Y)}{H(X) + H(Y)} \tag{12}$$

In order to reduce the redundancy between signal features, the calculation steps of the FCBF method are as follows:

Step 1: Calculation the $SU_{\max}(x_i, c)$ value for each feature x_i, where i the i-th feature and c is the class vector.

Step 2: Delete the irrelevant feature x_i, whose $SU_{\max}(x_i, c) < \delta$, where δ is a predefined threshold.

Step 3. List the remaining features in descending order, according to their $SU_{\max}$ value and label the result as S_{list}.

Step 4. Define the first element x_m in S_{list} as the predominant feature, append x_m to s_{select} and remove it from S_{list}. For the remaining features, calculate the $SU_{\max}(x_m, x_n)$. Remove redundant features based on conditions similar to Markov blankets. So, if $SU_{\max}(x_m, x_n) > SU_{\max}(x_n, c)$ and $SU_{\max}(x_m, c) > SU_{\max}(x_n, c)$, remove x_n from s_{list}.

Step 5. Regard the remaining feature next to x_m in the S_{list} as the new predominant feature and repeat step 4 until $S_{list} = \phi$. Finally, the relevant but non-redundant feature set s_{select} is obtained.

SUPPORT VECTOR MACHINE FOR FAULT CONDITION RECOGNITION

For an ME marine diesel engine, the fault sample is relatively insufficient. SVM as one of the supervised classifiers which is especially suitable for small sample cases; it is based on the principle of minimising the structural risk in statistical learning theory. SVM was originally developed for binary classification problems. However, the fault diagnosis of a marine diesel engine is usually a multi-classification problem. To address this issue, one-verse-one and one-verse-all are proposed. According to the literature [33], researchers decided to select the style of one-verse-one mode method and optimise parameter g and the penalty parameter c through particle swarm optimisation (PSO).

THE PROPOSED FAULT DIAGNOSIS METHOD

In order to realise the fault diagnosis of an ME diesel engine, a novel fault diagnosis method based on IRCMDE, FBCF and SVM is proposed in this paper. The flowchart of the proposed method is displayed in Fig. 7 and the calculating steps of the method are described as follows.

Step 1: Signal acquisition. Installing the relevant transducer to collect the signal under different working conditions. In this research, we installed a pressure and vibration transducer on the high pressure oil pipe of an ME diesel engine.

Step 2: Feature extraction. The IRCMDE method was used to extract the fault feature from the raw signal.

Step 3. Feature selection. The FCBF method was used to select the more sensitive features.

Step 4. Condition classification. The SVM method was used to classify the fault conditions.
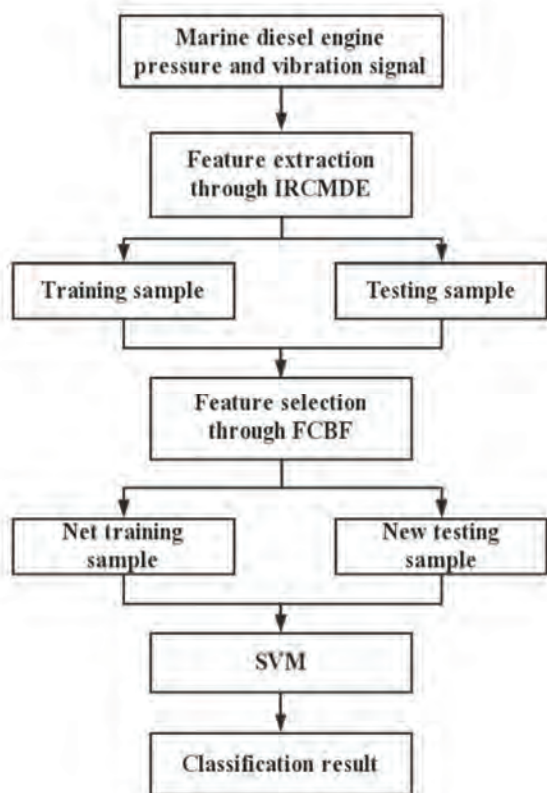
Fig. 7. Flowchart of the proposed method

EXPERIMENTAL VERIFICATION

EXPERIMENTAL SETUP DESCRIPTION AND DATA COLLECTION

To verify the effectiveness and applicability of the proposed method, experiments on an ME diesel engine were conducted. The ME diesel engine was located in Shanghai Maritime University Automation Engine Room Laboratory, as shown in Fig. 8. I was a MAN B&W 6S35ME-B9 type engine and the main parameters are listed in Table 10.

Table 10. Main parameters of ME diesel engine

Number	Parameter	Value
1	Number of strokes	2
2	Firing sequence	1-5-3-4-2-6
3	Rated Power	3570 kW
4	Rated speed	140 r/min
5	Compression ratio	21
6	Cylinder bore/Stoke	350 mm/1550 mm
7	Connecting rod length	1550 mm
8	Intake mode	Supercharging cooling

(a)

(b)
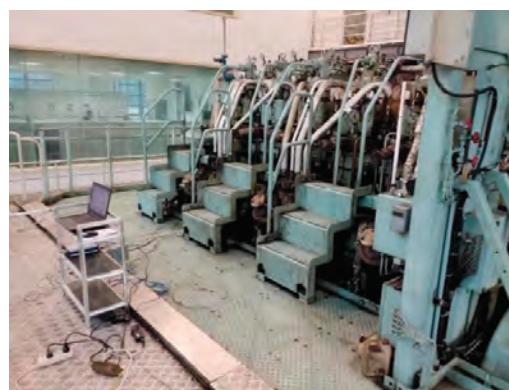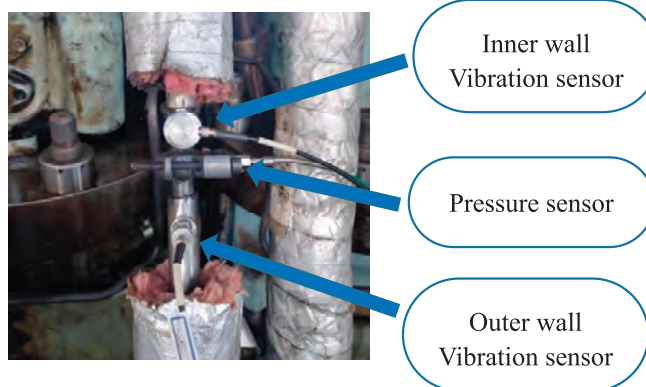
Fig. 8. Experimenalt rig

The fuel injector is the part of the fuel injection system most prone to malfunction, therefore three common injector failures, including reduced pressure at the opening valve, clogged spray holes and worn needle valves, were experimentally studied. In general, the vibration signal of the high-pressure fuel line was measured to obtain fault

information [34]. However, for ME diesel engines, the high-pressure fuel pipe is a double-walled pipe with a channel between the walls for oil return, in case of leakage. In addition, because the pressure in high-pressure oil pipes can sometimes reach 100 MPa, a double-walled structure is also beneficial for increasing safety. This double-wall construction leads to the possibility of inaccurate fault diagnosis by measuring the vibration signal on the outer wall of the high-pressure fuel pipe. Therefore, in this experiment, the pressure signal was measured by drilling holes in the inner wall of the high-pressure oil pipe. The pressure sensor model used for the experiment was a Kistler 4067E3000DS with a maximum measurement range of 300 MPa. For the comparison study, the vibration signals of the inner and outer walls of the high-pressure fuel line were measured simultaneously. During the experiment, in order to improve safety and prevent the high-pressure oil pipe from bursting at the perforation, woven bags were used for wrapping, as shown in the red box in Fig. 8(a). Fig. 8(b) is the detailed sensor installation location diagram, including one pressure sensor and two vibration sensors. The signals are collected by a PC via a COINV system. The speed of the main bearing was set at 90 r/min and 30% rated power, and the sampling rate was 2048 Hz. The sampling time for each condition lasted 50 s, i.e. there were 50*2048 points under each working condition. In order to validate the proposed method, all of the 102,400 points were selected as the sample sets. According to the analysis in Section 3, there are 2048 points per sample, so there are 50 samples per working state. Moreover, we randomly selected 30 samples as the training set and the remaining 20 samples as the test set. Thereby, a total of 120 training samples and 80 testing samples could be acquired. A detailed description of the fuel injector working condition is shown in Table 11.

Table 11. Detailed description of the fuel injector working condition

Working condition	Training samples	Testing samples	Label
Normal	30	30	1
Low valve opening pressure	30	30	2
Orifice blockage	30	30	3
Needle valve wear	30	30	4

The time-domain waveform of each working condition is shown in Fig. 9-12 and each state contains 3 graphics,

including pressure waveform, inner wall vibration waveform and outer wall vibration waveform, from top to bottom. It can be seen that different working conditions have similar waveforms, so it is necessary to apply the intelligent fault diagnosis method to accurately identify different working conditions. Moreover, the instantaneous pressure of fuel injection can reach up to 70 MPa and the vibration is also the most severe at this time. However, based on our experience, the vibration signal of the outer wall is more susceptible to external interference and contains more high-frequency noise. In order to verify which type of signal enables better injector fault diagnosis, a comparative analysis was carried out later, using pressure signals and vibration signals, respectively.
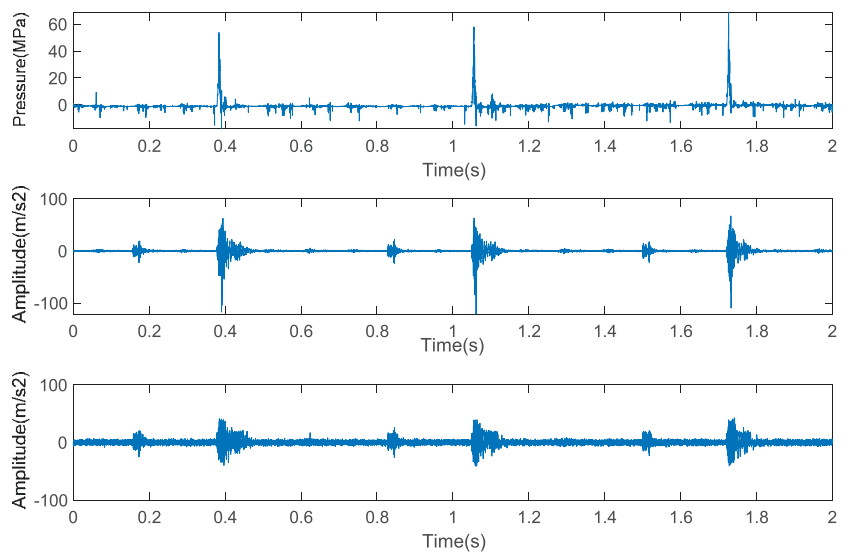

Fig. 9. Time domain waveform of signal under normal condition
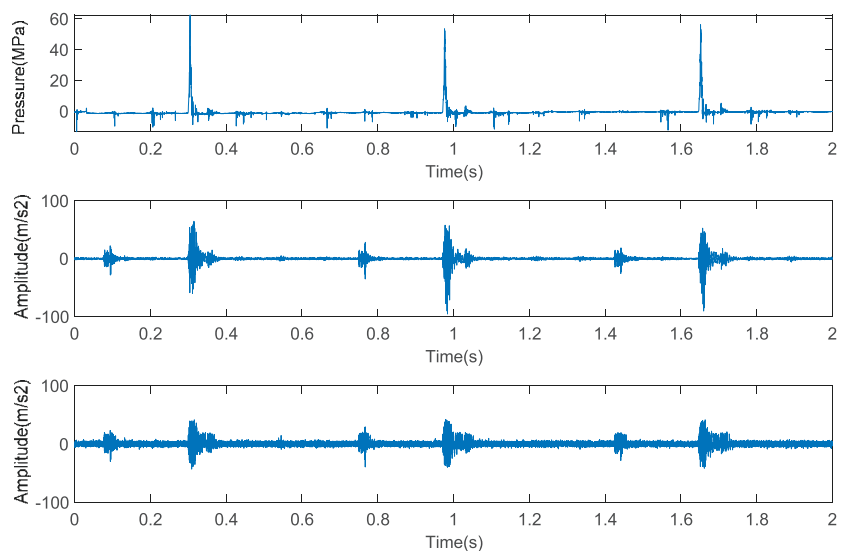
Fig. 10. Time domain waveform of signal under low valve opening pressure
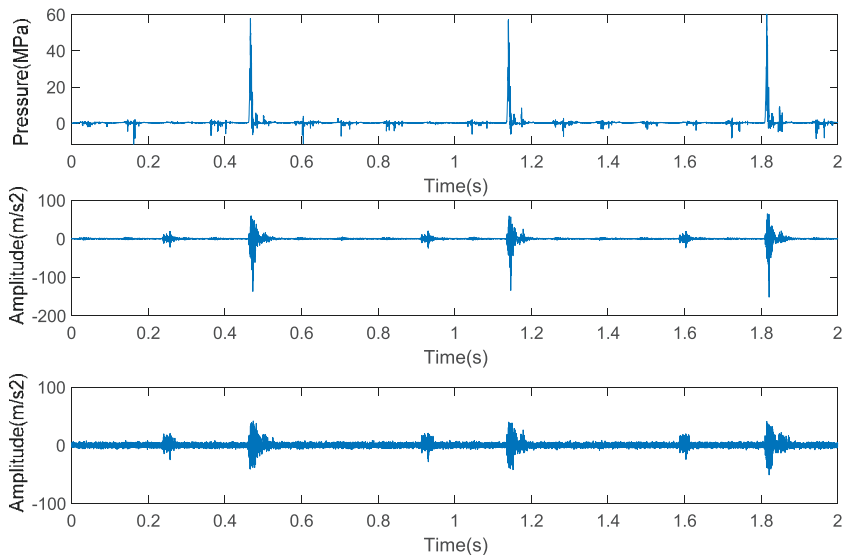
Fig. 11. Time domain waveform of signal under orifice blockage
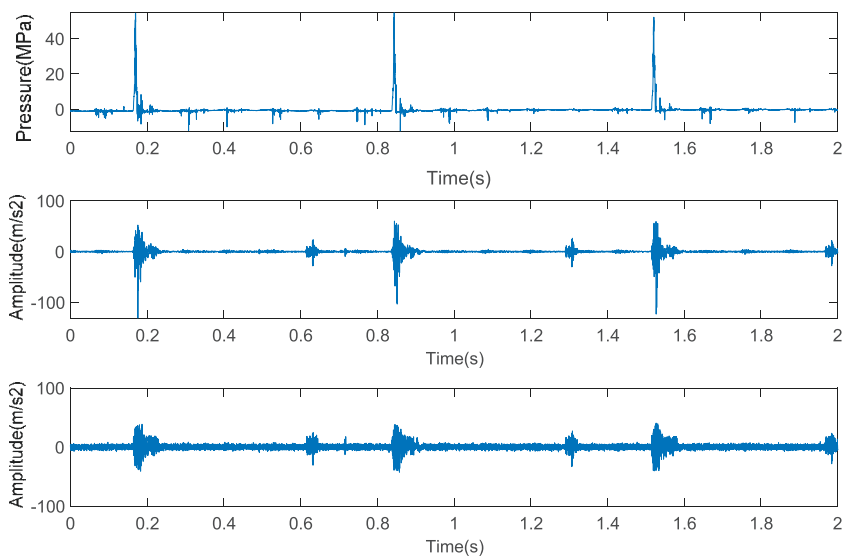
Fig. 12. Time domain waveform of signal under needle valve wear

DIAGNOSIS RESULTS AND ANALYSIS

According to the flowchart of the proposed method in Fig 7, IRCMDE is first used to extract the fault features from the fuel injection pressure signal and the calculation results of each extracted multi-scale features is shown in Fig. 13. It can be seen that the entropy values are different under most working conditions. However, in the cases of condition 1 and condition 3, the entropy curve shows a cross phenomenon because, when the injector nozzle is blocked, it will cause an increase in valve opening pressure. However, the blockage of the nozzle will generally be accompanied by a decrease in valve opening spring stiffness, both of which cause the valve opening pressure to be consistently normal. Therefore, the entropy value of the pressure wave is also approximately the same. Meanwhile, condition 4 has the maximum entropy value at all scales, indicating that needle valve wear faults contain more information. In order to verify the effect of needle valve wear on injector performance, the injector was tested on the injector opening pressure test rig and found to have very large fluctuations in opening pressure. This unstable operating condition resulted in a larger entropy value as well.

Because each sample has eighteen features, some of them may affect classification accuracy, due to interference. It is necessary to reduce the dimension of the feature set. Therefore, FCBF is used to select the main features according to their superiority and correlations. As a comparison, three entropy methods including RCMDE, MDE and MPE are also calculated, and FCBF is used to calculate the sensitivity on all the scales of the above methods. Table 12 shows the main features of the different methods. Then, the selected training sample of entropy values were used to train the SVM model and the selected testing sample entropy values were used to test the model. Before training SVM, the parameters of penalty factor c and kernel function parameter g need to be set. Here, we decides to use PSO to obtain the optimal parameters and the PSO theory can be found in the literature [35]. After 60 iterations, the optimal parameters c=10 and g=1 were obtained. The detailed fault diagnosis results can be seen from the confusion matrix, as is shown in Fig. 14. The proposed method of IRCMDE has the highest fault diagnosis rate, with an accuracy rate of 91.25%. The accuracy rates of the other three methods are 88.75%, 81.25% and 78.75%, respectively. As can been seen from the four methods above, fault condition 2 had the lowest classification accuracy. This is because, after long-term operation of marine diesel engines and frequent use of heavy oil, the internal spring stiffness of the fuel injector will naturally decrease, resulting in a lower valve opening pressure. So the failure of reducing valve opening pressure can easily cause confusion with other faults.

Table 12. Main features of the different methods.

Method	Feature scale			
IRCMDE	18	6	10	2
RCMDE	11	18	4	7
MDE	8	10	3	6
MPE	5	16	8	12
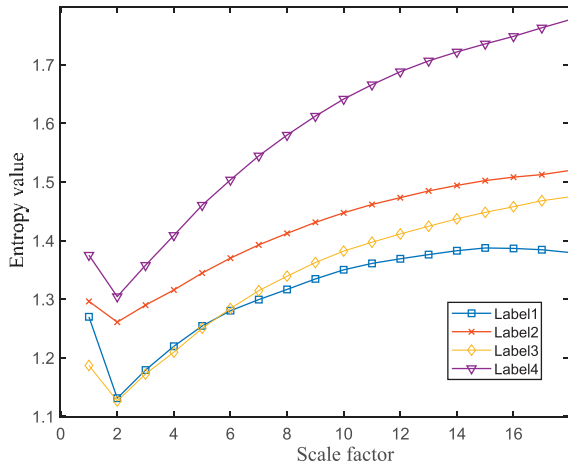
Fig. 13. IRCMDE values under four working conditions.

To further validate the effectiveness of the proposed algorithm, the fault diagnosis rate of each method was calculated twenty times, and the results are shown in Fig. 15. Five comparative indexes of the four methods in 20 trials are listed in Table 13, which includes the maximum, minimum, mean, SD and calculation time of accuracy for 20 trials. From Fig. 15 and Table 13, it can be concluded that the proposed method has the best accuracy and the SD value is relatively smaller. That indicates that the proposed method not only has

better classification accuracy, but is also more stable. There are several reasons for the illustrated comparative results. Firstly, PE is greatly affected by the signal amplitude while DE improves stability through nonlinear mapping. Secondly, IRCMDE and RCMDE fully consider the relationship between adjacent elements at each scale and generate more template vectors for short-term time series. Besides this, IRCMDE also considers the relative energy between the signals.
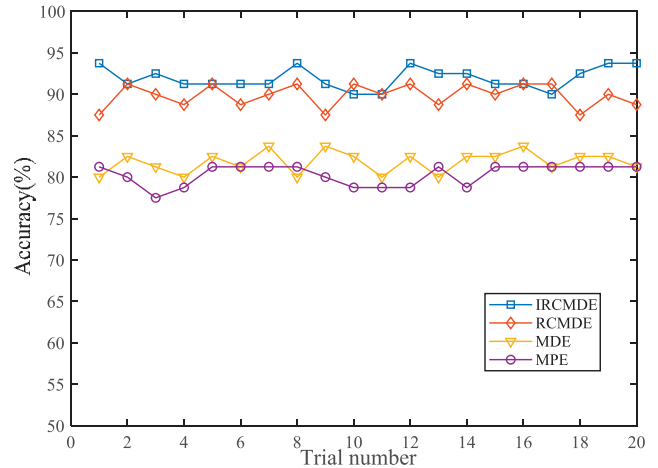
Fig. 15. Accuracy of four methods

(a) IRCMDE

(b) RCMDE

(c)MDE

(d) MPE
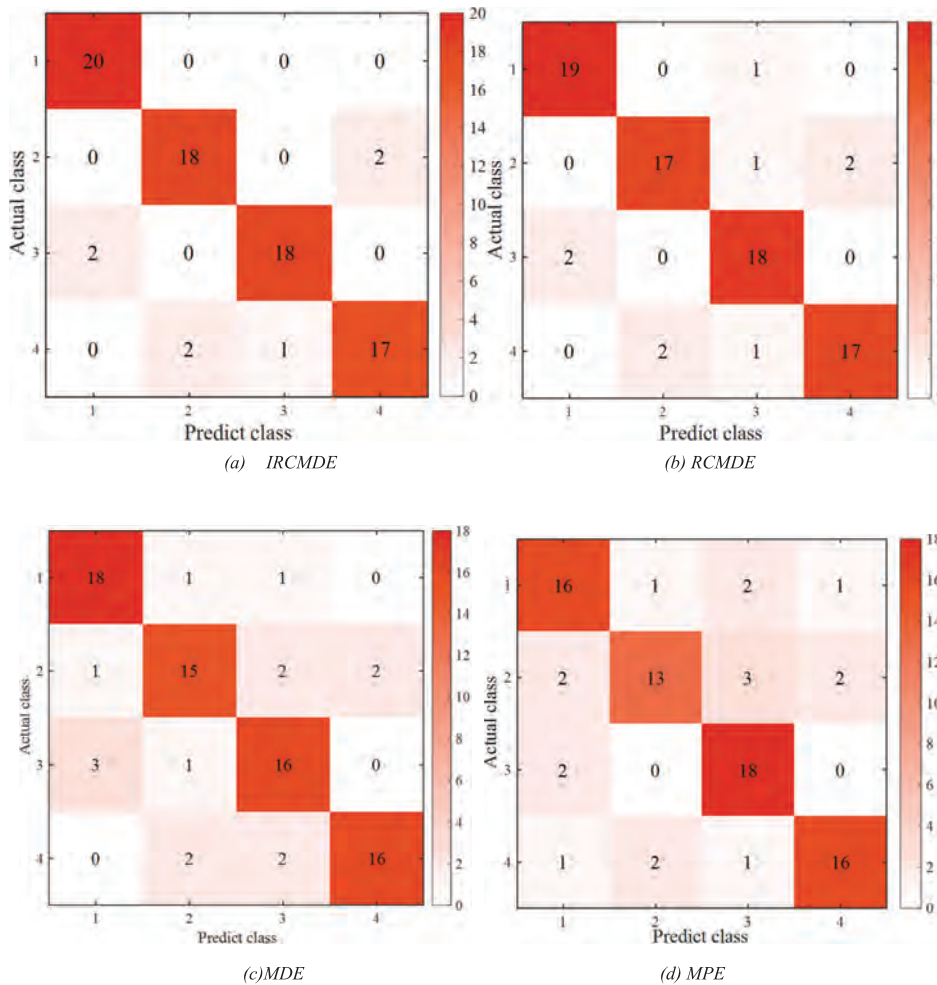
Fig. 14. Multi-class confusion matrix of different methods.

Table 13. Comparative indexes of different methods

Method	Comparative indexes			
	Maximum	Minimum	Mean	SD
IRCMDE	93.75	90.0	92.12	1.0512
RCMDE	91.25	87.5	89.50	1.3079
MDE	83.75	80.0	81.75	1.7396
MPE	81.25	77.5	78.94	1.6351

COMPARATIVE ANALYSIS OF USING PRESSURE AND VIBRATION SIGNALS

It can be seen, from Fig. 9 to 12, that, when the pressure in the high-pressure oil pipe increases, the vibration signal will also be significantly enhanced. However, the vibration signal is more susceptible to the influence of other cylinders. For example, there are two significant increases in the vibration signal waveform within a working cycle. Because our experiment was conducted on cylinder 1 at a speed of 90 r/min, it can be concluded that the most obvious vibration is the process of fuel injection and ignition in cylinder 1. According to the ignition sequence 1-5-3-6-2-4, the second most obvious vibration signal is the process of fuel injection and ignition in cylinder 2. As a comparison, inner wall vibration signals and outer wall vibration signals of the double-walled high pressure fuel pipe were used to diagnose fuel injector faults. As can be seen from Fig. 16, there is a phenomenon of entropy crossover, and the entropy crossover of the outer wall vibration signal is particularly severe. This means that the feature differentiation is not clear enough, which is not conducive to fault classification. A confusion matrix showing the effects of fault diagnosis is shown in Fig. 17, where the outer wall's fault diagnosis rate is 47.5% and the inner wall's fault diagnosis accuracy rate is 61.25%. This demonstrates that fault diagnosis in injectors is not well achieved using high pressure fuel pipe vibration signals. To explain this phenomenon, the high-pressure fuel pipe was sawn off and, as a result, the wall thickness of the inner pipe was found to be as high as 5 mm by measurement; the gap between the inner pipe and the outer pipe was 1 mm. This structure of the high-pressure tube improved the operational safety, to a certain extent but, on the other hand, it also weakened the internal pressure transmission of the high-pressure tube. Therefore, the accuracy of fault diagnosis based on vibration signals is relatively low.
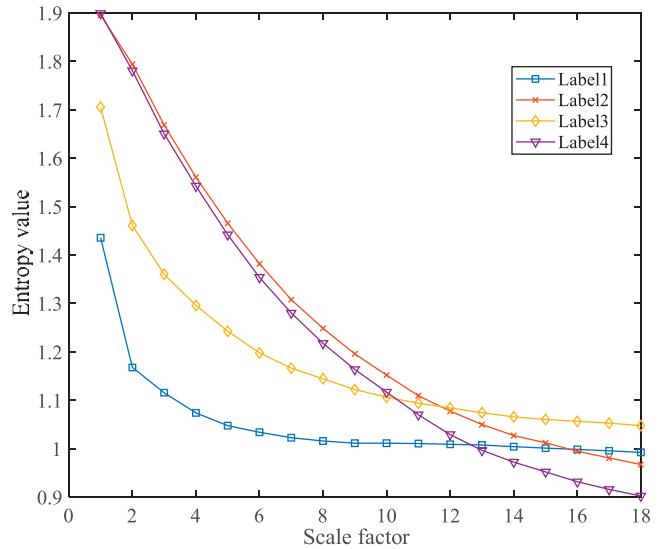
(a)   Entropy value of inner tube vibration signal
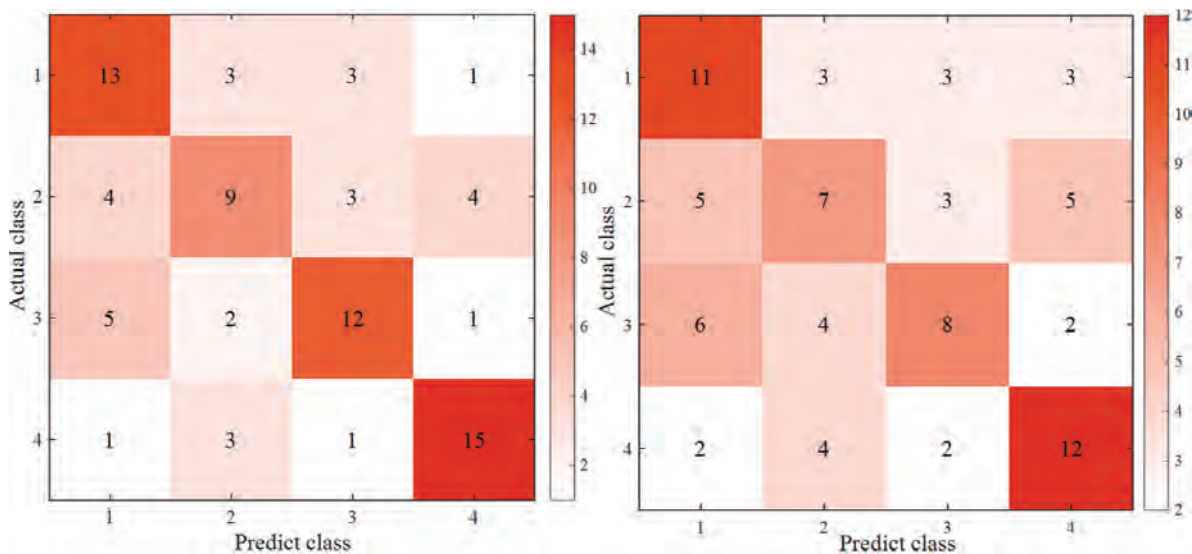
(a)   Inter- tube vibration signal

(b) Outer tube vibration signal

Fig. 17. Multiclass confusion matrix of different vibration signals
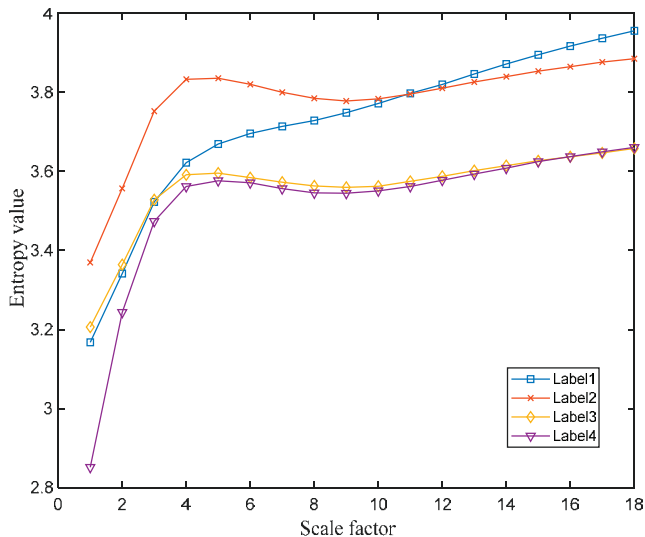
(b) Entropy value of outer tube vibration signal

Fig. 16. IRCMDE values of different vibration signals

CONCLUSION

Considering the non-stationary and nonlinear characteristics of the fuel injection pressure signal and vibration signal of a high-pressure fuel pipe, a novel intelligent fault diagnosis method, based on IRCMDE and FCBF, is proposed. The IRCMDE can extract more fault features from the original different working condition signals, which is beneficial for improving the accuracy of fault diagnosis. Then, FCBF should be used to select the sensitive features and SVM employed to classify the working condition. The main contribution of this paper can be concluded as follows:

It is the firstly time the fuel injection pressure signal has been measured on a large marine two-stroke MAN B&W 6S35ME-B9 diesel engine. The literature showed that most research has been carried out based on four-stroke diesel engines. Besides this, some research was based on model simulation to study fuel injector faults. (2) In this manuscript, IRCMDE is proposed, which overcomes the neutralisation phenomenon during the coarse-graining process. It can extract feature information from the complex signal more effectively and its parameter selection criterion has also been discussed in detail. The superiority of IRCMDE is validated using both simulation and experimental signals, compared with RCMDE, MDE, and MPE. (3) It is also the first time that both the fuel injection pressure signal and vibration signal of a high-pressure fuel pipe has been measured simultaneously on a marine two-stroke large diesel engine, in states such as reduced injector opening valve pressure, blocked spray holes, and worn needle valves. The experimental results showed that 92.15% fault diagnosis accuracy could be achieved for the pressure signal using IRCMDE; however, vibration signals of the inner and outer wall of the high pressure fuel pipe could only reach 61.25% and 47.5%, respectively.

DECLARATION OF COMPETING INTERESTS

The authors declare that they have no known competing financial interests or personal relationships that could have appeared to influence the work reported in this paper.

REFERENCES

1. C.G. Rodriguez, M.I. Lamas, J.D. Rodriguez and A. Abbas, "Analysis of the Pre-Injection System of a Marine Diesel Engine Through Multiple-Criteria Decision-Making and Artificial Neural Networks," Pol. Marit. Res., vol. 28, no. 4, pp. 88-96, 2022, doi: 10.2478/pomr-2021-0051.

2. F. Gao, "An integrated risk analysis method for tanker cargo handling operation using the cloud model and DEMATEL method," Ocean Eng., vol. 266, pp. 113021, 2022, doi: 10.1016/j.oceaneng.2022.113021.

3. R. Varbanets, et al., "Concept of Vibroacoustic Diagnostics of the Fuel Injection and Electronic Cylinder Lubrication Systems of Marine Diesel Engines," Pol. Marit. Res., vol. 29, no. 4, pp. 88-96, 2022, doi: 10.2478/pomr-2022-0046.

4. J. Kowalski, "An Experimental Study of Emission and Combustion Characteristics of Marine Diesel Engine with Fuel Injector Malfunctions," Pol. Marit. Res., vol. 23, no. 1, pp. 77-84, 2016, doi: 10.1515/pomr-2016-0011.

5. M.G. Thurston, M.R. Sullivan and S.P. McConky, "Exhaust-gas temperature model and prognostic feature for diesel engines," Appl. Therm. Eng., vol. 229, pp. 120578, 2023, doi: 10.1016/j.applthermaleng.2023.120578.

6. Y. Li, W. Zhou and Y. Zi, "A graphic pattern feature-mapping-based data-driven condition monitoring method for diesel engine malfunction identification and classification," Proceedings of the Institution of Mechanical Engineers, Part C: Journal of Mechanical Engineering Science, vol. 233, no. 1, pp. 202-212, 2019, doi: 10.1177/0954406218755186.

7. M. Zhang, Y. Zi, L. Niu, S. Xi and Y. Li, "Intelligent Diagnosis of V-Type Marine Diesel Engines Based on Multifeatures Extracted From Instantaneous Crankshaft Speed," IEEE T. Instrum. Meas., vol. 68, no. 3, pp. 722-740, 2019, doi: 10.1109/TIM.2018.2857018.

8.	Y. Yang, A. Ming, Y. Zhang and Y. Zhu, "Discriminative non-negative matrix factorisation (DNMF) and its application to the fault diagnosis of diesel engine," Mech. Syst. Signal Pr., vol. 95, pp. 158-171, 2017, doi: 10.1016/j.ymssp.2017.03.026.

9.	E. Ftoutou and M. Chouchane, "Diesel engine injection faults' detection and classification utilizing unsupervised fuzzy clustering techniques," Proceedings of the Institution of Mechanical Engineers, Part C: Journal of Mechanical Engineering Science, vol. 233, no. 16, pp. 5622-5636, 2019, doi: 10.1177/0954406219849089.

10.	S.M. Ramteke, H. Chelladurai and M. Amarnath, "Diagnosis of Liner Scuffing Fault of a Diesel Engine via Vibration and Acoustic Emission Analysis," Journal of Vibration Engineering & Technologies, vol. 8, no. 6, pp. 815-833, 2020, doi: 10.1007/s42417-019-00180-7.

11.	A. Zabihi-Hesari, S. Ansari-Rad, F.A. Shirazi and M. Ayati, "Fault detection and diagnosis of a 12-cylinder trainset diesel engine based on vibration signature analysis and neural network," Proceedings of the Institution of Mechanical Engineers, Part C: Journal of Mechanical Engineering Science, vol. 233, no. 6, pp. 1910-1923, 2019, doi: 10.1177/0954406218778313.

12.	L. Li, S. Tiexiong, F. Ma and Y. Pu, "Research on a small sample fault diagnosis method for a high-pressure common rail system," Advances in Mechanical Engineering, vol. 13, no. 9, pp. 2072279549, 2021, doi: 10.1177/16878140211046103.

13.	A. Zabihi-Hesari, S. Ansari-Rad, F.A. Shirazi and M. Ayati, "Fault detection and diagnosis of a 12-cylinder trainset diesel engine based on vibration signature analysis and neural network," Proceedings of the Institution of Mechanical Engineers, Part C: Journal of Mechanical Engineering Science, vol. 233, no. 6, pp. 1910-1923, 2019, doi: 10.1177/0954406218778313.

14.	A. Taghizadeh-Alisaraei and A. Mahdavian, "Fault detection of injectors in diesel engines using vibration time-frequency analysis," Appl. Acoust., vol. 143, pp. 48-58, 2019, doi: 10.1016/j.apacoust.2018.09.002.

15.	Y. Chen, T. Zhang, Z. Luo and K. Sun, "A Novel Rolling Bearing Fault Diagnosis and Severity Analysis Method," Applied Sciences, vol. 9, no. 11, pp. 2356, 2019, doi: 10.3390/app9112356.

16.	Y. Shang, G. Lu, Y. Kang, Z. Zhou, B. Duan and C. Zhang, "A multi-fault diagnosis method based on modified Sample Entropy for lithium-ion battery strings," J. Power Sources, vol. 446, pp. 227275, 2020, doi: 10.1016/j.jpowsour.2019.227275.

17.	K. Zhu and H. Li, "A rolling element bearing fault diagnosis approach based on hierarchical fuzzy entropy and support vector machine," Proceedings of the Institution of Mechanical Engineers, Part C: Journal of Mechanical Engineering Science, vol. 230, no. 13, pp. 2314-2322, 2016, doi: 10.1177/0954406215593568.

18.	Y. Ma, J. Cheng, P. Wang, J. Wang and Y. Yang, "Rotating machinery fault diagnosis based on multivariate multiscale fuzzy distribution entropy and Fisher score," Measurement, vol. 179, pp. 109495, 2021, doi: 10.1016/j.measurement.2021.109495.

19.	C. Ma, Y. Li, X. Wang and Z. Cai, "Early fault diagnosis of rotating machinery based on composite zoom permutation entropy," Reliab. Eng. Syst. Safe., vol. 230, pp. 108967, 2023, doi: 10.1016/j.ress.2022.108967.

20.	S. Wu, P. Wu, C. Wu, J. Ding and C. Wang, "Bearing Fault Diagnosis Based on Multiscale Permutation Entropy and Support Vector Machine," Entropy-Switz., vol. 14, no. 8, pp. 1343-1356, 2012, doi: 10.3390/e14081343.

21.	Y. Li, G. Li, Y. Wei, B. Liu and X. Liang, "Health condition identification of planetary gearboxes based on variational mode decomposition and generalised composite multi-scale symbolic dynamic entropy," Isa T., vol. 81, pp. 329-341, 2018, doi: 10.1016/j.isatra.2018.06.001.

22.	H. Azami and J. Escudero, "Amplitude- and Fluctuation-Based Dispersion Entropy," Entropy-Switz., vol. 20, no. 3, pp. 210, 2018, doi: 10.3390/e20030210.

23.	C. Gu, X. Qiao, H. Li and Y. Jin, "Misfire Fault Diagnosis Method for Diesel Engine Based on MEMD and Dispersion Entropy," Shock Vib., vol. 2021, pp. 1-14, 2021, doi: 10.1155/2021/9213697.

24.	X. Yan and M. Jia, "Intelligent fault diagnosis of rotating machinery using improved multiscale dispersion entropy and mRMR feature selection," Knowl.-Based Syst., vol. 163, pp. 450-471, 2019, doi: 10.1016/j.knosys.2018.09.004.

25.	Y. Ke, C. Yao, E. Song, Q. Dong and L. Yang, "An early fault diagnosis method of common-rail injector based on improved CYCBD and hierarchical fluctuation dispersion entropy," Digit. Signal Process., vol. 114, pp. 103049, 2021, doi: 10.1016/j.dsp.2021.103049.

26.	R. Dhandapani, I. Mitiche, S. McMeekin and G. Morison, "A Novel Bearing Faults Detection Method Using Generalised Gaussian Distribution Refined Composite Multiscale Dispersion Entropy," IEEE T. Instrum. Meas., vol. 71, pp. 1-12, 2022, doi: 10.1109/TIM.2022.3187717.

27.	Y. Ma, J. Cheng, P. Wang, J. Wang and Y. Yang, "Rotating machinery fault diagnosis based on multivariate

multiscale fuzzy distribution entropy and Fisher score," Measurement, vol. 179, pp. 109495, 2021, doi: 10.1016/j.measurement.2021.109495.

28. Y. Liu, J. Zhang and L. Ma, "A fault diagnosis approach for diesel engines based on self-adaptive WVD, improved FCBF and PECOC-RVM," Neurocomputing, vol. 177, pp. 600-611, 2016, doi: 10.1016/j.neucom.2015.11.074.

29. M. Zhang, Y. Zi, L. Niu, S. Xi and Y. Li, "Intelligent Diagnosis of V-Type Marine Diesel Engines Based on Multifeatures Extracted From Instantaneous Crankshaft Speed," IEEE T. Instrum. Meas., vol. 68, no. 3, pp. 722-740, 2019, doi: 10.1109/TIM.2018.2857018.

30. C. Zhao, J. Sun, S. Lin and Y. Peng, "Rolling mill bearings fault diagnosis based on improved multivariate variational mode decomposition and multivariate composite multiscale weighted permutation entropy," Measurement, vol. 195, pp. 111190, 2022, doi: 10.1016/j.measurement.2022.111190.

31. Y. Ma, J. Cheng, P. Wang, J. Wang and Y. Yang, "Rotating machinery fault diagnosis based on multivariate multiscale fuzzy distribution entropy and Fisher score," Measurement, vol. 179, pp. 109495, 2021, doi: 10.1016/j.measurement.2021.109495.

32. Y. Liu, J. Zhang and L. Ma, "A fault diagnosis approach for diesel engines based on self-adaptive WVD, improved FCBF and PECOC-RVM," Neurocomputing, vol. 177, pp. 600-611, 2016, doi: 10.1016/j.neucom.2015.11.074.

33. B. Mei, L. Sun, G. Shi and X. Liu, "Ship Maneuvering Prediction Using Grey Box Framework via Adaptive RM-SVM with Minor Rudder," Pol. Marit. Res., vol. 26, no. 3, pp. 115-127, 2019, doi: 10.2478/pomr-2019-0052.

34. Y. Ke, C. Yao, E. Song, Q. Dong and L. Yang, "An early fault diagnosis method of common-rail injector based on improved CYCBD and hierarchical fluctuation dispersion entropy," Digit. Signal Process., vol. 114, pp. 103049, 2021, doi: 10.1016/j.dsp.2021.103049.

35. L. Zhang, J. Sun and C. Guo, "A Novel Multi-Objective Discrete Particle Swarm Optimisation with Elitist Perturbation for Reconfiguration of Ship Power System," Pol. Marit. Res., vol. 24, no. s3, pp. 79-85, 2017, doi: 10.1515/pomr-2017-0108.

SYNERGISTIC PERFORMANCE DEGRADATION OF MARINE STRUCTURAL ELEMENTS: CASE STUDY OF POLYMER-BASED COMPOSITE AND STEEL HYBRID DOUBLE LAP JOINTS

Halis Haluk Baykal
Dokuz Eylül University Graduate School of Natural and Applied Sciences, Turkey
Gokdeniz Neser * ⓘ
Dokuz Eylul University Institute of Marine Sciences and Technology, Turkey

_____

* Corresponding author: *gokdeniz.neser@deu.edu.tr (G. Neser)*

ABSTRACT

The degradation of structures under the influence of a marine environment tends to be rapid and disruptive compared to that of structures that are far away from these influences. Efforts to consider these impacts in the design phase are increasing, with a view to the construction of more sustainable structures. However, experimental data from which designers and builders can benefit cannot be found in the relevant literature, especially when it comes to the effects of composite degradation. In this study, we experimentally investigate the combined effects of degradation factors such as a drying-wetting cycle, the shape of the structure, the variety of materials used in the structure, and the differences in the manufacturing of the materials . The structure chosen as an example is a hybrid structural double lap joint composed of epoxy resin, fibreglass composite, and steel, which is widely used in ship structures. The experiments considered four aging periods (zero, 30, 60 and 90 days) under a wet-dry cycle in a programmable corrosion chamber, two overlap lengths (short and long), two surface roughnesses of the steel parts (50 and 90 μm), and two surface preparation alternatives (uncoated and coated with epoxy primer). The synergistic effects of these parameters on the tensile strength, deformation and toughness of the joints were evaluated, and suggestions are made for ship designers. The attention of interested parties, and particularly ship designers, is drawn to the comparative effects of these degradation agents on performance.

Keywords: Wet-dry cycle; Double lap joint; Polymer composite-steel joints; Surface roughness; Aging in marine environment

INTRODUCTION

It is well-known that water, despite being the source of life and well-being for humans, is less kind to the materials and structures that come into contact with it or are located close to it. Water helps initiate and drive natural phenomena that lead to the weakening of mechanical properties established in the design phase, thereby increasing the need for repair and reconstruction, and shortening the expected life of related materials and structures. Material degradation is a global phenomenon that increases costs related to construction and operation, as well as the carbon footprint of a structure.

For example, it has been estimated that the economic and ecological effects of corrosion reach 3–4% of the gross domestic product of industrialised countries, especially in regard to metallic structures [1]. In order to achieve more sustainable structures, the resistance of marine structures to degradation needs to be increased and their service life extended.

In a seawater environment, the water itself is not the only element that causes these irreversible effects on the materials and structures; other degrading factors include salt (which is composed of different minerals depending on the geography), wetting/drying and freezing/thawing cycles,

moisture, weathering (including rain, sand erosion, etc.), UV radiation, microorganisms (e.g. fouling/boring organisms), and chemicals (acids, alkalis, solvents, oxygen, etc.) [2].

Although these factors often interact, research has focused on a single mechanism of degradation for a single material. In the design of ship structures, where designers tend to use the results of experimental studies, the synergistic effect of different combinations must be taken into account. It would be appropriate to refer to the total degradation effect, which occurs as a result of the action of many agents on the material according to many different mechanisms in the marine environment, as synergistic degradation.

As floating marine structures, ships are exposed to conditions that can be divided into three zones: underwater, the splash zone and the atmospheric zone (Figure 1). Degradation in the splash zone occurs more rapidly due to the high chloride and oxygen content and the cyclic wetting and drying action (WDA), which causes accumulation of chloride and increased intrusion and transfer of moisture into the structure [3].
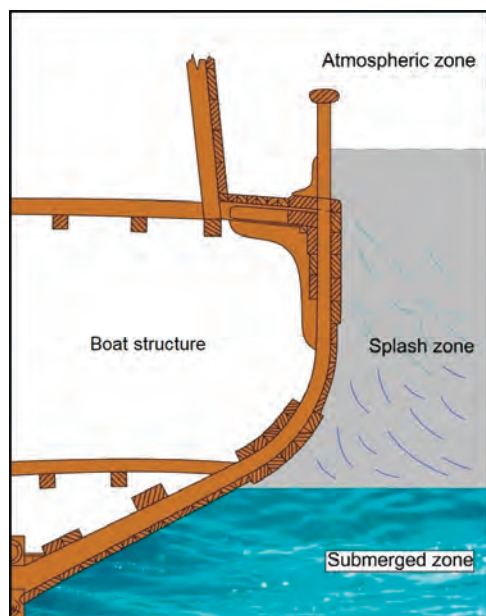

Fig. 1. Zones of the marine environment acting on a ship

As in other fields of engineering, the main aim of naval architecture is to achieve the lightest possible structure. To this end, naval architects tend to use lighter materials even for heavy floating metal structures, which mainly include composites based on fibre-reinforced polymers (FRP) [4]. These are used in a variety of industrial marine applications, including coastal structures, due to their high specific strength and stiffness. FRPs are also characterised by high corrosion resistance, good impact strength, and fatigue resistance, which make them attractive for use in marine applications such as propellers, boats, ships, turbine blades (wind and tidal turbines), and sails [5].

FRPs are also used to reinforce coastal structures such as ports and piers, either in the form of bars as a replacement

for reinforcing steel, or as strips that are bonded to concrete for the external reinforcement of structural members or delineation of columns. The beneficial effects of their use in rehabilitation, which arise from their ease of installation, high chemical resistance and reduced architectural impact and/or increased mechanical or fatigue resistance, are well known and have been described in the literature.

The water around the glass fibres becomes an alkaline solution as alkali ions dissolve out of the glass, and the glass fibres gradually decompose [6]. In general, the moisture concentration initially increases with time and eventually approaches a saturation point (equilibrium) after several days of exposure. The time needed to reach the saturation point depends on the properties of the materials and the ambient temperature, and although drying can reverse the process it may not lead to full recovery of the original properties [7]. This degradation often leads to damage to the FRP, such as microcracking of the matrix, fibre/matrix interfacial debonding and delamination, plasticisation and swelling of the matrix materials (making the polymer more ductile and lowering its glass transition temperature), and hydrolysis, leading to the ultimate failure of the structure [8]. In particular, for epoxy resins, a decrease in the elasticity modulus of this material has been observed under wetting-drying action (WDA). It has been reported that in long-term tests on glass/epoxy composites, about half of the tested specimens failed at a sustained stress of only 50% of the ultimate load after about seven years [9].

In the absence of chemical interactions, salt crystallisation occurs in saline environments, which physically damages the materials. This damage is caused by internal stress resulting from the formation of salt crystals in the material pores when the solution inside the pores becomes supersaturated [10]. Salt crystallisation occurs under two circumstances: the evaporation of the pore solution with the capillary rise, which is the action of a liquid moving across a small space without the aid of, or even against, any external forces like gravity, and WDA [11].

In one of the first studies in this field, by Gellert and Turley [12], it was shown that the glass fibre-reinforced plastics (GFRP) used in marine applications, which are composed of various resins such as polyester, phenol, and two types of vinyl esters, lose 15–25% of their mechanical properties during aging. During the tests, specimens were immersed in seawater and unloaded and loaded at high service temperatures in the range 30–50°C, and continuous solar radiation increased the temperature of the structure [13, 14]. There was a greater loss of mechanical properties from immersion at 50°C, which was accompanied by signs of abnormal degradation. The researchers also included an oven drying phase in their experiment to account for this effect, at temperatures of 45–80°C. Higher temperatures were used to increase the rate of water evaporation and to significantly shorten the duration of the test. Alhozaimy et al. [15] found that the corrosion of steel became more severe when the temperature was increased from 28.5°C to 34.5°C. This was due to the catalytic effect of a higher temperature

on chloride, which destroys the passivity of the steel.

However, it must be mentioned that there are some difficulties with joining polymer-based composites with metalelements of a marine structure, which are related to the large differences in mechanical properties (stiffness, coefficient of thermal expansion, etc.) between the adherents, and the strong anisotropy of composites.

Joints cause the local accumulation of stress, which can lead to discontinuities in the shape of the structure and the material properties. When designing and manufacturing a joint that is reliable over the long term, the effects of the marine environment in terms of degradation must be considered, as well as the elements of the joint and its shape, in order to minimise stress accumulation. The influence of the environment on materials significantly increases in the WDA zone. With a view to predicting potential degradation in the properties of materials, in situ data and data from accelerated aging simulations in materials laboratories have been used to overcome the difficulties of conducting long-term tests in natural environments. Studies of accelerated aging using distilled water and seawater have been reported in the literature, beginning in the early 1980s. In these studies, where the main corrosive element of the marine environment was salt from sea air, it was mentioned that aging leads to a reduction in the mechanical properties of materials, such as their stiffness and ultimate strength [16].

In addition to these effects, the steel parts of a hybrid joint may be roughened, which greatly complicates the prediction of its performance. The effects of surface roughness have not been extensively investigated in existing studies of composite-steel joints. Some type of surface pretreatment is required to achieve adequate bond strength and resistance to environmental degradation. Surface pretreatments are primarily used to remove contaminants and wear layers from surfaces, to increase the surface area, and to ensure that all mechanisms of adhesion are activated. The strength of bonded joints is increased if the surface is textured and made rougher before bonding, for example by mechanical abrasion, although the relationship between roughness and adhesion is not yet fully understood. This relationship may be explained by the large effective surface area or by some mechanical interlocking, and numerous studies have focused on the use of different metrics to describe roughness and its relationship to mechanical strength.

In composite shipbuilding, many types of adhesive joints are used, such as single and double lap joints, docking joints, bevel joints and trapezoidal joints, both to maintain the light weight of the structure and to improve its mechanical and physical properties [17]. Bonded and bolted double lap joints are prominently used for the connection of polymer-based composite–steel structures. It is well known that bonded joints have several advantages over conventional joints (bolted, welded, riveted, etc.), such as their ability to join dissimilar materials, better stress distributions, weight reduction, applicability to complex shapes, improved hydrodynamic surface resistance, and better corrosion and fatigue resistance [18]. In a study by Bohlman and Fogarty [19], bolted and bonded joints were compared in terms of joining a composite superstructure to the steel hull of a naval ship, and bolted joints were found to be more expensive to manufacture and maintain. The plates are not weakened or damaged during the joining process. The strength-to-weight ratio is also high for these joints [20]. Le Lan et al. [21], who studied both bolted and bonded joints, also developed bonded joints for French Lafayette frigates. Bonded double lap joints have been used in the study of metal-to-metal, metal-to-composite and composite ship elements, and have also been used to explore the interfacial fracture of the corresponding structure. In ship structures, double lap joints are preferable because they can resist transverse shear forces due to blast or sea pressure on a panel [22].

Damage to composite materials is one of the most important topics of current research, and numerical and experimental models have been developed specifically to study damage to composite joints. For example, Yang et al. [23] proposed an efficient model based on peridynamic theory to estimate the damage around a hole at the connection points of bolted composite joints. In addition, dynamic effects such as low-velocity impacts have been investigated due to their negative effects on the lifecycle of composite materials [24].

In a study by van Dam et al. [25], a shear test on a single lap joint showed that the dominant factor affecting the initial adhesion between the epoxy adhesive and the steel substrate was the roughness of the substrate. In addition, specimens with different surface morphologies but comparable average levels of roughness showed significant improvements in initial adhesion. The porous morphologies of etched and blasted surfaces gave superior adhesion performance, and appear to be key factors in the development of potential mechanical interlock. This occurs when the adhesive penetrates the pores of the surface and creates an area known as the microcomposite interphase zone.

In this study, experiments were conducted to predict the performance of double lap joints with lower and upper parts made of e-glass fibre-reinforced epoxy composites and a middle part made of ship-grade steel. We considered four aging periods (zero, 30, 60 and 90 days) under a wet-dry cycle in a programmable corrosion chamber, two overlap lengths (short and long), two surface roughnesses (50 and 90 µm) of the steel parts, and two surface preparation alternatives (uncoated and coated with epoxy primer). The synergistic effects of the above parameters on the joint performance were evaluated, and suggestions were drawn up for marine designers.

MATERIALS AND METHOD

SPECIMENS

Specimens of hybrid double overlap joints were fabricated, consisting of e-glass reinforced epoxy composite layers and a steel member between these layers, to comply with ASTM D3528-96 [26]. These specimens had two different lengths of

overlap (short and long), which were used as a performance variable for the joint (Figure 2).

Fig. 2. Geometry (in mm) of the specimens for the hybrid double lap joints: (a) short overlap, (b) long overlap

The reinforcement of the composite part was a stitched multiaxial [0, −45°, 45°, 90°] e-glass fibre with an area weight of 850 g/m², manufactured by Metyx [27] under code Q850E10B. The resin used in this composite was an epoxy resin made by Duratek [28], code 1000, which was recommended by the manufacturer for vacuum bagging, and was used with a hardener from the same manufacturer. It is worth mentioning that the sides of the composite parts were coated with an epoxy paint to prevent water from being absorbed.

The steel layers were Grade A St37 marine steel manufactured by Erdemir Iron and Steel Mill Corp. of Turkey [29]. The specimens, consisting of the composite material and a steel layer, were vacuum-bagged in a serial manner using a system developed by the authors (Figure 3), since vacuum-assisted methods cause fewer manufacturing defects than conventional hand lay-up methods [30]. To ensure that the steel parts did not touch each other and were aligned correctly, strips of PVC foam material were placed between them. In this way, it was prevented that the epoxy fills the gap between the steel parts.

PREPARATION OF STEEL PARTS

The surface roughness of the steel part of the joint was considered as another performance variable in this study. To evaluate the effect of this parameter on the performance, the surface of some specimens was textured with two different roughness values, Rz (average distance between the highest peak and lowest valley in each sampling length of the measured surface), of 50 μm and 90 μm. To obtain these roughness values, the steel layers were blasted using steel balls with diameters of 1 and 2.5 mm, respectively. The resulting roughness values of the surfaces were measured with a Mitutoyo SJ-301 (Neuss) instrument.

Before the roughened steel parts were used to make the double lap joint, a primer was applied to the surface of some parts. The application of the primer was also considered as a performance variable for the joints.

AGING

In order to simulate the effect of wet-dry cycling in a marine environment, the specimens were stored in a programmable cyclic corrosion test chamber (salt spray booth) [Ascoot CC 1000 IP, Staffordshire, UK]. A daily cycle was programmed in which the specimens in the chamber were covered with salt fog (a 2.5% solution of sodium chloride, NaCl) during the first eight hours of the day under the conditions specified in the ASTM B 117 standard [31] and at a temperature in the range 45–60°C. The specimens were then exposed to a relative humidity of 100% at a constant temperature of 60°C for the second period of eight hours. These two eight-hour periods represented the wetting phase of aging. During the final eight hours of the day, the specimens were exposed to a temperature from 60°C to 45°C without humidity. This last period represented the drying phase of aging. The weekly wet-dry aging cycle is shown in Figure 4. Specimens were grouped and aged for 30, 60 and 90 days to investigate the effect of the duration of aging on the joint performance, and were weighed with a precision balance at the end of each

Fig. 3. Specimen fabrication with vacuum bagging technique

period to determine the degree of water absorption.
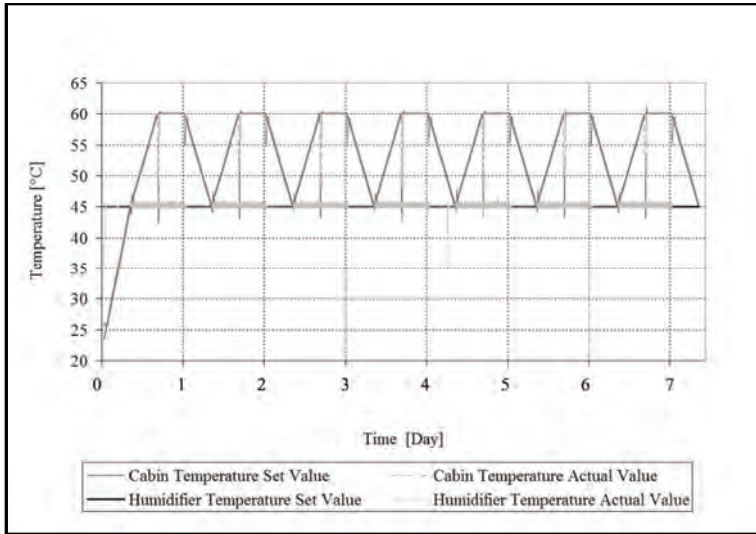
Fig. 4. Weekly aging cycle

TENSILE TESTS

To measure the strength of the joints (i.e. the maximum force that the joints could withstand), tensile tests were carried out in the Mechanics Laboratory of Dokuz Eylül University Engineering Faculty using a tester [Shimadzu Autogarph AG-IS, Kyoto, Japan] which complied with the ASTM D3528-96 standard [26], at a speed of 1.27 mm/min. The data were recorded and the equipment was controlled using Trapezium software.

SPECIMEN CODING

Specimens were coded as X-YY-ZZ, where X represented the overlap length (S indicated short and L long), YY was 50 or 90 (the values of the surface roughness), and ZZ represented the use of primer (where PN indicated without primer and PY with primer). For example, a specimen labelled L-90-PY had a long overlap, a surface roughness of 90 μm, and primer applied. For each condition (code), five specimens were tested in order to minimise the error rate, resulting in a total of 160 specimens tested.

RESULTS

The samples were weighed under ambient conditions to determine the water absorbed in the composite parts of the joints, and were then quickly returned to the exposure environment It was found that the amount of water absorbed was 1.3% of the total weight of the specimens after 30 days of aging, and and the same value was found for the materials at the second weighingafter 60 days of aging. At the last weighing, the amount of absorbed water decreased to the value of 1.1% of the total weight This deabsorption may have been due to the drying effect of the cycle. In addition, the water-repellent effect of salt crystals accumulating in the pores of the material should be noted. During the aging process, it was observed that the colour of the specimens changed from white to yellow, due to the time spent in the corrosion chamber.

The general results of the tensile tests are given below:

1. The tensile strength of the specimens increased with the aging time up to 60 days, and then started to decrease up to 90 days of aging. Samples with a longer overlap showed better performance (Figure 5). However, for S-50-PY and L-50-PY, the decrease in tensile strength started after the 30-day period. This indicates that the accumulation of salt crystals in the pores of the material, which led to a temporary increase in strength during the aging process, was prevented by the low surface roughness and the application of a primer coating.

2. Coating with primer resulted in better strength values for the specimens with a higher surface roughness than those with lower roughness. The strength of specimens with lower roughness coated with primer increased up to the end of the 30-day aging period, after which it began to decrease steadily. For the uncoated specimens, the strength of the joints increased steadily over the 90-day aging period. Uncoated joints with lower roughness showed a higher strength performance than those with higher roughness.

3. The length of the overlap had a positive effect on the performance of the joint. For uncoated joints, the ratio between the strength of specimens with lower roughness and those with higher roughness was almost 1.3 for shorter overlaps, but was 1.5 for longer ones. This ratio gradually decreased to 1.25 for longer joints at the end of the 90-day aging period, while it remained constant for shorter joints. It could be concluded that longer overlapped joints had higher strength due to the longer curing time at the relatively high temperature in the aging chamber. For coated joints, the shorter overlap/ lower roughness or longer overlap/higher roughness required for desired performance. As with the uncoated joints, specimens coated with primer with higher roughness gradually became stronger than those with lower roughness during the aging process. However, the performance of the joints did not increase in proportion to the overlap length. It was found that the reason for this nonlinearity was due to the adhesive performance of the joints during vacuum bagging, especially those with higher roughness, where the interface between the composite and steel consisted of micro voids. Despite cleaning, the roughened surface also contained small particles. Joint failure was triggered by these voids/ particles, and joint joints began to separate nonlinearly, if the tensile force was sustained.

4. Except for joints with low surface roughness/primer coating/short overlap, the shorter joints showed nearly

the same performance as the longer ones as aging progressed.

Fig. 5. Tensile strength of the specimens

5. The failure displacement increased throughout the aging process, indicating that aging made the joints much more ductile (Figure 6).

Fig.6. Maximum displacement of specimens

6. The failure energy (area under the force–displacement curve) increased with the aging time (Figure 7).

Fig. 7. Failure energy of the test specimens

CONCLUSIONS

In this study, bonded double lap joints consisting of glass fibre-reinforced epoxy composites and steel members were experimentally investigated with the aim of contributing to the design of marine structures in general and small marine craft in particular. For this purpose, a wet-dry cycle was used; the shape of the joints, the surface preparation of the steel part and the use of a primer were selected as performance parameters for the corresponding joints, and the effects of these parameters were discussed in detail.

This study provides deeper insight into the effects of WDA on the mechanical performance of the joints through experimental research. The following conclusions can be drawn from the study:

1. WDA exacerbates joint degradation depending on properties such as the duration, temperature and external loading. A combination of several mechanisms was investigated, and the results suggest that WDA makes the surfaces more susceptible to degradation.

2. Tests should be conducted in a real environment, which would allow the laboratory simulation of WDA to be further improved through the collection of extensive field data.

For designers of marine structures who wish to combine polymer composites with steel structures, the following points should be considered:

(1) It is advantageous to keep the overlaps of double lap joints short, for ease of fabrication. However, in this case, it is necessary to remove the roughness of the steel parts to enable effective bonding, and a primer may have to be used for this.

(2) When exposed to environmental agents for more than three months, the performance of structures such as the double lap joints in this study decreases. In general, measures should be applied (effective coatings, planned maintenance, etc.) to keep materials away from the exposure of the corrosive effects of the marine environment away from these effects.

(3) Although some experimental data are available for the study of the degrading effects of environmental factors on individual materials, further experimental tests are needed to understand the effects of more than one factor, as in this study. Conducting aging tests under real or simulated conditions during the design phase of structures operating under such synergistic effects is very important for the long-term reliability of the structure.

From this study, it can be concluded that the best solution for joining two different materials is to use an uncoated steel part with low surface roughness and composite parts with longer overlaps, which should be joined with a vacuum-assisted technique. In case of steel parts with higher surface roughness, the use of a primer coating is highly advisable. To produce a much stronger joint, an additional bolt could be placed in the location at which separation is initiated.
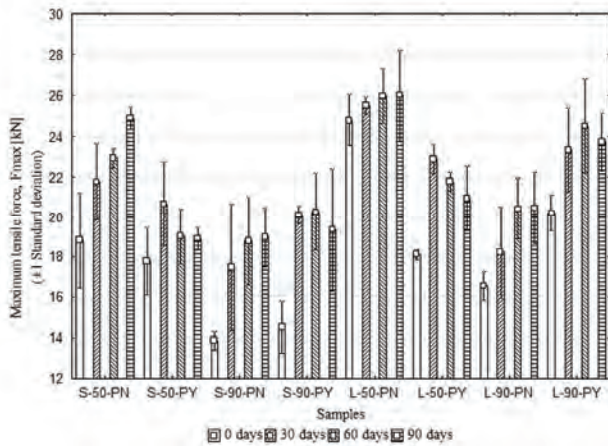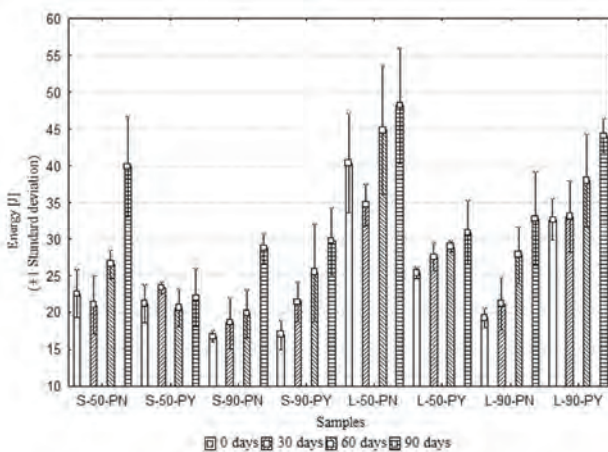
REFERENCES

3. A. R. Prased, A. Kunyankandy and A. Joseph, "Corrosion inhibition in oil and gas industry: Economic considerations," in Corrosion Inhibition in Oil and Gas Industry, V.S. Saji and S.A. Umoren, eds. 2020, pp. 135-150, Wiley-VCH Verlag GmbH & Co. KGaA.

4. A. S. Maxwell, W. R. Broughton, G. Dean, and G. D. Sims, Review of Accelerated Ageing Methods and Lifetime Prediction Technique for Polymeric Materials. Middlesex: National Physical Laboratory Report DEPC MPR 016, 2005.

5. M. Z. Y. Ting, K. S. Wong, M. E. Rahman, and S. J. Meheron, "Deterioration of marine concrete exposed to wetting-drying action," J Celan Prod, no. 278, p. 123383, 2021, https://doi.org/10.1016/j.jclepro.2020.123383.

6. A. P. Mouritz, E. Gellert, P. Burchill, and K. Challis, "Review of advanced composite structures for naval ships and submarines," Compos Struct, vol. 53, no. 1, pp. 21–41, 2001, https://doi.org/10.1016/S0263-8223(00)00175-6.

7. J. Cao and J. L. Grenestedt, "Design and testing of joints for composite sandwich/steel hybrid ship hulls," Compos Part A- Appl S, no. 35, pp. 1091–1105, 2004, https://doi.org/10.1016/j.compositesa.2004.02.010.

8. M. A. G. Silva, B. S. Da Fonseca, and H. Biscaia, "On estimates of durability of FRP based on accelerated tests," Compo Structures, no. 116, pp. 377–287, 2014, https://doi.org/10.1016/j.compstruct.2014.05.022.

9. J. D. Garcia-Espinel, D. Castro-Fresno, P. P. Gayo, and F. Ballester-Munoz, "Effect of sea water environment on glass fiber reinforced plastic materials used for marine civil engineering constructions," Mater Design, no. 66, pp. 46–50, 2015, https://doi.org/10.1016/j.matdes.2014.10.032.

10. E. J. Trujillo, C. R. Gonzales, and J. A. R. Gonzales, "Seawater aging effect on the mechanical properties of composites with different fiber and matrix types," Compos Mater, vol. 53, no. 23, pp. 3229–3241, 2019, https://doi.org/10.1177/0021998318811514.

11. L. J. Malvar, "Durability of composites in reinforced concrete," in Proc. of CDCC'98, First International Conference on Durability of Composites for Construction, 1998, Sherbrooke, Québec, p. 1–12.

12. N. Thaulow and S. Sahu, "Mechanism of concrete deterioration due to salt crystallization," MaterCharact, vol. 53, no. 2–4, pp.123–127, 2004, https://doi:10.1016/j.matchar.2004.08.013.

13. E. Nadelman and K. Kurtis, "Durability of Portland-limestone cement-based materials to physical salt attack," Cement Concrete Res, no. 125, p. 105859, 2019, https://doi.org/10.1016/j.cemconres.2019.105859.

14. E. P. Gellert and D. M. Turley, A Comparison of Normal and Accelerated Ageing of GRP Laminates Immersed in Seawater, Report No. DSTO-TR-0668, Melbourne: Department of Defense Science and Technology Organization (DSTO) Aeronautical and Maritime Research Laboratory, 1998.

15. K. K. Guan, "Surface and ambient air temperatures associated with different ground material: A case study at the University of California, Berkeley," EnvironmSci, no. 196, pp. 1–14, 2011.

16. C. L. Tan, N. H. Wong, and S. K. Jusuf, "Effects of vertical greenery on mean radiant temperature in the tropical urban environment," Landscape Urban Plan, no. 127, pp. 52–64. 2014, https://doi.org/10.1016/j.landurbplan.2014.04.005.

17. A. Alhozaimy, R. R. Hussain, R. Al-Zaid, and A. Al-Negheimish, "Coupled effect of ambient high relative humidity and varying temperature marine environment on corrosion of reinforced concrete," Constr Build Mater, vol. 28, no. 1, pp. 670–679, 2012, https://doi.org/10.1016/j.conbuildmat.2011.10.008.

18. B. S. Phull, S. J. Pikul, and R. M. Kain, "Thirty-eight years of atmospheric corrosivity monitoring," in: S. W. Dean, G. H. D. Delgaldillo, and J. B. Bushman, eds. Marine Corrosion in Tropical Environments, ASTM STP 1399, West Conshohocken, PA: American Society for Testing and Materials, pp. 60–74, 2000.

19. X. Li, Z. Zhu, Y. Li, and Z. Hu. "Design and mechanical analysis of a composite T-type connection structure for marine structures," Pol Marit Res, vol. 27, pp. 145–156, 2020, https://doi.org/ 10.2478/pomr-2020-0036.

20. N. Choupani, "Characterization of fracture in adhesively bounded double-lap joints," Intl JAdhes Adhes, vol. 29, no. 8, pp. 761–773, 2009, https://doi.org/10.1016/j.ijadhadh.2009.05.002.

21. R. E. Bohlman and J. H. Fogarty, "Demonstration of a composite to steel deck joint on a navy destroyer," in Proc. 9th International Conference on Marine Applications of Composite Materials, Melbourne, Florida, USA, pp. 19–21, 2002.

22. A. K. Mitra and B. Ghosh, "Interfacial stresses and deformations of an adhesive bounded double strap butt joint under tension," Compos Struct, vol. 55, no. 4, pp. 687–694, 1995, https://doi.org/10.1016/0045-7949(94)00430-B.

23. J. Y. Le Lan, P. Livory and P. Parneix, "Steel/composite bonding principle used in the connection of composite superstructure to metal hull," in Proc. 2nd International Conference on Sandwich Construction, vol. II, Gainesville, Florida, USA, 9–12 March 1992, pp. 857–872.

24. H. Osnes and D. McGeorge, "Experimental and analytical strength analysis of double-lap joints for marine applications," Compos Part B- Eng, no. 40, pp. 29–40, 2009, https://doi.org/10.1016/j.compositesb.2008.07.002.

25. N. N. Yang, T. Y. Zhao, J. G. Gu, and Z. P. Chen, "Damage and fracture analysis of bolted joints of composite materials based on peridynamic theory," Pol Marit Res, vol. 26, pp. 22–32, 2019, https://doi.org/ 10.2478/pomr-2019-0022.

26. Z. Zhu, X. Li, Q. Chen, Y. Cai, and Y. Xiong, "Simulations and tests of composite marine structures under low-velocity impact," Pol Mar Res, vol. 28, no. 1(109), pp. 59–71, 2021, https://doi.org/ 10.2478/pomr-2021-0006.

27. J. P. B. Van Dam, S. T. Abrahami, A. Yilmaz, Y. Gonzales-Garcia, H. Terryn and J. M. C. Mol, "Effect of surface roughness and chemistry on the adhesion and durability of a steel-epoxy adhesive interface," Int J Adhes Adhes, no. 92, p. 102450, 2020, https://doi.org/10.1016/j.ijadhadh.2019.102450.

28. ASTM D3528-96, Standard Test Method for Strength Properties of Double Lap Shear Adhesive Joints by Tension Loading, ASTM International, West Conshohocken, PA, 2016.

29. Metyx Composites Inc., "Multiaxials," 2022. [Online] Available: http://tr.metyx.com/cokyonlorguler.html# [Accessed: July 17, 2022].

30. Duratek Inc., "Epoxy and Polyurethane Systems," 2022. [Online] Available: http://www.duratek.com.tr/eng/products/composite/product-list/ [Accessed: July 17, 2022].

31. Erdemir Corp., "Products," 2002. [Online] Available: https://www.erdemir.com.tr/corporate/products-and-services/products/ [Accessed: July 17, 2022].

32. T. Niksa-Rynkiewicz, M. Landowski, and P. Szalewski, "Application of Apriori algorithm in the lamination process in yacht production," Pol Marit Res, vol. 27, no. 3(107), pp. 59–70, 2020, https://doi.org/ 10.2478/pomr-2020-0047.

33. ASTM B117-16, Standard Practice for Operating Salt Spray (Fog) Apparatus. ASTM International, West Conshohocken, PA, 2016.

EVENT-TRIGGERED ADAPTIVE NEURAL NETWORK TRAJECTORY TRACKING CONTROL FOR UNDERACTUATED SHIPS UNDER UNCERTAIN DISTURBANCE

Wenxue Su*
Qiang Zhang
School of Navigation and shipping, Shandong Jiaotong University, China
Yufeng Liu
University of Toronto OISE, China

Corresponding author: *71837989@qq.com (Wenxue Su)*

ABSTRACT

An adaptive neural network (NN) event-triggered trajectory tracking control scheme based on finite time convergence is proposed to address the problem of trajectory tracking control of underdriven surface ships. In this scheme, both NNs and minimum learning parameters (MLPS) are applied. The internal and external uncertainties are approximated by NNs. To reduce the computational complexity, MLPs are used in the proposed controller. An event-triggered technique is then incorporated into the control design to synthesise an adaptive NN-based event-triggered controller with finite-time convergence. Lyapunov theory is applied to prove that all signals are bounded in the tracking system of underactuated vessels, and to show that Zeno behavior can be avoided. The validity of this control scheme is determined based on simulation results, and comparisons with some alternative schemes are presented.

Keywords: Keywords: event-triggered control; underactuated marine surface vessels; adaptive neural network; trajectory tracking; finite-time

INTRODUCTION

Since the 20th century, surface transport via marine shipping has received unprecedented amounts of research attention [1][2]. The use of intelligent ships, for example based on artificial intelligence and digital twins, is an important development in the area of ocean transportation, and motion control of such ships is an essential aspect of achieving intelligent operation [3][4]. Trajectory tracking control for ships is an influential line of research in the domain of ship motion control, and the issue of how to achieve fast, high-precision tracking has always been one of the main focuses in this field [5].

However, the shipping itself is characterised by high inertia, long time lags, and nonlinearity. In addition, there are various other factors that affect the internal dynamic uncertainties and cause external disturbances, thereby creating great difficulties for high-precision trajectory tracking control. To solve these problems, control algorithms such as neural networks (NNs) [6]-[9], fuzzy methods [10]-[14], sliding modes [15]-[17], and adaptive backstepping [18]-[20] have been developed, and many of these have been applied to achieve trajectory tracking control of ships. Control schemes based on these algorithms have solved the problems described above to a certain extent, but can only obtain asymptotically stable results when the system time tends to infinity.

Achieving high-precision tracking control of ships within a limited time can solve a series of engineering problems. For example, when a ship is operating in a complex environment and detects other ships or obstacles in the sea ahead, fast, high-precision tracking allows it to avoid these obstacles promptly, thereby improving the safety of operation. Research into finite-time trajectory tracking control in shipping therefore has many practical implications for engineering applications. In [21], a finite-time control scheme based on the sliding mode and adaptive theory was designed for the formation control of UAVs. In [22], a synergistic heading control strategy based on a hyperbolic tangent guidance method was designed to enable the ship to complete tracking control within a limited time. In [23], a composite perturbation was estimated by a finite-time perturbation observer; virtual control was also achieved using a finite-time command filter, and a control scheme was designed under full constraints. In [24], a finite time was applied to the problem of power positioning control, and when combined with a non-singular fast terminal sliding mode strategy, the convergence speed and immunity of the system were greatly improved.

Research into the finite-time control schemes mentioned above has greatly improved the convergence speeds of such systems. However, with the recent advances in control accuracy, a higher energy output is often required. In practical engineering terms, this will undoubtedly increase the wear and tear of the thruster and controller. To solve these problems, event-triggered (ET) techniques have begun to be applied to ship motion control. In [25], an ET control scheme with static trigger conditions was first developed. In [26], time-triggered control schemes with dynamic trigger conditions were developed to further extend the interaction time. In [27], ET control schemes with periodicity were investigated with the aim of relaxing the restrictions on the monitoring of trigger conditions. Following the introduction of stringent policies for energy reduction and environmental protection nationwide, applications involving event triggering for ship motion and control are also being developed [28][29].

Inspired by these research studies, this paper presents the design of an ET trajectory tracking control scheme based on finite-time convergence for underdriven ships with adaptive NNs. The main contributions of this study are as follows:
(1) Under conditions of dynamic uncertainty and external disturbance, a finite-time trajectory tracking control scheme is proposed that combines finite-time control theory, NNs, minimum learning parameters (MLPs), and depth information robust adaptive methods to achieve tracking control of underactuated ships within a finite time.
(2) The proposed finite-time trajectory tracking control scheme is combined with a fixed-threshold ET method to decrease the update frequency of the controller, reduce the losses of the actuator, and avoid Zeno behavior.

MATHEMATICAL MODELLING OF SHIP MOTION

A general mathematical model with three degrees of freedom for underdriven surface ship tracking control can be expressed in the following form [30]:

$$\begin{cases} \dot{x} = u\cos(\psi) - v\sin(\psi) \\ \dot{y} = u\sin(\psi) + v\cos(\psi) \\ \dot{\psi} = r \end{cases} \tag{1}$$

$$\begin{cases} \dot{u} = f_u(u,v,r) + \dfrac{1}{m_u}\left[\tau_u + d_u\right] \\ \dot{v} = f_v(u,v,r) + \dfrac{1}{m_v}d_v \\ \dot{r} = f_r(u,v,r) + \dfrac{1}{m_r}\left[\tau_r + d_r\right] \end{cases} \tag{2}$$

$$\begin{cases} f_u(u,v,r) = \dfrac{1}{m_u}(m_v vr - Y_r r^2 + X_u u + X_{u|u|}|u|u) \\ f_v(u,v,r) = \dfrac{1}{m_v}(Y_v v + Y_{|v|v}|v|v + Y_{|r|v}|r|v + Y_r r - m_u ur + Y_{|v|r}|v|r + Y_{|r|r}|r|r) \\ f_r(u,v,r) = \dfrac{1}{m_r}[(m_u - m_v)uv + Y_r ur + N_v v + N_r r + N_{|r|v}|r|v + N_{|v|v}|v|v + N_{|v|r}|v|r + N_{|r|r}|r|r] \end{cases} \tag{3}$$

In Eq. (3), x, y, ψ are the attitude variables of the ship's position coordinates and bow angle, respectively; u, v, r are the ship's velocity variables; d_u, d_v, d_r denote unmeasured, unknown disturbances; τ_u, τ_r are the input moments; and $f_u(u,v,r)$, $f_v(u,v,r)$, $f_r(u,v,r)$ are higher-order hydrodynamic terms.

Assumption 1: $f_i(u,v,r)$, m_i and $i = \{u,v,r\}$ are unknown, but their external disturbances d_i, $i = \{u,v,r\}$ are unknown and bounded; that is say, there exist unknown positive constants σ_u, σ_v, σ_r such that d_u, d_v, d_r satisfy $|d_u| \le \sigma_u$, $|d_v| \le \sigma_v$, $|d_r| \le \sigma_r$.

Definition: The nonlinear control system is described as in Eq. (4):

$$\dot{x} = f(x), \, x(0) = x_o, \, x \in \Omega_0 \subset R^n \tag{4}$$

where $x \in R^n$ is the state variable of the system, Ω_0 is a spherical domain containing the origin, and $f(x)$ is a continuous function. For arbitrary initial conditions x_0, the system in Eq. (4) can be said to be semi-globally stable within a finite time, in practice, if there exists a constant $\Im > 0$ and a settling time function $0 < T(\Im, x_o) < \infty$ such that $\|x(t)\| \le \Im$, $t \ge T(x_0)$ [31].

CONTROLLER DESIGN

The trajectory tracking control process is shown in Fig. 1.
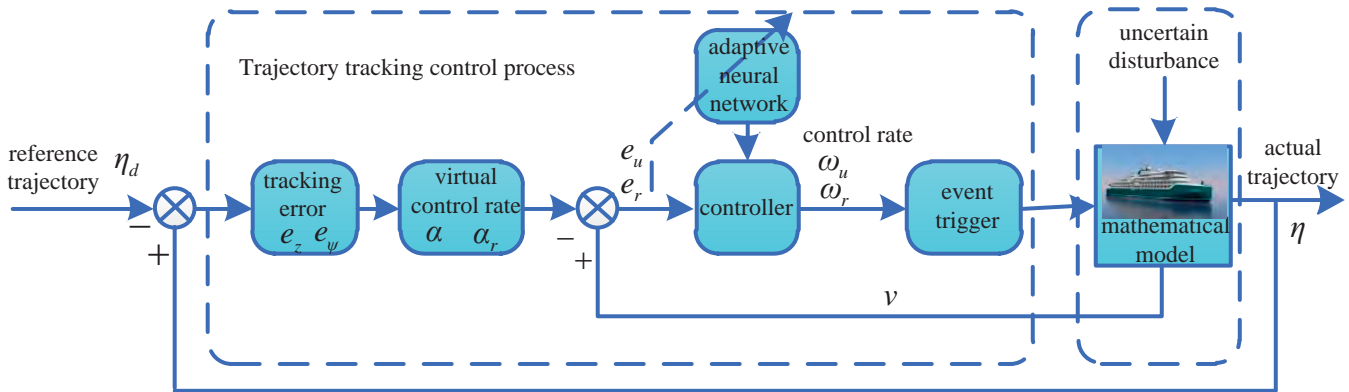
Fig. 1 Control flow diagram for trajectory tracking

To solve the problem of lateral drive mismatch of underdriven ships, a method from the existing literature [32] is used, and the following transformations are performed. First, we define the tracking error for an underdriven surface ship:

$$\begin{cases} e_x = x - x_d \\ e_y = y - y_d \\ e_\psi = \psi - \psi_d \end{cases} \tag{5}$$

where x_d, y_d, ψ_d represent the desired position and heading angle. A transformation of Eq. (5) yields

$$e_z = \begin{bmatrix} x - x_d \\ y - y_d \end{bmatrix} \tag{6}$$

From Eq. (6), we have

$$\dot{e}_z = u g_u(\psi) + v g_v(\psi) - \begin{pmatrix} \dot{x}_d \\ \dot{y}_d \end{pmatrix} \tag{7}$$

where $g_u(\psi) = \begin{bmatrix} \cos\psi \\ \sin\psi \end{bmatrix}$, $g_v(\psi) = \begin{bmatrix} -\sin\psi \\ \cos\psi \end{bmatrix}$.

To stabilise the tracking error e_z and e_ψ, we can construct the Lyapunov functions $V_1 = \frac{1}{2} e_z^T e_z + \frac{1}{2} \psi_e^2$. We can then design dummy control variables with the following form:

$$\begin{cases} \alpha = -k_{11} e_z - \dfrac{k_{12} e_z}{\sqrt{\|e_z\|^2 + \varsigma_z^2}} - v g_v(\psi) + \begin{pmatrix} \dot{x}_d \\ \dot{y}_d \end{pmatrix} \\[4mm] \alpha_r = -k_{31} e_\psi - \dfrac{k_{32} e_\psi}{\sqrt{\|e_\psi\|^2 + \varsigma_\psi^2}} + \dot{\psi}_d \end{cases} \tag{8}$$

The desired forward velocity, turning bow angular velocity and heading angle are expressed as shown in Eq. (9):

$$\begin{cases} u_d = \alpha_u = \|\alpha\| \\[2mm] r_d = \alpha_r = -k_{31} e_\psi - \dfrac{k_{32} e_\psi}{\sqrt{\|e_\psi\|^2 + \varsigma_\psi^2}} + \dot{\psi}_d \\[4mm] \psi_d = \arctan(\alpha_y, \alpha_x) \end{cases} \tag{9}$$

where ψ_d is obtained from $u_d = \alpha_u = \|\alpha\|$ inverse solution, and α_x, α_y are the virtual control rates of the position coordinates.

We define the error variables for the velocities as:

$$\begin{cases} e_u = u - \alpha_u \\ e_r = r - \alpha_r \end{cases} \tag{10}$$

From Eq. (10), we obtain

$$\begin{cases} \dot{e}_u = f_u\left(u,v,r\right) + \dfrac{1}{m_u}\left(\tau_u + d_u\right) - \dot{\alpha}_u \\[2mm] \dot{e}_r = f_r\left(u,v,r\right) + \dfrac{1}{m_r}\left(\tau_r + d_r\right) - \dot{\alpha}_r \end{cases} \qquad \text{(11)}$$

Lemma 1: For any given continuous smooth function defined on a compact set $\Omega \subset R^n$ [33][34], we have

$$h(x) = W^{*T}s(x) + \varepsilon, \forall x \in \Omega \qquad \text{(12)}$$

where ε is the approximation error, and for all $x \in \Omega$, there is a vector $\varepsilon^* > 0$ that satisfies $|\varepsilon| \le \varepsilon^*$; W^* is the weight vector under ideal conditions, and $s(x)$ is the central function. In general, the vector of ideal NN weights is unknown, and needs to be estimated. This problem can be interpreted as minimising $|\varepsilon|$ on $x \in \Omega \subset R^n$ to W, i.e.,

$$W^* = \arg \min_{W \in R^l} \left\{ \sup_{x \in \Omega} \left| h(x) - W^T s(x) \right| \right\} \qquad \text{(13)}$$

Assumption 2: In the compact set $\Omega_x \subset R^n$, the RBF neural network W^* used to approximate the unknown vector has bounded weights; that is, $\left\| W^* \right\| \le W_M$, W_M is a positive constant.

Due to the unknown dynamic uncertainties of $f_u\left(u,v,r\right)$ and $f_r\left(u,v,r\right)$, they cannot be used in the design of the controller. We therefore use RBF NNs to approximate $f_u\left(u,v,r\right)$ and $f_r\left(u,v,r\right)$, as follows:

$$\begin{cases} f_u\left(u,v,r\right) = W_u^T \sigma_u\left(\eta\right) + \varepsilon_u \\[2mm] f_r\left(u,v,r\right) = W_r^T \sigma_r\left(\eta\right) + \varepsilon_r \end{cases} \qquad \text{(14)}$$

where W_u and W_r are the matrices of NN weights; $\sigma_u\left(\eta\right)$ and $\sigma_r\left(\eta\right)$ are functions of the NN; and ε_u, ε_r are the approximation errors. The expressions in Eq. (14) are then substituted into Eq. (11) to give

$$\begin{cases} \dot{e}_u = W_u^T \sigma_u\left(\eta\right) + \varepsilon_u + \dfrac{1}{m_u}\left(\tau_u + d_u\right) - \dot{\alpha}_u \\[2mm] \dot{e}_r = W_r^T \sigma_r\left(\eta\right) + \varepsilon_r + \dfrac{1}{m_r}\left(\tau_r + d_r\right) - \dot{\alpha}_r \end{cases} \qquad \text{(15)}$$

Combined with a design concept based on the robust adaptive depth information method and using RBFNNs and MLPs, the following expressions can be obtained:

$$\begin{cases} \left\| W_u^T \sigma_u\left(\eta\right) + \varepsilon_u + \dfrac{d_u}{m_u} \right\| \le \left\| W_u^T \right\| \left\| \sigma_u\left(\eta\right) \right\| + \left| \varepsilon_u + \dfrac{d_u}{m_u} \right| \\[3mm] \qquad\qquad = \Theta_u \zeta_u\left(Z\right) \\[3mm] \left\| W_r^T \sigma_r\left(\eta\right) + \varepsilon_r + \dfrac{d_r}{m_r} \right\| \le \left\| W_r^T \right\| \left\| \sigma_r\left(\eta\right) \right\| + \left| \varepsilon_r + \dfrac{d_r}{m_r} \right| \\[3mm] \qquad\qquad = \Theta_r \zeta_r\left(Z\right) \end{cases} \qquad \text{(16)}$$

where $\begin{cases} \Theta_u = \max\left\{ \left\| W_u^T \right\|, \left| \varepsilon_u + \dfrac{d_u}{m_u} \right| \right\} \\[3mm] \Theta_r = \max\left\{ \left\| W_r^T \right\|, \left| \varepsilon_r + \dfrac{d_r}{m_r} \right| \right\} \end{cases}$ $\begin{cases} \zeta_u\left(Z\right) = \left\| \sigma_u\left(\eta\right) \right\| + 1 \\[2mm] \zeta_r\left(Z\right) = \left\| \sigma_r\left(\eta\right) \right\| + 1 \end{cases}$.

Through this transformation, the learning parameters of adaptive parameters are obviously reduced.

Based on this result, the Lyapunov function $V_2 = \dfrac{1}{2}u_e^2 + \dfrac{1}{2}r_e^2$ is constructed and the following expressions for the control rate are designed:

$$\begin{cases} \omega_u\left(t\right) = m_u\left[-k_{21}e_u - \dfrac{k_{22}e_u}{\sqrt{\left\| e_u \right\|^2 + \varsigma_u^2}} - c_1 e_u \hat{\Theta}_u \zeta_u^2(Z) + \dot{\alpha}_u \right] \\[4mm] \omega_r\left(t\right) = m_r\left[-k_{41}e_r - \dfrac{k_{42}e_r}{\sqrt{\left\| e_r \right\|^2 + \varsigma_r^2}} - c_2 e_r \hat{\Theta}_r \zeta_r^2(Z) + \dot{\alpha}_r \right] \end{cases} \qquad \text{(17)}$$

The adaptive rates are then as follows:

$$\begin{cases} \dot{\hat{\Theta}}_u = \acute{y}_1 \varsigma_u^2(Z)\left\| e_u \right\|^2 - {}_1\Theta \\[3mm] \dot{\hat{\Theta}}_r = \acute{y}_2 \varsigma_r^2(Z)\left\| e_r \right\|^2 - {}_2\Theta \end{cases} \qquad \text{(18)}$$

where k_{11}, k_{12}, k_{21}, k_{22}, c_1, c_2, $\acute{y}_1$, $\acute{y}_2$ are design parameters with values greater than zero.

The measurement errors are defined as:

$$\begin{cases} e_{\xi_u}\left(t\right) = \omega_u\left(t\right) - \tau_u\left(t\right),\ t \in \left[t_k, t_{k+1}\right) \\[2mm] e_{\xi_r}\left(t\right) = \omega_r\left(t\right) - \tau_r\left(t\right),\ t \in \left[t_k, t_{k+1}\right) \end{cases} \qquad \text{(19)}$$

where t is the trigger time interval; $\tau_u\left(t\right)$, $\tau_r\left(t\right)$ are the values for the controller at the previous departure time; and

$\tau_u(t)$, $\tau_r(t)$ are kept constant by the zero-order holder from the trigger time t_k until the trigger time is updated.

The event triggering conditions are designed as follows [35]:

$$\begin{cases} \tau_u(t) = \omega_u(t_k), \forall t \in [t_k, t_{k+1}) \\ t_{k+1} = \inf\left\{ t \in R \middle\| e_{\xi_u}(t) \middle| \geq \eta_u \right\} \end{cases} \quad (20)$$

$$\begin{cases} \tau_r(t) = \omega_r(t_k), \forall t \in [t_k, t_{k+1}) \\ t_{k+1} = \inf\left\{ t \in R \middle\| e_{\xi_r}(t) \middle| \geq \eta_r \right\} \end{cases} \quad (21)$$

where η_u and η_r are design parameters with values greater than zero. When the trigger condition is violated, the update time for the controller is marked as t_{k+1}, and the control signal for the controller is simultaneously updated to $\omega_u(t_{k+1})$ as the control input to the system.

STABILITY ANALYSIS

We select the following Lyapunov function for the control system:

$$V = V_1 + V_2 + \frac{1}{2g_u}\left(\Theta_u - g_u\hat{\Theta}_u\right)^2 + \frac{1}{2g_r}\left(\Theta_r - g_r\Theta_r\right)^2 \quad (22)$$

During the event trigger interval $[t_k, t_k+1)$, since $\omega_i(t) - \tau_i(t) \leq m_i$, $i = u, r$. Hence, there is a continuous time-varying parameter $\Xi(t)$ that satisfies the conditions $\Xi(t_k) = 0$, $\Xi(t_{k+1}) = \pm 1$, $\Xi(t) \leq 1$, meaning that $\forall t \in [t_k, t_{k+1})$ is not difficult to obtain.

$$\begin{cases} \omega_u(t) = \tau_u(t) + \Xi_u(t)\eta_u \\ \omega_r(t) = \tau_r(t) + \Xi_r(t)\eta_r \end{cases} \quad (23)$$

If $\Delta_e = ug_u(\psi) - u^* g_u(\psi^*)$, according to Young's inequality, $e_z\Delta_e \leq \frac{e_z^T e_z}{10} + \frac{5}{2}\|\Delta_e\|^2$ can be obtained. From the time derivative of Eq. (22), we can obtain expressions as follows:

$$\dot{V} \leq -e_z^T(k_{11} - 0.1)e_z - \frac{e_z^T k_{12} e_z}{\sqrt{\|e_z\|^2 + \varsigma_z^2}} + \frac{5}{2}\|\Delta_e\|^2 + e_u m_u^{-1}\tau_u + \|e_u\|\Theta_u\zeta_u(Z) \quad (24)$$

$$-\left(\Theta_u - g_u\hat{\Theta}_u\right)\dot{\Theta}_u - k_{31}e_\psi^2 - \frac{k_{32}e_\psi^2}{\sqrt{\|e_\psi\|^2 + \varsigma_\psi^2}} + e_r m_r^{-1}\tau_r + \|e_r\|\Theta_r\zeta_r(Z) - \left(\Theta_r - g_r\Theta_r\right)\dot{\Theta}_r$$

From Young's inequality $\lambda\gamma \leq \frac{1}{2}\lambda^2 + \frac{1}{2}\gamma^2$, we obtain

$$\dot{V} \leq -e_z^T(k_{11} - 0.1)e_z - \frac{e_z^T k_{12} e_z}{\sqrt{\|e_z\|^2 + \varsigma_z^2}} + \frac{5}{2}\|\Delta_e\|^2 - g_u\left(k_{21} + \frac{1}{2}\right)e_u^2 \quad$$

$$-\frac{g_u k_{22} e_u^2}{\sqrt{\|e_u\|^2 + \varsigma_u^2}} - c_1 g_u\hat{\Theta}_u\zeta_u^2(Z)e_u + \frac{1}{2}\|\Xi_u(t)m_u^{-1}\eta_u\|^2 + \|e_u\|\Theta_u\zeta_u(Z) \quad (25)$$

$$-\left(\Theta_u - g_u\hat{\Theta}_u\right)\dot{\Theta}_u - k_{31}e_\psi^2 - \frac{k_{32}e_\psi^2}{\sqrt{\|e_\psi\|^2 + \varsigma_\psi^2}} - g_r\left(k_{41} + \frac{1}{2}\right)e_r^2 - \frac{g_r k_{42} e_r^2}{\sqrt{\|e_r\|^2 + \varsigma_r^2}} \quad$$

$$-c_2 g_r\hat{\Theta}_r\zeta_r^2(Z)e_r + \|e_r\|\Theta_r\zeta_r(Z) + \frac{1}{2}\|\Xi_r(t)m_r^{-1}\eta_r\|^2 - \left(\Theta_r - g_r\hat{\Theta}_r\right)\dot{\Theta}_r$$

Based on Young's inequality, the following expressions can be obtained:

$$\begin{cases} \|e_u\|\Theta_u\zeta_u(Z) \leq \Theta_u\|e_u\|^2\zeta_u^2(Z) + \frac{\Theta_u}{4c_1} \\ \|e_r\|\Theta_r\zeta_r(Z) \leq \Theta_r\|e_r\|^2\zeta_r^2(Z) + \frac{\Theta_r}{4c_2} \end{cases} \quad (26)$$

Eq. (26) is then substituted into Eq. (25) to give

$$\dot{V} \leq -e_z^T\kappa_{11}e_z - \frac{e_z^T\kappa_{12}e_z}{\sqrt{\|e_z\|^2 + \varsigma_z^2}} + \frac{5}{2}\|\Delta_e\|^2 - g_u\kappa_{21}e_u^2 - \frac{g_u\kappa_{22}e_u^2}{\sqrt{\|e_u\|^2 + \varsigma_u^2}} - \kappa_{11}e_\psi^2 \quad (27)$$

$$-\frac{\kappa_{11}e_\psi^2}{\sqrt{\|e_\psi\|^2 + \varsigma_\psi^2}} + \frac{1}{2}\|\Xi_u(t)m_u^{-1}\eta_u\|^2 - g_r\kappa_{21}e_r^2 - \frac{g_r\kappa_{22}e_r^2}{\sqrt{\|e_r\|^2 + \varsigma_r^2}} + \iota_1\left(\Theta_u - g_u\hat{\Theta}_u\right)\dot{\Theta}_u$$

$$+\iota_2\left(\Theta_r - g_r\hat{\Theta}_r\right)\dot{\Theta}_r + \frac{\Theta}{4c_1} + \frac{\Theta}{4c_2} + \frac{1}{2}\|\Xi_r(t)m_r^{-1}\eta_r\|^2$$

where $\kappa_{11} = \min\left\{(k_{11} - 0.1), k_{31}\right\}$, $\kappa_{21} = \min\left\{k_{21} + 0.5, k_{41} + 0.5\right\}$, $\kappa_{12} = \min\left\{k_{12}, k_{32}\right\}$, $\kappa_{22} = \min\left\{k_{22}, k_{42}\right\}$.

We use the following Young's inequality:

$$\begin{cases} \left(\Theta_u - g_u\hat{\Theta}_u\right)\Theta_u \leq -\frac{1}{2g_u}\left(\Theta_u - g_u\Theta_u\right)^2 + \frac{\Theta_u^2}{2g_u} \\ \left(\Theta_r - g_r\hat{\Theta}_r\right)\Theta_r \leq -\frac{1}{2g_r}\left(\Theta_r - g_r\Theta_r\right)^2 + \frac{\Theta_r^2}{2g_r} \\ \frac{\iota_1}{2g_u}\left|\Theta_u - g_u\hat{\Theta}_u\right| \leq \frac{\iota_1}{4g_u}\left|\Theta_u - g\Theta_u\right|^2 + \frac{\iota_1}{4g_u} \\ \frac{\iota_2}{2g_r}\left|\Theta_r - g_r\hat{\Theta}_r\right| \leq \frac{\iota_2}{4g_r}\left|\Theta_r - g_r\Theta_r\right|^2 + \frac{\iota_2}{4g_r} \end{cases} \quad (28)$$

By adding or subtracting $\begin{cases} \dfrac{l_1}{2g_u}\left|\Theta_u - g_u\hat{\Theta}_u\right| \\ \dfrac{l_2}{2g_r}\left|\Theta_r - g_r\hat{\Theta}_r\right| \end{cases}$ to both

sides of Eq. (27) and combining with Eq. (28), the following equation can be obtained:

$$\dot{V} \le -e_z^{\ T}\kappa_{11}e_z - \frac{e_z^{\ T}\kappa_{12}e_z}{\sqrt{\|e_z\|^2 + \varsigma_z^{\ 2}}} + \frac{5}{2}\|\Delta_e\|^2 - g_u\kappa_{21}e_u^{\ 2} - \frac{g_u\kappa_{22}e_u^{\ 2}}{\sqrt{\|e_u\|^2 + \varsigma_u^{\ 2}}} - \kappa_{11}e_\psi^{\ 2} - \frac{\kappa_{11}e_\psi^{\ 2}}{\sqrt{\|e_\psi\|^2 + \varsigma_\psi^{\ 2}}}$$
$$- g_r\kappa_{21}e_r^{\ 2} - \frac{g_r\kappa_{22}e_r^{\ 2}}{\sqrt{\|e_r\|^2 + \varsigma_r^{\ 2}}} - \frac{l_1}{4g_u}\left(\Theta_u - g_u\hat{\Theta}_u\right)^2 - \frac{l_2}{4g_r}\left(\Theta_r - g_r\Theta_r\right)^2 - \frac{l_1}{2g_u}\left|\Theta_u - g_u\Theta_u\right| \quad \textbf{(29)}$$
$$- \frac{l_2}{2g_r}\left|\Theta_r - g_r\hat{\Theta}_r\right| + \frac{l_1}{4g_u} + \frac{l_2}{4g_r} + \frac{l_1\Theta_u^{\ 2}}{2g_u} + \frac{l_2\Theta_r^{\ 2}}{2g_r} + \frac{\Theta_u}{4c_1} + \frac{\Theta_r}{4c_2} + \frac{1}{2}\left\|\Xi_u(t)m_u^{-1}\eta_u\right\|^2 + \frac{1}{2}\left\|\Xi_r(t)m_r^{-1}\eta_u\right\|^2$$

Lemma 2: For any constant $\varsigma > 0$ and any scalar $\upsilon \in R$, the inequality in Eq. (30) holds [36]:

$$0 \le |\upsilon| - \frac{\upsilon^2}{\sqrt{\upsilon^2 + \varsigma^2}} < \varsigma \quad \textbf{(30)}$$

From Lemma 2, we obtain

$$\begin{cases} -\dfrac{e_z^{\ T}\kappa_{12}e_z}{\sqrt{\|e_z\|^2 + \varsigma_z^{\ 2}}} < \kappa_{12}\left(\varsigma_z - \|e_z\|\right) \\[4mm] -\dfrac{g_u\kappa_{22}e_u^{\ 2}}{\sqrt{\|e_u\|^2 + \varsigma_u^{\ 2}}} < \kappa_{22}\left[g_u\left(\varsigma_u - \|e_u\|\right)\right] \\[4mm] -\dfrac{\kappa_{12}e_\psi^{\ 2}}{\sqrt{\|e_\psi\|^2 + \varsigma_\psi^{\ 2}}} < \kappa_{12}\left(\varsigma_\psi - \|e_\psi\|\right) \\[4mm] -\dfrac{g_r\kappa_{22}e_r^{\ 2}}{\sqrt{\|e_r\|^2 + \varsigma_r^{\ 2}}} < \kappa_{22}\left[g_r\left(\varsigma_r - \|e_r\|\right)\right] \end{cases} \quad \textbf{(31)}$$

Eq. (32) is substituted into Eq. (29).

$$\dot{V} \le -e_z^{\ T}\kappa_{11}e_z - \kappa_{12}\|e_z\| + \frac{5}{2}\|\Delta_e\|^2 - g_u\kappa_{21}e_u^{\ 2} - g_u\kappa_{22}\|e_u\| - \kappa_{11}e_\psi^{\ 2} - \kappa_{12}\|e_\psi\| \quad \textbf{(32)}$$
$$- g_r\kappa_{21}e_r^{\ 2} - g_r\kappa_{22}\|e_r\| + \varsigma_{max}\left(\kappa_{12} + \kappa_{22}\right) - \frac{l_1}{4g_u}\left(\Theta_u - g_u\hat{\Theta}_u\right)^2 - \frac{l_2}{4g_r}\left(\Theta_r - g_r\Theta_r\right)^2$$
$$- \frac{l_1}{2g_u}\left|\Theta_u - g_u\hat{\Theta}_u\right| - \frac{l_2}{2g_r}\left|\Theta_r - g_r\Theta_r\right| + \frac{l_1}{4g_u} + \frac{l_2}{4g_r} + \frac{l_1\Theta_u^{\ 2}}{2g_u} + \frac{l_2\Theta_r^{\ 2}}{2g_r} + \frac{\Theta_u}{4c_1} + \frac{\Theta_r}{4c_2}$$
$$+ \frac{1}{2}\left\|\Xi_u(t)m_u^{-1}\eta_u\right\|^2 + \frac{1}{2}\left\|\Xi_r(t)m_r^{-1}\eta_u\right\|^2$$
$$\le -\upsilon_1 V - \upsilon_2 V^{\frac{1}{2}} + \theta$$

where $\upsilon_1 = \min\left\{2\kappa_{11}, 2g_u\kappa_{21}, 2g_r\kappa_{21}, \dfrac{l_1}{2}, \dfrac{l_2}{2}\right\}$,

$\rho_2 = \min\{\sqrt{2}\kappa_{12}, \sqrt{2}g_u\kappa_{22}, \sqrt{2}g_r\kappa_{22}, \dfrac{l_1}{\sqrt{2g_u}}, \dfrac{l_2}{\sqrt{2g_r}}\}$,

and

$$\theta = \frac{l_1}{4g_u} + \frac{l_2}{4g_r} + \frac{l_1\Theta_u^{\ 2}}{2g_u} + \frac{l_2\Theta_r^{\ 2}}{2g_r} + \frac{\Theta_u}{4c_1} + \frac{\Theta_r}{4c_2} +$$
$$+ \varsigma_{max}\left(\kappa_{12} + \kappa_{22}\right) + \frac{5}{2}\|\Delta_e\|^2 + \frac{1}{2}\left\|\Xi_u(t)m_u^{-1}\eta_u\right\|^2 + \frac{1}{2}\left\|\Xi_r(t)m_r^{-1}\eta_u\right\|^2$$

Lemma 3: For the nonlinear system in Eq. (4), we assume that there exists a positive definite Lyapunov function $V(x)$: $\Omega_0 \to R$ and any scalar $a > 0$ $b > 0$, $0 < \kappa < 1$ such that the inequality $\dot{V}(x) + aV(x) + bV^\kappa(x) \le 0$ holds. The system in Eq. (4) is then finite time stable, and its regulation time meets the condition [37]:

$$T \le \frac{1}{a(1-t)}\ln\frac{aV^{1-\kappa}(x_0) + b}{b} \quad \textbf{(33)}$$

where $V(x_0)$ is the initial value of $V(x)$.

From Eq. (32), we obtain

$$\dot{V} \le -\phi\upsilon_1 V - (1-\phi)\upsilon_1 V - \upsilon_2 V^{\frac{1}{2}} + \theta \quad \textbf{(34)}$$

where $\phi = \min\{\phi_1, \phi_2\}$, $0 < \phi < 1$.

If $V > \dfrac{\upsilon}{\phi\upsilon_1}$, we obtain

$$\dot{V} \le -(1-\phi)\upsilon_1 V - \upsilon_2 V^{\frac{1}{2}} \quad \textbf{(35)}$$

According to Lemma 3, the system will stabilise in finite time to the region $\Omega_V = \left\{V : V \le \dfrac{\theta}{\phi\upsilon_1}\right\}$, and the stabilisation time is

$$T \le \frac{4}{(1-t)\upsilon_1}\ln\left[\frac{(1-t)\upsilon_1 V^{1/2}(0) + \upsilon_2}{\upsilon_2}\right] \quad \textbf{(36)}$$

From Eq. (19), the following expressions ,can be obtained:

$$\begin{cases} \dfrac{d}{dt}\left|e_{\xi_u}\right| = \dfrac{d}{dt}\left(e_{\xi_u}*e_{\xi_u}\right) \\ \qquad = sign\left(e_{\xi_u}\right)\dot{e}_{\xi_u} \le \left|\dot{\omega}_u\left(t\right)\right| \\ \dfrac{d}{dt}\left|e_{\xi_r}\right| = \dfrac{d}{dt}\left(e_{\xi_r}*e_{\xi_r}\right) \\ \qquad = sign\left(e_{\xi_r}\right)\dot{e}_{\xi_r} \le \left|\dot{\omega}_r\left(t\right)\right| \end{cases} \qquad (37)$$

Furthermore, from Eq. (17), we know that

$$\dot{\omega}_u = m_u\{-k_{21}\dot{e}_u - \frac{k_{22}\dot{e}_u}{\sqrt{\|e_u\|^2 + \varsigma_u^2}} - [c_1\dot{e}_u\hat{\Theta}_u\zeta_u^{\,2}(Z) + c_1e_u(\dot{\hat{\Theta}}_u\zeta_u^{\,2}(Z) + 2\Theta_u\zeta_u(Z)\dot{\zeta}_u(Z)] + \ddot{\alpha}_u\}$$

$$\dot{\omega}_r = m_r\{-k_{41}\dot{e}_r - \frac{k_{42}\dot{e}_r}{\sqrt{\|e_r\|^2 + \varsigma_r^2}} - [c_2\dot{e}_r\hat{\Theta}_r\zeta_r^{\,2}(Z) + c_2e_r(\dot{\hat{\Theta}}_r\zeta_r^{\,2}(Z) + 2\Theta_r\zeta_r(Z)\dot{\zeta}_r(Z)] + \ddot{\alpha}_r\}$$

$$(38)$$

From Eq. (39), $\dot{\omega}_i$, $i = u, r$ is a smooth and derivable function, and $\dot{\omega}_i$ is therefore a continuous function. Since all its variables are globally bounded, $\lambda_i > 0$ gives $\left|\dot{\omega}_i\right| \le \lambda_i$. When $t = t_k$, $e_{\xi_i}\left(t_k\right) = 0$ and $\lim_{t \to t_k} e_{\xi_i}\left(t\right) = \eta_i$. Hence there exists a time interval t_k satisfying $t \ge \dfrac{\eta_i}{\lambda_i}$, and Zeno behavior does not occur.

SIMULATION

In this study, a Cybership 2 ship model from the Norwegian University of Science and Technology was used as the controlled object for simulation tests. The ship had a total length $L = 1.255$ m, a mass $m = 23.8$ kg, and other parameters as detailed in the literature [38].

Two different sets of equations, giving a circular and a trapezoidal trajectory, were used for the simulation, as shown in Eqs. (39) and (40).

The equations for the circular trajectory were as follows:

$$\begin{cases} x_d = 25\sin\left(0.01\pi t\right) \\ y_d = 25 - 25\cos\left(0.01\pi t\right) \end{cases} \qquad (39)$$

The equations for the trapezoidal trajectory were:

$$\begin{cases} y_d = 10 & t \le 47 \\ y_d = \sqrt{100-\left(t-47\right)^2} & 47 < t \le 53 \\ y_d = \dfrac{65-t}{1.5} & 53 < t \le 62 \\ y_d = 10 - \sqrt{100-\left(t-68\right)^2} & 62 < t \le 68 \\ y_d = 0 & 68 < t \le 112 \\ y_d = 10 - \sqrt{100-\left(t-112\right)^2} & 112 < t \le 118 \\ y_d = \dfrac{t-115}{1.5} & 118 < t \le 127 \\ y_d = \sqrt{100-\left(t-133\right)^2} & 127 < t \le 133 \\ y_d = 10 & 133 < t \le 200 \end{cases} \qquad (40)$$

To verify the effectiveness of the control scheme (ETC) proposed in this paper, two other approaches were selected for comparison:

Control scheme 1: Finite-time control scheme without event triggering (ANNs+FT) [39];

Control scheme 2: Adaptive control scheme using MLPs and ANNs (ANNs+MLPs) [40].

The virtual control rates, control rates, and adaptive laws for adaptive ANN trajectory tracking control using MLPs were as follows:

$$\begin{cases} \alpha_u = \left\| -k_{11}e_z - vg_v\left(e_\psi\right) + \begin{pmatrix} \dot{x}_d \\ \dot{y}_d \end{pmatrix} \right\| \\ \alpha_r = -k_{31}e_\psi + \dot{\psi}_d \end{cases} \qquad (41)$$

$$\begin{cases} \tau_u = m_u\left[-k_{21}e_u - c_1e_u\hat{\Theta}_u\zeta_u^{\,2}(Z) + \dot{\alpha}_u\right] \\ \tau_r = m_r\left[-k_{41}e_r - c_2e_r\hat{\Theta}_r\zeta_r^{\,2}(Z) + \dot{\alpha}_r\right] \end{cases} \qquad (42)$$

$$\begin{cases} \dot{\hat{\Theta}}_u = c_1\varsigma_u^{\,2}(Z)\|e_u\|^2 - \iota_1\hat{\Theta} \\ \dot{\hat{\Theta}}_r = c_2\varsigma_r^{\,2}(Z)\|e_r\|^2 - \iota_2\hat{\Theta} \end{cases} \qquad (43)$$

To simulate the sea state, the first-order Markov equations in Eq. (44) were used to describe the environmental disturbance, as shown in Fig. 2. This approach can reflect the coupling between the high and low frequencies of the waves more realistically than using sinusoidal waves [38].

$$\begin{cases} \dot{d}_{wu} = -d_{wu} + 0.05 * \omega_u \\ \dot{d}_{wo} = -d_{wv} + 0.05 * \omega_v \\ \dot{d}_{wr} = -d_{wr} + 0.5 * \omega_r \end{cases} \quad \text{(44)}$$
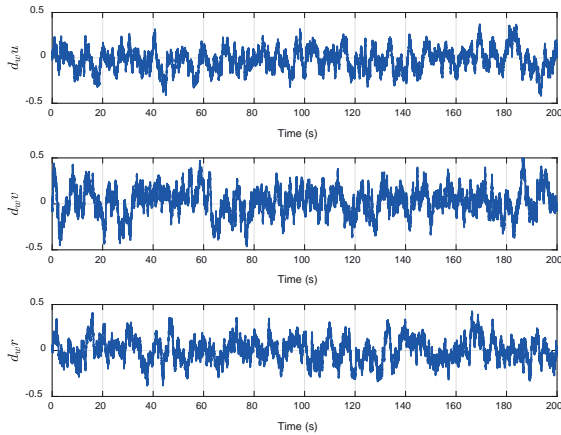

Fig. 2 Time evolution of the disturbances

In Fig. 2, $d_{wi} = d_i / m_i$, $i = \{u, v, r\}$ are three independent white noise variables with a variance of one.

Based on the condition that both model parameters m_u, m_v, m_r, $f_u(u, v, r)$ and $f_v(u, v, r)$ are unknown, we set the parameters $k_{11} = 0.3$, $k_{12} = 0.1$, $k_{21} = 0.2$, $k_{22} = 0.5$, $k_{31} = 3.5$, $k_{32} = 0.5$, $k_{41} = 2$, $k_{42} = 0.1$, $c_1 = 0.5$, $c_2 = 0.01$, $\iota_1 = 0.01$, $\iota_2 = 1$, $\varsigma_z = \varsigma_\psi = \varsigma_u = \varsigma_r = 0.05$, $\eta_u = 0.05$, $\eta_r = 0.5$. The initial position and velocity of the ship for the circular trajectory were $(x_0; y_0; \psi_0; u_0; v_0; r_0) = (0; 10; 0; 0; 0; 0)$. The initial position and velocity of the ship for the trapezoidal trajectory were $(x_0; y_0; \psi_0; u_0; v_0; r_0) = (3; 7; 75 / 57.3; 0; 0; 0)$.

The simulation results for the circular trajectory shown in Figs. 3–11 illustrate the tracking effect of the actual trajectory, and it can be seen that the three control schemes can track the target with good performance. Figs. 3–6 show the tracking of the ship's position, heading angle and speed. Figs. 2–6 show that the tracking effect of the system is greatly improved after the introduction of finite time and event triggering in the control scheme, and that there is no significant degradation in the control performance of the system after the introduction of event triggering. Figs. 7 and 8 show the ephemeral curves for the positional and velocity errors of the system. After introducing finite time to the control scheme, the convergence speed of the system errors is improved, and the upper and lower bounds on the errors are smaller. When event triggering is added, the tracking accuracy of the system is basically the same as that of the finite time control scheme. Fig. 9 shows the ephemeral curves for the control inputs of the system, and it can be seen that the number of updates to the control inputs of the event-triggered control scheme has been reduced. Fig. 10 shows the interval times between triggering events. In summary, the control performance of both control schemes

proposed in this paper is greatly improved, and the number of updates to the controller is significantly reduced after the introduction of event triggering.
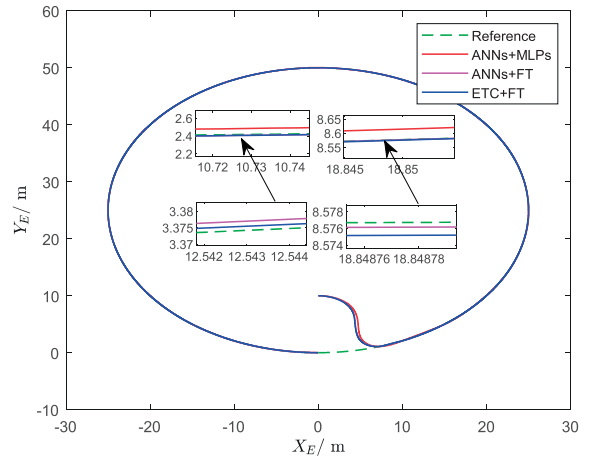

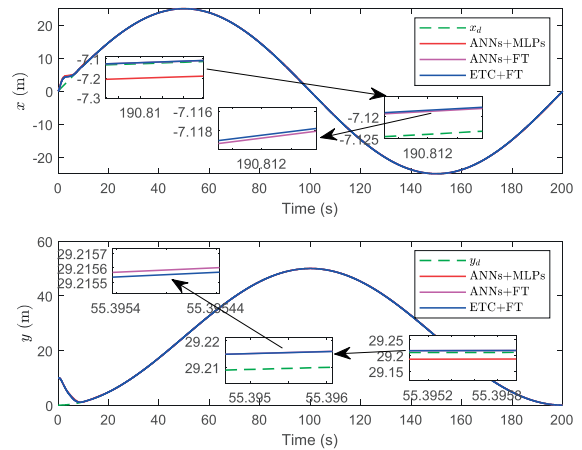Fig. 3 Actual and reference trajectories in the (x, y) plane

Fig. 4 Actual and reference positions
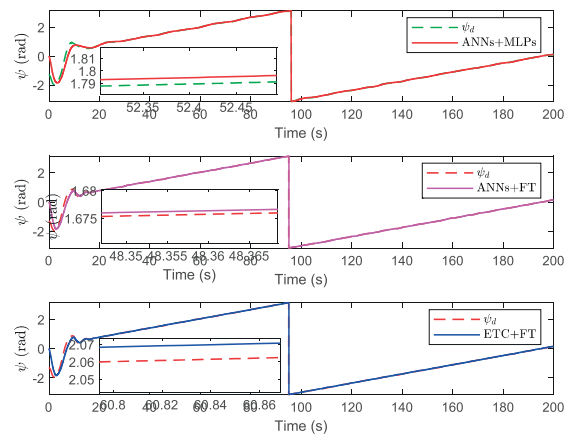
Fig. 5 Actual and reference yaw angles

Fig .6 Surge velocity u

Fig.7 Yaw rate r
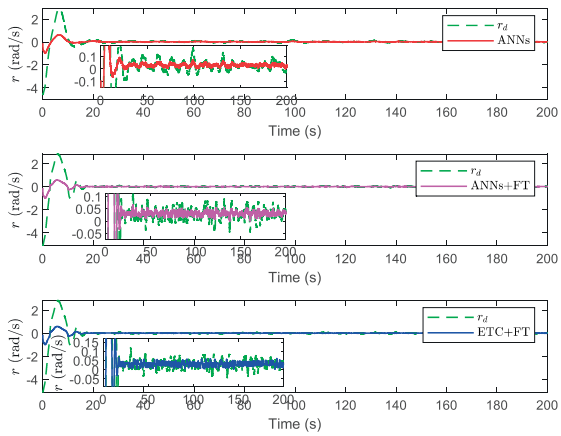
Fig. 8 Time evolution of the attitude errors

Fig. 9 Time evolution of the velocity errors
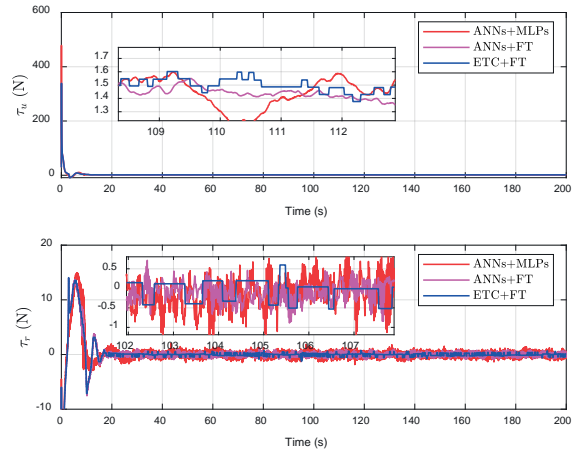
Fig. 10 Control input of τ_i ($i = u, r$)
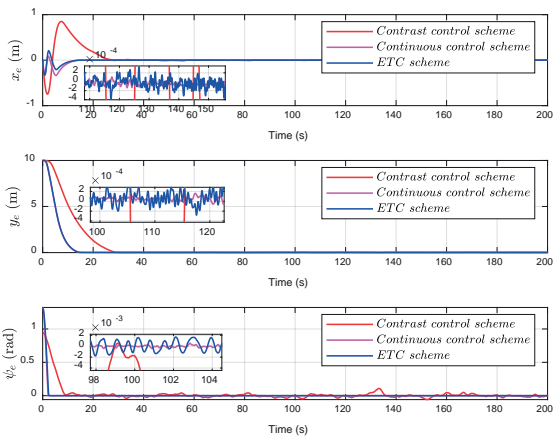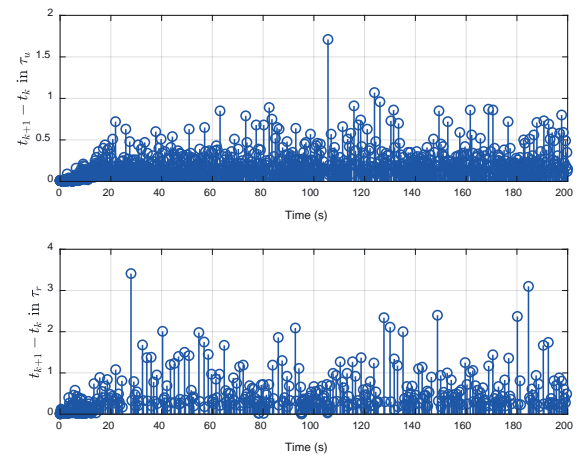
Fig. 11 Simulation of inter-event times

The simulation results for the trapezoidal trajectory are shown in Figs. 12–20. From the tracking effect and the error time curve, we see that the two control schemes proposed in this paper performed better than the control schemes without finite time and event triggering, and that the performance of the finite-time control scheme was not degraded when event triggering was added. As the trapezoidal trajectory was composed of multiple smaller trajectories, overshoot occurred at the points of trajectory switching. However, the tracking accuracy of the ET control scheme and the finite-time control scheme was better than for the non-ET and finite-time control schemes. Moreover, the results showed that the two control schemes presented in this paper could accomplish the task of tracking better under the condition of constant controller parameters. It is not difficult to see that the two control schemes designed in this paper have stronger robustness. As shown in Fig. 18, the ephemeral curves for the control inputs show that the number of controller updates was significantly reduced after the introduction of event triggering to the system.
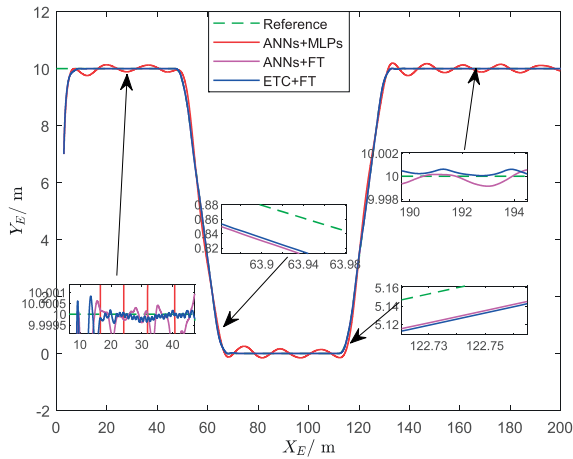
Fig. 12 Actual and reference trajectories in the $(x\ y)$ plane
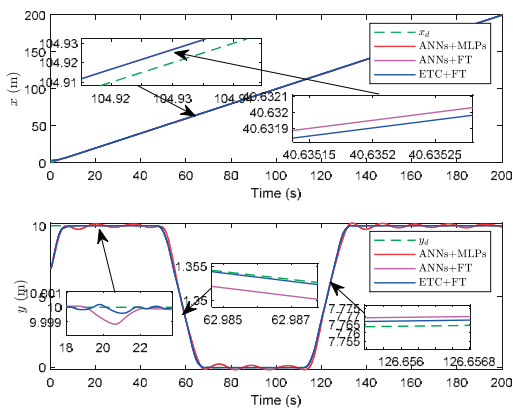
Fig. 13 Actual and reference positions
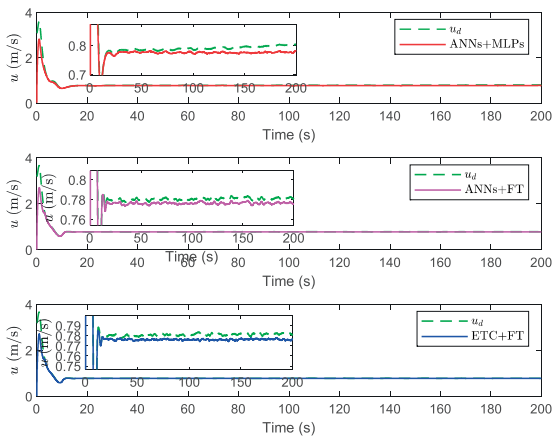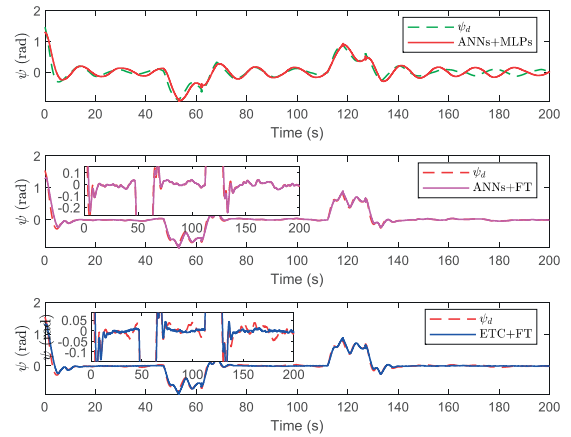

Fig. 14 Actual and reference yaw angles
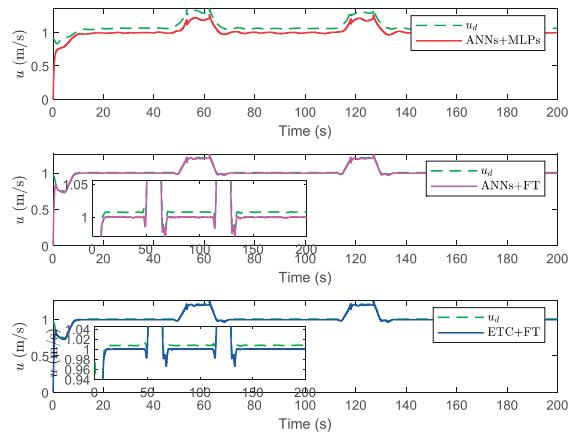
Fig. 15 Surge velocity u
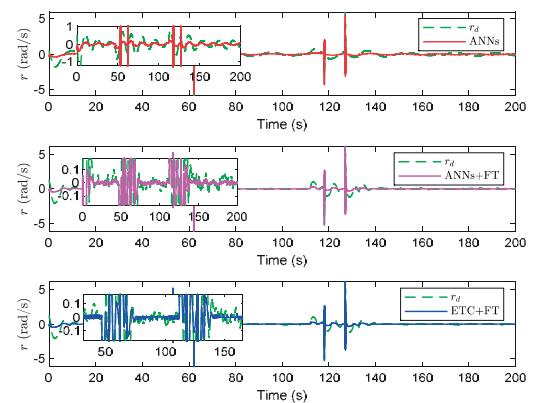
Fig. 16 Yaw rate r
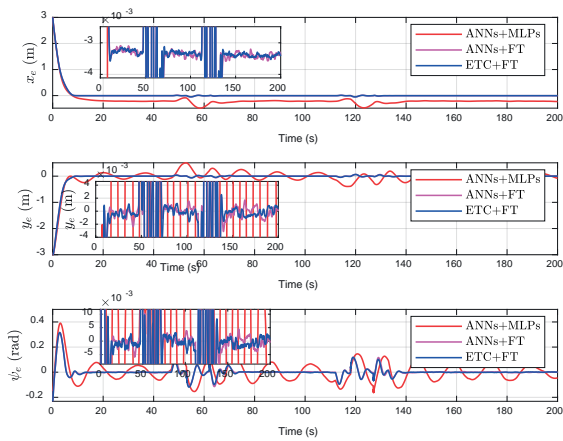
Fig. 17 Time evolution of the attitude errors
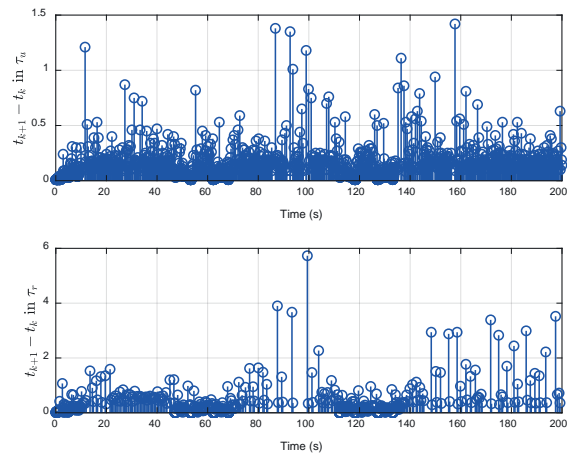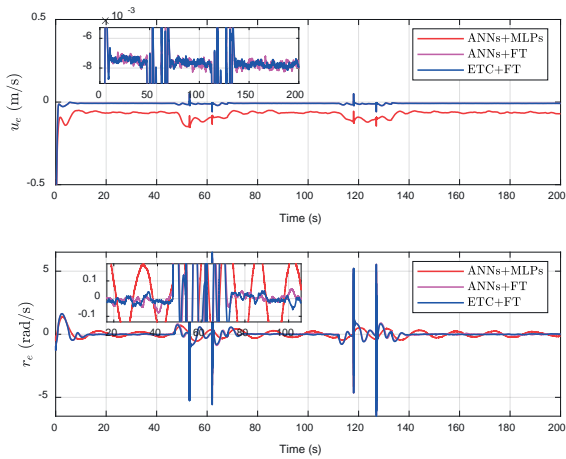
Fig. 18 Time evolution of the velocity errors

Fig. 19 Control input of τ_i ($i = u, r$)

Fig. 20 Simulation of inter-event times
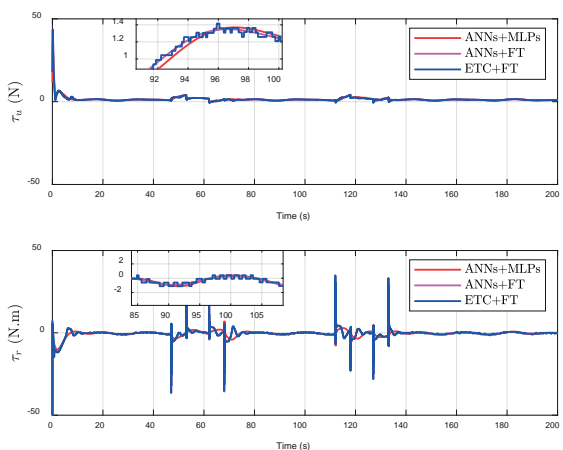
CONCLUSION

With the aim of tackling the problem of trajectory tracking for underactuated ships affected by internal and external uncertainties, this paper has presented an adaptive NN ET trajectory tracking control scheme for underactuated ships based on finite time convergence. The introduction of finite time was shown to greatly accelerate the convergence of system errors, and to further improve the tracking accuracy of the system. When combined with event triggering, the number of controller updates was also significantly reduced under the condition of ensuring the control accuracy of the system.

Compared with existing trajectory tracking control schemes, the controller structure of the control scheme in this paper is simpler and more suitable for engineering applications. However, the upper bound on the composite perturbation was approximated by an adaptive law with certain conservativeness, and the event trigger condition considered in this paper was essentially a static trigger. Further research is needed to design a more accurate perturbation compensation scheme and an event trigger condition that is more in line with engineering reality.

REFERENCES

1. H. W. He, Z. J. Zou, and Z. H. Zeng, 'Adaptive neural network-sliding mode path following control for underactuated surface vessels,' Journal of Shanghai Jiaotong University, 2020, 54(09): 890-897, doi: 10.16183/j.cnki.jsjtu.2019.122.

2. H. Y. Xu, M. F. Zhu, W. Z. Yu, and X. Han, 'Robust adaptive control of automatic berthing for intelligent ships,' Journal of Huazhong University of Science and Technology (Natural Science Edition), 2020, 48(03): 25-29+40, doi: 10.13245/j.hust.200305.

3. N. Wang and H. R. Karimi, 'Successive waypoints tracking of an underactuated surface vehicle,' IEEE Transactions on Industrial Informatics, 2020, 16(2): 898-908, doi: 10.1109/TII.2019.2922823.

4. K. Jonghoek, 'Target following and close monitoring using an unmanned surface vehicle,' IEEE Transactions on Systems Man & Cybernetics Systems, 2020, 50(11): 4233-4242, doi: 10.1109/TSMC.2018.2846602.

5. G. Zhu, Y. Ma, and S. Hu, 'Single parameter learning based finite-time tracking control of underactuated MSVs under input saturation,' Control Engineering Practice, 2020, 105, doi: 10.1016/j.conengprac.2020.104652.

6. G. Zhu, Y. Ma, and Z. Li, 'Event-triggered adaptive neural fault-tolerant control of underactuated MSVs with input saturation,' IEEE Transactions on Intelligent Transportation Systems, 2021, PP (99): 1-13, doi: 10.1109/TITS.2021.3066461.

7. Y. Ma, G. Zhu, and Z. L, 'Error-driven-based nonlinear feedback recursive design for adaptive NN trajectory tracking control of surface ships with input saturation,' IEEE Intelligent Transportation Systems Magazine, 2019, PP (2): 1-1. doi:10.1109/MITS.2019.2903517.

8. C. J. Zhang, C. Wang, and W. Cao, 'Underactuated USV neural network adaptive trajectory tracking control,' Journal of Harbin Institute of Technology, 2020, 52(12): 7-13 doi: 10.11918/201905049.

9. W. J. Wang and J. Li, 'A direct adaptive sliding mode trajectory tracking control design based on an RBF neural network,' Machinery Design & Manufacture, 2020(11): 183-187, doi: 10.19356/j.cnki.1001-3997.2020.11.046.

10. N. Wang and H. He, 'Dynamics-level finite-time fuzzy monocular visual servo of an unmanned surface vehicle,' IEEE Transactions on Industrial Electronics, 2020, 67(11): 9648-9658, doi: 10.1109/TIE.2019.2952786.

11. Y. Cheng, Z. Sun, and Y Huang, 'Fuzzy categorical deep reinforcement learning of a defensive game for an unmanned surface vessel,' International Journal of Fuzzy Systems, 2019, 21(2): 592-606, doi: 10.1007/s40815-018-0586-0.

12. Y. Lu, 'Adaptive-fuzzy control compensation design for direct adaptive fuzzy control,' IEEE Transactions on Fuzzy Systems, 2018, 26(6): 3222-3231, doi: 10.1109/TFUZZ.2018.2815552.

13. N. Wang, Z. Sun, and J. Yin, 'Fuzzy unknown observer-based robust adaptive path following control of underactuated surface vehicles subject to multiple unknowns,' Ocean Engineering, 2019, 176: 57-64, doi: 10.1016/j.oceaneng.2019.02.017.

14. Y. Deng, X. Zhang, and N. Im, 'Adaptive fuzzy tracking control for underactuated surface vessels with unmodeled dynamics and input saturation,' ISA Transactions, 2020, 103, doi: 10.1016/j.isatra.2020.04.010.

15. D. Mu, G. Wang, and Y. Fan, 'Trajectory tracking control for underactuated unmanned surface vehicle subject to uncertain dynamics and input saturation,' Neural Computing and Applications, 2021, (6), doi: 10.1007/s00521-021-05922-x.

16. X. Zhang, 'Backstep sliding mode control for trajectory tracking of underactuated surface unmanned vehicles,' Digital Technology & Application, 2020, 38(01): 180-183, doi: CNKI:SUN:SZJT.0.2020-01-090.

17. S. Wang and Y. Tuo, 'Robust trajectory tracking control of underactuated surface vehicles with prescribed performance,' Polish Maritime Research, 2020, 27(4): 148-156, doi: 10.2478/pomr-2020-0075.

18. N. Wang, Y. Gao, and H. Zhao, 'Reinforcement learning-based optimal tracking control of an unknown unmanned surface vehicle,' IEEE Transactions on Neural Networks and Learning Systems, 2020, PP(99): 1-12, doi: 10.1109/TNNLS.2020.3009214.

19. B. Qiu, G. Wang, and Y. Fan, 'Path following of underactuated unmanned surface vehicle based on trajectory linearization control with input saturation and external disturbances,' International Journal of Control Automation and Systems, 2020, 18(4): 1-12, doi: 10.1007/s12555-019-0659-3.

20. Q. Zhang, Z. Ding, and M. Zhang, 'Adaptive self-regulation PID control of course-keeping for ships,' Polish Maritime Research, 2020, 27(1): 39-45, doi: 10.2478/pomr-2020-0004.

21. D. D. Wang, Q. Zong, and B. Y. Zhang, 'Fully distributed limited-time formation control of multiple UAVs,' Control

and Decision, 2019, 34(12): 154-158, doi: 10.13195/j. kzyjc.2018.0314.

22. N. Wang and C. K. Ahn, 'Hyperbolic-tangent LOS guidance-based finite-time path following of underactuated marine vehicles,' IEEE Transactions on Industrial Electronics, 2020, 67(10): 8566-8575, doi: 10.1109/TIE.2019.2947845.

23. M. Y. Hu, S. H. Yu, and Y. Y. Li. 'Finite time trajectory tracking control of ocean surface vessels based on command filtering with full state constraints,' Journal of Nanjing University of Science and Technology, 2021, 45(3): 10, doi: 10.14177/j.cnki.32-1397n.2021.45.03.003.

24. H. L. Chen, H. X. Ren, and B. C. Yang, 'Design of finite time controller for ship dynamic positioning based on LS-SVM,' Ship Engineering, 2020, 42(2): 8, doi: 10.13788/j. cnki.cbgc.2020.02.14.

25. P. Tabuada, 'Event-triggered real-time scheduling of stabilizing control tasks,' IEEE Transactions on Automatic Control, 2007, 52(9): 1680-1685, doi: 10.1109/ TAC.2007.904277.

26. A. Girard, 'Dynamic triggering mechanisms for event-triggered control,' IEEE Transactions on Automatic Control, 2013, 60(7): 1992-1997, doi: 10.1109/TAC.2014.2366855.

27. W. Heemels and M. Donkers, 'Model-based periodic event-triggered control for linear systems,' Automatica, 2013, 49 (3): 698-711, doi: 10.1016/j.automatica.2012.11.025.

28. S. Gao, Z. Peng, and L. Liu, 'Coordinated target tracking by multiple unmanned surface vehicles with communication delays based on a distributed event-triggered extended state observer,' Ocean Engineering, 2021, 227(4): 108283, doi: 10.1016/j.oceaneng.2020.108283.

29. S. J. Yoo and B. S. Park, 'Guaranteed connectivity based distributed robust event-triggered tracking of multiple underactuated surface vessels with uncertain nonlinear dynamics,' Nonlinear Dynamics, 2020, 99(3): 2233-2249, doi: 10.1007/s11071-019-05432-5.

30. Y. Deng, X. Zhang, and N. Im, 'Model-based event-triggered tracking control of underactuated surface vessels with minimum learning parameters,' IEEE Transactions on Neural Networks and Learning Systems, 2020, 31(10): 1-14, doi: 10.1109/TNNLS.2019.2951709.

31. F. Wang, B. Chen, and X. Liu, 'Finite-time adaptive fuzzy tracking control design for nonlinear systems,' IEEE Transactions on Fuzzy Systems, 2017, 26(3), 1207-1216, doi: 10.1109/TFUZZ.2017.2717804.

32. W. T. Wu, N. Gu, and Z. H. Peng, 'Distributed time-varying formation control of multi-pilot guided unmanned ship swarms,' Chinese Journal of Ship Research, 2020, 15(01): 21-30, doi: 10.19693/j.issn.1673-3185.01734.

33. Q. Zhang, G. Zhu, and X. Hu, 'Adaptive neural network auto-berthing control of marine ships,' Ocean Engineering, 2019, 177(APR.1): 40-48, doi: 10.1016/j.oceaneng.2019.02.031.

34. B. Xu and Y. Shou, 'Composite learning control of MIMO systems with applications,' IEEE Transactions on Industrial Electronics, 2018, PP(99):1-1, doi: 10.1109/ TIE.2018.2793207.

35. M. Li, T. Li, and X. Gao, 'Adaptive NN event-triggered control for path following of underactuated vessels with finite-time convergence,' Neurocomputing, 2020, 379(Feb.28): 203-213, doi: 10.1016/j.neucom.2019.10.044.

36. Q. Zhang, M. Zhang, and R. Yang, 'Adaptive neural finite-time trajectory tracking control of MSVs subject to uncertainties,' International Journal of Control Automation and Systems, 2021, 19(6): 2238-2250, doi: 10.1007/s12555-020-0130-5.

37. Y. Huang and Y. Jia, 'Adaptive fixed-time six-DOF tracking control for noncooperative spacecraft fly-around mission,' IEEE Transactions on Control Systems Technology, 2019, 27(4): 1-9, doi: 10.1109/TCST.2018.2812758.

38. R. Skjetne, T. I. Fossen, and P. V. Kokotovi, 'Adaptive maneuvering, with experiments, for a model ship in a marine control laboratory,' Pergamon Press, Inc. 2005, 41(2): 289-298.

39. C. Y. Wu, L. L. Fan, and H. H. Ji, 'Finite-time consensus control by using adaptive neural networks control,' Engineering of China, 2022, 29(03): 455-463, doi: 10.14107/j. cnki.kzgc.20210489.

40. Q. Zhang, Y. C. Hu, and A. Q. Wang, 'Nonlinear adaptive control algorithm based on dynamic surface control and neural networks for ship course-keeping controller,' Journal of Applied Science and Engineering, 2017, 20(2): 157-163, doi: 10.6180/jase.2017.20.2.03.

FAULT DIAGNOSIS OF BEARINGS BASED ON SSWT, BAYES OPTIMISATION AND CNN

Guohua Yan ⓘD
Yihuai Hu * ⓘD
Qingguo Shi ⓘD
 Merchant Marine College, Shanghai Maritime University, China

* Corresponding author: *yhhu@shmtu.edu.cn (Yihuai Hu)*

ABSTRACT

Bearings are important components of rotating machinery and transmission systems, and are often damaged by wear, overload and shocks. Due to the low resolution of traditional time-frequency analysis for the diagnosis of bearing faults, a synchrosqueezed wavelet transform (SSWT) is proposed to improve the resolution. An improved convolutional neural network fault diagnosis model is proposed in this paper, and a Bayesian optimisation method is applied to automatically adjust the structure and hyperparameters of the model to improve the accuracy of bearing fault diagnosis. Experimental results from the accelerated life testing of bearings show that the proposed method is able to accurately identify various types of bearing fault and the different status of these faults under complex running conditions, while achieving very good generalisation ability.

Keywords: Fault diagnosis; Bearing; PMSM; Bayesian optimisation; CNN

INTRODUCTION

As bearings support the rotation of rotating bodies, they are important components of rotating machinery and transmission systems, and are widely used in industrial production and transportation. In harsh working environments, such as in ocean-going ships, bearings work at high temperatures and humidity, under corrosion from salt and alkalis, and are overloaded for long periods; they are therefore subject to wear and impact over the long term, which makes them extremely prone to various types of failure. In some types of equipment, bearings are the components that are most prone to failure. A statistical analysis has shown that the failure rate of bearings accounts for 30–40% of total motor failures [1], meaning that fault diagnosis of bearings could reduce or even prevent accidents, with very significant effects in terms of ensuring the safety of personnel and equipment.

Over the past few decades, researchers and engineers have developed a variety of methods for the diagnosis of bearing faults, which can be divided into analytical model-based, signal-based, and data-driven approaches [2]. Analytical model-based methods require a very good understanding of the operating mechanism of the motor and an accurate mathematical model, and diagnose the fault by analysing the difference between the model output and the actual output [3]. This method has poor flexibility and capability, and cannot be adapted to complex real-world applications. Signal-based methods do not require a complete model, and extract the features of the fault on the device from the time domain, frequency domain, or time-frequency domain [4]. Machine learning algorithms such as support vector machine (SVM) [5], an error backpropagation neural network (BPNN) [6] or K-means [7] can also be used to diagnose a fault; however, each feature extraction algorithm has certain limitations, and the extraction determines the final

result of diagnosis. Data-driven methods rely on big datasets, and can establish a mapping relationship between signals and faults from a large amount of historical data. They are very suitable for fault diagnosis in noisy environments.

Unlike traditional machine learning algorithms such as SVM and BPNN, deep learning algorithms with multiple nonlinear layers have a multi-layer feature learning capability, and can extract more high-quality feature information from a large amount of data; this means they can solve the problems inherent to traditional machine learning, and they are therefore widely used for bearing fault diagnosis. Deep autoencoders, deep belief networks, recurrent neural networks and convolutional neural networks (CNNs) are the most commonly used deep learning models for fault diagnosis [8]. Of these, the CNN is one of the most important, and has become a leading and fast-growing architecture for fault diagnosis. Zhang et al. [9] proposed a one-dimensional CNN algorithm for fault diagnosis from rotating machinery based on residual learning, which was shown to have higher accuracy than other commonly used deep learning fault diagnosis models. Pan et al. [4] proposed a combination of a one-dimensional CNN and an LSTM for bearing fault diagnosis, which made full use of the powerful feature extraction capability of the CNN and the good temporal modelling property of LSTM. Huang et al. [10] proposed a one-dimensional deep decoupled CNN fault diagnosis model that identified single and compound faults via feature learning and decoupled classification. However, the power of the CNN lies in its image processing capability, and there are many fault diagnosis methods that use two-dimensional CNNs. Time-frequency domain signal preprocessing methods are often used in combination with two-dimensional CNNs: this method uses time-frequency domain signal processing techniques to generate time-frequency spectra, and then exploits the powerful image processing capability of CNN to diagnose motor bearing faults. The wavelet transform (WT) method is a commonly used time-frequency analysis method. The WT time-frequency spectrum is based on wavelets, with the addition of time and scale variables, and can effectively handle nonstationary nonlinear signals. Ding et al. [11] proposed a multi-scale bearing fault feature extraction method with energy fluctuations using a wavelet packet energy map and a deep convolutional network. Verstraete et al. [12] used a WT, a short-time Fourier transform and a Hilbert-Huang transform (HHT) of the time-frequency spectrum as the input to a CNN to achieve automatic feature extraction and classification.

Although a WT has a high time-frequency resolution, it is still affected by the Heisenberg uncertainty principle, and the time-frequency resolution is somewhat limited, which makes the time-frequency spectrum blurred [13] and reduces the effectiveness of feature extraction in practical environments. In order to accurately describe nonstationary nonlinear vibration signals, many new methods have been proposed that improve on traditional WT methods, such as the synchrosqueezed WT (SSWT) [14] and the dual-core noise-reducing simultaneous squeezed WT [15]. Of these, SSWT is the most traditional, with good noise immunity and time-frequency resolution, and high robustness.

A CNN is a multi-layer feed-forward neural network, and a deep-learning-based CNN fault diagnosis model typically consists of two parts: filtering and classification. The filter stage is mainly used to extract the features of the input data, and includes a convolution layer, a batch normalisation layer, an active layer and a pooling layer. The classification module processes and classifies the extracted features, and includes a dropout layer and a fully connected layer. The training efficiency of a CNN is improved by reducing the number of parameters for model training through a parameter sharing mechanism and the use of sparse connections between the filtering and classification levels [16]. A CNN has a complex structure with many hyperparameters, and there is no mature theory to guide the design of the network structure; a trial-and-error method is generally used, and the results of experience and training are combined in an effort to obtain the right network architecture and hyperparameters. This requires numerous attempts and a considerable amount of time, and therefore poses a great challenge. Many hyperparameter optimisation methods have been developed, such as grid search, stochastic search, dynamic resource allocation, and Bayesian optimisation. Of these, Bayesian optimisation is notable as a classical adaptive optimisation method that takes the current optimal hyperparameters as a reference and predicts the next combination that will offer the greatest benefit.

To solve problems such as a blurred spectrum, a high level of noise and the difficulty of CNN design for traditional WT, a SSWT-Bayes-CNN fault diagnosis model is proposed in this paper. First, the SSWT method is used to increase the accuracy of representation of nonlinear, non-smooth vibration signals and to reduce noise interference in the signal. The SSWT time-frequency spectrum is used as input to the CNN, and the Bayesian optimisation algorithm is applied to achieve automatic optimisation of network hyperparameters, thereby reducing the dependence on network design experience. This process finally creates a high-performance CNN architecture, and can achieve rapid deployment of a bearing fault diagnosis model.

FAULT DIAGNOSIS METHOD BASED ON SSWT, BAYES OPTIMISATION AND CNN

SSWT

SSWT is a new mathematical transform tool that was developed on the basis of the WT, in a similar way to empirical mode decomposition (EMD) [17]. The WT can be seen as the result of a folded product of the signal with the mother wavelet after a telescopic translation, which forms the time-frequency spectrum and completes the sparse representation of the signal. The SSWT transform of the time signal $f(t)$ is based on the wavelet transform as [17]:

$$W_S(a, b) = \langle f(t), \varphi_{a, b}(t) \rangle = \frac{1}{\sqrt{a}} \int_{-\infty}^{+\infty} s(t) \varphi^*\left(\frac{t-b}{a}\right) dt \quad \text{(1)}$$

where $W_S(a, b)$ are the wavelet coefficients, and $\langle f(t), \varphi_{a, b}(t) \rangle$ denotes the wavelet transform of the vibration signal $f(t)$. $\varphi(a, b)$

is the wavelet function, which is obtained from scaling and translating the wavelet basis function φ, i.e. [18]:

$$\varphi_{a,b}(t) = \frac{1}{\sqrt{a}} \varphi(\frac{t-b}{a}) \qquad (2)$$

where a, b are the scaling and scale factors, respectively, . The coefficient is normalised to the wavelet energy. According to Plancherel's theorem, Equation (1) can be written as an expression in the wave number domain, as follows [17]:

$$W_S(a,b) = \frac{A\sqrt{a}}{4\pi} \varphi^*(a\omega)e^{ib\omega} \qquad (3)$$

Using the relationship between scale and frequency, the computed wavelet coefficients $W_S(a,b)$ can be mapped from the time scale plane to the time-frequency plane $(b,a) \to b$, $W_S(a,b)$. The coefficients of SSWT lie only in the frequency interval $[(\omega_l-\Delta\omega/2), (\omega_l+\Delta\omega/2)]$, centered at ω, while $\Delta\omega=\omega_l-\omega_{l-1}$. Since the scaling factor a and the scale factor b are discrete values, a scaling step $\Delta a_k=a_k-a_{k-1}$ is taken to isolate the discrete scale a_k [18], and then its wavelet decomposition is computed using Equation (3). The SSWT is [14]:

$$T_S(\omega_l, b)=(\Delta\omega)^{-1} \sum_{a_k:[W(a_k,b)-W_l]\leq\Delta\ a_k} W_S(a_k, b)a_k^{-3/2}\Delta a_k \quad (4)$$

From Equation (4), it can be seen that the SSWT compresses the wavelet coefficients only in the frequency direction. This compression process preserves the phase information of the wavelet coefficients, and the simultaneous compression WT can be reconstructed with the inverse transform as [14]:

$$S(b) = Re[C_\Psi^{-1} \sum T_S(\omega_l, t) (\Delta\omega) \qquad (5)$$

To illustrate the advantages of SSWT, a simple segment of the signal $f(t)$ was constructed with the following signal:

$$f(t) = 2sin(600t)+3sin(300t)+5sin(150t) \qquad (6)$$

Noise with a signal-to-noise ratio (SNR) of 15 dB was added to the signal $f(t)$ to simulate a complex signal with nonlinear nonstationarity, and three mainstream time-frequency analysis methods Continuous Wavelet Transform (CWT), HHT and SSWT) were applied to the signal $f(t)$ for comparison. The results are shown in Fig. 1. CWT has a very vague time-frequency performance, whereas HHT can clearly express the main components of the signal, although the resolution is not high and the detection band is wide. Unlike the vague time-frequency information representation of CWT, SSWT overcomes the problem of low time-frequency resolution of the signal, and characterises the time-frequency relationship of the signal more clearly and accurately.

BAYESIAN OPTIMISATION

The Bayesian optimisation algorithm can predict the maximum of a function based on existing sample points when the equation of the function is unknown. Its probabilistic agent model uses Gaussian processes (GPs). In our deep learning model, the combination of hyperparameters to be optimised is assumed to be $x=\{x_1, x_2..., x_n\}$. The objective function $f(x)$ of the Bayesian optimisation algorithm is the classification error of the trained deep learning model on the validation set. The classification of each dataset in the test set is considered an independent event with a certain probability of success, meaning that the number of datasets with classification errors follows a binomial distribution [19]:

$$f(t) = GP(\mu, k(x,x)) \qquad (7)$$

where GP is the Gaussian distribution, μ is the mean, and $k(x,x)$ is the covariance function.

After $n-1$ iterations of the Bayesian optimisation algorithm on the dataset $D_{n-1}=\{(x_1, f(x_1)), (x_2, f(x_2)),...,(x_{n-1}, f(x_{n-1}))\}$, the next step is to predict the observation $f(x_n)$ at the point x_n. It is generally assumed that these n observations are samples of an n-dimensional Gaussian distribution, i.e.:

$$[\frac{f_{1:n-1}}{f_n}] \sim GP(\mu, [\frac{K,k^T}{k,k(x_n,x_t)}]) \qquad (8)$$
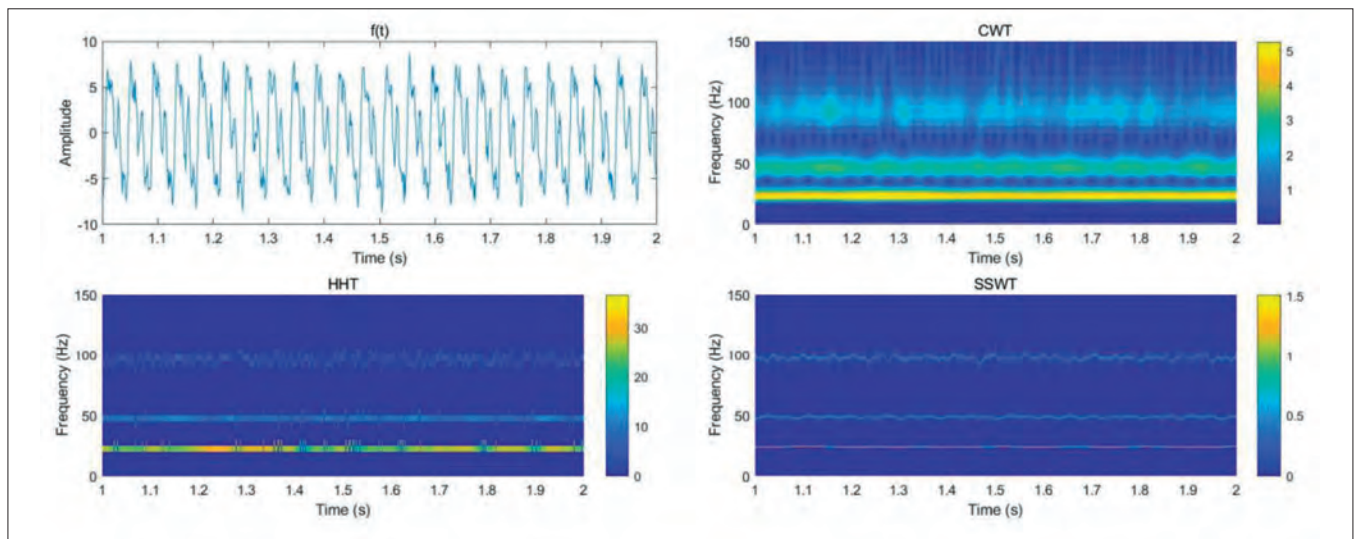

Fig. 1. SSWT and CWT time spectra

where
$$K = \begin{bmatrix} k(x_1, x_1) & \cdots & k(x_1, x_{n-1}) \\ \vdots & \ddots & \vdots \\ k(x_{n-1}, x_1) & \cdots & k(x_{n-1}, x_{n-1}) \end{bmatrix},$$

$$k = \left[(x_n, x_1), (x_n, x_2), \ldots, (x_n, x_{n-1}) \right].$$

This gives a Gaussian distribution for f_n:

$$P(f_n | D, x_n) = GP(\mu(x_n), \delta^2(x_n)) \qquad \textbf{(9)}$$

where $u(x_i)=kK^{-1}f_{1:n-1}$ is the predicted mean, and $\delta^2(x_n)=k(x_n, x_n)-kK^{-1}k^T$ is the predicted covariance. $(x_n, f(x_n))$ is the final data item for the nth observation point.

In order to use as few samples as possible, to make the Gaussian distribution of f_n closer to the true distribution, and to reduce the number of samples taken from the sample space, the acquisition function is used to determine whether a sample can can improve the model. The larger the gain, the closer the modified Gaussian process will be to the true distribution of objective function. The expected improvement (EI) function can reduce the probability of local optimisation, and is therefore chosen as the acquisition function.

IMPROVED CNN MODEL

The current trend in CNN models is to increase the number of network layers and decrease the size of the convolutional kernels. Smaller convolutional kernels can obtain better local information, whereas deeper networks can obtain better global information. An improved CNN model is proposed as shown in Fig. 2. In Conv_1, the number of layers is indeterminate for information filtering, feature extraction and size compression of the SSWT time spectrum, where the number of layers is determined by the actual needs. Each convolutional layer in Conv_1 includes batch normalisation (BN) to speed up convergence of the network and prevent overfitting, and ReLU is used as the activation function. Conv_2 and Conv_3 have the same internal structure and number of layers as Conv_1; the only difference is that Conv_1 uses 16 convolutional kernels, whereas Conv_2 uses 32 and Conv_3 uses 64. The number of convolutional kernels increases with the depth of the network. The deeper the network, the smaller the computation, and the additional convolutional kernels can use these computational capabilities. In addition, the deeper the network, the more abstract the feature information that is extracted. An increase in the number of convolutional kernels allows the feature information previously learned by the network to be better combined, meaning that various features

can be covered more comprehensively. The fully connected layer (FC) can obtain all the feature information extracted from the convolutional layer, but it suffers from too many parameters and redundancy, which tends to cause overfitting of the network. The addition of another FC layer can improve the overfitting situation, but makes the network more bloated. The Global Average Pooling (GAP) layer can integrate the high-dimensional information output from the convolutional layer, thus directly achieving a significant reduction in the number of feature parameters. This layer has no parameters, thereby avoiding overfitting, and has better robustness. The final classification layer applies a softmax function, which is used to output the probability of each fault.

BEARING FAULT DIAGNOSIS BASED ON BAYESIAN OPTIMISATION AND CNN

The hyperparameters of the CNN model have an important impact on the training process and model representation, and include the depth of the convolutional layer n, the momentum factor, the L2 regularisation, and the initial learning rate. Overfitting means that although the model has a very low error on the training set (original dataset), it has a very high error on the unseen test set (new dataset), i.e. the model has poor generalisation ability, and cannot be generalised effectively from the original dataset to another dataset. Underfitting means that the model cannot obtain a sufficiently low error on the training set. The larger the size of the L2 regularisation parameter, the stricter the constraint, and the easier it is to cause underfitting of the model. If the parameter is too small, the constraint is loose, and does not act as a constraint, which tends to produce overfitting [20]. An initial learning rate that is too large will result in a model that fails to converge and an unstable training process, whereas a rate that is too small will result in a model that converges particularly slowly or fails to learn. The momentum-based stochastic gradient descent method (SGDM) introduces a momentum factor that ameliorates the problem of traditional stochastic gradient descent (SGD) oscillations. When the network tends to converge in the middle and late stages of training, the network parameters oscillate back and forth around local minima, which also helps the network to jump out of local boundaries and find better network parameters. If the momentum factor is too high, it may cause the model to oscillate in the parameter space and fail to converge stably, whereas a momentum factor that is too small may cause the model to converge too slowly or even to fall into a local minimum. The hyperparameters of the Bayesian optimisation-based CNN bearing fault diagnosis model are the convolutional layer depth n, the momentum factor, the L2
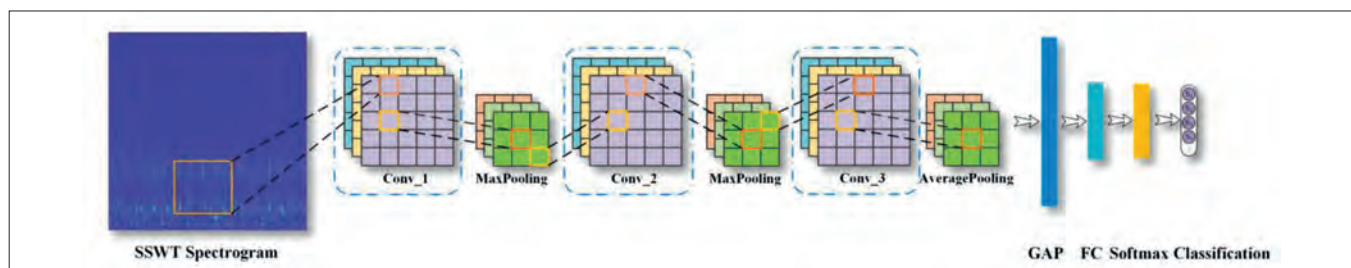

Fig. 2. Improved CNN model

regularisation, and the initial learning rate, as shown in Fig. 3. In general, when a supervised deep learning model is trained, the data are divided into training, validation and test sets. The results on the validation set can accurately reflect the current training status of the network, and can verify the generalisation ability of the model. The error on the validation set after completion of training is therefore used in this paper as the objective function for Bayesian optimisation, denoted as $f(x)$, and the optimisation objective is to minimise the error on the validation set.
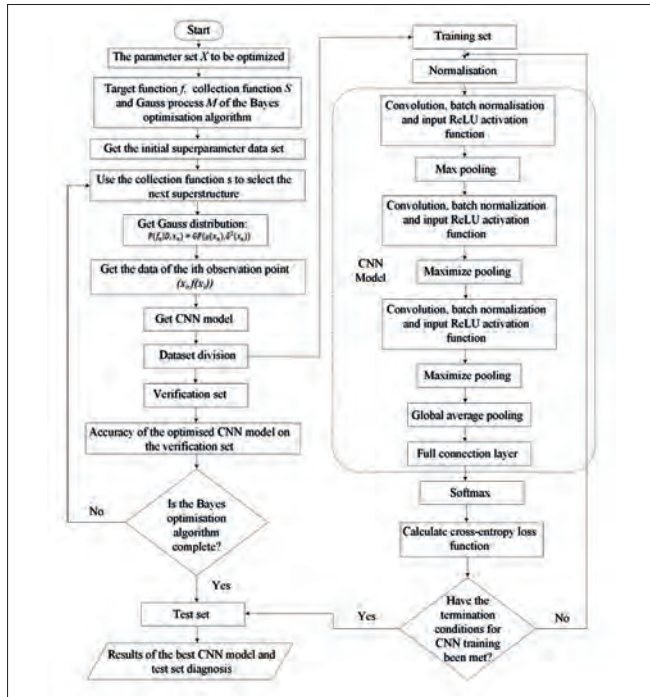
Fig.3. Fault diagnosis model based on Bayesian optimisation of a CNN

TEST ANALYSIS AND BEARING FAULT DIAGNOSIS

TEST DATA

The acquisition of high-quality bearing fault signals is still a difficult task, due to the limitations of data acquisition techniques, the time and cost required to obtain natural fault data, and other problems. Fortunately, some research institutions have published such datasets, including the Case Western Reserve University (CWRU) bearing dataset [21], the MFPT fault dataset [22], and the Paderborn dataset [23]. The CWRU dataset is one of the most commonly used for bearing fault diagnosis; however, all of the the bearings in this dataset are artificially damaged and operate under simple conditions, unlike actual bearings. The Paderborn dataset, provided by Paderborn University, Germany, contains a variety of fault types and severities; the working conditions of the bearings are diverse; both artificial and actual damage are considered; and the dataset is relatively comprehensive. Lessmeier et al. [23] carried out a detailed study using WPD and FFT to extract fault features, and compared the

results from popular machine learning classification algorithms such as a neural network (NN), random forest (RF) and SVM, which gave good accuracy on both artificial and actual damage datasets. However, when a model is trained on an artificial damage dataset and tested on actual damage dataset, poor diagnostic results are generally obtained. This indicates that there are significant differences between artificial damage and actual faults, and that artificial faults cannot accurately represent real ones. Hence, in order to more closely match the failure situation in real industrial scenarios, only real failure data are selected from accelerated life tests, as shown in Fig. 4. The dataset uses 6,203 grooved ball bearings, including single and repeated damage to the inner ring, single and repeated damage to the outer ring, and compound damage to the inner and outer rings. Based on the length of the damage and the percentage size of the pitch circumference, the faults are divided into five levels indicating their severity, as shown in Table 1.

(a) *Apparatus used for accelerated life time test*

(b) *Bearing damage from accelerated life test*
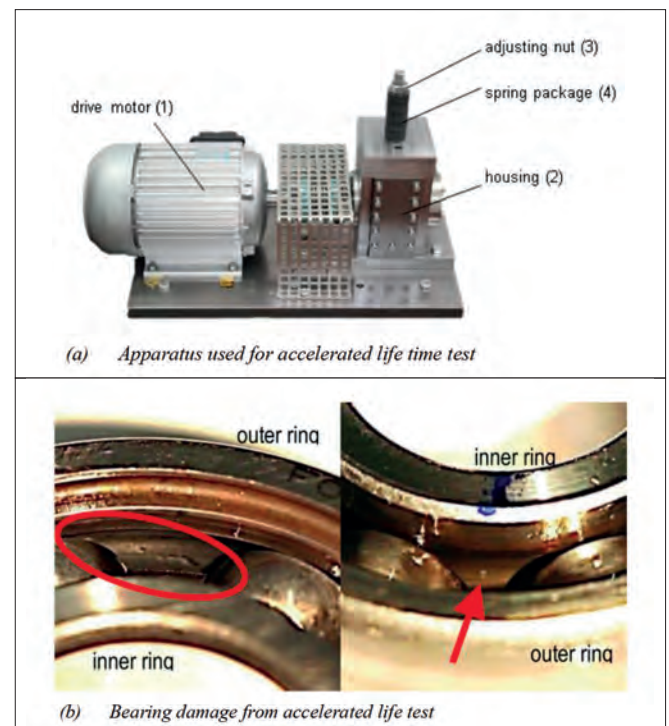
Fig.3. Fault diagnosis model based on Bayesian optimisation of a CNN

Tab. 1. Bearing fault levels [21]

Damage level	Assigned percentage values	Limits for bearing 6203
1	0–2%	≤ 2 mm
2	2–5%	> 2 mm
3	5–15%	> 4.5 mm
4	15–35%	> 13.5 mm
5	>35%	> 31.5 mm

The sampling frequency of the vibration signal was 64 kHz, the sampling length was 4 s, and a total of 20 samples were considered for each fault. Detailed information on the samples is shown in Table 2.

Bearing status	Working conditions	Damage level	Operating state
Health	• n = 700 r/min, M = 0.7 Nm • n = 1500 r/min, M = 0.1 Nm • n = 1500 r/min, M = 0.7 Nm	0	H
Damage to inner ring	• n = 700 r/min, M = 0.7 Nm • n = 1500 r/min, M = 0.1 Nm • n = 1500 r/min, M = 0.7 Nm	1	IR I
	• n = 700 r/min, M = 0.7 Nm • n = 1500 r/min, M = 0.1 Nm • n = 1500 r/min, M = 0.7 Nm	2	IR II
	• n = 700 r/min, M = 0.7 Nm • n = 1500 r/min, M = 0.1 Nm • n = 1500 r/min, M = 0.7 Nm	3	IR III
Damage to outer ring	• n = 700 r/min, M = 0.7 Nm • n = 1500 r/min, M = 0.1 Nm • n = 1500 r/min, M = 0.7 Nm	1	OR I
	• n = 700 r/min, M = 0.7 Nm • n = 1500 r/min, M = 0.1 Nm • n = 1500 r/min, M = 0.7 Nm	2	OR II
Damage to both inner and outer rings	• n = 700 r/min, M = 0.7 Nm • n = 1500 r/min, M = 0.1 Nm • n = 1500 r/min, M = 0.7 Nm	1	IR+OR I
	• n = 700 r/min, M = 0.7 Nm • n = 1500 r/min, M = 0.1 Nm • n = 1500 r/min, M = 0.7 Nm	2	IR+OR II
	• n = 700 r/min, M = 0.7 Nm • n = 1500 r/min, M = 0.1 Nm • n = 1500 r/min, M = 0.7 Nm	3	IR+OR III

SSWT PRE-PROCESSING

As can be seen from Table 2, there are nine possible operating states of the bearings under three different working conditions. For each working condition, the dataset contains 20 samples, meaning that it is very rich. Data of length 0.1 s are selected as samples. The original vibration data are sliced, with 9 working conditions and 2400 samples were obtained for each working condition, each sample length is 6400. Each sliced sample is

processed via SSWT to obtain a time-frequency spectrum of size 227×227×3, which is used as the input to the network. Fig. 5 shows the CWT and SSWT time-frequency spectra of the real bearing vibration signal. It can be seen that the SSWT method greatly improves the time-frequency resolution of the signal, and can express the time-frequency relationship of the signal more accurately and clearly.

OPTIMISATION OF THE CNN HYPERPARAMETERS

The SSWT time data were divided into three groups: a training set, a validation set and a test set. The test set for each working condition was a 240 fixed group, and the training set and validation set were randomly assigned in the ratio of 4:1 in the remaining sample. The final numbers of samples in the training, validation and test sets for each working condition were 1728, 432 and 240, respectively. The datasets were input into the CNN fault diagnosis model with the objective of minimising the validation set error,, and a Bayesian algorithm is used to optimise the four hyper-parameters in the model to find the minimum value of the objective function $f(x)$, as shown in Table 3. Table 4 shows the main options for training the CNN fault diagnosis model. To reduce the possibility of overfitting in the training process, data enhancement techniques were applied to the training set, including random scaling, rotation and panning of the images.

Tab. 3. Optimised hyperparameters and ranges

Hyperparameters	Search space	Data type
Section depth	1 – 3	int
Initial learning rate	$5×10^{-3}$ – 1	log
Momentum	0.8 – 0.98	log
L2 regularisation	$1×10^{-10}$ – 0.01	log
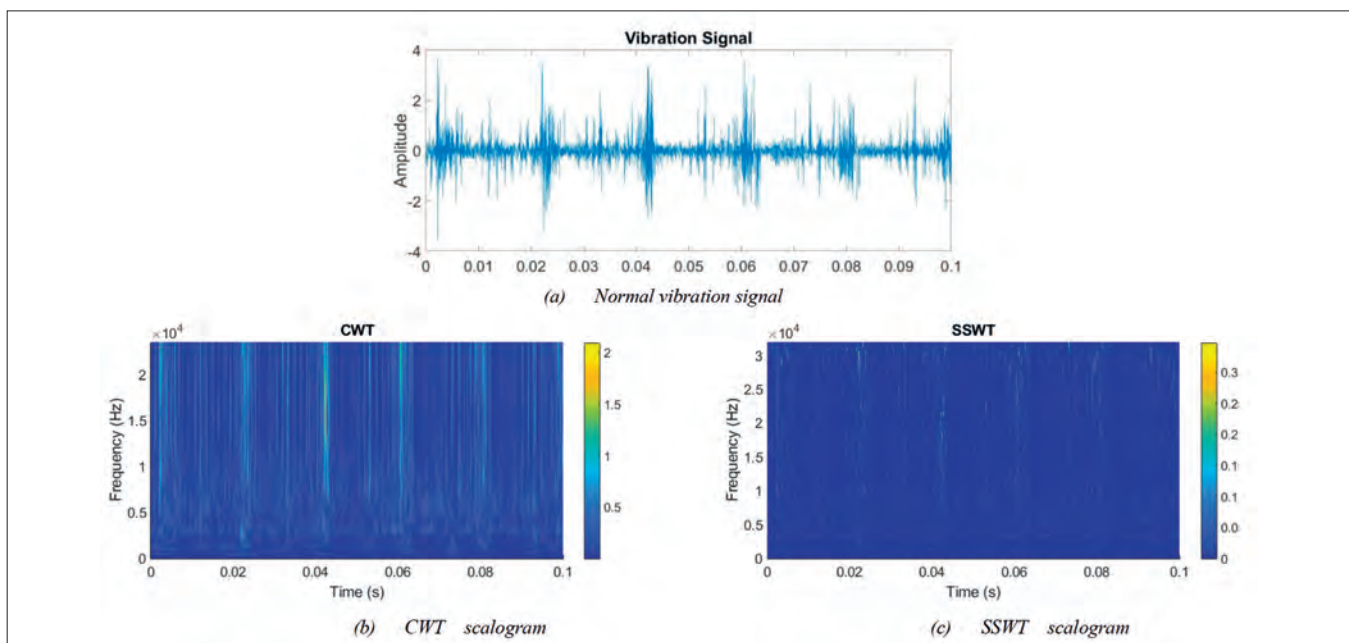
Fig. 5. CWT and SSWT time spectra for a normal bearing vibration signal

Optimisation algorithm	SGDM	Shuffle	Every epoch
Learning rate drop factor	0.5	Validation frequency	Every epoch
Learning rate drop period	10	MaxEpochs	50
Learn rate schedule	Piecewise	Minibatch size	128

The number of Bayesian optimisations was set to 35, to train the CNN fault diagnosis model using the SGDM optimiser, the optimiser stores the hyperparameters for each optimisation and the accuracy of the validation set. The prediction of the current objective function was calculated by a Gaussian process, nd the next set of hyperparameters are selected using the gain function. The CNN model was retrained using new hyperparameters for ,Fig. 6 shows the minimum objective function versus the number of Bayesian optimisations, and it can be seen that the minimum objective function is obtained after the 23rd optimisation, which represents the optimal combination of hyperparameters. The depth of the CNN network is three, the initial learning rate is 0.022158, the momentum for the stochastic gradient descent is 0.89684, and the coefficient of L2 regularisation is 2.2395×10^{-7}. Fig. 7 shows the accuracy on the validation set after each optimisation. The accuracy on the validation set after the fourth optimisation is much lower than at the other points, which is due to the fact that the hyperparameters chosen for this optimisation trap the network in a local minimum, thus resulting in low accuracy.
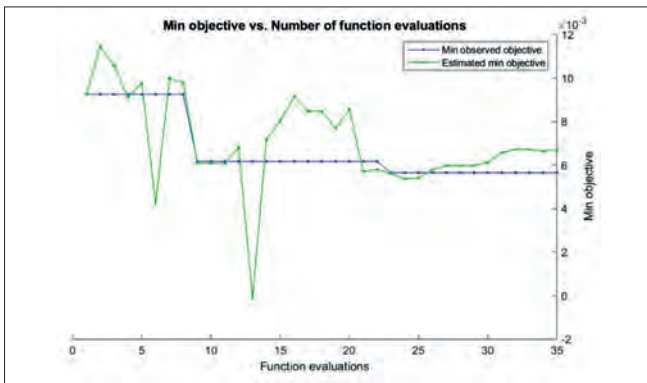
Fig. 6. Predicted values, observed values and evaluation times for the minimum objective function
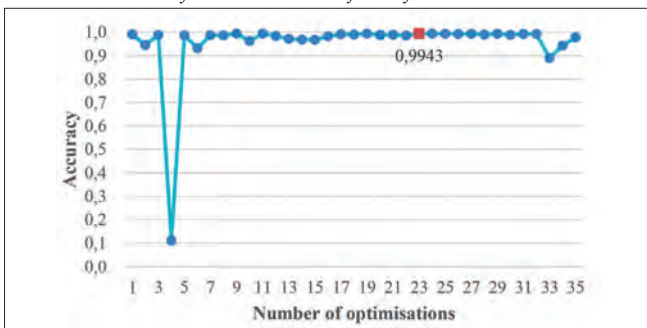
Fig. 7. Accuracy on the verification set vs. number of evaluations

The test set was used to verify the trained CNN fault diagnosis model. The accuracy of the test set can be used to measure the performance of the model, and is expressed as:

$$Accuracy = \frac{n}{N} \times 100\% \qquad (10)$$

where n is the number of correctly classified samples, and N is the total number of samples in the test set. Fig. 8 shows the test results in the form of a confusion matrix, and it can be seen that the proposed method obtained an accuracy of 99.40%. The confusion matrix shows that the proposed model can distinguish between normal operation and a fault on the bearing with 100% accuracy; the locations of the bearing faults are almost all accurately classified, and the main problem with misclassification is associated with the severity of the damage. The highest diagnostic error rates are seen for the fault statuses of the inner rings II and III. This is because the faults are located in the inner ring, with high similarity between the two characteristics, which increases the difficulty of classification. Multiple failure types, severities and operating conditions mean that the bearing operating characteristics have more diversity and similarity, but this also increases the difficulty of classification. Despite the complex and diverse working conditions of the bearings, the proposed fault diagnosis model achieves very good results.
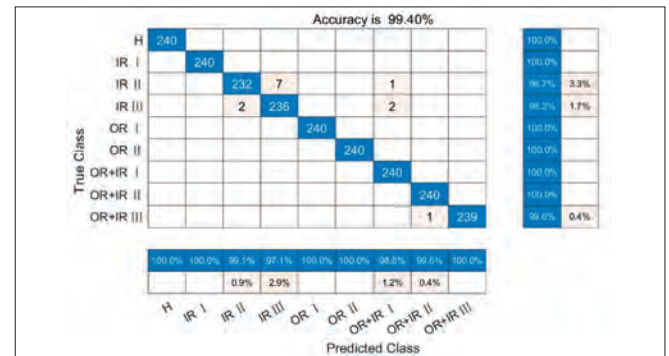
Fig. 8. Confusion matrix for the classification results from the optimal CNN model on the test set

In the testing process, the classification of each image in the test set is considered an independent event with a certain probability of success, i.e. the number of misclassified images follows a binomial distribution, where there are only two classification outcomes for each image: correct or incorrect. The Wald test for CNN fault diagnosis models consists of two steps, as follows:

(i) Calculate the standard error of for the test set:

$$TestErrorSE = \sqrt{\frac{Accuracy(1-accuracy)}{N}} \qquad (11)$$

(ii) Calculate the 95% confidence interval for the standard error:

$$TestError95CI = \left[1 - Accuracy - 1.96^* \, TestErrorSE, \right.$$

$$\left. 1 - Accuracy + 1.96^* \, TestErrorSE \right] \qquad (12)$$

where *Accuracy* is the accuracy on the test set obtained from Equation (10). Both the standard error for the test set and the 95% confidence interval of the standard error reflect the performance of the proposed CNN fault diagnosis model, and

the standard variance reflects the degree of dispersion of the results for the test set. The larger the standard variance, the more samples in the test set are misclassified, whereas the smaller the 95% confidence interval, the more samples in the test set are correctly classified. The result for *TestErrorSE* is 0.0017, and the *TestError95CI* interval is [0.0028, 0.0093]; both of these are very small, indicating that the CNN fault diagnosis model proposed in this paper has very good performance.

GENERALISATION AND ROBUSTNESS TESTING OF MODELS IN NOISY ENVIRONMENTS

A bearing operates in a variety of environments under actual operating conditions, and the collected signals contain some random interference noise, which affects the effectiveness of fault diagnosis. The SNR is the ratio of the average power of the effective signal to the average power of the noise, as follows:

$$SNR = 10 log_{10} \frac{P_{Signal}}{P_{Noise}} \qquad (13)$$

where P_{Signal} is the energy of effective signal and P_{Noise} is the energy of the noise. The smaller the SNR, the higher the level of noise in the signal.

Gaussian white noise signals with values for the SNR of 0–80 dB at 10 dB intervals were added to the original vibration signals, and nine levels of noise intensity were applied as a way to simulate the acquisition of bearing vibration signals under different actual environments. These values covered most operating environments. The bearing vibration signals under different noise conditions were processed by SSWT. The CNN model and the hyperparameters were trained and tested, and the results are shown in Fig. 9. It can be seen that the noise intensity affects the accuracy of fault diagnosis; however, the accuracy of the proposed model is greater than 99% for the low-noise case, 98% in the medium-noise case, and higher than 90% in the high-noise case. It can therefore be concluded that the proposed fault diagnosis model gives good diagnostic results even in a high-noise environment.
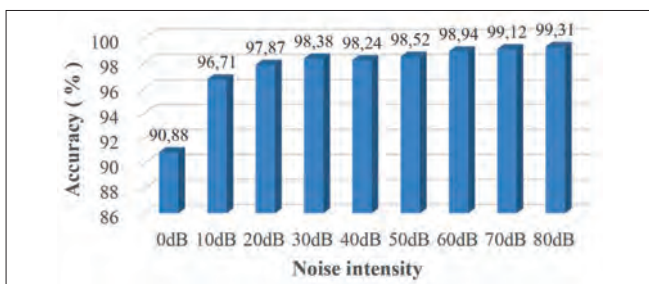
Fig. 9. Accuracy of CNN models trained and tested with different levels of noise

COMPARISON WITH OTHER FAULT DIAGNOSIS METHODS

CWT can closely model the detailed characteristics of vibration signals, and is widely used in the diagnosis of bearing faults. A Fourier simultaneous squeeze transform (FSST) is also a method for improving the time-frequency

resolution. In a similar way to SSWT, FSST improves the time-frequency resolution of STFT by rearranging the time-frequency coefficients with a simultaneous squeeze operator. The raw vibration signal from the bearing was processed with both CWT and FSST, and the same CNN network model and hyperparameters as mentioned above were used for training and testing. The results are shown in Fig. 10, and it can be seen that SSWT gives the best diagnostic performance.
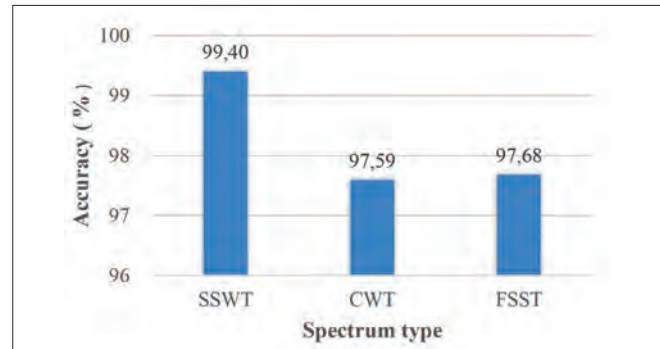
Fig. 10. Accuracy of the model using three time spectra

AlexNet was the first modern deep convolutional network model, and won the ImageNet image classification competition in 2012 [25]. During the recent boom in deep learning, other classical deep convolutional network models such as GoogLeNet and ResNet were developed. Using the original vibration signal and the spectrogram after SSWT processing under different noise signals, the classical models mentioned above were used for training and testing, and the results are shown in Fig. 11. It can be seen that the model proposed in this paper gave the best diagnostic performance under all levels of noise intensity.
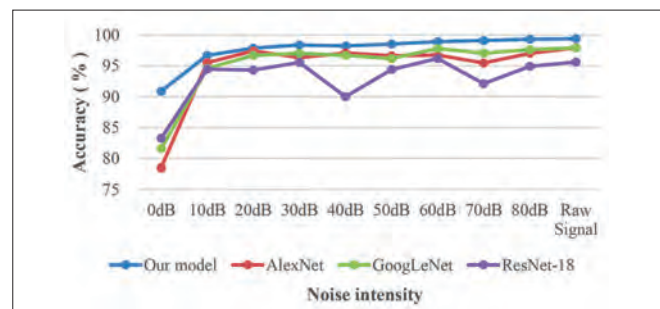
Fig. 11. Accuracy of different models under varying noise conditions

CONCLUSION

An adaptive bearing fault diagnosis method (SSWT-Bayes-CNN) has been proposed in this paper with the aim of adapting to the changable characteristics of bearing fault signals under complex operating conditions. The SSWT method is used to improve the resolution of the time-frequency spectrum, in order to highlight the most important information in the complex signal. To address the difficulty of selecting an CNN structure and appropriate hyperparameters, an improved CNN model was proposed, and a Bayesian optimisation method was applied to determine the optimal structure and hyperparameters for

the CNN, which provided a solution to the selection problem of multiple hyperparameter coupling. Experimental results confirmed that the proposed bearing fault diagnosis method could effectively diagnose different types and severities of bearing faults under complex operating conditions, with very high accuracy and very good generalisation ability. The use of accelerated life test data also provided a reference for the application of our model to practical fault diagnosis.

ACKNOWLEDGEMENTS

DECLARATION OF COMPETING INTERESTS

The authors declare that they have no known competing financial interests or personal relationships that could have appeared to influence the work reported in this paper.

REFERENCES

1. S. Zhang, S. Zhang, B. Wang, and T. G. Habetler, "Deep learning algorithms for bearing fault diagnostics—A comprehensive review," *IEEE Access*, vol. 8, pp. 29857–29881, 2020, doi: 10.1109/ACCESS.2020.2972859.

2. J. A. Reyes-Malanche, F. J. Villalobos-Pina, E. Cabal-Yepez, R. Alvarez-Salas, and C. Rodriguez-Donate, "Open-circuit fault diagnosis in power inverters through currents analysis in time domain," *IEEE Transactions on Instrumentation and Measurement*, vol. 70, pp. 1–12, 2021, Art no. 3517512, doi: 10.1109/TIM.2021.3082325.

3. X. Chen, P. Qin, Y. Chen, J. Zhao, W. Li, Y. Mao, and T. Zhao, "Inter-turn short circuit fault diagnosis of PMSM," *Electronics*, vol. 11, no. 10, p. 1576, 2022, https://doi.org/10.3390/electronics11101576.

4. H. Pan, X. He, S. Tang, and F. Meng, "An improved bearing fault diagnosis method using one-dimensional CNN and LSTM," 2018, bearing fault diagnosis; CNN; LSTM vol. 64, no. 7–8, p. 10, 2018.

5. S. Liang, Y. Chen, H. Liang, and X. Li, "Sparse representation and SVM diagnosis method for inter-turn short-circuit fault in PMSM," *Applied Sciences*, vol. 9, no. 2, p. 224, 2019, https://doi.org/10.3390/app9020224.

6. Z. Zhao, Q. Xu, and M. Jia, "Improved shuffled frog leaping algorithm-based BP neural network and its application in bearing early fault diagnosis," *Neural Computing and Applications*, vol. 27, no. 2, pp. 375–385, 2016.

7. L.-K. Chang, S.-H. Wang, and M.-C. Tsai, "Demagnetization fault diagnosis of a PMSM using auto-encoder and K-means clustering," *Energies*, vol. 13, no. 17, doi: 10.3390/en13174467.

8. J. Jiao, M. Zhao, J. Lin, and K. Liang, "A comprehensive review on convolutional neural network in machine fault diagnosis," *Neurocomputing*, vol. 417, pp. 36–63, 2020.

9. W. Zhang, X. Li, and Q. Ding, "Deep residual learning-based fault diagnosis method for rotating machinery," *ISA Transactions*, vol. 95, pp. 295–305, 2019.

10. R. Huang, Y. Liao, S. Zhang, and W. Li, "Deep decoupling convolutional neural network for intelligent compound fault diagnosis," *IEEE Access*, vol. 7, pp. 1848–1858, 2019, doi: 10.1109/ACCESS.2018.2886343.

11. X. Ding and Q. He, "Energy-fluctuated multiscale feature learning with deep ConvNet for intelligent spindle bearing fault diagnosis," *IEEE Transactions on Instrumentation and Measurement*, vol. 66, no. 8, pp. 1926–1935, Aug. 2017, doi: 10.1109/TIM.2017.2674738.

12. D. Verstraete, A. Ferrada, E. L. Droguett, V. Meruane, and M. Modarres, "Deep learning enabled fault diagnosis using time-frequency image analysis of rolling element bearings," *Shock and Vibration*, vol. 2017, p. 5067651, 2017.

13. Z. Shi, X. Yang, Y. Li, and G. Yu, "Wavelet-based synchroextracting transform: An effective TFA tool for machinery fault diagnosis," *Control Engineering Practice*, vol. 114, p. 104884, 2021.

14. C. Su, et al., "Damage assessments of composite under the environment with strong noise based on synchrosqueezing wavelet transform and stack autoencoder algorithm," *Measurement*, vol. 156, p. 107587, 2020.

15. J. Yuan, Z. Yao, Q. Zhao, Y. Xu, C. Li, and H. Jiang, "Dual-core denoised synchrosqueezing wavelet transform for gear fault detection," *IEEE Transactions on Instrumentation and Measurement*, vol. 70, pp. 1–11, 2021, Art no. 3521611, doi: 10.1109/TIM.2021.3094838.

16. Y. LeCun, Y. Bengio, and G. Hinton, "Deep learning," *Nature*, vol. 521, no. 7553, pp. 436–444, 2015.

17. G. W. Chang, Y.-L. Lin, Y.-J. Liu, G. H. Sun, and J. T. Yu, "A hybrid approach for time-varying harmonic and interharmonic detection using synchrosqueezing wavelet transform," *Applied Sciences*, vol. 11, no. 2, p. 752, 2021.

18. H. Wang and D.-Y. Yeung, "Towards Bayesian deep learning: A framework and some existing methods," *IEEE Transactions on Knowledge and Data Engineering*, vol. 28, no. 12, pp. 3395–3408, Dec. 2016, doi: 10.1109/TKDE.2016.2606428.

19. M. Jiaocheng, S. Jinan, Z. Xin, and Z. Peng, "Bayes-DCGRU with Bayesian optimization for rolling bearing fault diagnosis," *Applied Intelligence*, vol. 52, no. 10, pp. 11172–11183, 2022.

20. W. A. Smith and R. B. Randall, "Rolling element bearing diagnostics using the Case Western Reserve University data: A benchmark study," *Mechanical Systems and Signal Processing*, vol. 64–65, pp. 100–131, 2015.

21. W. A. Smith and R. B. Randall, "Rolling element bearing diagnostics using the Case Western Reserve University data: A benchmark study," Mechanical Systems and Signal Processing, vol. 64-65, pp. 100-131, 2015.

22. USA. The Vibration Institute, Condition Based Maintenance Fault Database for Testing of Diagnostic and Prognostics Algorithms. [Online]. https://www.mfpt.org/fault-data-sets..

23. C. Lessmeier, J. K. Kimotho, D. Zimmer, and W. Sextro, "Condition monitoring of bearing damage in electromechanical drive systems by using motor current signals of electric motors: A benchmark data set for data-driven classification," In: Editor. Pub Place; 2016. pp. 5–8.

24. Germany. University of Paderborn, Department of Design and Drive Technology, Condition Monitoring (CM) Experimental Bearing Dataset Based on Vibration and Motor Current Signals. [Online]. https://mb.uni-paderborn. de/kat/forschung/kat-datacenter/bearing-datacenter/data-sets-and-download

25. A. Krizhevsky, I. Sutskever, and G. E. Hinton, "ImageNet classification with deep convolutional neural networks," *Commun*. ACM, vol. 60, no. 6, pp. 84–90, 2017.

DESIGN OF AN AUTONOMOUS IOT NODE POWERED BY A PEROVSKITE-BASED WAVE ENERGY CONVERTER

Marcin Drzewiecki * [ID]
Jarosław Guziński [ID]
Department of Electric Drives and Energy Conversion, Faculty of Electrical and Control Engineering,
Gdańsk University of Technology, Poland

* Corresponding author: *marcin.drzewiecki@pg.edu.pl (M. Drzewiecki)*

ABSTRACT

This paper presents the results of experimental research focused on wave energy harvesting and its conversion to power Internet of Things (IoT) devices. The harvesting and conversion process was performed using a wave energy converter (WEC) consisting of a lead zirconate titanate piezoelectric ceramic perovskite material and a prototype power electronic circuit. The designed WEC was considered as a power supply for an end node device (END) of an IoT network. The END consisted of a long-range radio module and an electronic paper display. A set of physical experiments were carried out, and the results confirmed that an energy surplus was supplied by WEC compared to the energy consumed by the END. Hence, the proposed scheme was experimentally validated as a convenient solution that could enable the autonomous operation of an IoT device. The use case presented here for the proposed WEC was analysed for selected sea areas on the basis of wave statistics. The novelty of this paper arises from an investigation that confirms that WECs can significantly contribute to the development of wireless and mobile IoT communication powered by freely available sea wave energy.

Keywords: wave energy converter; renewable energy; internet of things; IoT applications; hydropower

INTRODUCTION

Wave energy converters (WECs) are devices intended for harvesting the energy of water waves and converting it into a useful form. The first patent associated with the harvesting and use of wave energy dates back to the 18th century [1,2], and related to a solution for the harvesting of water wave energy and its conversion into a useful mechanical form. Since then, many patents and implementations regarding WEC have emerged, in regard to both model-scale laboratory conditions and full-scale sea conditions [3]. Solutions have also been proposed for harvesting the mechanical energy of water waves and converting it into electrical form, through the use of

electrical machines operating as generators [4]. Since then, numerous considerations have been made regarding WEC, and such devices are still being developed [5,6]. Additional approaches in terms of applied materials and methods of harvesting and converting this energy into a useful electrical form have also been introduced over recent years [7,8]. The solutions described in these works show that for certain applications, electric machines that require maintenance can be replaced with maintenance-free piezoelectric materials (PMs) or dielectric elastomers (DEs). These materials generate electrical energy under the mechanical influence of water waves. The main motivation for the work described in the current paper, and its novelty compared to related works, is

an investigation of the possibility of harvesting the energy of water waves and converting it into electrical form via PMs, for use in powering distributed and autonomous elements of communication networks located onshore, nearshore, or offshore.

The concept of an integrated network consisting of software and hardware elements in which nodes received data packets at radio frequencies was formulated in an early paper in the 1990s [9]. In later works published in the 2000s, this concept began to be referred to as the Internet of Things (IoT) [10]. Over time, IoT solutions became more advanced [11], lower in power [12] and more common [13].

Both of the technologies described above, WEC and IoT, are still under development, and their role in meeting human needs is expected to grow significantly. If current trends continue [2,11], the use of WECs for the IoT is going to be one of the most essential aspects of sustainable development in the areas of wireless and mobile communication. A ceramic perovskite material called lead zirconate titanate (PZT) is applied in the present work. PZT was chosen due to its ability to convert mechanical energy into electrical form at low cost, its ease of operation, and its widespread availability [14]. The objectives and scope of this work were to design and validate a PZT-based WEC that was capable of powering IoT communication by harvesting freely available sea wave energy.

ENERGY CONVERSION

The energy of water waves was discussed in [19]. Below is a study on the availability of mechanical wave energy when harvested and converted into electrical form. The energy of a water wave can be expressed as follows in the time domain and in the discrete frequency domain. The mechanical energy E_A contained in a progressive sinusoidal water wave consists of potential energy E_p and kinetic energy E_k. The amount of energy in such a wave per unit surface area of the water is given by Eq. (1) [15]:

$$E_A = E_p + E_k = \frac{1}{2}\rho g z_A{}^2 \qquad (1)$$

where ρ is the density of water and g is the acceleration due to gravity. z_A is the amplitude of the two-dimensional progressive sinusoidal wave, as shown in Fig. 1.
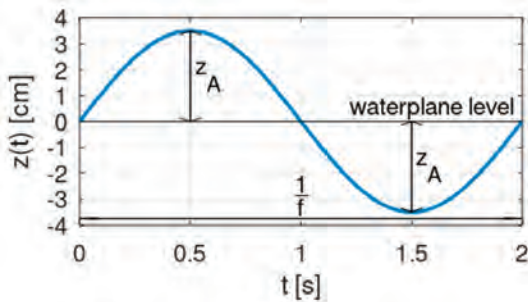
Fig. 1. Two-dimensional progressive sinusoidal wave at the surface of the water [19].

A water wave passing through an energy harvesting point in an area of water can be considered as a sum of two-dimensional progressive sinusoidal waves, as shown in Eq. (2) [16]:

$$z(t) = \sum_{i=1}^{\infty} z_{Ai}\cos\left(2\pi f_i t + \varepsilon_k\right) \qquad (2)$$

where z_{Ai} is the amplitude of the sinusoidal component with frequency f_i. The parameter εk is the phase of each component, and is randomly applied in the range of 0–2π to reflect the space-time randomness of the wave process in the area of water. The summation of the two-dimensional progressive sinusoidal waves given in Eq. (2) is illustrated in Fig. 2.
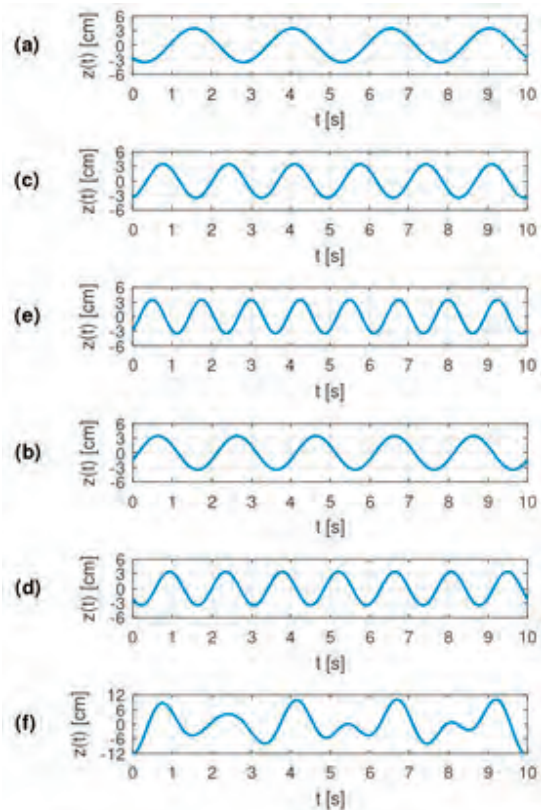
Fig. 2. A water wave (f) can be considered as the sum of several two-dimensional progressive sinusoidal wave harmonics with amplitudes of 3.5 cm and frequencies of: (a) 0.4 Hz, (b) 0.5 Hz, (c) 0.6 Hz, (d) 0.7 Hz, (e) 0.8 Hz. [19]

The energy E contained per unit surface area of the water for the water waves formulated in Eq. (2) can be calculated using Eq. (3):

$$E = \frac{1}{2}\rho g \sum_{i=1}^{\infty} z_{Ai}{}^2 \qquad (3)$$

The time domain mathematical model in Eq. (2) can be transformed into the frequency domain and expressed as harmonics with frequencies fi and amplitudes z_{Ai}. The model of waves on the surface of the water can be considered as a power spectrum of harmonics $S(f_i)$, as given in Eq. (4) [17]:

$$S(f_i) = \frac{A}{f_i{}^5} \exp\left(\frac{-B}{f_i{}^4}\right) \qquad \textbf{(4)}$$

The values of A and B are determined based on the type [17] and state of the sea under consideration [18]. The energy $E(f_t)$ related to the power spectrum harmonics and expressed per unit surface area of the water can be represented in the frequency domain as:

$$E(f_i) = \rho g S(f_i) \qquad \textbf{(5)}$$

The energy expressed above in the form of harmonics, which occurs naturally in areas of water, can be converted into a useful electrical form via the piezoelectric effect. The piezoelectric effect occurs in certain materials, including PZT, and involves the generation of an electric charge when the material is deformed [14]. Based on the physical definition of work, it can be considered that the harmonic energy expressed in Eq. (3) can be transferred to a floating body (e.g. a buoy) by applying a harmonic force F_{Vi} along a vertical displacement Z_{Ai}. The energy is transferred with efficiency η_i. Hence, the harmonic of the force vertical component F_{Vi} per unit surface area of the water can be expressed as shown in Eq. (6):

$$F_{Vi} = \eta_i \frac{1}{2} \rho g z_{Ai} \qquad \textbf{(6)}$$

When the energy is transferred by the further application of a harmonic force component F_{Vi} from the buoy to the PZT, such that the force component points in the same direction as the polarisation of the PZT material, then the generated static voltage V_{si} is given as shown in Eq. (7) [20]:

$$V_{Si} = \frac{g_{33} F_{Vi} t}{C} \qquad \textbf{(7)}$$

where g_{33} is a piezoelectric voltage constant for the case where the force F_{Hi} is directed the same way as the PZT polarisation; C is the cross-sectional area of the PZT; and t is its layer thickness. In view of the above, the energy E of the water waves given in Eq. (3) can be transferred as work done by the force F_{Vi} in Eq. (6) and converted into a useful electrical form at a voltage V_{si} as shown in Eq. (7). This conversion takes place with efficiency η_i. The electrical form of energy obtained in this way can be used to power IoT devices.

OSCILLATING BODY SYSTEM WAVE ENERGY CONVERTER

A wave energy converter was designed and constructed in the form of an oscillating body system, following the WECs classification [2]. It consisted of three-body heaving cylindrical buoys trapped in a fixed frame with an openwork structure. Each cylindrical buoy was 240 mm high and 65 mm in diameter, and had a mass of 80 g. The openwork frame was 160 mm wide, 130 mm deep, and 450 mm high. The openings of the openwork structure were 50 mm in diameter. All of the elements were made of polypropylene, and are

illustrated in Fig. 3.
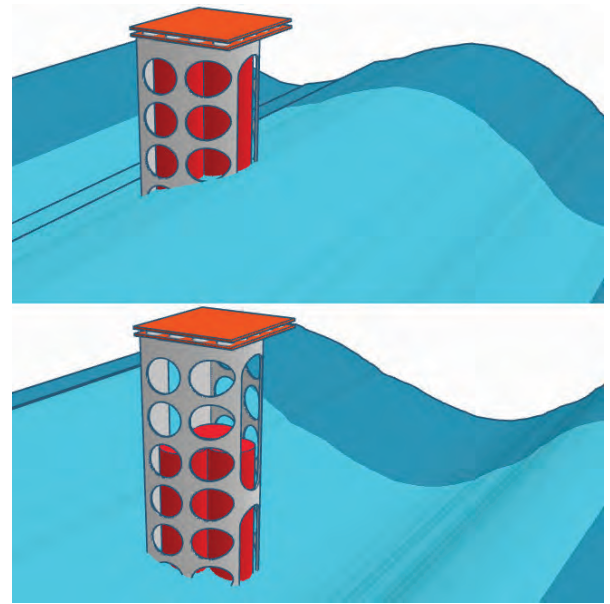
Fig. 3. Wave energy absorber consisting of three body heaving cylindrical buoys (red) trapped in a fixed frame with an openwork structure (white) working in waves (top dead centre position on the top and bottom dead centre position on the bottom).

The heaving buoys were intended to move with the motion of the water surface, and to act as a force on the PZT transducers fixed to the frame. The piezoelectric module was constructed in the form of 20 PZT/brass disk transducers, fixed to a common surface. The disk transducers consisted of PZT and brass plates, with diameters 19 mm (PZT) and 27 mm (brass) and an overall thickness of 0.24 mm. Each transducer had a capacitance of 45 nF, an impedance of 250 Ω and a resonant frequency of 2500 Hz. The PZT electrodes were led out with LgY0.5 wires with a stranded core structure and a core section of 0.5 mm². The brass plates were soldered to the common copper surface. The piezoelectric module is shown in Fig. 4.

Fig. 4. PZT converter, consisting of 20 PZT/brass disk transducers fixed to a common copper surface.

The energy converted by the PZT into electrical form was further processed via a prototype power electronic circuit (PEC), as illustrated in the schematic diagram in Fig. 5.
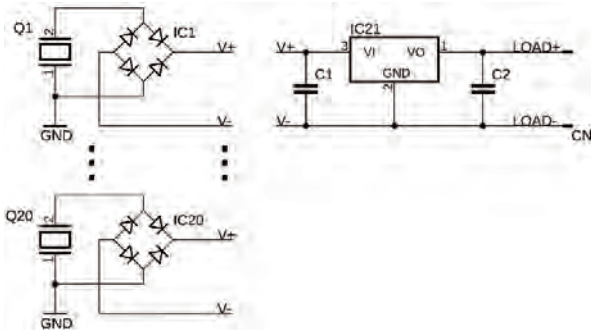
Fig. 5. Schematic diagram of a prototype power electronic circuit consisting of PZT/brass disk transducers (Q1–Q20), full-wave single-phase bridge rectifiers (IC1–IC20), input capacitor C1, very low-dropout voltage regulator IC21, output capacitor C2, and male connector CN for the load.

The implementation of the PEC is shown in Fig. 6. The system was constructed on a prototype PU26 universal board with a width of 60 mm, a height of 90 mm and a thickness of 1.6 mm.
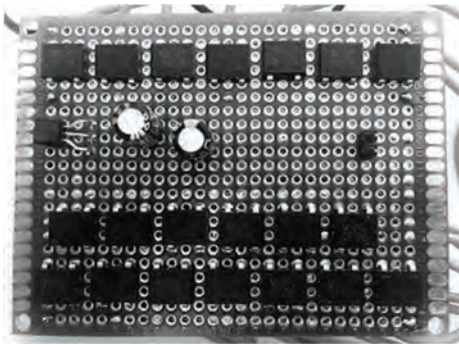
Fig. 6. Implementation of the prototype power electronic circuit.

The prototype board consisted of the components listed in Table 1.

Table 1. Components of the prototype power electronic circuit.

Item	Reference	Description	Value	MPN [1]	Quantity
1	IC1–IC20	Bridge recti-fiers	N/A	DF06	20
2	IC21	Voltage regula-tor	N/A	LE33	1
3	C1	Input capaci-tor	10 µF	KE10/100	1
4	C2	Output capaci-tor	47 uF	KE47/50	1
5	CN	Male conne-ctor	N/A	87220-2	1

1 Manufacturer part number

In the operation of the PEC, the piezoelectric voltage of the PZT electrodes is full-wave rectified by single-phase bridges (IC1–IC20). The input capacitor (C1) of the very low-dropout voltage regulator (IC21) is then charged at the rectified voltage. Next, the output current of the IC21 charges the output capacitor (C2) at the voltage that is applied to the load. In this way, the load is powered with the harvested energy.

INTERNET OF THINGS END NODE DEVICE

The IoT END considered under the present investigation consisted of a 2.71" e-paper display [21] and an STM32WL55JC ultra-low-power microcontroller with an embedded radio module enabling the LoRa modulation [22].

An electronic paper display (EPD), commonly referred to as an e-paper, is an electronic display that looks and feels similar to regular paper. EPDs contain microcapsules that are filled with electrically charged ink particles: black ink particles are negatively charged, while white ones are positively charged. Although colour EPDs are available, monochrome EPDs have lower power needs and are therefore considered in the current study. When an appropriate charge is applied to the display surface, it is possible to create very detailed images with similar contrast and legibility to those of traditional printing. The e-paper screen consumes electricity only when the displayed content changes, and once the ink particles are in place, they remain there for years. The details of e-paper technology have been thoroughly described by its manufacturer [21]. The 2.71" e-paper display used in the present study is shown in Fig. 7.

Fig. 7. The 2.71" black and white e-paper display used in the present study, with an example of graphical content.

The 2.71" display had an active area size of 57.3 × 38.2 mm, a resolution of 264 × 176 px, a density of 117 DPI, and a 2-bit colour depth, which corresponds to four shades of gray. Its visual similarity to regular paper can be seen in Fig. 8.

LoRa is a long-range, low-power wireless modulation technique. It is derived from chirp spread spectrum (CSS) technology and encodes information about radio waves using pulses (known as chirp pulses) in a manner similar to that used by dolphins and bats [24]. A modulated LoRa transmission is resistant to interference, and can be received over long distances of many kilometres. These distances can reach more than 22 km for transmission over seawater [25] or even more than 830 km for stratospheric balloons [26]. LoRa

is a solution used in applications that send small amounts of data, and these data can be transmitted over long distances compared to technologies such as Wi-Fi, Bluetooth or BLE, at relatively low digital transmission speeds. These features make *LoRa* well-suited to sensors and actuators that operate in a very low-power mode [24]. A comparison of *LoRa* with other selected wireless communication technologies in terms of bandwidth and range is presented in Fig. 9. The *LoRa* radio modules available on the market are characterised by very low power consumption, and are referred to by manufacturers as ultra-low-power solutions [22]. *LoRa* can operate in licence-free sub-gigahertz bands, such as at 915, 868, and 433 MHz. It can also operate in the 2.4 GHz band to achieve higher data rates compared to sub-gigahertz bands, at the cost of a lower range. These frequencies belong to the ISM bands, which are reserved worldwide for industrial, scientific, and medical purposes [24].

Fig. 8. Top image: 2.71" vertically oriented display; bottom image: regular paper. A normal view is shown on the left and a 50× magnification using a USB Delta Optical DO Smart microscope on the right.

Fig. 9. Comparion of LoRa with other selected wireless communication technologies in terms of bandwidth and range.

Our experimental *LoRa* setup consisted of a *The Things Indoor Gateway* based on a Semtech SX1308 chipset and an end node based on the STM32WL55JC microcontroller. The transmission power of the gateway was 27 dBm, corresponding to 500 mW, and its receiving sensitivity was −140 dBm. The transmission power of the end node radio module was 15 dBm, corresponding to 32 mW, and its receiving sensitivity was −148 dBm. The time on air was 0.4 s, meaning that a duty cycle of longer than 40 s was required to maintain 1% time

on air. A frequency of 868 MHz was used.

An IoT END prototype was developed, re-constructed to operate with the STM32WL55JC microcontroller, and researched by the author in cooperation with the MpicoSys Embedded Pico Systems (MpicoSys) company. This IoT END module is commercially offered and produced by MpicoSys, a company that provides complete solutions in the field of design, engineering, production, and rapid prototyping of e-paper for ultra-low-power and no-power technologies [27]. The IoT END device used in this study, in the form of an air quality indicator made of e-paper, is shown in Fig. 10. The device displays the results of air quality measurements at a station in Gdynia, Poland. These measurements are shared online by the Chief Inspectorate of Environmental Protection and acquired by the IoT END via *LoRa* communication.
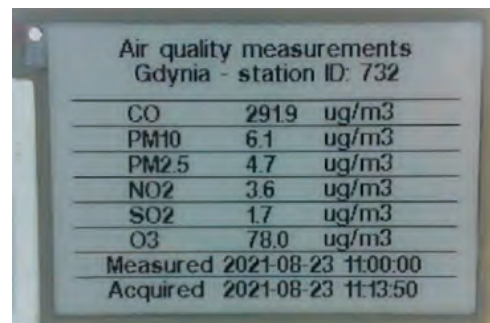
Fig. 10. IoT END device in the form of an air quality indicator made of e-paper.

EXPERIMENTAL RESEARCH

Our research consisted of a set of physical experiments. Two series of measurements were carried out to enable us to compare the results for the energy consumed by the IoT END with the energy supplied by the WEC. These measurements were carried out separately, and the results were compared.

The energy consumption of the IoT END was investigated in one of the possible use cases. The use case was considered in accordance with one of the solutions developed by the author and offered on the market by MpicoSys. The scenario included periodic data acquisition and refreshing of the display with user-directed information on air quality. The data were acquired and refreshed every 10 minutes, and the information displayed on the IoT END was acquired over *LoRa*. The IoT END consisted of two elements that consumed energy: a 2.71" EPD, and a STM32WL55JC microcontroller enabling the *LoRa* modulation. The STM32WL55JC microcontroller was equipped with firmware that performed low-power functions, and which received the data via the *LoRa* communication. Both of these elements were powered by DC voltage and consumed varying current depending on their needs, which was measured using an Otii Arc energy consumption analysis tool. Measurements were made over the *LoRa* communication cycle including the reception of 215 bytes of data and the

idle state and full refresh of the 2.71-inch EPD. A sampling frequency of 1 kHz and a resolution of 2.5 µA were used. Measurements of the current were performed at a DC supply voltage of 3.3 V set in the Otii Arc.

The energy supplied by the WEC was investigated in one possible application case. It can be mounted on breakwaters, piers, piles or other coastal structures. In the use case, it was assumed that the WEC would be positioned in a coastal zone where waves break and turbulise, meaning that the mechanical impacts have a higher frequency that is particularly suitable for piezoelectric materials such as PZT, due to their relatively high resonant frequency. The wave energy absorber of the WEC was submerged in a test tank at a depth of 30 cm, as shown in Fig. 11.
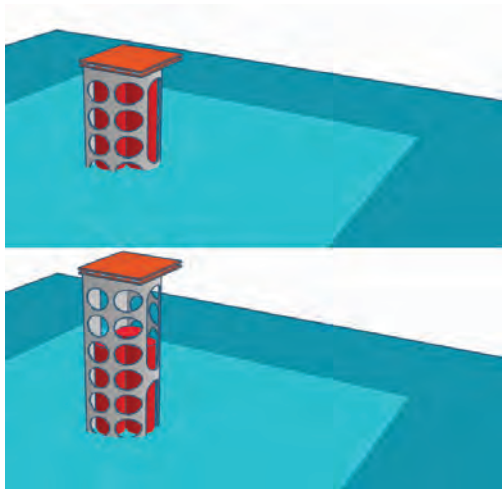
Fig. 11. The wave energy absorber submerged in water in a test tank – top dead centre position on the top and bottom dead centre position on the bottom.

The construction of the PZT converter and the mechanical bumpers before assembly is shown in Fig. 12. Mechanical bumpers were needed as interlayers between the impact surface of the buoy and the PZT. Each bumper was 13 mm in diameter, 5 mm thick and made of polyvinyl chloride.
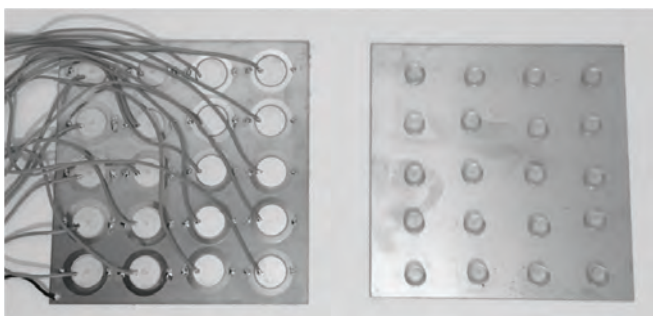
Fig. 12. View before assembly: PZT converter (left); mechanical bumpers (right)

The components shown in Fig. 12 were assembled as shown in Fig. 13.
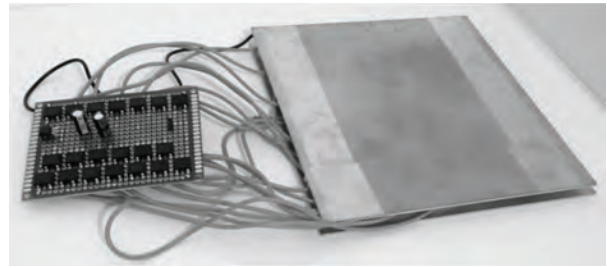
Fig. 13. After assembly: PZT converter and mechanical bumpers, connected to the power electronic circuit.

After assembly with the mechanical bumpers, the PZT converter was attached to the top of the wave energy absorber for the duration of the measurements, meaning that the vertical force from the moving buoys acted on the PZT. From Eq. (7) and considering that the vertical force is involved in energy conversion, the equivalent of the formation of waves on the water surface was the heaving of the WEC absorber relative to the water surface. Consequently, the WEC was heaved up and down into the water to model the action of the force. The vertical movements were performed at a frequency corresponding to the wave whose vertical action was modelled. The energy supplied by the WEC was measured using an STM32F429ZIT6U microcontroller equipped with firmware to perform the analogue-to-digital (ADC) conversion of the voltage acquired from the LOAD+ and LOAD- output terminals (Fig. 5). The measured voltage acquired and processed using a 12-bit ADC converter was subsequently sent to the RS232 terminal of the personal computer via the UART interface and recorded. A sampling frequency of 25 Hz was used, with a resolution of 0.732 mV. Measurements of the generated voltage were made with a 2.94 kΩ load resistor connected to the LOAD+ and LOAD-WEC output terminals, and the results from the generated voltage with a fixed load resistance allowed us to calculate the current flowing in the circuit and hence the energy generated by the WEC.

In the case study considered here, important messages (such as air or water quality, alerts or weather forecasts) could be transmitted in coastal areas via long-range wireless communication using wave energy. It was essential to ensure that the energy produced by WEC exceeded the energy consumed by the IoT END for this application. The results are presented and discussed in the following section.

RESULTS

According to research performed on the IoT END and described in this paper, the STM32WL55JC microcontroller handling the *LoRa* modulation consumed an average current of 684 µA. This current consumption occurred at a supply voltage of 3.3 V DC during one *LoRa* communication cycle in which 215 B of data were received. This is shown in Fig. 14 over the time period 0.2–5.7 s.

The STM32WL55JC microcontroller consumed an average current of 2.42 µA in the idle state at a supply voltage of

3.3 V DC. This is shown in Fig. 14 over the time period 5.7–10 s.
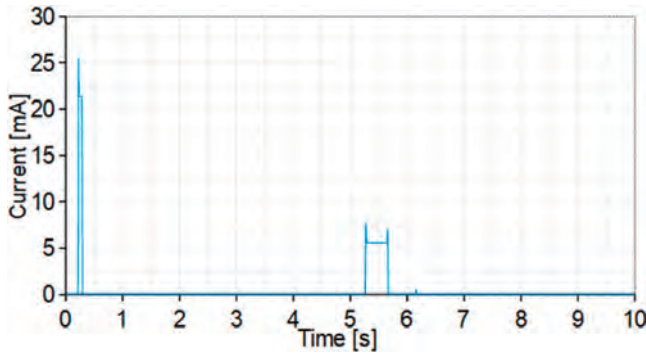
Fig. 14. Current consumed by the STM32WL55JC at a supply voltage of 3.3 V DC, showing the LoRa communication cycle receiving 215 B of data from 0.2 to 5.7 s, and the idle state from 5.7 to 10 s, measured using Otii Arc.

The 2.71" EPD consumes an average current of 1.72 mA at a supply voltage of 3.3 V DC during the update cycle when the display is refreshed. It is shown in Fig. 15 over the time period 0.1–1.7 s.
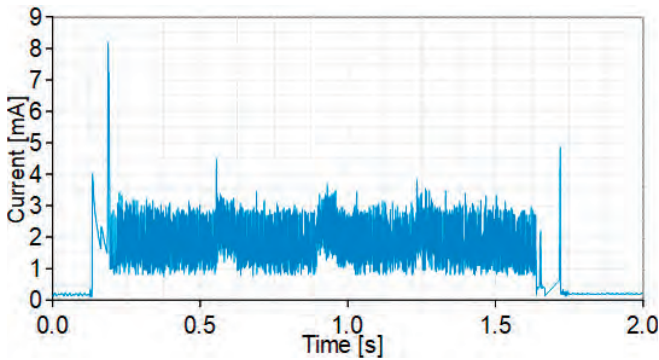
Fig. 15. Current consumed by the 2.71" EPD at a supply voltage of 3.3 V DC, showing the display update cycle (when the display area of 264 ×176 px is refreshed) between 0.1 and 1.7 s.

A summary of the energy consumed by the IoT EPD for the use case considered here, for a data acquisition and display refresh cycle of 10 min, is presented in Table 2.

Table 2. Summary of IoT EPD energy consumption for one data acquisition/ display update cycle

State	Average current[1] [μA]	Period[2] [s]	Energy consumption [mJ]
Idle	2.42	592.9	4.74
Communication	684	5.5	12.42
Display update	1720	1.6	9.08
Total	N/A	600	26.23

[1] For a supply voltage of 3.3 V DC

[2] For a data acquisition and display update period of 10 min

From these results, it can be seen that the energy consumption of the IoT END over one 10 min period of data acquisition via *LoRa* and display update was equal to 26.23 mJ.

The experiments performed on the WEC showed that the converter supplied an average current of 90 μA at an average voltage of 263 mV, generated under the impact of a vertical force resulting from a modelled wave with a height of 30 cm and a frequency of 1.3 Hz. These conversion parameters were found for a load with a 2.94 kΩ resistor. The mean values reported here were calculated from the pulsating value of the generated voltage measured at the WEC output terminals (Fig. 5). The results of the generated voltage measurements are shown in Fig. 16.

An amplitude of 30 cm for the vertical movement was measured on a centimetre measuring scale. The frequency of 1.3 Hz for the vertical movement was measured and registered (it corresponded to the frequency of the WEC's voltage generated).

The wave frequency of 1.3 Hz was chosen as an optimum trade off between the harmonic energy density of natural water waves and their high dynamics, desirable for the PZT element. Based on the classification of ocean waves in terms of their frequencies [28], a harmonic value of 1.3 Hz corresponds to the region of wind sea waves, whereas higher frequencies correspond to the region of capillary waves. Since the energy density decreases from the wind wave region to the capillary wave region, a higher harmonic energy density would be too low for harvesting. The geometric dimensions of the WEC were selected to ensure that it was compact and easy to use for harvesting the energy of breaking waves and turbulised water near offshore, onshore and coastal structures.
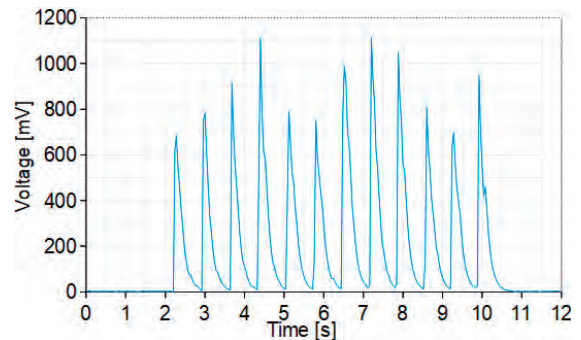
Fig. 16. Measured voltage generated at the output terminals of the WEC under a load and force resulting from the modelled vertical impact of a water wave with a height of 30 cm at a frequency of 1.3 Hz.

The pulsating current was calculated for the known value of the load resistor, and the results are shown in Fig. 17.
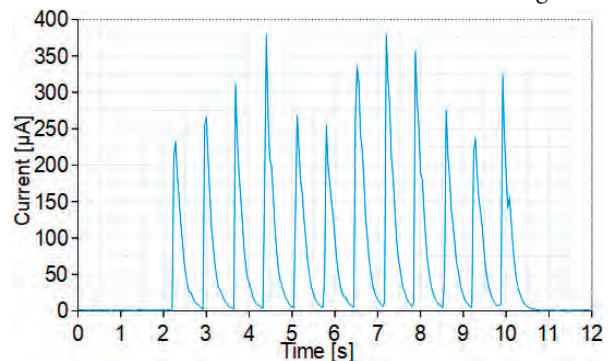
Fig. 17. Current supplied to the output terminals of the WEC at a voltage generated under a load and force resulting from the modelled vertical impact of a water wave with a height of 30 cm at a frequency of 1.3 Hz.

The variation in the power was then calculated for the known values of the voltage and current, and the results are shown in Fig. 18.
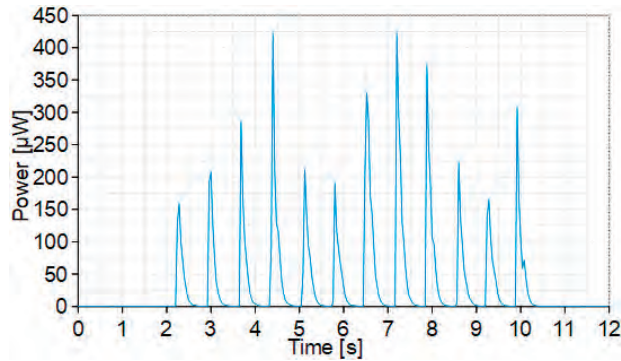
Fig. 18. Power supplied from the WEC to the load under the force resulting from the modelled vertical impact of a water wave with a height of 30 cm at a frequency of 1.3 Hz.

From the 12-s measurement gates presented in Figs. 16, 17, and 18, a time range from 2.2 to 10 s was considered for further analysis, which corresponded to the active impact of the modelled wave.

A summary of the energy conversion performance of the WEC under the applied load and the modelled impact of the wave is presented in Table 3.

Table 3. Summary of WEC energy conversion performance under the load and the modelled impact of the wave

Parameter	Average value[1]	Units
Voltage	263	mV
Current	90	µA
Power	51	µW
Energy[2]	30.3	mJ
Load	2.94	kΩ
Wave height	30	cm
Wave frequency	1.3	Hz

1 Average value from 2.2 s to 10 s
2 For the 10-min IoT END period

The results show that the amount of the energy converted into electrical form was 30.3 mJ, whereas the amount of energy consumed by the IoT END was 26.23 mJ. Both of these values correspond to one cycle of data acquisition and display updating for the IoT END over a 10 min period.

The output power of the IoT END transmitter reached up to 32 mW. The power generated by the WEC was of 51 µW. However, the transmission time was short enough to balance the energy consumption and generation. Our experimental results confirmed that an energy surplus was supplied by the WEC compared to the energy consumption of the IoT END, indicating that wireless and mobile communication could be powered by freely available sea wave energy.

Balancing the energy generated and consumed requires the use of energy storage elements such as capacitors or micro-supercapacitors. The selection and validation of reliable energy storage elements will be performed in future work.

The piezoelectric voltage constant g_{33} resulting from the material dimensions of the piezoelectric and the design of the wave energy absorber both have a significant impact on the parameters of energy conversion and WEC performance. Optimisation of the piezoelectric material and the wave energy absorber falls outside the scope of the present study, and will be considered in future work.

DISCUSSION OF MARINE AREAS

The use case presented here for the proposed WEC was analysed for use in selected marine coastal areas. This study was conducted using information from the EU Copernicus Marine Service [29], and an analysis was performed using acquired values for the:
- Significant height of sea surface waves H_s,
- Period of sea surface waves at a variance spectral density maximum T_p.

The significant height H_s is the average height of the highest one-third of the waves. The sea surface wave period at variance spectral density maximum T_p is also known as the modal period or the peak period.

Data from 19th February 2023 were acquired for the following marine coastal areas, in alphabetical order:
1. Algeria, Bay of Algiers: 36.797N, 3.128E;
2. Estonia, Tallinn: 59.492N, 24.734E;
3. Finland, Oulu: 65.129N, 25.204E;
4. France, Dunkirk: 51.139N, 2.308E;
5. Israel, Haifa: 32.836N, 34.963E;
6. Japan, Hamamatsu: 34.636N, 137.748E;
7. Lithuania, Klaipeda: 55.652N, 21.076E;
8. Netherlands, Hague: 52.666N, 4.562E;
9. Norway, Trondheim: 64.294N, 10.373E;
10. Poland, Gdańsk Bay: 54.460N, 18.628E;
11. Poland, Jastrzębia Góra: 54.846N, 18.299E;
12. Poland, Międzyzdroje: 53.937N, 14.429E;
13. South Africa, Cape of Good Hope: 34.358S, 18.470E;
14. Sweden, Malmo: 55.629N, 12.979E;
15. United Arab Emirates, Dubai: 25.242N, 55.242E;
16. United Kingdom, Kingsbridge: 50.279N, 3.904W;
17. United States of America, California, San Francisco: 37.761N, 122.539W.

To carry out an energy analysis based on the values acquired from the global wave system, the relationship between the energy contained in the water waves and H_s needed to be obtained as follows.

An expression for the amplitude spectrum harmonics Z_{Ai} in terms of the power spectrum harmonics S_i is given in Eq. (8):

$$S_i = \frac{1}{2} z_{Ai}{}^2 \qquad (8)$$

Following [30], H_s can be related to the power spectrum harmonics S_i as shown in Eq. (9):

$$H_s = 4\sqrt{\sum_{i=1}^{\infty} S_i} \qquad (9)$$

By substituting Eq. (8) into Eq. (9) and simplifying the equation, an expression for Z_{Ai} can be formulated as shown in Eq. (10):

$$\sum_{i=1}^{\infty} z_{Ai} = \frac{1}{\sqrt{8}} H_s \qquad (10)$$

We combine Eqs. (10) and (3) to find the energy E expressed per unit of the water surface and contained in the water waves in terms of H_s, as shown in Eq. (11):

$$E = \frac{1}{16} \rho g H_s^{\,2} \qquad (11)$$

Using the equation given above, values for E were calculated as listed in Table 4. The parameter ρ was set to 998.7739 kg/m³, and g was assumed to be equal to the standard value of 9.80665 m/s² in for the calculations. The value of ρ corresponds to an average annual temperature of the surface waters of the oceans of 17°C.

Table 4. Energy contained in water waves and expressed per unit of surface area of water for selected marine coastal areas

Coastal area[1]	H_s [m]	T_p [s]	f_p [Hz]	E [J/m²]
1	0.21	3.78	0.26	27
2	0.82	7.25	0.14	412
3	0.11	1.86	0.54	7
4	1	4.72	0.21	612
5	0.31	2.82	0.35	59
6	1.59	8.27	0.12	1548
7	1.5	6.39	0.16	1377
8	1.05	5.82	0.17	675
9	3.62	10.91	0.09	8022
10	0.78	6	0.17	372
11	0.98	5.58	0.18	588
12	0.67	3.91	0.26	275
13	1.62	12.06	0.08	1607
14	0.56	3.39	0.29	192
15	1.49	7.11	0.14	1359
16	0.8	12.4	0.08	392
17	1.06	12.12	0.08	688

[1] Numbering follows the list of marine coastal areas in alphabetical order given above

The solution presented in the previous sections ensured that the energy supplied by the WEC exceeded the energy consumed by the IoT END. This amount of energy was generated under the vertical impact of a modelled water wave with height 30 cm and frequency 1.3 Hz. The energy contained in this water wave was 441 J/m², a value calculated using Eq. (1). The parameter ρ was set to 999.6991 kg/m³ and g was taken as the standard value of 9.80665 m/s² for the calculations. This value of ρ corresponds to a water temperature of 10°C in the test tank.

The WEC converted the energy of the wave at a frequency of 1.3 Hz, corresponding to a period of 0.77 s. The value of Tp found for the data acquired from the global wave system ranged from 1.86 s to 12.4 s. However, the proposed WEC is intended to be mounted on nearshore coastal structures, where the waves break and turbulise, and the local wave period is therefore expected to increase significantly, meaning that the mechanical impact is expected to have a higher frequency, closer to the tested value of 1.3 Hz.

The topology of the coastal structures and the presence of wave breakers or turbulisers have a significant impact on the parameters of a broken wave; however, this type of breaking falls outside the scope of the present study, and will be considered in future work.

Our energy analysis based on data acquired for 19th February 2023 show that the use of the IoT END with the proposed WEC is suitable for coastal areas 4, 6, 7, 8, 9, 11, 13, 15, 17. For coastal areas 1, 2, 3, 5, 10, 12, 14, 16, the update period of the IoT END needs to be extended to allow the generated energy to exceed that consumed by the IoT END.

CONCLUSIONS

The use of the proposed WEC to power an IoT device was successfully verified for the case study considered here. The perovskite-based WEC designed and constructed as part of this study was experimentally proven to be capable of generating the energy required by distributed and autonomous IoT ENDs. In the event of insufficient wave energy, the update period for the IoT END can be extended to allow the generated energy to exceed the IoT END energy consumption. The solution presented here can make significant contributions to the sustainable development of wireless and mobile communication powered by freely available sea wave energy.

The main advantage of our technical solution compared to existing alternatives is that it is very compact and can harvest energy directly at the point where it is consumed by the distributed, autonomous elements of an IoT network located onshore, nearshore, or offshore. A further advantage over related schemes introduced in recent years [4] is that the proposed solution uses an innovative method of energy conversion based on PZT ceramic perovskite material. In addition, other related systems are based on electrical machines that require maintenance, whereas the solution proposed in this paper uses maintenance-free piezoelectric materials. This feature is a particular advantage for a distributed, energy-autonomous IoT network operating in marine conditions.

In future research, we intend to consider and implement optimised piezoelectric materials and a wave energy absorber to improve the performance of the WEC. Further research will also be carried out to match the piezoelectric materials

to the frequency of water waves, and to apply a matching inductance to the piezoelectric circuit, which will increase the efficiency of the water wave energy conversion. In future, it will also be useful to analyse the topology of coastal structures, wave breakers or turbulisers and their impacts on the wave energy conversion parameters. In further work to extend the current scheme, the experimental system will be tested and demonstrated in real environments.

REFERENCES

1. P. Girard and S. Girard, Brevet D'invention De Quinze Ans, "Pour divers moyens d'employer les vagues de la mer, comme moteurs," a patent for invention, Paris 1799, 349.

2. T. Aderinto and H. Li, "Ocean wave energy converters: Status and challenges," Energies, vol. 11, p. 1250, 2018. doi:/10.3390/en11051250.

3. A. Clément et al., "Wave energy in Europe: Current status and perspectives," Renewable and Sustainable Energy Reviews, vol. 6, p. 5, 2002. doi:10.1016/S1364-0321(02)00009-6.

4. M. S. Lagoun, A. Benalia, and M. E. H. Benbouzid, "Ocean wave converters: State of the art and current status," Proceedings of the 2010 IEEE ENERGYCON, Manama (Bahraïn), December 2010, pp. 636–642.

5. A. Maria-Arenas et al., "Control strategies applied to wave energy converters: State of the art," Energies, vol. 12, p. 3115, 2019. doi:10.3390/en12163115.

6. M. A. Jusoh et al., "Hydraulic power take-off concepts for wave energy conversion system: A review," Energies, vol. 12, p. 4510, 2019. doi:10.3390/en12234510.

7. S. Chiba et al., "Consistent ocean wave energy harvesting using electroactive polymer (dielectric elastomer) artificial muscle generators," Applied Energy, vol. 104, pp. 497–502, 2013. doi:10.1016/j.apenergy.2012.10.052.

8. X. Chou et al., "All-in-one filler-elastomer-based high-performance stretchable piezoelectric nanogenerator for kinetic energy harvesting and self-powered motion monitoring," Nano Energy, vol. 53, pp. 550–558, 2018. doi:10.1016/j.nanoen.2018.09.006.

9. M. Weiser, "The computer for the 21st century," Scientific American, vol. 265, pp. 94–104, 1991.

10. R. Qiu and Z. Zhang, "Design of enterprise Web servers in support of instant information retrievals," IEEE RFID Virtual Journal, pp. 2661-2666, vol. 3, 2003. doi:10.1109/ICSMC.2003.1244286.

11. M. H. Miraz et al., "A review on Internet of Things (IoT), Internet of Everything (IoE) and Internet of Nano Things (IoNT)," IEEE Spectrum, pp. 219–224, 2015. doi:10.1109/ITechA.2015.7317398.

12. T. Hiramoto et al., "Ultra-low power and ultra-low voltage devices and circuits for IoT applications," IEEE Silicon Nanoelectronics Workshop (SNW), pp. 146–147, 2016. doi:10.1109/SNW.2016.7578025.

13. S. K. Vishwakarma et al., "Smart energy efficient home automation system using IoT," IEEE 4th International Conference on Internet of Things: Smart Innovation and Usages (IoT-SIU), pp. 1–4, 2019. doi:10.1109/IoT-SIU.2019.8777607.

14. K. Wasa, et al., "Thin films of PZT-based ternary perovskite compounds for MEMS," IEEE Ultrasonics Symposium, pp. 213–216, 2008. doi:10.1109/ULTSYM.2008.0052.

15. J. Dudziak, "Dynamika środowiska," in Teoria okrętu, Wydawnictwo Morskie, Gdańsk, Poland, 1988, p. 338 (in Polish).

16. A. Iafrati et al., "Laboratory modelling of waves: Regular, irregular and extreme events," in Proceedings of the Specialist Committee on Modeling of Environmental Conditions, 28th ITTC, Wuxi, China, 17–22 September 2017, p. 8.

17. C. T. Stansberg et al., "Final report and recommendations to the 23rd ITTC," in Proceedings of the 23rd ITTC, Volume II, Specialist Committee on Waves, Venice, Italy, 8–14 September 2002, p. 517, pp. 544–551.

18. G. G. Cox et al., "Report of the Seakeeping Committee," in Proceedings of the 17th ITTC, Volume I, Seakeeping Committee, 17th ITTC, Goteborg, Sweden, 8–15 September 1984, p. 482.

19. M. Drzewiecki and J. Guziński, "Fuzzy control of waves generation in a towing tank," Energies, vol. 13, p. 2049, 2020. doi:10.3390/en13082049.

20. APC International, Ltd., "Modes of vibration for common piezoelectric ceramic shapes," in Piezoelectric Ceramics: Principles and Applications, APC International, Ltd.: Mackeyville, PA, USA, 2011, Table 1.8.

21. Pervasive Displays 2.71" E-ink display. Accessed: Feb. 11, 2023 [Online]. Available: https://www.pervasivedisplays.com/product/2-71-e-ink-display/

22. STM32WL55JC Sub-GHz Wireless Microcontrollers. Dual-core Arm Cortex-M4/M0+ @48 MHz with 256 Kbytes of Flash memory, 64 Kbytes of SRAM. LoRa, (G)FSK, (G)MSK, BPSK modulations. AES 256-bit. Multiprotocol System-on-Chip. Accessed: Feb. 11, 2023). [Online] Available:

https://www.st.com/en/microcontrollers-microprocessors/stm32wl55jc.html

23. Pervasive Displays, "How low-power e-paper displays enhance IoT applications." Accessed Feb. 11, 2023. [Online]. Available: https://www.pervasivedisplays.com/how-e-paper-works/

24. The Things Network, "What are LoRa and LoRaWAN?" Accessed Feb. 11, 2023. [Online]. Available: https://www.thethingsnetwork.org/docs/lorawan/what-is-lorawan/

25. N. Jovalekic et al., "Experimental study of LoRa transmission over seawater," Sensors, vol. 18, p. 2853, 2018. doi: 10.3390/s18092853.

26. The Things Network Global Team, "LoRaWAN® distance world record broken, twice." Accessed Feb. 11, 2023. [Online]. Available: https://www.thethingsnetwork.org/article/lorawan-world-record-broken-twice-in-single-experiment-1

27. "MPICOSYS Low Power Innovators Invent, Design & Produce For You." Accessed Feb. 11, 2023. [Online]. Available: https://www.mpicosys.com/

28. L. H. Holthuijsen, Waves in Oceanic and Coastal Waters. Cambridge: Cambridge University Press, 2007, p. 4.

29. Copernicus Marine Service Information, "Global Ocean Waves Analysis and Forecast," doi:10.48670/moi-00017. Accessed Feb. 19, 2023. [Online]. Available: https://data.marine.copernicus.eu/product/GLOBAL_ANALYSISFORECAST_WAV_001_027/description

30. P. Gualeni et al., "Confidence intervals for significant wave height and modal period," In Recommended Procedures and Guidelines, Specialist Committee on Stability in Waves of the 28th ITTC, Wuxi, China, 17–22 September 2017, p. 4.

EXPERIMENTAL STUDY OF THE NONLINEAR BEHAVIOUR OF DEEP-SEA MOORING POLYESTER FIBRE ROPES

He Zhang [ID] [1]
Ji Zeng * [2]
Bowen Jin [1]
Chiate Chou [3]
Hangyu Li [3]
Hailei Dong [3]

[1] Merchant Marine College, Shanghai Maritime University, Shanghai, China

[2] College of Ocean Science and Engineering, Shanghai Maritime University, Shanghai, China

[3] Zhejiang Four Brothers Rope Co. Ltd., Taizhou, China

* Corresponding author: *zengji@shmtu.edu.cn (Ji Zeng)*

ABSTRACT

Mooring ropes are essential components of ships and offshore floating structures and they are subjected to cyclic axial loads. This study investigates the evolution of the full-cycle stiffness of fibre polyester ropes under long-term static and dynamic loading. First, the static stiffness characteristics of the ropes, including the rope elongation properties at different stages, shrinkage rates, and creep coefficients after an idle period, are examined under static loads; an empirical formula for static stiffness is established. Second, the dynamic stiffness characteristics of the ropes are investigated under cyclic loads that are typical of platform production operations. The stabilities of the structure under different tensions are compared; the effects of mean tension, tension amplitude, and load cycle on the dynamic stiffness of the ropes are analysed and an empirical formula is established to predict the dynamic stiffness during the engineering design phase. The results of this study can be helpful for the rational design of deep-sea taut-leg mooring systems because they present the evolution of the full-cycle stiffness characteristics of mooring ropes.

Keywords: polyester fibre ropes; static stiffness; creep coefficient; long-term cyclic loads; dynamic stiffness

INTRODUCTION

As China continues to implement its marine strategy, the development of deep-sea oil and gas resources has become important for strengthening its maritime power. This development depends on the support of platform-positioning technology, and mooring ropes play a decisive role in the lifeline of the mooring system. In the 1960s, Vecchio and Moraes [1] proposed using synthetic fibres in deep-water taut-leg mooring systems. Kota et al. [2] compared the mooring performances of polyester ropes and steel cables at water depths of 1000–3000 m and found that polyester ropes were more advantageous compared with steel cables. However, unlike steel cables, synthetic fibre materials exhibit viscoelastic and viscoplastic behaviour [3], and the stretching behaviour of ropes made of such materials

exhibits nonlinear characteristics, which are influenced by factors such as load size and frequency. To understand the mooring performances of floating structures, numerous researchers have conducted extensive investigations on the mechanical properties of synthetic fibre ropes.

To examine the tensile properties of ropes, the American Bureau of Shipping (ABS) [4] developed a method for detecting their breaking strengths, which is one of the simplest mechanical parameters. Beltran and Williamson [5–7] established a numerical analysis model to study changes in the static curve and breaking strength under monotonic loading. This model can be used to predict rope performance under various loads. Williams et al. [8], Lanquetin et al. [9], and Lian et al. [10] evaluated the effects of different degrees of damage on the tensile forces of ropes by considering specimens with structural damage states. This

can further help us to understand the changes in mechanical performance when ropes are damaged during use. Davies et al. [11] found that most researchers only focused on the impact of the form of the load on the tension of ropes and ignored the impact of synthetic materials and weaving techniques. Therefore, they considered the influences of these factors on rope performance. Li et al. [12] considered the weaving structure and rope diameter in their mechanical research and further explored the influence of the rope's structure on its mechanical characteristics. Bain et al. [13] studied specific quantitative indicators of rope wear and the effects of different loading directions and strengths on stretching behaviour. These studies provide an important theoretical basis and experimental references for the design, manufacturing, and use of ropes.

Stiffness is one of the indicators used to determine the flexibility and bending performance of ropes and it is an important parameter for evaluating their performance and safety in engineering applications. In practical engineering, an appropriate assessment of rope stiffness can help engineers and designers choose suitable rope materials and structural forms, thereby ensuring the safety, reliability, and service life of ropes. Suitable testing methods and analytical tools are needed to accurately measure and analyse rope stiffness. Davies et al. [14] studied the dynamic stiffness evolution of three synthetic-fibre-rope types under short-term cyclic testing, namely: polyester, aramid, and high-molecular-weight polyethylene (HMPE). The results revealed that the mean tension was the main factor affecting the dynamic stiffness. Thus, they proposed an empirical formula for dynamic stiffness by considering the influence of the mean tension. Subsequently, Liu et al. [15] conducted dynamic stiffness tests on aramid, polyester, and HMPE ropes, Lian et al. [16] conducted tests on polyester and HMPE ropes, and Davies et al. [11] conducted tests on HMPE and aramid ropes. The results showed that, in addition to the mean tension, the tension amplitude and load cycle have a considerable impact on dynamic stiffness. Therefore, an empirical formula that integrates these three factors was proposed to improve the accuracy of the prediction model. Xu et al. [17] applied the Kalman filter to identify the parameters of an empirical formula and found that the Kalman filter could estimate the parameters of the empirical expression reliably and accurately. These studies revealed that rope stiffness testing is important, not only for the installation and use of ropes in practical engineering applications, but also, for clarifying the mechanical behaviour of synthetic fibre ropes [18–20]. However, certain problems require further investigation owing to the different degrees of rope wear, uncertainty in the accurate determination of elongation and stiffness, and ambiguity in rope creep during stiffness testing.

In this study, the axial tensile and complete stiffness characteristics of polyester ropes under load conditions were investigated through tension tests. To ensure the uniformity of the internal force on the rope, an empirical formula for stiffness was established by combining experimental data, including the static stiffness of the rope after installation and aging, and the dynamic stiffness of the rope under the influence of different mean tensions, tension amplitudes, and load cycles, considering the creep coefficient.

BASES FOR POLYESTER FIBRE ROPE TESTS

STIFFNESS TEST EQUIPMENT

For the stiffness test, a 3000-t microcomputer-controlled horizontal heavy-duty tension-testing machine (Zhejiang Four Brothers Rope Co., Ltd.) was used. The machine consists of an equipment base, a stator-end/stator hydraulic device, a test-end/test hydraulic device, and a water environment system, as shown in Fig. 1 [21]. The tensioner was 22 m long, with a capacity of 3000 t and a maximum error of 0.2%. The tests were conducted at room temperature (25°C) and 65% humidity. The elongation rate ΔL of the test rope was recorded four times per second using displacement sensors and strain gauges.

Fig. 1. Structural diagrams of 3000-t and rope-tension-reciprocating testing machine

For the test specimen, a polyester fibre rope with 1×12 strands was selected. Its parameters are specified in Table 1. The rope specimen was fixed to the testing equipment using the eye-splice method. The total length of the rope specimen was 14 m, which included an eye-splice length of approximately 3 m. To avoid the influence of eye-splice weaving on the mechanical properties of the rope and ensure that the rope specimen had a sufficient undisturbed area, the middle $L_0 = 5$ m segment was selected for measurements during the test, as shown in Fig. 2.

Tab. 1. Specifications of the polyester fibre rope test specimen

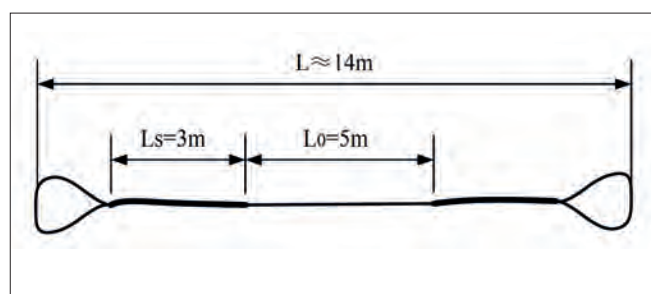|	Material	Pitch	Weaving	Diameter	Total length	Minimum breaking strength
Specimen	Polyester	300 mm	1×12 strands	68 mm	14 m	1786.4 kN

Fig. 2 . Diagram of test segment of polyester fibre rope

STIFFNESS CALCULATION

The elongation characteristics of a rope are typically related to the morphological structure of the corresponding material. The internal structures of the fibres include crystalline and amorphous forms. When the force is slowly loaded, the crystalline and amorphous parts of the structure have sufficient reaction time to act on the external forces. The mean stiffness of these two parts is called the 'static stiffness' of the rope. When the rope is subjected to periodic loading, the amorphous part of the structure cannot respond quickly to external forces, and only the crystalline part bears the load. The stiffness of this part is defined as the 'dynamic stiffness'. Generally speaking, the dynamic stiffness of a rope is approximately 2–3 times greater than its static stiffness.

Rope stiffness can be calculated by Eq. (1), and Eq. (2), after normalisation using the minimum breaking strength (MBS).

$$EA = \Delta T / \Delta \varepsilon \qquad (1)$$

$$K_r = EA / \text{MBS} = \frac{(T_n^p - T_{n-1}^v)/\text{MBS}}{\varepsilon_n^p - \varepsilon_{n-1}^v} \qquad (2)$$

where: E is the elastic modulus; A is the cross-sectional area; ΔT is the axial force increment; $\Delta \varepsilon$ is the strain increment; K_r is the stiffness coefficient; T_n^p and ε_n^p are the peak tension and corresponding strain in the n -th cycle, respectively; and T_{n-1}^v and ε_{n-1}^v are the valley tension and corresponding strain in the (n − 1)th cycle, respectively.

Here, K_r consists of a static stiffness coefficient, K_{rs}, and dynamic stiffness coefficient, K_{rd}. François and Davies [22] introduced the concept of 'quasi-static stiffness', to account for the influence of time-dependent characteristics of fibre mooring lines in mooring analysis. Additionally, the ABS has also defined the calculation method for static stiffness, as shown in Eq. (3).

$$K_{rs} = (T_2 - T_1) / [\varepsilon_2 - \varepsilon_1 + C\lg(t)], \qquad (3)$$

where: T_1 is the initial tension; T_2 is the final tension; ε_1 is the initial strain; ε_2 is the final strain; C is the creep factor (its determination is reported in the next section); and t is the creep time.

The calculation of the dynamic stiffness coefficient consists of three types: an upper and lower boundary model, a single-factor model, and a multifactor model. In a previous study [23], experimental data regarding the dynamic stiffness of polyester mooring ropes were collected from the relevant literature and the factor T_m was found to be an important factor influencing the dynamic stiffness of the rope, thus leading to the derivation of Eq. (4) for its calculation. However, the precise definition of the values for the upper and lower boundaries in the model was not provided. In another study [14], the dynamic stiffness calculation in Eq. (5) was derived for polyester mooring ropes influenced by factor T_m, avoiding the drawback of uncertain boundary values.

$$\begin{cases} 1.\ K_{rd} = 23 + 0.25T_m \quad \textit{lower limit} \\ \\ 2.\ K_{rd} = 17 + 0.2T_m \quad \textit{upper limit} \end{cases} \qquad (4)$$

$$K_{rd} = 18.5 + 0.33T_m . \qquad (5)$$

However, a series of model tests, conducted previously [24], revealed that the influence of the tension amplitude T_A and load cycle N on the dynamic stiffness cannot be ignored; a multifactor dynamic stiffness prediction formula was proposed, as shown in Eq. (6). In this study, a multifactor formula was adopted that considers the mean tension, tension amplitude, and load cycle to predict the dynamic stiffness of polyester ropes.

$$K_{rd} = \alpha + \beta T_m + \gamma T_A + \delta\lg(N) , \qquad (6)$$

where: T_m is the ratio of the mean tension to the average breaking strength (%MBS); T_A is the ratio of the tension amplitude to the average breaking strength (%MBS); N is the number of cycles; and α, β, γ and δ are the parameters of the empirical formula.

To ensure the accuracy of the derived dynamic stiffness equation, the accuracy of the dynamic stiffness model is evaluated using the error ratio ΔK_{rd}, mean error (ME), and mean squared error (MSE), as shown in Eqs. (7)–(9).

$$\Delta K_{rd} = (K_{rd_o} - K_{rd_o\,m}) / K_{rd_o\,m} , \qquad (7)$$

$$ME = \frac{1}{n} \sum_{t=1}^n (K_{rd,m}^t - \bar{K}_{rd}^t) , \qquad (8)$$

$$MSE = \frac{1}{n} \sum_{t=1}^n (K_{rd,m}^t - \bar{K}_{rd}^t)^2 , \qquad (9)$$

where: n is the sample size; $K_{rd,m}$ represents the experimental values of the dynamic stiffness of the model; $\bar{K}_{rd}$ represents the estimated values of the dynamic stiffness calculated using the nonlinear fitting function 'nlinfit' in MATLAB; and t is the number of steps in the discrete observation process.

STIFFNESS PRELOADING TEST

Before the stiffness tests were conducted, each sample rope was pre-processed by performing a preloading test. This test was conducted to determine whether the internal structure of the rope was stable and to ensure that each fibre in the rope was in an equivalent tensile state, thereby guaranteeing the accuracy of the subsequent tests. To simulate the marine environment better, the sample rope was immersed in freshwater for at least 4 h. A pre-processed sample rope was then installed between the two anchors of the tension-testing machine and a strain gauge and measuring gauge were attached to the test specimen to record the elongation of the rope. First, 1% MBS was applied and held for 5 min. Next, the load was gradually increased to 13% MBS and held for 2 h. Subsequently, the load was increased to 40% MBS and held for 3 h (if the load dropped by more than 5% MBS, it was increased back to 40% MBS). Finally, the load was reduced back to 13% MBS and held for 6 h to complete the installation of the preloading test.

Fig. 3 shows the variation in the test rope with the load during the preloading test. The maximum elongation rate of the sample rope was 6.49%, which decreased to 4.58% as the load decreased, thus indicating a positive correlation between the rope elongation rate and load size. After 6 h of static settling,
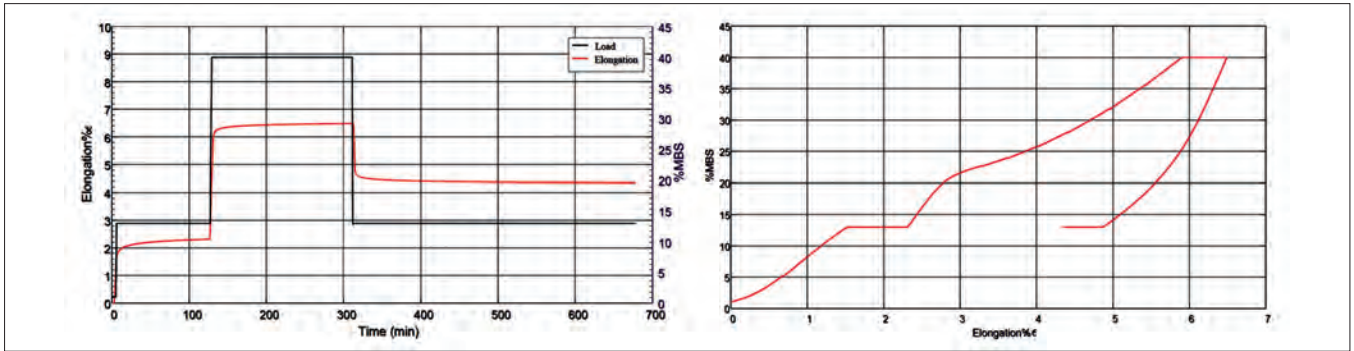
Fig. 3. Deformation of rope under different loads in the preloading test: (a) time-variation curve and (b) stress–strain curve

the elongation rate decreased to 4.345%, which is 0.23% less than that at the beginning of unloading. This indicates that some structural deformation inside the rope was not completely eliminated, thus resulting in a slight contraction of the rope. Therefore, fully tearing and wearing the rope is necessary.

STATIC STIFFNESS TEST OF POLYESTER FIBRE ROPES

The static stiffness test of the pre-treated ropes included initially installed ropes and aged ropes. In this study, periodic dynamic loads were considered to simulate the aging of the ropes. The pretension of 13% MBS was increased to 65% MBS and maintained for 100 min. Then, 1000 consecutive dynamic loads were applied within a tension range of 35–65% and cycles of 12–35 s. Finally, the tension of the last cycle was reduced to 13% MBS, and the aging of the rope was completed after 100 min. The experimental processes for studying the dynamic

stiffness of the initially installed ropes and aged ropes were identical, and the specific force loading conditions are shown in Fig. 4.

The tensile characteristics, creep coefficients, and empirical formulas were determined for the static stiffness of the ropes at the installation stage under different loads. Fig. 4 shows that the tension during the static stiffness test process increased from 3% to 30% MBS and was maintained for 100 min. The tension was increased from 45% to 60% MBS and maintained for 100 min before unloading to the initial tension of 13% MBS. The strains of the ropes are shown in Fig. 5. The strains after loading and unloading of the initially installed and aged ropes were 7.835 and 7.952%, respectively; the corresponding strains for the pretension of 13% MBS were 5.192% and 5.441%. After remaining static for 200 min, the strains were 4.729% and 5.002%, respectively. The change in rope elongation shows that, after a static period, the initially installed and aged ropes shrank by 0.463% and 0.439%, respectively, and the shrinkage rates of the two were almost the same.
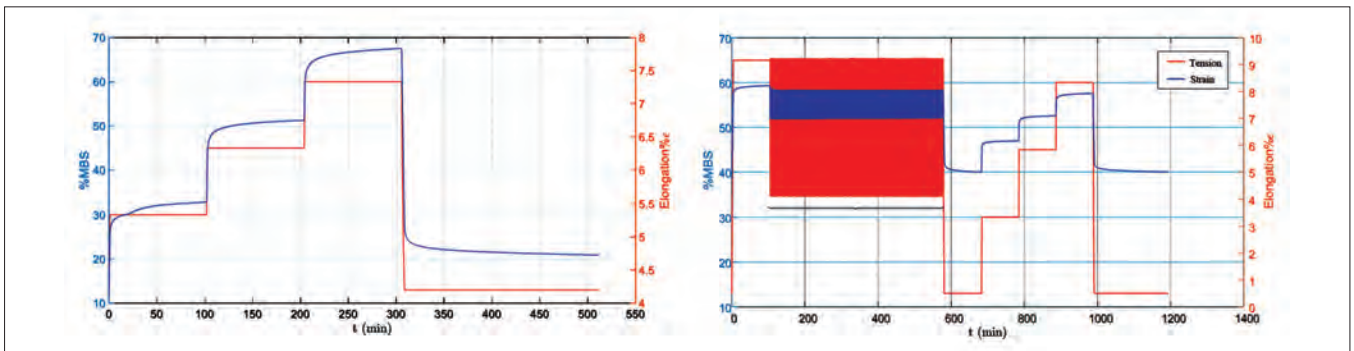
Fig. 4. Time curves of tension/strain in static stiffness test: (a) initially installed ropes and (b) aged ropes
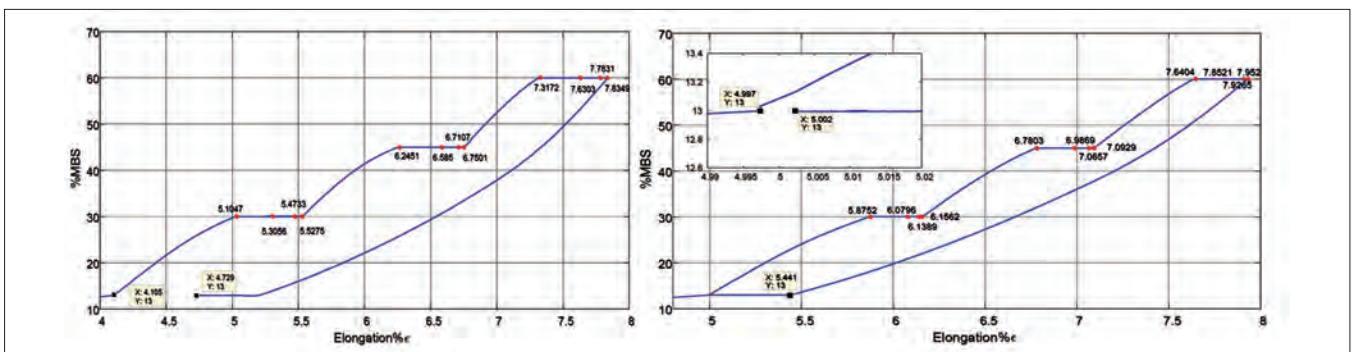
Fig. 5. Stress–strain curves of static stiffness test: (a) initially installed ropes and (b) aged ropes
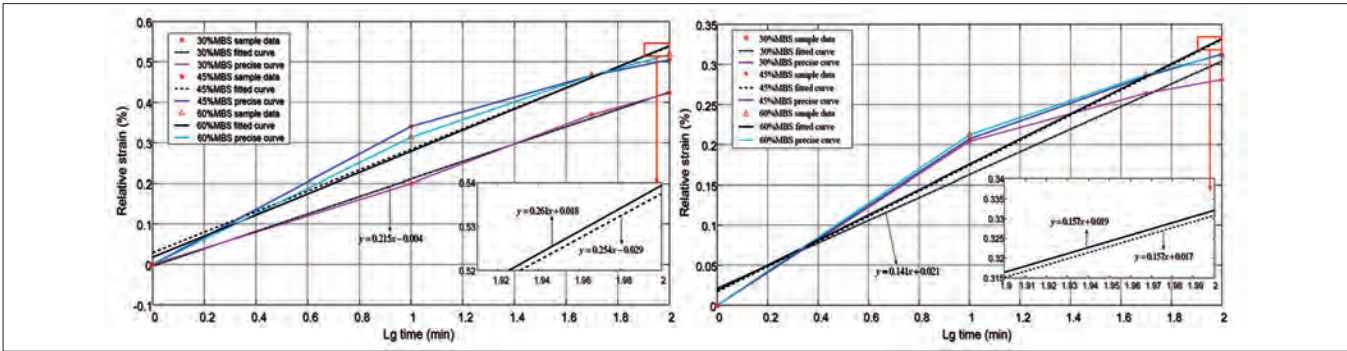
Fig. 6. Determination of creep coefficient of ropes based on static stiffness: (a) initially installed ropes and (b) aged ropes

Because different tensile loads correspond to unique creep coefficients, the rope elongation was measured and recorded at 1, 10, 50, and 100 min, to obtain the creep coefficients under different loads. For the convenience of calculation, the corresponding strain was assumed to be zero at the beginning of the test. The data for determining the creep coefficient under the static stiffness of the rope are presented in Table 2 and are derived from Fig. 5.

Tab. 2. Creep data for static stiffness testing of ropes with 30%, 45%, and 60% MBS

| Load (%MBS)	Time (t, min)	Lg (t)	Initially installed rope strain (ε)	Aged rope strain (ε)	Relative strain of initially installed rope (%)	Relative strain of aged ropes (%)
30	1	0	5.1047	5.8752	0.000	0.000
30	10	1	5.3056	6.0796	0.200	0.204
30	50	Lg (50)	5.4733	6.1389	0.369	0.264
30	100	2	5.5275	6.1562	0.423	0.281
45	1	0	6.2451	6.7803	0.000	0.000
45	10	1	6.5850	6.9869	0.340	0.207
45	50	Lg (50)	6.7107	7.0657	0.466	0.285
45	100	2	6.7501	7.0929	0.505	0.313
60	1	0	7.3172	7.6404	0.000	0.000
60	10	1	7.6303	7.8521	0.313	0.212
60	50	Lg (50	7.7831	7.9265	0.466	0.287
60	100	2	7.8949	7.9520	0.518	0.312

The objective of this study was to determine the creep coefficient C, under different loads. The experimental data listed in Table 2 and the linear regression analysis performed using MATLAB software were utilised to obtain the results displayed in Fig. 6. As the applied load increased, the slopes of the regression curves for the initially installed and aged ropes increased in the order of 0.125, 0.254, and 0.261; and 0.141, 0.157, and 0.157, respectively. The creep rates corresponding to 30%, 45%, and 60% MBS were determined. As the tension load increased over time, the corresponding strain gradually increased, and the creep coefficient increased proportionally with the tension load. This indicates that the larger the tension load, the larger the creep coefficient of the rope.

The tension, strain, and fitted C values were substituted into Eq. (3) to solve the static stiffness equations for the ropes under 30%, 45%, and 60% MBS loads, as shown in Eq. (10). The derived formulas were used to predict the static stiffness of the rope material in advance and provide theoretical guidance for engineering production.

The dynamic stiffness values of initially installed ropes are:

$$K_{rs} = 17 / [1.423 + 0.144 \lg(t)] \quad (\text{Load} = 30\% \text{MBS})$$
$$K_{rs} = 32 / [2.222 + 0.641 \lg(t)] \quad (\text{Load} = 45\% \text{MBS})$$
$$K_{rs} = 47 / [2.802 + 0.171 \lg(t)] \quad (\text{Load} = 60\% \text{MBS})$$

(10)

The dynamic stiffness values of aged ropes are:

$$K_{rs} = 17 / [1.159 + 0.141 \lg(t)] \quad (\text{Load} = 30\% \text{MBS})$$
$$K_{rs} = 32 / [1.815 + 0.157 \lg(t)] \quad (\text{Load} = 45\% \text{MBS})$$
$$K_{rs} = 47 / [2.361 + 0.157 \lg(t)] \quad (\text{Load} = 60\% \text{MBS})$$

(11)

Fig. 7 shows a line graph of the six static stiffness equations derived, which can facilitate the prediction of static stiffness during the rope production and design phases. The load applied during the test can be considered to be equivalent to the actual forces the rope would experience in a marine environment. Fig. 7 shows that the static stiffness increases with increasing load and decreases with increasing duration of the load. Aged ropes exhibit greater static stiffness than initially installed ropes under the same load, primarily because aged ropes undergo sufficient wear and tear, thus resulting in less residual strain in the internal structure and a greater ability to resist external deformation.
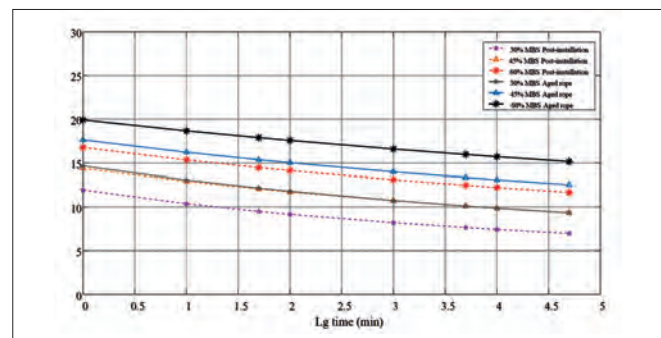

Fig. 7. Static stiffness line graph for polyester fibre ropes

DYNAMIC STIFFNESS TESTING OF POLYESTER FIBRE ROPES

The design of the dynamic stiffness test conditions for the polyester fibre ropes includes two main types of load: tension and tightening. The load cycles were selected based on the inherent periods of swaying, rolling, and heaving during the production operation of offshore floating platforms. The test conditions are listed in Table 3.

Tab. 3. Design of dynamic stiffness test conditions for polyester ropes

Test	Mean tension T_m (%MBS)	Tension amplitude T_A (%MBS)	Minimum tension T_{min} (%MBS)	Maximum tension T_{max} (%MBS)	Load cycle T_m (S)
1	15	2	13	17	30
2	15	5	10	20	30
3	15	2	13	17	150
4	15	3	12	18	150
5	35	10	25	45	40
6	35	15	20	50	15
7	35	15	20	50	150
8	40	10	30	50	40
9	40	20	20	60	40
10	40	15	25	55	15
11	40	15	25	55	150
12	50	10	40	60	40
13	50	15	35	65	15
14	50	15	35	65	150
15	60	10	50	70	15
16	60	10	50	70	150
17	60	15	45	75	30
18	65	5	60	70	150

The testing procedure for dynamic stiffness followed the following steps.
(1) For each wave frequency test case, the rope was cycled 40 times between T_{min} and T_{max}, and the load and elongation were recorded at a frequency of at least 1 Hz.
(2) For each low-frequency test case, the rope was cycled 20 times under tension between T_{min} and T_{max}, and the load and elongation were recorded at a frequency of at least 0.25 Hz.
(3) The test for the entire matrix was continuous without significant interruptions.

Fig. 8 shows the time-varying load in the dynamic stiffness testing of the rope. The parallel peaks and valleys of the tension in the figure indicate that the test system can provide long-term stable cyclic loads. Moreover, the graph indicates that this study considered the effects of three factors (mean tension, tension amplitude, and cycle period) on the dynamic stiffness of the rope. For example, tests 8–10 considered the effect of the tension

amplitude on the dynamic stiffness, whereas the mean tension was the same. Tests 6, 10, and 13 considered the effect of the mean tension on the dynamic stiffness.
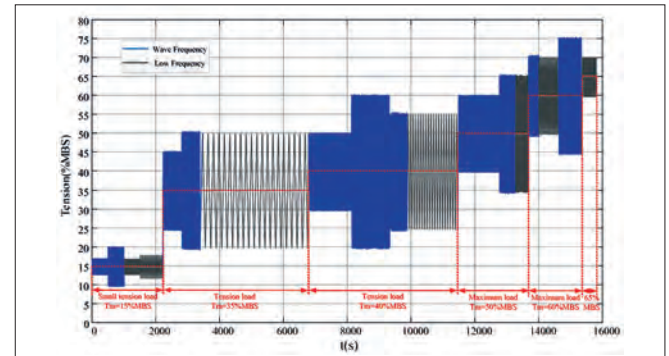
Fig. 8. Load curves for dynamic stiffness tests under working conditions

DYNAMIC STIFFNESS UNDER DIFFERENT TENSION AMPLITUDES

The pre-stretched rope was fixed on the tension-testing machine, and tests 8–10 were conducted to examine the influence of the tension amplitude (T_A) on the dynamic stiffness of the rope when the mean tension (T_m) was determined. The cyclic load acting on the rope was applied through the harmonic motion of the free end of the testing machine. Fig. 9 depicts the variation in force and strain with time. The figure indicates that the mean tension on the test rope was 40% MBS and the tension peak and tension valley were parallel, demonstrating that the test system could provide a long-term stable cyclic load of both the mean tension and the tension amplitude. The figure also shows that the strain increased with increasing tension amplitude; the strain is a maximum at $T_A = 20\%$ MBS.
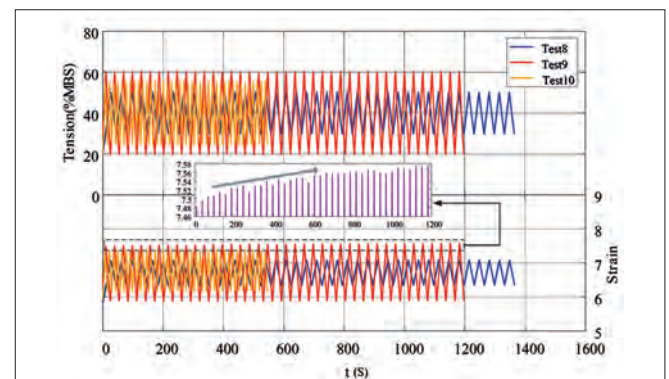
Fig. 9. Time curves of force and strain under different tension amplitudes

Fig. 10 shows the variation in rope tension and strain with time under different tension amplitudes (taking the results for the last five cycles, as an example). The test results show that the tension and strain change nonlinearly, and that a hysteresis loop forms owing to the nonlinear viscoelastic and viscoplastic behaviour. The area of the hysteresis loop represents the energy dissipation caused by the production and accumulation of the rope heat. In this test, a water-cooling system was used to cool the fibre rope, thus eliminating heat accumulation. The high degree of coincidence of the hysteresis loops in the last five cycles

indicates that the internal structure of the rope tends to be stable. The test also demonstrates that tension amplitude and strain are positively correlated and this result can be further extended to practical engineering. More specifically, the ability of a rope to resist dynamic deformation under high-amplitude loads is poor.
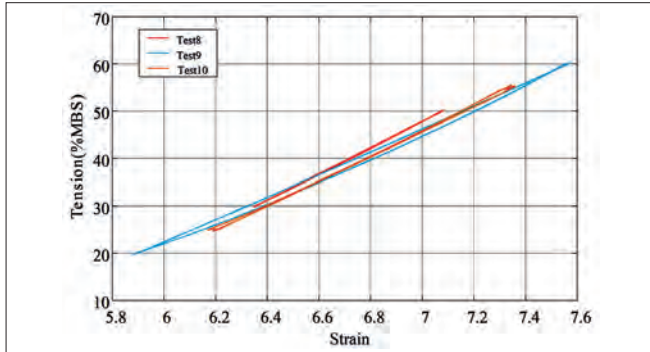
Fig. 10. Rope strains under different tension amplitudes in the last five cycles

Based on these tests, the evolution curve of the dynamic stiffness of polyester ropes with cyclic loads can be plotted using Eq. (2). Fig. 11 indicates that, even under tension amplitudes of 10%, 15%, and 20%, the effect of the tension amplitude on the dynamic stiffness is significant, and the tension amplitude and dynamic stiffness are negatively correlated. In particular, as the tension amplitude increases, the dynamic stiffness decreases. Therefore, the influence of the tension amplitude T_A cannot be ignored in the empirical formula for rope dynamic stiffness. At the same time, as the cycle load period increases, the fluctuation of the dynamic stiffness of the rope decreases, thus indicating a relatively stable internal structure of the cable rope. Thus, the dynamic stiffness of the rope, ultimately, tends to stabilise.
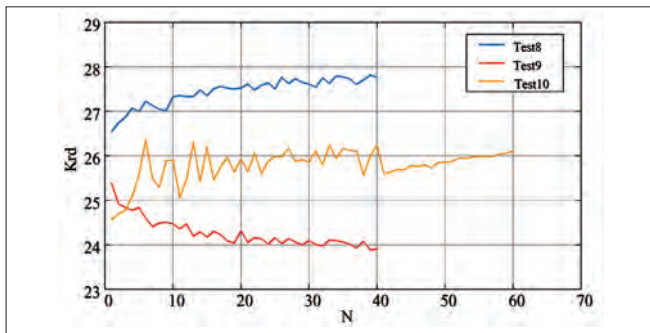
Fig. 11. Dynamic stiffness evolution under different tension amplitudes

DYNAMIC STIFFNESS UNDER DIFFERENT MEAN TENSIONS

Based on test conditions 7, 11, and 14, the influence of the mean tension (T_m) on the dynamic stiffness was examined. Fig. 12 shows the variations in the cyclic load and strain over time. When the load amplitude was 15% MBS, the strain ($\Delta L/L$) increased with increasing mean tension (T_m). Thus, the impact on the stability and deformation of the rope structure was greater under larger tension values. Combining the strain distribution of the rope under the last five cycles, as shown in Fig. 13, reveals that the residual strain accumulated in the initial stage of the test was considerable. With increasing time, the strain response to the

cyclic load gradually reached a steady state and the hysteresis loops ultimately overlapped, indicating that the deformation of the rope tended to stabilise.
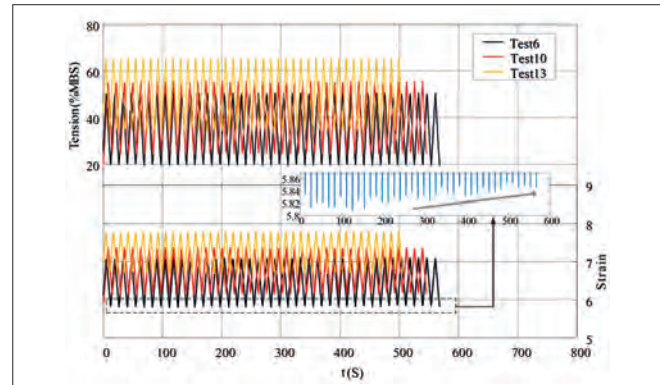
Fig. 12. Time curves of force and strain under different mean tensions
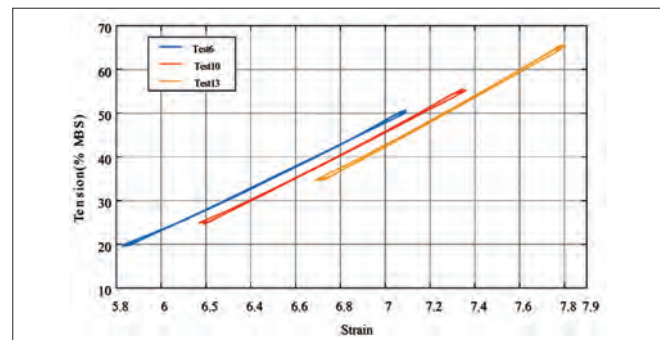
Fig. 13. Rope strains under different tension amplitudes in the last five cycles

Based on these experiments, the evolution curve of the dynamic stiffness of polyester ropes with periodic loads can be obtained by calculating and organising the test data using Eq. (2). Fig. 14 shows that the dynamic stiffness of the tested rope gradually increased with time and stabilised at $N = 40$; the dynamic stiffness of the rope was largest under $T_m = 50\%$ MBS, compared with the other two test conditions. In particular, the dynamic stiffness increased with an increase in the mean tension. The main reason for this was that the twisting changed the fibre structure inside the rope and was significant under a large load; the twisting angle between the structures decreased with an increase in the mean load. More specifically, the structure became more stable under high tension, owing to the smaller twisting angle between the fibres/strands. Thus, the rope had a greater ability to resist external deformation, thereby resulting in a larger dynamic stiffness.
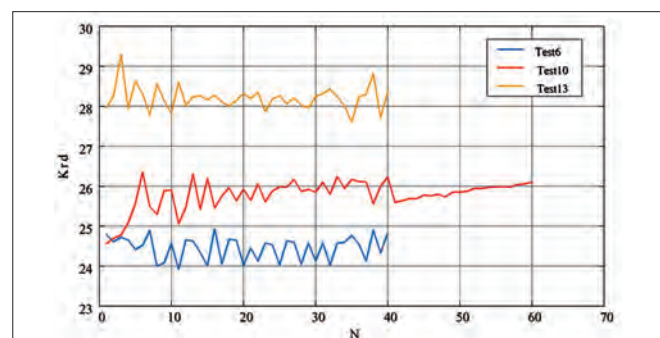
Fig. 14. Evolution of dynamic stiffness under different mean tensions
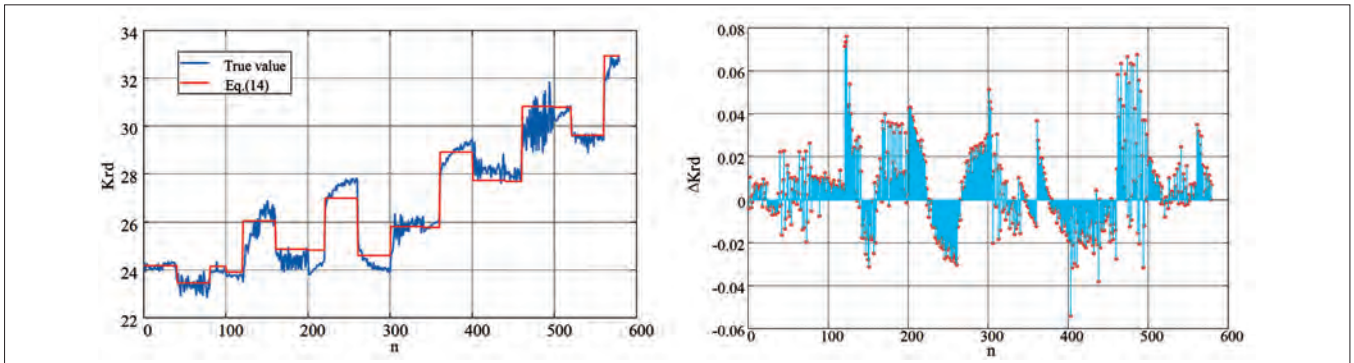
Fig. 15. Numerical analysis of rope dynamic stiffness: (a) dynamic stiffness value and (b) relative error

Based on the experimental data and the influence of the mean tension (T_m), tension amplitude (T_A), and load cycle (N), an empirical expression for the dynamic stiffness of polyester ropes was established, as shown in Eq. (12), where the parameters have the same meanings as previously mentioned.

$$K_{rd} = \alpha + \beta T_m + \gamma T_A + \delta \lg(N) . \qquad (12)$$

Using the experimental data obtained under the 18 operating conditions designed in this test (Table 4), the relevant parameters in Eq. (17) were solved using the nonlinear fitting function in MATLAB, where α, β, γ, and δ were 21.87, 0.19, −0.24, and 0.04, respectively, as shown in Eq. (14).

$$K_{rd} = 21.87 + 0.19T_m - 0.24T_A - 0.04\lg(N) . \qquad (14)$$

A comparison of the dynamic stiffness of the ropes is shown in Fig. 15, including the measured values $K_{rd,m}$ and the predicted values K_{rd} based on the empirical formulas. In Fig. 15(b), an error occurs between $N \approx 120$ and $N \approx 500$ rather than in the initial loading phase with the fastest growth rate. This is related to the relaxation and instability of the internal structure of the sample. When dynamic stiffness values are substituted into Eqs. 8) and (9), the calculated ME and MSE are 0.125 and 0.279, respectively. To a certain extent, this empirical formula can reflect the dynamic stiffness of polyester fibre ropes.

During the rope design phase, the use of predicted empirical formulas makes an advance estimation of stiffness possible, thereby reducing the need for extensive testing and lowering economic costs. To examine the flexibility of the different empirical equations for predicting the dynamic stiffness of polyester ropes, the measured dynamic stiffness (last cycle) was compared with the empirical equations under different conditions, as presented in Table 4. Clearly, the equation derived in this study provides the most-accurate calculations.

Fig. 16 indicates the existence of a significant error in Eqs. (4) 1 and (5); additionally, Eq. (4) 2 exhibits noticeable fluctuations. This indicates that the accuracy of the empirical equations used to predict the dynamic stiffness of the ropes is not entirely reliable. The determination of these empirical formulas may be influenced by such factors as the rope manufacturing processes, weaving structures, testing procedures, and equipment errors. Even with the same rope material, different weaving structures or testing procedures can lead to deviations in the predicted results of the empirical formulas. Therefore, further research is

Tab. 4. Comparison of measured and calculated values of dynamic stiffness of polyester ropes

Polyester	Measured K_{rd}	Eq. (4)		Eq. (5)	Eq. (14)
		1	2	1	1
Test 1	23.659	26.75	20.00	23.45	24.18
	Relative error (%)	13.06	15.47	0.88	2.20
Test 2	23.223	26.75	20.00	23.45	23.46
	Relative error (%)	15.19	13.88	0.98	1.02
Test 3	23.918	26.75	20.00	23.45	24.15
	Relative error (%)	11.84	16.38	1.96	0.97
Test 4	23.819	26.75	20.00	23.45	23.91
	Relative error (%)	12.31	16.03	1.55	0.38
Test 5	26.183	31.75	24.00	30.05	26.06
	Relative error (%)	21.26	8.34	14.77	0.47
Test 6	24.828	31.75	24.00	30.05	24.87
	Relative error (%)	27.88	3.34	21.03	0.17
Test 7	24.393	31.75	24.00	30.05	24.83
	Relative error (%)	30.16	1.61	23.19	1.79
Test 8	27.762	33.00	25.00	31.70	27.01
	Relative error (%)	18.87	9.95	14.18	2.71
Test 9	23.904	33.00	25.00	31.70	24.61
	Relative error (%)	38.05	4.58	32.61	2.95
Test 10	26.234	33.00	25.00	31.70	25.82
	Relative error (%)	25.79	4.70	20.84	1.58
Test 11	26.104	33.00	25.00	31.70	25.78
	Relative error (%)	26.42	4.23	21.44	1.24
Test 12	29.459	35.50	27.00	35.00	28.91
	Relative error (%)	20.50	8.35	18.81	1.86
Test 13	28.354	35.50	27.00	35.00	27.72
	Relative error (%)	25.20	4.77	23.44	2.24
Test 14	28.466	35.50	27.00	35.00	27.68
	Relative error (%)	24.71	5.15	22.95	2.76
Test 15	30.337	38.00	29.00	38.30	30.82
	Relative error (%)	25.26	4.41	26.25	1.59
Test 16	30.836	38.00	29.00	38.30	30.78
	Relative error (%)	23.23	5.95	24.21	0.18
Test 17	29.418	38.00	29.00	38.30	29.61
	Relative error (%)	29.17	1.42	30.19	0.65
Test 18	32.714	39.25	30.00	39.95	32.93
	Relative error (%)	19.98	8.30	22.12	0.66

needed to improve the universality of these empirical formulas for predicting rope dynamic stiffness.
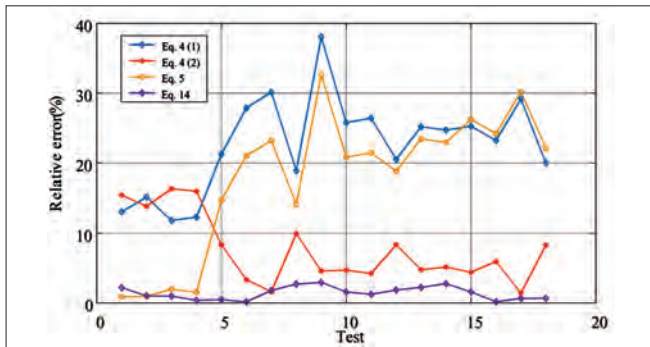

Fig. 16. Comparison of results from empirical formulas for dynamic stiffness of ropes

CONCLUSION

To study the tensile properties and stiffness characteristics of polyester fibre ropes, several tensile tests were conducted. The mechanical characteristics of the ropes were explored under static loads during three stages: preloading, initial installation, and aging. The experimental results demonstrated a positive correlation between the elongation rate and the tensile strength of the ropes. A reversible elongation rate of approximately 0.23% was observed during the preloading stage under small loads. By contrast, the reversible elongation rates during the initial installation and aging stages under large loads were similar (approximately 0.45%). This indicates that the axial force disrupts the internal structure of the ropes; however, once they are sufficiently worn, the elongation rate and reversible elongation rate tend to stabilise at a fixed value.

To facilitate the prediction of the static stiffness during the design phase, an empirical formula for the static stiffness of polyester ropes was established based on the creep coefficient. We found that the static stiffness of the rope is linearly correlated with the duration of the load. Furthermore, the aged ropes had a higher static stiffness than the initially installed ropes. This is mainly attributed to the fact that the ropes that had been used underwent sufficient stretching, resulting in a smaller residual strain and a more stable structure, thus leading to increased stiffness. Comparing the creep coefficients under different loads revealed that the coefficient increases as the load increases.

The cyclic load test considered the effects of different mean loads and load amplitudes on the dynamic stiffness of the rope. The dynamic stiffness increased with an increase in the mean load and decreased with an increase in the load amplitude. An empirical formula for the dynamic stiffness was established and multiple empirical formulas were compared with experimental measurements. Overall, all of the empirical formulas significantly underestimated the dynamic stiffness. The determination of empirical formulas is influenced greatly by such factors as the rope manufacturing process, braiding structure, testing procedure, and equipment errors.

REFERENCES

1. D. Vecchio and C.J. Moraes, 'Light weight materials for deep water moorings', University of Reading, 1992.

2. R.S. Kota, W. Greiner, and R.B.D'Souza, 'Comparative assessment of steel and polyester moorings in ultradeep water for spar- and semi-based production platforms', Proceedings of the Offshore Technology Conference. 1999, https://doi.org/10.4043/10909-MS.

3. G.P. Foster, 'Advantages of fibre rope over wire rope', Journal of Industrial Textiles. 2002, doi: 10.1106/152808302031656.

4. American Bureau of Shipping, 'Guidance notes on the application of fibre rope for offshore mooring'. 2011.

5. J.F. Beltran and E.B. Williamson, 'Degradation of rope properties under increasing monotonic load'. Ocean Engineering. 2005, https://doi.org/10.1016/j.oceaneng.2004.10.004.

6. J.F. Beltran and E.B. Williamson, 'Investigation of the damage-dependent response of mooring ropes', Journal of Engineering Mechanics. 2009, https://doi.org/10.1061/(ASCE)0733-9399(2009)135:11(1237).

7. J.F. Beltran and E.B. Williamson, 'Numerical simulation of damage localization in polyester mooring ropes'. Journal of Engineering Mechanics. 2010, https://doi.org/10.1061/(ASCE)EM.1943-7889.0000129.

8. J.G. Williams, A. Miyase, D. Li, and S.S. Wang, 'Small-scale testing of damaged synthetic fibre mooring ropes'. Proceedings of the Offshore Technology Conference. 2002, https://doi.org/10.4043/14308-MS.

9. E.G. Lanquetin, R.R. Ayers, S.J. Banfiel, N. O'Hear, C.E. Smith, and T. Laurendine, 'The residual strength of damaged polyester rope'. Proceedings of the Offshore Technology Conference. 2006, https://doi.org/10.4043/18150-MS.

10. Y. Lian, B. Zhang, J. Zheng, H. Liu, G. Ma, S.C. Yim, and Y. Zhao, 'An upper and lower bound method for evaluating residual strengths of polyester mooring ropes with artificial damage'. Ocean Engineering. 2022, https://doi.org/10.1016/j.oceaneng.2022.112243.

11. P. Davies, Y. Reaud, L. Dussud, and P. Woerther, 'Mechanical behaviour of HMPE and aramid fibre ropes for deep sea handling operations'. Ocean Engineering. 2011, https://doi.org/10.1016/j.oceaneng.2011.10.010.

12. G. Li, W. Li, S. Lin, H. Li, Y. Ge, and Y. Sun, 'Dynamic stiffness of braided HMPE ropes under long-term cyclic loads: A full-scale experimental investigation'. Ocean Engineering. 2021, https://doi.org/10.1016/j.oceaneng.2021.109076.

13. C. Bain, P. Davies, G. Bles, Y. Marco, and J. Barnet, 'Influence of bedding-in on the tensile performance of HMPE fibre ropes'. Ocean Engineering. 2020, https://doi.org/10.1016/j.oceaneng.2020.107144.

14. P. Davies, M. François, F. Grosjean, P. Baron, K. Salomon, and D. Trassoudaine, 'Synthetic mooring lines for depths to 3000 meters'. Proceedings of the Offshore Technology Conference. 2002, https://doi.org/10.4043/14246-MS.

15. H. Liu, W. Huang, Y. Lian, and L. Li, 'An experimental investigation on nonlinear behaviours of synthetic fibre ropes for deepwater moorings under cyclic loading'. Applied Ocean Research. 2014, https://doi.org/10.1016/j.apor.2013.12.003.

16. Y. Lian, H. Liu, L. Li, and Y. Zhang, 'An experimental investigation on the bedding-in behaviour of synthetic fibre ropes'. Ocean Engineering. 2018, https://doi.org/10.1016/j.oceaneng.2018.04.071.

17. S. Xu, S. Wang, H. Liu, Y. Zhang, L. Li, and C.G. Soares, 'Experimental evaluation of the dynamic stiffness of synthetic fibre mooring ropes'. Applied Ocean Research. 2021, https://doi.org/10.1016/j.apor.2021.102709.

18. S. Xu and C. Guedes Soares, 'Dynamics of an ultra-deepwater mooring line with embedded chain segment'. Marine Structures. 2020, https://doi.org/10.1016/j.marstruc.2020.102747.

19. S.D. Weller, L. Johanning, P. Davies, and S.J. Banfield, 'Synthetic mooring ropes for marine renewable energy applications'. Renewable Energy. 2015, https://doi.org/10.1016/j.renene.2015.03.058.

20. W. Huang, H. Liu, Y. Lian, and L. Li, 'Modeling nonlinear creep and recovery behaviours of synthetic fibre ropes for deepwater moorings'. Applied Ocean Research. 2013, https://doi.org/10.1016/j.apor.2012.10.004.

21. L. Maoben, L. Yanxi, L. Hangyu, L. Ji, '3000 tons and below rope tension reciprocating tester'. Patent CN108548738A.

22. M. Francois and P. Davies, 'Characterization of polyester mooring lines'. Proceedings of the ASME International Conference on Offshore Mechanics & Arctic Engineering. 2008.

23. C. Wibner, T. Versavel, and I. Masetti, 'Specifying and testing polyester mooring rope for the Barracuda and Caratinga FPSO deepwater mooring systems'. Proceedings of the Offshore Technology Conference. 2003, OTC-15139-MS.

24. H. Liu, Y. Lian, L. Li, Y. Zhang, 'Experimental investigation on dynamic stiffness of damaged synthetic fibre ropes for deepwater moorings. Journal of Offshore Mechanics and Arctic Engineering. 2015.

RESEARCH ON THE MODIFIED ECHO HIGHLIGHT MODEL FOR UNDERWATER VEHICLES WITH COMBINED STRUCTURES

Xin Xie [1]
Fanghua Liu [1]
Guangwen Jin [2]
Jinwei Liu [3]
Cong Xu [3]
Zilong Peng [4] *

[1] School of Mechanical Engineering, Jiangsu University of Science and Technology, Zhenjiang, Jiangsu 212100, China

[2] Shanghai Marine Equipment Research Institute, Shanghai 200031, China

[3] School of Energy and Power, Jiangsu University of Science and Technology, Zhenjiang, Jiangsu 212100, China

[4] Jiangsu University of Science and Technology, Zhenjiang, China,

* Corresponding author: *zlp_just@sina.com (Zilong Peng)*

ABSTRACT

The highlight model is widely used as a simple and convenient method in the radar field but its accuracy is not high. Based on the traditional highlight model, the algorithm has been improved to address the acoustic scattering problems of underwater vehicles with more complex line shapes. The basic idea is to partition the model into micro-bodies to calculate the scattered sound pressure, consider the phase interference of each part, and then synthesise the scattered sound pressure to approximate the target's actual shape. A computational model of the wedge-shaped convex structure on the back of the underwater vehicles is developed using a highlight model of a trapezoidal plate. The results of the calculations using the highlight model approach are consistent with those of the planar element method. Utilising the modified highlight model method, the accuracy of acoustic scattering characteristics calculations for the stern and overall structures of underwater vehicles has proven satisfactory. Finally, fast acoustic scattering prediction software is developed for underwater vehicles, enabling the calculation of the acoustic scattering characteristics for individual structures, combined structures, and coated silent tiles. This software provides algorithmic support for the fast prediction of the acoustic stealth performance of underwater vehicles.

Keywords: modified highlight model, wedge-shaped convex structure, piecewise synthesis method, acoustic scattering calculation software

INTRODUCTION

Predicting the acoustic scattering of complex underwater targets is an important research direction in modern hydroacoustics. The characteristics of target acoustic scattering serve as a crucial foundation for active sonar in detecting and recognising underwater targets [1]. The methods for studying the acoustic scattering characteristics of underwater targets can be categorised as either numerical or approximate methods. Among the numerical methods, the Rayleigh normal mode solution [2,3] is primarily used to predict the acoustic scattering characteristics of simple targets; the integral equation

method [4-6] can lead to singularities in the integral equation or uniqueness of the solution; the finite element/boundary element method [7-10] is suitable for small-sized targets at low frequencies; and the T-matrix method [11,12] exhibits low computational efficiency. The approximation method is mainly employed for high-frequency problems. Lee and Seong [13] derived a time-domain solution of the impedance polygon facet from the Kirchhoff formula. Fan and Tang [14–16] introduced the Planar Elements Method, which they continuously modified. Abawi [17] developed a method for solving both frequency-domain and time-domain solutions for arbitrarily shaped scattered sound fields, based on the Kirchhoff approximation.

Stanton [18,19] proposed the deformed cylinders method, building upon the concept of a radiating sound field from an inhomogeneous line source. Tang [20] proposed the highlight model after summarising research results on target acoustic scattering, describing the highlight characteristics with three parameters: amplitude, time delay, and phase factors. Theoretical analysis and experimental results demonstrate that, in the case of high frequency, complex targets can be represented as combinations of several highlights, each producing an echo. The total echo results from the interference superposition of these highlight echoes. Liu [21] and Chen [22] conducted investigations into the echo highlight of complex targets. In the present study, the highlight model is utilised to calculate the echoes of the complex underwater vehicles model, but it exhibits limited accuracy in the target echoes.

In this paper, we modified the highlight model by utilising the piecewise synthesis method [23,24] to further enhance the computational accuracy of the highlight model. The modified highlight method was employed to calculate the acoustic scattering characteristics of the wedge-shaped convex structure and several sub-structures of the underwater vehicles. The results were compared with those of the planar element method and they showed relatively consistent findings. Finally, based on the theoretical work, we summarised the highlight model method and developed two software programs: 'Target Strength Prediction Software for Simple Convex Structure of Underwater Vehicles' and 'Target Strength Fast Prediction Software for Multi-Highlight Interference of Underwater Vehicles'.

HIGHLIGHT MODEL FOR ACOUSTIC SCATTERING FROM A FINITE ELLIPTICAL CYLINDER

The shape of the sail and rudder of early underwater vehicles is similar to that of an elliptical cylinder, making them suitable for approximation using the scattering highlight of an elliptical cylinder, as depicted in Fig. 1. We employed the physical acoustic method and the saddle point approximation method to derive two equivalent edge highlights for the upper and lower edges of the elliptical cylinder, resulting in the transfer function [25]:

$$H(\vec{r},\omega) = H_1(\vec{r},\omega) + H_2(\vec{r},\omega) \qquad (1)$$

$$H_1(\vec{r},\omega) = \frac{C}{D} e^{2jk(\sqrt{(Aa)^2+(Bb)^2} + L\cos\theta)-j\frac{5\pi}{4}} \qquad (2)$$

$$H_2(\vec{r},\omega) = \frac{C}{D} e^{2jk(\sqrt{(Aa)^2+(Bb)^2} + L\cos\theta)-j\frac{\pi}{4}} \qquad (3)$$

where $A = \sin\theta \cos\varphi$, $B = \sin\theta \sin\varphi$, $C = ab(A^2+B^2)$, and $D = 4\sqrt{k}\pi\cos\theta((Aa)^2+(Bb)^2)^{3/4}$.

When $a = b$, Eq. (1) represents the highlight transfer function for a finite cylinder.

We further calculated the target strength for an elliptical cylinder with dimensions $a = 3$ m, $b = 1$ m, and $L = 5$ m, using the highlight model method and the planar element method, respectively, in the frequency band of 1-10 kHz; the results are depicted in Fig. 2.
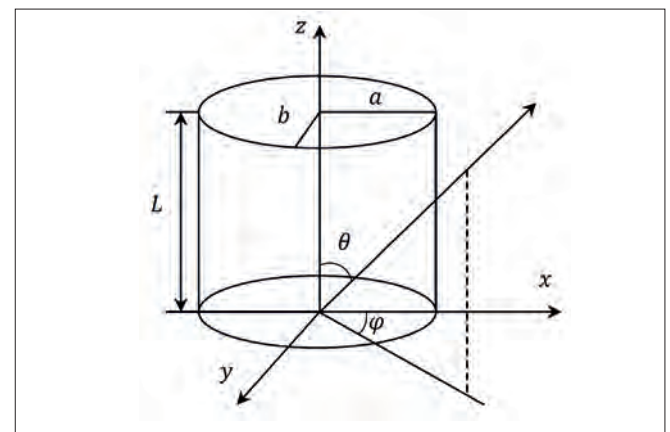
Fig. 1. Geometry of the elliptical cylinder

SIMPLE STRUCTURAL HIGHLIGHT MODEL METHODOLOGY AND VALIDATION

The underwater vehicles have a bulged back structure [26], which can be seen as a stretched trapezoidal plate, usually behind the sail or as a whole, filled above the hulling cylinder. The convex sides and top of the structure are similar to a plate, so a trapezoidal plate structure can be used as an approximate substitute, as depicted in Fig. 3.
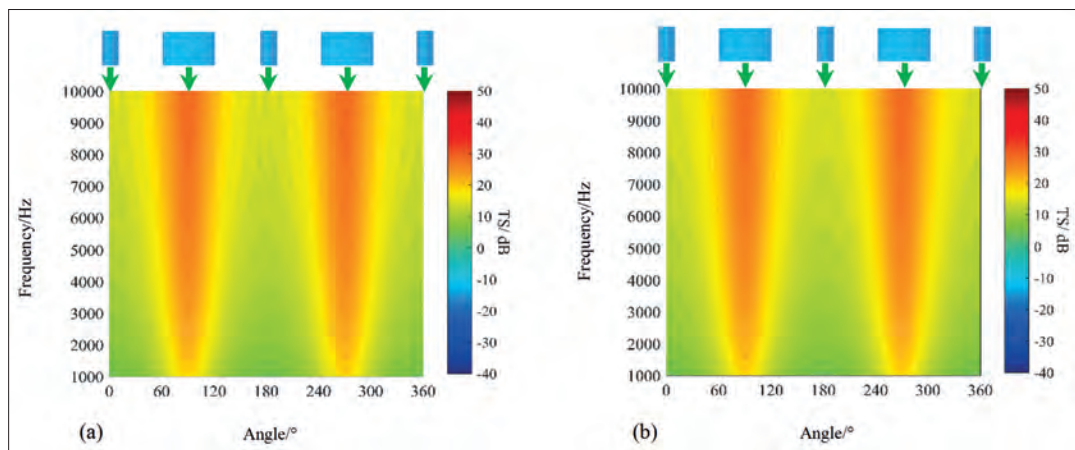
Fig. 2. Echo characteristics of finite elliptical cylinder a) planar element method b) highlight model method
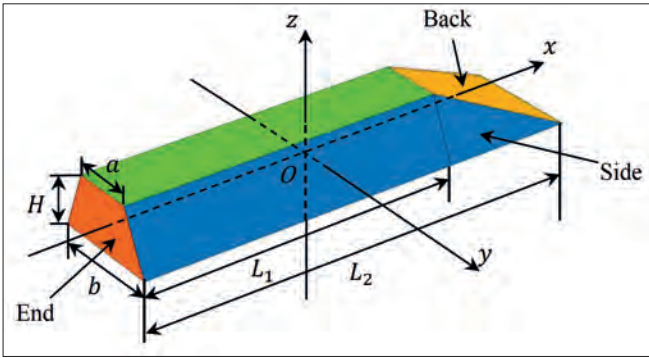
Fig. 3. 3D model of wedge-shaped structure
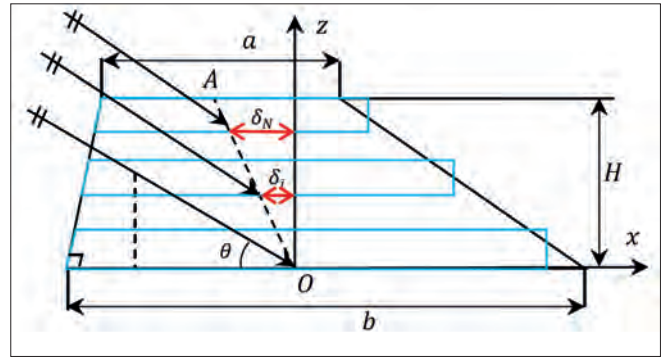
Fig. 4. Schematic diagram of the calculation of the highlight model of a right-angle trapezoidal plate

RIGHT-ANGLE TRAPEZOIDAL PLATE HIGHLIGHT MODEL

For a rectangular plate, the four edges produce four highlights when the sound waves are obliquely incident to the plate, and so the transfer function of the rectangular plate is [1]:

$$I = ab \cos\theta \frac{\sin(ka \sin\theta \cos\varphi)}{ka \sin\theta \cos\varphi} \frac{\sin(kb \sin\theta \sin\varphi)}{kb \sin\theta \sin\varphi} \quad (4)$$

When $\varphi = 0°$, the transfer function simplifies to:

$$I = ab \cos\theta \frac{\sin(ka \sin\theta)}{ka \sin\theta} \quad (5)$$

A right-angled trapezoidal plate can be regarded as an isosceles trapezoidal plate with the centre of the upper edge (point A in Fig. 4) shifted by l with respect to the origin O. Right-angled edges are common edges in a micro-rectangular plate. The eccentricity equation $y = f(x)$ is obtained by connecting the centres of the upper and lower edges. The reference point for the phase difference calculation is the origin O, the centre of the side length of the micro-rectangular plate is the intersection of the lower edge of the micro-trapezoidal plate and the equation $y = f(x)$; the distance δ_i between the intersection and the origin O is the phase distance.

Assuming a transfer function of I_i for a micro-rectangular plate, the transfer function, after considering the phase, is:

Fig. 5. Computational results comparison: a) planar element method b) highlight model method (=60) c) Target strength curve at 5 kHz d) Target strength curve at 8 kHz

$$\begin{cases} I_1' = I_1 e^{-2jk\delta_1 \sin\theta} \\ I_2' = I_2 e^{-2jk\delta_2 \sin\theta} \\ I_3' = I_3 e^{-2jk\delta_3 \sin\theta} \\ \cdots \\ I_N' = I_N e^{-2jk\delta_N \sin\theta} \end{cases}$$

(6)

The equation for calculating the target strength of a right-angled trapezoidal plate is:

$$TS = 10\lg\left(\left|\Sigma_{i=1}^N I_i'\right| / \lambda\right)^2$$

(7)

Tab. 1. Computing time for the angular-frequency spectrum

	Planar element	Highlight model
mesh quantity / pcs	538	$N = 60$
Time / s	16.334	2.480

We further calculated the target strength for a right-angled trapezoidal plate with an upper edge of $a = 4$ m, lower edge of $b = 8$ m and height of $H = 3$ m, using the planar element method and the highlight model method in the frequency band of 1-10 kHz. The results are presented in Fig. 5 and the time required for the two calculation methods is presented in Table 1.

SIDE PLATE HIGHLIGHT MODEL
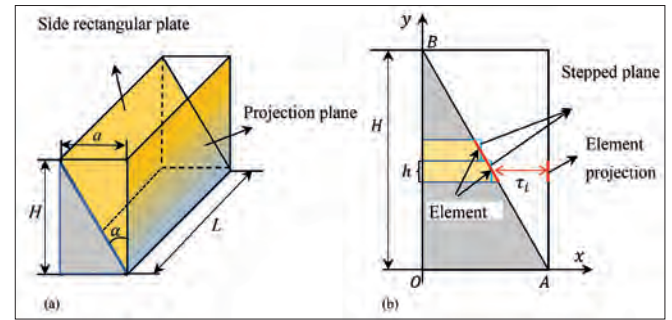
Fig. 6. Local model schematic diagram a) 3D view b) front view

Fig. 6 shows that the normal direction of the side plate is not in the coordinate plane, so the side plate needs to be further divided and approximated. For a certain angle α between the side plate and the projection plane, the projection plane is parallel to the *xoz* plane and the projection plane is used as a reference for the calculation of phase differences.

If the side plate in the *OB* direction is segmented and the divided inclined plane is projected into the projection plane, an inclined plane is equivalent to a stepped plane, as shown in Fig. 6(b). The height of any section of the projection plane is $h = H/N$, the distance between the stepped plane and the projection plane is the sound path difference, and the sound path difference τ_i is:

Fig. 7. Computational results comparison a) planar element method b) highlight model method (=60) c) Target strength curve at 5 kHz d) Target strength curve at 8 kHz

$$\tau_i = L_{OA} - y^{-1}(x_i) \tag{8}$$

L_{OA} is the distance between point O and point A, $y^{-1}(x_i)$ is the x-coordinate of the line equation $y(x)$ between A and B, and x_i is the x-coordinate of the intersection between the midpoint of each inclined plane height and the function $y(x)$.

The tilt of each inclined plane is described by the sound path difference τ_i between each inclined plane and its projection. Let the transfer function of any stepped plane be I_i, and the transfer function, considering the sound path difference τ_i, is:

$$I_i^1 = I_i e^{2jk\tau_1 \cos\theta} \tag{9}$$

So the transfer function of the side plate is:

$$I_i^2 = I_i^1 \, e^{2jk\tau_1 \cos\theta} \, e^{2jk\delta_i \sin\theta} \tag{10}$$

We further calculated the target strength of a side plate with $a = 1.5$ m, $H = 3$ m and $L = 5$ m using the planar element method and the highlight model method, respectively, for the frequency band 1-10 kHz. The results are presented in Fig. 7 and the time required for the two calculation methods is presented in Table 2.

Tab. 2. Computing time for the angular-frequency spectrum

	Planar element	Highlight model
mesh quantity / pcs	227	$N = 60$
Time / s	15.937	1.749

The results in Figs. 5 and 7 show that:

(1) There is strong agreement between the results obtained through the highlight model method and the planar element method, in terms of key features;

(2) When the calculation frequency increases, the number of segments N also needs to be increased appropriately;

(3) The angular-frequency spectrum of the acoustic target strength and the variation curve of the target strength, calculated using the highlight model method, are consistent with the results of the planar element method.

Therefore, the combinations of a rectangular plate can be used to approximate the highlight parameters of a trapezoidal plate and an inclined rectangular plate.

VALIDATION OF THE WEDGE-SHAPED STRUCTURE HIGHLIGHT MODEL METHOD

The previous section is the basis for modelling the highlight model of the wedge-shaped structure. The geometric parameters of the wedge-shaped structure are the upper edge of the end panel $a = 1$ m, the lower edge $b = 1.8$ m, and the heights $H = 1$ m, $L_1 = 5$ m, $L_2 = 7$ m. The acoustic wave is incident along the negative direction of the x-axis, the sound target strength is calculated using the planar element method and the highlight model method, respectively; the
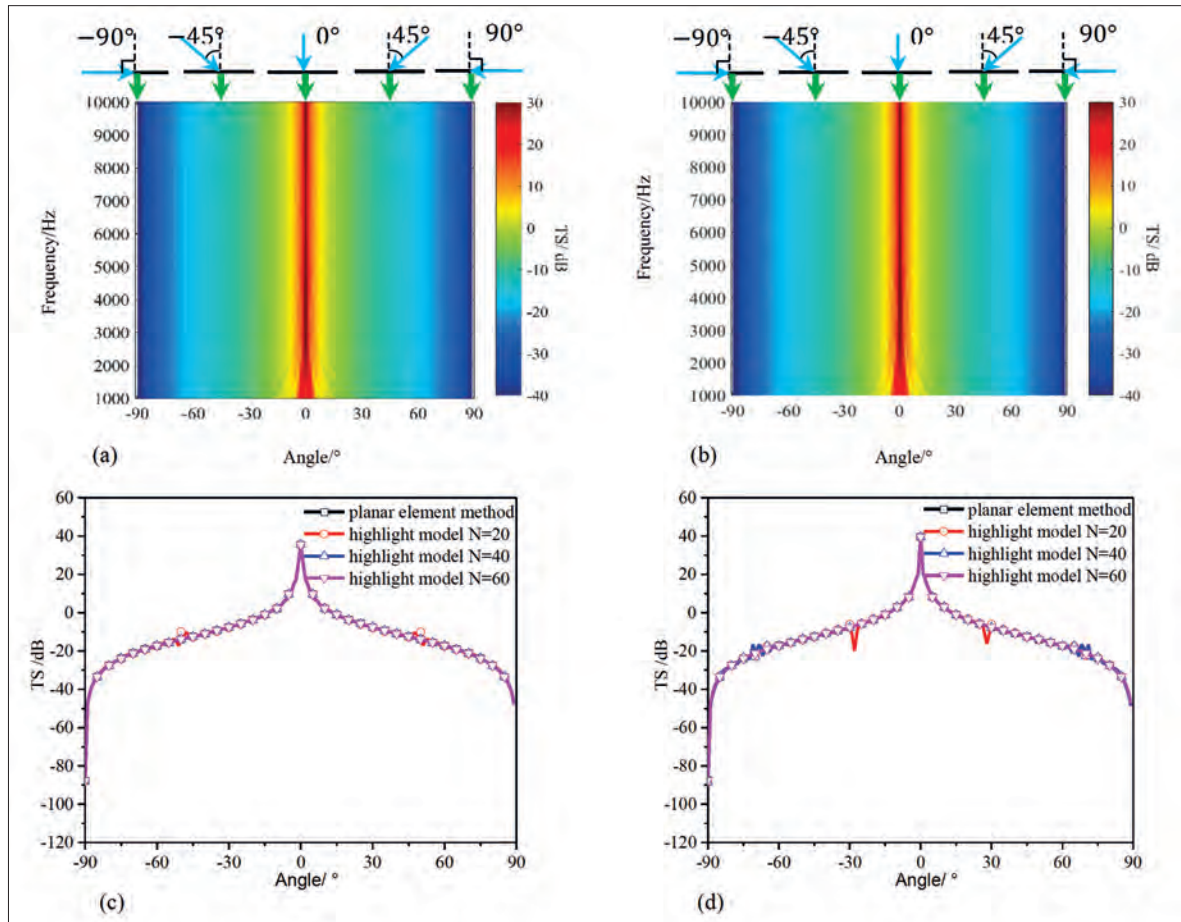

Fig. 8. Computational results comparison a) planar element method b) highlight model method (=60) c) Target strength curve at 5 kHz d) Target strength curve at 8 kHz

calculated frequency band is 1-10 kHz, the calculation results are presented in Fig. 8, and the time required by the two calculation methods is presented in Table 3.

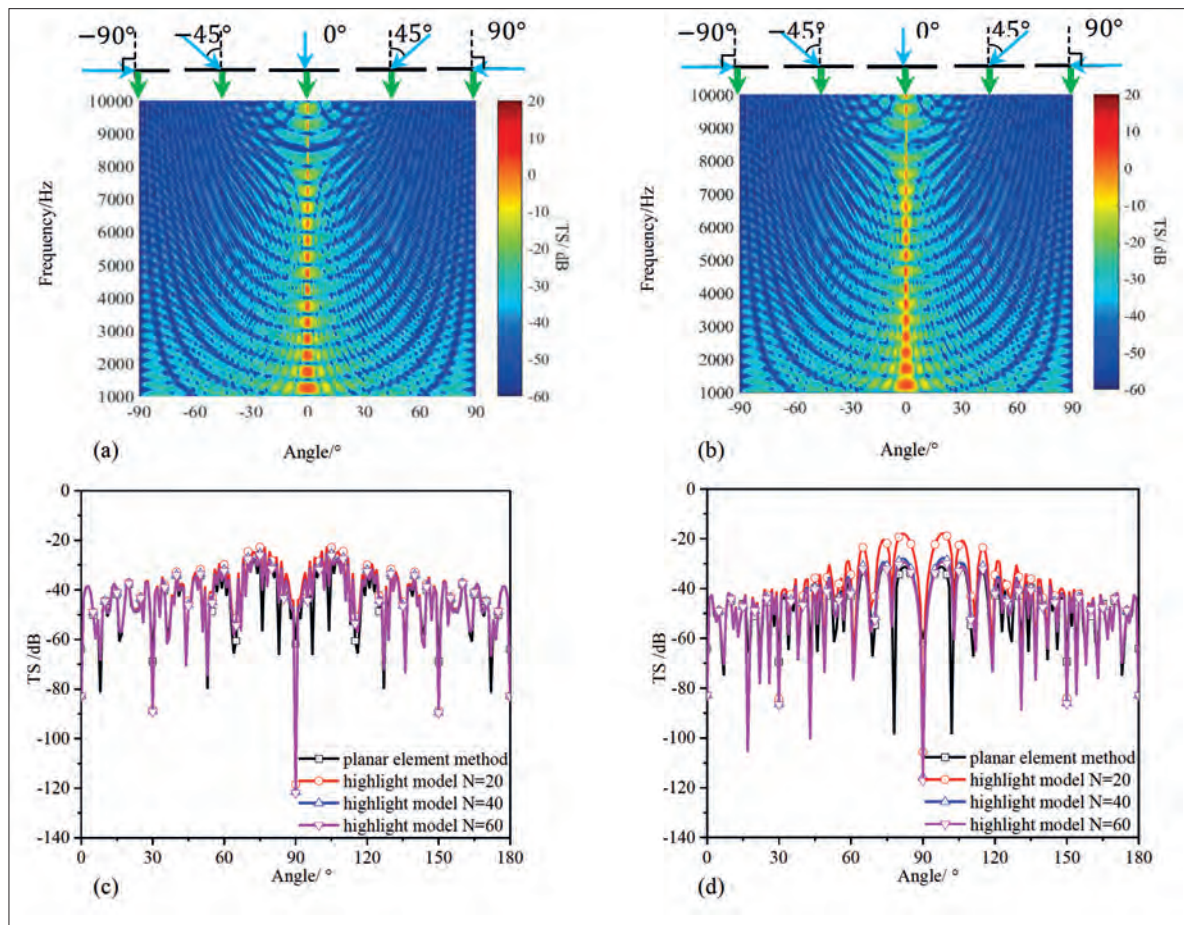|	Planar element	Highlight model
mesh quantity / pcs	938	$N = 60$
Time / s	15.654	6.923

(1) Choosing the appropriate segments N in the range 0-90° can bring the results of the modified highlight model method calculations into high agreement with those of the planar element method.

(2) The calculation results of the highlight model method can reflect the influence of the wedge-shaped structure on the highlight echoes. The low amplitude of the target strength at some frequency points is due to inaccurate phase calculations between the back plate, the end plate, and the side plate.

VALIDATION OF THE STERN STRUCTURE HIGHLIGHT MODEL

The generatrix of the hull stern model is determined by Eq. (11) [27]. To obtain micro-element targets, the model was evenly segmented along the x-axis direction, as depicted in Fig. 9. The radius of the bottom surface of each elliptical truncated cone can be found by substituting the abscissa of the bottom surface into the function $y = f(x)$. This allows us to establish the transfer function of any elliptical truncated cone $H_i(\vec{r}, \omega)$. Since changes in the computing centre can lead to phase variations and highlight interference phenomena, we utilise coherent superposition to combine the transfer function and calculate the scattered sound pressure or target strength of the model. The transfer function of the elliptical truncated cone is described by Eq. (12).

$$y = 0.5d - \left(\frac{1.45d}{c^2} - \frac{\tan\theta}{c}\right)(x - c + 0.5L)^2 - \left(\frac{d}{c^3} - \frac{\tan\theta}{c^2}\right)(x - c + 0.5L)^3 \tag{11}$$
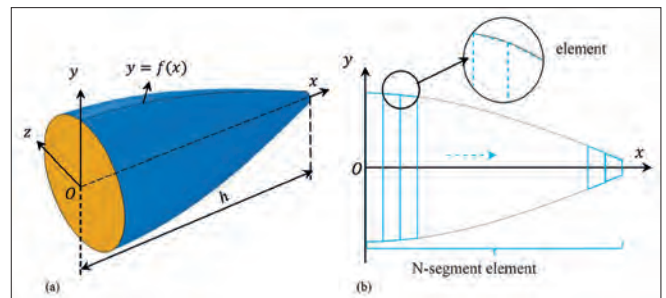
Fig. 9. A rotating body structure with convex smooth generatrix
a) 3D model b) Division diagram
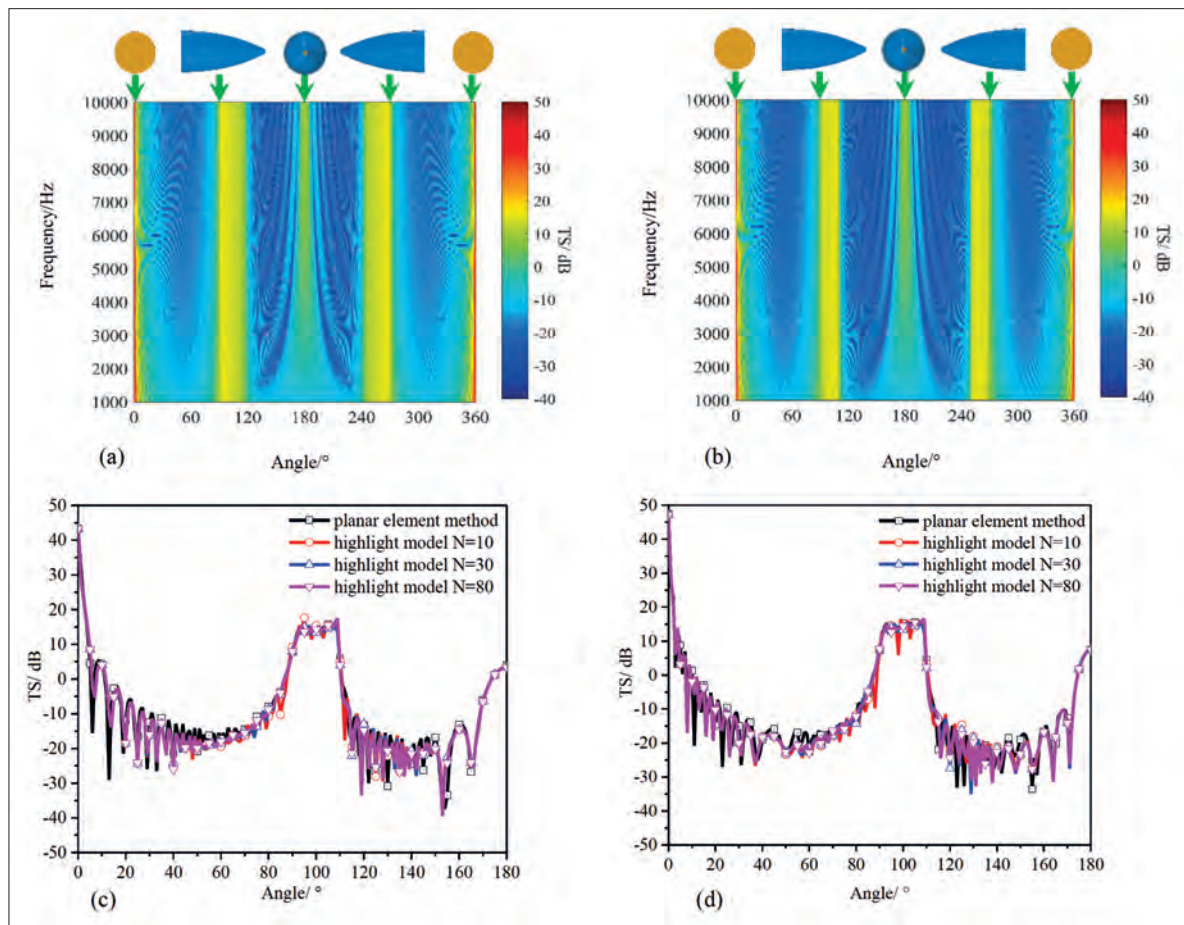
Fig. 10. Computational results comparison a) planar element method b) highlight model method (=80) c) Target strength curve at 5 kHz d) Target strength curve at 8 kHz

$$\begin{cases} H_1'(\vec{r},\omega) = H_1(\vec{r},\omega)e^{-2jk(L_1)\cos(\theta)} \\ H_2'(\vec{r},\omega) = H_2(\vec{r},\omega)e^{-2jk(L_2+h_0)\cos(\theta)} \\ H_3'(\vec{r},\omega) = H_3(\vec{r},\omega)e^{-2jk(L_3+2h_0)\cos(\theta)} \\ \cdots \\ H_N'(\vec{r},\omega) = H_N(\vec{r},\omega)e^{-2jk(L_N+(N-1)h_0)\cos(\theta)} \end{cases}$$

(12)

where $H_i'(\vec{r},\omega)$ is the transfer function of the i-segment elliptical truncated cone with respect to the 1-segment elliptical truncated cone; and $L_1, L_2, L_3, \ldots, L_N$ denotes the height of the elliptical truncated cone.

The highlight transfer function of a convex body structure is obtained by using the coherent superposition method, and the target strength calculation is:

$$TS = 10\lg(|\textstyle\sum_{i=1}^{N} H_i'(\vec{r},\omega)|^2)$$

(13)

By orienting the large bottom surface at 0° and the small bottom surface at 180°, we calculated the target strength using the planar element method and the highlight model method, respectively. The calculated incidence angle ranges from 0-360° and the calculation frequency band is 1-10 kHz. The calculated results are presented in Fig. 10.

(1) The graph shows that the calculation results of both methods are highly consistent. In addition, with the increase of N, the target of the combination of micro elliptical truncated cones will be closer to the original target and the accuracy of the calculation increases.

(2) In theory, as N increases, the higher the accuracy of the calculation but, in practice, there is an upper limit to the accuracy of the calculation. The number of segments N is too large and affects the efficiency of the calculation. The value of N is related to the calculation frequency and the generatrix type.
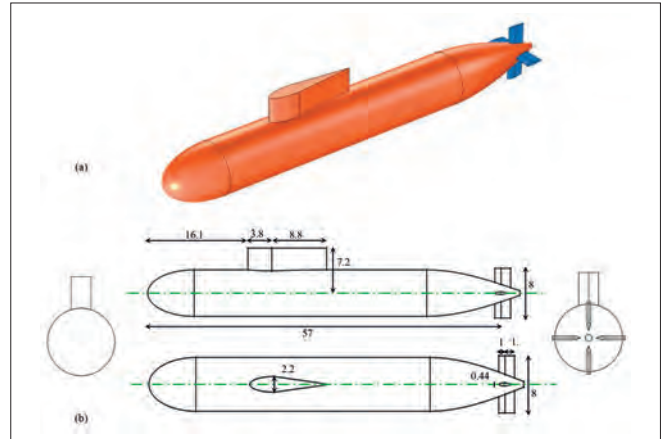
Fig. 11. The mono-hull underwater vehicle a) 3D model b) geometric parameter schematic
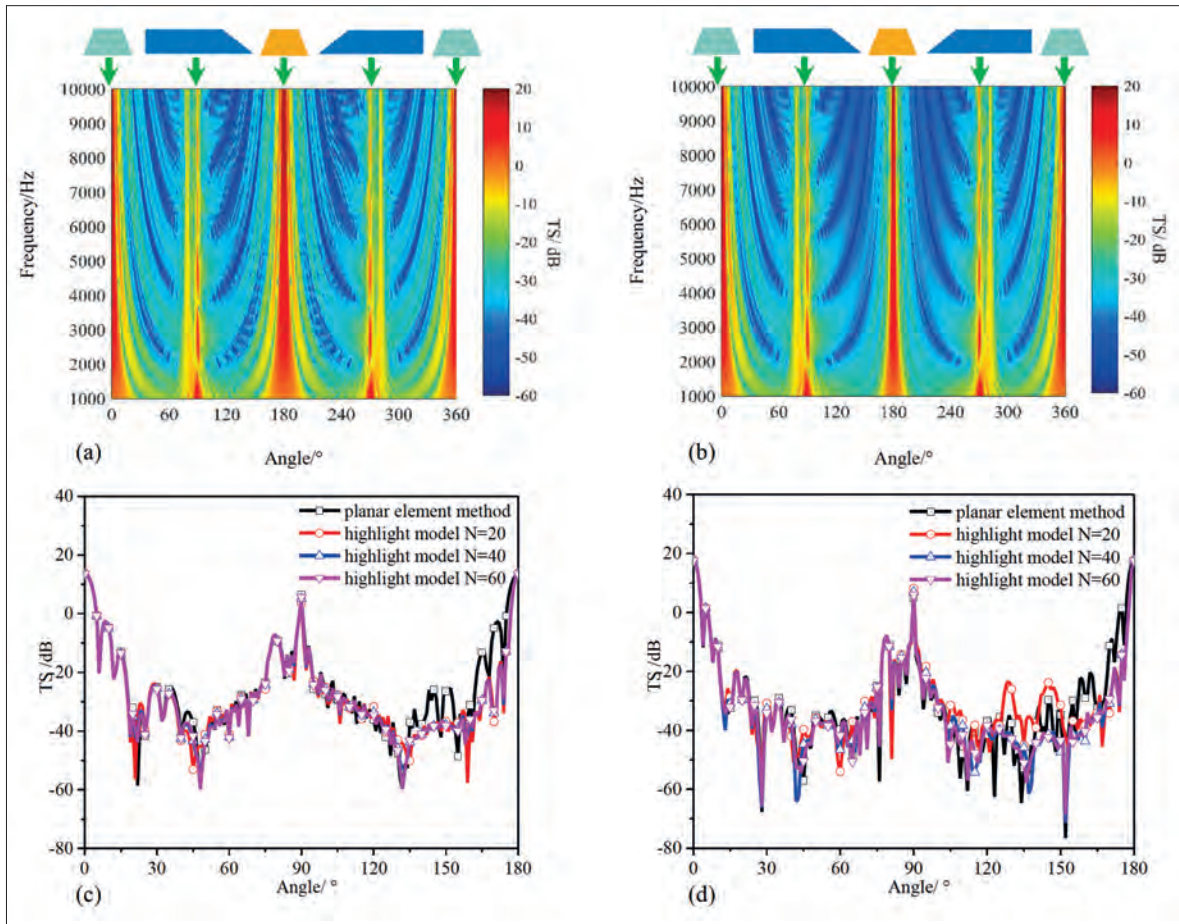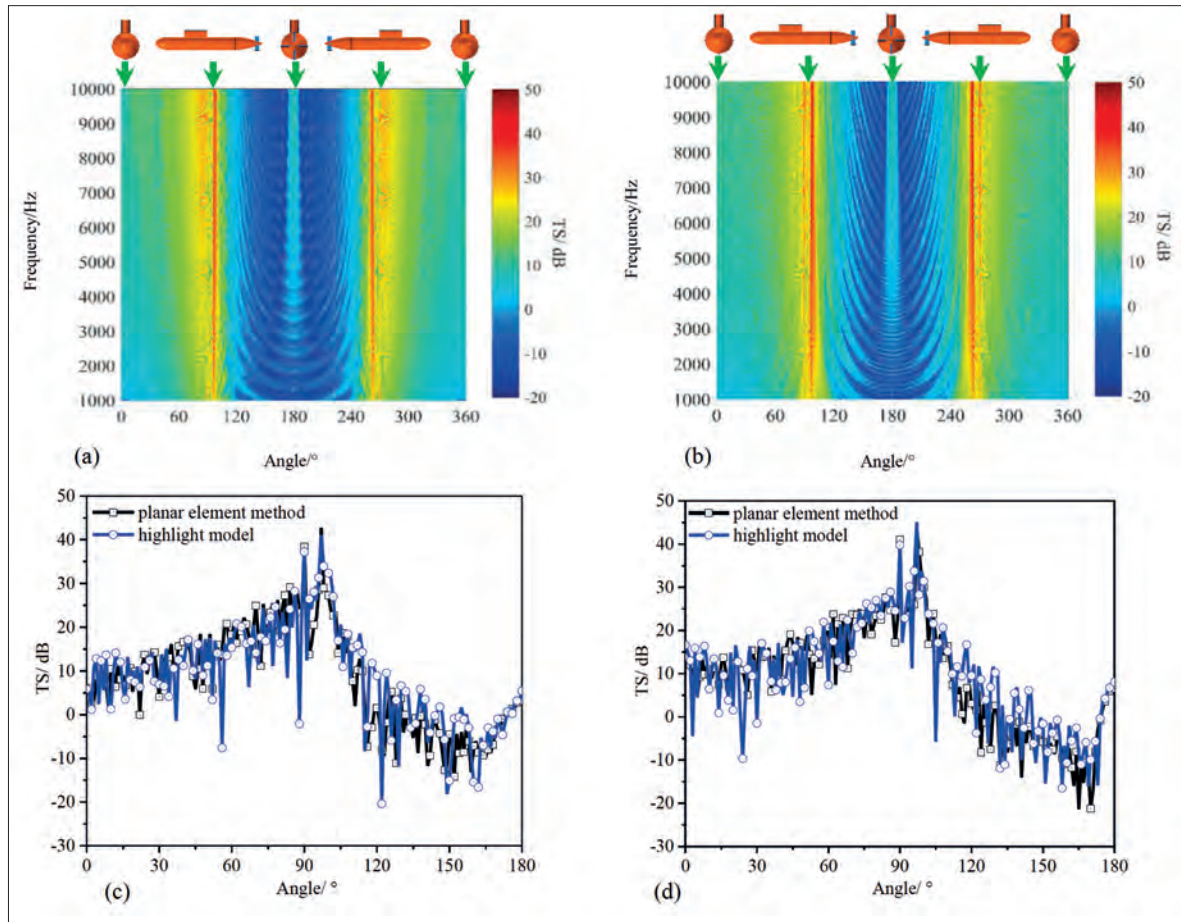

Fig. 12. Computational results comparison a) planar element method b) highlight model method (=100) c) Target strength curve at 5 kHz d) Target strength curve at 8 kHz

VALIDATION OF A HIGHLIGHT MODEL FOR ACOUSTIC SCATTERING FROM MONO-SHELL UNDERWATER VEHICLES

The 3D model of the mono-shell underwater vehicle under study is illustrated in Fig. 11(a) and its geometric parameters are detailed in Fig. 11(b). In this model, the shape of the cross rudder is the same as that of the sail and its geometric parameters are configured based on the rudder of the Benchmark underwater vehicles model, which was adjusted to 8 m.

The planar element method and the highlight model component method were used to calculate the target strength of a mono-shell underwater vehicle. The calculation results are presented in Fig. 12.

Tab. 4. Computing time for the angular-frequency spectrum

	Planar element method	Highlight model method
mesh quantity / pcs	21120	$N = 00$(stern)
Time / s	118.494	14.386

(1) The highlight model component method, which considers phase, can effectively predict the scattered sound field of large, complex underwater targets and has some engineering applications.

(2) In the range 0-90°, the target strength changes greatly due to the increase in the calculation frequency; there is a strong interference phenomenon between the highlights of each component due to the phase difference. Between 90-180°, the calculation results of the highlight model component method are slightly higher than those of the planar element method because the sail contributes significantly to the scattered sound field of the underwater vehicles.

(3) The calculation time of the highlight model component method is only 14.386 seconds, which is about 8.5 times faster than the planar element method.

RESEARCH ON THE DEVELOPMENT OF FAST-PREDICTION SOFTWARE FOR ACOUSTIC SCATTERING CHARACTERISTICS OF UNDERWATER VEHICLES

By integrating the highlight model of underwater vehicle sub-structures, utilising the traditional highlight model and a modified version of it, we developed two software applications: 'Target Strength Prediction Software for Simple Convex Structure of Underwater Vehicles' and 'Target Strength
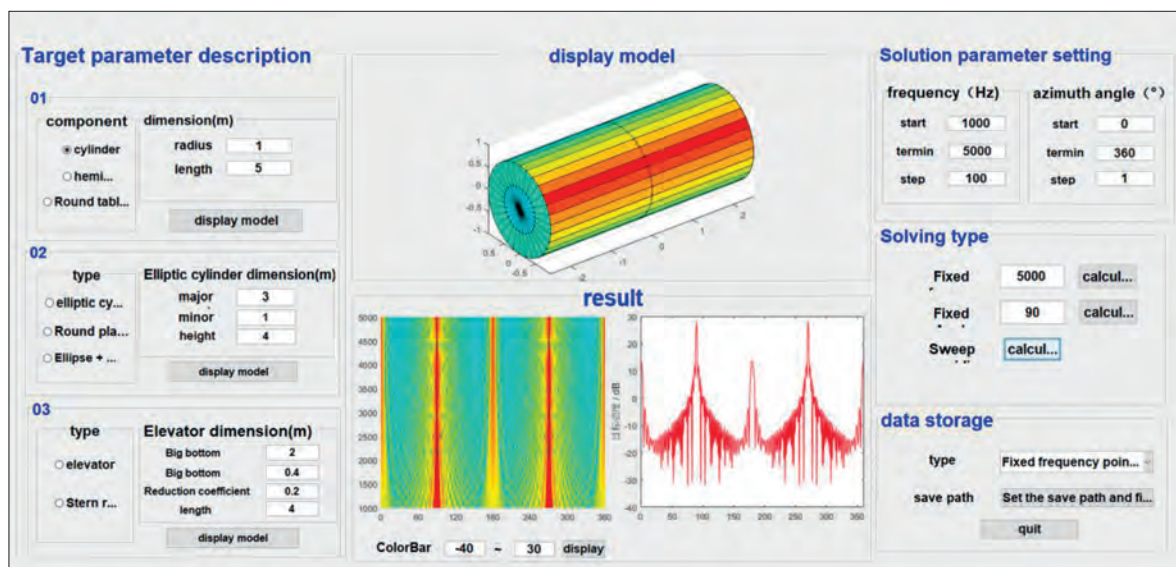
Fig. 13. Software demonstration interface
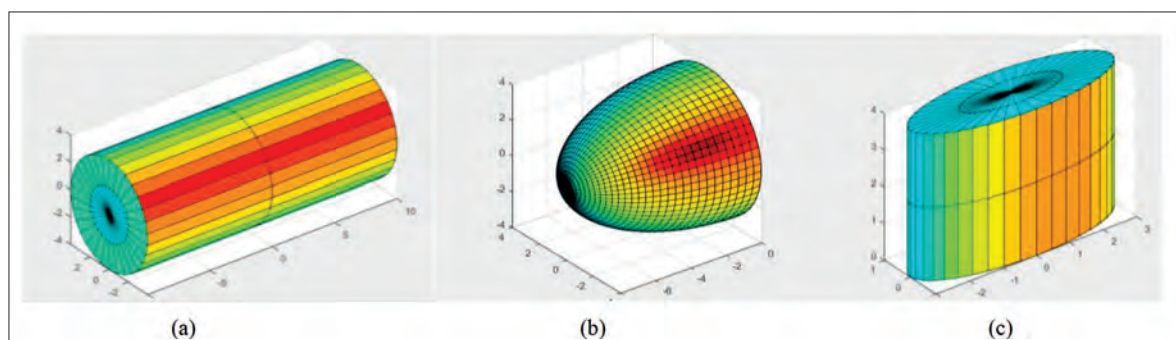
Fig. 14. The modelling results a) Hull Cylinder b) Bow of the hull c) Elliptic cylinder

Fast Prediction Software for Multi-Highlight Interference of Underwater Vehicles'. These software tools were created using the 'MATLAB GUI' platform and were primarily designed for predicting the scattered sound field of the main convex bodies, their attachment structures on underwater vehicles, and the scattered sound field of bare shells or coated silent tiles on mono-shell or double-shell underwater vehicles, as well as mono-shell and double-shell hybrid underwater vehicles.

TARGET STRENGTH PREDICTION SOFTWARE FOR SIMPLE CONVEX STRUCTURES OF UNDERWATER VEHICLES

The demonstrative interface of the software is exhibited in Fig. 13, which can be divided into three main functional areas:
(1) Calculation object selection area: According to the main components of underwater vehicles, the target can be divided into 'hull', 'superstructure' and 'rudder' components, each of which can be further divided into different sub-targets. Fig. 14 shows a few of the modelling results.
(2) Calculation parameter setting area: The main function of this section is setting parameters, such as calculation frequency and angle, but also post-processing modules.
(3) Display area for calculation results: The main function of this section is to display the modelling results and calculation results.

TARGET STRENGTH FAST PREDICTION SOFTWARE FOR MULTI-HIGHLIGHT INTERFERENCE OF UNDERWATER VEHICLES

Software introduction

The software interface of the 'Target Strength Fast Prediction Software for Multi-Highlight Interference of Underwater Vehicles' contains a modelling window, defining acoustic coverage layer window, modelling visualisation window, defining calculation parameter window, calculation result viewing window, and post-processing window, as shown in Fig. 15. The interface specifically includes the following major sections:
(1) Modelling section: a mono-shell underwater vehicles model, double-shell underwater vehicles model, and mono-shell and double-shell hybrid underwater vehicles model can be modelled in the software.
(2) Calculation section: For different types of underwater vehicles, target strength angle frequency spectrum, target strength variation curve with incident angle, and frequency response curve can be calculated. Taking the double-shell underwater vehicles as an example, the inner shell target strength, the outer shell target strength, and the total target strength of the underwater vehicles can be calculated. At the same time, an acoustic cover layer can be defined for the underwater vehicles and the calculation is the same as above.
(3) Post-processing section: The data can be exported to a designated folder, according to the requirements to further analyse the scattering characteristics of underwater vehicles.

The calculation parameters in the software include: calculation frequency, angle, and pitch angle. The calculation conditions include the type of underwater vehicles, whether to install the coated silent tiles or introduce reflection and transmission coefficients, etc.

Software features

(1) Taking full advantage of the 'MATLAB GUI' interface with excellent human-machine interaction, the software incorporates various coloured treatments for different underwater vehicles, enabling users to observe the entire modelling process.
(2) The software system defines the relative position parameters of the sub-targets, minimising user input requirements and keeping the modelling process fast and straightforward.
(3) The calculation data can be easily exported to a specified path as needed, streamlining calculations and saving time, thus simplifying subsequent processing.
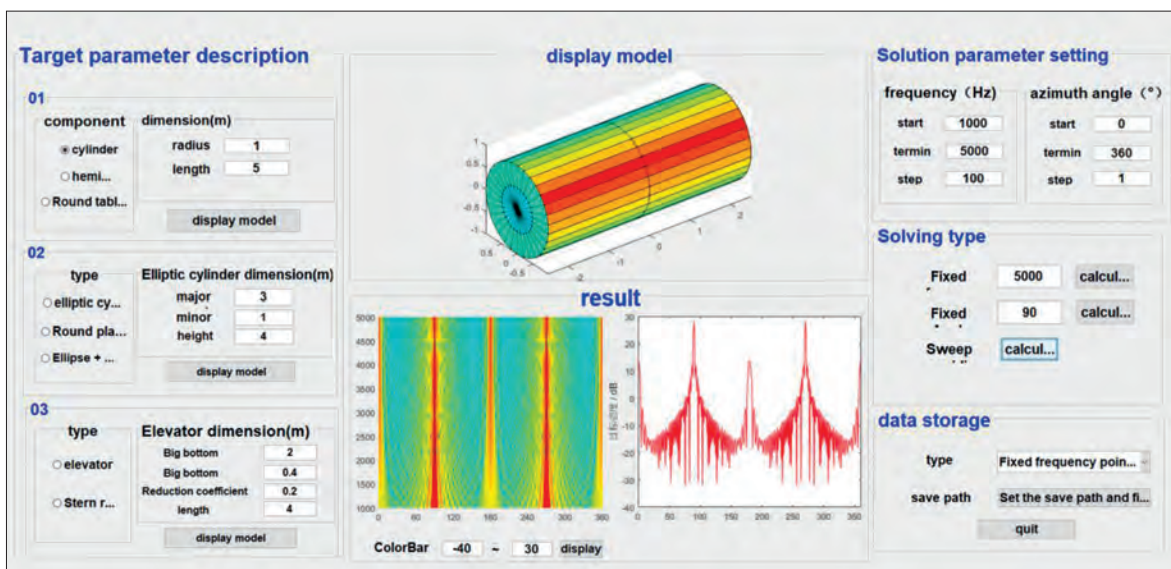
Fig. 15. Software demonstration interface

CONCLUSION

In this paper, the scattered sound field of a wedge-shaped structure is studied based on the modified highlight model. The highlight model of the wedge-shaped structure is finally obtained by calculating the trapezoidal plate through the 'segmentation-approximation-combination' method. The highlight models of other sub-structures of underwater vehicles are also calculated and the calculation results of the highlight model are compared with those of the planar element method.

The main conclusions are given as follows:

(1) It is important to choose an appropriate number of segments N when using the modified highlight model method. As the calculation frequency increases, N also needs to be increased appropriately. A small value of N will lead to a lack of precision, while a large value will lead to inefficient calculations.

(2) The modified highlight model method is highly consistent with the calculation results of the planar element method, in terms of changing trend and amplitude size, when it is used to calculate the angle frequency spectrum of sound target strength and the curve of sound target strength.

(3) For irregular targets, utilising a modified highlight model and taking into account the phase interference of different components can make the calculation results more accurate.

(4) The research results have certain engineering significance with the development of 'Target Strength Prediction Software for Simple Convex Structure of Underwater Vehicles' and 'Target Strength Fast Prediction Software for Multi-Highlight Interference of Underwater Vehicles'.

This research enriches the model library of highlight models and the developed software has high engineering significance, providing greater space for the prediction of underwater vehicles.

REFERENCES

1. W. Tang, J. Fan, and Z. Ma, 'Acoustic scattering of underwater target', Beijing: Science Press, 2018. (in Chinese)

2. Y. Sun, 'Wide-Frequency-Range prediction method of target strength of underwater structure and its application for submarine sails', Huazhong University of Science and Technology, 2019, doi: 10.27157/d.cnki.ghzku.2019.000843. (in Chinese)

3. H. Überall, R. Doolittle, and J. McNicholas, 'Use of sound pulses for a study of circumferential waves', The Journal of the Acoustical Society of America, vol. 39, no. 3, pp. 564-578, 1966, doi: 10.1121/1.1909929.

4. H. Zheng, R. Cai, and L. Pan, 'A modified Galerkin FEM for 1D Helmholtz equations', Applied Acoustics, vol. 74, no. 1, pp. 211-216, 2013, doi: 10.1016/j.apacoust.2012.06.014.

5. W. Murphy, V. Rokhlin, and M. Vassiliou, 'Solving electromagnetic scattering problems at resonance frequencies', Journal of Applied Physics, vol. 67, no. 10, pp. 6061-6065, 1990, doi: 10.1063/1.345217.

6. H. Schenck, 'Improved integral formulation for acoustic radiation problems', The Journal of the Acoustical Society of America, vol. 44, no. 1, pp. 41-58, 1968, doi: 10.1121/1.1911085.

7. H. Wu, L. Yu, and W. Jiang, 'A coupling FEM/BEM method with linear continuous elements for acoustic-structural interaction problems', Applied Acoustics, vol. 150, pp. 44-54, 2019, doi: 10.1016/j.apacoust.2019.02.001.

8. H. Li, Z. Lu, Y. Ke, Y. Tian, and W. Luo, 'A fast optimization algorithm of FEM/BEM simulation for periodic surface acoustic wave structures', Information, vol. 10, no. 3, p. 90, 2019, doi: 10.3390/info10030090.

9. W. Zhao, S. Marburg, and H. Chen, 'A FEM/BEM based topology optimization of submerged bi-material shell structures under harmonic excitations', INTER-NOISE and NOISE-CON Congress and Conference Proceedings, Institute of Noise Control Engineering, pp.763-774, 2018.

10. H. Chen and W. Zhao, 'A FEM/BEM based topology optimization of submerged bi-material shell structures under harmonic excitations', INTER-NOISE and NOISE-CON Congress and Conference Proceedings, Institute of Noise Control Engineering, pp. 5031-5015, 2017.

11. P. Waterman, 'Matrix theory of elastic wave scattering', The Journal of the Acoustical Society of America, vol. 60, no. 3, pp. 567-580, 1969, doi: 10.1121/1.381130.

12. F. Ingenito, 'Scattering from an object in a stratified medium', The Journal of the Acoustical Society of America, vol. 82, no. 6, pp. 2051-2059, 1987, doi: 10.1121/1.395649.

13. K. Lee and W. Seong, 'Time-domain Kirchhoff model for acoustic scattering from an impedance polygon facet', The Journal of the Acoustical Society of America, vol. 126, no. 1, pp. EL14-EL21, 2009, doi: 10.1121/1.3141887.

14. J. Fan, W. Tang, and L. Zhuo, 'Planar elements method for forecasting the echo characteristics from sonar targets', Journal of Ship Mechanics, vol. 16, no. Z1, pp.171-180, 2012. (in Chinese)

15. G. Zheng, J. Fan, and W. Tang, 'A modified planar elements method considering occlusion and secondary scattering', ACTA ACUSTICA, Chinese version, vol. 36, no. 04, pp. 377-383, 2011, doi: 10.15949/j.cnki.0371-0025.2011.04.010. (in Chinese)

16. W. Wang, B. Wang, J. Fan, and J. Zhou, 'An iterative planar elements method for calculating multiple acoustic scattering

from concave targets', Proceedings of the 18th Symposium on Underwater Noise of Ships, Wuxi: Key Laboratory of Ship Vibration and Noise, pp. 121-126, 2021, doi: 10.26914/c.cnkihy.2021.056714 . (in Chinese)

17. A. Abawi, 'Kirchhoff scattering from non-penetrable targets modeled as an assembly of triangular facets', The Journal of the Acoustical Society of America, vol. 140, no. 3, pp. 1878-1886, 2016, doi: 10.1121/1.4962735.

18. T. Stanton, 'Sound scattering by cylinders of finite length. I. Fluid cylinders', The Journal of the Acoustical Society of America, vol. 83, no. 1, pp. 55-62, 1988, doi: 10.1121/1.396184.

19. T. Stanton, 'Sound scattering by spherical and elongated shelled bodies', The Journal of the Acoustical Society of America, vol. 88, no. 3, pp. 1619-1633, 1990, doi: 10.1121/1.400321.

20. W. Tang, 'Highlight model of echoes from sonar targets', ACTA ACUSTICA, Chinese version , vol. 19, no. 2, pp. 92-100, 1994, doi: 10.15949/j.cnki.0371-0025.1994.02.002. (in Chinese)

21. W. Liu, J. Zhao, Y. Song, and J. Zhang, "Underwater target modelling technology based on modified highlight model", Torpedo Technology, vol. 18, no. 5, pp. 352-356, 2010. (in Chinese)

22. Y. Chen, "The research of target highlight modelling based on the planar elements clustering", China Ship Research and Development Academy, 2019. (in Chinese)

23. X. Zhang, J. Zhao, R. Wang, and J. Han, 'Modelling and simulation of scattering field for bistatic sonar', Journal of System Simulation, no. 5, pp. 562-565, 2002. (in Chinese)

24. C. Partridge and E. Smith, 'Acoustic scattering from bodies: Range of validity of the deformed cylinder method', The Journal of the Acoustical Society of America, vol. 97, no. 2, pp. 784-795, 1995, doi: 10.1121/1.412943.

25. J. Fan, 'Study on echo characteristics of underwater complex targets', Shanghai Jiao Tong University, 2001. (in Chinese)

26. Y. Guo, 'Nuclear submarine profile recognition', Ordnance Knowledge, no. 5, pp. 54-55, 2003, doi: 10.19437/j.cnki.11-1470/tj.2003.05.020. (in Chinese)

27. B. Li, 'Anti-active detection underwater target acoustic stealth shape optimization design', Jiangsu University of Science and Technology, 2020, doi: 10.27171/d.cnki.ghdcc.2020.000294. (in Chinese)

GLASS MICROSPHERES THERMO-DEFORMATION SINTERING PROCESSES IN THE TECHNOLOGIES OF OBTAINING MATERIALS FOR UNDERWATER TECHNICAL EQUIPMENT

Yuliia Kazymyrenko [1]
Natalya Solomoniuk *[1]
Oxana Drozd [2]

[1] Department of Information Control Systems and Technologies Admiral Makarov National University
of Shipbuilding, Mykolaiv, Ukraine

[2] Kherson Branch of the Admiral Makarov National University of Shipbuilding, Kherson, Ukraine

* Corresponding author: *natalysolomonuk@gmail.com (N. Solomoiuk)*

ABSTRACT

In this work, the important scientific and technical problem of creating multifunctional composite materials for shipbuilding and ocean engineering was solved. The work aimed to study the thermal deformation processes of sintering glass microspheres to obtain lightweight glass composites with a cellular structure that provides positive buoyancy and sound insulation properties. For this purpose, glass microspheres of $Na_2O–SiO_2$ and $Na_2O–B_2O_3–SiO_2$ composition with a dispersion of 10 to 60 µm were used as raw materials. They were sintered to form a closed, porous structure. The theoretical substantiation of technological parameters is based on the concepts of solid state and glassy state chemistry and physicochemical concepts of glass softening processes. The process of hot-pressing glass microspheres without plasticisers and additives was investigated. The author's own laboratory equipment was used for the experiments. The sintering intensity was determined from the results of shrinkage processes; the kinetic shrinkage curves were constructed in semilogarithmic coordinates. The glass composite samples were examined by optical and electron microscopy. As a criterion, the storage of spherical microspheres under the influence of simultaneous heating to 700 ℃ with the application of pressure in the range of 0,5 to 1,5 MPa was chosen. It was established that the formation of a predominantly closed-porous structure of glass composites with a density of 350...600 kg/m³ occurs by the mechanisms of viscous glass phase flow through liquefaction processes in the walls of microspheres. At the same time, shrinkage processes in the linear direction reach up to 50%.

The acoustic properties were investigated by measuring the differences in sound pressure levels in octave frequency bands using a Kundt pipe. The water absorption of the glass composite samples was determined at hydrostatic pressures up to 20 MPa. The research results were compared with the characteristics of analogue composites, such as syntactic foams and foam glass. The developed materials can be used in the design and manufacture of technical equipment for research and maintenance of underwater infrastructure. The prospects for further research are related to the feasibility study and marketing research on implementing the developed glass composites.
.

Keywords: temperature, pressing pressure, structure, porosity, sphericity, fiberglass composites, subsea equipment, and infrastructurecharacteristics

INTRODUCTION

The main purpose of creating a network of subsea infrastructure is to service offshore mineral production and the technical equipment for lifting and transporting them [1, 2]. Today, oil and gas exploration are carried out at great depths (from 2 to 6-7 km) [3, 4] and not only in sedimentary basins but also in crystalline Precambrian rocks, both onshore and offshore [5]. Moreover, in recent decades, the world has been successfully developing fundamentally new gas deposits - gas from "tight reservoirs" located in shale, siltstone, and fine-grained sandstones ("shale" and "central basin" gas) [6]. Improving and developing methods for developing subsea deposits is very important for finding new sources of raw materials for energy and industry. This research is being conducted in almost 70 countries and covers the shelves of

all continents. By 2000, more than 3,000 offshore oil and gas fields had been discovered [7]. Products are delivered to land using special product pipelines that are laid on the seabed on special supports or buried in the ground [8]. They are in difficult operating conditions, and in addition to the working pressure of the transported product, they are also loaded with external hydrostatic water pressure. Pipelines can also be affected by waves and currents. They must be insulated to protect against corrosion and lined to protect the coating from mechanical damage [9]. Unlike deep-water drilling, offshore mining takes place at a depth of 100...200 meters. However, the work is complicated due to water surface disturbance, rock washout, and its release into the habitat of marine life, which is a threat to the environment [10]. Most underwater vehicles operating at these depths have a limited carrying capacity, which can be increased by equipping them with buoyancy modules (Fig. 1), which are installed externally in a space free of equipment and supporting structures.

Fig. 1. Buoyancy modulus [10]

They can have a variety of configurations and consist of separate blocks that are not identical in size and shape [11]. They are an integral part of the combined buoyancy systems that are placed in volumes free of load-bearing structures and are subject to hydrostatic pressure during operation.

Problematic issues in their design and operation are the combination of strength characteristics of structures with reduced weight and dimensions and functional capabilities to operate under extreme conditions of wave, hydrostatic, and acoustic loads. Solutions include the development and use of highly specialised and multifunctional composite materials.

Due to a set of valuable physical and mechanical properties, the use of inorganic glass shells, glass, and alumina ceramics is considered universal in deep-water technologies. Theoretical and experimental studies of their strength have shown that, along with lightness and strength, shell structures made of these materials are non-magnetic, radiotransparent, and chemically resistant.

Buoyancy materials are subject to the requirements of low density, optimal buoyancy, ability to withstand hydrostatic loads, high specific strength, corrosion and chemical resistance, and resistance to atmospheric and bacterial action. PVC is used for small depths [12]. Also, polyurethane foams will meet these requirements. Each kilogram of polyurethane foam provides a lifting force of approximately 300 N (density as low as 100 kg/m³), so its use is effective in raising sunken vessels, removing them from reefs, shoals, and underwater pipeline equipment. Polyurethane foams are also used to make life-saving equipment such as rafts, belts, bibs, lapel pins, and dinghies. They are used as coatings on the sides of heavy ships and on the floors and ceilings of shipboard accommodations [13]. However, their low strength characteristics do not allow them to be used in technologies for manufacturing additional buoyancy blocks for underwater exploration and research vehicles. The maximum immersion depth of polyurethane foam is 350 meters (density 0.4 kg/m³). In addition, they are flammable, toxic, and unable to operate for a long time at temperatures above 60 °C.

Syntactic foams are considered to be more competitive composite materials. They are synthesised by filling a polymer matrix with glass, ceramic, and carbon microspheres. The existing experience in producing composite materials and coatings based on non-metallic microspheres is based on low-temperature technologies for the preparation of colloidal solutions. Phenolic, polyester, polyamide, and, most often, epoxy matrices are used for the manufacture of composites. They ensure homogeneity of composition, a certain density, and increased adhesion strength. Glass inclusions are evenly distributed in the polymer matrix (Fig. 2a). The use of this material as part of the buoyancy material provides an apparent density in the range of 450...700 kg/m³ with a possible operating depth to 12,000 m [14]. An important disadvantage of syntactic foams is the impossibility of their long-term operation at temperatures above 110 to 130 °C due to the presence of a polymeric thermosetting binder.

The choice of materials is an important and difficult stage in solving design problems. Most polymer compositions are characterised by increased flammability and toxicity, and they lose their thermal insulation properties with increasing temperature and water absorption. Alternative buoyancy composite materials that combine high hydrostatic strength with thermal insulation capacity are foam glasses with a density of 300...700 kg/m³ [15]. The technology for their production is based on the sintering of glass powders with a dispersion of 20...150 μm in a particular sodium silicate composition, with a gas-forming agent (Fig. 2b). As a result, a porous structure is formed, making this material indispensable for use in combined buoyancy units of underwater vehicles with a submergence depth of up to 2000 m.

Thus, the analysis of the problems of using modern composite materials in the technologies of designing and manufacturing underwater technical means has shown the prospects of introducing materials with a cellular structure that provides a set of valuable operational properties. The choice of raw materials for their creation is based on the principles of forming cells with a certain geometry. For this purpose, dispersed substances such as glass powders or hollow microspheres are suitable. Reducing the density of the compositions will be facilitated by the choice of high-temperature technologies, such as sintering, which will exclude the use of polymeric binders. However, the influence of technological parameters, in particular temperature and pressure, on the processes of structure formation during the sintering of microspheres without additional impurities remains insufficient.

The aim of the work is to study the thermo-deformation processes of sintering hollow glass microspheres to obtain lightweight glass composites with a cellular structure that provides positive buoyancy and sound insulation properties.
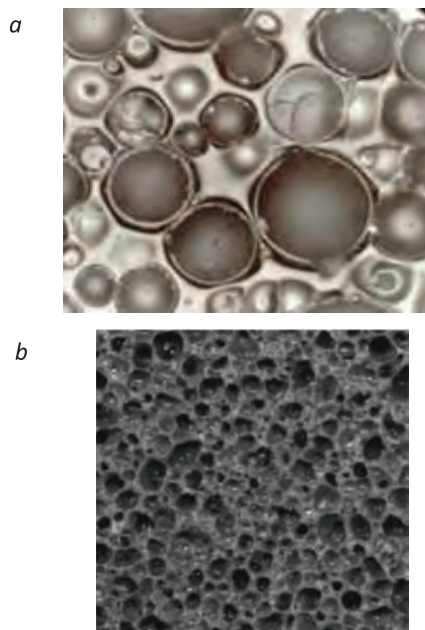
Fig. 2. Optical micrographs of the structure of buoyancy materials: a – syntactic foam (×600); b - foam glass (1:3) [Microphotographs were taken using the BIOLAM optical microscope]

EXPERIMENTAL DETAILS

The experimental work consists of obtaining samples from glass microspheres sintered using hot pressing technology and studying their performance properties.

For sintering, the glass microspheres used were bulk inorganic powders with a dispersion of 10 to 60 µm and a shell thickness of $\delta = 0.5$ to 2.0 µm. They were made of sodium silicate glass from the Na_2O-SiO_2 system (chemical composition (wt. %): SiO_2 – 77.0; Na_2O_3 - 23.0) and sodium borosilicate glass from the Na_2O - B_2O_3 - SiO_2 system (chemical composition (wt. %): SiO_2 - 69.0; B_2O_3 - 7.5; CaO - 6.0; Na_2O_3 - 13.5; ZnO -2.0; F - 2.0). The sintering process was carried out in a hermetically sealed graphite container which was filled with microspheres without additives and plasticisers. The theoretical substantiation of the technological parameters is based on the provisions of solid-state chemistry [16] and glassy-state, physicochemical concepts of glass-softening processes [17].

For the experimental work, the author's own model of the installation for sintering powders in an oxidising environment at temperatures up to 900 °C [18] was used. The peculiarity of the equipment is the presence of a mechanical pressing device (Fig. 3) with an indicator of the movement of the mould punch, which is used to measure shrinkage processes every minute. This allows for careful control of the sintering process and stopping it when the material reaches a certain structure or to prevent distortion of the geometric dimensions of the samples.

The formation of the interface between the microspheres

during heating to a temperature of 700 °C with a pressure of 0,5 to 1,5 MPa was studied by optical and electron microscopy (BIOLAM-I and REMMA-102-02 microscopes). The purpose of forming the structure of glass composites is to store microspheres of a spherical shape, which provides hydrostatic strength.

Fig. 3. Pressing device of the sintering setup

The acoustic properties of fibreglass composites with a density of 320...500 kg/m³ were investigated by measuring the sound pressure level drops in octave frequency bands, for which a Kundt tube wasater absorption of glass composite samples was determined at a hydrostatic pressure of up to 20 MPa. The studies were carried out in a hydrostatic chamber (Fig. 4, a), using distilled water as the working environment.
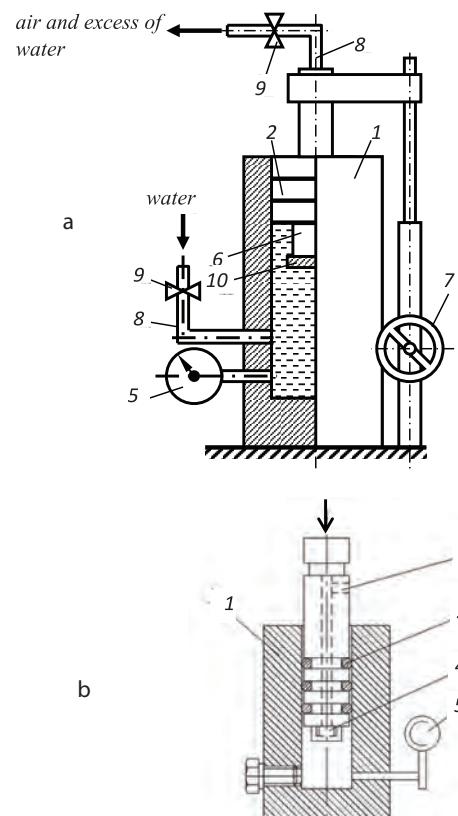
Fig. 4 Scheme of the test chamber for determining the hydrostatic strength of samples.
1 - chamber body; 2 - rod; 3 - sealing ring; 4 - piezoelectric element; 5 - pressure gauge; 6 - syntactic glass sample; 7 - lifting mechanism for controlling the rod; 8 - nozzles; 9 - taps; 10 - ballast.

The sample was subjected to hydrostatic pressures of 2, 5, 15, and 20 MPa, and the exposure of the pressure time was 3 - 5 min at a rate of 0.01 MPa/s. The water absorption was determined by hydrostatic weighing after each loading; the relative error in the measurements did not exceed ± 5 %. The number of destroyed microspheres was determined by a method based on the readings of thermal sensors with piezoelectric elements (Fig. 4, b). The method is based on registering acoustic emission waves caused by the destruction of microspheres [19].

RESULTS

The sintering kinetics of the glass composite samples was analysed (influence of temperature and pressure). Changes in the material structure are shown in Fig. 5. The microstructure was investigated for the glass-microspheres of the Na_2O-SiO_2 system (Fig. 5a) and Na_2O-B_2O_3-SiO_2 system (Fig. 5b). The sintering temperature was 650 °C.
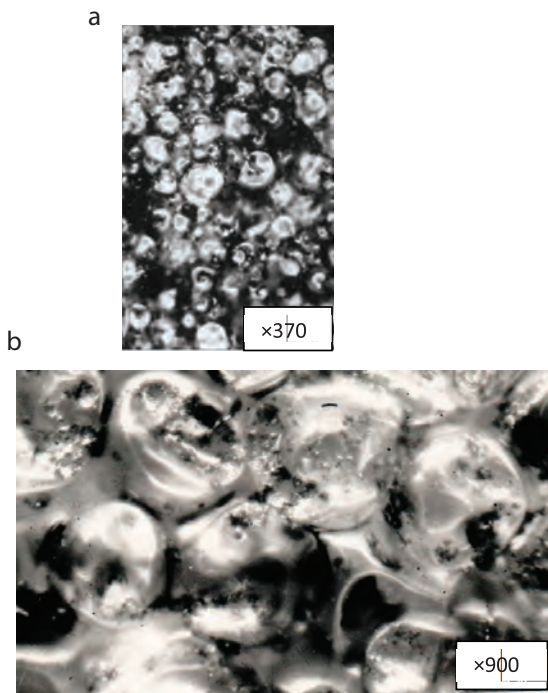
Fig. 5 Changes in the glass-microspheres' structure during sintering

The pressure was applied to the heated container with microspheres. The heating temperature was controlled by a chromium-aluminium thermocouple inserted directly into the microsphere mixtureThe density of the material at the stage of its formation is 250 – 270 kg/m³. Heating to a temperature of 650 °C with a pressure of 0.5 – 1.5 MPa contributes to their compaction by the mechanism of contact cauterisation with the shells deforming by 20 to 25% of their original size, as shown in the microstructure (Fig. 5b). The physicochemical processes in the formation of a contact area (perimeter of 30 - 50 μm) are explained by the chemical composition of the glasses. The deformation criterion of glass

microspheres is the change in their shape factor as the ratio of the minimum particle size to the maximum (from 1.0 to 0.75). The more complex chemical composition of the sodium boron silicate glass microspheres determines the presence of fusible components that contribute to forming the liquid phase and more intensive sintering of microspheres, as shown in Fig. 6b.
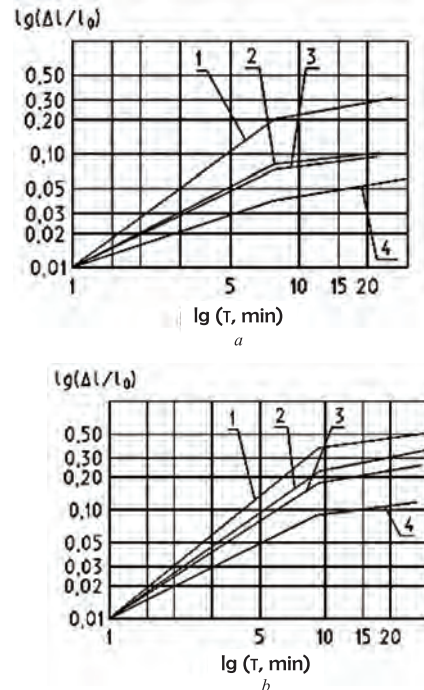
Fig. 6. Sintering kinetics of microspheres from glass systems: a - Na_2O-SiO_2-glass system; b - Na_2O-B_2O_3-SiO_2-glass system; 1 – p = 1,5 MPa; 2 – 1,2 MPa; 3 – 1,0 MPa; 4 – 0,5 MPa

Line 1 characterises the pressure of 1.5 MPa, 2 – 1.2 MPa, 3 – 1.0 MPa, 4 – 0.5 MPa.

The sintering intensity of glass microspheres was determined by the results of the shrinkage processes. The kinetic shrinkage curves were plotted in semilogarithmic coordinates. The results of studies of the acoustic characteristics of glass composites are shown in Fig. 7.Curve 1 characterises the sound signal for octave frequency bands without samples in the Kundt tube. Curves 3 and 5 determine the sound pressure level for glass composites obtained by sintering microspheres of Na_2O-SiO_2 glass (curve 3) and microspheres of Na_2O-B_2O_3-SiO_2 glass (curve 5). For a qualitative assessment, the acoustic characteristics of foam rubber (curve 2) [20] and foam plastic (curve 4) samples were investigated [21].
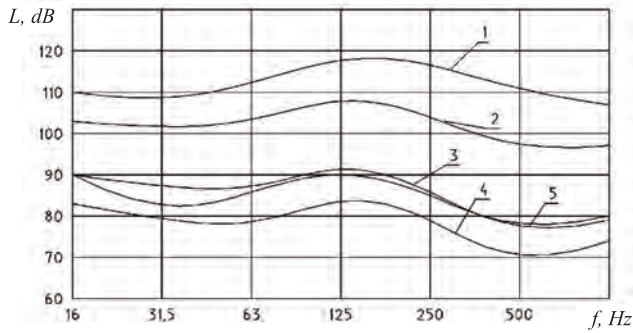
Fig. 7. Sound pressure levels in octave frequency bands

Figure 8 shows the graphical dependence of the water absorption values of samples with densities of 320 kg/m³ (curve 1), 400 kg/m³ (curve 2), and 500 kg/m³ (curve 3) under conditions of gradual loading with all-round hydrostatic pressure.
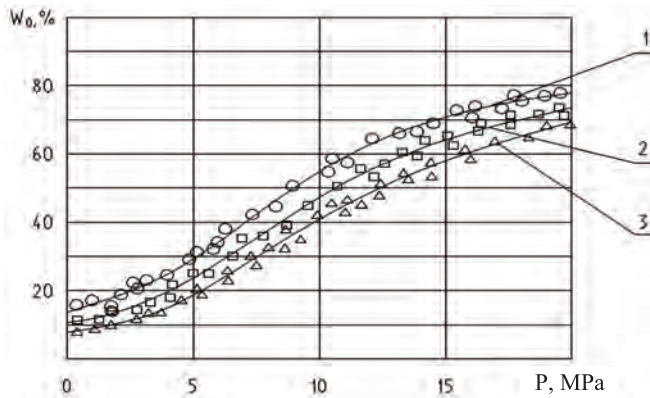
Fig. 8. Water absorption of samples under hydrostatic pressure

The local destruction of microspheres in the sintered composite material was determined by experimental studies of loading samples with hydrostatic pressures from 5 to 45 MPa, where the criterion was the number of destroyed microspheres, Np, expressed in per cent. The quantitative destruction of microspheres for glass microspheres of the Na_2O-SiO_2 system (curve 1) and glass microspheres of the Na_2O-B_2O_3-SiO_2 system (curve 2) is shown graphically in Fig. 9.
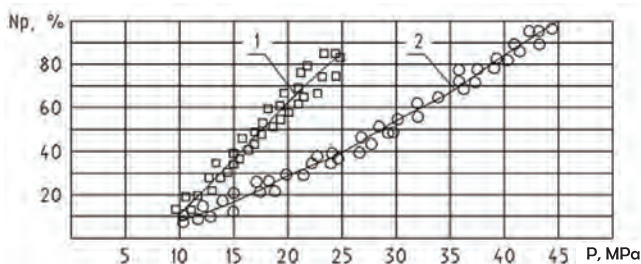
Fig. 9. Dependence of the number of destroyed microspheres on the hydrostatic pressure.

DISCUSSION

The glass composites obtained by sintering glass microspheres are new competitive analogues of syntactic foams in terms of their structure and properties - composite materials consisting of a polymer matrix and hollow spherical particles made of glass, ceramics, polymer, etc. The absence of a polymeric binder helps to obtain lightweight compositions whose density is 20% lower than syntactic foams with glass microspheres. The possibility of obtaining such materials will help to improve the design of subsea equipment for offshore development and research. Their hydrostatic strength is due to the spherical shape of the closed-loop cells. This structure (Fig. 5) is formed during the sintering of glass microspheres under selected temperature and strain conditions. The graphical interpretation of the kinetic shrinkage curves (Fig. 6) indicates the identity of the thermo-deformation processes of sintering microspheres from sodium silicate and sodium borosilicate glasses. From the angle of inclination of the curves to the abscissa axis, it can be established that during isothermal heating at 650 °C, the sintering process of microspheres lasts 25 - 30 min and is most intense in the first 8 min. However, the results of thermometric control showed that shrinkage begins long before reaching the isothermal holding mode: for Na_2O - SiO_2 glasses at 550 °C and Na_2O - B_2O_3 - SiO_2 glasses at 500 °C. This is due to the liquefaction softening processes that occur in the walls of glass microspheres, which is confirmed by comparing the results with the state diagrams of the corresponding silicate systems [22, 23]. The strength of the obtained glass composites is formed through contact curing of glass microspheres by the mechanisms of viscous glass phase flow. The formation of the contact area between the microspheres (Fig. 2b) occurs due to the application of a small pressure (up to 1.5 MPa) to the heated mixture (mass, weight), an increase which will contribute to a more intense sintering process. As shown in Fig. 6, the value of linear shrinkage can reach 50%. However, the results of experimental studies have shown that exceeding the selected temperature and strain modes of sintering leads to a violation of the spherical shape of the particles, which will negatively affect the performance properties of glass composites.

Experimental studies of the acoustic characteristics of the obtained glass composite samples (Fig. 7) showed the prospects of their use as sound insulation. The sound pressure level in the octave frequency bands is lower than that of foam samples. This effect can be explained by the peculiarities of the porous structure of the prototypes. During sintering, closed and open pores are formed between the glass microspheres. The shape and size of the pores depend on the thermo-deformation parameters of sintering, mainly on pressure. The open porosity of glass composites has a positive effect on their soundproofing properties, while the closed porosity reduces water absorption and increases buoyancy.

The results of hydrostatic tests (Fig. 8) showed the ability of glass composites to operate under conditions of comprehensive hydrostatic loading up to 20 MPa and

characterised the dynamics of their damage. The increase in volumetric water absorption is associated with the filling of micropores formed between the microspheres during sintering with water. The analysis of the experimentally obtained results on the destruction of microspheres under higher hydrostatic pressure (Fig. 9) confirms the theoretical ideas about the mechanisms of sintering without binders of Na_2O-SiO_2 and Na_2O-B_2O_3-SiO_2 glasses' microspheres and indicates the possibility of using the developed materials. In this regard, using the developed materials as a filler in combined shell structures is recommended.

Prospects for further research are related to computer modelling of fracture under hydrostatic loads, a feasibility study, and marketing research on the implementation of the developed glass composites.

CONCLUSIONS

The article solves an important scientific and technical problem of creating polyfunctional composite materials for shipbuilding and deep-sea engineering.

The thermal deformation processes of sintering sodium silicate and sodium borosilicate microspheres, which will directly affect the structure formation of glass composites with sound insulation properties and hydrostatic strength, were investigated.

The developed materials can be used in the design and manufacture of technical equipment for research and the maintenance of underwater infrastructures.

REFERENCES

1. Transporting Oil by Sea. In Planète Energies. January 14, 2015, https://www.planete-energies.com/en/media/article/transporting-oil-sea.

2. B.Wetzel. Oil in Motion: How Crude Oil Transportation Works. In Breakthrough group. November 1, 2019, https://www.breakthroughfuel.com/blog/oil-in-motion-visibility-into-crude-oil-transportation/.

3. V. Kobolev. The Black Sea's oil and gas potential: the reality and prospects of drilling a unique ultra-deep well on Zmiiny Island. In Mining of Mineral Deposits 2017. November 1, 2017. Retrieved from https://oil-gas.com.ua.

4. O. Lukin, I. Gafych, G. Goncharov, V. Makogon and T. Prygarina. 'Hydrocarbon potential in entrails of the earth of Ukraine and main trend of its development', Mineral Resources of Ukraine, vol. 11, no. 4, pp. 28 – 38, 2020, doi.org/10.31996/mru.2020.4.28-38.

5. Offshore Oil and Gas. In Planete Energies. November 8, 2015, https://www.planete-energies.com/en/media/article/offshore-oil-and-gas-production.

6. M. Xinhua, X. Jun. 'The progress and prospects of shale gas exploration and development in southern Sichuan Basin. SW China - Petroleum exploration and development', Online English edition of the Chinese language journal. vol. 45, no. 1, 2018, doi.org/10.1016/S1876-3804(18)30018-1.

7. G. Zhang, H. Qu, G. Chen, C. Zhao, F. Zhang, H. Yang, Z. Zhao and M. Ma. 'Giant discoveries of oil and gas fields in global deep waters in the past 40 years and the prospect of exploration', Natural Gas Geoscience, vol. 28, no. 4, pp. 1 – 28, 2019, doi: 10.1016/j.jnggs.2019.03.002.

8. Transportation of oil. In Energy Education. June 2014, https://energyeducation.ca/encyclopedia/ Transportation_of_oil.

9. A. Bahadori. Thermal Insulation Handbook for the Oil, Gas, and Petrochemical Industries. 1st Edition, School of Environment, Science & Engineering, Southern Cross University, Lismore, NSW, Australia, 2014. doi.org/10.1016/C2013-0-13424-1.

10. Deep-sea mining for rare metals will destroy ecosystems, say scientists. In The Guardian, March 2023, https://www.theguardian.com/environment/2023/mar/26/deep-sea-mining- for-rare-metals-will-destroy-ecosystems-say-scientists.

11. С. В. Копійка, І. О. Захарова та О. Г. Єгоров. 'Обґрунтування раціональної конструкції блоків плавучості підводних апаратів' (S. Kopiyka, I. Zakharova and A. Egorov. 'Substantiation of the rational design of buoyancy blocks of under-water vehicles'), Збірник наукових праць Національного університету кораблебудування. vol. 5, no. 2, pp. 28 – 32, 2017, doi.org/10.15589/jnn20170204.

12. V. Kumar. 'Buoyancy materials for marine instrumentation', National Institute of Oceanography, Goa, India, 2015, doi.org/10.13140/RG.2.1.2228.4964.

13. G. J. Meyer. Low-density polyurethane foam for subsea buoyancy systems. In Sea technology. August 5, 2015, https://sea-technology.com/feature-article-low-density-polyurethane-foam-for-subsea-buoyancy-systems.

14. D. Choqueuse, P. Davies, D. Perreux, L.Sohier and J-Y Cognard. 'Mechanical behaviour of syntactic foams for deep sea thermally insulated pipeline', Applied Mechanics and Materials, vol. 24 - 25, pp. 97 – 102, 2010, doi.org/10.4028/www.scientific.net/AMM.24-25.97.

15. Н. Соломонюк. Удосконалення конструкції підводного апарату блоками плавучості підвищеної теплостійкості. (N. Solomoniuk. Improvement of the underwater vehicle design by increased heat resistance buoyancy blocks) Ph.D. thesis, Admiral Makarov National University of Shipbuilding, Ukraine, 2012.

16. L. Smart and E. Moore. Solid state chemistry. In Taylor & Francis Group. 2005, https://www.uobabylon.edu.iq/eprints/publication_10_10256_250.pdf.

17. J. Dyre. 'Colloquium: The glass transition and elastic models of glass-forming liquids', American Physical Society, 2006, doi.org/10.1103/RevModPhys.78.953.

18. Y. Kazymyrenko, 'Installation for manufacturing of powdered products'. Utility model patent of Ukraine UA01414197, December 30, 2014.

19. W. Sikorski. Acoustic Emission - Research and Applications. InTech, pp.225, 2013.

20. Flexible cellular polymeric materials - Polyurethane foam for laminate use — Specification, ISO 6915:2019, 04 - 2020. Available: https://www.iso.org/ru/standard/77358.html.

21. Rigid cellular plastics. Thermal insulation products for buildings. Specifications. ISO 4898:2018, 03-2018.

22. W. Wong-Ng. 'Phase Equilibria and Crystallography of Ceramic Oxides', Journal of Research of the National Institute of Standards and Technology. 2011, doi.org/10.6028/jres.106.059.

23. J. Safarian, G. Tranell and M. Tangstad. 'Thermodynamic and kinetic behaviour of B and Na through the contact of B-doped silicon with Na2O-SiO2 slags', Metallurgical and Materials Transactions. 2013, doi.org/10.1007/s11663-013-9823-y.

TOWARD SAFE AND EFFICIENT RECOVERY OF GAS MUNITIONS DUMPED AT SEA

Lech Rowiński* (ID)
Gdansk University of Technology, Institute of Naval Architecture, Poland
Thanh Hai Truong
Phuoc Quy Phong Nguyen
PATET Research Group, Ho Chi Minh City University of Transport, Ho Chi Minh City, Viet Nam

Corresponding author: *lech.rowinski@pg.edu.pl (Lech Rowiński)*

ABSTRACT

The proposal of a system for the safe recovery of unexploded ordnance (UXO), chemical weapons (CW) and chemical warfare agents (CWA) dumped at sea mainly after WWI and WWII is described in this work. The proposed solution addresses the tasks required to neutralise thousands of tons of dumped material and the currently available solutions and proposed ideas. Requirements concerning the features of a recovery system are defined and scrutinised, these being intended to ensure the safety of this phase of the UXO/CW neutralisation process. To meet this requirement, the concept of a remotely operated, two-component working size underwater vehicle is proposed, supplemented by a properly sized and outfitted surface platform that is an important part of the recovery system. Finally, the basic components of the proposed system configuration are characterised, together with their functions during the recovery of dangerous CWA-related objects.

Keywords: remotely operated robot vehicle, chemical warfare agent, unexploded ordnance disposal

INTRODUCTION

Seen from a land based perspective, the marine environment seems to be endless in three dimensions and perfectly sustainable. The appearance of a water body at any instant depends on the weather, but ultimately the waves or a calm water surface seem always to be the same and self-healing. This is the reason why people have considered the ocean as both an unlimited source of wealth and an unlimited sink for all anthropogenic wastes. However, within the ocean, one kind of such waste is unused and unexploded munitions. This includes munitions (chemical weapons – CW) filled with chemical warfare agents (CWAs) of various kinds and containers filled with unused CWAs. According to Beldowski [1], there are roughly 150 to 300 sites worldwide with dumped chemical weapons. That number includes around 50 sites along the American coastlines, with a significant proportion in Hawaii. The total amount is unknown but a group of researchers from the Middlebury Institute of International Studies in Monterey, California, calculated that the total amount of chemical munitions in known locations amounts to 1.6 million tons, while roughly the same amount has been dumped elsewhere [2], and the identified sites can be seen on an interactive map [3]. The

most comprehensive description of the current knowledge of Baltic Sea dumping sites, which includes the characterisation of threats, is published by HELCOM (https://helcom.fi/) [4].

When first dumped, CW devices containing chemical warfare agents (CWAs) posed no direct, large-scale threat to people or the marine environment. They were contained in sealed shells and were not provided with detonators. Sometimes the dumped CWs contain bursting and priming charges, but, as far as is known, there have been no explosions during actions to finds chemical warfare bombs in the Baltic [5]. However, during the dumping operations some containers were damaged and released poisonous chemicals to the environment. This resulted in several fatal accidents during the first few decades after WW II. With time, people learned how to avoid such hazards. However, bomb shells and CWA containers were usually made of thin sheets of iron alloys, and due to corrosion processes they have now often completely faded away. The remaining semi-solidified mustard gas lumps often contain both priming and bursting charges, as shown in **Fig. 1**.
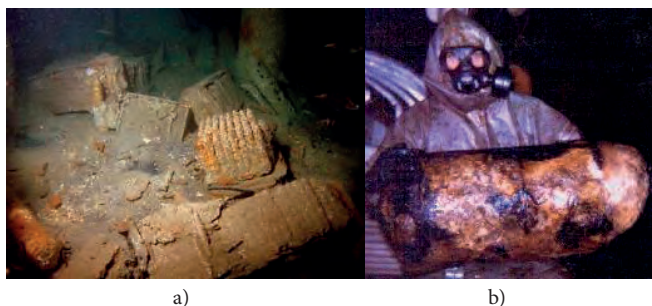

Fig. 1. Possible material forms of dumped CW devices and CWA: (a) Camera image of the sea bottom at a dumping site; (b) Semi-solid lump of mustard gas reflecting the shape of a gas-filled aerial bomb after its casing corroded completely [5][6]

A number of solutions have been proposed for some of the components of recovery and transportation tasks. One of the most serious recent proposals is the concept of a munition neutralisation barge to be operated in the Baltic and other areas (). This concept was developed by the Remontowa Group (Poland) based on the experience and solutions of the modular disposal line from Dynasafe Demil Systems AB [12][13][14]. The concept involves a double hull platform with a length of 105 m and width of 24 m. Manned with 40 persons, the facility would be capable of disposing of approximately 1250 kg of ammunition per day. This seems a substantial amount, but the neutralisation of 100,000 tons would take a single installation some 300 years to accomplish. This means that, in practice, only the most dangerous (threatening) dumping sites can be cleared. The concept prepared by the Remontowa – Dynasafe consortium demonstrates an understanding of the seriousness of the undertaking, indicating the approximate dimensions of the hypothetical surface platform required for operation with the neutralisation facility located at the dumping site. The solution apparently eliminates problems with the long-range transportation of the recovered CWs, but does not answer the question of how to safely recover and transfer

them to the neutralisation barge. Their proposal "*to pre-load (simply) the ammunition into the recovery containers while still underwater and prepare the underwater cache for collection by groups of navy divers-miners and specialist diving service providers*" seems unrealistic. However, the consortium indicates the requirement for an increase in capacity, "*through the provision of specialist robots and heavy suits, which eliminate the diver's contact with the external environment and hazardous substances*" [13]. Less practically developed ideas can be found in some descriptions of patents and patents pending. The US4621562A patent proposes the application of a wheeled manipulator to handle dumped UXO, as shown in **Fig. 2a** [15]. This is a remotely controlled robot vehicle that includes at least two pairs of wheels, at least one pair of which is driven, the said pairs of wheels being mounted on a support secured to the vehicle, whose supports are each mounted for pivotal movement about a generally horizontal axis extending longitudinally from the vehicle, with the wheels on the same side of the vehicle being capable of being driven synchronously. The vehicle carries a manipulation arm with a claw that allows for the handling of dumped shells. Another bottom-positioned device is described in the US7363844 B2 patent and concerns a remotely operated underwater non-destructive ordnance recovery system, which includes a powered remote controller, a floating remote-controlled transceiver wired to a remote disposal unit having a hydraulic grapple, and an ordnance recovery basket, together with the method by which these devices are used to extract unexploded underwater ordnance, as depicted in **Fig. 2b** [16]. The remote disposal unit includes an electrically driven internal hydraulic pump with bio-degradable hydraulic fluid in a closed loop system. A base includes variable footplates to stabilise the hydraulic grapple by remotely adjustable telescoping legs. A control head that receives signals from control cables and transfers them into hydraulic value actuation, an extendable fully rotating boom, two ballast tubes, a rotating grapple, and illuminated underwater cameras on the control box and ballast tubes are also included in the remote disposal unit.

Moreover, the objective of an invention described in EP3479052B1 is to create a method and a corresponding device to quite significantly reduce the harm to humans and the environment and is described non-exhaustively below by way of an example in the course of clearing UXO while avoiding any detonation underwater, as shown in **Fig. 3a** [17]. The object is reached according to the invention first exposed, and excavated sufficiently to permit its identification. In a second step, the UXO is separated from the surrounding seawater by placing it into a closable chamber, which is emptied of seawater once closed. Then, the casing of the UXO is cut open by means of water jet cutting. A device described in patent WO2020030558A1 is also suspended from the surface. This patent relates to an apparatus and a method for deactivating unexploded ordnance located underwater having at least one fuse, as illustrated in **Fig. 3b** [18], in which the apparatus (1) comprises a housing (2) that can be closed under water and from which water can be removed, a holder (4) for receiving the unexploded ordnance (5), the holder
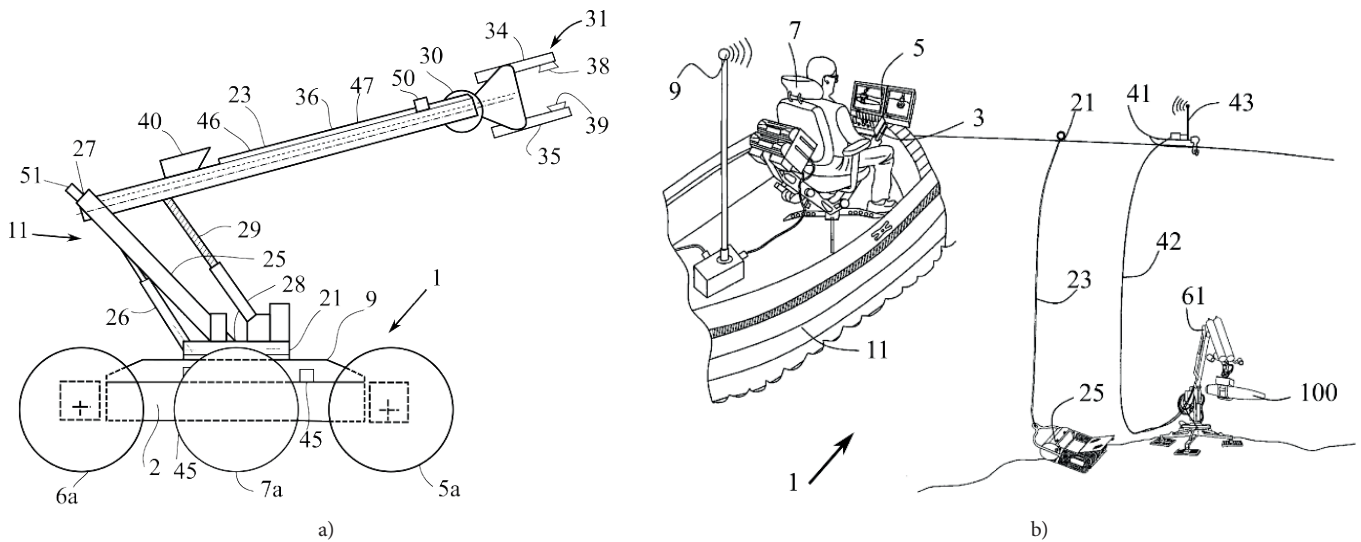
Fig. 2. Proposals of bottom equipment for remotely operated recovery of water-dumped unexploded munitions:
(a) Bottom driving wheeled munition lifting robot according to US4621562A patent [15];
(b) Remotely operated UXO recovery system composed of bottom located manipulator and separate lifting device US7363844 B2 [16]

being fixed in position in the housing (2), location means for precisely determining the location of the fuse (8) of the unexploded ordnance (5), a manipulator (10) having cutting means, and a gripper for removing and isolating the fuse (8) once cut free from the rest of the unexploded ordnance (5).

The invention is intended for sea mines and other ordnance filled with explosives, and provides that the UXO will be cut to pieces underwater by the device itself. However, it is rather unsuitable for direct use on chemical weapons.
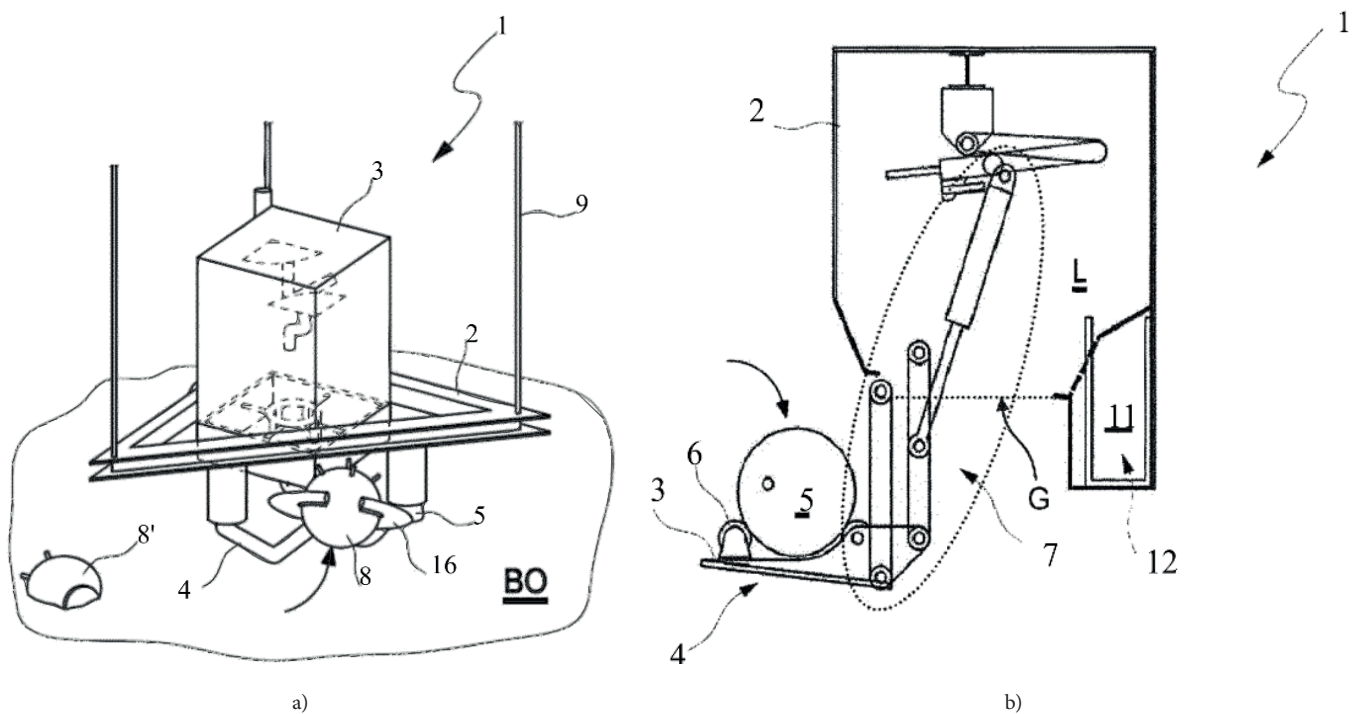
Fig. 3. UXO recovery devices suspended from surface platforms: (a) UXO recovery using device suspended from surface autonomous platform according to EP3479052B1 [17]; (b) UXO recovery using device suspended from surface autonomous platform according to WO2020030558A1 [18]

PROCESS OF NEUTRALISATION OF GAS MUNITIONS

The process of neutralisation of sea-dumped CWs is composed of four basic phases:

1. Investigation of the suspected site and identification of local threats;
2. Handling and recovery of the identified object to the surface;
3. Transport to recover the object to a neutralisation plant;
4. Neutralisation of the object in the plant.

All the phases of this process need to be organised and equipped to minimise the threat of incidental contamination of people and the environment. By definition, the CWAs involved are designed to kill irrespective of the cost to humanity and the environment. This threat is still real, in particular when large-scale operations are considered. Before any organisation can start the neutralisation of sea-dumped CWs and CWAs, it must prepare all feasible safety measures for every phase of the process. Particular difficulties with the neutralisation of gas munitions dumped at sea are the consequence of the fact that some tasks must be executed in spite of the instability of the operational conditions. This is an obvious situation when working at sea, where the weather can change dramatically within a single hour.

The investigation phase is the least threatening phase of the process of the neutralisation of the CWs. Except for cases where dumping sites were not properly marked on maps, the dumping sites can be detected and well documented by various available means. Remote sensing is mostly utilised during this phase, with TV cameras, photo cameras, sonars, magnetic and electromagnetic sensors used for this purpose. Chemical sensors and sample analyses of water sediments and living creatures are also utilised. Investigation is performed using remotely operated and autonomous vehicles, but commercial divers can be involved if required. Direct contact of equipment and people with CWAs can usually be avoided. From the safety point of view, it is important that particular missions in this phase can be terminated at any time, without significant consequences. This may be necessitated by unfavourable weather conditions or any other unexpected circumstances. Investigation efforts are continuously performed by many institutions, while, from time to time, investigation "campaigns" are organised by local authorities and international consortia. In general, the practical results of such investigations and wider campaigns to date have been decisions "not to disturb deposits" and to allow the threat to slowly deteriorate (meaning to corrode, hydrolyse and dissolve) [7].

In the majority of cases, this is probably the most efficient approach as no technology has been developed and tested that allows the safe neutralisation of the indicated masses of CWs. However, this well-established approach is less feasible if the containers are deteriorating too fast or the dumping sites are located in environmentally or economically valuable areas. From the point of view of local citizens and enterprises, the areas with dumped CWs are always valuable, and the potential threat caused by their presence is always direct.

The technologies for the destruction of CW during the last phase of neutralisation processes are also comparatively well developed. This is particularly true in the case of gas-filled artillery shells. This is due to the well-known structure of the particular designs and the intrinsic robustness of the artillery shells. As seen in Fig. 4, their structures are well defined by procurement processes. If the shells are intact and have no detonators, they pose no serious safety problems. To allow the neutralisation of Cold War stockpiles of gas-filled projectiles, efficient industrial processing lines were developed [8][9]. Neutralisation plants are active in many countries but their capacity is very limited. Usually, they are based on heat processes (incineration and controlled detonation) that are quite well developed. Such permanent, land-based facilities require the munitions to be transported from their storage sites. Portable neutralisation facilities are also available, but devoted to single pieces of munition.
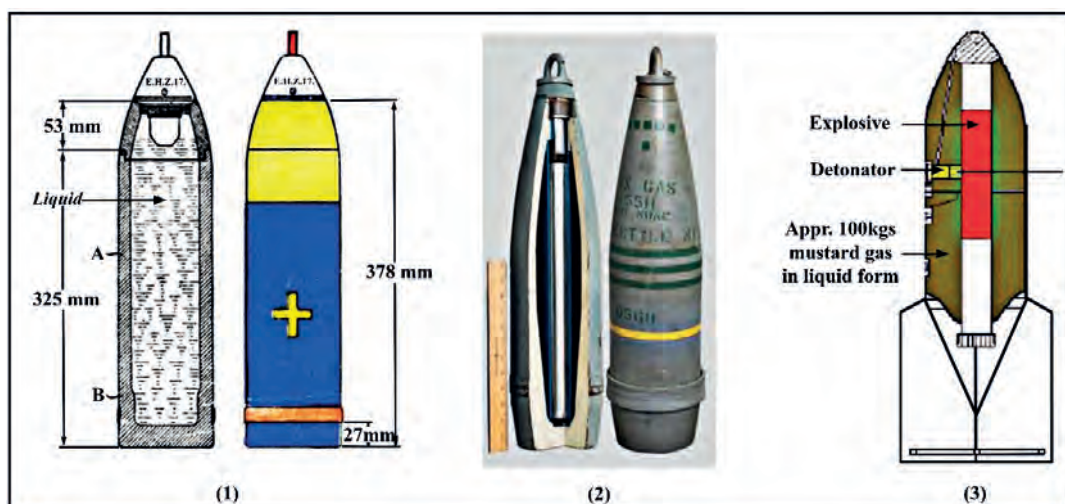

Fig. 4. Typical arrangement of gas-filled artillery shell: 1. German WWI mustard gas shells [10]; 2. US 155 mm chemical, M121A1 shell, chemical warfare agents (CWA) [11]; 3. German WWII mustard gas bomb KC 250 [5]

Similarly, in many cases, CWs in the form of artillery projectiles dumped at sea can be safely recovered and transported to incineration facilities. The difference, in comparison with new shells, is the questionable possibility of recovering the bursting explosive from aged devices before the chemical fill can be incinerated. In the case of gas containers and aerial bombs, the situation is much more complicated as these devices were less robust and are more susceptible to mechanical damage and corrosion. Such devices with chemicals exposed (Fig. 1) may not be simple to handle, recover and transport to the neutralisation facility. As mentioned above, the best solution in such cases is a decision "not to disturb". Such deposits need to wait until procedures and technical means that ensure the safe recovery and transportation of large numbers of damaged containers and solidified chemical lumps are developed.

RECOVERY PHASE

Following the above statement, it is apparent that technical means that are able to ensure the safe recovery and transportation of dangerous objects need to be developed. This concerns the filled shells, leaking containers and even exposed chemicals. This is the pre-condition for safe, large-scale clearance of the sea bottom. The first step in the development process of a CW recovery system is the definition of requirements ensuring the fulfilment of operational and safety needs. The proposed requirements are listed below. While a CW recovery system must be well integrated, it is divided into two components: recovery equipment and a surface platform system, the latter being a platform from which the recovery equipment is launched and operated. The reason for the separate definition of requirements is the possibility of better identification of the required features and capabilities of each part of the system.

REQUIREMENTS REGARDING EQUIPMENT FOR CW RECOVERY PHASE

The recovery equipment is the least defined component in the whole process of CW neutralisation. This is why it needs to be defined to meet the requirements of the specific application. Of course, if a remotely operated underwater vehicle is considered, it must be built as a reliable work system that is able to operate at the required depth and sea current. According to the author's analyses, the equipment (underwater vehicle) employed for the detailed investigation and recovery of dumped munitions and CWs in particular would also possess the following abilities:
1. Assess the chemical composition of the local environment, with constant monitoring of contamination levels from the CW during the recovery operation;
2. Firmly stabilise the equipment (work vehicle) on the bottom to allow detailed investigation of objects deposited on the bottom and buried in sediments without agitating these sediments;

3. Firmly stabilise the equipment (work vehicle) on the bottom to allow all kinds of manipulation tasks without agitating these sediments;
4. Move horizontally while in contact with the bottom with minimum agitation of bottom sediments;
5. Remove amounts of sediments to expose objects of interest without spreading the CW in the environment;
6. Accomplish the manipulation tasks required for assessment of the condition of an investigated object;
7. Remove semi-solid CWA from a site, without spreading the CWA in the environment;
8. Collect objects with mass of up to 250 kg (1000 kg if aerial bombs are included);
9. Isolate CWs and other objects containing CWA in dedicated containers;
10. Ascend with collected object without agitation of sediments by the operating thrusters.

REQUIREMENTS REGARDING SURFACE PLATFORM AND ITS OUTFIT

The requirements regarding the platform from which the recovery equipment is launched and operated are easier to define than those of the recovery equipment itself. Its minimum size is defined by the operating conditions and physical properties (size and weight) of the recovery equipment and its assumed functionality. As a minimum, it can be assumed that the functionality is limited to storage and transport of the recovered CW to a neutralisation facility. The remaining features and abilities ensure safety during normal operation and in emergencies.

Such a surface system (surface platform) used for the recovery of dumped munitions, and CWs in particular, would possess the following abilities:
1. Provide safe operation conditions for recovery equipment in the expected location (sea worthiness);
2. Provide protection for people (crew) against accidental contamination by the recovered CW;
3. Self-decontamination of the ship deck and deck equipment;
4. Decontamination of people (crew);
5. Decontamination of divers and diving equipment;
6. Decontamination of recovery equipment;
7. Storage of contaminated fluids;
8. Storage of recovered objects;
9. Storage of insulating containers with recovered objects;
10. Remotely controlled operation of the surface platform in the case of emergency contamination.

The requirements regarding the features listed above are considered to be the minimum for safe recovery and storage of recovered CWs. The neutralisation phase that needs to follow can be accomplished locally, or the recovered objects may need to be transported to an external neutralisation plant. The solution adopted would depend on the scale of the operation. For a small-scale intervention (removal of some insulated pieces of CW), transport to a land-based facility may be feasible. In the case of large-scale "bottom cleaning", the application of a neutralisation ship (barge) seems to be more efficient.

PROPOSED SOLUTIONS

The dumped CW can be recovered using the well-established technology of classical diving. The equipment (classical diving suits) used for diving protects the persons (divers) involved from contact with chemicals and can be easily decontaminated. The recovered items can be insulated from the environment using simple, sealed containers. However, manual work at significant depth must be limited to individual cases, as it requires hard physical work that is difficult to accomplish at substantial depths. At depths greater than 50 m (for example Bornholm Deep and Gdansk Deep), saturation diving will be essential. It will be difficult to exclude accidents also. Of course, mechanical equipment (excavators and lifting machines) can be developed to support divers, but in fact, such equipment can be operated remotely without involving divers.

CONCEPT OF AN INTEGRATED CW RECOVERY SYSTEM BASED ON REMOTELY OPERATED VEHICLE

Based on the requirements listed above, the concept of a complete CW recovery system was defined. The system according to this proposal is used to recover and store (destroy) dangerous objects. Recovery and storage (destruction) activities are carried out using a surface platform with dimensions adapted to the expected environmental conditions and the size and amount of the recovered objects. The surface platform needs to be equipped with all means necessary for

safe operation of a work size, remotely controlled underwater vehicle and accompanying devices. The equipment used to recover hazardous objects from the bottom has the form of a two-component underwater remotely operated vehicle. The total mass of the vehicle is estimated at between 3 and 5 tons, depending on the assumed size and mass of recovered objects. One part of the vehicle is a transport or propulsion module and the second part is a bottom module. All the bottom activity is performed by the bottom module, while the propulsion module transports equipment and recovered objects between the bottom and surface platform. This solution was selected to minimise the agitation of bottom sediments by the hovering submersible. This is an important feature according to the requirements listed above. The transport module is equipped with an observation unit, a navigation suite, a propulsion system and a very capable ballast system. The ballast system adjusts the buoyancy of the transport module in a range suitable for moving the bottom module in the water space and for lifting the expected objects from the bottom. For the majority of cases, the buoyancy changes would be in the range of 0 to 2.5 kN. If handling of aerial bombs or large barrels is considered, buoyancy changes in the range of 0 kN to 10 kN or an even wider range needs to be provided. The transporting module is designed with the minimal number of appendages as these would be difficult to decontaminate. An insulating container is attached to the bottom of the transport module and utilised for transportation of the most dangerous objects after they are lifted from the bottom. The concept of the insulating container is shown in Fig. 5.

(1) (2) (3)
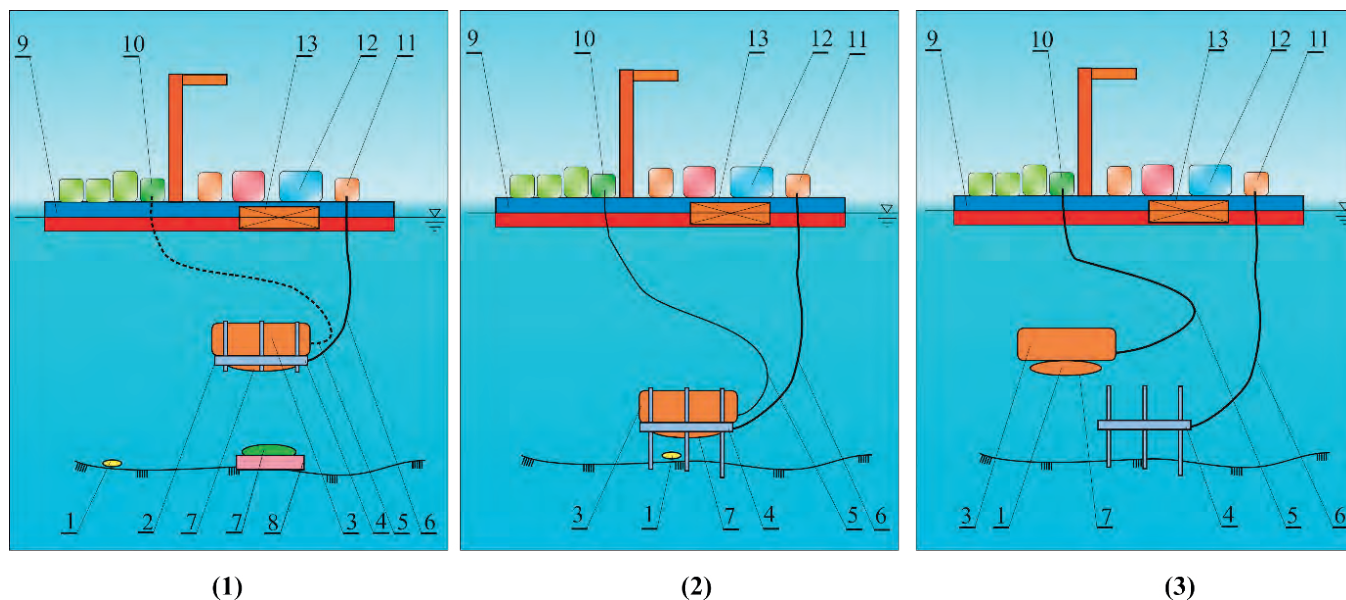
Fig. 4 General arrangement of the proposed gas munition recovery system: 1. The vehicle consisting of a drive module and a bottom module, swimming to a dangerous object; 2. The vehicle over an UXO with the legs extended and stabilised on the bottom; 3. The drive module with the container floats to the surface while the bottom module remains on the bottom near the next object to be lifted from the bottom, or waiting to be moved by the drive unit to a new job site. 1. UXO; 2. ROV; 3. Transporting module; 4. Bottom module; 5. Umbilical of transporting module; 6. Umbilical of bottom module; 7. Insulating container; 8. Temporary storage frame; 9. Surface platform; 10. Transporting module winch; 11. Bottom module winch; 12. Decontamination compartment; 13. Contaminated water tank
[Author's drawing]
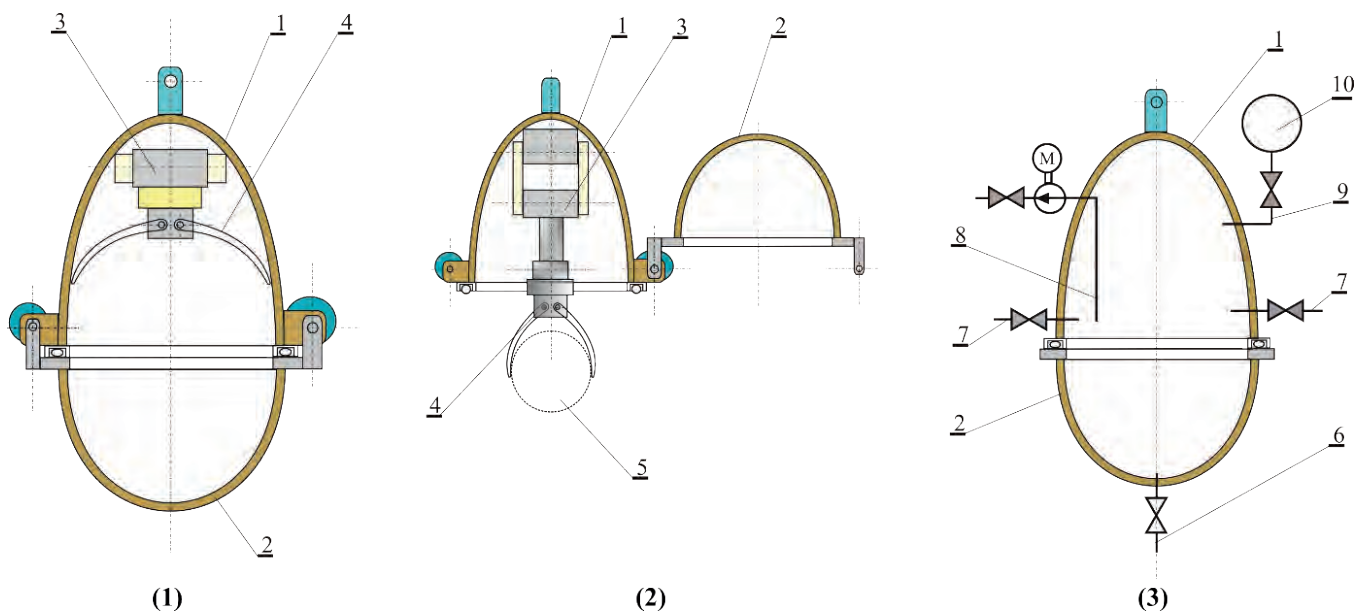
Fig. 5. Concept of an insulating container for recovered leaking CW and badly damaged containers with exposed CWA. 1. General arrangement of the insulating container with internally mounted manipulation and CW object handling; 2. The insulating container in open configuration and CW object in the manipulator; 3. Tubular outfit of the insulation container that allows for control of atmosphere inside the closed container. 1. Insulating container; 2. Container cover; 3. Manipulator arm; 4. Manipulator claws; 5. Recovered object; 6. Drain pipe; 7. Chemical treatment pipes; 8. Water removal pipe; 9. Gas purging pipe; 10. Gas canister
[Author's drawing]

The second part of the underwater vehicle is the bottom module. Initially, it is attached to the transport module in a detachable manner and transferred to the munition dump site. The bottom module is a working platform capable of walking on the bottom on six legs and stabilising the vehicle during handling (manipulation) activities. The spider-like configuration of the motion system, which allows for movement in any direction, was selected to meet the requirement regarding the minimum agitation of sediments during relocation of the bottom module. It also allows for significant movement in the horizontal plane without retracting the legs from the sediment, levelling of the platform and control of the distance between the chassis of the bottom module and the bottom itself. The majority of the manipulating devices applied in the recovery of CWs are fixed to the chassis of the bottom module, together with the illumination devices, cameras and sensors used to assess the contamination levels. This solution minimises the possibility of accidental surfacing of equipment contaminated with CWAs. An important feature is the capability of the design to allow precise cleaning of objects of interest using water jetting of sediments and the object surface to remove rust and other debris. At the same time, any developing slurry can be pumped out to some distance from the working vehicle or pumped to the surface for treatment or/and storage. This arrangement allows for the recovery of liquid and semi-solid CWAs without the need to recover lumps of chemicals that may be difficult to handle. Semi-solid CWAs can be cut to small pieces mechanically or using high-pressure water-jets and sucked off.

Both modules of the underwater vehicle are connected by means of two separate umbilicals to equipment mounted on the surface platform. These umbilicals are connected to two dedicated winches mounted on the surface platform. The umbilical of the transporting module has a typical ROV positive buoyancy structure, containing power and communication components. The umbilical of the bottom module contains additional components in the form of an elastic pipe (hose). This is provided for pumping of the contaminated water and slurry generated during handling of leaking CWs and CWAs without containers. Therefore, the dedicated winch of the bottom module is designed to transfer contaminated fluids and suspended solids to storage tanks and treatment facilities.

The surface platform is basically designed to support the operation of the underwater part of the system. For this purpose, it is equipped with appropriate lifting devices and cranes, control rooms, and power supply devices (generators). For safety reasons, the surface platform is anchored at some distance from the work site. The distance needs to be sufficient to exclude damage due to any possible underwater explosion. To allow the handling of CWs and CWAs, dedicated containers (rooms) and tanks are provided. These are used for the deactivation and storage of hazardous objects, fluids and gases. It is recommended that a complete line for destroying UXO of all types and CWAs in containers at any technical condition will be assembled on the surface platform.

In order to extract a dangerous object from the bottom, the position of the surface platform is stabilised in the vicinity of the object or set of such objects (i.e. a dumping site). Then, the underwater vehicle composed of the two modules is launched from the deck of the surface vessel by means of a crane specific for the handling of ROVs. When the vehicle is submerged, the winches located on the platform unwind appropriate lengths

of both umbilicals. After reaching a dangerous object, the underwater vehicle stands on the bottom on extendable legs. The pressure the vehicle exerts on the bottom is regulated by means of ballast devices. Then, using the mobility properties of the legs, the vehicle moves towards the dangerous object so that it is under the body of the vehicle and within reach of the manipulating arms. By means of observation, aided by handling activities, including washing out and sucking out debris and corrosion products of the elements of the potentially dangerous object, it is identified and evaluated. It is envisaged that the water contaminated with chemicals is sent to the ship's neutralising equipment. After a thorough inventory of the object in terms of the type, degree of damage and level of danger, the object or its elements are lifted by the internal manipulator of the hermetic insulating container and closed inside it. After enclosing the dangerous object in the insulating container, the underwater vehicle separates into the bottom module and the transport module. The bottom module remains anchored on the bottom with its legs in the sediments. The transport module floats to the surface after balancing the weight of the object by means of the buoyancy control system. Then it is lifted by the ship's crane and placed in the insulating sluice of the decontamination system. In this sluice, the transport container is detached from the transport module. Another transport container is then attached to the transport module, which is lowered back into the water and down to the bottom module standing on the bottom.

After reconnecting the drive module and the bottom module, lifting of objects from the bottom continues. In the case of recovering multiple objects located in proximity, the vehicle combined with the transporting module approaches the next ones (objects) using leg movements. Of course, while dealing with safe objects (not damaged or leaking), the recovery operation can be simplified. In such a case, CWA-filled shells or containers can be loaded (several pieces) into unsealed recovery containers using manipulators and lifted to the surface platform.

If, when lifting a dangerous object into an insulating container, the surface of this container and the transport module is heavily contaminated (e.g. when lifting a lump of chemical agent from a corroded container), the vehicle puts the container with the dangerous object on the storage frame located at the bottom and picks up another container from this frame. The storage frame with insulating containers containing dangerous objects is lifted to the surface after the contamination drops to a level considered safe. According to available data, such "natural" decontamination of thin layers of chemicals usually requires less than 24 h exposure to sea water [4]. After removing all the hazardous objects from the bottom, the legs of the vehicle are released from the bottom sediments and the underwater vehicle is moved to another location to perform further tasks. If work is finished at one spot, the vehicle swims to the surface and is lifted on board the surface platform, cleaned and prepared for the next operation.

(1) **(2)**
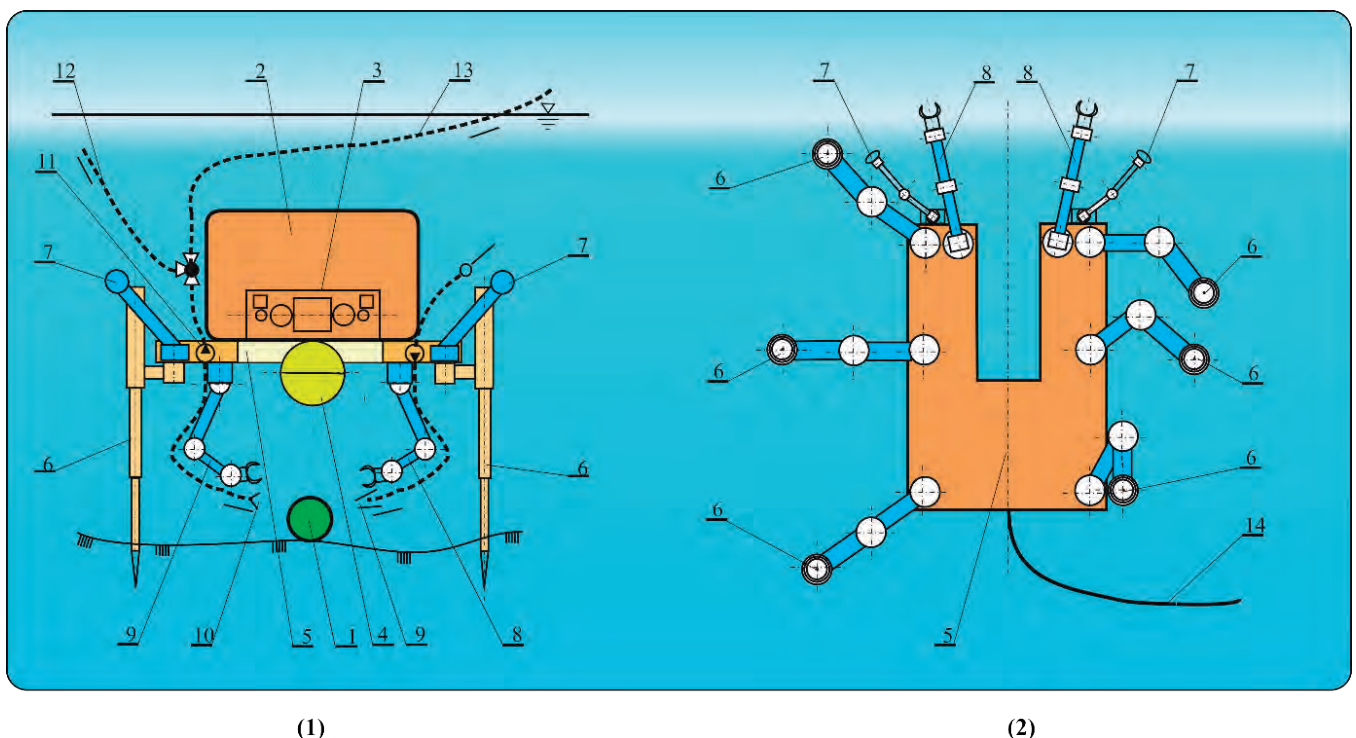
Fig. 6. Basic features of gas munition recovery vehicle composed of legged bottom module and transportation module equipped with insulating container.
1. UXO; 2. Transporting module; 3. Observation equipment; 4. Insulating container; 5. Bottom module; 6. Leg; 7. Lamp; 8. Manipulator; 9. Water jetting nozzle;
10. Sediment/CWA slurry suction cup; 11. Slurry transfer pump; 12. Sediment slurry discharge hose; 13. Sediment/CWA slurry hose for surface treatment;
14. Umbilical of the bottom module
[Author's drawing]

SUMMARY

It is apparent that the large-scale neutralisation of sea-dumped warfare materials is a really great challenge to the nations, governments and international organisations involved. One can assume that the recovery of some 100,000 items from the most threatening European deposits will realistically take 10 years. An operation on this scale would require the procurement of some 50 active and efficient recovery and neutralisation systems manned with 5000 personnel. As seen from a brief investigation of the current solutions, the availability of adequate "industrial" technologies is very problematic. Safe neutralisation of unexploded ordnance, chemical weapons and warfare chemical agents, in particular those dumped at sea, requires the development of suitable technologies, equipment and procedures. Due to under-development of the recovery phase of the neutralisation process, strong (inter-governmental) support for research and development in dedicated equipment is required. It is apparent that for the scale of the task of "cleaning" the bottom, really substantial development effort is required. Based on the discussed requirements, other new proposals need to be created, developed and tested in practice. Testing in practice means testing on real dumping sites. This needs to be done before the selected method and equipment are approved as safe for people and the environment. Otherwise, the only practical solution will remain "not to disturb" and to allow the dumped materials to slowly deteriorate with time.

REFERENCES

1. J. Bełdowski *et al.*, "Chemical munitions search & assessment - An evaluation of the dumped munitions problem in the Baltic Sea," *Deep. Res. Part II Top. Stud. Oceanogr.*, vol. 128, 2016, doi: 10.1016/j.dsr2.2015.01.017.

2. I. Wilkinson, (Middlebury Institute of International Studies in Monterey), "Chemical weapon munitions dumped at sea: An interactive map," 2017. https://nonproliferation.org/chemical-weapon-munitions-dumped-at-sea/

3. Anonymous, "Chemical weapons material dumped at sea; Interactive map," 2017. https://www.google.com/maps/d/viewer?ll=5.368292378570265%2C0&z=2&mid=1ALnyOrN5JQ8H50znwJqI_Sj8IwE

4. J. Beldowski, "Chemical munitions dumped in the Baltic Sea. Report of the ad hoc expert group to update and review the existing information on dumped chemical munitions in the Baltic Sea (HELCOM MUNI)," in *Baltic Sea Environment Proceedings (BSEP),* No. 142, p. 128, 2013. [Online]. Available: https://helcom.fi/wp-content/uploads/2019/08/Dumped-chemical-munitions-in-the-Baltic-Sea.pdf

5. Anonymous, "A framework for developing national guidelines for fishermen on how to deal with encounters conventional and chemical munitions," 2004. [Online]. Available: http://www.environet.eu/pub/pubwis/rura/20070113123123.pdf

6. Anonymous, "Overview of past dumping at sea of chemical weapons and munitions in the OSPAR Maritime Area 2010 update," 2010. [Online]. Available: https://www.ospar.org/ospar-data/p00519_2010 revised dumping at sea of munitions and weapons.pdf

7. Anonymous, "Government won't remove thousands of tons of potentially toxic chemical weapons dumped off US coasts," 2017. https://underwatermunitions.org/2017/10/17/government-wont-remove-thousands-of-tons-of-potentially-toxic-chemical-weapons-dumped-off-us-coasts/

8. M. Geuss, "In southeastern Colorado, robots carefully disarm WWII-era chemical weapons," 2017. https://arstechnica.com/science/2017/02/in-southwestern-colorado-robots-carefully-disarm-wwii-era-chemical-weapons/

9. M. de Yoanna, "In Pueblo, America's chemical weapons era nears an end," 2019. https://www.kunc.org/news/2019-08-08/in-pueblo-americas-chemical-weapons-era-nears-an-end

10. S. Jones, "Yellow Cross: the advent of mustard gas in 1917," 2007. https://simonjoneshistorian.com/2014/02/04/yellow-cross-the-advent-of-mustard-gas-in-1917/

11. Anonymous, "US Projectile, 155mm Chemical, M121A1." https://www.bulletpicker.com/projectile_-155mm-chemical_-m4.html

12. R. Miętkiewicz, "Do WWII weapons dumped in the Baltic Sea pose a threat to wind energy?," 2022. https://balticwind.eu/do-wwii-weapons-sunk-in-the-baltic-sea-pose-a-threat-to-wind-energy/

13. Anonymous, "Removal of hazardous substances from the bottom of the Baltic Sea – solution of Remontowa Holding," 2021. https://www.polandatsea.com/removal-of-hazardous-substances-from-the-bottom-of-the-baltic-sea-solution-of-remontowa-holding/

14. J. Donovan, "Method and apparatus for the destruction of suspected terrorist weapons by detonation in a contained environment," WO2001048437A1, 1999 [Online]. Available: https://patents.google.com/patent/WO2001048437A1/en

15. M. J. R. Carr, C. Sennett, and B. Wilkinson, "Remote control robot vehicle," US Patent 4621562, 1986. [Online]. Available: http://www.google.com/patents?hl=en&lr=&vid=USPAT4621562&id=fqQzAAAAEBAJ&a

mp;oi=fnd&dq=Remote+control+robot+vehicle&printsec=abstract. [Accessed: Feb. 11, 2012].

16. J. Barton, "Remotely operated, underwater non-destructive ordnance recovery system and method," US 7363844 B2, 2006 [Online]. Available: https://patents.google.com/patent/US7363844B2/en?oq=US+7%2C363%2C844+B2+

17. J. Koebel, "Method and device for disposing of a piece of unexploded ordnance lying under water," EP3479052B1, 2017 [Online]. Available: https://patents.google.com/patent/EP3479052B1/en?oq=EP3479052B1

18. N. Scheffer and M. Freudenthal, "Method and apparatus for deactivating unexploded ordnance located under water," WO2020030558A1, 2018 [Online]. Available: https://patents.google.com/patent/WO2020030558A1/de?oq=WO2020030558A1

ROLE OF GREEN LOGISTICS IN THE CONSTRUCTION OF SUSTAINABLE SUPPLY CHAINS

Nguyen Dang Khoa Pham (iD)
PATET Research Group, Ho Chi Minh city University of Transport, Ho Chi Minh city, Vietnam
Gia Huy Dinh (iD)
Institute of Graduate Studies, Ho Chi Minh City University of Transport, Ho Chi Minh city, Vietnam
Hoang Thai Pham (iD)
Maritime Academy, Ho Chi Minh City University of Transport, Ho Chi Minh city, Vietnam
Janusz Kozak (iD)
Gdansk University of Technology, Institute of Naval Architecture, Poland
Hoang Phuong Nguyen* (iD)
Academy of Politics Region II, Ho Chi Minh city, Vietnam

Corresponding author: *nghoangphuong11@gmail.com (Hoang Phuong Nguyen)*

ABSTRACT

The global supply chain has been growing strongly in recent years. This development brings many benefits to the economy, society, and human resources in each country but also causes a large number of concerns related to the environment since traditional logistics activities in the supply chain have been releasing a significant amount of emissions. For that reason, many solutions have been proposed to deal with these environmental pollution problems. Among these, three promising solutions are expected to completely solve environmental problems in every supply chain: (i) Application of blockchain in the supply chain, (ii) Use of renewable energy and alternative fuels, and (iii) Design of a closed supply chain. However, it seems to lack a comprehensive study of these solutions aiming to overcome the drawbacks of traditional logistics. Indeed, this work focuses on analyzing and evaluating the three above-mentioned solutions and the impacts of each solution on solving problems related to traditional logistics. More importantly, this work also identifies critical factors and challenges such as policies, laws, awareness, and risks that are found to be remarkable difficulties in the shifting progress of traditional logistics to green logistics. Finally, directions for developing and deploying green solutions to the logistics, supply chain, and shipping sectors toward decarbonization strategies and net-zero goals are discussed in detail.

Keywords: green logistics, supply chain, environmental pollution, sustainable development

INTRODUCTION

With the current trends towards globalisation, the supply chain is expanding to meet the increasing needs of society [1]. However, when the supply chain develops too quickly, it will have negative effects, the most obvious of which are problems with environmental pollution [2]. This forces businesses to pay attention to their environmental impacts and to find ways to address them [3][4]. a common aim of businesses and organisations operating in all sectors is to continuously improve their tools and operating methods to create sustainable development, without causing negative impacts on the environment, while still optimising their operating costs [5]. Of the latest solutions put forward, the green supply chain stands out as a viable and potential system for managing the supply chains of organisations and solving problems with environmental pollution [6][7]. In addition, trends towards globalisation have promoted the expansion of the supply chain, and an inevitable consequence of this is a significant increase in logistics activities [8]. This puts great pressure on the environment when solutions for limiting negative aspects are either incomplete or not yet operational [9]. According to data from 2016, emissions in transportation activities account for about one-quarter of total emissions;

more specifically, CO_2 emissions are currently about 8 Gt, representing an increase of about 71% compared to 1990 [10]. Among these, emissions from freight activities account for 42% of all transportation emissions [11][12][13], and are expected to reach 60% by 2050 [14]. Moreover, the remarkable decline of NOx, PM, and CO_2 emissions during lockdown due to the COVID-19 pandemic could be considered as believable proof of the significant contribution of transport activities to pollutant emissions [15][16][17]. Due to this reason, the International Energy Agency (IEA) has developed a Sustainable Development Scenario with a primary emphasis on lowering transportation-related CO_2 emissions. Direct CO_2 emissions from transport using fossil fuels are projected to decrease by over 90%, from 8.1 Gt in 2019 to 1 Gt in 2070, under the Sustainable Development Scenario [18]. Fig. 1 shows the pathway for achieving net-zero CO_2 pollution from energy around the world by 2070.
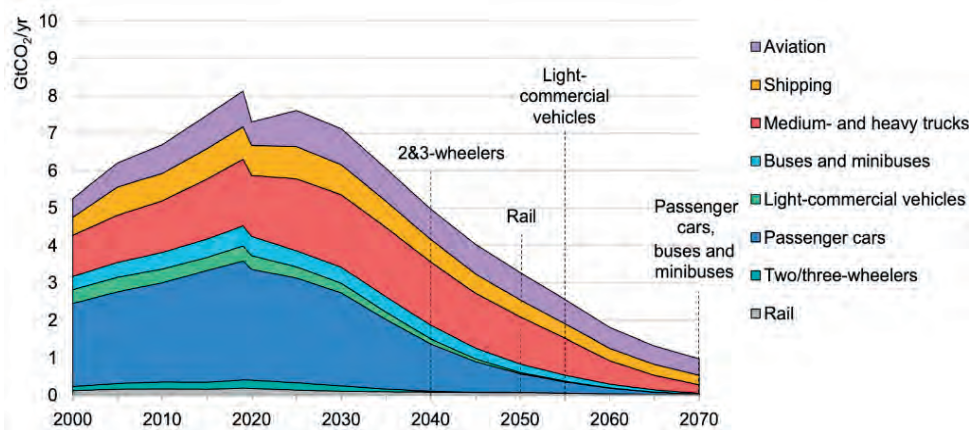
Fig. 1. Expected global CO_2 emissions from various modes of transport from 2000 to 2070, according to the Sustainable Development Scenario [18]

The requirements for the sustainable development of supply chains and transportation are of great interest to many countries and governments, although the outcomes achieved in each country have been very different [19]. It is, therefore, essential to consider the factors affecting sustainable development when comparing the efficiency of supply chain and logistics operations across countries with a view to moving towards green logistics (GL). Reducing harm to the environment is not only one of the great challenges in achieving a sustainable development strategy, but is also mandatory for organisations and businesses in all sectors, with logistics businesses being no exception [20]. The vital role of transport and logistics activities in the economy and social stability of countries cannot be denied, but they are also one of the main sources of environmental pollution [21]

[22][23]. Environmental policies toward logistics businesses are becoming increasingly stringent; the two main reasons for this are the growing influence of the supply chain on the environment (in terms of higher congestion, lower safety, and greater environmental pollution) and the feasibility of building sustainable logistics systems. The demand for GL services is therefore rising by the day, leading to ever more initiatives being designed and deployed in this area. Supply chains are not only expanding in number, but also in terms of the complexity of supplier and enterprise networks, meaning that ways of managing these networks effectively are required [24]. Links between the implementation of green solutions in logistics management, economic growth, and the minimisation of negative impacts on the environment have been reported in studies by Aldakhil et al. [25] and Nguyen et al. [26]. In addition, the effective maintenance of green operations in logistics activities has been proven to help achieve both economic and environmental sustainability goals [27]. Karaman et al. [28] and Seroka-Stolka et al. [29] have reported that GL activities help the economic circle run more smoothly, thereby strongly boosting the overall economy of the country. Important practices include eco-friendly packaging design, and the adoption of green transport, storage, and processing practices. Fig. 2 shows the links between economic development, environmentally friendly operation, and sustainable supply chains [30].

In general, freight and logistics operations are the lifeblood of the supply chain, as they are concerned with the movement and storage of materials and products throughout the entire supply chain. Most supply chains today operate on the just-in-time model, which requires continuous and rapid movement of materials and products, management, and expansion of logistics activities, meaning that transportation becomes a vital element of the economy. The growth in road transport activities has therefore been considerably higher than for

Fig. 2. Connections between sustainability issues, economic development, and the supply chain [30]

other transport activities [31]. However, in the absence of sustainable options for implementation, these processes cause negative environmental and social impacts. Indeed, Piecyk et al. [32] showed that freight transport accounted for a much higher share of emissions than other emissions related to transportation. The main reason for this was the abuse of just-in-time approaches to promote small but fast and continuous deliveries, mainly by trucks [33]. Most businesses still rely heavily on road transport, even though other means of transport such as air, waterways, and railways have significantly improved, primarily due to its low cost, high flexibility, and fast response times [34]. The consequence of this overuse of vehicles is that their CO_2 emissions are overwhelming compared to other causes; they account for 30–40% of the total emissions from the industry [35]. For all of these reasons, green transport strategies need to be implemented throughout the supply chain and logistics operations. In addition, it is necessary to continuously check and measure the operational efficiency, as this is important in determining the ability to implement and maintain a strategy as well as the success of the strategy; it therefore affects the economic aspects of the business, and requires a meaningful green transport strategy. a paradigm for environmentally friendly logistics, founded on the operational concepts of environmentally friendly growth and logistics, is presented below in Fig. 3 [36].
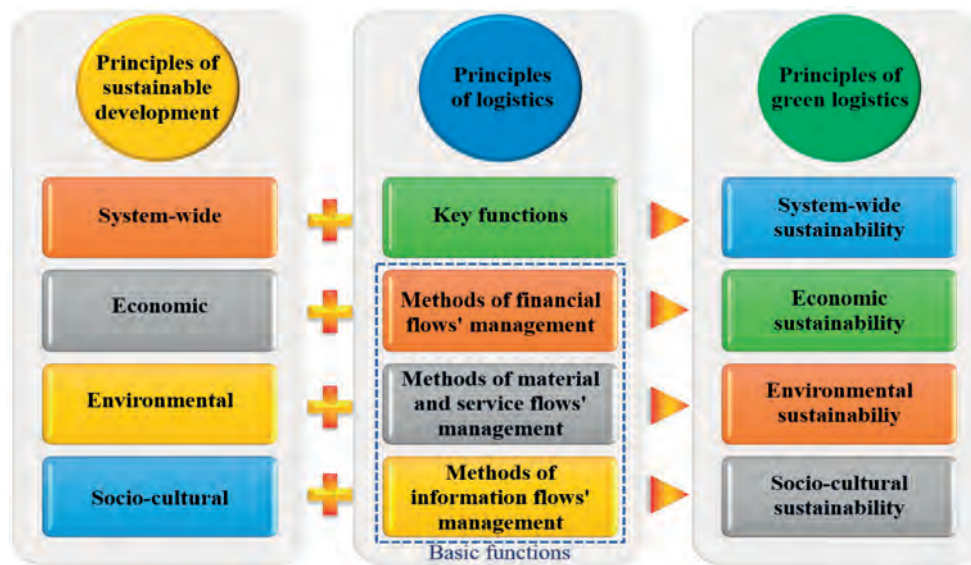
Fig. 3: Green logistics: a conceptual framework [36]

From Fig 3, it could be seen that benchmarks for measuring transport business success include factors relating to sustainable development, these factors are particularly important for the logistics field. However, there have been limits in understanding, developing, and deploying green logistics. Therefore, the main focus of this work is on highlighting the most important aspects of the role of GL in establishing a sustainable supply chain. The paper consists of five parts, in which Section 2 reviews the theoretical foundations of existing research, while Section 3 describes recent trends in the use of GL systems to build a sustainable supply chain. In addition, applications and future trends in GL in this section is also reviewed in this section. Section 4 discusses perspectives and future directions for GL in the construction of a sustainable supply chain. The final section presents the conclusions and key findings of this work.

THEORETICAL BACKGROUND

CONCEPTUAL BASIS OF GREEN LOGISTICS

Effective supply chain management is a leading factor in the sustainable development of a business. Over the past few decades, researchers, scientists, managers, and politicians around the world have strived to develop a general concept of sustainable development that can be combined with social and environmental goals without affecting economic success. Bajdor et al. [37] claim that the concept of sustainable development has changed the approaches and business strategies of modern companies, which aim to maintain and develop their economic and financial profits while also ensuring social order and minimising the negative impacts on the environment. With a view to adapting and optimising the transport policies of enterprises while still being able to protect resources and the environment, today's supply chain and logistics systems are oriented towards green transport [38][39][40][41][42]. Green transport is an important link in the logistics chain, and is commonly defined as a way of transporting supplies (raw materials and products) that minimises the negative impacts on the environment. Enterprises or organisations often consider integrating green transport into the supply chain, with the desire to maintain and improve the smooth operation of the system while still being able to meet the strict requirements of the law on environmental issues and the performance of suppliers and customers [43]. It is, therefore, necessary to evaluate and analyse the important factors affecting the development of an appropriate greening roadmap [44][45][46]. In particular, small and medium enterprises are less involved in (or even completely left out of) the trend towards globalisation, and find complicated policies more difficult to apply. Issues such as organisational management, corporate culture, and social attitudes to change present major barriers

to the practice of sustainable development, not only in the field of logistics but also in the management of the whole business stalled [47][48][49].

The fact shows that GL is not only a scientific or economic concept but also the next stage in the development of enterprise logistics. Since most logistics concepts are very close to reality and dynamic, the ability to access and operate GL will provide a special competitive advantage to transport companies, thereby demonstrating the strategic vision of the business [50][51][52]. In addition to improving the economic and environmental aspects of businesses, GL also has positive effects on both the state and society. The key element of GL is to protect the environment by solving or reducing problems related to road traffic emissions. As reported, the composition and degree of toxicity of exhaust gas emissions caused by vehicles are determined based on the design of the engine, the quality and the composition of the used fuel, the fuel types, and the technical conditions of vehicles [50][53][54][55]. Due to this reason, a large number of advanced technologies relating to the use of additives or alternative fuels [56][57][58][59], the application of hybrid/electric vehicles [60][61][62][63], the improvement of the combustion process of engines [64][65][66][67], and the application of advanced injection technology and post-treatment technology for exhaust gas [68][69][70] have been considered as efficient solutions to reduce pollutant emissions from internal combustion engines-based vehicles that are used for logistics activities. The fact shows that in most businesses, logistics is one of the primary areas considered for improvement with the aim of reducing costs and optimising profits [71]. This term is not new, and is widely used in most business fields and in financial statements. However, in recent years, the concept of GL has gradually emerged to replace existing concepts, in which GL is defined as all efforts and measures undertaken to minimise the negative environmental impacts of logistics activities on the ecosystem. a large body of scientific literature has been published by researchers, indicating that GL has received special attention in recent years, and it has close relevance to the goal of sustainable development [72][73][74][75][76][77][78][79][80][81][82][83]. Fig. 4 illustrates the main targets of GL in practice.

It could be observed from Fig. 4 that there is a strong relationship between GL and sustainable development via activities such as green transportation, green storage, green packaging, green organisation, GL data collection and management, and waste management [85][86][87][88][89]. In a study by Karia and Asaari [90], it was stated that green packaging involves the use of economically sustainable materials, environmental and social responsibility, and processes such as recycling and reuse; green storage involves space optimisation and energy consumption reserves; and green transport involves using green vehicles and fuels, and contributing to sustainable development in areas such as economics, the environment and society. In order to maintain the consistency of economic, environmental and social aspects, planning is necessary in regard to the control, monitoring and evaluation of GL.
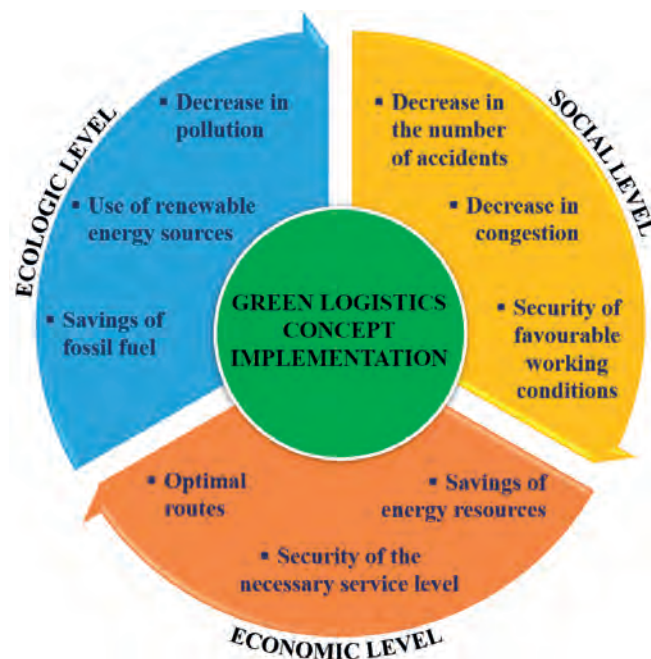
Fig. 4. Primary aims of green logistics in practice [84]

Thanks to advanced management, software and information systems, GL data collection and processing activities have not only been significantly improved, but the use of paper documents has also been minimised, which is a valuable part of the greening of management activities. Despite some differences between definitions, some common terms can be easily recognised [91], such as ‚supply chain environmental management' [92], ‚green purchasing and procurement' [93], ‚green logistics and environmental logistics' [94], and ‚sustainable supply network management' [95].

BENEFITS OF GREEN LOGISTICS

The increasing amounts of emissions from vehicles in the supply chain have attracted the attention of governments around the world. While most industrial firms are only interested in reducing logistics costs rather than being aware of environmental issues, there have been many studies, showing that reducing logistics costs in the right way can also reduce negative impacts on the environment. The concept of GL was born from this finding. The most pressing problems of environmental pollution, such as climate change, are consequences of global warming and the greenhouse effect [96]. Another problem is air pollution, which is mainly caused by CO_2 emitted during transportation by trucks and other types of transport [97]. Therefore, if an efficient distribution centre can be built, the amount of transportation needed will be reduced, leading to reductions in transportation costs and emissions to the environment. In contrast, a lack of systematic and effective organisation will cost businesses in terms of both money and time, and will also affect the living environment. Fig. 5 illustrates the environmental impacts

of logistics operations such as the handling of materials and physical distribution flow management aiming to attain the GL goals.
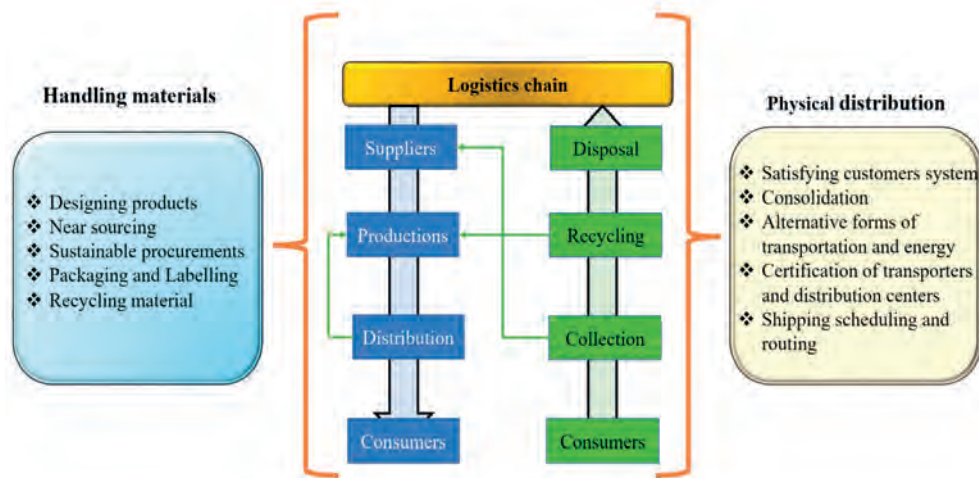
Fig. 5. Ecological impacts of the logistics chain [98]

There are many studies that have highlighted the benefits of GL activities from different perspectives. Khan [21], Richnak et al. [85], Maas et al. [99], Azevedo et al. [100], and Sureeyatanap et al. [86] demonstrated that the implementation of GL activities in the supply and transport chains would significantly improve the economic profitability of enterprises, build customer trust and satisfaction, and improve economic performance, while also making business operations smoother and more efficient, thereby enabling sustainable development. Chu et al. [101] stated in one of their studies that although GL would increase investment and training costs in the beginning, it would optimise costs and energy consumption in the long run in all stages of operation, in accordance with sustainable development criteria. In their research, Nguyen et al. [102][103] suggested the possibility of creating a green seaport as a means of lowering CO_2 emissions while also contributing to the intelligent and more environmentally friendly development of transportation in this area. Other studies have shown that an improvement in the image of an enterprise leads to a special competitive advantage in the market [28][104][105]. a business goal of minimising negative impacts on the environment and society can not only significantly reduce operating costs, but can also ensure the satisfaction of loyal and potential customers [100][105][106]. Tuzün et al. [107] reported that GL could help improve business and commercial activities while increasing the favorability of the organisation's image, which could increase market share, while enabling the company to use resources efficiently and to recycle them. In their pioneering research, Patra [105] and Evangelista [108] showed that there are four main benefits to implementing GL: reducing emissions (especially CO_2 emissions), reducing costs in the long term, reducing noise and other harmful agents to the environment, and diversifying the business and managing

additional directions (reverse logistics). In one study, Zaman [109] evaluated the effects of logistics activities on economies of scale in several European countries. Research has demonstrated that the use of logistics performance indices (LPIs) for timeliness and cargo and logistics tracking systems can significantly increase the energy consumption of operations. While infrastructure improves energy efficiency and reduces CO_2 emissions, service metrics increase CO_2 significantly. Zaman [109] showed that cross-border shipments with LPIs can significantly reduce CO_2 emissions. In contrast, however, the timeliness of logistics increases CO_2 emissions. In this case, the implementation of GL has clearly not been effective. More recently, Nguyen et al. [110] evaluated the growth of smart ports and with their progress in terms of creating a sustainable maritime environment in order to lower CO_2 pollution and use energy in an efficient manner. Based on the above analysis, it could be concluded that minimising the environmental impacts of logistics activities is considered a primary GL activity, and the close monitoring of logistics flows represents the first step in this reduction.

CURRENT TRENDS IN GREEN LOGISTICS

APPLICATION OF BLOCKCHAIN TECHNOLOGY

Nowadays, the use of information technology in logistics is mandatory to avoid being left behind in a fiercely competitive market. Many enterprises have combined their information technology and supply chain management systems. Decentralised applications based on blockchain technology for supply chain management have been shown to increase performance efficiency, reduce waste, and boost customer satisfaction [111]. Sustainable supply chain management based on blockchain technology can become more honed, open, specific, and realistic if end-to-end mass customisation is implemented. Suppliers will become more productive as routine physical operations and product design planning are automated [112]. However, the application of these technologies in GL is still very limited, despite results that prove its effectiveness. Indeed, Tan et al. [113] established a framework that combined blockchain technology with GL. Their model consisted of seven layers: the physical layer, the perception layer, the network layer, the blockchain layer, the management layer, the application layer, and the user layer. Based on this framework, the authors proposed several

specific applications for GL, such as tracing logistics activities and reducing the operating energy, thereby helping businesses maximise their ability to use resources, directly increasing their financial profits, and reducing the impact of operations on the environment.

Saberi et al. [114] argued that blockchain was likely to become an important technology. Thery indicated that four characteristics of the blockchain make it suitable for contributing to a sustainable supply chain: (i) thanks to its superior traceability, the blockchain can help to reduce product recalls and rework; (ii) the blockchain makes it easy for regulators to trace products and calculate the exact amount of carbon tax that each company is required to pay; (iii) it can create incentives to engage in recycling behaviors by providing deposit-based recycling programs; (iv) it can improve operational efficiency by minimising fraud and increasing system integrity. Zhang et al. [115] designed a framework that combined the blockchain with edge computing in a design consisting of five layers: the knowledge layer, the intelligent layer, the application layer, the green supply chain enterprise layer, and the market trend layer. Each layer was separate and required hierarchical permissions, making this design very secure and reliable. Enterprise users could therefore trust green supply chains without concerns regarding security risks, which would enable green supply chain knowledge to be shared among related businesses. Trivellas et al. [116] conducted a study on green supply chains for agro-food products, and pointed out the links between green supply chains, business performance, and the ability to control environmental dynamics. Their research results once again proved that logistics and transportation networks have an extremely strong influence on business performance and sustainable development goals. When blockchain technology is integrated into operational processes, agricultural products are completely under control, and can be tracked and displayed by all licensees from farmers to distribution agents. Moreover, the traceability of blockchain technology means that stakeholders can access data consistently, with high reliability, which directly reduces unnecessary losses of resources such as raw materials, contributing to economic benefits for enterprises [113]. Rane and Thakker [117] researched the applications of blockchain technology to the supply chain in the field of procurement. The performance history of a supplier and their green impacts can be easily traced using the blockchain and IoT networks. Smart contracts and IoT can be reliable indicators for suppliers when they implement green initiatives or have good environmental performance [118]. Another issue related to green procurement is the management of raw materials and output products, and this is also a strength of blockchain technology. As mentioned above, long-term historical data and convenient data extraction can help stakeholders determine the exact origin, quality, and time requirements of a product [119]. With the aim of boosting competitive performance and advancing logistics services, Nguyen [120] also investigated the use of the blockchain in supply chain management, and provided suggestions for long-term growth based on this technology. This type of information can also help in tracking green performance and assessing the recyclability, utilisation and carbon footprint of a product. For products that require particular disposal methods at the end of their life, such as those containing graphite or hazardous materials, information can also be provided to assist stakeholders in taking appropriate action. Saberi et al. [121] highlighted these problems in their study. In general, Fig. 6 illustrates the main problems, which include intra-organisational, inter-organisational, and system-related issues, and external limitations as applying blockchain to green supply chains.
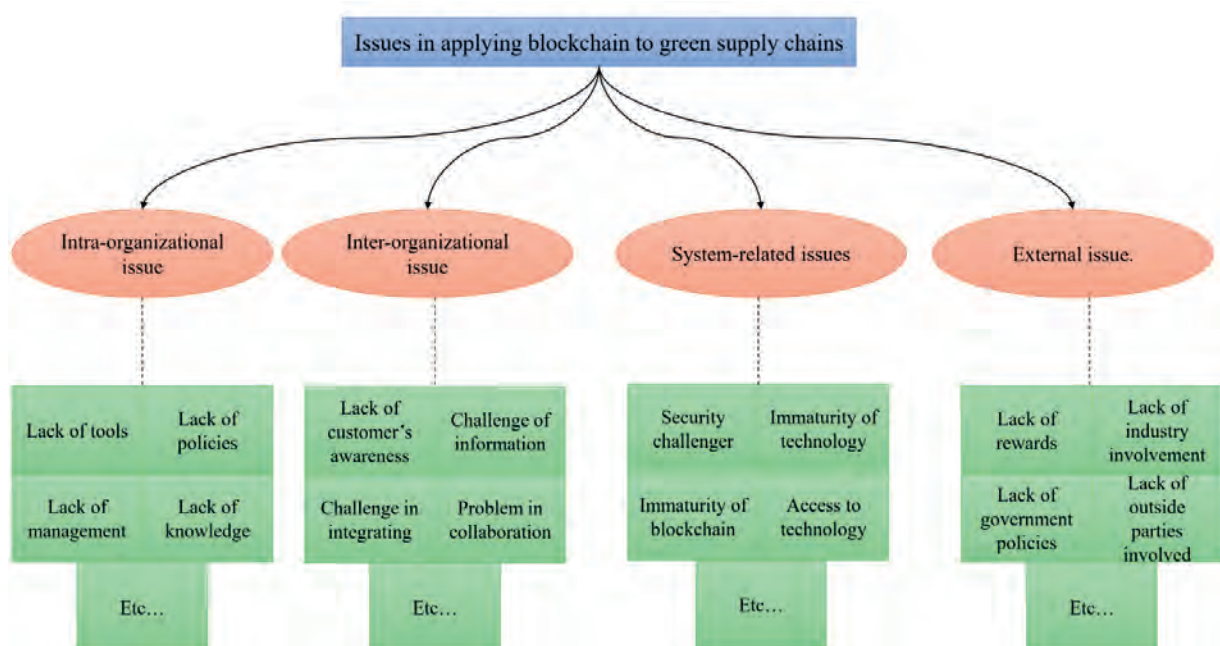

Fig. 6. Obstacles to the widespread application of blockchain technology in green supply chains [121]

USE OF ALTERNATIVE FUELS AND RENEWABLE ENERGY

After the ISO 20400 standard was introduced in 2017, the introduction of green and sustainable supply chains began to be seen as an inevitable trend. Research on green supply chain management and construction is also of particular interest. In 2018, Teixeira et al. [122] described a scenario in which green supply chain and green procurement were applied, and discussed their contributions. The two main conclusions of their research were as follows: (i) in terms of operations and organisation, supply chain and green procurement can increase the level of awareness and competitiveness in the market thanks to improvements from harmonising strategies with the strategic goals of the organisation; (ii) in terms of the environment, supply chain and green procurement can also contribute to a significant reduction in CO_2 emissions through efforts to use environmentally friendly fuel sources, and transport activities can be regulated accordingly. In addition, the use of supply chain and green procurement can help organisations to cut operating costs, improve internal communication technologies, and gradually train personnel to achieve sustainability goals [123].

It was also found that the use of alternative fuels or fuel management could be considered an efficient solution for GL, since these types of fuel could reduce carbon emissions and hence reduce environmental pollution [124][125][126]. As reported in the literature, a large number of alternative fuel types could be used for transportation means aiming to reduce pollutant emissions into the environment, such as hydrogen [127][128][129][130], biogas [131][132], biodiesel [133][134][135], LPG, LNG or CNG [136][137][138], alcohol [139][140], ether [141][142], bio-oil [143][144], and ammonia [145].

Various methods of reducing emissions from transportation means such as hydrogen fuel-cell technologies and phase change materials, have also been presented in the literature [146][147][148]. This technology converts energy directly from a fuel (such as liquid hydrogen) into electricity via an electrochemical process in a fuel cell, and then supplies it to an electric motor [149]. Fuel cells produce electricity directly from liquid hydrogen as input, with water as a by-product, meaning that under normal conditions, a hydrogen fuel cell has no negative impact on the environment and releases only water [150]. For example, in the maritime field, Geertsma et al. [151] carried out a thorough analysis of the current and potential future use of conventional and advanced electrical propulsion systems by commercial vessels. The authors provided an in-depth comparison and analysis to help businesses make the best decision when switching to electric or hybrid powertrain systems for their fleets, with a focus on the configuration, electric power source, and propulsion. a report from the International Maritime Organization (IMO) identified and compared four potential fuels that could be used to replace traditional fuels in the future: biodiesel, LNG, DME (methanol–dimethyl ether), and nuclear power [152][153][154]. Another recent report from the IMO presented a comparative analysis of prospective fuels for use as alternatives to conventional fuels based on several key criteria, including a reduction in CO_2 emissions, a decrease in black carbon emissions, the capacity to reduce NOx emissions, the possibility of reducing SOx emissions, the level of technological maturity, and the time required for widespread adoption [155][156][157][158]. In general, characteristics of using LNG, dimethyl ether, methanol, and nuclear energy for maritime sectors are summarised in Table 1.

Tab. 1: Summary of alternative fuels as an abatement option (NR: not reported)

Abatement measure	↓CO2 %			↓BC %			↓NOx	↓SOx	Technology maturity	Uptake time	Remarks	Ref.
	Low	Mid	High	Low	Mid	High						
Biodiesel – 100%	−5	NR	−11	50	NR	75	No	Yes	Demonstration	<12 months	Fuel availability	[155] [159] [160] [161]
Biodiesel – 20%	−1	NR	−3	10	NR	30	No	Yes	Demonstration	<12 months	Fuel availability	[155] [160] [162] [161]
LNG	15	NR	30	88	NR	99	Yes	Yes	Commercially available	1 to 5 years	Engine/fuel storage retrofit. Port supply of LNG. Fugitive emissions	[155] [163] [164] [165]
Methanol/ DME	NR	−9	NR	NR	97	100	Yes	Yes	Demonstration	5 to 10 years	Fuel storage retrofit and onboard catalysis units required	[155] [166] [167]
Nuclear	NR	NR	95	NR	NR	95	Yes	Yes	Not available	>10 years → Unlikely to be implemented	Design, security, and waste issues. CO2 and BC emissions from fuel production/ disposal	[155]

Besides the alternative fuels mentioned above, renewable energy has also emerged as one option for solving problems related to the demand for reducing greenhouse gas emissions and it is attracting the significant interests of all countries, scientists and policymakers [168][169][170]. Therefore, the use of renewable energy is also found to play an important role in GL and green supply chains aiming to attain net-zero goals [171][172]. Of these types of renewable energy used for maritime sector (ships and ports), the most prominent are wind and solar power [173][174]. In the maritime sector, research in the field of wind power has often focused on the application of wind-driven propulsion systems [175][176]. The use of this particular engine variant has gained in popularity as a viable solution for mitigating carbon emissions in the maritime and logistics industries [177]. Specific conditions, such as ships traveling at slow speeds (less than 16 knots) and ships with small loads (e.g., 3000–10,000 tons), were considered in studies by Smith et al. [178][179], and it was found that wind-assisted propulsion would help ships move more smoothly. One of the few commercially successful products has been the SkySails propulsion system, which consists of a towing kite tied to a rope that propels the ship forward in the direction of the wind. According to its manufacturers, the SkySails system can reduce the fuel consumption of ships by up to 50% under optimal weather conditions, and can yield reductions in annual fuel consumption of between 10% and 15% on average [180]. Besides wind, solar power is one of the most widely researched types of renewable energy for transportation and logistics. Merchant ships using solar power have been proven to have reduced CO_2 emissions [181][173]. In a study by Karatuğ et al. [182], a special type of ship called a RO-RO was also examined in terms of the arrangement of solar arrays during the trip between Pendik, Turkey and Trieste, Italy. a favorable result was obtained, as 0.312 tons of SOx, 3,942 tons of NOx, 232,393 tons of CO_2,

and 0.114 tons of PM were prevented from being emitted into the environment. In addition to these two forms of renewable energy, other types should be mentioned, such as biomass, hydrogen, and geothermal energy that could be used for ports, this could also contribute to the reduction of total greenhouse gases for supply chains [183][184].

DESIGN OF GREEN CLOSED-LOOP SUPPLY CHAIN

Traditional supply chains start with the import of raw materials, pass to production and processing, and end with distribution to customers. When the demand increases significantly but technologies cannot keep up, these traditional supply chains are shown to have many shortcomings, especially with regard to environmental aspects [185]. In addition to the most obvious cause, which is the amount of emissions released by transportation into the environment, a great deal of waste such as plastics and certain difficult-to-treat materials in the supply chain do not yet have effective treatment measures. If a closed supply chain could be designed, reasonable solutions to dealing with the waste created by the production process could be found, which would significantly contribute to improving the environment [186]. Moreover, a closed supply chain can help businesses get input from recycled materials, thereby helping to improve profit margins. According to Govindan et al. [187], a closed supply chain can provide two benefits: firstly, it can ensure that the customer's needs are met, and secondly, the after-use waste products from customers' products can be collected and the most suitable treatment measures can be offered. Fig. 7 illustrates a closed supply chain consisting of a forward supply chain (raw material import, processing, assembling, distribution/retailing, and consuming) and a reverse supply chain (repairing, reconditioning, remanufacturing, recycling, and disposing), operating in parallel.
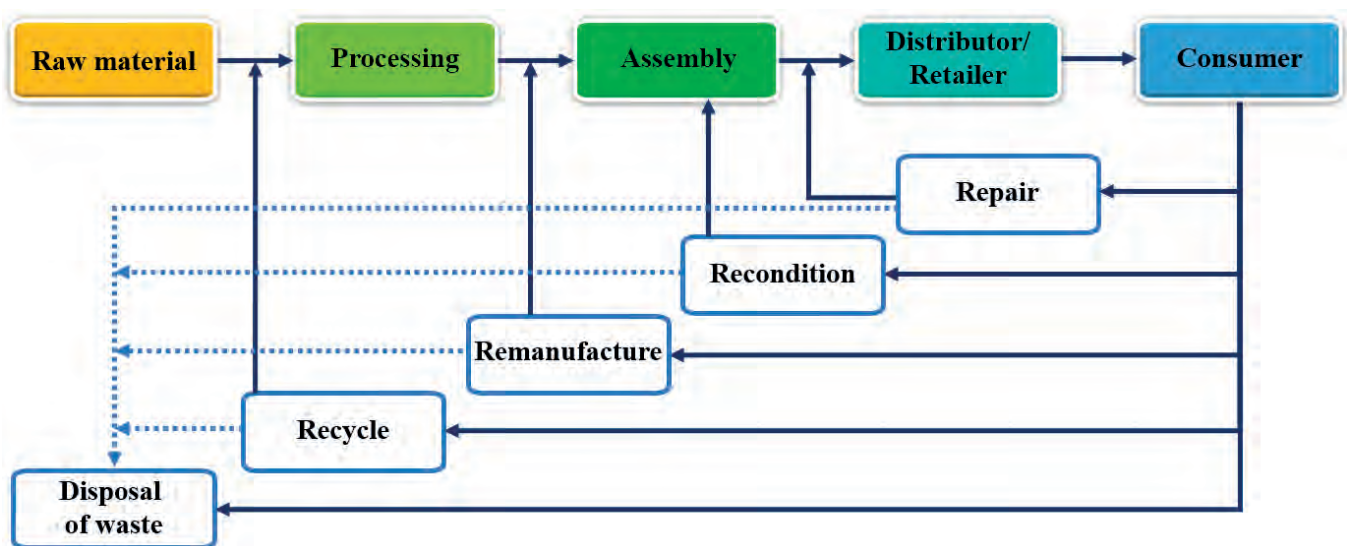

Fig. 7. General illustration of a closed-loop supply chain [188]

Soleimani et al. [189] addressed the research gap by creating a completely closed supply chain. a multi-level, multi-product, and multi-stage closed-loop supply chain was designed in which product ingredients and raw materials could be identified. This model was shown to generate both high profits and customer satisfaction, as it was possible to easily meet the customer's needs while still meeting strict requirements and maintaining responsibility for the environment and society. The results of the study were promising, which can provide a solution with small errors at the appropriate time. The model was tested under six randomized scenarios, and the results for each were presented. Mohtashami et al. [190] studied a green supply chain that included two forward and reverse phases. The model was shown to reduce the negative impact on the environment while reducing the energy consumption of transport fleets by accounting for loading/unloading and production rates, which directly affect lead times and delivery. Some small-scale computations were also discussed based on the NLP model. In addition, on a larger scale, a metaheuristics approach was applied to problem-solving. Zhen et al. [191] researched a green and sustainable closed-loop supply chain network with uncertain needs. This study applied a stochastic bio-objective mixed-integer programming approach to optimise and balance the cost and CO_2 emissions in the closed-loop supply chain network. Experimental results verified the effectiveness and feasibility of the proposed model and method. In the same area of research but with a different approach, Yavari et al. [192] addressed the problem of perishability in products, unexpected events that cause delays in the supply chain, and grid-related problems, and the authors recommended strategies for building a green closed supply chain. Five different strategies were suggested for overcoming disruptions: (i) the use of an intermediate facility; (ii) lateral transshipments; (iii) stockpiling; (iv) capacity storage; and (v) the integration of interdependent networks. The results showed that combining a strategy of integrating interdependent networks with the other strategies mentioned above, especially the first and second, could greatly improve the efficiency of the integrated network. In addition, the product was found to have a longer lifespan and the overall performance of the proposed model was enhanced, which confirmed the ability of the supply chain to respond to disruptions in the power grid using the tactic of integrating of dependent networks.

PERSPECTIVES AND PROSPECTS

In the past, industrialisation and modernisation have created some negative impacts on the environment, and the rapidly increasing trend towards globalisation in most countries has made the situation even worse, especially in terms of greenhouse gas emissions and waste [193][194]. The implementation of green and smart supply chains would optimise the entire operation process, thereby reducing adverse impacts on the environment, moving towards the goal of sustainable development, and balancing the goals of economic development, social stability, and environmental protection. With unexpected effects in both economic and environmental terms, the GL system was oriented to popularise in the supply chain from the perspective of sustainable development. The synthesis and analysis of recognised studies in the GL and supply chain sectors reveal proven and applied implementation methods as well as regulatory principles on sustainability issues that have been built and are gradually being completed [195]. However, a unified and widely accepted principle in the field of GL has yet to be adopted, meaning that the systems, methods, and tools needed to implement this process are still inconsistent. At the present time, the benefits of Industry 4.0 technologies are gradually becoming clear to businesses, with logistics being one of these. a combination of GL and smart logistics on a traditional logistics platform is forecast to be a likely direction; however, several difficulties in this area were identified in a study by Edirisuriya et al. [196]. Table 2 summarises current challenges in regard to combining and transforming traditional logistics, sustainable logistics, and smart logistics.

Tab. 2: Difficulties faced by the logistics business in the shift towards 4.0 technologies [196]

Reference	Training and development	Infrastructure and network services are being built	Adaptability of technology	Standardisation, collaboration, and government oversight
[197]		x	x	x
[198]	x	x	x	x
[199]	x	x	x	x
[200]	x	x	x	x
[201]	x	x	x	x
[202]	x	x	x	
[203]	x	x	x	x
[204]	x	x	x	

The logistics industry is also largely responsible for the problems of environmental degradation, as the main fuel used for these operations is still fossil fuels [205][206]. Regulatory organisations and governments are putting pressure on the logistics industry to implement measures to reduce or even completely replace procurement, storage, packaging, and delivery processes that have adverse effects on the environment [207][208]. The concept of GL was developed in this context and has become increasingly popular, as it refers to the use of environmentally friendly methods in the field of logistics and supply [209]. In order to promote the popularisation of GL systems, a number of studies have proposed and established tactical models as a solution to mitigate negative environmental effects. Pishvaee et al. [210] built a bi-objective credibility-based fuzzy mathematical programming model for GL systems with uncertain initial conditions. This model could help to balance the total cost

of setup with the accompanying environmental factors, thus helping businesses choose the right solutions. The model included the full range of supply chain elements, including CO_2 emissions, material reuse and recycling, waste handling, and energy efficiency. Abduaziz et al. [211] built an integrated model based on systems dynamics and discrete event simulation, which could assist decision-makers in gaining an intuitive view of the environmental impacts as well as the necessary costs.

As mentioned above, research on GL and supply chains has been widely published in recent decades. However, without the determination of managers and governments around the world, it would have taken a long time for the approaches reported in these studies to be put into common use. In addition to dialogue between authorities, residents and entrepreneurs, influencers also need to continuously focus on changing people's perceptions of the environment and society [212]. Governments should continuously emphasise the importance of the environment and society in order to change perceptions, while developing and perfecting mandatory standards for logistics and supply chain activities. Zhang et al. [213] showed that although GL policies were related to many different aspects, they could be divided into two main types: (i) efficient fuel use and emission reductions; and (ii) methods of evaluating and building complete GL policies. Finding alternative energy sources during the operation of the supply chain can not only bring sustainable development to a country but also help to increase the country's energy security, as economic benefits can be gained by exporting energy [214]. Hence, more and more governments are paying special attention to GL, as reflected in policies to promote activities such as taxation or recycling. According to statistics from Liu et al. [215], innovative strategies have helped to reduce the environmental pollution of the logistics industry significantly: for example, the emissions generated by vehicles decreased by 26.9%, and green packaging and green warehouse data systems were updated, meaning that the accuracy of the transferred information increased to 45.97%. By cutting unnecessary costs and improving profit margins, businesses at the forefront of building GL systems could also become leaders in the development of the logistics industry in the future. Zhang et al. [216] reviewed and evaluated policies, public support, laws and regulations, green awareness, green technology innovations, consumer demand, and the quantity and quality of GL talent as the most important factors. Social factors shown through government support were a necessary condition for the general development of the entire logistics industry. However, support for GL facilities was a sufficient condition to develop GL comprehensively. These authors noted that enterprises needed to build and develop smart logistics systems, integrating technologies that do not pollute the environment, and needed to upgrade existing facilities in a goal-friendly direction with the environment. New facilities need to be carefully and scientifically planned based on the current state of the existing facilities, to avoid wasting time, money, material and effort, which was contrary to the existing facilities' original goal. Information technology, and especially information management, needs to be applied in the supply chain to help improve the speed, accuracy, and transparency of information circulating in the system. The ability to easily set up plans or real-time schedules can help stakeholders to be in a state of complete information awareness and to provide the most appropriate and accurate solutions, thereby reducing the cost of logistics activities [217][218]. In addition to barriers related to technology, information technology, policy, and awareness, the geographical location of production facilities and logistics centres is also a barrier that needs to be addressed by local planning regulations, governments, and planners [219][220][221]. When determining the location of logistics facilities, there is a need to consider many factors, such as the geographical locations of site selection points and demand points, economic cost, service efficiency, and consumer satisfaction [222][223].

Despite these barriers, the move towards GL is a significant trend in business. With the goal of sustainable development for industry and society and to create a better public image, businesses are making great efforts to transform. With support from modern technologies in the era of Industry 4.0, logistics and green supply chains are becoming more efficient, and represent a promising solution to the problems facing humanity. Making the world's supply chains more sustainable and reliable could go hand in hand with the common development of the world.

CONCLUSIONS

Environmental issues are a top concern in modern society because of the impact they have on all countries around the world. In particular, logistics and supply chain activities have made this problem worse due to increasing demand for transportation. In order to solve key environmental problems, this article specifically presents the current global green supply chain development trends. The application of blockchain technology allows product traceability, control, and tracking to the end of the life cycle, which is very effective in saving operating energy, materials, raw materials, and the ability to control environmental dynamics. The trend toward using alternative fuels and renewable energy shows high efficiency in reducing harmful emissions to the environment. The green closed-loop supply chain helps to improve efficiency in the recycling and processing of products as well as ensuring the supply of raw materials for the supply chain, which has been highly effective in improving the environment. These trends have significant effects on the development of green supply chains, contributing to the sustainability of the supply chain and the environment. In addition, this work also indicates the difficulties that businesses and governments face in implementing work towards green supply chains and logistics, such as limited technology and renewable energy policies in many countries or inadequacies in logistics center connection planning, suggesting that policy studies that are tailored to the unique characteristics and circumstances of each country and region should be critically conducted.

Last but not least, the close and strategic combinations of green technology and policy are found to play an important role in applying and expanding logistics activities in green supply chains. In the future, combining models between public policies and advanced technology, as well as assessing the risks of applying advanced technologies to green supply chains should be considered as potential studies.

REFERENCES

1. H. L. Lee and C. S. Tang, "Socially and Environmentally Responsible Value Chain Innovations: New Operations Management Research Opportunities," Manage. Sci., vol. 64, no. 3, pp. 983–996, Mar. 2018, doi: 10.1287/mnsc.2016.2682.

2. T. T. Le et al., "Management strategy for seaports aspiring to green logistical goals of IMO: Technology and policy solutions," Polish Marit. Res., vol. 30, no. 2, pp. 165–187, 2023, doi: 10.2478/pomr-2023-0031.

3. C. R. Carter and M. M. Jennings, "Logistics Social Responsibility: An Integrative Framework," J. Bus. Logist., vol. 23, no. 1, pp. 145–180, Mar. 2002, doi: 10.1002/j.2158-1592.2002.tb00020.x.

4. S. Vachon and R. D. Klassen, "Environmental management and manufacturing performance: The role of collaboration in the supply chain," Int. J. Prod. Econ., vol. 111, no. 2, pp. 299–315, Feb. 2008, doi: 10.1016/j.ijpe.2006.11.030.

5. B. Beloff, M. Lines, and D. Tanzil, Transforming Sustainability Strategy into Action: The Chemical Industry. John Wiley & Sons, 2005.

6. Q. Zhu, J. Sarkis, and K. Lai, "Confirmation of a measurement model for green supply chain management practices implementation," Int. J. Prod. Econ., vol. 111, no. 2, pp. 261–273, Feb. 2008, doi: 10.1016/j.ijpe.2006.11.029.

7. S. Saberi, M. Kouhizadeh, J. Sarkis, and L. Shen, "Blockchain technology and its relationships to sustainable supply chain management," Int. J. Prod. Res., vol. 57, no. 7, pp. 2117–2135, Apr. 2019, doi: 10.1080/00207543.2018.1533261.

8. P. Ceniga and V. Sukalova, "Future of Logistics Management in the Process of Globalization," Procedia Econ. Financ., vol. 26, pp. 160–166, 2015, doi: 10.1016/S2212-5671(15)00908-9.

9. Y. Lai, H. Sun, and J. Ren, "Understanding the determinants of big data analytics (BDA) adoption in logistics and supply chain management," Int. J. Logist. Manag., vol. 29, no. 2, pp. 676–703, May 2018, doi: 10.1108/IJLM-06-2017-0153.

10. IEA, "CO_2 Emissions from Fuel Combustion Highlights." International Energy Agency, Paris, France, 2018.

11. J. Manners-Bell and K. Lyon, "The Future of Logistics: What Does the Future Hold for Freight Forwarders?" Kewill, London, UK, pp. 1–16, 2015.

12. IEA, "The Future of Trucks: Implications for energy and the environment." International Energy Agency, Paris, France, pp. 1–164, 2017.

13. V. G. Nguyen et al., "An extensive investigation on leveraging machine learning techniques for high-precision predictive modeling of CO 2 emission," Energy Sources, Part a Recover. Util. Environ. Eff., vol. 45, no. 3, pp. 9149–9177, Aug. 2023, doi: 10.1080/15567036.2023.2231898.

14. A. McKinnon, "Green Logistics: The Carbon Agenda," LogForum, vol. 6, no. 3, pp. 1–9, 2010.

15. V. V. Le et al., "A remarkable review of the effect of lockdowns during COVID-19 pandemic on global PM emissions," Energy Sources, Part a Recover. Util. Environ. Eff., pp. 1–16, Dec. 2020, doi: 10.1080/15567036.2020.1853854.

16. X. P. Nguyen, A. T. Hoang, A. I. Ölçer, and T. T. Huynh, "Record decline in global CO 2 emissions prompted by COVID-19 pandemic and its implications on future climate change policies," Energy Sources, Part a Recover. Util. Environ. Eff., pp. 1–4, Jan. 2021, doi: 10.1080/15567036.2021.1879969.

17. H. Zhang et al., "Global association between satellite-derived nitrogen dioxide (NO2) and lockdown policies under the COVID-19 pandemic," Sci. Total Environ., vol. 761, p. 144148, Mar. 2021, doi: 10.1016/j.scitotenv.2020.144148.

18. IEA, "Energy Technology Perspectives 2020," Paris, 2020. doi: 10.1787/ab43a9a5-en.

19. S. A. R. Khan, D. I. Godil, C. J. C. Jabbour, S. Shujaat, A. Razzaq, and Z. Yu, "Green data analytics, blockchain technology for sustainable development, and sustainable supply chain practices: evidence from small and medium enterprises," Ann. Oper. Res., Oct. 2021, doi: 10.1007/s10479-021-04275-x.

20. J. Elliott, An introduction to sustainable development. Routledge, 2012.

21. S. A. R. Khan, "The Effect of Green logistics on Economic growth, Social and Environmental sustainability: An Empirical study of Developing countries in Asia," Preprints, pp. 1–23, 2019, doi: 10.20944/preprints201901.0104.v1.

22. I. Ibrahim, V. P. K. Sundram, E. N. Omar, N. Yusoff, and A. Amer, "The determinant factors of green practices adoption for logistics companies in Malaysia. a case study of PKT logistics group Sdn. Bhd.," J. Emerg. Econ. Islam. Res., vol. 7, no. 1, pp. 1–10, 2019.

23. P. Centobelli, R. Cerchione, and E. Esposito, "Environmental sustainability in the service industry of transportation and logistics service providers: Systematic literature review and research directions," Transp. Res. Part D Transp. Environ., vol. 53, pp. 454–470, Jun. 2017, doi: 10.1016/j.trd.2017.04.032.

24. C. Bratt, R. Sroufe, and G. Broman, "Implementing Strategic Sustainable Supply Chain Management," Sustainability, vol. 13, no. 15, p. 8132, Jul. 2021, doi: 10.3390/su13158132.

25. A. M. Aldakhil, A. A. Nassani, U. Awan, M. M. Q. Abro, and K. Zaman, "Determinants of green logistics in BRICS countries: An integrated supply chain model for green business," J. Clean. Prod., vol. 195, pp. 861–868, Sep. 2018, doi: 10.1016/j.jclepro.2018.05.248.

26. Hoang Phuong Nguyen and Van Tai Pham, "Toward The Green Logistics By Developing Sustainable Transportation: a Case Study From Vietnam," GIS Bus., vol. 15, no. 1, pp. 127–141, Jan. 2020, doi: 10.26643/gis.v15i1.17959.

27. Z. Yu, H. Golpîra, and S. A. R. Khan, "The relationship between green supply chain performance, energy demand, economic growth and environmental sustainability: An empirical evidence from developed countries," Logforum, vol. 14, no. 4, pp. 479–494, Dec. 2018, doi: 10.17270/J.LOG.2018.304.

28. A. S. Karaman, M. Kilic, and A. Uyar, "Green logistics performance and sustainability reporting practices of the logistics sector: The moderating effect of corporate governance," J. Clean. Prod., vol. 258, p. 120718, Jun. 2020, doi: 10.1016/j.jclepro.2020.120718.

29. O. Seroka-Stolka, and A. Ociepa-Kubicka, "Green logistics and circular economy," Transp. Res. Procedia, vol. 39, pp. 471–479, 2019, doi: 10.1016/j.trpro.2019.06.049.

30. Z. Yu, H. Golpîra, and S. A. R. Khan, "THE RELATIONSHIP BETWEEN GREEN SUPPLY CHAIN PERFORMANCE, ENERGY DEMAND, ECONOMIC GROWTH AND ENVIRONMENTAL SUSTAINABILITY: AN EMPIRICAL EVIDENCE FROM DEVELOPED COUNTRIES," Logforum, vol. 14, no. 4, pp. 479–494, Dec. 2018, doi: 10.17270/J.LOG.2018.304.

31. F. Kamakaté and L. Schipper, "Trends in truck freight energy use and carbon emissions in selected OECD countries from 1973 to 2005," Energy Policy, vol. 37, no. 10, pp. 3743–3751, Oct. 2009, doi: 10.1016/j.enpol.2009.07.029.

32. M. I. Piecyk and A. C. McKinnon, "Forecasting the carbon footprint of road freight transport in 2020," Int. J. Prod. Econ., vol. 128, no. 1, pp. 31–42, Nov. 2010, doi: 10.1016/j.ijpe.2009.08.027.

33. B. Fahimnia, J. Sarkis, and A. Eshragh, "A tradeoff model for green supply chain planning:A leanness-versus-greenness analysis," Omega, vol. 54, pp. 173–190, Jul. 2015, doi: 10.1016/j.omega.2015.01.014.

34. G. P. Kiesmüller, A. G. de Kok, and J. C. Fransoo, "Transportation mode selection with positive manufacturing lead time," Transp. Res. Part E Logist. Transp. Rev., vol. 41, no. 6, pp. 511–530, Nov. 2005, doi: 10.1016/j.tre.2005.07.003.

35. ITF, "Reducing Transport Greenhouse Gas Emissions: Trends and Data 2010." International Transport Forum, Leipzig, Germany, pp. 1–94, 2010.

36. A. Rakhmangulov, A. Sladkowski, N. Osintsev, and D. Muravev, "Green Logistics: Element of the Sustainable Development Concept. Part 1," Naše more, vol. 64, no. 3, pp. 120–126, Nov. 2017, doi: 10.17818/NM/2017/3.7.

37. P. Bajdor, I. Pawełoszek, and H. Fidlerova, "Analysis and Assessment of Sustainable Entrepreneurship Practices in Polish Small and Medium Enterprises," Sustainability, vol. 13, no. 7, p. 3595, Mar. 2021, doi: 10.3390/su13073595.

38. D. D., G. R., A. Hariharasudan, I. Otola, and Y. Bilan, "Reactive Power Optimization and Price Management in Microgrid Enabled with Blockchain," Energies, vol. 13, no. 23, p. 6179, Nov. 2020, doi: 10.3390/en13236179.

39. A. Gaur and D. A. Vazquez-Brust, "Sustainable Development Goals: Corporate Social Responsibility? a Critical Analysis of Interactions in the Construction Industry Supply Chains Using Externalities Theory," in Sustainable Development Goals and Sustainable Supply Chains in the Post-global Economy, Greening o., Yakovleva, N., R. Frei, and S. Rama Murthy, Eds. Springer, Cham, 2019, pp. 133–157.

40. M. Krynke, "Application of linear programming in supply chain management in the foundry," in Proceedings 29th International Conference on Metallurgy and Materials, 2020, pp. 1280–1286, doi: 10.37904/metal.2020.3648.

41. J. Grabara, "Sustainable Development - Never Fulfilled Dream," Qual. - Access to Success, vol. 20, pp. 565–570, 2019.

42. J. Grabara, M. Dabylova, and G. Alibekova, "Impact Of Legal Standards On Logistics Management In The Context Of Sustainable Development," Acta Logist., vol. 7, no. 1, pp. 31–37, Mar. 2020, doi: 10.22306/al.v7i1.155.

43. A. Mesjasz-Lech and P. Michelberger, "Sustainable Waste Logistics and the Development of Trade in Recyclable Raw Materials in Poland and Hungary," Sustainability, vol. 11, no. 15, p. 4159, Aug. 2019, doi: 10.3390/su11154159.

44. S. Lazar, D. Klimecka-Tatar, and M. Obrecht, "Sustainability Orientation and Focus in Logistics and Supply Chains," Sustainability, vol. 13, no. 6, p. 3280, Mar. 2021, doi: 10.3390/su13063280.

45. M. Drljača, S. Petar, M. Raad, and I. Štimac, "The role and position of Airport City in the Supply Chain," Prod. Eng. Arch., vol. 26, no. 3, pp. 104–109, Sep. 2020, doi: 10.30657/pea.2020.26.21.

46. H. P. Nguyen and V. D. Bui, "Sustainable development of Vietnam's transportation from analysis of car freight management," Int. J. Knowledge-Based Dev., vol. 12, no. 2, pp. 77–96, 2021, doi: 10.1504/IJKBD.2021.121707.

47. D. Klimecka-Tatar and M. Niciejewska, "Small-sized enterprises management in the aspect of organizational culture," Rev. Gestão Tecnol., vol. 21, no. 1, pp. 4–24, Mar. 2021, doi: 10.20397/2177-6652/2021.v21i1.2023.

48. M. Suchacka, "Corporate Digital Responsibility - a New Dimension of the Human - Technology Relations," Syst. Saf. Hum. - Tech. Facil. - Environ., vol. 2, no. 1, pp. 1–8, Mar. 2020, doi: 10.2478/czoto-2020-0001.

49. K. Teplická and S. Hurná, "New Approach of Costs of Quality According their Trend of During Long Period in Industrial Enterprises in SMEs," Manag. Syst. Prod. Eng., vol. 29, no. 1, pp. 20–26, Mar. 2021, doi: 10.2478/mspe-2021-0003.

50. M. Ingaldi and D. Klimecka-Tatar, "People's Attitude to Energy from Hydrogen—From the Point of View of Modern Energy Technologies and Social Responsibility," Energies, vol. 13, no. 24, p. 6495, Dec. 2020, doi: 10.3390/en13246495.

51. A. Jazairy, R. von Haartman, and M. Björklund, "Unravelling collaboration mechanisms for green logistics: the perspectives of shippers and logistics service providers," Int. J. Phys. Distrib. Logist. Manag., vol. 51, no. 4, pp. 423–448, May 2021, doi: 10.1108/IJPDLM-09-2019-0274.

52. J. Karcz and B. Ślusarczyk, "Criteria of quality requirements deciding on choice of the logistic operator from a perspective of his customer and the end recipient of goods," Prod. Eng. Arch., vol. 27, no. 1, pp. 58–68, Mar. 2021, doi: 10.30657/pea.2021.27.8.

53. G. Kovács, "Combination of Lean value-oriented conception and facility layout design for even more significant efficiency improvement and cost reduction," Int. J. Prod. Res., vol. 58, no. 10, pp. 2916–2936, May 2020, doi: 10.1080/00207543.2020.1712490.

54. P. Szymanski, M. Zolnieruk, P. Oleszczyk, I. Gisterek, and T. Kajdanowicz, "Spatio-Temporal Profiling of Public Transport Delays Based on Large-Scale Vehicle Positioning Data From GPS in Wrocław," IEEE Trans. Intell. Transp. Syst., vol. 19, no. 11, pp. 3652–3661, Nov. 2018, doi: 10.1109/TITS.2018.2852845.

55. M. Tutak, J. Brodny, D. Siwiec, R. Ulewicz, and P. Bindzár, "Studying the Level of Sustainable Energy Development of the European Union Countries and Their Similarity Based on the Economic and Demographic Potential," Energies, vol. 13, no. 24, p. 6643, Dec. 2020, doi: 10.3390/en13246643.

56. A. A. Yusuf et al., "Investigating the influence of plastic waste oils and acetone blends on diesel engine combustion, pollutants, morphological and size particles: Dehalogenation and catalytic pyrolysis of plastic waste," Energy Convers. Manag., vol. 291, p. 117312, Sep. 2023, doi: 10.1016/j.enconman.2023.117312.

57. A. Sule, Z. A. Latiff, M. A. Abbas, I. Veza, and A. C. Opia, "Recent Advances in Diesel-Biodiesel Blended with Nano-Additive as Fuel in Diesel Engines: a Detailed Review," Automot. Exp., vol. 5, no. 2, pp. 182–216, Apr. 2022, doi: 10.31603/ae.6352.

58. L. M.I., R. C.G., T. J., and R. J.D., "Numerical Analysis of Emissions from Marine Engines Using Alternative Fuels," Polish Marit. Res., vol. 22, no. 4, pp. 48–52, Dec. 2015, doi: 10.1515/pomr-2015-0070.

59. A. Tuan Hoang et al., "Understanding behaviors of compression ignition engine running on metal nanoparticle additives-included fuels: a control comparison between biodiesel and diesel fuel," Fuel, vol. 326, p. 124981, Oct. 2022, doi: 10.1016/j.fuel.2022.124981.

60. G. Zhao, X. Wang, M. Negnevitsky, and H. Zhang, "A review of air-cooling battery thermal management systems for electric and hybrid electric vehicles," J. Power Sources, vol. 501, p. 230001, Jul. 2021, doi: 10.1016/j.jpowsour.2021.230001.

61. M. Ehsani, K. V. Singh, H. O. Bansal, and R. T. Mehrjardi, "State of the Art and Trends in Electric and Hybrid Electric Vehicles," Proc. IEEE, vol. 109, no. 6, pp. 967–984, Jun. 2021, doi: 10.1109/JPROC.2021.3072788.

62. P. Gełesz, A. Karczewski, J. Kozak, W. Litwin, and Ł. Piątek, "Design Methodology for Small Passenger Ships On the Example of the Ferryboat Motława 2 Driven by Hybrid Propulsion System," Polish Marit. Res., vol. 24, no. s1, pp. 67–73, Apr. 2017, doi: 10.1515/pomr-2017-0023.

63. P. Geng, X. Xu, and T. Tarasiuk, "State of Charge Estimation Method for Lithium-Ion Batteries in All-Electric Ships Based on LSTM Neural Network," Polish Marit. Res., vol. 27, no. 3, pp. 100–108, Sep. 2020, doi: 10.2478/pomr-2020-0051.

64. R. Mahmoodi, M. Yari, J. Ghafouri, and K. Poorghasemi, "Effect of reformed biogas as a low reactivity fuel on performance and emissions of a RCCI engine with reformed biogas/diesel dual-fuel combustion," Int. J. Hydrogen Energy, vol. 46, no. 30, pp. 16494–16512, 2021, doi: 10.1016/j.ijhydene.2020.09.183.

65. D. Dobslaw, K. H. Engesser, H. Störk, and T. Gerl, "Low-cost process for emission abatement of biogas internal combustion engines," J. Clean. Prod., vol. 227, no. 2, pp. 1079–1092, 2019, doi: 10.1016/j.jclepro.2019.04.258.

66. S. Serbin, B. Diasamidze, V. Gorbov, and J. Kowalski, "Investigations of the Emission Characteristics of a Dual-Fuel Gas Turbine Combustion Chamber Operating Simultaneously on Liquid and Gaseous Fuels," Polish Marit. Res., vol. 28, no. 2, pp. 85–95, Jun. 2021, doi: 10.2478/pomr-2021-0025.

67. D. Cuper-Przybylska, V. N. Nguyen, C. D. Nam, and J. Kowalski, "High Quality Multi-Zone and 3D CFD Model of Combustion in Marine Diesel Engine Cylinder," Polish Marit. Res., vol. 30, no. 2, pp. 61–67, Jun. 2023, doi: 10.2478/pomr-2023-0021.

68. T. C. Zannis et al., "Marine Exhaust Gas Treatment Systems for Compliance with the IMO 2020 Global Sulfur Cap and Tier III NOx Limits: a Review," Energies, vol. 15, no. 10, p. 3638, May 2022, doi: 10.3390/en15103638.

69. A. T. Hoang, "Waste heat recovery from diesel engines based on Organic Rankine Cycle," Appl. Energy, vol. 231, pp. 138–166, Dec. 2018, doi: 10.1016/j.apenergy.2018.09.022.

70. S. V. Khandal, N. R. Banapurmath, V. N. Gaitonde, and S. S. Hiremath, "Paradigm shift from mechanical direct injection diesel engines to advanced injection strategies of diesel homogeneous charge compression ignition (HCCI) engines- a comprehensive review," Renew. Sustain. Energy Rev., vol. 70, pp. 369–384, Apr. 2017, doi: 10.1016/j.rser.2016.11.058.

71. P. Bajdor, "Comparison between sustainable development concept and green logistics – The Literature Review COMPARISON BETWEEN SUSTAINABLE DEVELOPMENT CONCEPT AND GREEN LOGISTICS – THE LITERATURE," no. January 2012, 2017.

72. A. Mckinnon, S. Cullinane, M. Browne, and A. Whiteing, Green Logistics: Improving the Environmental Sustainability of Logistics. 2012.

73. A. Kutkaitis and E. Župerkienė, "Darnaus vystymosi koncepcijos raiška uosto logistinėse organizacijose," Vadyb. Moksl. ir Stud. verslų ir jų infrastruktūros plėtrai, vol. 2, no. 26, pp. 130–137, 2011.

74. A. McKinnon and A. Kreie, "Adaptive Logistics: Preparing Logistical Systems for Climate Change," in Proceedings of the 15th Annual Logistics Research Network Conference: Volatile and Fragile Supply Chains, 2010, pp. 1–8.

75. S. Emmett and V. Sood, Green Supply Chains: An Action Manifesto. John Wiley & Sons, Inc., 2010.

76. A. Palmer and M. Piecyk, "Time, cost and CO_2 effects of rescheduling freight deliveries," in Towards the Sustainable Supply Chain: Balancing the Needs of Business. Economy and the Environment 8th–10th September, 2010, pp. 1–8.

77. Y. Guochuan, "Constraints and counter measures of China's Green Logistics Development," J. Bus. Econ., vol. 2, pp. 18–23, 2010.

78. A. Sbihi and R. W. Eglese, "Combinatorial optimization and Green Logistics," Ann. Oper. Res., vol. 175, no. 1, pp. 159–175, Mar. 2010, doi: 10.1007/s10479-009-0651-z.

79. T. Cherrett, F. McLeod, S. Maynard, A. Hickford, J. Allen, and M. Browne, "Understanding retail supply chains to enable 'greener' logistics," in 14th Annual Logistics Research Network Conference, 2009, pp. 80–87.

80. D. Bagdonienė, A. Galbuogienė, and E. Paulavičienė, "Darnios organizacijos koncepcijos formavimas visuotinės kokybės vadybos pagrindu," Ekon. ir Vadyb., vol. 14, pp. 1044–1053, 2009.

81. M. Monnet, "The Intermediary Conditions of Logistics Service Providers in the Context of Sustainable Development," Supply Chain Forum An Int. J., vol. 9, no. 2, pp. 78–87, Jan. 2008, doi: 10.1080/16258312.2008.11517201.

82. S. K. Srivastava, "Green supply-chain management: a state-of-the-art literature review," Int. J. Manag. Rev., vol. 9, no. 1, pp. 53–80, Mar. 2007, doi: 10.1111/j.1468-2370.2007.00202.x.

83. J.-P. Rodrigue, B. Slack, and C. Comtois, "Green Logistics," in Handbook of Logistics And Supply-Chain Management, London: Pergamon/Elsevier, 2001.

84. A. V. Vasiliauskas, V. Zinkevičiūtė, and E. Šimonytė, "Implementation of the Concept of Green Logistics Reffering to it Applications for Road Freight Transport Enterprises," Verslas Teor. ir Prakt., vol. 14, no. 1, pp. 43–50, Mar. 2013, doi: 10.3846/btp.2013.05.

85. P. Richnák and K. Gubová, "Green and Reverse Logistics in Conditions of Sustainable Development in Enterprises in Slovakia," Sustainability, vol. 13, no. 2, p. 581, Jan. 2021, doi: 10.3390/su13020581.

86. P. Sureeyatanapas, P. Poophiukhok, and S. Pathumnakul, "Green initiatives for logistics service providers: An investigation of antecedent factors and the contributions to corporate goals," J. Clean. Prod., vol. 191, pp. 1–14, Aug. 2018, doi: 10.1016/j.jclepro.2018.04.206.

87. A. Rakhmangulov, A. Sladkowski, N. Osintsev, and D. Muravev, "Green Logistics: a System of Methods and Instruments—Part 2," Naše more, vol. 65, no. 1, pp. 49–55, May 2018, doi: 10.17818/NM/2018/1.7.

88. A. Kumar, "Green Logistics for sustainable development: an analytical review," IOSRD Int. J. Bus., vol. 1, no. 1, pp. 7–13, 2015.

89. P. Trivellas, G. Malindretos, and P. Reklitis, "Implications of Green Logistics Management on Sustainable Business and Supply Chain Performance: Evidence from a Survey in the Greek Agri-Food Sector," Sustainability, vol. 12, no. 24, p. 10515, Dec. 2020, doi: 10.3390/su122410515.

90. N. Karia and M. Asaari, "Transforming green logistics practice into benefits: a case of third-party logistics (3PLs)," in Proceedings of the 2016 International Conference on Industrial Engineering and Operations Management, 2016, pp. 1–6.

91. J. Sarkis, Q. Zhu, and K. Lai, "An organizational theoretic review of green supply chain management literature," Int. J. Prod. Econ., vol. 130, no. 1, pp. 1–15, Mar. 2011, doi: 10.1016/j.ijpe.2010.11.010.

92. M. P. Sharfman, T. M. Shaft, and R. P. Anex, "The road to cooperative supply-chain environmental management: trust and uncertainty among pro-active firms," Bus. Strateg. Environ., vol. 18, no. 1, pp. 1–13, Jan. 2009, doi: 10.1002/bse.580.

93. H. Min and W. P. Galle, "Green Purchasing Strategies: Trends and Implications," Int. J. Purch. Mater. Manag., vol. 33, no. 2, pp. 10–17, Jun. 1997, doi: 10.1111/j.1745-493X.1997.tb00026.x.

94. P. R. Murphy and R. F. Poist, "Green logistics strategies: an analysis of usage patterns," Transp. J., vol. 40, no. 2, pp. 5–16, 2000.

95. A. Young, "Sustainable Supply Network Management," Corp. Environ. Strateg., vol. 8, no. 3, pp. 260–268, Sep. 2001, doi: 10.1016/S1066-7938(01)00122-1.

96. P. R. Murphy and R. F. Poist, "Green perspectives and practices: a 'comparative logistics' study," Supply Chain Manag. An Int. J., vol. 8, no. 2, pp. 122–131, May 2003, doi: 10.1108/13598540310468724.

97. H. Bakır et al., "Forecasting of future greenhouse gas emission trajectory for India using energy and economic indexes with various metaheuristic algorithms," J. Clean. Prod., vol. 360, p. 131946, Aug. 2022, doi: 10.1016/j.jclepro.2022.131946.

98. J.-P. Rodrigue, The Geography of Transport Systems. Fifth edition. | Abingdon, Oxon ; New York, NY : Routledge, 2020.: Routledge, 2020.

99. S. Maas, T. Schuster, and E. Hartmann, "Stakeholder Pressures, Environmental Practice Adoption and Economic Performance in the German Third-party Logistics Industry—A Contingency Perspective," J. Bus. Econ., vol. 88, no. 2, pp. 167–201, Feb. 2018, doi: 10.1007/s11573-017-0872-6.

100. S. G. Azevedo, H. Carvalho, and V. Cruz Machado, "The influence of green practices on supply chain performance: a case study approach," Transp. Res. Part E Logist. Transp. Rev., vol. 47, no. 6, pp. 850–871, Nov. 2011, doi: 10.1016/j.tre.2011.05.017.

101. Z. Chu, L. Wang, and F. Lai, "Customer pressure and green innovations at third party logistics providers in China," Int. J. Logist. Manag., vol. 30, no. 1, pp. 57–75, Feb. 2019, doi: 10.1108/IJLM-11-2017-0294.

102. H. P. Nguyen, P. Q. P. Nguyen, and T. P. Nguyen, "Green Port Strategies in Developed Coastal Countries as Useful Lessons for the Path of Sustainable Development: a case study in Vietnam," Int. J. Renew. Energy Dev., vol. 11, no. 4, pp. 950–962, Nov. 2022, doi: 10.14710/ijred.2022.46539.

103. H. P. Nguyen, P. Q. P. Nguyen, D. K. P. Nguyen, V. D. Bui, and D. T. Nguyen, "Application of IoT Technologies in Seaport Management," JOIV Int. J. Informatics Vis., vol. 7, no. 1, p. 228, Mar. 2023, doi: 10.30630/joiv.7.1.1697.

104. R. Raut, M. Kharat, S. Kamble, and C. S. Kumar, "Sustainable evaluation and selection of potential third-party logistics (3PL) providers," Benchmarking An Int. J., vol. 25, no. 1, pp. 76–97, Feb. 2018, doi: 10.1108/BIJ-05-2016-0065.

105. P. K. Patra, "Green logistics: Eco-friendly measure in supply-chain," Manag. Insight, vol. 14, no. 1, pp. 65–71, 2018.

106. X. Wang, "Study on relationship between green logistics activity and logistics performance," Cluster Comput., vol. 22, no. S3, pp. 6579–6588, May 2019, doi: 10.1007/s10586-018-2344-3.

107. S. TÜZÜN RAD and Y. S. GÜLMEZ, "Green Logistics For Sustainability," Int. J. Manag. Econ. Bus., vol. 13, no. 3, pp. 0–0, Sep. 2017, doi: 10.17130/ijmeb.2017331327.

108. P. Evangelista, "Environmental sustainability practices in the transport and logistics service industry: An exploratory case study investigation," Res. Transp. Bus. Manag., vol. 12, pp. 63–72, Oct. 2014, doi: 10.1016/j.rtbm.2014.10.002.

109. K. Zaman and S. Shamsuddin, "Green logistics and national scale economic indicators: Evidence from a panel of selected European countries," J. Clean. Prod., vol. 143, pp. 51–63, Feb. 2017, doi: 10.1016/j.jclepro.2016.12.150.

110. H. P. Nguyen, N. D. K. Pham, and V. D. Bui, "Technical-Environmental Assessment of Energy Management Systems in Smart Ports," Int. J. Renew. Energy Dev., vol. 11, no. 4, pp. 889–901, Nov. 2022, doi: 10.14710/ijred.2022.46300.

111. H.-C. Pfohl, B. Yahsi, and T. Kurnaz, "The impact of Industry 4.0 on the supply chain," in Innovations and Strategies for Logistics and Supply Chains: Technologies, Business Models and Risk Management. Proceedings of the Hamburg International Conference of Logistics (HICL), Vol. 20, 2015, pp. 31–58.

112. G. Sowmya and A. Polisetty, "Smart practices in green supply chain management using blockchain technology," in Green Blockchain Technology for Sustainable Smart Cities, Elsevier, 2023, pp. 217–235.

113. B. Q. Tan, F. Wang, J. Liu, K. Kang, and F. Costa, "A Blockchain-Based Framework for Green Logistics in Supply Chains," Sustainability, vol. 12, no. 11, p. 4656, Jun. 2020, doi: 10.3390/su12114656.

114. B. Esmaeilian, J. Sarkis, K. Lewis, and S. Behdad, "Blockchain for the future of sustainable supply chain management in Industry 4.0," Resour. Conserv. Recycl., vol. 163, p. 105064, Dec. 2020, doi: 10.1016/j.resconrec.2020.105064.

115. H. Zhang, S. Li, W. Yan, Z. Jiang, and W. Wei, "A Knowledge Sharing Framework for Green Supply Chain Management Based on Blockchain and Edge Computing," 2019, pp. 413–420.

116. D. Prashar, N. Jha, S. Jha, Y. Lee, and G. P. Joshi, "Blockchain-Based Traceability and Visibility for Agricultural Products: a Decentralized Way of Ensuring Food Safety in India," Sustainability, vol. 12, no. 8, p. 3497, Apr. 2020, doi: 10.3390/su12083497.

117. S. B. Rane and S. V. Thakker, "Green procurement process model based on blockchain–IoT integrated architecture for a sustainable business," Manag. Environ. Qual. An Int. J., vol. 31, no. 3, pp. 741–763, Dec. 2019, doi: 10.1108/MEQ-06-2019-0136.

118. A. Awasthi, S. S. Chauhan, and S. K. Goyal, "A fuzzy multicriteria approach for evaluating environmental performance of suppliers," Int. J. Prod. Econ., vol. 126, no. 2, pp. 370–378, Aug. 2010, doi: 10.1016/j.ijpe.2010.04.029.

119. B. Aquilani, C. Silvestri, A. Ruggieri, and C. Gatti, "A systematic literature review on total quality management critical success factors and the identification of new avenues of research," TQM J., vol. 29, no. 1, pp. 184–213, Jan. 2017, doi: 10.1108/TQM-01-2016-0003.

120. H. P. Nguyen, "Blockchain-an indispensable development trend of logistics industry in Vietnam: Current situation and recommended solutions," Int. J. e-Navigation Marit. Econ., vol. 13, pp. 14–22, 2019.

121. S. Saberi, M. Kouhizadeh, J. Sarkis, and L. Shen, "Blockchain technology and its relationships to sustainable supply chain management," Int. J. Prod. Res., vol. 57, no. 7, pp. 2117–2135, Apr. 2019, doi: 10.1080/00207543.2018.1533261.

122. C. R. B. Teixeira, A. L. Assumpção, A. L. Correa, A. F. Savi, and G. A. Prates, "The contribution of green logistics and sustainable purchasing for green supply chain management," Indep. J. Manag. Prod., vol. 9, no. 3, p. 1002, Sep. 2018, doi: 10.14807/ijmp.v9i3.789.

123. S. Vakili, A. I. Ölçer, A. Schönborn, F. Ballini, and A. T. Hoang, "Energy-related clean and green framework for shipbuilding community towards zero-emissions: a strategic analysis from concept to case study," Int. J. Energy Res., vol. 46, no. 14, pp. 20624–20649, Nov. 2022, doi: 10.1002/er.7649.

124. V. N. Nguyen et al., "Understanding fuel saving and clean fuel strategies towards green maritime," Polish Marit. Res., vol. 30, no. 2, pp. 146–164, 2023, doi: 10.2478/pomr-2023-0030.

125. V. G. Nguyen et al., "Using Artificial Neural Networks for Predicting Ship Fuel Consumption," Polish Marit. Res., vol. 30, no. 2, pp. 39–60, Jun. 2023, doi: 10.2478/pomr-2023-0020.

126. I. Shancita, H. H. Masjuki, M. A. Kalam, I. M. Rizwanul Fattah, M. M. Rashed, and H. K. Rashedul, "A review on idling reduction strategies to improve fuel economy and reduce exhaust emissions of transport vehicles," Energy Convers. Manag., vol. 88, pp. 794–807, Dec. 2014, doi: 10.1016/j.enconman.2014.09.036.

127. S. Serbin, K. Burunsuz, D. Chen, and J. Kowalski, "Investigation of the Characteristics of a Low-Emission Gas Turbine Combustion Chamber Operating on a Mixture of Natural Gas and Hydrogen," Polish Marit. Res., vol. 29, no. 2, pp. 64–76, Jun. 2022, doi: 10.2478/pomr-2022-0018.

128. R. Zhao et al., "A Numerical and Experimental Study of Marine Hydrogen–Natural Gas–Diesel Tri–Fuel Engines," Polish Marit. Res., vol. 27, no. 4, pp. 80–90, Dec. 2020, doi: 10.2478/pomr-2020-0068.

129. V. G. Bui et al., "Flexible syngas-biogas-hydrogen fueling spark-ignition engine behaviors with optimized fuel compositions and control parameters," Int. J. Hydrogen Energy, Oct. 2022, doi: 10.1016/j.ijhydene.2022.09.133.

130. P. Murugesan et al., "Role of hydrogen in improving performance and emission characteristics of homogeneous charge compression ignition engine fueled with graphite oxide nanoparticle-added microalgae biodiesel/diesel blends," Int. J. Hydrogen Energy, vol. 47, no. 88, pp. 37617–37634, 2022, doi: 10.1016/j.ijhydene.2021.08.107.

131. V. G. Bui, T. M. T. Bui, A. T. Hoang, S. Nižetić, T. X. Nguyen Thi, and A. V. Vo, "Hydrogen-Enriched Biogas Premixed Charge Combustion and Emissions in Direct Injection and Indirect Injection Diesel Dual Fueled Engines: a Comparative Study," J. Energy Resour. Technol., vol. 143, no. 12, Dec. 2021, doi: 10.1115/1.4051574.

132. V. G. Bui et al., "Optimizing operation parameters of a spark-ignition engine fueled with biogas-hydrogen blend integrated into biomass-solar hybrid renewable energy system," Energy, vol. 252, p. 124052, Aug. 2022, doi: 10.1016/j.energy.2022.124052.

133. Y. Pramudito et al., "Comparative analysis of filterability behavior of B30 and B40 biodiesel blends on various porosity and dimension of fuel filter," Int. J. Renew. Energy Dev., vol. 12, no. 4, pp. 760–767, Jul. 2023, doi: 10.14710/ijred.2023.52801.

134. A. T. Hoang et al., "Rice bran oil-based biodiesel as a promising renewable fuel alternative to petrodiesel: a review," Renew. Sustain. Energy Rev., vol. 135, p. 110204, Jan. 2021, doi: 10.1016/j.rser.2020.110204.

135. V. G. Nguyen, M. T. Pham, N. V. L. Le, H. C. Le, T. H. Truong, and D. N. Cao, "A comprehensive review on the use of biodiesel for diesel engines," Int. J. Renew. Energy Dev., vol. 12, no. 4, pp. 720–740, Jul. 2023, doi: 10.14710/ijred.2023.54612.

136. P. Balcombe, D. A. Heggo, and M. Harrison, "Total Methane and CO 2 Emissions from Liquefied Natural Gas Carrier Ships: The First Primary Measurements," Environ. Sci. Technol., vol. 56, no. 13, pp. 9632–9640, Jul. 2022, doi: 10.1021/acs.est.2c01383.

137. A. T. Le, T. D. Quoc, T. T. Tam, H. A. Tuan, and P. Van Viet, "Performance and combustion characteristics of a retrofitted CNG engine under various piston-top shapes and compression ratios," Energy Sources, Part a Recover. Util. Environ. Eff., 2020, doi: 10.1080/15567036.2020.1804016.

138. Y. Li, B. Li, F. Deng, Q. Yang, and B. Zhang, "Research on the Application of Cold Energy of Largescale Lng-Powered Container Ships to Refrigerated Containers," Polish Marit. Res., vol. 28, no. 4, pp. 107–121, Jan. 2022, doi: 10.2478/pomr-2021-0053.

139. G. Labeckas, S. Slavinskas, J. Rudnicki, and R. Zadrąg, "The Effect of Oxygenated Diesel-N-Butanol Fuel Blends on Combustion, Performance, and Exhaust Emissions of a Turbocharged CRDI Diesel Engine," Polish Marit. Res., vol. 25, no. 1, pp. 108–120, Mar. 2018, doi: 10.2478/pomr-2018-0013.

140. M. Svanberg, J. Ellis, J. Lundgren, and I. Landälv, "Renewable methanol as a fuel for the shipping industry," Renew. Sustain. Energy Rev., 2018, doi: 10.1016/j.rser.2018.06.058.

141. S. Wang and L. Yao, "Effect of engine speeds and dimethyl ether on methyl decanoate HCCI combustion and emission characteristics based on low-speed two-stroke diesel engine," Polish Marit. Res., 2020.

142. Q. B. Doan, X. P. Nguyen, T. M. H. Dong, M. T. Pham, and T. S. Le, "Performance and emission characteristics of diesel engine using ether additives: a review," Int. J. Renew. Energy Dev., vol. 11, no. 1, pp. 255–274, 2022.

143. X. Yuan et al., "Applications of bio-oil-based emulsions in a DI diesel engine: The effects of bio-oil compositions on engine performance and emissions," Energy, vol. 154, pp. 110–118, Jul. 2018, doi: 10.1016/j.energy.2018.04.118.

144. S. Rajamohan et al., "Optimization of operating parameters for diesel engine fuelled with bio-oil derived from cottonseed pyrolysis," Sustain. Energy Technol. Assessments, vol. 52, p. 102202, Aug. 2022, doi: 10.1016/j.seta.2022.102202.

145. Y. Bicer and I. Dincer, "Environmental impact categories of hydrogen and ammonia driven transoceanic maritime vehicles: a comparative evaluation," Int. J. Hydrogen Energy, vol. 43, no. 9, pp. 4583–4596, Mar. 2018, doi: 10.1016/j.ijhydene.2017.07.110.

146. F. Abbasov, T. Earl, C. C. Ambel, B. Hemmings, and L. Gilliam, "Roadmap to Decarbonising European Shipping." Transport & Environment, Brussels, Belgium, pp. 1–22, 2018.

147. T. Tarasiuk, W. Cao, P. Geng, and X. Xu, "Energy management strategy considering energy storage system degradation for hydrogen fuel cell ship," Polish Marit. Res., vol. 30, no. 2, pp. 95–104, 2023, doi: 10.2478/pomr-2023-0025.

148. M. Subramanian et al., "A technical review on composite phase change material based secondary assisted battery thermal management system for electric vehicles," J. Clean. Prod., vol. 322, p. 129079, Nov. 2021, doi: 10.1016/j.jclepro.2021.129079.

149. M. Muthukumar, N. Rengarajan, B. Velliyangiri, M. A. Omprakas, C. B. Rohit, and U. Kartheek Raja, "The development of fuel cell electric vehicles – a review," Mater. Today Proc., vol. 45, pp. 1181–1187, 2021, doi: 10.1016/j.matpr.2020.03.679.

150. O. Bethoux, "Hydrogen Fuel Cell Road Vehicles: State of the Art and Perspectives," Energies, vol. 13, no. 21, p. 5843, Nov. 2020, doi: 10.3390/en13215843.

151. R. D. Geertsma, R. R. Negenborn, K. Visser, and J. J. Hopman, "Design and control of hybrid power and propulsion systems for smart ships: a review of developments," Appl. Energy, vol. 194, pp. 30–54, May 2017, doi: 10.1016/j.apenergy.2017.02.060.

152. H. Xing, C. Stuart, S. Spence, and H. Chen, "Alternative fuel options for low carbon maritime transportation: Pathways to 2050," J. Clean. Prod., vol. 297, p. 126651, May 2021, doi: 10.1016/j.jclepro.2021.126651.

153. A. Mukherjee, P. Bruijnincx, and M. Junginger, "A Perspective on Biofuels Use and CCS for GHG Mitigation in the Marine Sector," iScience, vol. 23, no. 11, p. 101758, Nov. 2020, doi: 10.1016/j.isci.2020.101758.

154. L. Bilgili, "A systematic review on the acceptance of alternative marine fuels," Renew. Sustain. Energy Rev., vol. 182, p. 113367, Aug. 2023, doi: 10.1016/j.rser.2023.113367.

155. IMO, "An update to the investigation of appropriate control measures (abatement technologies) to reduce Black Carbon emissions from international shipping (as an annex of the report (No. PPR 5/INF.7) submitted by Canada to PPR)," 2017.

156. A. Sharafian, P. Blomerus, and W. Mérida, "Natural gas as a ship fuel: Assessment of greenhouse gas and air pollutant reduction potential," Energy Policy, vol. 131, pp. 332–346, Aug. 2019, doi: 10.1016/j.enpol.2019.05.015.

157. Q. Zhang, Z. Wan, B. Hemmings, and F. Abbasov, "Reducing black carbon emissions from Arctic shipping: Solutions and policy implications," J. Clean. Prod., vol. 241, p. 118261, Dec. 2019, doi: 10.1016/j.jclepro.2019.118261.

158. A. T. Hoang, V. D. Tran, V. H. Dong, and A. T. Le, "An experimental analysis on physical properties and spray characteristics of an ultrasound-assisted emulsion of ultra-low-sulphur diesel and Jatropha-based biodiesel," J. Mar. Eng. Technol., vol. 21, no. 2, pp. 73–81, Mar. 2022, doi: 10.1080/20464177.2019.1595355.

159. A. Petzold et al., "Operation of marine diesel engines on biogenic fuels: Modification of emissions and resulting climate effects," Environ. Sci. Technol., 2011, doi: 10.1021/es2021439.

160. J. Xue, T. E. Grift, and A. C. Hansen, "Effect of biodiesel on engine performances and emissions," Renew. Sustain. Energy Rev., vol. 15, no. 2, pp. 1098–1116, Feb. 2011, doi: 10.1016/j.rser.2010.11.016.

161. V. Jayaram, H. Agrawal, W. A. Welch, J. W. Miller, and D. R. Cocker, "Real-Time Gaseous, PM and Ultrafine Particle Emissions from a Modern Marine Engine Operating on Biodiesel," Environ. Sci. Technol., vol. 45, no. 6, pp. 2286–2292, Mar. 2011, doi: 10.1021/es1026954.

162. US-EPA, "A Comprehensive Analysis of Biodiesel Impacts on Exhaust Emissions - Draft Technical Report (EPA420-P-02-001)," 2002.

163. CAIP, "Compressed Natural Gas versus Diesel, Results of Vehicle Testing at Misr Lab," 2004.

164. P. Coroller, G. Plassat, and T. Seguelong, "Comparative Study on Exhaust Emissions from Diesel- and CNG-Powered Urban Buses." pp. 1–24, 2003.

165. T. W. Hesterberg, C. A. Lapin, and W. B. Bunn, "A Comparison of Emissions from Vehicles Fueled with Diesel or Compressed Natural Gas," Environ. Sci. Technol., vol. 42, no. 17, pp. 6437–6445, Sep. 2008, doi: 10.1021/es071718i.

166. NORDEN, "SPIRETH – Alcohol (Spirits) and Ethers as marine fuel," 2012.

167. C. Duwig, P. Gabrielsson, and P. E. Højlund-Nielsen, "SPIRETH - Methanol fuelled Diesel engine using the OBATE technology," 2011.

168. X. P. Nguyen, N. D. Le, V. V. Pham, T. T. Huynh, V. H. Dong, and A. T. Hoang, "Mission, challenges, and prospects of renewable energy development in Vietnam," Energy Sources, Part a Recover. Util. Environ. Eff., pp. 1–13, Aug. 2021, doi: 10.1080/15567036.2021.1965264.

169. Z. Said et al., "Nanotechnology-integrated phase change material and nanofluids for solar applications as a potential approach for clean energy strategies: Progress, challenges, and opportunities," J. Clean. Prod., vol. 416, p. 137736, Sep. 2023, doi: 10.1016/j.jclepro.2023.137736.

170. V. N. Nguyen et al., "Combination of solar with organic Rankine cycle as a potential solution for clean energy production," Sustain. Energy Technol. Assessments, vol. 57, p. 103161, Jun. 2023, doi: 10.1016/j.seta.2023.103161.

171. S. Gawusu, X. Zhang, S. A. Jamatutu, A. Ahmed, A. A. Amadu, and E. Djam Miensah, "The dynamics of green supply chain management within the framework of renewable energy," Int. J. Energy Res., vol. 46, no. 2, pp. 684–711, Feb. 2022, doi: 10.1002/er.7278.

172. H.-M. Wee, W.-H. Yang, C.-W. Chou, and M. V. Padilan, "Renewable energy supply chains, performance, application barriers, and strategies for further development," Renew. Sustain. Energy Rev., vol. 16, no. 8, pp. 5451–5465, Oct. 2012, doi: 10.1016/j.rser.2012.06.006.

173. Y. Shi and W. Luo, "Application of Solar Photovoltaic Power Generation System in Maritime Vessels and Development of Maritime Tourism," Polish Marit. Res., vol. 25, no. s2, pp. 176–181, Aug. 2018, doi: 10.2478/pomr-2018-0090.

174. A. T. Hoang et al., "Energy-related approach for reduction of CO_2 emissions: a critical strategy on the port-to-ship pathway," J. Clean. Prod., vol. 355, p. 131772, Jun. 2022, doi: 10.1016/j.jclepro.2022.131772.

175. L. Walther, C. Jahn, and T. Lade, "Weather routing for a wind driven hybrid merchant vessel," in OCEANS 2015 - Genova, May 2015, pp. 1–7, doi: 10.1109/OCEANS-Genova.2015.7271557.

176. Z. Y. Tay and D. Konovessis, "Sustainable energy propulsion system for sea transport to achieve United Nations sustainable development goals: a review," Discov. Sustain., vol. 4, no. 1, p. 20, Apr. 2023, doi: 10.1007/s43621-023-00132-y.

177. H. Zhang, Y. Hu, and J. He, "Wind Tunnel Experiment of Multi-Mode ARC Sail Device," Polish Marit. Res., vol. 28, no. 4, pp. 20–29, Jan. 2022, doi: 10.2478/pomr-2021-0046.

178. T. Smith, P. Newton, G. Winn, and A. Grech La Rosa, "Analysis techniques for evaluating the fuel savings associated with wind assistance," Low carbon Shipp. Conf., 2013.

179. T. Smith et al., "CO_2 emissions from international shipping: Possible reduction targets and their associated pathways," UMAS London, UK, 2016.

180. T.-T. Orthodontic and D. Supplies, "Product Brochure," Rochester, Minnesota, vol. 55902, p. 16.

181. A. A. Salem and I. S. Seddiek, "Techno-Economic Approach to Solar Energy Systems Onboard Marine Vehicles," Polish Marit. Res., vol. 23, no. 3, pp. 64–71, Sep. 2016, doi: 10.1515/pomr-2016-0033.

182. Ç. Karatuğ and Y. Durmuşoğlu, "Design of a solar photovoltaic system for a Ro-Ro ship and estimation of performance analysis: a case study," Sol. Energy, 2020, doi: 10.1016/j.solener.2020.07.037.

183. I. Sadek and M. Elgohary, "Assessment of renewable energy supply for green ports with a case study," Environ. Sci. Pollut. Res., vol. 27, no. 5, pp. 5547–5558, Feb. 2020, doi: 10.1007/s11356-019-07150-2.

184. I. S. Seddiek, "Application of renewable energy technologies for eco-friendly sea ports," Ships Offshore Struct., vol. 15, no. 9, pp. 953–962, Oct. 2020, doi: 10.1080/17445302.2019.1696535.

185. T. Roy, J. A. Garza-Reyes, V. Kumar, A. Kumar, and R. Agrawal, "Redesigning traditional linear supply chains into circular supply chains–A study into its challenges," Sustain. Prod. Consum., vol. 31, pp. 113–126, May 2022, doi: 10.1016/j.spc.2022.02.004.

186. D. F. Blumberg, Introduction to management of reverse logistics and closed loop supply chain processes. CRC press, 2004.

187. K. Govindan and H. Soleimani, "A review of reverse logistics and closed-loop supply chains: a Journal of Cleaner Production focus," J. Clean. Prod., vol. 142, pp. 371–384, Jan. 2017, doi: 10.1016/j.jclepro.2016.03.126.

188. K. Khor and Z. Udin, "Impact of Reverse Logistics Product Disposition towards Business Performance in Malaysian E&E Companies," J. Supply Chain Cust. Relatsh. Manag., pp. 1–19, Feb. 2012, doi: 10.5171/2012.699469.

189. H. Soleimani, K. Govindan, H. Saghafi, and H. Jafari, "Fuzzy multi-objective sustainable and green closed-loop supply chain network design," Comput. Ind. Eng., vol. 109, pp. 191–203, Jul. 2017, doi: 10.1016/j.cie.2017.04.038.

190. Z. Mohtashami, A. Aghsami, and F. Jolai, "A green closed loop supply chain design using queuing system for reducing environmental impact and energy consumption," J. Clean. Prod., vol. 242, p. 118452, Jan. 2020, doi: 10.1016/j.jclepro.2019.118452.

191. L. Zhen, L. Huang, and W. Wang, "Green and sustainable closed-loop supply chain network design under uncertainty," J. Clean. Prod., vol. 227, pp. 1195–1209, Aug. 2019, doi: 10.1016/j.jclepro.2019.04.098.

192. M. Yavari and H. Zaker, "Designing a resilient-green closed loop supply chain network for perishable products by considering disruption in both supply chain and power networks," Comput. Chem. Eng., vol. 134, p. 106680, Mar. 2020, doi: 10.1016/j.compchemeng.2019.106680.

193. Y.-S. Peng and S.-S. Lin, "Local Responsiveness Pressure, Subsidiary Resources, Green Management Adoption and Subsidiary's Performance: Evidence from Taiwanese Manufactures," J. Bus. Ethics, vol. 79, no. 1–2, pp. 199–212, Apr. 2008, doi: 10.1007/s10551-007-9382-8.

194. R. Inglehart, Modernization and postmodernization: Cultural, economic, and political change in 43 societies. Princeton university press, 2020.

195. S. A. Rehman Khan, Y. Zhang, M. Anees, H. Golpîra, A. Lahmar, and D. Qianli, "Green supply chain management, economic growth and environment: a GMM based evidence," J. Clean. Prod., vol. 185, pp. 588–599, Jun. 2018, doi: 10.1016/j.jclepro.2018.02.226.

196. A. Edirisuriya, S. Weerabahu, and R. Wickramarachchi, "Applicability of Lean and Green Concepts in Logistics 4.0: a Systematic Review of Literature," in 2018 International Conference on Production and Operations Management Society (POMS), Dec. 2018, pp. 1–8, doi: 10.1109/POMS.2018.8629443.

197. L.-E. Gadde and K. Hulthén, "Logistics outsourcing and the role of logistics service providers from an industrial network perspective," Ind. Mark. Manag., vol. 38, pp. 633–640, 2009.

198. M. Maslarić, S. Nikoličić, and D. Mirčetić, "Logistics Response to the Industry 4.0: the Physical Internet," Open Eng., vol. 6, no. 1, Nov. 2016, doi: 10.1515/eng-2016-0073.

199. S. Y. Teng, X. J. Li, Z. Zhao, P. L. Qin, and Y. Y. Lu, "Countermeasure Analysis on Internet Logistics," E3S Web Conf., vol. 38, p. 01036, Jun. 2018, doi: 10.1051/e3sconf/20183801036.

200. J. M. Müller, D. Kiel, and K.-I. Voigt, "What Drives the Implementation of Industry 4.0? The Role of Opportunities and Challenges in the Context of Sustainability," Sustainability, vol. 10, no. 1, p. 247, Jan. 2018, doi: 10.3390/su10010247.

201. K. Zhou, Taigang Liu, and Lifeng Zhou, "Industry 4.0: Towards future industrial opportunities and challenges," in 2015 12th International Conference on Fuzzy Systems and Knowledge Discovery (FSKD), Aug. 2015, pp. 2147–2152, doi: 10.1109/FSKD.2015.7382284.

202. J. Posada et al., "Visual Computing as a Key Enabling Technology for Industrie 4.0 and Industrial Internet," IEEE Comput. Graph. Appl., vol. 35, no. 2, pp. 26–40, Mar. 2015, doi: 10.1109/MCG.2015.45.

203. M. Rüßmann et al., "Industry 4.0: The future of productivity and growth in manufacturing industries," Bost. Consult. Gr., vol. 9, no. 1, pp. 54–89, 2015.

204. M. K. Wyrwicka and B. Mrugalska, "'INDUSTRY 4.0'—TOWARDS OPPORTUNITIES AND CHALLENGES OF IMPLEMENTATION," DEStech Trans. Eng. Technol. Res., no. icpr, Mar. 2018, doi: 10.12783/dtetr/icpr2017/17640.

205. Z. He, P. Chen, H. Liu, and Z. Guo, "Performance measurement system and strategies for developing low-carbon logistics: a case study in China," J. Clean. Prod., vol. 156, pp. 395–405, Jul. 2017, doi: 10.1016/j.jclepro.2017.04.071.

206. K. Rashidi and K. Cullinane, "Evaluating the sustainability of national logistics performance using Data Envelopment Analysis," Transp. Policy, vol. 74, pp. 35–46, Feb. 2019, doi: 10.1016/j.tranpol.2018.11.014.

207. K. Hung Lau, "Benchmarking green logistics performance with a composite index," Benchmarking An Int. J., vol. 18, no. 6, pp. 873–896, Oct. 2011, doi: 10.1108/14635771111180743.

208. K. Lai and C. W. Y. Wong, "Green logistics management and performance: Some empirical evidence from Chinese manufacturing exporters," Omega, vol. 40, no. 3, pp. 267–282, Jun. 2012, doi: 10.1016/j.omega.2011.07.002.

209. H. Wu and S. C. Dunn, "Environmentally responsible logistics systems," Int. J. Phys. Distrib. Logist. Manag., vol. 25, no. 2, pp. 20–38, Mar. 1995, doi: 10.1108/09600039510083925.

210. M. S. Pishvaee, S. A. Torabi, and J. Razmi, "Credibility-based fuzzy mathematical programming model for green logistics design under uncertainty," Comput. Ind. Eng., vol. 62, no. 2, pp. 624–632, Mar. 2012, doi: 10.1016/j.cie.2011.11.028.

211. O. Abduaziz, J. K. Cheng, R. M. Tahar, and R. Varma, "A Hybrid Simulation Model for Green Logistics Assessment in Automotive Industry," Procedia Eng., vol. 100, pp. 960–969, 2015, doi: 10.1016/j.proeng.2015.01.455.

212. W. Zhang, M. Zhang, W. Zhang, Q. Zhou, and X. Zhang, "What influences the effectiveness of green logistics policies? a grounded theory analysis," Sci. Total Environ., vol. 714, p. 136731, Apr. 2020, doi: 10.1016/j.scitotenv.2020.136731.

213. W. Zhang, M. Zhang, W. Zhang, Q. Zhou, and X. Zhang, "What influences the effectiveness of green logistics policies? a grounded theory analysis," Sci. Total Environ., vol. 714, p. 136731, Apr. 2020, doi: 10.1016/j.scitotenv.2020.136731.

214. S. A. R. Khan, Y. Zhang, A. Kumar, E. Zavadskas, and D. Streimikiene, "Measuring the impact of renewable energy, public health expenditure, logistics, and environmental performance on sustainable economic growth," Sustain. Dev., vol. 28, no. 4, pp. 833–843, Jul. 2020, doi: 10.1002/sd.2034.

215. C. Liu and T. Ma, "Green logistics management and supply chain system construction based on internet of things technology," Sustain. Comput. Informatics Syst., vol. 35, p. 100773, Sep. 2022, doi: 10.1016/j.suscom.2022.100773.

216. M. Zhang, M. Sun, D. Bi, and T. Liu, "Green Logistics Development Decision-Making: Factor Identification and Hierarchical Framework Construction," IEEE Access, vol. 8, pp. 127897–127912, 2020, doi: 10.1109/ACCESS.2020.3008443.

217. P. Lee, O. Kwon, and X. Ruan, "Sustainability Challenges in Maritime Transport and Logistics Industry and Its Way Ahead," Sustainability, vol. 11, no. 5, p. 1331, Mar. 2019, doi: 10.3390/su11051331.

218. A. Abdi, A. Abdi, A. M. Fatollahi-Fard, and M. Hajiaghaei-Keshteli, "A set of calibrated metaheuristics to address a closed-loop supply chain network design problem under uncertainty," Int. J. Syst. Sci. Oper. Logist., vol. 8, no. 1, pp. 23–40, Jan. 2021, doi: 10.1080/23302674.2019.1610197.

219. V. Yadav, P. Gaur, and R. Jain, "On adoption of green logistics: a literature review," Int. J. Logist. Syst. Manag., vol. 40, no. 2, p. 193, 2021, doi: 10.1504/IJLSM.2021.118736.

220. L. B. Prataviera, A. Creazza, and S. Perotti, "A call to action: a stakeholder analysis of green logistics practices," Int. J. Logist. Manag., Jul. 2023, doi: 10.1108/IJLM-09-2022-0381.

221. C. C. Fen, N. K. Kamaruddin, and N. M. Nor, "Drivers and Barriers Implementing Green Logistics Among Logistics Companies in Selangor, Malaysia," Res. Manag. Technol. Bus., vol. 1, no. 1, pp. 41–54, 2020.

222. Y. Xu, H. Jia, Y. Zhang, and G. Tian, "Analysis on the location of green logistics park based on heuristic algorithm," Adv. Mech. Eng., vol. 10, no. 5, p. 168781401877463, May 2018, doi: 10.1177/1687814018774635.

223. V. D. Bui and H. P. Nguyen, "A Systematized Review on Rationale and Experience to Develop Advanced Logistics Center System in Vietnam," Webology, vol. 18, pp. 89–101, 2021.